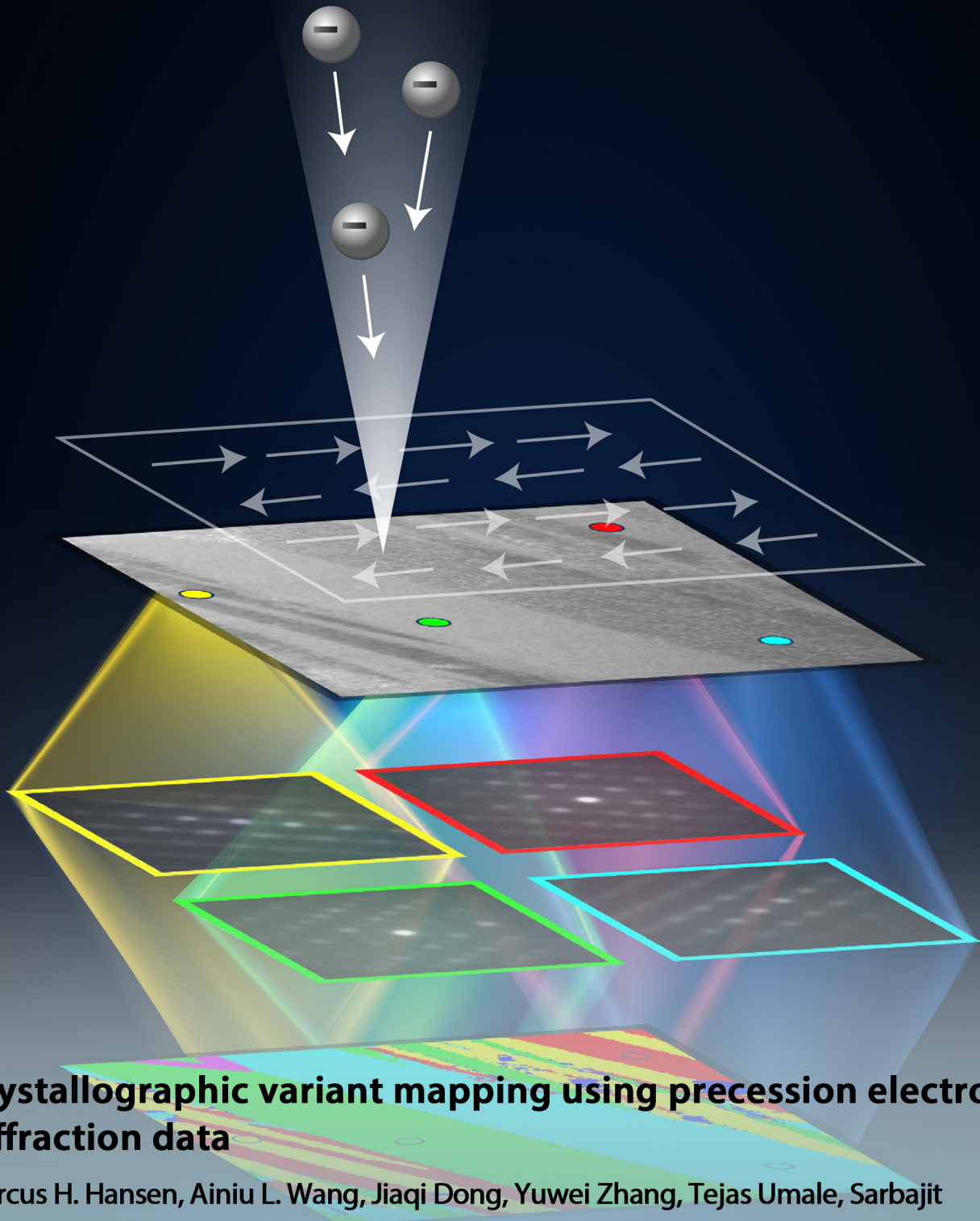


MICROSTRUCTURES

Editor-in-Chief: Prof. Shujun Zhang



Crystallographic variant mapping using precession electron diffraction data

Marcus H. Hansen, Ainiu L. Wang, Jiaqi Dong, Yuwei Zhang, Tejas Umale, Sarbajit Banerjee, Patrick Shamberger, Matt Pharr, Ibrahim Karaman, Kelvin Y. Xie



ISSN 2770-2995 (Online)



www.microstructj.com

EDITORIAL BOARD

Editor-in-Chief

Shujun Zhang (Australia)

Executive Editors

Jun Chen (China)

Xiaozhou Liao (Australia)

Junior Executive Editors

Zibin Chen (China)

Shiqing Deng (China)

Associate Editors

Yida Deng (China)

Ning Gao (China)

Lin Gu (China)

Jiamian Hu (USA)

Xiaoning Jiang (USA)

Liangzhi Kou (Australia)

Fei Li (China)

Charlene Lobo (Australia)

Yang Ren (USA)

Andrea Sanson (Italy)

Lianzhou Wang (Australia)

Yandong Wang (China)

Chengtie Wu (China)

Qian Yu (China)

Ting Zhu (USA)

Xiaoying Zhuang (Germany)

Senior Editorial Board Members

Nazanin Bassiri-Gharb (USA)

Daolun Chen (Canada)

Zhi-Gang Chen (Australia)

Neus Domingo (USA)

Yi Du (Australia)

Alexei Gruverman (USA)

Zaipeng Guo (Australia)

Xiaodong Han (China)

Sergei V. Kalinin (USA)

Huijun Li (Australia)

Jiangyu Li (China)

Yun Liu (Australia)

Yunhau Ng (China)

Timon Rabczuk (Germany)

Dong Su (China)

Litao Sun (China)

Jian Wang (USA)

Yin Xiao (Australia)

Shanqing Zhang (Australia)

Chun-Xia Zhao (Australia)

Yuntian Zhu (USA)

Rongkun Zheng (Australia)

Editorial Board Members

Matthew Cabral (USA)

Shaobo Cheng (China)

Charlotte Cochard (UK)

Zhanxi Fan (China)

Xuwen Fu (China)

Sophia Gu (Australia)

Yuxiao Lai (China)

Si Lan (China)

Ting Li (China)

Junhao Lin (China)

Danmin Liu (China)

Shen Liu (China)

Hongshi Ma (China)

Kasra Momeni (USA)

Mojca Otoničar (Slovenia)

Zhihua Sun (China)

Chunming Wang (China)

Dawei Wang (China)

Haitao Li (China)

Xiupeng Wang (Japan)

Zhenglong Xu (China)

Tao Yang (China)

Yulin Zhong (Australia)

Chunqiang Zhuang (China)

Sarina Sarina (Australia)

Xusheng Yang (China)

Yang Cao (China)

GENERAL INFORMATION

About the Journal

Microstructures, ISSN 2770-2995 (Online), is a peer-reviewed and continuously published online journal with print on demand compilation of articles published. The journal's full text is available online at www.jcmtjournal.com. The journal allows free access (Open Access) to its contents and permits authors to self-archive final accepted version of *Microstructure*, which is the nature, quantity and distribution of structural elements or phases that make up materials, determines the properties of materials. Understanding microstructure-properties relationships is critical for the design of materials. With the increase of demand and investment in new materials around the globe, there has been a great deal of interest in the exploration and manipulation of microstructure in materials science and engineering.

Information for Authors

Manuscripts should be prepared in accordance with Author Instructions.

Please check www.microstructj.com/pages/view/author_instructions for details.

All manuscripts should be submitted online at <https://oaemesas.com/login?JournalId=microstructures>.

Copyright

The entire contents of the *Microstructures* are protected under international copyrights. The journal, however, grants to all users a free, irrevocable, worldwide, perpetual right of access to, and a license to copy, use, distribute, perform and display the work publicly and to make and distribute derivative works in any digital medium for any reasonable purpose, subject to proper attribution of authorship and ownership of the rights. The journal also grants the right to make small numbers of printed copies for their personal use under the Creative Commons Attribution 4.0 License.

Copyright is reserved by © The Author(s) 2023.

Permissions

For information on how to request permissions to reproduce articles/information from this journal, please visit www.microstructj.com.

Disclaimer

The information and opinions presented in the journal reflect the views of the authors and not of the journal or its Editorial Board or the Publisher. Publication does not constitute endorsement by the journal. Neither the *Microstructures* nor its publishers nor anyone else involved in creating, producing or delivering the *Microstructures* or the materials contained therein, assumes any liability or responsibility for the accuracy, completeness, or usefulness of any information provided in the *Microstructures*, nor shall they be liable for any direct, indirect, incidental, special, consequential or punitive damages arising out of the use of the *Microstructures*. The *Microstructures*, nor its publishers, nor any other party involved in the preparation of material contained in the *Microstructures* represents or warrants that the information contained herein is in every respect accurate or complete, and they are not responsible for any errors or omissions or for the results obtained from the use of such material. Readers are encouraged to confirm the information contained herein with other sources.

Publisher

OAE Publishing Inc.

245 E Main Street st112, Alhambra, CA 91801, USA

Website: www.oaepublish.com

Contacts

E-mail: editorialoffice@microstructj.com

Website: www.microstructj.com

Research Article

2023027 Grain engineering of high energy density BaTiO₃ thick films integrated on Si
Jun Ouyang, Xiaoman Teng, Meiling Yuan, Kun Wang, Yuyao Zhao, Hongbo Cheng, Hanfei Zhu, Chao Liu, Yongguang Xiao, Minghua Tang², Wei Zhang, Wei Pan

2023028 Structure, magnetism and low thermal expansion in Tb_{1-x}Er_xCo₂Mn_y intermetallic compounds
Yanming Sun, Yili Cao, Yang Ren, Saul H. Lapidus, Qiang Li, Jinxia Deng, Jun Miao, Kun Lin, Xianran Xing

2023029 Crystallographic variant mapping using precession electron diffraction data
Marcus H. Hansen, Ainiu L. Wang, Jiaqi Dong, Yuwei Zhang, Tejas Umalel, Sarbajit Banerjee, Patrick Shamberger, Matt Pharr, Ibrahim Karaman, Kelvin Y. Xie

Review

2023030 Physiological and pathological/ectopic mineralization: from composition to microstructure
Yuqing Mu, Wendong Gao, Yinghong Zhou, Lan Xiao, Yin Xiao

2023031 Constructing and regulating nanochannels in two-dimensional-material-based membranes for specified separation applications
Chao Xing, Mengchen Zhang, Lingfeng Liu, Zehua Zheng, Ming Zhou, Shanqing Zhang, Changyu Liu

Research Article

2023032 Synthesis strategies of metal-organic frameworks for CO₂ capture
Meng Sun, Xiaokang Wang, Fei Gao, Mingming Xu, Weidong Fan, Ben Xu, Daofeng Sun

2023033 Influence of kinks on the interaction energy between ferroelastic domain walls in membranes and thin films
Guangming Lu, Kimura Hideo, Xiangdong Ding, Zhijun Xu, Ruiqing Chu, Guillaume F. Nataf, Ekhard K. H. Salje

2023034 Optimizing the energy storage performance of NaNbO₃ ceramics by rare-earth-based composite perovskite Sm(Mg_{0.5}Zr_{0.5})O₃ modification
Mingzhao Xu, Dafu Zeng, Xiang Wang, Peng Nong, Yue Pan, Qinpeng Dong, Jiaming Wang, Huanfu Zhou, Xiuli Chen

2023035 Investigation of BiFeO₃-BaTiO₃ lead-free piezoelectric ceramics with nonstoichiometric bismuth
Hailan Qin, Jianwei Zhao, Xiaoxin Chen, Hongtian Li, Shenghao Wang, Yuxiao Du, Huanfu Zhou, Peifeng Li, Dawei Wang

2023036 Improving orientation mapping by enhancing the diffraction signal using Auto-CLAHE in precession electron diffraction data
Ainiu L. Wang, Marcus H. Hansen, Yi-Cheng Lai, Jiaqi Dong, Kelvin Y. Xie

Review

2023037 Machine learning assisted intelligent design of meta structures: a review

Liangshu He, Yan Li, Daniel Torrent, Xiaoying Zhuang, Timon Rabczuk, Yabin Jin

2023038 The concept, structure, and progress of seawater metal-air batteries

Yuanyuan Guo, Yanhui Cao, Junda Lu, Xuerong Zheng, Yida Deng

2023039 Metal-organic frameworks as promising flame retardants for polymeric materials

Boyou Hou, Ye-Tang Pan, Pingan Song

Perspective

2023040 Scanning transmission electron microscopy for advanced characterization of ferroic materials

Matthew J. Cabral, Zibin Chen, Xiaozhou Liao

Research Article

2023041 What lies beneath? Investigations of atomic force microscopy-based nano-machining to reveal sub-surface ferroelectric domain configurations in ultrathin films

Lynette Keeney, Louise Colfer, Debismita Dutta, Michael Schmidt, Guannan Wei

2023042 Influence of hydrogel and porous scaffold on the magnetic thermal property and anticancer effect of Fe₃O₄ nanoparticles

Man Wang, Rui Sun, Huajian Chen, Xiaohan Liu, Toru Yoshitomi, Masaki Takeguchi, Naoki Kawazoe, Yingnan Yang, Guoping Chen

Review

2023043 Cryogenic atom probe tomography and its applications: a review

Ziyang Zhou, Zhengquan Wang, Ranming Niu, Pang-Yu Liu, Chao Huang, Yi-Hsuan Sun, Xiutong Wang, Hung-Wei Yen, Julie M. Cairney, Yi-Sheng Chen

2023044 Magnetic structures and correlated physical properties in antiperovskites

Sihao Deng, Hongde Wang, Lunhua He, Cong Wang

Research Article

2023045 Temperature dependence of dielectric nonlinearity of BaTiO₃ ceramics

Ichiro Fujii, Susan Trolier-McKinstry

2023046 Varied domain structures in 0.7Pb(Mg_{1/3}Nb_{2/3})O₃-0.3PbTiO₃ single crystals


Dawei Zhang, Lei Wang, Linglong Li, Pankaj Sharma, Jan Seidel

Research Article

Open Access



Grain engineering of high energy density BaTiO₃ thick films integrated on Si

Jun Ouyang^{1,2,3} , Xiaoman Teng¹, Meiling Yuan^{3,4}, Kun Wang^{3,5}, Yuyao Zhao³, Hongbo Cheng^{1,3}, Hanfei Zhu^{1,3}, Chao Liu¹, Yongguang Xiao², Minghua Tang², Wei Zhang^{3,6}, Wei Pan⁷

¹Institute of Advanced Energy Materials and Chemistry, Jinan Engineering Laboratory for Multi-Scale Functional Materials, School of Chemistry and Chemical Engineering, Qilu University of Technology (Shandong Academy of Sciences), Jinan 250353, Shandong, China.

²Key Laboratory of Key Film Materials & Application for Equipment, School of Material Sciences and Engineering, Xiangtan University, Xiangtan 411105, Hunan, China.

³Key Laboratory for Liquid-Solid Structure Evolution and Processing of Materials (Ministry of Education), School of Materials Science and Engineering, Shandong University, Jinan 250061, Shandong, China.

⁴Academic Affairs Office Civil Aviation University of China, Tianjin 300300 China.

⁵China Tobacco Shandong Industrial Co., Ltd., Jinan 250014, Shandong, China.

⁶College of Electronic and Optical Engineering, Nanjing University of Posts and Telecommunications, Nanjing 210023, China.

⁷State Key Laboratory of New Ceramics and Fine Processing, Tsinghua University, Beijing 100084, China.

Correspondence to: Prof./Dr. Jun Ouyang, School of Chemistry and Chemical Engineering, Qilu University of Technology, #3501 Daxue Road, Jinan 250353, Shandong, China. E-mail: ouyangjun@qlu.edu.cn

How to cite this article: Ouyang J, Teng X, Yuan M, Wang K, Zhao Y, Cheng H, Zhu H, Liu C, Xiao Y, Tang M, Zhang W, Pan W. Grain engineering of high energy density BaTiO₃ thick films integrated on Si. *Microstructures* 2023;3:2023027. <https://dx.doi.org/10.20517/microstructures.2023.22>

Received: 5 May 2023 **First Decision:** 22 May 2023 **Revised:** 30 May 2023 **Accepted:** 2 Jun 2023 **Published:** 13 Jun 2023

Academic Editor: Shujun Zhang **Copy Editor:** Fangling Lan **Production Editor:** Fangling Lan

Abstract

Ferroelectric (FE) ceramics with a large relative dielectric permittivity and a high dielectric strength have the potential to store or supply electricity of very high energy and power densities, which is desirable in many modern electronic and electrical systems. For a given FE material, such as the commonly-used BaTiO₃, a close interplay between defect chemistry, misfit strain, and grain characteristics must be carefully manipulated for engineering its film capacitors. In this work, the effects of grain orientation and morphology on the energy storage properties of BaTiO₃ thick films were systematically investigated. These films were all deposited on Si at 500 °C in an oxygen-rich atmosphere, and their thicknesses varied between ~500 nm and ~2.6 μm. While a columnar nanograined BaTiO₃ film with a (001) texture showed a higher recyclable energy density W_{rec} (81.0 J/cm³ vs. 57.1 J/cm³ @3.2 MV/cm, ~40% increase) than that of a randomly-oriented BaTiO₃ film of about the same thickness (~500 nm), the latter showed an improved energy density at a reduced electric field with an increasing film thickness. Specifically, for the 1.3 μm and 2.6 μm thick polycrystalline films, their energy storage densities W_{rec}



© The Author(s) 2023. **Open Access** This article is licensed under a Creative Commons Attribution 4.0 International License (<https://creativecommons.org/licenses/by/4.0/>), which permits unrestricted use, sharing, adaptation, distribution and reproduction in any medium or format, for any purpose, even commercially, as long as you give appropriate credit to the original author(s) and the source, provide a link to the Creative Commons license, and indicate if changes were made.



reached 46.6 J/cm³ and 48.8 J/cm³ at an applied electric field of 2.31 MV/cm (300 V on 1.3 μm film) and 1.77 MV/cm (460 V on 2.6 μm film), respectively. This ramp-up in energy density can be attributed to increased polarizability with a growing grain size in thicker polycrystalline films and is desirable in high pulse power applications.

Keywords: Energy storage, ferroelectric, grain engineering, BaTiO₃, film capacitors, Si

INTRODUCTION

With the development of various energy-harvesting technologies and associated applications, devices that can provide both high-density storage and rapid electricity supply have become increasingly important. Dielectric capacitors using ferroelectric (FE) ceramics with a high relative dielectric permittivity have demonstrated such a potential^[1-5]. However, there are compromises that hinder the further development of FE ceramic capacitors for energy storage applications. These compromises include complex compositions, high composition sensitivity, and high processing temperatures, which are especially challenging for integrated film capacitors^[6-8]. Therefore, the development of simple composition FE film capacitors with a high energy density, such as BaTiO₃, has become an emergent challenge for the future of electric energy storage using dielectric capacitors.

Once a manufacturable composition was selected, the performance of FE film capacitors was mostly affected by the substrate, which imposes a clamping effect^[9] and a residual strain^[10], the deposition chemistry^[11], and the crystalline or grain characteristics^[12,13]. These factors are usually intertwined, and hence it is difficult to separate out their contributions to the energy storage performance of the film. In this work, we chose the prototype FE of BaTiO₃ for its simple composition and broad application in electro ceramics, especially ceramic capacitors. Established deposition chemistry, i.e., sputtering deposition in an oxygen-rich atmosphere, was used for the preparation of BaTiO₃ film capacitors on a Si substrate^[13]. Therefore, in this work, we were able to focus on the grain effects on the energy storage performance of the FE film capacitors, including the effects of grain orientation and grain morphology.

Our previous investigations on preparing high energy density BaTiO₃-based film capacitors^[13-15] have focused on a columnar nanograin design via a low-temperature process (350-400 °C) and a buffer-layer technique. This approach resulted in a densely-packed nanograin array, which shows a (001)-texture, an in-plane grain diameter down to 10-20 nm, and a grain length extending through the thickness of the film. Due to periodic gradients in the electric polarization and relative dielectric permittivity, the total dielectric displacement of such a film is confined and experiences a significantly delayed saturation under an external field. Consequently, such a grain structure is endowed with a high breakdown field and a large energy storage density. For example, a recyclable energy density of ~130 J/cm³ at ~650 MV/m^[13] and ~229 J/cm³ at 875 MV/m^[15] was achieved in columnar-grained BaTiO₃ films of ~350 nm and ~160 nm thick, respectively. However, these high energy densities were achieved under very large electric fields, corresponding to a much-reduced relative dielectric permittivity. This is not always the optimum solution for the storage and/or supply of electric energy, especially in cases where high pulsed power is demanded under middle-to-low electric fields.

In this work, we aimed to manipulate the grain characteristics, including grain orientation and morphology, to achieve a high energy density at a reduced electric field in BaTiO₃ film capacitors. To achieve this goal, a higher growth temperature at 500 °C was used, and a compromise was made between improved crystallinity, which enhances the dielectric response, and increased average grain size, which reduces the

maximum applicable electric field. By using a thick LaNiO_3 buffer layer (~ 110 nm) on platinized Si and a fast deposition rate, we successfully suppressed the growth of randomly-oriented, discontinuous columnar grains in the BaTiO_3 film directly deposited on the Pt electrode. Instead, we achieved a (001)-textured, continuous columnar nanograin structure. This structure is similar to those obtained at low deposition temperatures^[9,10] but with an increased average grain size (~ 50 - 60 nm vs. 10 - 20 nm), resulting in an enhanced dielectric response. In comparison to the unbuffered films, the LaNiO_3 -buffered BaTiO_3 films exhibited a higher dielectric polarization under the same applied electric field (320 MV/m), leading to a $\sim 40\%$ boost in the recyclable energy density of a film capacitor (81.0 J/cm³ vs. 57.1 J/cm³ @ 3.2 MV/cm). Furthermore, to break down the aspect-ratio conservation of the continuous columnar nanograin microstructure and its associated thickness scalable energy storage performance^[13], we went back to the classic random polycrystalline BaTiO_3 film directly deposited on platinized Si. The rapid growth of its grain size with deposition time led to an increasing polarizability/relative dielectric permittivity with the film thickness. Consequently, an enhanced energy storage density close to 50 J/cm³ was achieved in device-level thick BaTiO_3 films (46.6 J/cm³ @ 300 V on a 1.3 μm thick film and 48.8 J/cm³ @ 460 V on a 2.6 μm thick film). These values are ~ 25 times higher than those of the BaTiO_3 ceramics and serve as an important benchmark for the future development of multilayer ceramic capacitors (MLCCs).

MATERIALS AND METHODS

For the preparation of the platinized Si substrate, a Pt/Ti bilayer bottom electrode was used. The Ti layer, with a thickness of ~ 10 nm, is the adhesion layer to bond with the Si substrate. The deposition process was carried out on a (100) Si substrate at 300 °C via dc magnetron sputtering in a pure Ar atmosphere. The resulting Pt layer showed a high degree of (111) texture. It is noteworthy that these platinized Si substrates are also commercially available for this purpose. The (100) Si substrates (10 mm \times 10 mm) and ceramic targets of BaTiO_3 and LaNiO_3 ($\Phi = 50$ mm, $t = 5$ mm, 99.9% purity) were purchased from the Anhui Institute of Optics, Chinese Academy of Science. The Pt and Ti sputtering targets ($\Phi = 50$ mm, $t = 3$ mm, 99.99% purity) were purchased from Zhongnuo Advanced Material Technology Co. Limited (Beijing, China). The key deposition parameters of the LaNiO_3 -buffered and unbuffered BaTiO_3 film heterostructures are summarized in Table 1. Dot-shaped Au top electrodes ($\Phi = 0.2$ mm) were sputtered through a masked plate at room temperature for electrical measurements.

The microstructure of the two types of BaTiO_3 thin film heterostructures was characterized by using X-ray diffraction (XRD) θ - 2θ scans in a commercial Rigaku Dmax-rc XRD diffractometer equipped with a Ni-filtered Cu K radiation source. The surface morphologies were analyzed via atomic force microscopy (AFM) on a MicroNano D-5A scanning probe microscope (Shanghai, China). The layer thicknesses and nanostructures of the BaTiO_3 thin film heterostructures were analyzed via transmission electron microscopy (TEM) using a JEM-2010 microscope (JEOL, Japan). The room temperature FE hysteresis loops (P-V) were measured at 100 Hz via a commercial Multiferroic™ FE tester (Radiant Technology, USA). The voltage-dependent capacitance (C-V) curves, from which the relative dielectric permittivity and loss tangent as functions of the applied voltage/field were obtained, were measured by using a B1505A impedance analyzer (Agilent Technologies, USA) at 5 kHz by applying a small ac signal of 50 mV. The voltage was swept from negative maximum to positive maximum and vice versa during the measurements.

RESULTS AND DISCUSSION

Figure 1 shows the XRD θ - 2θ scan patterns of the $\text{BaTiO}_3/\text{Pt}/\text{Ti}/\text{Si}$ [Figure 1A] and $\text{BaTiO}_3/\text{LaNiO}_3/\text{Pt}/\text{Ti}/\text{Si}$ [Figure 1B] thin film heterostructures, respectively. It can be clearly seen that while the unbuffered BaTiO_3 film showed a typical polycrystalline structure, the LaNiO_3 buffered BaTiO_3 film was (001)-textured, as reported in our previous publications^[13-15]. Furthermore, the degree of crystallinity was significantly

Table 1. Magnetron sputtering parameters of BaTiO₃ film heterostructures

Structure type	BaTiO ₃ /Pt/Ti	BaTiO ₃ /LaNiO ₃ /Pt/Ti
Base pressure	2×10^{-4} Pa	2×10^{-4} Pa
Pt/Ti layer sputtering pressure	0.3 Pa	0.3 Pa
Pt/Ti layer thickness	~150-200 nm	
Buffer layer sputtering temperature	N/A	500 °C
Buffer layer sputtering atmosphere	N/A	Ar:O ₂ (4:1)
Buffer layer sputtering pressure	N/A	0.3 Pa
Buffer layer thickness	N/A	~100 nm
BaTiO ₃ sputtering temperature	500 °C	500 °C
BaTiO ₃ sputtering atmosphere	Ar:O ₂ (4:1)	Ar:O ₂ (4:1)
BaTiO ₃ sputtering pressure	0.3 Pa	1.2 Pa
BaTiO ₃ deposition rate	~7 nm/min	~10 nm/min
BaTiO ₃ layer thickness (nm)	435 nm, 845 nm, 1,305 nm, 2,610 nm	510 nm
Cooling atmosphere (pressure)	Pure O ₂ (2.5 Pa)	Pure O ₂ (2.5 Pa)

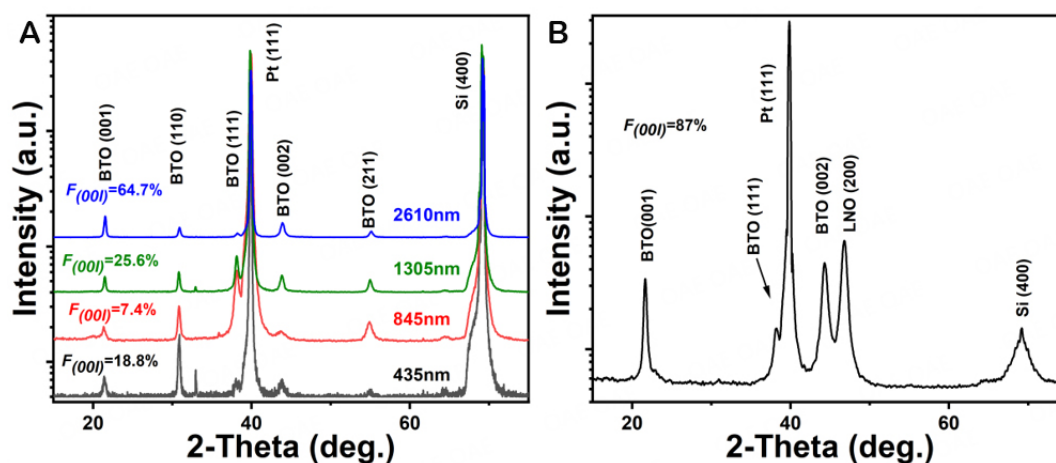


Figure 1. XRD θ - 2θ scan patterns of the thin film heterostructures of (A) BaTiO₃/Pt/Ti/Si (with various thicknesses of the BaTiO₃ layer) and (B) BaTiO₃/LaNiO₃/Pt/Ti/Si (with a 510 nm thick BaTiO₃ layer).

improved in the thicker polycrystalline BaTiO₃ film, as evidenced by their stronger and sharper diffraction peaks. The preferred crystalline orientation, which was (110) in the 435 nm thick film, changed into (111) in the 845 nm and 1,305 nm thick films and finally became (001) in the 2,610 nm thick film. The degree of grain (00l)-orientation of unbuffered BaTiO₃ film was evaluated using the Lotgering factor $F_{(00l)} = 64.7\%$ [Figure 1A]^[16] and compared with those of the standard powder XRD pattern of BaTiO₃ (JCPDS 05-0626). The growth of BaTiO₃ on (111) Pt involves a competition between various factors, including the channeling effect^[17], interface energy, and surface energy. The dominance of the channeling effect is evident in the thinnest film, leading to a preferred orientation of the closest-packed plane of (110) in perovskite. As the film thickness increases, the interface energy, primarily influenced by misfit strain energy, becomes more significant. This leads to the (111) orientation, which is the best match to the (111) Pt base plane, taking over as the preferred crystalline orientation. Lastly, in the thickest film where the residual misfit approached zero, (001) crystalline planes with the minimum surface energy emerged as the preferred orientation. On the other hand, in the LaNiO₃-buffered BaTiO₃ film, since the (100)-textured growth of LaNiO₃ on Pt^[18] has been preset, the (001) orientation of the BaTiO₃ film satisfies the requirement of minimum energy, which is now dominated by the interface/surface energy term. The Lotgering factor $F_{(00l)}$ for buffered BaTiO₃ film is

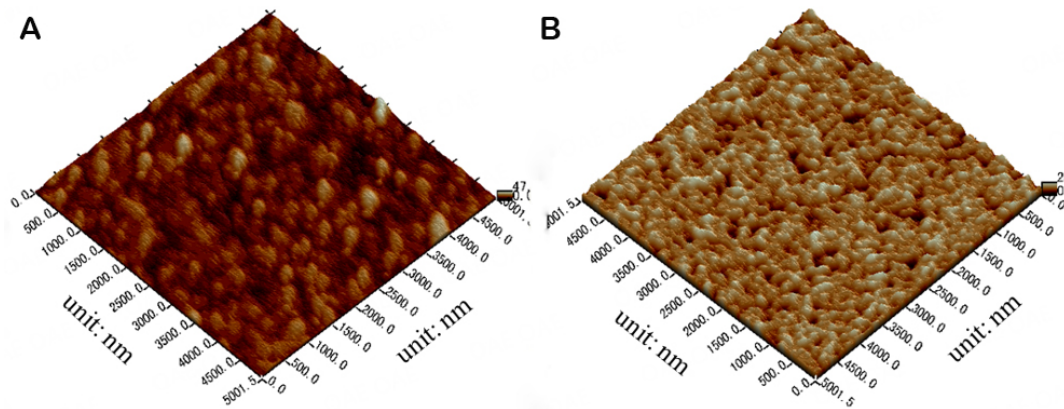


Figure 2. AFM surface scan images of (A) the 435 nm thick BaTiO₃ film grown on Pt/Ti/Si and (B) the 510 nm thick BaTiO₃ film grown on LaNiO₃/Pt/Ti/Si.

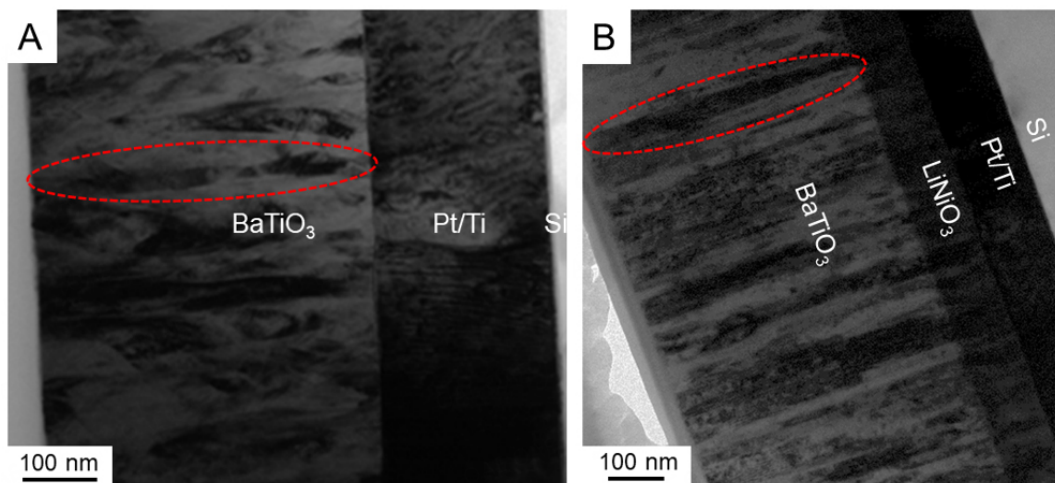


Figure 3. Cross-sectional TEM images of (A) the BaTiO₃ (435 nm) /Pt/Ti/Si and (B) the BaTiO₃ (510 nm)/LaNiO₃/Pt/Ti/Si heterostructures.

87% [Figure 1B].

According to the study by Zhang *et al.*, the relative dielectric permittivity of a polycrystalline BaTiO₃ film deposited on a Pt electrode^[19] is expected to be higher than that of the (001)-textured film. Moreover, the presence of larger grain sizes in the thicker films warrants an improved dielectric response, which can be attributed to extrinsic sources such as domain wall movements^[20] and grain re-orientations. Next, we will compare their nanostructure characteristics, including grain and interface morphologies, of the 510 nm thick buffered and the 435 nm thick unbuffered BaTiO₃ film samples to complement the XRD results.

Figure 2A and B displays the surface AFM image of the two films. Both films showed a dense and granular surface, with a root mean square roughness (Ra) of 2.868 (A) and 2.007 nm (B), respectively. Figure 3A and B presents the cross-sectional TEM image of the two BaTiO₃ films. The unbuffered film consists of discontinuous columnar nanograins, occasionally displaying twisted or canted orientations. In contrast, the bi-layer film of BaTiO₃/LaNiO₃ constitutes continuous arrays of columnar nanograins that extend from the LaNiO₃/Pt bottom electrode interface to the surface of the BaTiO₃ layer. These

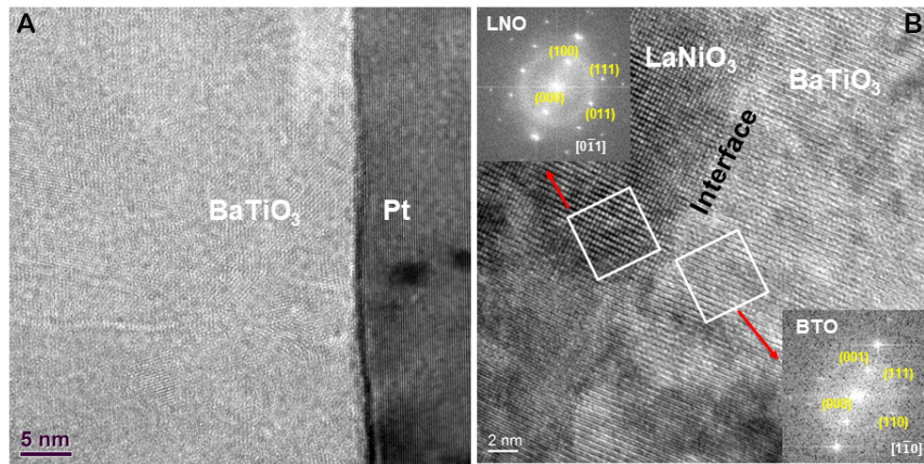


Figure 4. High-resolution TEM images near (A) BaTiO₃/Pt and (B) BaTiO₃/LaNiO₃ interfaces in the unbuffered and buffered BaTiO₃ film heterostructures, respectively. Insets are Fast-Fourier-Transformed (FFT) selected area electron diffraction (SAED) patterns of the local BaTiO₃ film and its underneath LaNiO₃ buffer layer.

nanostructures are characteristic of sputtered perovskite/Pt^[17] and perovskite/perovskite heterostructures^[13]. For the BaTiO₃/Pt case, the XRD analysis revealed the competition between multiple crystalline orientations, leading to a “broken” nanograin morphology with twisted/canted grain variants. In contrast, the presence of the lattice-matched, (100)-oriented LaNiO₃ buffer layer provides local coherency within each grain nucleus of BaTiO₃. This has promoted a (001)-textured, continuous growth of the columnar nanograins in the LaNiO₃/BaTiO₃ bi-layer film^[13]. From TEM images, the unbuffered and LaNiO₃-buffered BaTiO₃ films showed an average grain diameter (in-plane) ~50-60 nm and ~30-40 nm, respectively. These grain sizes are much larger than those of the low-temperature deposited BaTiO₃ films with a superfine columnar nanograin structure^[13-15], which showed a boosted energy storage density at a high field by sacrificing their relative dielectric permittivity. Therefore, these two types of BaTiO₃ films deposited at 500 °C are expected to show an enhanced dielectric response and boosted energy storage performance at middle-to-low electric fields.

In [Figure 4](#), we present the high-resolution TEM images near the BaTiO₃/Pt (A) and BaTiO₃/LaNiO₃ interfaces in the unbuffered and buffered BaTiO₃ film heterostructures, respectively. The BaTiO₃/Pt interface exhibits a clean-cut interface with a narrow boundary layer of ~1-2 nm, indicating a limited degree of interdiffusion. This is consistent with the medium deposition temperature (@500 °C) and is supported by an elemental line scan analysis via energy dispersive spectroscopy (EDS) in a Scanning Transmission Electron Microscope. In [Figure 4B](#), the imaged section of the BaTiO₃ film, located inside a single grain, showed an “atomically smooth” and locally-coherent growth on the underlying LaNiO₃ layer. This indicates a locally coherent or “heteroepitaxial” growth inside the grain. The Fast-Fourier-Transformation of [Figure 4B](#) led to a selected area electron diffraction (SAED) pattern that complements the XRD results. It not only verifies an out-of-plane (001)_{BaTiO₃}//(100)_{LaNiO₃} crystalline correlation but also reveals an in-plane crystalline correlation of [100]_{BaTiO₃}//(010)_{LaNiO₃}. Overall, the high-quality surfaces and interfaces, together with the dense nanograin morphology, will contribute to a high breakdown strength and a large energy storage density of the BaTiO₃ films. Specifically, for the unbuffered BaTiO₃ films, since the grain shape is irregular and preferred grain orientation varies with film thickness, the energy storage density at a given field will be thickness-dependent. Taking into consideration that the degree of crystallinity, especially the grain size, increases with the film thickness, we would expect a higher relative dielectric permittivity in a thicker film, together with a higher energy density at a low electric field. This is due to an enhanced

“polarizability”, i.e., early saturation of the electric polarization in comparison to that of the low-temperature deposited BaTiO₃ films.

In [Figure 5A](#), we present typical polarization-electric field (*P-E*) hysteresis loops of the LaNiO₃ buffered BaTiO₃ film at successively increasing voltages of 100 V, 120 V, and 160 V. The *P-E* loops did not show signs of saturation until under the largest applied voltage of 160 V, at which the applied electric field approached 314 MV/m and the electric polarization reached ~75 C/cm². The recyclable energy densities W_{rec} as functions of the applied electric field were computed via the integration of the *P-E* loops ($W_{\text{rec}} = \int_{P_r}^{P_{\text{max}}} E dP$)^[13]. The relative dielectric permittivity ϵ_r , $\epsilon_r = (2 \int_0^P E dP) / (E^2 \epsilon_0)$, where $\int_0^P E dP$ is the total stored electric energy under field *E*, was obtained from monopolar *P-E* loops (not shown here). [Figure 5B](#) presents the W_{rec} and ϵ_r values of the LaNiO₃-buffered BaTiO₃ along with those of a BaTiO₃ ceramic^[21]. Under an applied maximum field of ~314 MV/m, the electric energy density W_{rec} of the buffered BaTiO₃ film reached ~81 J/cm³, and the relative dielectric permittivity ϵ_r ranged between 470 (@low field) and ~215 (@low field). In contrast, the maximum electric energy density W_{rec} of the BaTiO₃ ceramic, which has the largest reported bulk dielectric strength^[21], is only ~1.8 J/cm³. The W_{rec} -*E* curves of the two materials overlap fairly well at low electric fields (< ~50 MV/m), but the corresponding ϵ_r -*E* curves are quite different. In the BaTiO₃ ceramic, ϵ_r quickly drops to ~200 at *E* = 30 MV/m and remains constant as the field increases until it reaches the breakdown limit of ~90 MV/m. In contrast, in the BaTiO₃ film, ϵ_r gradually decreases from ~300 at *E* = 30 MV/m to ~215 at *E* ~314 MV/m, indicating a much slower saturation of the electric polarization compared to the bulk BaTiO₃. The grain size of BaTiO₃ thin films is only several tens of nanometers, which is much smaller than that of its ceramic counterpart (ranging from a few micrometers to tens of micrometers). Due to this extremely small grain size, a full polarization alignment in BaTiO₃ thin films becomes very difficult under an intermediate electric field (~10 MV/m). In bulk ceramics, this level of field is usually sufficient to saturate the electric polarization. However, in the nanoscale grains of the BaTiO₃ thin films, a field level of about one order of magnitude higher (~100 MV/cm) is required to align all accessible polarization vectors, resulting in a slow electric polarization saturation. The delayed saturation of the electric polarization enables the absorption of additional electrical energy and greatly extends the electric breakdown limit. Consequently, our BaTiO₃ films exhibit outstanding energy storage capacities under electric fields of several hundred MV/m.

Furthermore, the unbuffered, randomly oriented BaTiO₃ films (on Pt/Ti/Si) showed a distinct energy storage feature compared to the (001)-textured, LaNiO₃-buffered BaTiO₃ films. Unlike the latter, which have shown a thickness-scalable relative dielectric permittivity ϵ_r /energy density^[13] by maintaining an aspect-ratio of in-plane diameter/grain length, the randomly oriented films demonstrate an increasing energy density W_{rec} and ϵ_r at a given low field with the film thickness [[Figure 6A](#) and [B](#), [Table 2](#)]. These behaviors, as predicted by the microstructural analyses, can be attributed to the discontinuous columnar nanograin morphology with mixed crystalline orientations and the growth of these nanograins with the film thickness. It is worth noting that at a high voltage of 460 V, the 2,610 nm thick film showed a low dielectric loss (< 3%) and a high electric polarization (> 75 C/cm²). This can be attributed to its large thickness (460 V corresponding to a low field of ~117 MV/m) and good film quality/robust insulation.

CONCLUSIONS

In summary, the study investigates the energy storage capabilities of BaTiO₃ thick films (~0.5 μm to ~2.6 μm) deposited at 500 °C, with two types of engineered grain structures. The films with a (001)-textured, continuous columnar nanograin structure showed a high recyclable energy density W_{rec} of ~81 J/cm³ at *E* = 314 MV/m. This represents a substantial improvement compared to films of the same type of films

Table 2. Energy storage densities of various BaTiO₃ film capacitors

BaTiO ₃ thin film heterostructures sputter-deposited on Si	Applied voltage (V)/Field (MV/m)	W_{rec} (J/cm ³)
Au/BaTiO ₃ (510 nm)/LaNiO ₃ /Pt/Ti	160/314	81.0
Au/BaTiO ₃ (435 nm)/Pt/Ti	140/322	57.1
Au/BaTiO ₃ (845 nm)/Pt/Ti	260/308	50.4
Au/BaTiO ₃ (1,305 nm)/Pt/Ti	300/231	46.6
Au/BaTiO ₃ (2,610 nm)/Pt/Ti	460/177	48.8

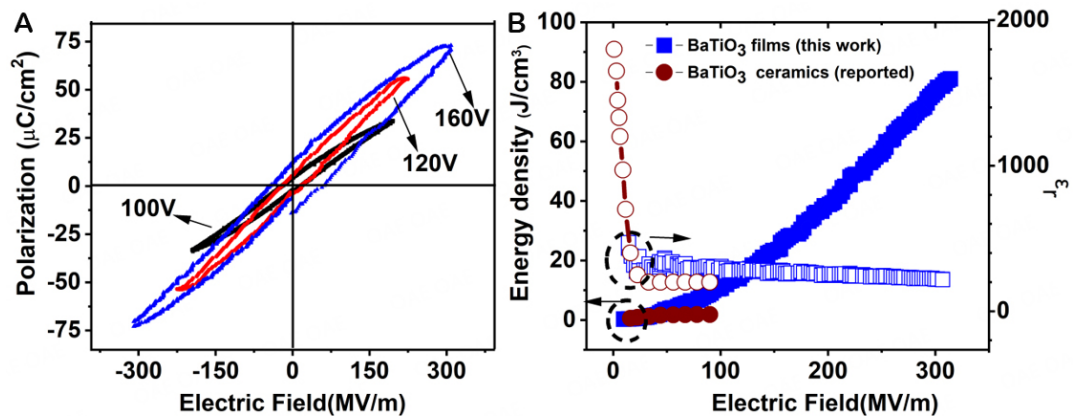


Figure 5. (A) Typical polarization-electric field hysteresis loops of the LaNiO₃ buffered BaTiO₃ film (~510 nm) and (B) the corresponding energy storage density W_{rec} and relative dielectric permittivity of the film in (A), as well as those of a BaTiO₃ ceramic, plotted as functions of the applied electric field.

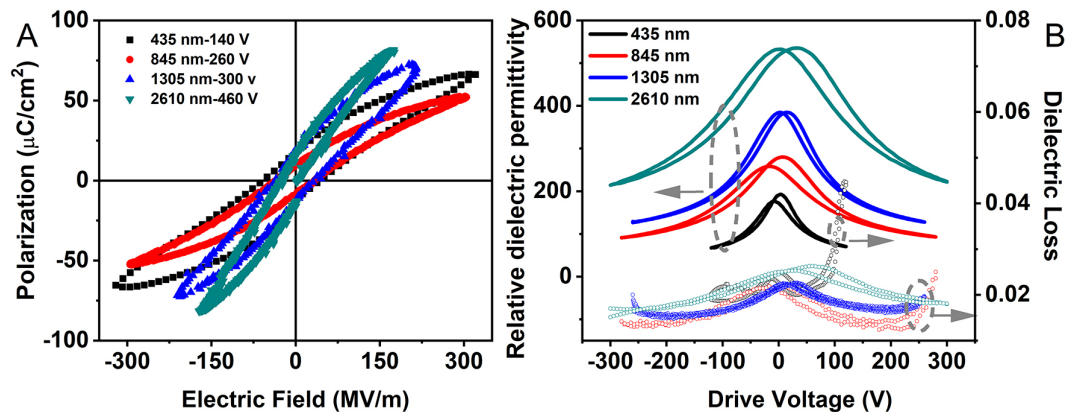


Figure 6. (A) Typical polarization-electric field (P-E) hysteresis loops of the four unbuffered BaTiO₃ films directly deposited on Pt/Ti/Si, with thicknesses ranging between 435 nm and 2610 nm; (B) The relative dielectric permittivity and loss tangents as functions of the applied voltage for the four films in (A).

prepared at lower temperatures^[13-15], making them promising for energy storage under middle-to-low electric fields. Meanwhile, films consisting of discontinuous columnar nanograins with mixed crystalline orientations showed an improved relative dielectric permittivity and a higher energy storage density at low fields, with increasing film thickness. Both types of BaTiO₃ films have shown good potential for dielectric energy storage applications under middle-to-low electric fields. However, the randomly-oriented films are better material candidates in high-voltage applications (several times the commercially used voltage of 220 V).

DECLARATIONS

Authors' contributions

Conceptualization and methodology; writing - original draft preparation: Ouyang J

Validation: Teng X, Yuan M, Wang K

Formal analysis: Yuan M, Wang K, Zhao Y, Cheng H

Investigation: Zhu H, Liu C, Xiao Y, Zhang W

Resources: Ouyang J, Tang M, Pan W

Data curation: Ouyang J, Teng X, Yuan M

Writing, review, and editing: Ouyang J, Yuan M

Visualization: Teng X, Yuan M, Ouyang J

Supervision: Ouyang J, Tang M

Project administration: Ouyang J, Pan W

Funding acquisition: Ouyang J, Cheng H, Zhu H, Liu C

All authors have read and agreed to the published version of the manuscript.

Availability of data and materials

Data will be available from the first author upon reasonable request.

Financial support and sponsorship

The authors are deeply grateful for the financial support from the National Natural Science Foundation of China (Grant No. 52072218 and 52002192), Natural Science Foundation of Shandong Province (Grant No. ZR2020QE042, ZR2022ZD39, ZR2022QB138, ZR2022ME031, and ZR2022YQ43), and the Science, Education and Industry Integration Pilot Projects of Qilu University of Technology (Shandong Academy of Sciences) (Grant No. 2022GH018 and 2022PY055). Jun Ouyang acknowledges the support from the Jinan City Science and Technology Bureau (Grant No. 2021GXRC055), the Education Department of Hunan Province/Xiangtan University (Grant No. KZ0807969), and the State Key Laboratory of New Ceramics and Fine Processing (Tsinghua University).

Conflicts of interest

All authors declared that there are no conflicts of interest.

Ethical approval and consent to participate

Not applicable.

Consent for publication

Not applicable.

Copyright

© The Author(s) 2023.

REFERENCES

1. Chu B, Zhou X, Ren K, et al. A dielectric polymer with high electric energy density and fast discharge speed. *Science* 2006;313:334-6. [DOI](#)
2. Yao K, Chen S, Rahimabady M, et al. Nonlinear dielectric thin films for high-power electric storage with energy density comparable with electrochemical supercapacitors. *IEEE Trans Ultrason Ferroelectr Freq Control* 2011;58:1968-74. [DOI](#)
3. Sigman J, Brennecke GL, Clem PG, Tuttle BA. Fabrication of perovskite-based high-value integrated capacitors by chemical solution deposition. *J Am Ceram Soc* 2008;91:1851-7. [DOI](#)

4. Dai L, Lin F, Zhu Z, Li J. Electrical characteristics of high energy density multilayer ceramic capacitor for pulse power application. *IEEE Trans Magn* 2005;41:281-4. DOI
5. Chen XF, Dong XL, Wang GS, Cao F, Wang YL. Doped Pb(Zr,Sn,Ti)O₃ slim-loop ferroelectric ceramics for high-power pulse capacitors application. *Ferroelectrics* 2008;363:56-63. DOI
6. Zhu L, Wang Q. Novel ferroelectric polymers for high energy density and low loss dielectrics. *Macromolecules* 2012;45:2937-54. DOI
7. Wang Y, Zhou X, Chen Q, Chu B, Zhang Q. Recent development of high energy density polymers for dielectric capacitors. *IEEE Trans Dielect Electr Insul* 2010;17:1036-42. DOI
8. Kim Y, Kathaperumal M, Smith OL, et al. High-energy-density sol-gel thin film based on neat 2-cyanoethyltrimethoxysilane. *ACS Appl Mater Interfaces* 2013;5:1544-7. DOI
9. Ouyang J, Yang SY, Chen L, Ramesh R, Roytburd AL. Orientation dependence of the converse piezoelectric constants for epitaxial single domain ferroelectric films. *Appl Phys Lett* 2004;85:278-80. DOI
10. Wang J, Su Y, Wang B, Ouyang J, Ren Y, Chen L. Strain engineering of dischargeable energy density of ferroelectric thin-film capacitors. *Nano Energy* 2020;72:104665. DOI
11. Niu M, Zhu H, Wang Y, et al. Integration-friendly, chemically stoichiometric BiFeO₃ films with a piezoelectric performance challenging that of PZT. *ACS Appl Mater Interfaces* 2020;12:33899-907. DOI
12. Su Y, Ouyang J, Zhao YY. Nanograins in ferroelectric films. In: Ouyang J, editor, *Nanostructures in ferroelectric films for energy applications*. Amsterdam: Elsevier; 2019; pp. 129-62.
13. Zhao Y, Ouyang J, Wang K, et al. Achieving an ultra-high capacitive energy density in ferroelectric films consisting of superfine columnar nanograins. *Energy Stor Mater* 2021;39:81-8. DOI
14. Wang K, Zhang Y, Wang S, et al. High energy performance ferroelectric (Ba,Sr)(Zr,Ti)O₃ film capacitors integrated on Si at 400 °C. *ACS Appl Mater Interfaces* 2021;13:22717-27. DOI
15. Zhu H, Zhao YY, Ouyang J, Wang K, Cheng H, Su Y. Achieving a record-high capacitive energy density on Si with columnar nanograined ferroelectric films. *ACS Appl Mater Interfaces* 2022;14:7805-13. DOI
16. Park S, Jang J, Ahn C, et al. Buffered template strategy for improving texture quality and piezoelectric properties of heterogeneous templated grain growth (K,Na)NbO₃-based ceramics through interface engineering. *J Eur Ceram Soc* 2023;43:1932-40. DOI
17. Yuan M, Zhang W, Wang X, Pan W, Wang L, Ouyang J. In situ preparation of high dielectric constant, low-loss ferroelectric BaTiO₃ films on Si at 500 °C. *Appl Surf Sci* 2013;270:319-23. DOI
18. Wakiya N, Azuma T, Shinozaki K, Mizutani N. Low-temperature epitaxial growth of conductive LaNiO₃ thin films by RF magnetron sputtering. *Thin Solid Films* 2002;410:114-20. DOI
19. Zhang W, Cheng H, Yang Q, Hu F, Ouyang J. Crystallographic orientation dependent dielectric properties of epitaxial BaTiO₃ thin films. *Ceram Int* 2016;42:4400-5. DOI
20. Xu F, Trolrier-mckinsty S, Ren W, Xu B, Xie Z, Hemker KJ. Domain wall motion and its contribution to the dielectric and piezoelectric properties of lead zirconate titanate films. *J Appl Phys* 2001;89:1336-48. DOI
21. Burn I, Smyth DM. Energy storage in ceramic dielectrics. *J Mater Sci* 1972;7:339-43. DOI

Research Article

Open Access



Structure, magnetism and low thermal expansion in $Tb_{1-x}Er_xCo_2Mn_y$ intermetallic compounds

Yanming Sun¹, Yili Cao¹, Yang Ren², Saul H. Lapidus³, Qiang Li¹, Jinxia Deng¹, Jun Miao¹, Kun Lin¹, Xianran Xing¹

¹Beijing Advanced Innovation Center for Materials Genome Engineering, Institute of Solid State Chemistry, Department of Physical Chemistry, University of Science and Technology Beijing, Beijing 100083, China.

²Department of Physics, City University of Hong Kong, Kowloon, Hong Kong, China.

³X-Ray Science Division, Argonne National Laboratory, Argonne, IL 60439, USA.

Correspondence to: Prof. Xianran Xing, Department of Physical Chemistry, University of Science and Technology Beijing, Xueyuan Rd. 30, Haidian District, Beijing 100083, China. E-mail: xing@ustb.edu.cn

How to cite this article: Sun Y, Cao Y, Ren Y, Lapidus SH, Li Q, Deng J, Miao J, Lin K, Xing X. Structure, magnetism and low thermal expansion in $Tb_{1-x}Er_xCo_2Mn_y$ intermetallic compounds. *Microstructures* 2023;3:2023028. <https://dx.doi.org/10.20517/microstructures.2023.03>

Received: 16 Jan 2023 **First Decision** 17 Feb 2023 **Revised:** 18 Apr 2023 **Accepted:** 6 Jun 2023 **Published:** 16 Jun 2023

Academic Editors: Andrea Sanson, Danmin Liu **Copy Editor:** Fangling Lan **Production Editor:** Fangling Lan

Abstract

Here, we obtained a series of controllable thermal expansion alloys $Tb_{1-x}Er_xCo_2Mn_y$ ($x = 0-0.5$, $y = 0-0.4$) by incorporating double rare earth doping and introducing non-stoichiometric Mn content. By varying the amount of Er or Mn, a low thermal expansion (LTE) is achieved in $Tb_{0.6}Er_{0.4}Co_2Mn_{0.1}$ (TECM, $\alpha_1 = 1.23 \times 10^{-6} K^{-1}$, 125-236 K). The macroscopic linear expansion and magnetic properties reveal that anomalous thermal expansion is closely related to the magnetic phase transition. Synchrotron X-ray powder diffraction results show that TECM is a cubic phase (space group: $Fd-3m$) at high temperatures, and a structural transition to a rhombohedral phase (space group: $R-3m$) occurs as temperature decreases. The negative thermal expansion c-axis compensates for the normal positive thermal expansion of the basal plane, resulting in the volumetric LTE. This study provides a new metallic and magnetic ZTE material.

Keywords: Zero thermal expansion, crystal structure, microstructure, magnetism

INTRODUCTION

By flexibly compensating for thermal expansion, negative thermal expansion (NTE) materials have gained



© The Author(s) 2023. **Open Access** This article is licensed under a Creative Commons Attribution 4.0 International License (<https://creativecommons.org/licenses/by/4.0/>), which permits unrestricted use, sharing, adaptation, distribution and reproduction in any medium or format, for any purpose, even commercially, as long as you give appropriate credit to the original author(s) and the source, provide a link to the Creative Commons license, and indicate if changes were made.



significant attention and development over the past three decades. The NTE is an important requirement for the development of zero thermal expansion (ZTE) materials, which exhibit no dimensional changes when subjected to heating. Materials with a coefficient of thermal expansion below $2 \times 10^{-6} \text{ K}^{-1}$ are defined as low thermal expansion (LTE) materials and find applications in various engineering environments, such as electronic devices, optical instruments, and spacecraft. An example is Invar alloy $\text{Fe}_{0.65}\text{Ni}_{0.35}$, which has been extensively used since its discovery in 1897^[1]. Over time, other LTE alloys such as Fe-Co-Cr stainless steel Invar alloys and other alloy compositions have emerged^[2]. In comparison with oxides^[3], fluorides^[4], and cyanides^[5], LTE alloys offer additional properties such as optical properties^[6], excellent electrical, thermal transport properties, and mechanical properties^[7-9]. Examples of such alloys include $(\text{Zr}, \text{Nb})\text{Fe}_2$ ^[10,11], $(\text{Sc}, \text{Ti})\text{Fe}_2$ ^[12], MnCoGe ^[13,14], $\text{La}(\text{Fe}, \text{Si}, \text{Al})_{13}$ ^[15,16], RECo_2 ($\text{RE} = \text{rare earth}$)^[17,18], REFe_{14}B ^[19], and $\text{RE}_2\text{Fe}_{17}$ ^[20,21]. The metallic ZTE is known to be correlated with the magneto-volume effect (MVE), which refer to volume changes induced by spontaneous magnetic ordering^[16,22].

Cubic Laves phase RECo_2 has been studied intensively due to its relatively simple crystal and magnetic structures. It belongs to a class of materials known for their magnetostrictive and magnetocaloric properties^[23]. The compound is composed of two magnetic sublattices: one involving the local magnetic moment of REs, and the other comprising the Co sublattice, which exhibits long-range magnetic ordering induced by the molecular field of RE atoms^[24,25]. In previous literature, samples TbCo_2Mn_y ($y = 0, 0.1, 0.2,$ and 0.3) were found to exhibit a rhombohedral structure (space group: $R\bar{3}m$) below the Curie temperature (T_C) and undergo a transition to a cubic structure (space group: $Fd\bar{3}m$) above T_C ^[26]. TbCo_2Mn_y were reported for the ZTE temperature window of about 40 K^[23]. Intriguingly, the introduction of the element Er in compound TbCo_2Mn_y gives the Laves phase of $\text{Tb}_{1-x}\text{Er}_x\text{Co}_2\text{Mn}_y$, and their ZTE temperature windows can be wider with increasing Er content. In the $(\text{RE}_{1-x}\text{RE}'_x)(\text{Co}_{1-y}\text{Mn}_y)_2$ compounds, the substitution of the RE' atoms for the RE atoms occurs only in the $16d$ atomic site, while the substitution of the M atoms for Co atoms takes place in the $8a$ site^[24]. This differs from the $(\text{RE}_{1-x}\text{RE}'_x)\text{Co}_2\text{Mn}_y$ compounds, where the Mn atoms can replace the $8a$ and $16d$ sites in the cubic structure with equal probability^[27]. This unusual modulation of multiple sites in $(\text{RE}_{1-x}\text{RE}'_x)\text{Co}_2\text{Mn}_y$ compounds significantly increases the T_C of the corresponding Mn-free compounds. In this study, new intermetallic compounds $\text{Tb}_{1-x}\text{Er}_x\text{Co}_2\text{Mn}_y$ ($x = 0, 0.1, 0.2, 0.4,$ and $0.5, y = 0$ and 0.1), with a MgCu_2 type cubic structure, are introduced. These compounds can be modulated by changing their components to achieve near ZTE.

MATERIALS AND METHODS

All the Laves-phase samples of $\text{Tb}_{1-x}\text{Er}_x\text{Co}_2\text{Mn}_y$ ($x = 0, 0.1, 0.2, 0.4,$ and $0.5, y = 0$ and 0.1) were prepared by arc melting under high-purity argon environment using raw materials with a purity of more than 99.9%, which were weighed at the designed ratio of raw materials. To ensure homogeneity, the samples were turned over and melted more than three times. At the end of the arc melting, the ingots are wrapped with molybdenum foil and annealed in a vacuum-sealed quartz tube at 1,173 K for one week. The purity of the samples was verified by a laboratory X-ray diffractometer (XRD, PANalytical X'Pert PRO) with $\text{Cu K}\alpha$ radiation. The scanning electron microscopy (SEM) imaging and X-ray energy dispersive spectroscopy (EDS) elemental analysis were performed using a scanning electron microscope system (1,720, EPMA, Shimadzu). All linear thermal expansion curves ($\Delta L/L_0$) were measured at a thermodilatometer (NETZSCH DIL402) with a heating rate of 5 K/min. The magnetic properties were measured by a Physical Property Measurement System (PPMS, Quantum Design company). Temperature dependence of the synchrotron X-ray diffraction (SXRD) of the sample was collected at beamline of 11-BM-B ($\lambda = 0.459073 \text{ \AA}$) in the Argonne National Laboratory (USA). All diffraction data were analyzed by the FULLPROF software.

RESULTS AND DISCUSSION

$\text{Tb}_{1-x}\text{Er}_x\text{Co}_2\text{Mn}_y$ ($x = 0, 0.1, 0.2, 0.4, \text{ and } 0.5, y = 0, 0.1, 0.2, 0.3$) were confirmed to be pure phases by XRD at room temperature (except $y = 0.4$). For example, at 300 K, the Rietveld refinement of the SXRD data for $\text{Tb}_{0.6}\text{Er}_{0.4}\text{Co}_2\text{Mn}_{0.1}$ (denoted as TECM) shows the cubic structure in [Supplementary Figure 1](#). In $\text{Tb}_{1-x}\text{Er}_x\text{Co}_2$ ($x = 0, 0.1, 0.2, 0.4, \text{ and } 0.5$, [Figure 1A and B](#)): It is cubic without Er ($x = 0, \text{ TbCo}_2$) and remains cubic with increasing Er content ($x \leq 0.5$). Meanwhile, it was observed that the peak (220) shifted to a higher angle due to the successful introduction of smaller radii Er atoms. In $\text{Tb}_{1-x}\text{Er}_x\text{Co}_2\text{Mn}_{0.1}$ ($x = 0, 0.1, 0.2, 0.4, \text{ and } 0.5$), the peak (220) shifted to a high angle with increasing Er content, while the Mn content being fixed at $y = 0.1$ and still maintaining the cubic phase [[Figure 1C and D](#)]. To investigate the effect of different Er contents on $\text{Tb}_{1-x}\text{Er}_x\text{Co}_2$ and $\text{Tb}_{1-x}\text{Er}_x\text{Co}_2\text{Mn}_{0.1}$, the cell parameters of which were obtained by fitting the XRD data [[Supplementary Figure 2 and Supplementary Table 1](#)]. In addition, we successfully synthesized $\text{Tb}_{0.6}\text{Er}_{0.4}\text{Co}_2\text{Mn}_y$ ($y = 0, 0.1, 0.2, 0.3, \text{ and } 0.4$) with increasing Mn content. The samples have a similar cubic structure below $y = 0.4$ [[Supplementary Figure 3](#)]. The cubic structure of the RECo_2 is shown in [Figure 1F](#). The rhombohedral structure is also presented in [Figure 1E](#) as the temperature decreases below T_C . The SEM images and EDS elemental mappings shown in [Figure 1G-K](#) and [Supplementary Table 2](#) illustrate the uniform distribution of elements Tb, Er, Co, and Mn in TECM (Tb:Er:Co:Mn = 0.58:0.37:2:0.09). The contents of Co and Mn were close to the nominal compositions, as evidenced by the ICP results shown in [Supplementary Table 3](#).

As shown in [Figure 2](#), the samples $\text{Tb}_{1-x}\text{Er}_x\text{Co}_2\text{Mn}_y$ ($x = 0, 0.1, 0.2, 0.4, \text{ and } 0.5, y = 0 \text{ and } 0.1$) exhibit a significantly different linear thermal expansion behavior. The NTE behavior of TbCo_2 occurs in a narrow temperature window. Interestingly, the anomalous thermal expansion of the $\text{Tb}_{1-x}\text{Er}_x\text{Co}_2$ ($x = 0, 0.1, 0.2, \text{ and } 0.4$) compounds ends at lower temperatures with increasing Er content. A large NTE coefficient of $\text{Tb}_{0.6}\text{Er}_{0.4}\text{Co}_2$ (denoted as TEC, $\alpha_l = -15.29 \times 10^{-6} \text{ K}^{-1}$, 131-167 K) was obtained [[Figure 2A](#)]. To obtain LTE, the ferromagnetic (FM) exchange interactions can be enhanced by introducing Mn atoms at the Tb/Er *8a* and Co *16d* sites^[28]. However, the samples $\text{Tb}_{1-x}\text{Er}_x\text{Co}_2\text{Mn}_{0.1}$ ($x = 0, 0.1, 0.2, 0.4, \text{ and } 0.5$) [[Figure 2B](#)], are different from the above. As Er replaces Tb, the volume shrinkage behavior of $\text{Tb}_{1-x}\text{Er}_x\text{Co}_2\text{Mn}_{0.1}$ decreases, and the LTE temperature window of $\text{Tb}_{1-x}\text{Er}_x\text{Co}_2\text{Mn}_{0.1}$ gradually appears and expands to $x = 0.4$. The LTE is obtained with TECM ($\alpha_l = 1.23 \times 10^{-6} \text{ K}^{-1}$, 125-236 K) when $x = 0.4$. For comparison, the coefficient of thermal expansion value of TECM is smaller than that of common metals such as Fe ($\alpha_l = 12.2(0) \times 10^{-6} \text{ K}^{-1}$), Al ($\alpha_l = 22.9(0) \times 10^{-6} \text{ K}^{-1}$), Cu ($\alpha_l = 16.3(1) \times 10^{-6} \text{ K}^{-1}$), etc. However, the coefficient of thermal expansion trends from negative to positive with increasing Er content [[Supplementary Figure 4](#)]. TECM has a wide temperature window of the LTE curves, which may offer promising prospects for both basic research and applications.

The magnetic phase transition of TbCo_2 was documented to be first-order, while that of the TbCo_2Mn_x compound obtained by the addition of Mn was second-order^[23]. The addition of Mn significantly increased the T_C of the compounds, for example, from 225 K for TbCo_2 to 347 K for $\text{TbCo}_2\text{Mn}_{0.4}$ ^[29]. The macroscopic FM behavior of $\text{Tb}_{1-x}\text{Er}_x\text{Co}_2\text{Mn}_y$ ($x = 0, 0.1, 0.2, 0.4, \text{ and } 0.5, y = 0 \text{ and } 0.1$) was determined by measurements of zero-field cooling (ZFC) and field cooling (FC) during heating in a 500 Oe magnetic field [[Figure 3A and B](#)]. It is obvious that the FM transition temperature of the compound TEC is 167 K [[Figure 3C](#)], and that of TECM is 236 K [[Figure 3D](#)]. In $\text{Tb}_{1-x}\text{Er}_x\text{Co}_2$ and $\text{Tb}_{1-x}\text{Er}_x\text{Co}_2\text{Mn}_{0.1}$ samples, the magnetic transition temperature shifts to the low temperature with increasing Er content. The above results can be obtained from the derivative curves of FC/ZFC. The introduction of Mn effectively increases the FM transition temperature, as shown by the curves of T_C in [Figure 3E](#), which is essential for obtaining LTE materials with a wide-temperature window. To further verify the FM transition temperature, isothermal magnetization curves $M-H$ for selected TEC and TECM are shown in [Figures 3F and](#)

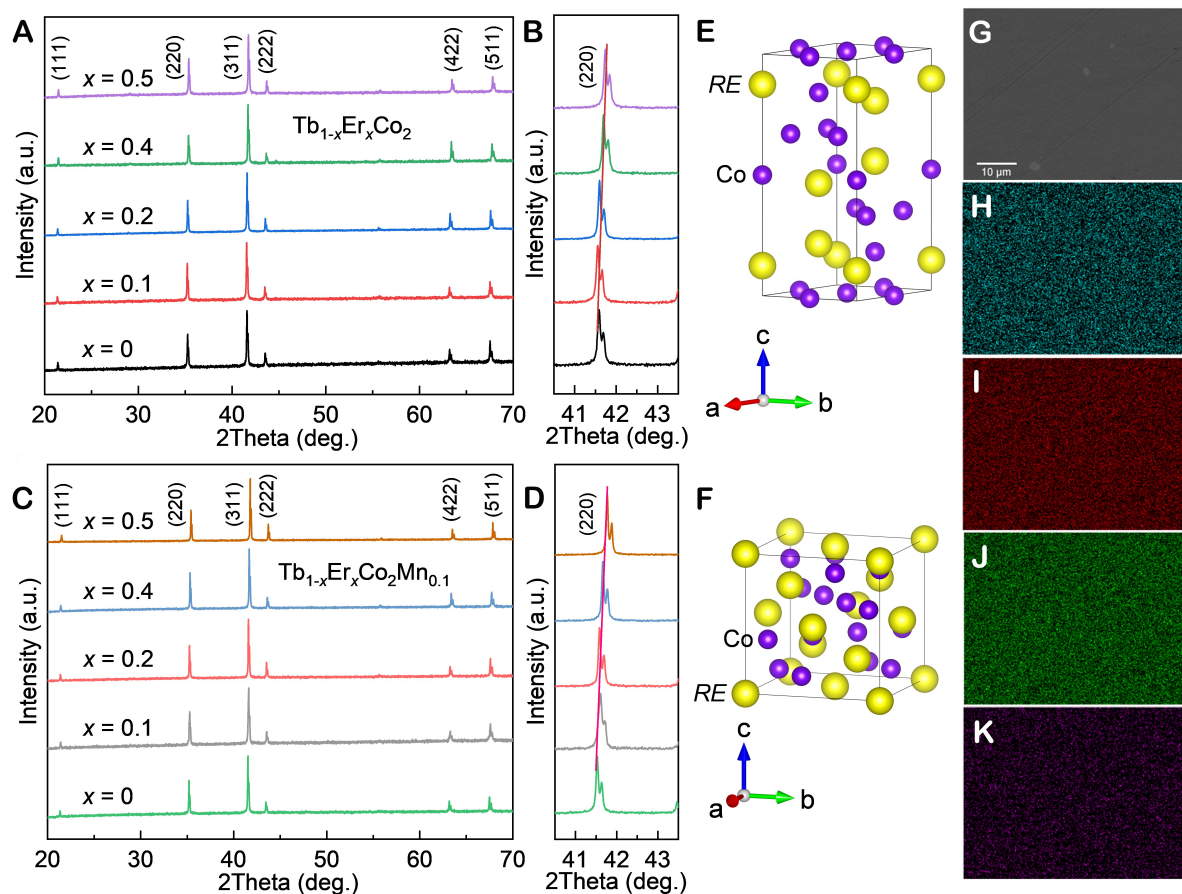


Figure 1. XRD patterns of the (A) $Tb_{1-x}Er_xCo_2$ ($x = 0, 0.1, 0.2, 0.4,$ and 0.5) and (C) $Tb_{1-x}Er_xCo_2Mn_{0.1}$ ($x = 0, 0.1, 0.2, 0.4,$ and 0.5). The corresponding enlarged diffraction peaks (220) are (B and D). The rhombohedral (E) and cubic (F) crystal structures of $RECo_2$ ($RE =$ rare earth, the orange ball is RE , and the purple ball is Co). (G) The SEM images and EDS elemental mappings of (H) Tb, (I) Er, (J) Co, and (K) Mn of TECM, showing the uniformity of each element.

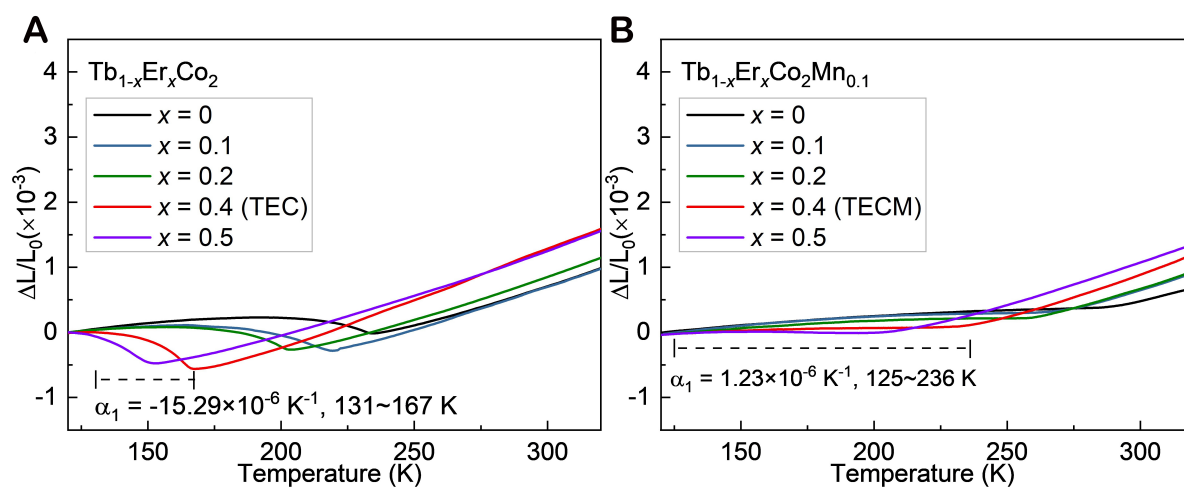


Figure 2. Linear thermal expansion ($\Delta L/L_0$) of (A) $Tb_{1-x}Er_xCo_2$ ($x = 0, 0.1, 0.2, 0.4,$ and 0.5) and (B) $Tb_{1-x}Er_xCo_2Mn_{0.1}$ ($x = 0, 0.1, 0.2, 0.4,$ and 0.5).

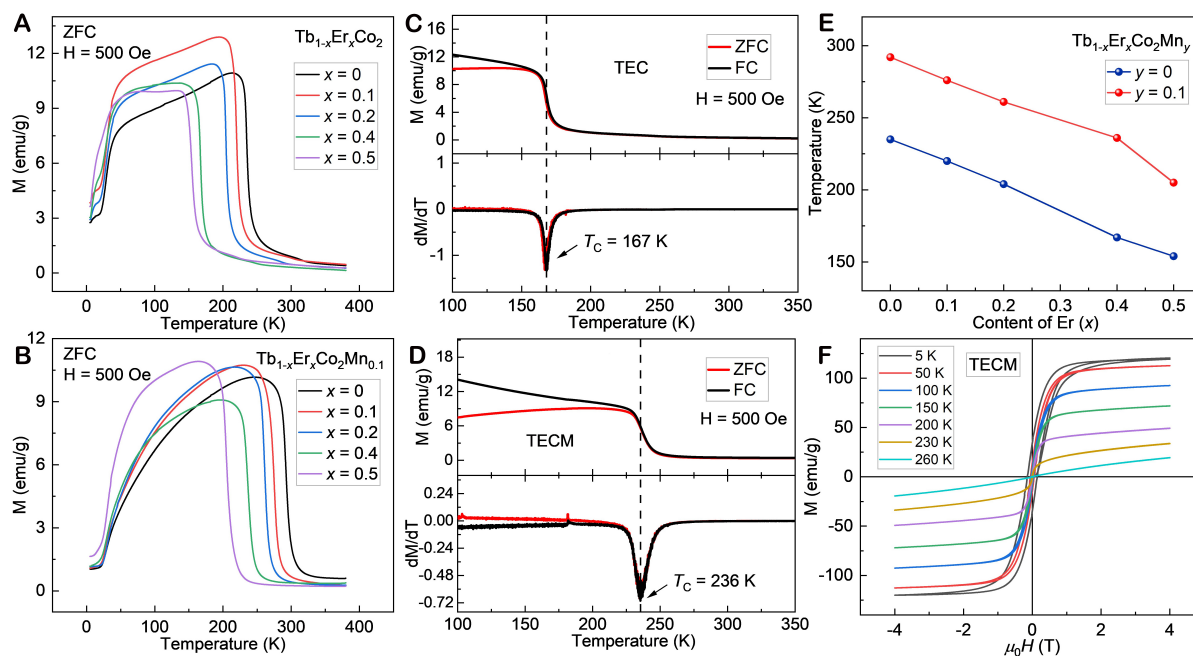


Figure 3. Temperature dependence of ZFC for the (A) Tb_{1-x}Er_xCo₂ and (B) Tb_{1-x}Er_xCo₂Mn_{0.1} compounds under an applied magnetic field of 500 Oe from 5 to 380 K. FC-ZFC and the derivative curves of FC/ZFC of (C) TEC and (D) TECM compounds, respectively. (E) Curie temperature for Tb_{1-x}Er_xCo₂Mn_y (the results are obtained from the derivative curves of FC/ZFC). (F) Isothermal *M*-*H* curves (-4 to 4 T) for TECM.

Supplementary Figure 5. The molecular magnetic moment of TEC is 6.32 μ_B/f.u., which is higher than that of TECM (6.10 μ_B/f.u.) at 5 K [Supplementary Figure 6]. As shown in Supplementary Figure 7, the introduction of Mn increases the phase transition temperature. A close correlation between structure, magnetic and thermal expansion. The crystal structural and magnetic transition temperature of TEC and TECM were found to be consistent with the point of the disappearance of NTE or ZTE, which would be helpful in plotting the curves of structural transition, ZFC-FC, and delta L/L₀ (T).

In the SXRDX intensity contour plot of the TECM compound [Figure 4A], a splitting of the peak at low temperatures near 20.85° was found. The crystal structure of TECM was determined by SXRDX, and it was demonstrated that it produces a phase transition from cubic (*Fd-3m* space group) to rhombohedral (*R-3m* space group) with decreasing temperature. Rietveld refinement results of TECM at T = 100 K and T = 275 K are shown in Figure 4B. By a refinement of the SXRDX pattern, this transition can be described in the inset of Figure 4B. The results show that the two peaks (110) and (104) of the rhombohedral structure are replaced by the peak (220) of the cubic structure. The temperature dependence of the unit lattice parameters and volume of TECM from 100 K to 325 K is shown in Figure 4C. From the correlation between the unit cell of the rhombohedral model (space group: *R-3m*) and the cubic model (space group: *Fd-3m*), it is clear that the amounts of $\sqrt{2}a$ and $c/\sqrt{3}$ (*a* and *c* are the lattice parameters of the rhombohedral) are equivalent to the cubic amounts^[30]. From thermodilatometer measurement and SXRDX calculation results [Figure 4C], it is clear that the linear thermal expansion of TECM is consistent.

CONCLUSIONS

In summary, a series of Tb_{1-x}Er_xCo₂Mn_y intermetallic compounds with a cubic MgCu₂-type structure were synthesized. The addition of Mn increases the T_C and contributes to a low thermal expansion with a wide temperature window. It has been confirmed by the high-resolution SXRDX, which signifies such LTE is

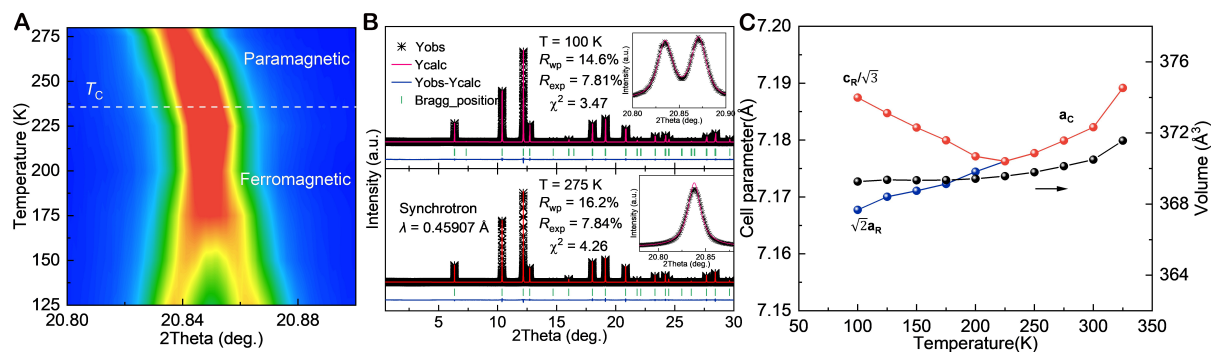


Figure 4. (A) Contour plot of the SXR intensity for TECM compound. (B) Full profile Rietveld refinements of the SXR patterns for the TECM compound at 100 K and 275 K. (The illustration shows the enlarged area. The experimental profiles are shown by star markers. Bragg reflections are indicated by ticks. Pink lines represent the calculated data, while black lines represent the difference between the observed and calculated data.) (C) Temperature dependence of the lattice parameters a , c , and V of TECM measured by SXR. (The amounts of $\sqrt{2}a$ and $c/\sqrt{3}$ (a and c are the lattice parameters of the rhombohedra) are equivalent to the cubic amounts).

attributed to magnetic-structural transition below T_c . The TECM compound shows a cubic ($Fd-3m$) structure above T_c while transforming to rhomboidal ($R-3m$) below T_c . TECM has a wide temperature window of the low thermal expansion curves, which offers good prospects for both basic research and applications. This work provides structural information and near ZTE properties of the compounds $Tb_{1-x}Er_xCo_2Mn_y$, which may guide future exploration of magnetic functional materials.

DECLARATIONS

Authors' contributions

Conceived and designed the study: Xing X

Prepared the samples and collected the data: Sun Y

Performed data analysis and wrote the main draft of the paper: Sun Y, Cao Y, Xing X

Analyzed the thermal expansion results: Li Q, Deng J, Miao J, Lin K

Conducted the SXR measurements: Ren Y, Lapidus SH

All authors discussed the results and commented on the manuscript.

Availability of data and materials

Not applicable.

Financial support and sponsorship

This work was supported by the National Key R&D Program of China (2020YFA0406202), the National Natural Science Foundation of China (22275015, 22090042, 21971009, and 21731001), and the Fundamental Research Funds for the Central Universities, China (FRF-IDRY-19-018 and FRF-BR-19-003B). This research used resources of the Advanced Photon Source, a U.S. Department of Energy (DOE) Office of Science User Facility operated for the DOE Office of Science by Argonne National Laboratory.

Conflicts of interest

All authors declared that there are no conflicts of interest.

Ethical approval and consent to participate

Not applicable.

Consent for publication

Not applicable.

Copyright

© The Author(s) 2023.

REFERENCES

1. Guillaume C. Recherches sur les aciers au nickel. *J Phys Theor Appl* 1898;7:262-74. DOI
2. Honda K. A new alloy, 'stainless-invar'. *Nature* 1933;131:587-587. DOI
3. Huang Q, Santoro A, Lynn JW, et al. Structure and magnetic order in $\text{La}_{1-x}\text{Ca}_x\text{MnO}_3$ ($0 < x < \sim 0.33$). *Phys Rev B* 1998;58:2684-91. DOI
4. Li Q, Lin K, Liu Z, et al. Chemical diversity for tailoring negative thermal expansion. *Chem Rev* 2022;122:8438-86. DOI
5. Chippindale AM, Hibble SJ, Bilbé EJ, et al. Mixed copper, silver, and gold cyanides, $(M_xM'_{1-x})\text{CN}$: tailoring chain structures to influence physical properties. *J Am Chem Soc* 2012;134:16387-400. DOI
6. Poornaprakash B, Subramanyam K, Vattikuti SP, Pratap Reddy MS. Achieving enhanced ferromagnetism in ZnTbO nanoparticles through Cu co-doping. *Ceram Int* 2019;45:16347-52. DOI
7. Tan Z, Miao P, Hagihala M, et al. Room temperature zero thermal expansion in a cubic cobaltite. *J Phys Chem Lett* 2020;11:6785-90. DOI
8. Guo X, Ni X, Li J, et al. Designing mechanical metamaterials with kirigami-inspired, hierarchical constructions for giant positive and negative thermal expansion. *Adv Mater* 2021;33:e2004919. DOI
9. Xu J, Wang Z, Huang H, et al. Significant zero thermal expansion via enhanced magnetoelastic coupling in kagome magnets. *Adv Mater* 2023;35:e2208635. DOI
10. Song Y, Sun Q, Yokoyama T, et al. Transforming thermal expansion from positive to negative: the case of cubic magnetic compounds of $(\text{Zr,Nb})\text{Fe}_2$. *J Phys Chem Lett* 2020;11:1954-61. DOI
11. Shiga M, Nakamura Y. Magnetovolume effects and invar characters of $(\text{Zr}_{1-x}\text{Nb}_x)\text{Fe}_2$. *J Phys Soc Jpn* 1979;47:1446-51. DOI
12. Wada H, Shimamura N, Shiga M. Thermal and transport properties of $\text{Sc}_{1-x}\text{Ti}_x\text{Fe}_2$. *J Phys Soc Jpn* 1994;63:283-8. DOI
13. Ren Q, Hutchison W, Wang J, et al. Negative thermal expansion of Ni-doped MnCoGe at room-temperature magnetic tuning. *ACS Appl Mater Interfaces* 2019;11:17531-8. DOI
14. Shen F, Zhou H, Hu F, et al. Cone-spiral magnetic ordering dominated lattice distortion and giant negative thermal expansion in Fe-doped MnNiGe compounds. *Mater Horizons* 2020;7:804-10. DOI
15. Hu F, Shen B, Sun J, Cheng Z, Rao G, Zhang X. Influence of negative lattice expansion and metamagnetic transition on magnetic entropy change in the compound $\text{LaFe}_{1.4}\text{Si}_{1.6}$. *Appl Phys Lett* 2001;78:3675-7. DOI
16. Fujita A, Fukamichi K, Wang J, Kawazoe Y. Large magnetovolume effects and band structure of itinerant-electron metamagnetic $\text{La}(\text{Fe}_x\text{Si}_{1-x})_{13}$ compounds. *Phys Rev B* 2003;68:104431. DOI
17. Khmelevskiy S, Mohn P. Theory of invar anomalies in the laves phase $R\text{Co}_2$ ($R = \text{Ho}, \text{Dy}$) intermetallic compounds. *J Magn Magn Mater* 2004;272-276:525-6. DOI
18. Hu J, Lin K, Cao Y, et al. Adjustable magnetic phase transition inducing unusual zero thermal expansion in Cubic $R\text{Co}_2$ -based intermetallic compounds ($R = \text{Rare earth}$). *Inorg Chem* 2019;58:5401-5. DOI
19. Yang N, Dennis K, McCallum R, Kramer M, Zhang Y, Lee P. Spontaneous magnetostriction in $R_2\text{Fe}_{14}\text{B}$ ($R = \text{Y}, \text{Nd}, \text{Gd}, \text{Tb}, \text{Er}$). *J Magn Magn Mater* 2005;295:65-76. DOI
20. Kuchin A, Medvedeva I, Gaviko V, Kazantsev V. Magnetovolume properties of $\text{Y}_2\text{Fe}_{17-x}\text{M}_x$ alloys ($M = \text{Si}$ or Al). *J Alloys Compd* 1999;289:18-23. DOI
21. Cao Y, Lin K, Khmelevskiy S, et al. Ultrawide temperature range super-invar behavior of $R_2(\text{Fe},\text{Co})_{17}$ materials ($R = \text{Rare Earth}$). *Phys Rev Lett* 2021;127:055501. DOI
22. Weiss RJ. The origin of the 'invar' effect. *Proc Phys Soc* 1963;82:281-8. DOI
23. Fang C, Wang J, Hong F, et al. Tuning the magnetic and structural transitions in TbCo_2Mn_x compounds. *Phys Rev B* 2017;96:064425. DOI
24. Bloch D, Lemaire R. Metallic alloys and exchange-enhanced paramagnetism. application to rare-earth-cobalt alloys. *Phys Rev B* 1970;2:2648-50. DOI
25. Duc NH, Goto T. Handbook on the physics and chemistry of rare earths. Amsterdam: Elsevier B.V.; 1999. pp. 1-413.
26. Inishev AA, Gerasimov EG, Mushnikov NV, Terent'ev PB, Gaviko VS. Structure, magnetic and magnetocaloric properties of nonstoichiometric TbCo_2Mn_x compounds. *Phys Met Metallogr* 2018;119:1036-42. DOI
27. Gerasimov E, Inishev A, Mushnikov N, Terentev P, Gaviko V, Anikin M. Magnetocaloric effect, heat capacity and exchange interactions in nonstoichiometric $\text{Er}_{0.65}\text{Gd}_{0.35}\text{Co}_2\text{Mn}$ compounds. *Intermetallics* 2022;140:107386. DOI
28. Bentouaf A, Mebsout R, Rached H, Amari S, Reshak A, Aïssa B. Theoretical investigation of the structural, electronic, magnetic and elastic properties of binary cubic C15-Laves phases TbX_2 ($X = \text{Co}$ and Fe). *J Alloys Compd* 2016;689:885-93. DOI
29. Gerasimov E, Inishev A, Terentev P, Kazantsev V, Mushnikov N. Magnetostriction and thermal expansion of nonstoichiometric TbCo_2Mn_x compounds. *J Magn Magn Mater* 2021;523:167628. DOI
30. Koley B, Ghanta S, Misra S, Jana PP. $\text{Rh}_8\text{Cd}_{43}$: a rhombohedral variant of a cubic giant cell structure. *J Alloy Compd* 2017;695:3760-6. DOI

Research Article

Open Access



Crystallographic variant mapping using precession electron diffraction data

Marcus H. Hansen¹, Ainiu L. Wang¹, Jiaqi Dong¹, Yuwei Zhang², Tejas Umale¹, Sarbajit Banerjee^{1,3}, Patrick Shamberger¹, Matt Pharr², Ibrahim Karaman¹, Kelvin Y. Xie¹

¹Department of Materials Science and Engineering, Texas A&M University, College Station, TX 77843, USA.

²Department of Mechanical Engineering, Texas A&M University, College Station, TX 77843, USA.

³Department of Chemistry, Texas A&M University, College Station, TX 77843, USA.

Correspondence to: Prof. Kelvin Y. Xie, Department of Materials Science and Engineering, Texas A&M University, College Station, TX, 77843, USA. E-mail: kelvin_xie@tamu.edu

How to cite this article: Hansen MH, Wang AL, Dong J, Zhang Y, Umale T, Banerjee S, Shamberger P, Pharr M, Karaman I, Xie KY. Crystallographic variant mapping using precession electron diffraction data. *Microstructures* 2023;3:2023029. <https://dx.doi.org/10.20517/microstructures.2023.17>

Received: 15 Apr 2023 **First Decision:** 4 May 2023 **Revised:** 7 Jun 2023 **Accepted:** 19 Jun 2023 **Published:** 5 Jul 2023

Academic Editor: Xiaozhou Liao **Copy Editor:** Fangyuan Liu **Production Editor:** Fangyuan Liu

Abstract

In this work, we developed three methods to map crystallographic variants of samples at the nanoscale by analyzing precession electron diffraction data using a high-temperature shape memory alloy and a VO₂ thin film on sapphire as the model systems. The three methods are (I) a user-selecting-reference pattern approach, (II) an algorithm-selecting-reference-pattern approach, and (III) a *k*-means approach. In the first two approaches, Euclidean distance, Cosine, and Structural Similarity (SSIM) algorithms were assessed for the diffraction pattern similarity quantification. We demonstrated that the Euclidean distance and SSIM methods outperform the Cosine algorithm. We further revealed that the random noise in the diffraction data can dramatically affect similarity quantification. Denoising processes could improve the crystallographic mapping quality. With the three methods mentioned above, we were able to map the crystallographic variants in different materials systems, thus enabling fast variant number quantification and clear variant distribution visualization. The advantages and disadvantages of each approach are also discussed. We expect these methods to benefit researchers who work on martensitic materials, in which the variant information is critical to understand their properties and functionalities.

Keywords: Crystallographic variant mapping, precession electron diffraction (PED), image similarity quantification, *k*-means



© The Author(s) 2023. **Open Access** This article is licensed under a Creative Commons Attribution 4.0 International License (<https://creativecommons.org/licenses/by/4.0/>), which permits unrestricted use, sharing, adaptation, distribution and reproduction in any medium or format, for any purpose, even commercially, as long as you give appropriate credit to the original author(s) and the source, provide a link to the Creative Commons license, and indicate if changes were made.



INTRODUCTION

The martensitic transformation is an important phenomenon, which is widely observed in many metals [e.g., steels, shape memory alloys (SMAs), *etc.*]^[1-5] and ceramics (e.g., ZrO₂, VO₂, *etc.*)^[6-8]. During a martensitic transformation, the martensite grains exhibit a well-defined crystallographic orientation relationship with the parent austenite grains. For example, in Ni_{36.5}Ti_{48.5}Hf₁₅ SMAs, the orientation relationship between the B2 austenite and B19' martensite is described as [100]B2//[100]B19' and (001)B2//(011)B19'^[9]. Moreover, although the number of martensite grains in the same prior austenite grain can be numerous, the martensite variant number is limited. Theoretical predictions based on the lattice correspondences of B2 and B19 showed that 12 martensite variants are permitted^[10]. Note that not all 12 martensite variants will show up due to self-accommodation constraints^[10]. For example, only four martensite variants were observed in a solution-treated Ni_{50.3}Ti_{29.7}Hf₂₀ SMA, and there are well-defined orientation relationships between the martensite variants^[11].

The transformation behavior and properties of solid-state phase change materials are dictated by their structure and substructure (e.g., martensite size, variant numbers, orientation relationship, the presence/absence of internal twins, *etc.*). However, martensite characterization, in particular identifying the martensite variant number and orientation relationship, has posed a challenge using conventional microscopy techniques. Traditional transmission electron microscopy (TEM) imaging can reveal the size of martensite grains but provides no information on the number of martensite variants and their distribution^[12,13]. Electron backscatter diffraction (EBSD) can be used to map martensite variants, but the orientation maps are generally very noisy, with low indexing rates^[14]. Because of its limited resolution, EBSD also fails to capture the crystallographic information if the martensite grains are small (e.g., plates or laths < 150 nm in width)^[14]. Hence, there is a demand for techniques that can efficiently reveal martensite variant information with high spatial resolution.

Precession electron diffraction (PED) is a powerful characterization technique to reveal the crystal structure and orientation information at the nanoscale^[15-22]. The electron beam in TEM is converged to a small probe (~ 1-3 nm) and rastered on the specimen. Precession (typically 0.3-0.8°) is applied to excite higher-order reflections and to reduce the dynamical effect^[15,23]. The experimentally acquired diffraction patterns from each pixel are compared to the simulated diffraction patterns in a database to determine the crystal structure and orientation. The information is then used to create phase (crystal structure) and orientation maps. Naturally, the PED should be the ideal technique to obtain the martensite variant information in various materials. Unfortunately, there are several associated challenges. First, many martensite grains contain high-density twins, which leads to additional spots (and streaking) in diffraction patterns^[11]. The simulated diffraction patterns in the database assume single crystals. Thus, the experimentally acquired diffraction patterns that contain both diffraction spots from the matrix and the twin cannot find a good match in the database and are considered bad indexing. Second, orientation indexing is generally poor for low-symmetry crystals (monoclinic, triclinic, *etc.*) in PED because the small differences between different sets of lattice planes cannot be easily distinguished by the orientation indexing software. The confusion leads to noisy orientation maps (an example, see [Figure 1](#)).

In this work, by taking advantage of the superior spatial resolution and the diffraction information from each pixel in PED, we developed three methods to create “crystallographic variant maps”. All methods identify the crystallographic variants by comparing the diffraction patterns in the PED data, with the first approach more manual and the second and third more automatic. The advantages and disadvantages of each approach are described. Different methods to quantify the similarity between diffraction patterns, as well as their influence on the final crystallographic variant maps, are also discussed. These new semi-

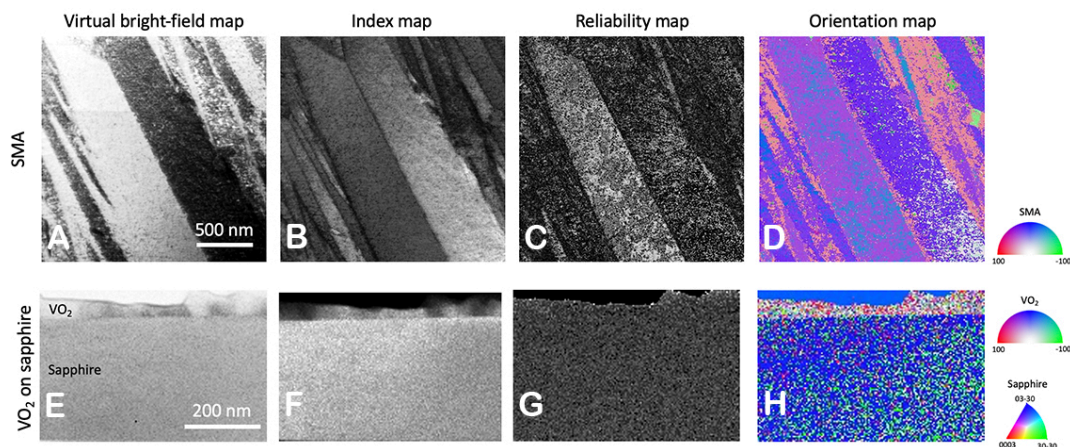


Figure 1. (A) VBF, (B) index, (C) reliability, and (D) orientation maps of the SMA sample. (E) VBF, (F) index, (G) reliability, and (H) orientation maps of the VO₂ on sapphire sample. Note the reliability and orientation maps are noisy in both samples.

automatic crystallographic mapping methods are open-source, easy to use, and less prone to human errors and can be useful tools for researchers who work on martensitic material systems.

MATERIALS AND METHODS

The two model systems we use in this study to develop the crystallographic variant mapping methods are (1) a Ni_{50.3}Ti_{29.7}Hf₂₀ SMA and (2) a VO₂ thin film deposited on a *c*-cut monocrystalline sapphire substrate. Both samples are martensitic at room temperature. The Ni_{50.3}Ti_{29.7}Hf₂₀ SMA has a monoclinic crystal structure, with $a = 3.052 \text{ \AA}$, $b = 4.089 \text{ \AA}$, $c = 4.887 \text{ \AA}$, and $\beta = 102.91^\circ$. The VO₂ also has a monoclinic crystal structure, with $a = 5.752 \text{ \AA}$, $b = 4.538 \text{ \AA}$, $c = 5.383 \text{ \AA}$, and $\beta = 122.65^\circ$ ^[12]. The *b*-axis of VO₂ is parallel to the *c*-axis of sapphire (hexagonal crystal structure, $a = 4.760 \text{ \AA}$ and $c = 12.994 \text{ \AA}$)^[24]. The detailed processing information of these samples can be found in our previous work^[11,25]. SMAs are known for their shape memory effect and super-elastic behavior, which make them widely used in mechanical, aerospace, and biomedical applications^[4,26]. VO₂ undergoes an insulator-to-metal transition when heated up above the phase transformation temperature and is a promising material for neuromorphic computing^[27,28]. The SMA sample was aged at 550 °C for 10 h to grow nanoscale precipitates. The diffraction patterns were obtained with a 200 kV FEI Tecna F20 ST TEM equipped with a NanoMEGAS ASTAR system with a Stingray CCD camera to acquire the PED data. The diffraction pattern acquisition rate is approximately 0.06 s per pixel. The precession angle is 0.3°, and the electron beam spot size is approximately 3 nm. The 0.3° precession angle was selected because it offers a good combination of reduction in the dynamical effect and retaining a decent beam spot size. While larger precession angles can further reduce the dynamical effect, they result in larger beam spot sizes and, consequently, poorer spatial resolution for mapping. The SMA map is 285 × 285 pixels. The diffraction patterns were acquired with a 144 × 144 pixel resolution. The VO₂ on the sapphire map is 150 × 100 pixels. The diffraction patterns were acquired with a 580 × 580 pixel resolution to evaluate the effect of noise and denoise on the final crystallographic variant maps. The denoise was achieved by applying a 5-pixel radius Gaussian filter.

For the PED data reading and then processing, the “.blo” file is loaded and read using Hyperspy, which converts the file into a usable 4D array^[29]. Hyperspy is an open-source Python library that provides tools to analyze multi-dimensional data, such as a function to read “.blo” files.

Regarding crystallographic variant mapping, three methods were developed. Both the first and second methods rely on comparing the diffraction patterns of each pixel to the reference patterns from the same PED dataset. The first method is more manual in that it requires the user to first choose the reference patterns. For each diffraction pattern in the dataset, the highest similarity value between all the reference patterns is used to determine which crystallographic variant it is most similar to. A crystallographic variant map is then generated based on the highest similarity values at each location in the data. The second method is more automatic, in which the algorithm will create new references when the similarity values between the test pattern and the existing reference patterns are lower than a threshold. In the first two methods, the Euclidean distance, Cosine, and Structural Similarity (SSIM) algorithms were used to quantify the similarity values between the diffraction patterns of each pixel to references.

The Euclidean distance algorithm^[30] flattens the 2D image arrays to create 1D number arrays. The 1D number arrays can be viewed as vectors. For 144×144 pixel resolution diffraction patterns, the i value is 20,736 (i.e., 144^2). Hence the 1D number arrays correspond to vectors in 20,736 dimensions. The Euclidean distance, $d(u, v)$, between the test diffraction pattern and the reference pattern is calculated as the distance between the two vectors in 20,736 dimensions, which is expressed as $d(u, v) = \sqrt{\sum_{i=1}^n (u_i - v_i)^2}$, where u and v are intensity values of each pixel in the test and reference diffraction patterns, respectively. In PED, the diffraction patterns are stored as 8-bit images with the values of u and v ranging from 0 to 255. To turn the Euclidean distances into similarity values that range from 0 to 1, we describe Euclidean similarity ($S_{Euclidean}$) as $S_{Euclidean} = 1 - \frac{d(u,v)}{|u|+|v|}$, where $|u|$ and $|v|$ are the magnitudes of the vectors corresponding to the test and reference patterns, respectively. The magnitude is calculated as $|u| = \sqrt{\sum_i^n u_i^2}$. The same applies to v in the reference pattern. A $S_{Euclidean}$ value of 1 indicates that the test and reference diffraction patterns are identical. For diffraction patterns acquired with 580×580 pixel resolution, the i value is 336,400 (i.e., 580^2), and the vectors are 336,400 dimensional. The Euclidean distances and the similarities are calculated in the same way as described above.

The Cosine image comparison method^[31] is similar to the Euclidean distance algorithm. The 2D image arrays are also transformed into 1D arrays (i.e., vectors at high dimensions). The Cosine method uses the angle between the two high-dimensional vectors describing the test and reference patterns. If the cosine angle between the arrays is low, the two images are similar. The Cosine similarity (S_{Cosine}) is calculated as $S_{Cosine} = 1 - \frac{|u \cdot v|}{|u||v|}$, where $u \cdot v$ is the dot product between the test (u) and reference (v) diffraction patterns. The S_{Cosine} value also ranges between 0 and 1, and a value of 1 means that the two images are the same and the angle between the corresponding two vectors is 0.

The SSIM image comparison method measures the structural similarity between two images (the reference and test diffraction patterns in this work), taking into account luminance, contrast, and structure^[32]. Luminance (l) measures the brightness difference between the two images and is defined as $l(x, y) = \frac{2\mu_x\mu_y + c_1}{\mu_x^2 + \mu_y^2 + c_1}$, where μ_x and μ_y are the pixel intensity means of two images x and y , and c_1 is a constant. Contrast (c) captures the variation of brightness in the images and is defined as $c(x, y) = \frac{2\sigma_x\sigma_y + c_2}{\sigma_x^2 + \sigma_y^2 + c_2}$, where σ_x and σ_y are the pixel intensity variances of two images x and y , and c_2 is also a constant. The structure (s) captures the patterns and texture in the image and is defined as $s(x, y) = \frac{\sigma_{xy} + c_3}{\sigma_x\sigma_y + c_3}$, where σ_{xy} is the pixel intensity covariance of images x and y , and c_3 is also a constant. The SSIM similarity combines the above measurements and is defined as $SSIM(x, y) = l(x, y) \cdot c(x, y) \cdot s(x, y)$. Similar to $S_{Euclidean}$ and S_{Cosine} , $SSIM(x, y)$ also ranges from 0 to 1, and

a value of 1 indicates that the two compared images are identical.

In the third crystallographic variant mapping method, the k -means method^[33] was used to cluster the diffraction patterns into different groups, with each group representing one crystallographic variant. The algorithm uses the *VGG16 Keras* model (a pre-trained deep learning model that consists of 16 convolutional layers and three fully connected layers used for feature extraction) to reduce all diffraction patterns in a dataset into feature vectors^[34]. The feature vectors capture key characteristics of each diffraction pattern, including structure and orientation. Next, the feature vectors are reduced from 4,096 to 100 components, each using kernel principal component analysis (kernel PCA) to lower the amount of data processed in the next step while retaining key information. Kernel PCA is a dimensionality reduction technique that uses kernel methods to transform nonlinear data^[35]. These vectors are input into a k -means++ algorithm (an extension of conventional k -means but with much better with centroid initialization)^[36]. The algorithm then sorts the vectors into k clusters, which are mapped to create a similarity map. For each k -value, the inertia (the sum of the squared distances of samples to their closest cluster centroid) is also calculated and shown in an “elbow graph” that can be used to manually determine an optimal k -value.

RESULTS AND DISCUSSION

Conventional PED characterization of the model systems

Figure 1 shows the virtual bright-field (VBF), index, reliability, and orientation maps of the SMA and VO₂ on sapphire, which are the model systems of this study. The VBF images are formed using the intensity of the direct beam in diffraction patterns and are similar to the conventional bright-field TEM micrographs but with less dynamical effect due to the beam precession. The index map is similar to the band contrast map in EBSD, in which brighter pixels indicate better matches between the experimentally acquired diffraction pattern and the simulated pattern. The reliability map is obtained by calculating the ratio of similarities between the best and second-best matches obtained through template matching. Brighter pixels in the reliability map indicate a higher level of confidence and reduced ambiguity between the best and second-best matches in orientation indexing. The concept of “reliability” will serve as a metric to assess the quality of our crystallographic mapping in subsequent sections of this work.

The SMA sample (B19', monoclinic crystal structure) shows a typical martensitic microstructure where the martensite grains are plate-like [Figure 1A]. The martensite plate thickness varies from tens to hundreds of nanometers. The corresponding index, reliability, and orientation maps [Figure 1B-D] show that multiple martensite variants exist in the sample, but the result is noisy. A VO₂ (monoclinic crystal structure at room temperature) thin film grows epitaxially on c -cut sapphire^[37], which exhibits three crystallographic variants^[38]. The VBF in Figure 1E shows that the VO₂ film is approximately 50-100 nm thick. The corresponding index, reliability, and orientation maps [Figure 1F-H] are extremely noisy, and the variants of VO₂ cannot be identified at all. The poor indexing of the martensitic SMA and VO₂ may be caused by the low symmetry nature of their monoclinic crystal structure, where the spacing and angles of different lattice planes are close to each other, leading to confusion when the software does the diffraction pattern indexing. Consequently, there is a demand for new methods to better illustrate the distribution of crystallographic variants in this wide group of materials.

Method 1: user-selecting-reference-pattern approach

In this method, the user will first peruse the dataset to identify how many crystallographic variants are present in the dataset and then select a reference pattern from each variant. We observed no apparent variation in the diffraction patterns among pixels within each crystallographic variant. This allows high flexibility in selecting the reference pattern for each variant by the user. Next, the diffraction pattern from

each pixel will be compared to all reference patterns, and the one with the highest similarity value will be used for the variant assignment of pixels. Each variant is represented by a color in the map. Before going into the detailed mapping results using the first method, we will briefly discuss similarity quantification using Euclidian distance, Cosine, and SSIM algorithms.

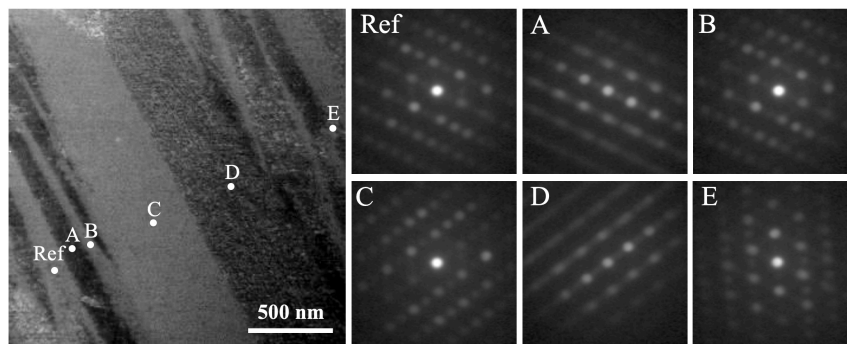
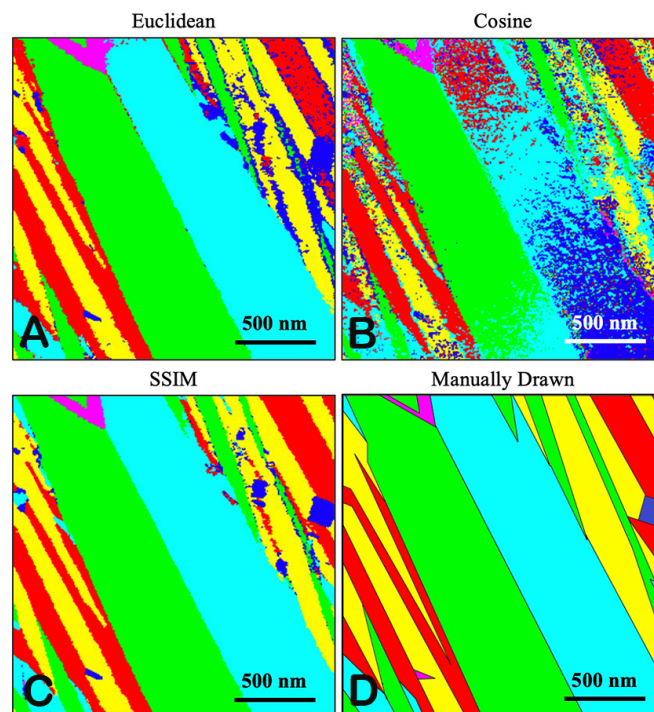
Figure 2 shows the VBF of the SMA sample (same as **Figure 1A** but with some brightness and contrast adjustment) and diffraction patterns from various martensite grains. One of the diffraction patterns was selected as the reference, whereas the others were compared to the reference. By visual inspection, it can be seen that the *Ref* and *B* patterns are from the same crystallographic variant, while each of the other patterns represents unique variants. Hence, we expect *Ref* and *B* patterns to display the highest similarity. The similarity results, calculated by Euclidian distance, Cosine, and SSIM algorithms, are shown in **Table 1**. Each comparison method returns a normalized similarity value ranging from 0 to 1. A 0 means the compared images are completely dissimilar, and a 1 means that they are exactly the same. As expected, diffraction pattern *B* has the highest similarity with the reference pattern for all three similarity methods. A major difference between the different methods is the overall spread in the similarity values between the patterns. Euclidean has a similarity value range of 0.081, Cosine has a small range of 0.026, and SSIM has the largest range of 0.137. We further examine the similarity comparison quality by calculating the reliability values. The reliability is calculated by dividing the highest similarity by the second highest similarity. Larger values indicate higher reliability. The reliability of the Euclidean, Cosine, and SSIM methods are 1.044, 1.006, and 1.083, respectively. The small range and low reliability for the Cosine algorithm may lead to inconclusive results when the two diffraction patterns are similar, which will be demonstrated shortly.

Figure 3 shows the crystallographic variant maps generated via the Euclidean distance [**Figure 3A**], Cosine [**Figure 3B**], and SSIM [**Figure 3C**] algorithms, along with a manually drawn map [**Figure 3D**]. The manually drawn map is created by a person inspecting the dataset to determine the variant regions and is treated as the baseline. Both the Euclidean and SSIM maps are exceptionally close to the manually drawn map. The four predominant variants (red, yellow, green, and cyan in color) and two minor variants (blue and magenta in color) are clearly revealed. Note that the Euclidean map is a bit noisy in the upper right region, while the SSIM maps provide a cleaner map. Unfortunately, the Cosine algorithm produced poor results. The map is noisy, and the large cyan variant in the center is split into three separate variants. This may be due to the varying diffraction pattern intensity along the variant. When generating the crystallographic maps using our methods [**Figure 3A-C**], the colors are selected on a hue saturation value (HSV) color wheel and spaced equally apart based on the number of reference points to distinguish them from each other. The colors were adjusted manually for clarity as needed. Generating the above maps [**Figure 3A-C**] only took tens of seconds or a few minutes using a computer with an Intel i7 13700K CPU and Nvidia RTX 3080 GPU, but it took a student several hours to generate the manually drawn map [**Figure 3D**].

To investigate the effect of noise of the diffraction patterns on the similarity quantification and the resultant crystallographic orientation maps, we used the VO₂ thin film deposited on a *c*-cut monocrystalline sapphire. The diffraction patterns were acquired with 580 × 580 resolution. The 144 × 144 diffraction pattern resolution in the previous SMA example was a result of binning the 580 × 580 original data by the NanoMEGAS commercial software during the data acquisition. Hence, the 580 × 580 resolution diffraction patterns in this case study are much noisier. **Figure 4** shows the VBF of the VO₂ thin film on the sapphire substrate with diffraction patterns taken from different pixels. A diffraction pattern from the sapphire substrate was selected as the reference pattern. The diffraction patterns from pixels A, B, C, and D are from sapphire, VO₂ variant 1, VO₂ variant 2, and vacuum, respectively. Since diffraction pattern A was also taken

Table 1. Euclidean distance, Cosine, and SSIM similarity values compared to the reference pattern, along with the reliability values, in the SMA sample

Diffraction pattern	Similarity method		
	Euclidean	Cosine	SSIM
A	0.904	0.971	0.834
B	0.964	0.997	0.903
C	0.918	0.986	0.777
D	0.883	0.986	0.766
E	0.923	0.991	0.820
Reliability	1.044	1.006	1.083

**Figure 2.** VBF image of the SMA sample (left) and the selected diffraction patterns (right) for similarity quantification.**Figure 3.** Crystallographic variant maps of the SMA sample generated using the (A) Euclidean distance, (B) Cosine, and (C) SSIM algorithms. (D) A manually drawn crystallographic variant map of the same area serving as a baseline.

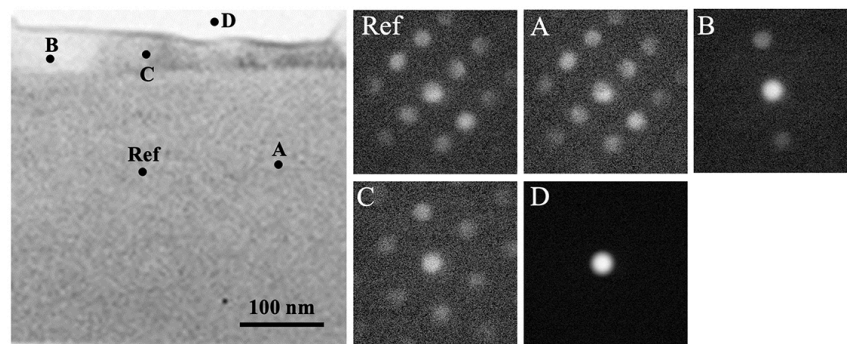


Figure 4. VBF image of VO₂ thin film on sapphire (left) and the selected diffraction patterns (right) for similarity quantification.

from the sapphire substrate, it is expected to have the highest similarity with the reference pattern. Diffraction pattern D was taken from the vacuum, in which there is only a direct beam without a diffracted beam; it is expected to have the least similarity with the reference pattern. Table 2 summarizes similarity values calculated between the selected diffraction patterns compared to the reference pattern using the Euclidean distance, Cosine, and SSIM algorithms. The Euclidean similarity shows the highest value for A and the lowest for D, as expected. The Cosine algorithm produced a similar distribution as the highest value for A and lowest for D while switching the order for B and C. In contrast, the SSIM method comparison had low overall similarity values and ranked pattern B higher than A. We also note that all the similarity values calculated here are generally lower than the binned case (the SMA example). This observation has two important implications. First, the presence of noise decreases the similarity values, although the two diffraction patterns are visually similar. Second, the presence of noise, though not significant to human eyes, can assign higher similarity values even to the visually dissimilar diffraction patterns.

As expected, the generated similarity maps generally display poor quality [Figure 5]. The Euclidean distance map [Figure 5A] is the best out of the three algorithms. The vacuum (black), sapphire substrate (red), and two variants of VO₂ (blue and green) were identified, but small parts VO₂ thin film were wrongly identified as the sapphire substrate. Note that there should be three variants of VO₂ on *c*-cut sapphire. Only two were captured in the figure due to the small mapping area. In the Cosine map [Figure 5B], large parts of the VO₂ thin film were mistakably identified as the sapphire substrate. The SSIM algorithm [Figure 5C] performed the worst, in which the film and substrate were not distinguished, albeit the two different variants in the VO₂ thin film. These observations suggest that the Euclidean distance method is most noise-tolerant when computing the similarity between two images. The accuracy of the SSIM method can be dramatically affected by noise in the diffraction patterns.

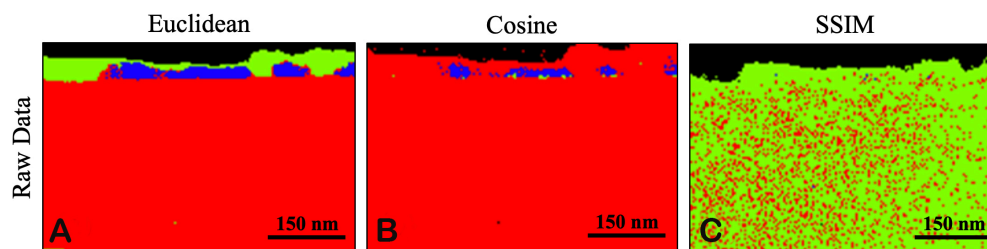
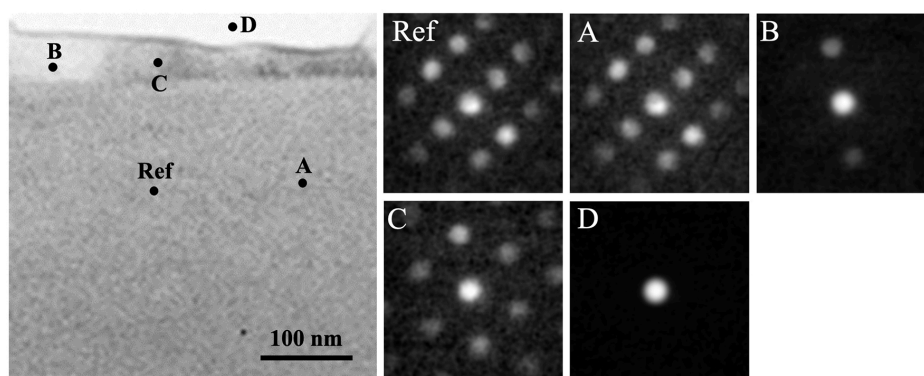
Removing the noise can dramatically improve the accuracy of diffraction pattern similarity quantification, which subsequently helps generate much improved crystallographic variant maps. One common way to denoise is by binning. For example, the NanoMEGAS commercial software can do binning that reduces the diffraction patterns from 580 × 580 to 144 × 144 resolution (an example see the SMA example in this work). Another common method is to apply a Gaussian filter^[39]. Here, we explore the effect of denoise on the similarity quantification and crystallographic variant mapping accuracy using a Gaussian filter. Figure 6 shows the data similar to Figure 4, but a Gaussian filter (radius = 5) was applied to all diffraction patterns in Figure 6. With the Gaussian filter, the overall noise in each diffraction pattern is reduced. The Gaussian filter improved the similarity values for all methods by increasing the range and more accurately identifying the most similar diffraction patterns [Table 3]. The Euclidean similarity between patterns A and Ref is 0.910 after filtering compared to 0.707 using the raw data. The filtered diffraction patterns from the two VO₂

Table 2. Euclidean, Cosine, and SSIM similarity values compared to the reference pattern, along with the reliability values, in the VO₂ on sapphire sample

Diffraction pattern	Similarity method		
	Euclidean	Cosine	SSIM
A	0.707	0.841	0.045
B	0.632	0.807	0.046
C	0.678	0.804	0.033
D	0.421	0.771	0.035
Reliability	1.043	1.042	1.022

Table 3. Euclidean, Cosine, and SSIM similarity values compared to the reference pattern, along with the reliability values, in the VO₂ on sapphire sample denoised with a Gaussian filter applied (radius = 5)

Diffraction pattern	Similarity method		
	Euclidean	Cosine	SSIM
A	0.910	0.919	0.846
B	0.600	0.907	0.666
C	0.723	0.903	0.718
D	0.412	0.284	0.276
Reliability	1.259	1.013	1.178

**Figure 5.** Crystallographic variant maps of the VO₂ thin film on sapphire sample generated using the (A) Euclidean distance, (B) Cosine, and (C) SSIM algorithms.**Figure 6.** VBF image of VO₂ thin film on sapphire (left) and the selected diffraction patterns (right) after Gaussian filtering (radius = 5) for similarity quantification.

variants are very different from the Ref pattern (similarity values are 0.600 and 0.723). The difference is the largest when comparing the vacuum diffraction pattern with the Ref pattern, which yields a similarity value

of only 0.412. The Cosine method correctly identified that pattern A has the highest similarity value (0.919), but the ones from the two VO₂ variants also showed high similarity values (0.907 and 0.903), which may lead to crystallographic variant misidentification. Among the three algorithms, the Cosine method yields the lowest reliability value. This shortcoming of the Cosine method is consistent with the observation made in the SMA samples [Table 1]. The SSIM algorithm yields a similar trend to the Euclidean distance approach but shows low similarity values in absolute numbers. Taken together, reducing noise with a Gaussian filter significantly improved the similarity quantification across the three algorithms.

Reducing noise also improved the crystallographic variant mapping. Figure 7 shows the crystallographic variant maps generated using the Euclidean distance, Cosine, and SSIM algorithms. All methods produced good results where the sapphire substrate (red), VO₂ variants (blue and green), and vacuum (black) are clearly resolved. A manually drawn baseline map is not provided here because the interface between the two VO₂ variants is curved and difficult to draw. A careful examination of the diffraction patterns in this dataset confirmed that the maps shown in Figure 7 are indeed correct.

Method 2: algorithm-selecting-reference-pattern approach

The previous method, though powerful and efficient in generating the crystallographic variant maps, requires user input to select all known crystallographic variants. In some cases, the number and location of the crystallographic variants are unknown. Here, we describe a new method that is built upon the user-selecting-reference-pattern approach (Method 1) but uses the algorithm to select reference patterns to generate crystallographic variant maps.

This method starts at a pixel in the PED data (0, 0) by default or a pixel position chosen by the user. The diffraction pattern corresponding to the pixel is treated as the first reference and is added to a list that will contain reference patterns in the dataset. Each reference pattern in the list represents a unique crystallographic variant. The diffraction patterns from the following pixels will be compared to the reference pattern, and the similarity values (using Euclidean distance, Cosine, or SSIM) will be calculated. The starting pixel will be compared to all other pixels, and the minimum similarity value will be used as the initial cut-off value. If the calculated similarity value of the pixel is greater than the cut-off value, the algorithm treats the pixel the same as the reference pattern variant. If the calculated similarity value is less than the cut-off value, the algorithm will save the diffraction pattern of the pixel as a new reference. The diffraction patterns from the following pixels will be compared to the two references to determine which variant they belong to. This process iterates. If a pixel has one or more similarity values greater than the cut-off, the variant is determined by the one with the highest similarity. If a pixel has all similarity values less than the cut-off, the pixel itself will be added to the reference list and serve as a new variant. This process repeats for all pixels. Once all the pixels have been compared, the cut-off value increases by a step; by default, there are 20 steps between the initial minimum similarity and the maximum similarity values. The process repeats using the increased cut-off value and starting with the list of unique crystallographic variants from the previous iteration.

The above-mentioned mapping method was first used on the SMA dataset to produce a series of similarity maps at varying cut-off values. In the SMA dataset, the (0, 0) point is located at a boundary between two variants that may skew the variant identification. A user-selected point in the middle of a large variant, (116, 168), was used, and the corresponding diffraction pattern serves as the first reference pattern. Figure shows the SSIM similarity maps with various cut-off values ranging from 0.705 to 0.787. The optional initial point and comparison method are the only user inputs using this method. Note the small cut-off range generates very different crystallographic maps. With low cut-off values, such as 0.705, the four predominant

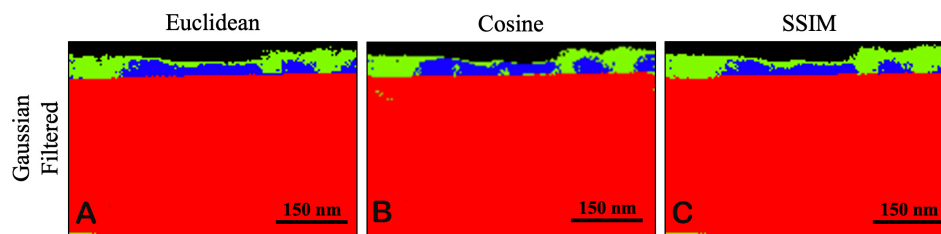


Figure 7. Crystallographic variant maps of the VO₂ thin film on sapphire sample generated using the (A) Euclidean distance, (B) Cosine, and (C) SSIM algorithms. The diffraction patterns in the PED data were filtered with a Gaussian filter (radius = 5) before generating the maps.

variants merged into only two “variants”. With increasing cut-off values, new variants emerge [Figure 8A]. With the cut-off value at 0.769 [Figure 8D], the crystallographic variant map agrees very well with the baseline map in Figure 3D, where both maps contain four predominant and two minor variants [Figure 8D]. Further increasing the similarity threshold splits variants into two or more pseudo-variants that are differentiated by small differences. For example, with the cut-off value of 0.787, a new dark green variant was generated from the yellow variant, and the magenta variant split from the cyan variant [Figure 8F]. The analysis and crystallographic variant mapping of this dataset took approximately 1 hour to complete.

This algorithm was also applied to the Gaussian-filtered VO₂ using the Euclidean similarity method. For this sample, the point (22, 13) in one of the VO₂ variants was selected as the initial point. Figure 9 shows the generated crystallographic variant maps with the cut-off increasing from 0.627 to 0.816. Again, such a relatively narrow range of cut-offs led to drastically different crystallographic variant maps. With a low cut-off value of 0.627, only the sample and vacuum were identified, but with low accuracy [Figure 9A]. Part of the VO₂ thin film was mistakably identified as vacuum. The sapphire substrate and two VO₂ variants were not resolved. The crystallographic variant identification improves as the cut-off value increases. At the cut-off value of 0.735, the most accurate map was generated [Figure 9C]. Further increasing the cut-off results in the variants splitting into pseudo-variants, as shown in Figure 9D and E. The analysis and crystallographic variant mapping of this dataset took approximately 20 min to complete.

The algorithm-selecting-reference-pattern approach can be a useful tool to accurately identify and map similar crystallographic variants in a dataset with minimal user input. Some user input is still needed to select the optional first point and to review the generated similarity maps to determine the ideal similarity cut-off threshold. However, this method is primarily automated and takes much less human effort than the user-selecting-reference-pattern approach (Method 1). Based on the observations made in the above two case studies, it can be seen that small changes in the cut-off value can result in large differences in the final crystallographic variant map output. Lower similarity cut-off values underestimate crystallographic variants, and higher similarity cut-off values overestimate them. User analysis is required to review the generated similarity maps to determine the optimal cut-off value for variant mapping. The computational time varies depending on the size of the dataset, the comparison method used, and the number of variants in the dataset. Typically, it is expected to take between 0.5 and 2 h to generate the similarity maps for a dataset.

Method 3: *k*-means approach

Unsupervised learning is widely used in image segmentation to group different regions in an image based on the pixel intensities and other features^[21,22,40,41]. Martineau *et al.* and Bergh *et al.* successfully applied unsupervised learning techniques (e.g., non-negative matrix factorization and fuzzy clustering) to learn significant microstructural features in the PED data to achieve dimensionality reduction and overlapping

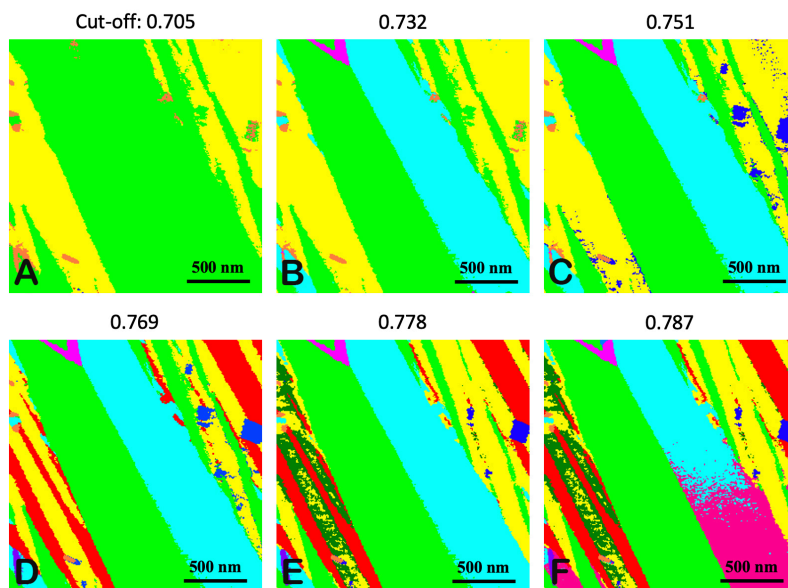


Figure 8. Crystallographic variant maps generated using the SMA dataset and the SSIM comparison method with (A) 0.705, (B) 0.732, (C) 0.751, (D) 0.769, (E) 0.778, and (F) 0.787 cut-off values.

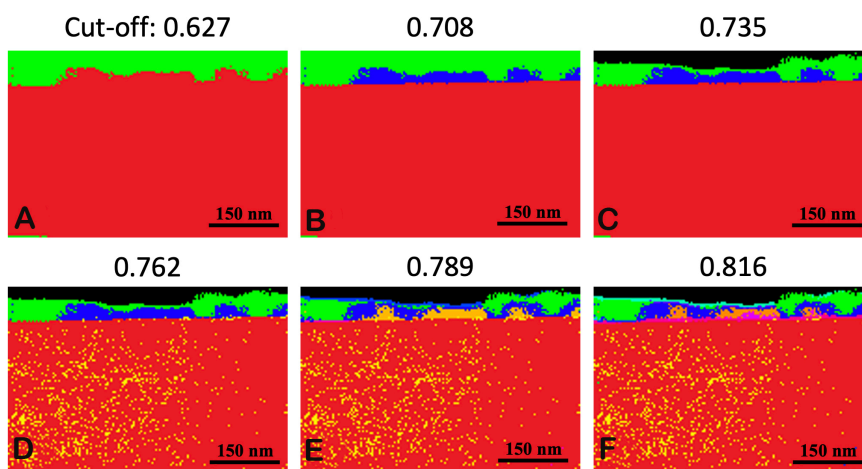


Figure 9. Crystallographic variant maps generated using the Gaussian-filtered VO₂ on sapphire dataset and the Euclidean comparison method with (A) 0.627, (B) 0.707, (C) 0.735, (D) 0.762, (E) 0.789, and (F) 0.816 cut-off values.

pattern unmixing^[21,22]. Here, we employed *k*-means (a common unsupervised learning algorithm) in an approach that is different from the previous two reference pattern-based methods. The advantage of this unsupervised clustering algorithm lies in its ability to partition unlabeled data. After loading the data with *HyperSpy*, each diffraction pattern is processed into a feature vector using the *VGG16* model from *Keras*^[34]. The dimensionality of each feature vector is then reduced with kernel PCA. In the user interface, the “elbow graph” is generated, allowing the user to determine an optimal *k*-value (the number of crystallographic variants in the data set) and input it into the *k*-means algorithm to create a crystallographic orientation map.

The elbow graph and the crystallographic variant maps for the SMA and Gaussian-filtered VO₂ on sapphire datasets with different k -values are shown in Figure 10. The SMA elbow graph [Figure 10A] has a rapidly dropping inertia from $k = 1$ to 3, after which the slope begins to flatten out. This indicates an optimal k -value of 3 or 4, as both the inertia and k at those points are minimized. From the previous discussion, the mapped region shows four predominant and two minor variants. Hence, the optimal k -value from k -means underestimates the variant numbers. Figure 10B shows crystallographic variant maps for $k = 3, 4,$ and 5. In $k = 4$, the four predominant martensite variants were identified, but the two minor variants were lost. When k increased to 5, the minor variants were not revealed. Instead, a high level of noise was observed in the martensite plates. The k -means analysis took roughly 7 h on the SMA dataset. Similar observations were made in the Gaussian-filtered VO₂ on sapphire datasets. The elbow graph in Figure 10C indicates an optimal k -value of 2 or 3. From the previous discussion, the dataset should contain four crystallographic variants (sapphire, two VO₂ variants, and vacuum). Again, the optimal k -value tends to underestimate the variant numbers. Figure 10D shows crystallographic variant maps for $k = 3, 4,$ and 5. In the map with $k = 3$, the sapphire substrate, VO₂ film, and vacuum were identified. However, part of the VO₂ film was erroneously marked as vacuum, as indicated by the arrows. In $k = 4$, the vacuum and thin film regions remain the same, but the sapphire substrate split into two pseudo-variants. In $k = 5$, the substrate region remains split, and the vacuum and thin film regions are accurately revealed, with the second VO₂ variant now showing. The k -means analysis took roughly 40 min on the cropped VO₂ on the sapphire dataset (100 × 100 pixels). Based on the above observations, the k -means method can provide general information on the crystallographic variants in the materials with minimal user input but can fail to capture minor variants and may falsely split variants into pseudo-variants.

It should be noted that while the k -means algorithm is well-suited for identifying similar-sized spherical clusters, it may not be the ideal choice for the SMA and VO₂ model systems. For example, in the case of the VO₂ on the sapphire dataset, sapphire, two variants of VO₂, and vacuum exhibit significant differences in data sizes, which can potentially lead to misidentifications when using $k = 3$ or 4. To address this challenge, alternative unsupervised machine learning techniques, such as density-based spatial clustering of applications with noise (DBSCAN), mean shift, and Gaussian mixture models (GMM), could be considered in future studies for more effective identification of crystallographic variants using the PED data^[42]. Nevertheless, the use of k -means serves as a baseline for comparing the performance of other unsupervised learning techniques in future applications.

Method comparison

Each approach described above has ideal use cases along with advantages and disadvantages. The user-selecting-reference-pattern approach (Method 1) is best suited when the number and location of crystallographic variants in the sample are known. A region can be mislabeled if a reference point for the diffraction pattern is not selected. Inversely, if more than one reference point is selected for a pattern, a variant region can be divided between the selected points. Hence, if the user is not familiar with the material, this method can be prone to human errors. When all the variants are selected correctly, this approach can produce the most accurate similarity maps with the lowest computational cost (generally a few minutes). Among the diffraction pattern similarity quantification algorithms, both the Euclidean and SSIM methods outperform the Cosine method in generating more accurate crystallographic variant maps.

The algorithmic-selecting-reference pattern approach (Method 2) omits the need for the user to select the reference pattern of each variant. This approach can generate similarity maps automatically with only user input to select the ideal cut-off threshold based on the generated maps. The cut-off values in each map govern the new variant generation. Too high of a value will capture the small differences of diffraction patterns within the same variant, thus splitting one variant into two or more pseudo-variants. Too low of a

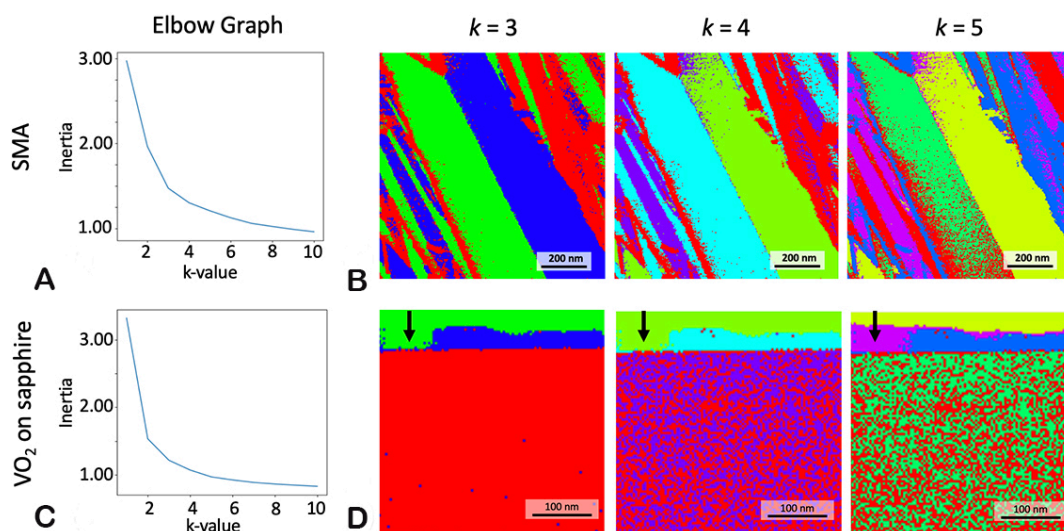


Figure 10. (A) Inertia vs. k -value elbow graph and (B) crystallographic variant maps with $k = 3$, $k = 4$, and $k = 5$ generated using the k -means clustering method on the SMA dataset. (C) Inertia vs. k -value elbow graph and (D) crystallographic variant maps with $k = 3$, $k = 4$, and $k = 5$ generated using the k -means clustering method on a portion of the Gaussian-filtered VO₂ on the sapphire dataset.

value will merge variants with different but similar diffraction patterns. Another challenge is that a small change of the cut-off value can lead to drastically different crystallographic variant maps. Generating the similarity maps with this method usually takes up to an hour on average.

The k -means approach (Method 3) can process the dataset and produce similarity maps automatically at various k -values. The only user input is the k -value (the crystallographic variant number of the mapped area). This number is more intuitive than the cut-off value in the previous method. Moreover, only one round of computation is required to generate the crystallographic orientation maps with various k -values. Changing the k -value and corresponding similarity map for a dataset is near instantaneous, allowing the user to quickly compare maps with varying numbers of diffraction pattern clusters. Unfortunately, the k -means approach tends to generate variant maps with the lowest quality. The generated similarity maps lack fine details, and noise and the number of pseudo-variants increase as the k -value increases. Additionally, the k -means approach is the slowest to compute, as it generally takes several hours to complete the analysis. This approach has room for improvement by experimenting with other unsupervised machine learning models.

These approaches can also be combined to help mitigate the shortcomings of a particular method. For example, in an unknown sample, the algorithm-assisted (Method 2) or the k -means method (Method 3) can be used to determine the approximate variant number and location, which can then be input into the user-assisted algorithm (Method 1), with a manual review, to create an accurate similarity map. It is also worth mentioning that although the methods developed in this work were designed to analyze PED datasets, the same approach can also be applied to the four-dimensional scanning transmission electron microscopy (4D-STEM) datasets, in which the diffraction patterns of each pixel are formed via convergent-beam electron diffraction^[43], to determine the crystallographic variants.

It is also worth noting that creating TEM specimens with generally uniform thickness is imperative for all algorithms to correctly identify the crystallographic variants. Uneven specimen thickness can significantly impact the diffraction patterns of individual pixels. For example, within a single variant, regions with

greater thickness will exhibit decreased diffraction spot intensity and increased background noise^[44]. Thick regions also limit the reduction of the dynamical effect, even with the application of precession^[45]. These factors ultimately affect similarity comparisons and can result in poor crystallographic variant mapping.

CONCLUSIONS

In this work, we developed new crystallographic mapping methods to quantify the variant numbers and reveal the variant distribution by analyzing PED data. An SMA sample and a VO₂ thin film on sapphire sample were used as the model systems. Here are some key take-away messages.

Three methods were developed to map the crystallographic variants of materials using PED data. These methods are (I) a user-selecting-reference-pattern approach; (II) an algorithm-selecting-reference-pattern approach; and (III) a *k*-means approach.

When applying the first two approaches, Euclidean, Cosine, and SSIM were used to calculate the similarities between diffraction patterns. The Euclidean and SSIM algorithms outperform the Cosine method and can generate reliable similarity values for crystallographic variant mapping.

Background noise in diffraction patterns is detrimental to the similarity quantification. Denoising, either via binning or applying a filter (e.g., Gaussian filter), can dramatically improve the crystallographic variant mapping quality.

In the first approach, the user will select the reference patterns, and each reference represents a unique crystallographic variant. All diffraction patterns in the dataset will then be compared to the reference patterns. The one with the highest similarity will be used for assigning the crystallographic variant. This approach is fast and accurate when using the Euclidean and SSIM similarities, but it requires the user to have a good understanding of the sample to correctly select the reference patterns for accurate crystallographic variant map generation.

The second approach is similar to the first one, but the algorithm, instead of the user, selects the reference patterns. When scanning through the dataset, a new reference (representing a new variant) will be created whenever the new diffraction patterns are dissimilar, based on a cut-off value, to the reference patterns stored in the list. Hence, it is a dynamic process. This approach is moderately fast and can generate high-quality crystallographic variant maps. However, the map quality is sensitive to the cut-off value used.

In the third approach, the algorithm uses the *k*-means to cluster similar diffraction patterns into different categories (variants). The only input is the *k*-value (variant number). Unfortunately, this approach is computationally expensive, and the crystallographic variant maps are of low quality. Nevertheless, this approach can still provide some information on the general variant number and distribution, which can be helpful if the user is not familiar with the material system.

DECLARATIONS

Acknowledgments

The authors would like to acknowledge the instrument and technical support from the Microscopy & Imaging Center (MIC) at Texas A&M University.

Authors' contributions

Designed this study and performed data analysis and interpretation: Hansen MH, Wang AL, Xie KY
Prepared the samples and performed data acquisition: Dong J, Zhang Y, Umale T
All authors contributed to the intellectual merit and writing of the manuscript.

Availability of data and materials

The code used for our algorithms can be found on GitHub (<https://github.com/TAMU-MHansen/PED-Similarity-Mapping>). A tutorial on how to use our code can be found on YouTube: https://www.youtube.com/watch?v=Jr_QxVrVcbg.

Financial support and sponsorship

Hansen MH, Wang AL, Dong J, Umale T, Karaman I and Xie KY acknowledge the funding support from the National Science Foundation (NSF-DMR, grant number: 2004752). Zhang Y, Shamberger P, Banerjee S, and Pharr M acknowledge partial support from the Department of Energy under DE-SC0023353.

Conflicts of interest

All authors declared that there are no conflicts of interest.

Ethical approval and consent to participate

Not applicable.

Consent for publication

Not applicable.

Copyright

© The Author(s) 2023.

REFERENCES

1. Nishiyama Z. Martensitic transformation. Amsterdam: Elsevier; 2012.
2. Bhadeshia H, Honeycombe R. Steels: microstructure and properties. Oxford: Butterworth-Heinemann; 2017.
3. Zaeferrer S, Ohlert J, Bleck W. A study of microstructure, transformation mechanisms and correlation between microstructure and mechanical properties of a low alloyed TRIP steel. *Acta Mater* 2004;52:2765-78. DOI
4. Lagoudas DC. Shape memory alloys: modeling and engineering applications. Berlin: Springer; 2008.
5. Otsuka K, Ren X. Physical metallurgy of Ti-Ni-based shape memory alloys. *Prog Mater Sci* 2005;50:511-678. DOI
6. Garvie RC, Nicholson PS. Phase analysis in zirconia systems. *J Am Ceram Soc* 1972;55:303-5. DOI
7. Morin FJ. Oxides which show a metal-to-insulator transition at the neel temperature. *Phys Rev Lett* 1959;3:34-6. DOI
8. Goodenough JB. The two components of the crystallographic transition in VO₂. *J Solid State Chem* 1971;3:490-500. DOI
9. Han X, Zou W, Wang R, Zhang Z, Yang D. Structure and substructure of martensite in a Ti_{36.5}Ni_{48.5}Hf₁₅ high temperature shape memory alloy. *Acta Mater* 1996;44:3711-21. DOI
10. Nishida M, Nishiura T, Kawano H, Inamura T. Self-accommodation of B19' martensite in Ti-Ni shape memory alloys - part I. morphological and crystallographic studies of the variant selection rule. *Philos Mag* 2012;92:2215-33. DOI
11. Dong J, Umale T, Young B, Karaman I, Xie KY. Structure and substructure characterization of solution-treated Ni_{50.3}Ti_{29.7}Hf₂₀ high-temperature shape memory alloy. *Scr Mater* 2022;219:114888. DOI
12. Evirgen A, Karaman I, Santamarta R, Pons J, Hayrettin C, Noebe R. Relationship between crystallographic compatibility and thermal hysteresis in Ni-rich NiTiHf and NiTiZr high temperature shape memory alloys. *Acta Mater* 2016;121:374-83. DOI
13. Karaca H, Saghaian S, Ded G, et al. Effects of nanoprecipitation on the shape memory and material properties of an Ni-rich NiTiHf high temperature shape memory alloy. *Acta Mater* 2013;61:7422-31. DOI
14. Cayron C. What EBSD and TKD tell us about the crystallography of the martensitic B2-B19' transformation in NiTi shape memory alloys. *Crystals* 2020;10:562. DOI
15. Rauch EF, Portillo J, Nicolopoulos S, Bultreys D, Rouvimov S, Moeck P. Automated nanocrystal orientation and phase mapping in the transmission electron microscope on the basis of precession electron diffraction. *Z Kristall* 2010;225:103-9. DOI
16. Rottmann PF, Hemker KJ. Experimental observations of twin formation during thermal annealing of nanocrystalline copper films using orientation mapping. *Scr Mater* 2017;141:76-9. DOI

17. Ma X, Zhao D, Yadav S, Sagapuram D, Xie KY. Grain-subdivision-dominated microstructure evolution in shear bands at high rates. *Mater Res Lett* 2020;8:328-34. DOI
18. Yadav D, Zhao D, Baldwin JK, Devaraj A, Demkowicz MJ, Xie KY. Persistence of crystal orientations across sub-micron-scale “super-grains” in self-organized Cu-W nanocomposites. *Scr Mater* 2021;194:113677. DOI
19. Johnstone DN, van Helvoort ATJ, Midgley PA. Nanoscale strain tomography by scanning precession electron diffraction. *Microsc Microanal* 2017;23:1710-1. DOI
20. Ånes HW, Andersen IM, van Helvoort ATJ. Crystal phase mapping by scanning precession electron diffraction and machine learning decomposition. *Microsc Microanal* 2018;24:586-7. DOI
21. Martineau BH, Johnstone DN, van Helvoort ATJ, Midgley PA, Eggeman AS. Unsupervised machine learning applied to scanning precession electron diffraction data. *Adv Struct Chem Imaging* 2019;3:5. DOI
22. Bergh T, Johnstone DN, Crout P, et al. Nanocrystal segmentation in scanning precession electron diffraction data. *J Microsc* 2020;279:158-67. DOI
23. Portillo J, Rauch EF, Nicolopoulos S, Gemmi M, Bultreys D. Precession electron diffraction assisted orientation mapping in the transmission electron microscope. In: *Materials Science Forum*; 2010. pp. 1-7. DOI
24. Zhang Y, Fincher CD, Gurrola RM, et al. Strategic texturation of VO₂ thin films for tuning mechanical, structural, and electronic couplings during metal-insulator transitions. *Acta Mater* 2023;242:118478. DOI
25. Zhao D, Patel A, Barbosa A, et al. A reference-area-free strain mapping method using precession electron diffraction data. *Ultramicroscopy* 2023;247:113700. DOI
26. Jani JM, Leary M, Subic A, Gibson MA. A review of shape memory alloy research, applications and opportunities. *Mater Des* 2014;56:1078-113. DOI
27. Schofield P, Bradicich A, Gurrola RM, et al. Harnessing the metal-insulator transition of VO₂ in neuromorphic computing. *Adv Mater* 2022:e2205294. DOI
28. Corti E, Gotsmann B, Moselund K, Ionescu AM, Robertson J, Karg S. Scaled resistively-coupled VO₂ oscillators for neuromorphic computing. *Solid State Electron* 2020;168:107729. DOI
29. de la Pena F, Ostasevicius T, Tonaas Fauske V, et al. Electron microscopy (big and small) data analysis with the open source software package hyperspy. *Microsc Microanal* 2017;23:214-5. DOI
30. Wang L, Zhang Y, Feng J. On the Euclidean distance of images. *IEEE Trans Pattern Anal Mach Intell* 2005;27:1334-9. DOI
31. Xia P, Zhang L, Li F. Learning similarity with cosine similarity ensemble. *Inf Sci* 2015;307:39-52. DOI
32. Wang Z, Bovik AC, Sheikh HR, Simoncelli EP. Image quality assessment: from error visibility to structural similarity. *IEEE Trans Pattern Anal Mach Intell* 2004;13:600-12. DOI
33. Lloyd S. Least squares quantization in PCM. *IEEE Trans Pattern Anal Mach Intell* 1982;28:129-37. DOI
34. Gulli A, Pal S. *Deep learning with Keras*. Birmingham: Packt; 2017.
35. Mika S, Schölkopf B, Smola A, Müller K-R, Scholz M, Rätsch G. Kernel PCA and de-noising in feature spaces. In: *advances in neural information processing systems*. Cambridge: MIT Press;1999: pp. 536-42.
36. Arthur D, Vassilvitskii S. k-means++: the advantages of careful seeding. Stanford, 2006. Available from: https://www.researchgate.net/publication/220778887_K-Means_The_Advantages_of_Careful_Seeding [Last accessed on 27 Jun 2023].
37. Zhao Y, Hwan Lee J, Zhu Y, et al. Structural, electrical, and terahertz transmission properties of VO₂ thin films grown on c-, r-, and m-plane sapphire substrates. *J Appl Phys* 2012;111:053533. DOI
38. Fan LL, Wu YF, Si C, Pan GQ, Zou CW, Wu ZY. Synchrotron radiation study of VO₂ crystal film epitaxial growth on sapphire substrate with intrinsic multi-domains. *Appl Phys Lett* 2013;102:011604. DOI
39. Gonzalez RC, Woods RE. *Digital image processing*. Pearson education: India; 2009.
40. Dhanachandra N, Mangle K, Chanu YJ. Image segmentation using k-means clustering algorithm and subtractive clustering algorithm. *Procedia Comput Sci* 2015;54:764-71. DOI
41. Ray S, Turi RH. Determination of number of clusters in K-means clustering and application in colour image segmentation. In: *4th International Conference on Advances in Pattern Recognition and Digital Techniques*. 2023 Jun 17-18; Sydney, Australia. pp. 137-43.
42. Ghahramani Z. Unsupervised learning. In: *Advanced Lectures on Machine Learning*. 2003 Feb 2-14; ML Summer Schools, Canberra, Australia. pp. 72-112 DOI
43. Ophus C. Four-dimensional scanning transmission electron microscopy (4D-STEM): from scanning nanodiffraction to ptychography and beyond. *Microsc Microanal* 2019;25:563-82. DOI PubMed
44. Williams DB, Carter CB. *Transmission Electron Microscopy: Diffraction, Imaging, and Spectrometry*. Springer; 2009.
45. Oleynikov P, Hovmöller S, Zou XD. Precession electron diffraction: observed and calculated intensities. *Ultramicroscopy* 2007;107:523-33. DOI PubMed

Review

Open Access



Physiological and pathological/ectopic mineralization: from composition to microstructure

Yuqing Mu^{1,2,3}, Wendong Gao^{2,3}, Yinghong Zhou^{2,4}, Lan Xiao^{2,3}, Yin Xiao^{1,2,3} 

¹School of Medicine and Dentistry & Menzies Health Institute Queensland, Griffith University (GU), Gold Coast, QLD 4222, Australia.

²The Australia-China Centre for Tissue Engineering and Regenerative Medicine (ACCTERM), Queensland University of Technology, Brisbane, QLD 4000, Australia.

³School of Mechanical, Medical and Process Engineering, Centre for Biomedical Technologies, Queensland University of Technology, Brisbane, QLD 4000, Australia.

⁴School of Dentistry, the University of Queensland, Brisbane, QLD 4006, Australia.

Correspondence to: Prof. Yin Xiao, School of Medicine and Dentistry & Menzies Health Institute Queensland, Griffith University (GU), Gold Coast, QLD 4222, Australia. E-mail: yin.xiao@griffith.edu.au

How to cite this article: Mu Y, Gao W, Zhou Y, Xiao L, Xiao Y. Physiological and pathological/ectopic mineralization: from composition to microstructure. *Microstructures* 2023;3:2023030. <https://dx.doi.org/10.20517/microstructures.2023.05>

Received: 18 Jan 2023 **First Decision:** 8 Mar 2023 **Revised:** 17 May 2023 **Accepted:** 21 Jun 2023 **Published:** 7 Jul 2023

Academic Editors: Xiupeng Wang, Yuxiao Lai **Copy Editor:** Fangling Lan **Production Editor:** Fangling Lan

Abstract

Biom mineralization is a process that leads to the formation of hierarchically arranged structures in mineralized tissues, such as bone and teeth. Extensive research has been conducted on the crystals in bones and teeth, with the aim of understanding the underlying mechanisms of the mineralization process. Pathological/ectopic mineralization, such as kidney stones, calcific tendinitis, and skeletal fluorosis, shares some similar features but different mechanisms to physiological mineralization. A better understanding will provide new perspectives for treating pathological/ectopic mineralization-related diseases. This review provides an overview of the mechanisms of the crystallization and growth of crystals in physiological and pathological conditions from a chemistry perspective. By linking the microstructures and functions of crystals formed in both conditions, potential approaches are proposed to treat pathological/ectopic mineralization-related diseases.

Keywords: Physiological mineralization, pathological/ectopic mineralization, apatite crystals, mineral crystallinity, dental tissues, bone remodeling



© The Author(s) 2023. **Open Access** This article is licensed under a Creative Commons Attribution 4.0 International License (<https://creativecommons.org/licenses/by/4.0/>), which permits unrestricted use, sharing, adaptation, distribution and reproduction in any medium or format, for any purpose, even commercially, as long as you give appropriate credit to the original author(s) and the source, provide a link to the Creative Commons license, and indicate if changes were made.



INTRODUCTION

Biom mineralization, an emerging interdisciplinary field, deals with the formation, structure, and mechanical strength of naturally formed mineralized tissues^[1]. The skeleton of animals provides mechanical support to counteract gravitational forces on land and hydrostatic pressure in the depths of the oceans. As a highly complex and exquisitely organized organ, the skeleton is structurally, and hence mechanically, heterogeneous owing to spatial distributions in the shape, size, and composition of its constituent building blocks, the mineralized collagen fibrils^[2].

Nature produces a diverse assortment of mineralized structures with a high degree of complexity. These hierarchical structures exhibit superior mechanical strength^[3-5] and are, therefore, of great interest to researchers in the disciplines of biotechnology and biomedical engineering. Biom mineralization on a template of organic molecules is used by many organisms to produce inorganic-organic nanocomposites that result in highly ordered multifunctional materials. The biosynthesis of bacterial magnetosome^[6], eggshell^[7], molluscan shell^[8], dental structures^[9], and skeletal system^[10] are all examples of biologically controlled mineral formation through organic/inorganic recognition and interaction. In the skeleton, for example, the organic matrix consists primarily of the fibrous protein collagen and around 10% of other non-collagenous proteins (NCPs)^[11] [Figure 1]. The inorganic phase is composed of tightly packed nanocrystals made of calcium phosphates (CaPs) with the incorporation of a number of essential trace elements.

In the field of biomaterial development, the *ex vivo* bioactivity of the material is often predicted by examining the formation of an apatite layer on its surface in a simulated body fluid (SBF)^[12]. Notably, slight differences in the SAED patterns of SBF-originated apatite on a Titanium substrate and bone apatite resulted from the random and ordered orientations, respectively, of apatite crystals [Figure 2]^[12-14]. However, there are other differences between SBF-derived apatite and bone apatite in terms of possible defects on the lattice of bone apatite due to the incorporation of trace elements in the body and crystal sizes affected by cells and cell-secreted bio-factors^[15,16].

Calcification has been increasingly recognized as an important component to fully understand the pathology of some diseases. For instance, the types of breast cancer have been shown to be related to the properties of calcification in the breast^[17-19]. The utilization of advanced characterization techniques within the field of material science has facilitated significant advancements in our comprehension of the formation of pathological crystals, such as X-ray diffraction (XRD), spectroscopic, and electron microscopic techniques^[20,21]. By comparing to crystals in physiological mineralization, understanding the characteristics and behaviors of crystals involved in pathological or ectopic calcification can offer valuable insights into the underlying mechanisms of calcification-related disorders. This knowledge may enable the development of novel disease management strategies.

Physiological mineralization is a complex process that is essential for the development of well-organized structures in bone and teeth^[22]. The intricate process occurs only in specific regions^[23,24]. The regulation of physiological mineralization is well-coordinated, involving both inhibitory and stimulatory factors. Some proteins, including osteopontin (OPN), matrix Gla protein, and pyrophosphate (PPi), have been identified as inhibitors of mineralization^[22,25]. In contrast, other factors, such as matrix vesicles that contain calcium (Ca) and inorganic phosphate (Pi), apoptotic bodies, and tissue non-specific alkaline phosphatase, have been shown to facilitate the initiation of mineralization^[26-28].

On the other hand, pathological/ectopic mineralization occurs in soft tissues and is associated with disease conditions or medical conditions, such as injury, inflammation, and aging, causing significant morbidity

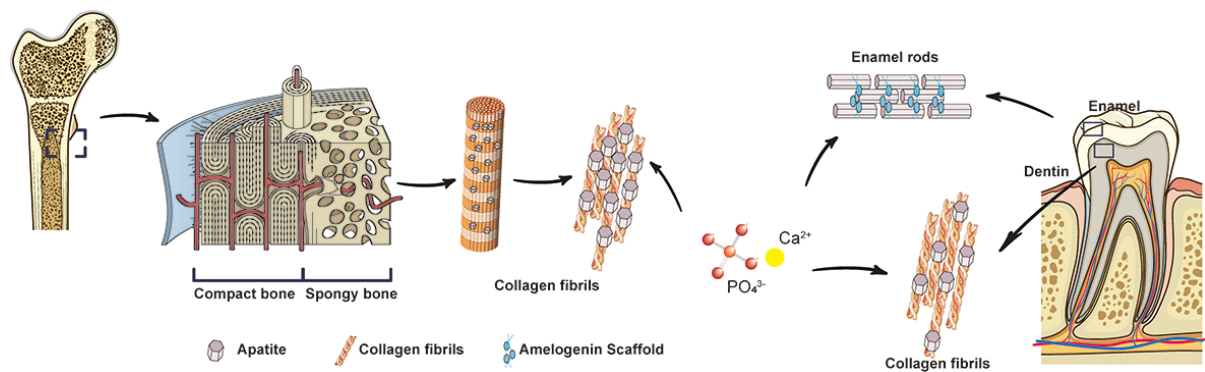


Figure 1. Physiological mineralization, mainly in bone and teeth, forms well-organized structures.

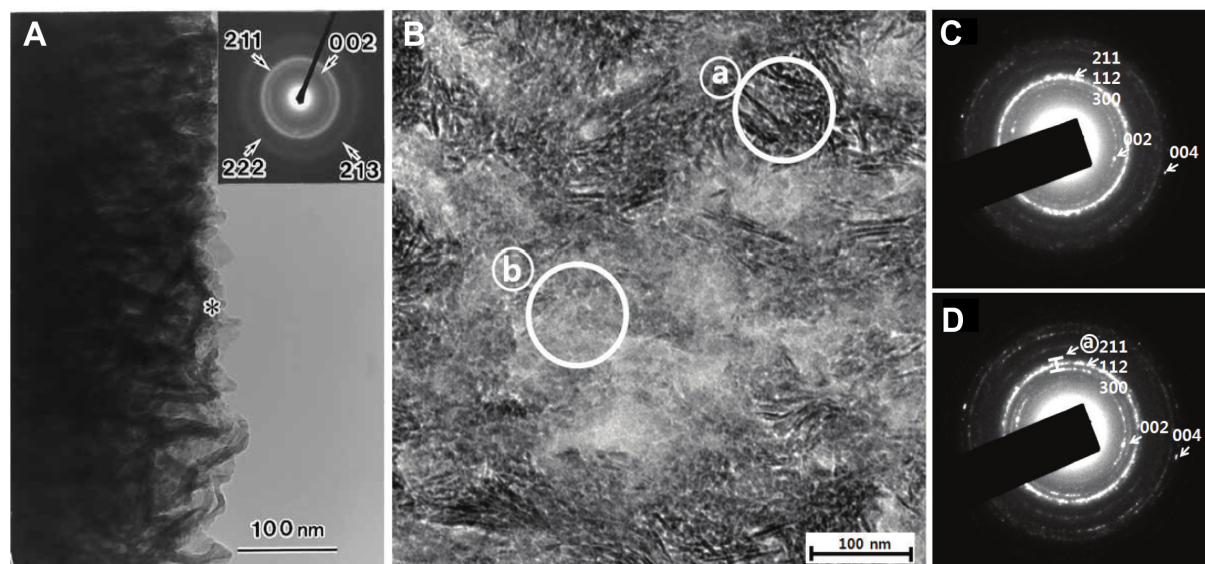


Figure 2. Transmission electron microscope (TEM) photographs of (A) SBF-originated apatite crystals on a Titanium substrate (inset: SAED pattern) (Reproduced with permission from Takadama et al.^[14]. Copyright 2001, John Wiley & Sons), (B-D) apatite crystals from mouse femur and their SAED patterns (Reproduced with permission from Taehoon et al.^[13]. Copyright 2010, SpringerOpen).

and mortality^[29-32]. Such mineralization consists of different Ca-containing minerals, including CaPs, calcium carbonates ($CaCO_3$), and calcium oxalates (CaO_x)^[20,31].

The current treatment of pathological mineralization in soft tissues includes reduced intake of Ca or reduced precipitation of Ca-containing complex. However, there are still no specific and effective treatments to prevent or counteract the condition^[32,33]. Pathological/ectopic mineralization is less understood than physiological mineralization, but the commonalities between physiological and pathological/ectopic mineralization have gradually been recognized over the years^[34-36]. There are still ongoing debates regarding the chemical compositions and crystal structures of pathological crystals, the dynamics of ion transport, the participation of cellular activities, the interactions of pathological crystals with surrounding tissues, and how these contribute to disease progression^[36]. The compositional and structural analysis of pathological mineralization would benefit the development of better disease management through advanced treatment and prevention. In this review, bone and teeth mineralization and crystal structures are recognized as the fundamental and physiological processes in biomineralization.

The comparison is made to unveil the similarities and differences in both physiological and pathological/ectopic mineralization. In addition, current approaches, with a focus on modulating crystal formation and growth on the progression of pathological mineralization, are discussed.

OVERVIEW OF THE PHYSIOLOGICAL MINERALIZATION PROCESS

The mineralization of self-assembled organic matrices results in the formation of hard tissues in the body, and its level (or the proportion of mineral contents in the tissue) varies from around 65% in the bone to close to 100% in dental enamel [Figure 1]^[37,38]. The fundamental form of both bone and teeth crystals is apatite. Its compositions and structures can be modified by accommodating a wide range of ion substitutions via cell uptake^[39,40]. The investigation regarding the nucleation process of apatite in solution started several decades ago, attempting to unveil the mystery of mineralization^[41-45]. Along with the emergence of edge-cutting equipment and the accumulation of knowledge over the years, a multi-stage nucleation process of apatite in aqueous solution was demonstrated to start with the aggregation of charged pre-nucleation complexes, $[\text{Ca}(\text{HPO}_4)_3]^{4-}$ (Ca/P(calcium/phosphorus) = 0.3-0.4)^[46]. After the formation of ribbon-like calcium-deficient octahydrogen phosphates (OCPs), $[\sim\text{Ca}_6(\text{HPO}_4)_4(\text{PO}_4)_2]^{2-}$ (Ca/P = 1.0) and elongated plate-like OCPs, $[\text{Ca}_8(\text{HPO}_4)_2(\text{PO}_4)_4]$ (Ca/P = 1.33) from amorphous calcium phosphates (ACPs), apatite is finally generated^[46]. It has been suggested that the evolution of the OCP structure to apatite occurred through the elimination of the hydrated shell on the surface of the nanocrystalline^[37,47]. The hydrated shell on the surface of freshly precipitated apatite contains exchangeable ionic species and some proteins^[37,48]. During the maturation of apatite in the solution, ions in the hydrated shell are easily exchanged, accompanied by proteins within the shell, and it leads to reduced surface reactivity and increasingly stable apatite^[37,49]. This suggests that metals (such as Ca, magnesium (Mg), sodium (Na), potassium (K), *etc.*), and possibly other ions are incorporated structurally into the collagenous matrices of calcified tissues^[50]. In earlier investigations of the composition of trace elements in human cortical bone and beef tendons, researchers have documented a regularity in the appearance of certain trace metals, namely copper (Cu), iron (Fe), and zinc (Zn)^[23,51,52]. Additionally, non-metal trace element, e.g., fluoride (F), has also been physio-chemically linked with the bone mineral matrix^[53].

Mineralization of bone

A similar crystal formation mechanism was proposed in bone based on the similarity of XRD patterns of bone mineral and crystal formed from the ACP in an aqueous solution^[41-43,45]. Bone minerals can be modeled as carbonate hydroxyapatite (CHAp) with a wide range of substitutions of hydroxide (OH^-) and phosphate (PO_4^{3-}) by carbonate (CO_3^{2-}) on the lattice and the substitutions of Ca^{2+} by other metal ions, such as strontium (Sr^{2+}), Mg^{2+} , *etc.* [Figure 3]^[49,54]. Its composition can vary depending on species, location, diet, sex, age, and pathological conditions^[37,55-57]. The substitution of carbonate results in the contraction of the *a*-axis and the expansion of the *c*-axis of the unit cell, as well as a decrease in crystallinity^[58]. The presence of vacancies on the apatite crystals results in lower binding energies, thus, more soluble than stoichiometric hydroxyapatite (HAp)^[25,59,60]. During the formation of bone minerals, ACP nanospheres formed on the site of bone formation or supplemented through blood are delivered and deposited within the collagen matrix by cells and further transformed into plate-like apatite via intermediates that resemble OCPs^[44,61-63]. While Crane *et al.* (2006) suggest this possibility, the finding remains unrepeated and is not widely accepted^[63]. However, recent evidence has shown the presence of OCPs in bone, specifically in combination with the protein osteocalcin^[64]. This suggests that OCPs may play a role in bone mineral formation, although further research is needed to fully understand this process. Moreover, bone mineralization is much more complicated with the involvement of extensive biological additives, acting as promoters or inhibitors, such as proteins, trace ions, and some small organic molecules^[42,65].

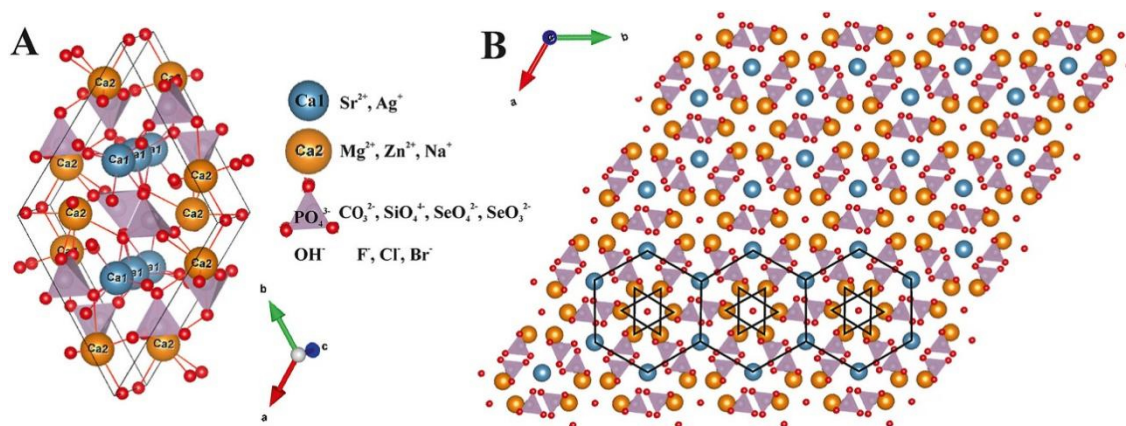


Figure 3. A schematic illustration of the crystal lattice of bone apatite (Reproduced with permission from Ressler et al.^[54]. Copyright 2021, Elsevier). (A) the unit cell of bone apatite; (B) the top view of the lattice of bone apatite.

Based on the discovery and transformation pathway from ACPs to apatite during bone mineralization, additives are believed to get involved by preventing unstable amorphous phases from crystallizing or dissolving before or during transport to the site of interest^[42]. It is also known as the polymer-induced liquid precursor (PILP) process. Numerous studies aimed at identifying influencing factors in the process over the years. For example, many NCPs found in bone growth regions regulate mineralization with acidic amino acid groups through the ability to bind Ca^{2+} , as well as high affinity for collagen fibrils, such as osteonectin and various phosphoproteins^[66-68]. Organic Pi or polyphosphates, as Pi sources, participate in and affect the crystallization process of ACPs in the form of orthophosphates after being digested by alkaline phosphatase^[32,69,70]. PPI, on the other hand, is a well-known inhibitor of apatite crystal formation^[71].

Mineralization of teeth

In general, teeth mineral $[\text{Ca}_{(10-x)}\text{Na}_x(\text{PO}_4)_{(6-y)}(\text{CO}_3)(\text{OH})_{(2-z)}\text{F}_z]$ (x, cation substitutions; y, carbonate substitutions; z, fluorine substitutions) varies from both stoichiometric HAP and bone apatite^[40]. Its chemical composition, the mineralization level of the organic matrix, and crystal size and orientation are tailored to meet different mechanical needs at different locations^[37,72,73]. Enamel and dentin are two kinds of hard tissues in teeth. Dentin is capped by enamel and, in the root, is covered by cementum.

Dentin is less mineralized and shares a similar mineralization pattern with bone, namely matrix-mediated mineralization^[74,75]. It is formed by the mineralization of the dentin matrix (composed of type I collagen), mediated by some non-collagenous matrix proteins (NCPs), such as dentin phosphoprotein (DPP), dentin sialoprotein (DSP), and dentin matrix protein-1 (DMP-1)^[76]. However, unlike bone, little or no remodeling takes place in dentin. Compared to enamel, dentin has a higher capacity for F uptake through systemic ingestion due to its less crystallinity and accumulation through life^[77].

Enamel is the hardest tissue in the vertebrate body, composed of crystalline HAP^[78]. In contrast to the bone, which uses collagen as the substrate for mineralization and goes through remodeling throughout its lifetime, enamel does not contain collagen and does not remodel^[76,79]. During enamel mineralization, the synthesized protein mixture assembles to form a matrix that regulates the precipitation of HAP^[80,81]. Once the full thickness of enamel has been formed, HAP crystals expand slowly into the space previously occupied by matrix proteins and water^[82]. Mature HAP crystals in enamel are ribbon-like fluoridated carbonate HAP, 50-70 nm in width and 20-25 nm in thickness^[83].

Cementum is a thin layer that covers the entire root surface and anchors the roots of teeth to the jaw. Similar to the bone, it is composed of water, an organic matrix (mainly collagen, glycoproteins, and proteoglycans), and minerals and is formed through the formation of HAp in deposited type I collagen by cementoblasts^[84-86]. Compared to dentin (70%) and enamel (> 95%), cementum (40%-50%) is less mineralized^[86]. In addition to HAp, small amounts of ACPs were also found in cementum^[85]. The presence of the amorphous phase results in a greater capacity of cementum for the adsorption of F and other elements over time and readily decalcification in acidic environments^[85]. For example, cementum contains F up to 0.9% ash weight and increases with age^[87]. Regulation of teeth mineralization is, in part, regulated by the ratio of Pi and PPI, as well as other factors, such as genetic modifications, age, diet, oral hygiene, and certain diseases, such as periodontal diseases, caries, root resorption, tumoral lesions, or trauma^[88,89].

Otoconia

Otoconia, which is composed of CaCO₃, is found in the inner ear of humans and other vertebrates. They are positioned to sense stimuli in directions and send signals to the brain to maintain bodily balance^[90]. Similar to the bone, the organic matrix in otoconia determines the orientation, sizes, and shapes of crystals by providing a framework^[91]. Additionally, otoconia contain high levels of Ca, Na, Mg, K, P, sulfur (S), and chloride (Cl)^[90]. However, the underlying molecular etiology remains unknown, neither the functions of otoconial proteins nor the crystal formation.

PATHOLOGICAL (ECTOPIC) MINERALIZATION IN MAJOR ORGANS

Physiological mineralization is restricted within the skeletal system, including bone, teeth, and calcified cartilage^[92]. In contrast, pathological (ectopic) mineralization can occur not only in the skeletal system but also in soft tissues, such as the breast, blood vessels, kidney, pancreas, and prostate, mostly composed of CaPs, CaCO₃, and CaO_x [Figure 4]^[22,31]. There are three structural types of deposits observed in ectopic calcification, single crystals, polycrystalline deposits, and calcified matrix. The specific type and characteristics of the deposits can vary, depending on the tissue and the underlying mechanisms. For example, single crystals are typically small and uniform in size and often are found in tendons and ligaments^[93,94]. The formation of single crystals can be initiated by the presence of specific proteins or molecules that act as nucleation sites. Polycrystalline deposits, on the other hand, consist of multiple small crystals randomly arranged in tissues, such as blood vessels and heart valves^[95]. In contrast, the calcified matrix consists of alternating layers of mineralized and non-mineralized tissues and can be found in a variety of tissues, including cartilage and blood vessels^[96]. Pathological/ectopic calcification occurs in both genetic and acquired clinical conditions and affects the prognosis of diseases^[32,97]. Pathological/ectopic calcification can occur through different mechanisms, depending on the involvement of cells, including cell-induced, cell-controlled, or spontaneously precipitated. For example, vascular calcification can be triggered by damage to the endothelial cells lining the blood vessels, leading to the recruitment and differentiation of smooth muscle cells into osteoblastic cells that actively deposit Ca and Pi^[35]. Cell-controlled calcification occurs with specific mineralization-related factors released by cells in response to injury, inflammation, or bacterial infection^[98,99]. Spontaneous deposition may happen as a result of changes in the environment without the involvement of cells, such as oxidative stress, local pH, and the supersaturation of ions^[100,101]. Understanding the formation, structure, and composition of crystals deposited in the physiological and pathological conditions will aid the development of therapeutic strategies to prevent and/or regulate pathological/ectopic calcification^[31,102] [Table 1].

Bone

Bone tissue undergoes continuous remodeling to maintain its density and strength in a stable state. The bone mineralization process is tightly regulated by osteoblasts (bone-forming cells) and osteoclasts (bone resorption cells). Osteocytes, which are embedded in the bone matrix, also play important roles in

Table 1. A summary of pathological/ectopic mineralization in terms of the composition and the involvement of cells

Tissue	Composition	Involvement of cellular activities	References
Bone	HAp	Cell-induced	[112]
Joint	CPPD, HAp, TCP, OCP, whitlockite, sodium urate	Cell-derived articular cartilage vesicles	[120,123,124,237]
Tendon	Carbonate HAp	Cell-induced	[94,128,130-132]
Teeth	Brushite, dicalcium phosphate dihydrate, OCP, HAp, whitlockite	Cell-mediated	[134,135]
Salivary gland	HAp, whitlockite, brushite, OCP	Unknown	[137-139]
Heart and blood vessel	HAp, whitlockite	Cell-induced	[20,35,140-142]
Kidney	CaOx, CaP, the mixture of struvite magnesium ammonium phosphate, carbonate HAp	Cell-mediated	[151,153-155]
Brain	HAp	Unknown	[171,172]
Ocular	Whitlockite, HAp	Unknown	[20,21]
Breast	CaPs (carbonate HAp and whitlockite), CaO _x	Cell-induced	[182-185]
Pancreas	CaCO ₃	Unknown	[188,189]
Prostate	Carbonate HAp, whitlockite, CaO _x	Cell-mediated	[191,192,238]
Placental	CaPs	Cell-mediated	[194,195]
Lymph nodes	HAp, whitlockite	Unknown	[197,198]

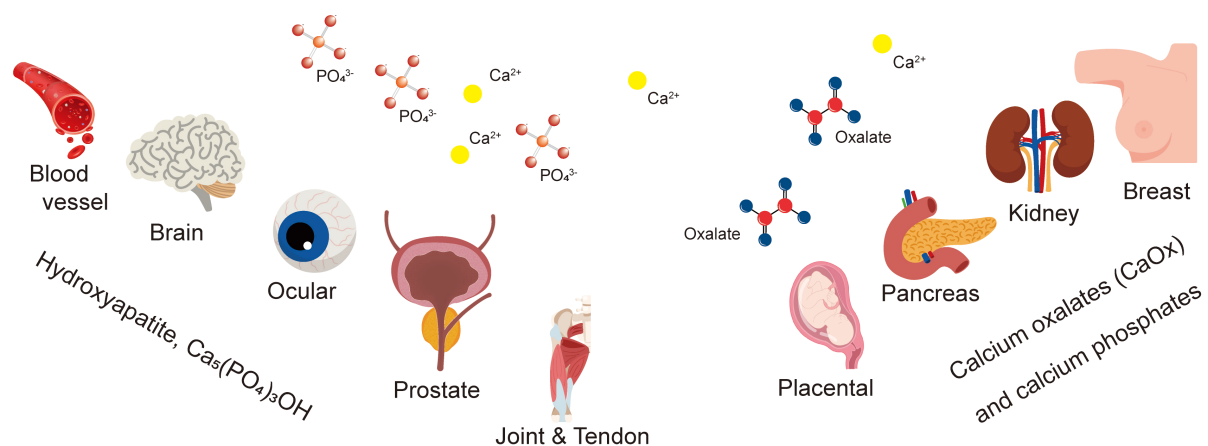


Figure 4. Pathological mineralization in soft tissues (blood vessels, brain, ocular, prostate, joint & tendon, placental, pancreas, kidney, and breast). The major forms of pathological/ectopic mineralization are calcium phosphates, calcium carbonate, and calcium oxalates.

regulating the bone remodeling process. The disruption in the balance between bone resorption and bone formation resulting from several pathological cues will affect bone health, metabolism, or homeostasis and lead to irregular remodeling activity and pathological bone mineralization^[103]. Pathological bone mineralization can be roughly categorized as hypomineralization, hypermineralization, and other abnormal mineralization patterns.

Hypomineralization

Hypomineralization refers to insufficient mineralization of the bone matrix, resulting in reduced bone density and increased fracture risk^[104]. Some several factors and conditions contribute to hypomineralization^[105-107]. Rickets and osteomalacia are examples of pathological hypomineralization conditions^[103]. Rickets, a disorder affecting children, and osteomalacia, its adult counterpart, can be caused by insufficient intake of essential nutrients, such as calcium and vitamin D, and hereditary factors^[103]. The

deficiency of calcium and vitamin D can result in a reduction in Ca that leads to impaired bone mineralization and a higher proportion of organic matrix compared to inorganic mineral content, which contributes to reduced mechanical strength and increased fracture risk^[105].

Besides, certain genetic disorders can induce abnormal bone development, such as osteogenesis imperfecta, a condition characterized by fragile bones due to the mutation in genes responsible for collagen production that leads to aberrant collagen production, and hypophosphatasia, an inherited disorder that results from a deficiency in alkaline phosphatase, which is essential for proper bone mineralization^[106,108].

Hypermineralization

Hypermineralization, characterized by abnormally high bone mineral density (BMD), is associated with hereditary and nonhereditary disorders^[104]. For example, in hereditary disorders, such as osteopetrosis and osteosclerosis, a dramatic decrease in osteoclast number or osteoclast activity and increased bone mass and density were observed. At the crystal level, low remodeling activities alter the crystal size/shape and increase the amount of highly mineralized bone tissues, leading to decreased toughness of bone tissues and thus increasing the risk of fracture^[104]. Skeletal fluorosis is another nonhereditary disorder associated with excessive ingestion of F. The accumulation of F results in abnormal bone deposition and adsorption. At the crystal level, the hydroxyl group in HAp is substituted by F, resulting in an increased crystallinity, crystal size, and elastic modulus^[109].

Other abnormal mineralization patterns

Osteoporosis, one of the most prevalent pathological abnormal mineralization conditions, is mainly related to menopause and aging^[104,110,111]. Osteoporosis is diagnosed based on low BMD and leads to reduced bone mass and deterioration in bone micro-architecture, which further increases the susceptibility to fracture^[110]. In osteoporosis, bone resorption exceeds bone formation, resulting in altered mineralization properties, including mineral content, composition, and crystal size, which leads to reduced fracture resistance^[110]. It has been reported that the bone tissue Ca/P ratio was reduced in osteoporosis patients and the imbalance increased the defect in the HAp network, thus resulting in a less rigid HAp crystal structure and further contributing to the increased fracture susceptibility in osteoporotic bones^[112]. Meanwhile, the uneven distribution of minerals in the bone matrix is observed in some pathological conditions, such as Paget's disease, which is a chronic disorder that the normal bone remodeling process is disrupted, leading to abnormally shaped, enlarged, and weakened bones that are more susceptible to fractures and deformities.

The presence of whitlockite in osteocyte lacunae (micropetrosis) is associated with pathological conditions, as it is primarily found in the pathological mineralization of various soft tissues, dental calculus, and occasionally in enamel and dentine^[113]. Notably, Mg-whitlockite [$\text{Ca}_{18}\text{Mg}_2(\text{HPO}_4)_2(\text{PO}_4)_{12}$] has been detected in post-apoptotic osteocyte lacunae in human alveolar bone, but this unusual mineral has not been found in the extracellular matrix of mammalian bone under normal conditions^[113]. The notion that Mg-whitlockite is a significant constituent of bone minerals remains unsubstantiated, and it is considered a pathological biomineral^[114]. Therefore, contrary to some claims, biomaterials containing Mg-whitlockite do not represent a bioinspired or biomimetic approach to bone repair^[113].

Joint

Cartilage calcification that has been observed in the hip and knee is pathological in almost all osteoarthritis (OA) patients^[115]. The deposition of calcium pyrophosphate dihydrate (CPPD) has been found in patients suffering from acute attacks of pseudogout in the joints^[116-118]. Other CaPs have also been found in synovial fluids, synovium, and cartilage of OA patients, such as carbonate HAp, tricalcium phosphate (TCP), and

OCP^[116,117,119,120]. Articular cartilage calcification that occurs in end-stage OA shows the accumulation of predominant HAp crystals^[116,121]. The deposition of HAp initiates from articular cartilage vesicles (ACVs) and induces stress in articular chondrocytes, which ultimately results in the phenotypic change of chondrocytes and the formation of more HAp crystals^[121,122]. Besides, whitlockite, another kind of CaP-based mineral, has also been found in the mineral phase of osteoarthritic articular cartilage and intervertebral disc^[123,124]. Under certain circumstances, such as elevated Mg concentrations, acidic microenvironments, and the presence of specific proteins or organic molecules, Mg partly substitutes Ca, inhibits apatite originating from ACP, and aids the precipitation of whitlockite.

Tendon

Tendon mineralization (calcific tendinitis) is the cell-mediated calcification of living tissues that causes joint pain^[94]. It typically affects the shoulder and hip, as well as other sites, such as the hand and wrist, foot and ankle, and neck^[125]. Four well-defined phases of calcific tendinitis are formative (pre-calcific), calcific, resorptive, and reparative^[94,126]. In the formative phase, a portion of the tendon undergoes a fibrocartilaginous transformation. During the calcific phase, calcium crystals are deposited in small vascular structures located between collagen fibrils^[126,127]. Followed by calcification, the appearance of thin-walled vascular channels at the periphery of the calcium deposits marks the initiation of the resorptive phase, which involves Ca removal by macrophages and multinucleated giant cells^[128]. Computed tomography studies showed the porous structure of calcific deposits throughout the tendon^[129]. Structural and compositional analysis revealed that the chemical composition of mineralized deposits in calcific tendinitis is poorly crystallized carbonate HAp, having a Ca/P molar ratio ranging between 0.9 and 1.5^[128,130-132].

Teeth

Pathological mineralization on teeth results from a variety of factors, such as changes in the oral environment, genetic predisposition, or underlying medical conditions^[88,89]. In dentin, pathological mineralization happens in the form of dentinogenesis imperfecta, causing weakened teeth that are prone to cavities and fractures^[133]. Dental calculus builds up on teeth (both supragingival and subgingival), is composed of inorganic components (brushite, dicalcium phosphate dihydrate, OCP, HAp, and whitlockite) and salivary proteins adsorbed on the tooth surface^[134,135]. The level of dental calculus is affected by oral hygiene habits, diet, age, systemic diseases, and medications^[135]. In enamel, pathological mineralization appears as spots on the surface of the tooth. It can be caused by malnutrition, high fever during childhood, or exposure to excessive F^[77].

Salivary gland

A salivary gland stone (salivary calculi or sialolithiasis) found in the salivary gland consists of a central organic core and a layered cortex of inorganic components^[136]. The crystals found in the salivary gland were randomly oriented carbonate HAp, whitlockite, and less frequently brushite and OCPs^[137-139].

Heart and blood vessels

Cardiovascular calcification, the deposition of apatite and whitlockite, is closely associated with increased risks of several mortal diseases, such as blood vessel stenosis, ischemia, stroke, and heart disease^[20,35,140-142]. Based on its histological appearance, the calcification can be distinguished as amorphous (lacking tissue architecture) and chondro-osseous (having the tissue architecture of cartilage or bone)^[143].

Calcification that occurs in the intimal layer of the arteries links to arterial obstruction and atherosclerotic plaque rupture, leading to stroke or myocardial infarction^[35,144]. Calcification that occurs in the medial layer, also known as Monckeberg's medial sclerosis, is associated with vessel stiffness, systolic hypertension, and progressively increased risks of diastolic dysfunction and heart failure^[35,145,146]. Even though the mechanism

of cardiovascular calcification is not fully understood, it is no longer acknowledged as a passive accumulation of minerals but an active inflammatory and/or osteogenesis-related signaling process^[147,148]. Several influencing factors have also been identified in the past few decades, such as the loss of inhibition, induction of osteogenesis, accumulation of nuclei, and cell death^[98]. For example, cell-secreted small membrane-bound microparticles, such as apoptotic bodies and matrix vesicles, showed their capacities to concentrate Ca and Pi and initiate crystal nucleation in response to inflammatory stimuli^[100,144]. Additionally, lipids and cytokines released by macrophages were also found to accelerate osteogenic differentiation and calcification of vascular smooth muscle cells (VSMCs)^[100,101].

Kidney

Kidney stones are one of the most common and painful urinary disorders^[149]. In most cases, they result from the nucleation and aggregation/growth of crystals from supersaturated urine [Figure 5]^[150,151]. Based on their composition and pathogenesis, kidney stones are commonly classified into five types: (a) Ca-containing crystals; (b) struvite or magnesium ammonium phosphate stones; (c) uric acid stones or urate; (d) cystine stones; and (e) drug-induced stones^[152].

Ca-containing stones are predominant renal stones, typically composed of CaO_x (50%), CaP (5%), or a mixture of both (45%)^[153]. CaO_x exists in the form of CaO_x monohydrate (COM, or whewellite), CaO_x dihydrate (COD, or weddellite), or a mixture of both forms^[151,154]. Struvite stones in the body are shown to be a mixture of struvite magnesium ammonium phosphate [$\text{MgNH}_4\text{PO}_4 \cdot 6\text{H}_2\text{O}$] and carbonate HAP^[155]. In addition to the most common Ca-containing stone that comprises 80% of urinary calculi, struvite accounts for 10%-15%, and uric acid stones account for 9%, leaving 1% of the rest of the stone types, including cystine stones and drug-induced stones^[152,156,157].

The pathogenesis of kidney stones is a multi-step process, including crystal nucleation, aggregation, and retention. The nucleation of calculus occurs in a supersaturated liquid, where Ca and oxalate combine to form insoluble micro-clusters or start with existing nucleation centers [Figure 5]^[150,152,157]. Crystal aggregation and secondary nucleation of crystals account for crystal growth and interactions between crystals and cells and extracellular matrix^[158]. The formation of kidney stones is affected by the supersaturation of Ca and oxalate in the urine, urinary pH, and some molecular modulators in the environment^[157,159,160]. For instance, the growth of CaO_x crystals is associated with a urinary pH range of 5.0 to 6.5; uric acid stones form at low urinary pH (pH < 5.05), whereas CaP and struvite favor a pH range over 7^[152]. In addition to factors that affect the formation of kidney stones by altering the environment, there are several modulators actively modulating the nucleation and aggregation of pathological crystals. For example, PPi and citrate reduce the nucleation and growth of Ca-containing crystals, as well as Mg^[157,160,161]; Biomolecules, such as OPN, prothrombin F1 fragment, and calgranulin, have been shown to inhibit the crystallization of CaO_x and CaP by binding to Ca and hindering crystal growth^[157,162-164].

Brain

Brain mineralization occurs in the basal ganglia and other regions, such as the cerebellum, thalamus, and brainstem^[165,166]. Patients presenting brain calcification exhibit impaired motor and cognition, such as dystonia, parkinsonism, psychosis, and dementia^[165,167,168]. It is associated with neurological or metabolic disorders (secondary hypoparathyroidism and mitochondrial diseases) and other acquired conditions, such as injuries (infection, ischemia, and trauma) and toxicity related to manganese (Mn), Fe, lead (Pb), carbon monoxide, and normal aging^[165,169,170]. The major composition of brain mineralization is HAP^[171,172]. Other components, such as Zn, Fe, and Mg, are also present in the deposits^[173]. However, currently, there is no established method to determine whether it is a passive process, which can be attributed to normal aging, or an active process mediated by cellular activities^[171,172].

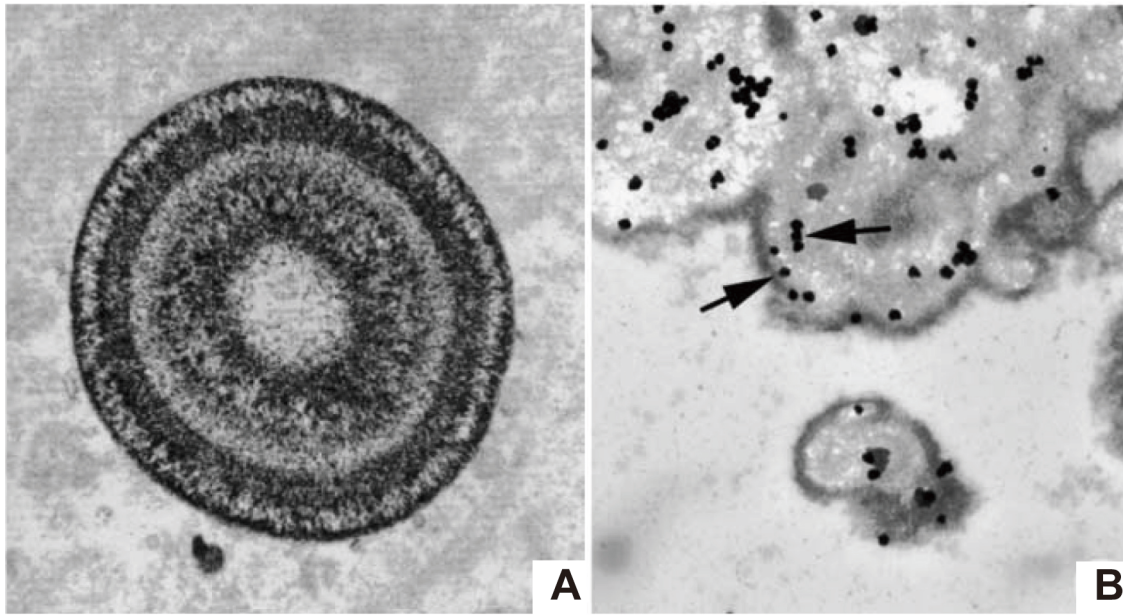


Figure 5. Crystal deposition in the urinary system (Reproduced with permission from Evan et al.^[150]. Copyright 2005, Elsevier). (A) The initial sites of the deposition of kidney stones in transmission electron microscopic images and (B) immunogold staining showed the localization of osteopontin in the plaque.

Ocular

Ocular mineralization can be found in the cornea, retina, optic nerve, and Bruch's membrane^[92,174-176]. In the aging eye, the accumulation of protein- and lipid-containing deposits external to the retinal pigment epithelium (RPE) can lead to macular degradation and, consequently, blindness^[92,177]. Three types of structures of minerals have been found in age-related macular degradation, spherules (whitlockite), plaques (amorphous apatite), and nodules (apatite)^[20,21]. However, the mechanism of the formation of calcified nodules remains unknown.

Breast

Breast mineralization, also called microcalcification, has been suggested to be a consequence of either injury or diseases, such as chronic kidney disease, hypertension, or metabolic syndrome^[178,179]. The formation of microcalcification is related to the acquisition of mesenchymal characteristics in breast cancer cells, affected by transforming growth factor beta (TGF- β) or nuclear factor kappa-light-chain-enhancer of activated B cells (NF- κ B)^[180,181]. Multiple phases of breast microcalcifications have been identified: CaPs (such as carbonate HAp and whitlockite), amorphous CaP, and, less commonly, CaO_x^[182-185]. However, the exact origins of minerals remained unclear. Nevertheless, the screening and evaluation of the morphology and distribution of microcalcification aid in determining the likelihood of whether the calcifications are benign, intermediate, or necessitate further investigation^[17]. For instance, CaOx (type I calcification) is detected in benign breast lesions or lobular carcinoma, whereas HAp calcification (type II calcification) is detected in both benign and malignant breast tissues^[18,19]. Compared to those formed in malignant ducts, type II microcalcification formed in benign ducts was found to contain a higher amount of CaCO₃ and a lower amount of protein^[186]. In some malignant specimens, Mg and Na have also been detected^[187]. Elevated Na levels have been found in malignant specimens, but no correlation has been found between the level of Mg and malignancy^[187].

Pancreas

Pancreatic stones (Pancreatic calculi) occur in the main ducts, side branches, or parenchyma^[188]. It contains an inner nidus core and outer shell, primarily constituting CaCO₃, in the form of calcite (major) and aragonite, besides Pi and other protein content^[188,189]. The inner protein nidus contained Fe, chromium (Cr), and nickel (Ni), whereas the outer calcite shell contained Ca and 17 other elements^[190].

Prostate

Prostatic calculi are usually found as apatite or whitlockite, less frequently CaO_x^[191,192]. They are classified as primary/endogenous or secondary/extrinsic stones^[193]. Endogenous stones are commonly caused by obstruction of the prostatic ducts or chronic inflammation; extrinsic stones are mainly caused by urine reflux^[193]. Klimas *et al.* suggested two mechanisms regarding the calcification of prostatic calculi: the calcification of the *corpora amylacea* (type I calculi, composed of Na, S, P, Ca, and Zn) and the precipitation of prostatic secretions (type II calculi, composed of Ca and P)^[191].

Placental

The placenta, a highly vascularized organ, mediates the communications between two circulatory systems. Placental calcification occurs when small calcium deposits build up on the placenta and is recognized as CaPs (the ratio of Ca/P = 2.00 ± 0.05) observed in placenta tissue^[194,195]. It is often found in both preterm and term birth and serves as a predictor of adverse pregnancy outcomes^[196]. However, the mechanisms of placental calcification are poorly understood^[194].

Lymph nodes

Calcification in the lymph nodes occurs following diseases such as granulomatous infections^[197]. Two patterns of calcification were found in the submandibular and neck regions: small blocks with different textures and islets surrounded by soft tissues, respectively^[198]. In the submandibular specimen, apatite, together with a minor amount of whitlockite, was found^[198]; In the neck specimen, whitlockite was found most frequently^[198].

POSSIBLE PREVENTION AND TREATMENTS OF PATHOLOGICAL MINERALIZATION

Current treatments for the removal of calcified plaque include mechanical removal using rotary blade ablation or chemically dissolving *in situ* with acid via a catheter device^[199-201]. In addition to mechanical and chemical debridement, reduced mineral ion intake from the diet or ions from bone stores have also been considered potential treatments for pathological/ectopic calcification in clinical practices^[201]. Other approaches have been explored in targeting regulatory molecules in the body. For example, the monoclonal antibody Denosumab was developed to interfere with osteoclast functions and serum Ca levels, and PPI inhibited uremic vascular calcification without interfering with the mineralization of bone^[202,203]. However, there are still no well-established and acknowledged treatments to prevent or counteract pathological/ectopic mineralization.

Current strategies targeting cellular mechanisms of calcification provided promising avenues for better administration of pathological mineralization in soft tissues, either reducing the nucleation of pathological crystals and crystal growth or reducing the circulating mineral ions in the serum^[204]. Several endogenous calcification inhibitors have been identified, such as fetuin-A, vitamin-K dependent matrix-Gla protein (MGP), PPI, and OPN^[23,33]. The serum protein fetuin-A is an important inhibitor of extra-skeletal calcification in the plasma and tissue fluids^[205]. It is derived from the liver and acts as a chaperone, stabilizing excess mineral ions by forming a colloid with mineral ions or completely insoluble calciprotein particles^[206-208]. MGP was the first inhibitor of artery calcification to be characterized *in vivo*^[24]. It serves as an inhibitor of bone morphogenic protein-2 (BMP2), driving changes in cells toward an osteogenic-like

phenotype and subsequent calcification^[209,210]. PPI is identified as the principal inhibitor of HAp deposition, evidenced by antagonizing the ability of Pi to crystallize with Ca to inhibit biomineralization and acquired clinical conditions regarding pathological calcification upon its deficiency^[32]. OPN is found to be associated with nascent mineralization foci during bone mineralization and present at interfaces where mineralization is needed to be quenched^[211,212].

Several approaches to regulating the metabolisms of these natural inhibitors exhibited promising results in treating pathological mineralization. For example, Vitamin K supplementation showed the effect of reducing the progression of vascular mineralization and subsequent arterial stiffness^[33,213]. Bisphosphonates, derivatives of PPI, stabilize the Pi groups by a phosphorus-carbon-phosphorus backbone. Compared to PPI, which can be easily hydrolyzed, bisphosphonates have extended plasma half-life and improved stability^[32]. Bisphosphonates showed their potency to reduce fractures in postmenopausal osteoporosis^[214]. They have also been found to reduce soft tissue calcification and interfere with osteoclast functions^[33,204]. Alendronate, a widely prescribed bisphosphonate, has shown good tolerance and improvements in several patients with brain calcification^[167]. Other bisphosphonates, such as etidronate, pamidronate, and ibandronate, have been demonstrated to inhibit aortic calcification both *in vitro* and *in vivo*^[202,215-218]. In addition to bisphosphonates, a few proteins associated with the metabolism of PPI have also been identified to be promising for targeted treatment of pathological mineralization, such as ectonucleotide pyrophosphatase/phosphodiesterase-1 (ENPP1), ATP binding cassette subfamily C member 6 (ABCC6), progressive ankylosis protein (ANK), and tissue-nonspecific alkaline phosphatase (TNAP)^[219-222]. Inspired by the inhibitory effect of acidic urinary macromolecules (e.g., OPN) on the formation of CaO_x *in vitro*, polymeric carboxylic amino acids, poly-L-glutamic and aspartic acid, were found to inhibit the crystallization of CaO_x^[223]. A similar inhibitory effect was also found to be achieved by acidic polyanion poly (acrylic acid)^[224-226]. Additionally, sodium thiosulfate (STS) treatment was found to inhibit calcium salt precipitation in calciphylaxis^[227-230]. Nevertheless, these results were limited either in the long-term efficacy or potential toxicity of the STS treatment^[33].

Moreover, the presence of trace elements has been shown to play a role in the crystal formation kinetics or external morphology of a growing crystal. It could be promising in designing therapeutic approaches against pathological mineralization^[102,231]. For example, Mg, Zn, aluminum (Al), Fe, and Cu are indicated as growth inhibitors of CaO_x at very low concentrations^[232-235]. Adding AlCl₃ or FeCl₃ to transplanted valves effectively delayed the onset of valve calcification by blocking TNAP activity^[236].

CONCLUSIONS AND FUTURE PERSPECTIVES

Our understanding of pathological/ectopic mineralization has been dramatically improved in parallel to bone biology and advanced characterization techniques widely used in the field of material science^[22,92,201]. Significant progress has been made in elucidating the properties of pathological crystals and the underlying mechanisms of pathological/ectopic calcification that occurred in soft tissues over the years. By elucidating the physiological mechanisms of bone mineralization and their relationship with mineralization phenomena, we can develop targeted therapeutic interventions to prevent, manage, or treat these disorders. However, there are still some debatable questions regarding (a) the composition and structure of pathological crystals mediated by cellular activities and factors in the surrounding environment; (b) the dynamics of ion transport; (c) the involvement of cells and related cellular activities; (d) the interactions between pathological crystals and the surrounding tissues; and (e) how these contribute to disease progression^[36]. Even though attempts have been made to simulate the crystallization process, it is still challenging to comprehend the *in situ* crystallization process due to the involvement of cellular activities. Nevertheless, a more comprehensive understanding of how the structures are formed, progressed, and adapted to changing needs enables us to conceive new insights into the progression of the pathological

condition and guide future therapeutic designs to prevent and manage pathological/ectopic mineralization.

DECLARATIONS

Authors' contributions

Conceptualization: Mu Y

Writing-original draft: Mu Y, Gao W

Writing-review and editing: Mu Y, Gao W, Zhou Y, Xiao L, Xiao Y

Availability of data and materials

Not applicable.

Financial support and sponsorship

This research is supported by the Joint Research Centre Fund from the Department of Environment and Science (2019-2023), Queensland.

Conflicts of interest

All authors declared that there are no conflicts of interest.

Ethical approval and consent to participate

Not applicable.

Consent for publication

Not applicable.

Copyright

© The Author(s) 2023.

REFERENCES

1. Weiner S, Dove PM. An overview of biomineralization processes and the problem of the vital effect. *Rev Mineral Geochem* 2003;54:1-29. [DOI](#)
2. Tai K, Dao M, Suresh S, Palazoglu A, Ortiz C. Nanoscale heterogeneity promotes energy dissipation in bone. *Nat Mater* 2007;6:454-62. [DOI](#) [PubMed](#)
3. Lichtenegger HC, Schöberl T, Bartl MH, Waite H, Stucky GD. High abrasion resistance with sparse mineralization: copper biomineral in worm jaws. *Science* 2002;298:389-92. [DOI](#) [PubMed](#)
4. Hamm CE, Merkel R, Springer O, et al. Architecture and material properties of diatom shells provide effective mechanical protection. *Nature* 2003;421:841-3. [DOI](#)
5. Tommasini SM, Wearne SL, Hof PR, Jepsen KJ. Percolation theory relates corticocancellous architecture to mechanical function in vertebrae of inbred mouse strains. *Bone* 2008;42:743-50. [DOI](#) [PubMed](#) [PMC](#)
6. Murat D, Falahati V, Bertinetti L, et al. The magnetosome membrane protein, MmsF, is a major regulator of magnetite biomineralization in *Magnetospirillum magneticum* AMB-1. *Mol Microbiol* 2012;85:684-99. [DOI](#) [PubMed](#) [PMC](#)
7. Gautron J, Stapane L, Le Roy N, Nys Y, Rodriguez-Navarro AB, Hincke MT. Avian eggshell biomineralization: an update on its structure, mineralogy and protein tool kit. *BMC Mol Cell Biol* 2021;22:11. [DOI](#)
8. Ramos-Silva P, Benhamada S, Le Roy N, et al. Novel molluscan biomineralization proteins retrieved from proteomics: a case study with Upsalin. *Chembiochem* 2012;13:1067-78. [DOI](#)
9. Beniash E, Simmer JP, Margolis HC. Structural changes in amelogenin upon self-assembly and mineral interactions. *J Dent Res* 2012;91:967-72. [DOI](#) [PubMed](#) [PMC](#)
10. Hosseini S, Naderi-Manesh H, Mountassif D, Cerruti M, Vali H, Faghihi S. C-terminal amidation of an osteocalcin-derived peptide promotes hydroxyapatite crystallization. *J Biol Chem* 2013;288:7885-93. [DOI](#) [PubMed](#) [PMC](#)
11. Weiner S, Wagner HD. The material bone: structure-mechanical function relations. *Annu Rev Mater Sci* 1998;28:271-98. [DOI](#)
12. Kokubo T, Takadama H. How useful is SBF in predicting in vivo bone bioactivity? *Biomaterials* 2006;27:2907-15. [DOI](#) [PubMed](#)
13. Jeon T. Analysis of microstructure in mouse femur and decalcification effect on microstructure by electron microscopy. *J Anal Sci Technol* 2010;1:124-9. Available from: https://www.researchgate.net/publication/49587402_Analysis_of_microstructure_in_mouse_femur_and_decalcification_effect_on_microstructure_by_electron_microscopy

[Last accessed on 5 July 2023].

14. Takadama H, Kim HM, Kokubo T, Nakamura T. TEM-EDX study of mechanism of bonelike apatite formation on bioactive titanium metal in simulated body fluid. *J Biomed Mater Res A* 2001;57:441-448. [PubMed](#)
15. Baino F, Yamaguchi S. The use of simulated body fluid (SBF) for assessing materials bioactivity in the context of tissue engineering: review and challenges. *Biomimetics* 2020;5:57. [DOI](#) [PubMed](#) [PMC](#)
16. Suchý T, Bartoš M, Sedláček R, et al. Various simulated body fluids lead to significant differences in collagen tissue engineering scaffolds. *Materials* 2021;14:4388. [DOI](#) [PubMed](#) [PMC](#)
17. Bonfiglio R, Scimeca M, Urbano N, Bonanno E, Schillaci O. Breast microcalcifications: biological and diagnostic perspectives. *Future Oncol* 2018;14:3097-9. [DOI](#) [PubMed](#)
18. Busing CM, Keppler U, Menges V. Differences in microcalcification in breast tumors. *Virchows Arch A* 1981;393:307-13. [DOI](#)
19. Barman I, Dingari NC, Saha A, et al. Application of Raman spectroscopy to identify microcalcifications and underlying breast lesions at stereotactic core needle biopsy. *Cancer Res* 2013;73:3206-15. [DOI](#) [PubMed](#) [PMC](#)
20. Tsolaki E, Bertazzo S. Pathological mineralization: the potential of mineralomics. *Materials* 2019;12:3126. [DOI](#) [PubMed](#) [PMC](#)
21. Tan ACS, Pilgrim MG, Fearn S, et al. Calcified nodules in retinal drusen are associated with disease progression in age-related macular degeneration. *Sci Transl Med* 2018;10:eaat4544. [DOI](#) [PubMed](#)
22. Kirsch T. Determinants of pathological mineralization. *Curr Opin Rheumatol* 2006;18:174-80. [DOI](#) [PubMed](#)
23. Reznikov N, Steele JAM, Fratzl P, Stevens MM. A materials science vision of extracellular matrix mineralization. *Nat Rev Mater* 2016;1:16041. [DOI](#)
24. Luo G, Ducey P, McKee MD, et al. Spontaneous calcification of arteries and cartilage in mice lacking matrix GLA protein. *Nature* 1997;386:78-81. [DOI](#)
25. Yagami K, Suh JY, Enomoto-Iwamoto M, et al. Matrix GLA protein is a developmental regulator of chondrocyte mineralization and, when constitutively expressed, blocks endochondral and intramembranous ossification in the limb. *J Cell Biol* 1999;147:1097-108. [DOI](#) [PubMed](#) [PMC](#)
26. Yuan FL, Xu RS, Ye JX, et al. Apoptotic bodies from endplate chondrocytes enhance the oxidative stress-induced mineralization by regulating PPI metabolism. *J Cell Mol Med* 2019;23:3665-75. [DOI](#) [PubMed](#) [PMC](#)
27. Wu LN, Genge BR, Dunkelberger DG, LeGeros RZ, Concannon B, Wuthier RE. Physicochemical characterization of the nucleational core of matrix vesicles. *J Biol Chem* 1997;272:4404-11. [DOI](#) [PubMed](#)
28. Sekaran S, Vimalraj S, Thangavelu L. The physiological and pathological role of tissue nonspecific alkaline phosphatase beyond mineralization. *Biomolecules* 2021;11:1564. [DOI](#) [PubMed](#) [PMC](#)
29. Franklin BS, Mangan MS, Latz E. Crystal formation in inflammation. *Annu Rev Immunol* 2016;34:173-202. [DOI](#) [PubMed](#)
30. Poloni LN, Ward MD. The materials science of pathological crystals. *Chem Mater* 2014;26:477-95. [DOI](#)
31. Bazin D, Daudon M, Combes C, Rey C. Characterization and some physicochemical aspects of pathological microcalcifications. *Chem Rev* 2012;112:5092-120. [DOI](#) [PubMed](#)
32. Ralph D, van de Wetering K, Uitto J, Li Q. Inorganic pyrophosphate deficiency syndromes and potential treatments for pathologic tissue calcification. *Am J Pathol* 2022;192:762-70. [DOI](#) [PubMed](#) [PMC](#)
33. Singh A, Tandon S, Tandon C. An update on vascular calcification and potential therapeutics. *Mol Biol Rep* 2021;48:887-96. [DOI](#) [PubMed](#)
34. Fuery MA, Liang L, Kaplan FS, Mohler ER. Vascular ossification: pathology, mechanisms, and clinical implications. *Bone* 2018;109:28-34. [DOI](#) [PubMed](#)
35. Durham AL, Speer MY, Scatena M, Giachelli CM, Shanahan CM. Role of smooth muscle cells in vascular calcification: implications in atherosclerosis and arterial stiffness. *Cardiovasc Res* 2018;114:590-600. [DOI](#) [PubMed](#) [PMC](#)
36. Vidavsky N, Kunitake JAMR, Estroff LA. Multiple pathways for pathological calcification in the human body. *Adv Healthc Mater* 2021;10:e2001271. [DOI](#) [PubMed](#) [PMC](#)
37. Cazalbou S, Combes C, Eichert D, Rey C. Adaptive physico-chemistry of bio-related calcium phosphates. *J Mater Chem* 2004;14:2148. [DOI](#)
38. Zipkin I. The inorganic composition of bones and teeth. In: Schraer H, editor. *Biological calcification: cellular and molecular aspects*. Boston: Springer; 1970. pp. 69-103. [DOI](#)
39. Elsharkawy S, Mata A. Hierarchical biomineralization: from nature's designs to synthetic materials for regenerative medicine and dentistry. *Adv Healthc Mater* 2018;7:e1800178. [DOI](#) [PubMed](#)
40. Abou Neel EA, Aljabo A, Strange A, et al. Demineralization-remineralization dynamics in teeth and bone. *Int J Nanomed* 2016;11:4743-63. [DOI](#) [PubMed](#) [PMC](#)
41. Eanes ED, Gillessen IH, Posner AS. Intermediate states in the precipitation of hydroxyapatite. *Nature* 1965;208:365-7. [DOI](#) [PubMed](#)
42. Habraken W, Habibovic P, Epple M, Bohner M. Calcium phosphates in biomedical applications: materials for the future? *Mater Today* 2016;19:69-87. [DOI](#)
43. Beniash E, Metzler RA, Lam RS, Gilbert PU. Transient amorphous calcium phosphate in forming enamel. *J Struct Biol* 2009;166:133-43. [DOI](#) [PubMed](#) [PMC](#)
44. Mahamid J, Aichmayer B, Shimoni E, et al. Mapping amorphous calcium phosphate transformation into crystalline mineral from the cell to the bone in zebrafish fin rays. *Proc Natl Acad Sci USA* 2010;107:6316-21. [DOI](#) [PubMed](#) [PMC](#)

45. Termine JD, Posner AS. Infrared analysis of rat bone: age dependency of amorphous and crystalline mineral fractions. *Science* 1966;153:1523-5. DOI PubMed
46. Habraken WJ, Tao J, Brylka LJ, et al. Ion-association complexes unite classical and non-classical theories for the biomimetic nucleation of calcium phosphate. *Nat Commun* 2013;4:1507. DOI
47. Brown WE, Schroeder LW, Ferris JS. Interlayering of crystalline octacalcium phosphate and hydroxylapatite. *J Phys Chem* 1979;83:1385-8. DOI
48. Wang Y, Von Euw S, Fernandes FM, et al. Water-mediated structuring of bone apatite. *Nat Mater* 2013;12:1144-53. DOI
49. Rey C, Combes C. What bridges mineral platelets of bone? *Bonekey Rep* 2014;3:586. DOI PubMed PMC
50. Dorvee JR, Veis A. Water in the formation of biogenic minerals: peeling away the hydration layers. *J Struct Biol* 2013;183:278-303. DOI PubMed PMC
51. Becker RO, Spadaro JA, Berg EW. The trace elements of human bone. *J Bone Joint Surg Am* 1968;50:326-34. DOI
52. Ellis EH, Spadaro JA, Becker RO. Trace elements in tendon collagen. *Clin Orthop Relat Res* 1969;65:195-8. Available from: <https://www.robertobecker.net/PDFs/BF050-CORR1969.pdf> [Last accessed on 5 July 2023].
53. Grynblas MD, Rey C. The effect of fluoride treatment on bone mineral crystals in the rat. *Bone* 1992;13:423-9. DOI
54. Ressler A, Žužić A, vanišević I, Kamboj N, Ivanković H. Ionic substituted hydroxyapatite for bone regeneration applications: a review. *Open Ceram* 2021;6:100122. DOI
55. Legros R, Balmain N, Bonel G. Age-related changes in mineral of rat and bovine cortical bone. *Calcif Tissue Int* 1987;41:137-44. DOI PubMed
56. Handschin RG, Stern WB. Crystallographic and chemical analysis of human bone apatite (Crista Iliaca). *Clin Rheumatol* 1994;13 Suppl 1:75-90. PubMed
57. Yao X, Carleton SM, Kettle AD, Melander J, Phillips CL, Wang Y. Gender-dependence of bone structure and properties in adult osteogenesis imperfecta murine model. *Ann Biomed Eng* 2013;41:1139-49. DOI PubMed PMC
58. Nelson DG. The influence of carbonate on the atomic structure and reactivity of hydroxyapatite. *J Dent Res* 1981;60 Spec No C:1621-9. DOI PubMed
59. Farlay D, Panczer G, Rey C, Delmas PD, Boivin G. Mineral maturity and crystallinity index are distinct characteristics of bone mineral. *J Bone Miner Metab* 2010;28:433-45. DOI PubMed PMC
60. Lacruz RS, Habelitz S, Wright JT, Paine ML. Dental enamel formation and implications for oral health and disease. *Physiol Rev* 2017;97:939-93. DOI PubMed PMC
61. Akiva A, Malkinson G, Masic A, et al. On the pathway of mineral deposition in larval zebrafish caudal fin bone. *Bone* 2015;75:192-200. DOI
62. Bennet M, Akiva A, Faivre D, et al. Simultaneous Raman microspectroscopy and fluorescence imaging of bone mineralization in living zebrafish larvae. *Biophys J* 2014;106:L17-9. DOI PubMed PMC
63. Crane NJ, Popescu V, Morris MD, Steenhuis P, Ignelzi MA Jr. Raman spectroscopic evidence for octacalcium phosphate and other transient mineral species deposited during intramembranous mineralization. *Bone* 2006;39:434-42. DOI PubMed
64. Simon P, Grüner D, Worch H, et al. First evidence of octacalcium phosphate@osteocalcin nanocomplex as skeletal bone component directing collagen triple-helix nanofibril mineralization. *Sci Rep* 2018;8:13696. DOI PubMed PMC
65. Nudelman F, Lausch AJ, Sommerdijk NA, Sone ED. In vitro models of collagen biomineralization. *J Struct Biol* 2013;183:258-69. DOI PubMed
66. Olszta MJ, Cheng X, Jee SS, et al. Bone structure and formation: a new perspective. *Mater Sci Eng R Rep* 2007;58:77-116. DOI
67. George A, Veis A. Phosphorylated proteins and control over apatite nucleation, crystal growth, and inhibition. *Chem Rev* 2008;108:4670-93. DOI PubMed PMC
68. Gower LB. Biomimetic model systems for investigating the amorphous precursor pathway and its role in biomineralization. *Chem Rev* 2008;108:4551-627. DOI PubMed PMC
69. Jonge LT, van den Beucken JJ, Leeuwenburgh SC, Hamers AA, Wolke JG, Jansen JA. In vitro responses to electrosprayed alkaline phosphatase/calcium phosphate composite coatings. *Acta Biomater* 2009;5:2773-82. DOI PubMed
70. Omelon SJ, Grynblas MD. Relationships between polyphosphate chemistry, biochemistry and apatite biomineralization. *Chem Rev* 2008;108:4694-715. DOI PubMed
71. Fleisch H, Bisaz S. Isolation from urine of pyrophosphate, a calcification inhibitor. *Am J Physiol* 1962;203:671-5. DOI PubMed
72. Cuy JL, Mann AB, Livi KJ, Teaford MF, Weihs TP. Nanoindentation mapping of the mechanical properties of human molar tooth enamel. *Arch Oral Biol* 2002;47:281-91. DOI PubMed
73. Tjäderhane L, Carrilho MR, Breschi L, Tay FR, Pashley DH. Dentin basic structure and composition-an overview. *Endod Topics* 2009;20:3-29. DOI
74. Linde A. Dentin mineralization and the role of odontoblasts in calcium transport. *Connect Tissue Res* 1995;33:163-70. DOI PubMed
75. Hao J, Ramachandran A, George A. Temporal and spatial localization of the dentin matrix proteins during dentin biomineralization. *J Histochem Cytochem* 2009;57:227-37. DOI PubMed PMC
76. Chatzistavrou X, Papagerakis S, Ma PX, Papagerakis P. Innovative approaches to regenerate enamel and dentin. *Int J Dent* 2012;2012:856470. DOI PubMed PMC
77. Vieira AP, Hancock R, Limeback H, Maia R, Grynblas MD. Is fluoride concentration in dentin and enamel a good indicator of dental fluorosis? *J Dent Res* 2004;83:76-80. DOI PubMed

78. White SN, Luo W, Paine ML, Fong H, Sarikaya M, Snead ML. Biological organization of hydroxyapatite crystallites into a fibrous continuum toughens and controls anisotropy in human enamel. *J Dent Res* 2001;80:321-6. DOI PubMed
79. Giacaman R, Perez V, Carrera C. Mineralization processes in hard tissues. In: *Biomaterialization and biomaterials*. Amsterdam, The Netherlands: Elsevier; 2016. pp. 147-85. DOI
80. Wang L, Guan X, Du C, Moradian-Oldak J, Nancollas GH. Amelogenin promotes the formation of elongated apatite microstructures in a controlled crystallization system. *J Phys Chem C Nanomater Interfaces* 2007;111:6398-404. DOI PubMed PMC
81. Robinson C, Kirkham J, Brookes SJ, Bonass WA, Shore RC. The chemistry of enamel development. *Int J Dev Biol* 1995;39:145-52. PubMed
82. Smith CE. Cellular and chemical events during enamel maturation. *Crit Rev Oral Biol Med* 1998;9:128-61. DOI PubMed
83. Moradian-Oldak J. Protein-mediated enamel mineralization. *Front Biosci* 2012;17:1996-2023. DOI PubMed PMC
84. Yamamoto T, Hasegawa T, Yamamoto T, Hongo H, Amizuka N. Histology of human cementum: its structure, function, and development. *Jpn Dent Sci Rev* 2016;52:63-74. DOI PubMed PMC
85. Gonçalves PF, Sallum EA, Sallum AW, et al. Dental cementum reviewed: development, structure, composition, regeneration and potential functions. *Braz J Oral Sci* 2005;4:651-8. Available from: <https://periodicos.sbu.unicamp.br/ojs/index.php/bjos/article/view/8641790> [Last accessed on 5 July 2023].
86. Neiders ME, Eick JD, Miller WA, Leitner JW. Electron probe microanalysis of cementum and underlying dentin in young permanent teeth. *J Dent Res* 1972;51:122-30. DOI PubMed
87. Nakagaki H, Weatherell JA, Strong M, Robinson C. Distribution of fluoride in human cementum. *Arch Oral Biol* 1985;30:101-4. DOI PubMed
88. Andras NL, Mohamed FF, Chu EY, Foster BL. Between a rock and a hard place: regulation of mineralization in the periodontium. *Genesis* 2022;60:e23474. DOI PubMed PMC
89. Foster BL, Nociti FH, Somerman MJ. Development and structure of cementum. In: Naji S, Rendu W, Gourichon L, editors. *Dental cementum in anthropology*. Cambridge University Press; 2022. pp. 46-64. DOI
90. Lundberg YW, Xu Y, Thiessen KD, Kramer KL. Mechanisms of otoconia and otolith development. *Dev Dyn* 2015;244:239-53. DOI PubMed PMC
91. Zhao X, Yang H, Yamoah EN, Lundberg YW. Gene targeting reveals the role of Oc90 as the essential organizer of the otoconial organic matrix. *Dev Biol* 2007;304:508-24. DOI PubMed PMC
92. Thompson RB, Reffatto V, Bundy JG, et al. Identification of hydroxyapatite spherules provides new insight into subretinal pigment epithelial deposit formation in the aging eye. *Proc Natl Acad Sci USA* 2015;112:1565-70. DOI
93. Landis WJ, Moradian-Oldak J, Weiner S. Topographic imaging of mineral and collagen in the calcifying turkey tendon. *Connect Tissue Res* 1991;25:181-96. DOI PubMed
94. Siegal DS, Wu JS, Newman JS, Del Cura JL, Hochman MG. Calcific tendinitis: a pictorial review. *Can Assoc Radiol J* 2009;60:263-72. DOI PubMed
95. Reynolds JL, Skepper JN, McNair R, et al. Multifunctional roles for serum protein fetuin-a in inhibition of human vascular smooth muscle cell calcification. *J Am Soc Nephrol* 2005;16:2920-30. DOI
96. Faria LL, Babler F, Ferreira LC, de Noronha Junior OA, Marsolla FL, Ferreira DL. Soft tissue calcifications: a pictorial essay. *Radiol Bras* 2020;53:337-44. DOI PubMed PMC
97. Wang D, Wang X, Huang L, et al. Unraveling an innate mechanism of pathological mineralization-regulated inflammation by a nanobiomimetic system. *Adv Healthc Mater* 2021;10:e2101586. DOI
98. Giachelli CM. Vascular calcification mechanisms. *J Am Soc Nephrol* 2004;15:2959-64. DOI PubMed
99. Schrijvers DM, De Meyer GR, Kockx MM, Herman AG, Martinet W. Phagocytosis of apoptotic cells by macrophages is impaired in atherosclerosis. *Arterioscler Thromb Vasc Biol* 2005;25:1256-61. DOI PubMed
100. Shanahan CM. Inflammation ushers in calcification: a cycle of damage and protection? *Circulation* 2007;116:2782-5. DOI PubMed
101. Pugliese G, Iacobini C, Blasetti Fantauzzi C, Menini S. The dark and bright side of atherosclerotic calcification. *Atherosclerosis* 2015;238:220-30. DOI
102. Stojewski M, Czerny B, Safranow K, et al. Microelements in stones, urine, and hair of stone formers: a new key to the puzzle of lithogenesis? *Biol Trace Elem Res* 2010;137:301-16. PubMed
103. Bala Y, Farlay D, Boivin G. Bone mineralization: from tissue to crystal in normal and pathological contexts. *Osteoporos Int* 2013;24:2153-66. DOI PubMed
104. Roschger P, Paschalis EP, Fratzl P, Klaushofer K. Bone mineralization density distribution in health and disease. *Bone* 2008;42:456-66. DOI PubMed
105. Roschger P, Misof B, Paschalis E, Fratzl P, Klaushofer K. Changes in the degree of mineralization with osteoporosis and its treatment. *Curr Osteoporos Rep* 2014;12:338-50. DOI PubMed
106. Kurdi MS. Chronic fluorosis: the disease and its anaesthetic implications. *Indian J Anaesth* 2016;60:157-62. DOI PubMed PMC
107. Rodan GA, Martin TJ. Therapeutic approaches to bone diseases. *Science* 2000;289:1508-14. DOI PubMed
108. Faibish D, Ott SM, Boskey AL. Mineral changes in osteoporosis: a review. *Clin Orthop Relat Res* 2006;443:28-38. DOI PubMed PMC
109. Feroz S, Khan AS. 7-fluoride-substituted hydroxyapatite. In: Khan AS, Chaudhry AA, editor. *Handbook of ionic substituted hydroxyapatites*, Soston, UK: Woodhead, 2020; pp. 175-96. DOI

110. Poole KE, Compston JE. Osteoporosis and its management. *BMJ* 2006;333:1251-6. DOI PubMed PMC
111. Tamimi I, Cortes ARG, Sánchez-Siles JM, et al. Composition and characteristics of trabecular bone in osteoporosis and osteoarthritis. *Bone* 2020;140:115558. DOI
112. Nobakhti S, Shefelbine SJ. On the relation of bone mineral density and the elastic modulus in healthy and pathologic bone. *Curr Osteoporos Rep* 2018;16:404-10. DOI PubMed
113. Shah FA. The many facets of micropetrosis - magnesium whitlockite deposition in bisphosphonate-exposed human alveolar bone with osteolytic metastasis. *Micron* 2023;168:103441. DOI PubMed
114. Shah FA. Magnesium whitlockite - omnipresent in pathological mineralisation of soft tissues but not a significant inorganic constituent of bone. *Acta Biomater* 2021;125:72-82. DOI
115. Meyer F, Dittmann A, Kornak U, et al. Chondrocytes from osteoarthritic and chondrocalcinosis cartilage represent different phenotypes. *Front Cell Dev Biol* 2021;9:622287. DOI PubMed PMC
116. Fuerst M, Bertrand J, Lammers L, et al. Calcification of articular cartilage in human osteoarthritis. *Arthritis Rheum* 2009;60:2694-703. DOI
117. Derfus BA, Kurian JB, Butler JJ, et al. The high prevalence of pathologic calcium crystals in pre-operative knees. *J Rheumatol* 2002;29:570-4. PubMed
118. Halverson PB, McCarty DJ. Patterns of radiographic abnormalities associated with basic calcium phosphate and calcium pyrophosphate dihydrate crystal deposition in the knee. *Ann Rheum Dis* 1986;45:603-5. DOI PubMed PMC
119. Nalbant S, Martinez JA, Kitumnuaypong T, Clayburne G, Sieck M, Schumacher HR Jr. Synovial fluid features and their relations to osteoarthritis severity: new findings from sequential studies. *Osteoarthr Cartil* 2003;11:50-4. Available from: <https://www.sciencedirect.com/science/article/pii/S1063458402908617> [Last accessed on 5 July 2023].
120. Rosenthal AK, Mattson E, Gohr CM, Hirschmugl CJ. Characterization of articular calcium-containing crystals by synchrotron FTIR. *Osteoarthr Cartil* 2008;16:1395-402. DOI PubMed PMC
121. Yan JF, Qin WP, Xiao BC, et al. Pathological calcification in osteoarthritis: an outcome or a disease initiator? *Biol Rev Camb Philos Soc* 2020;95:960-85. DOI
122. Rosenthal AK. Articular cartilage vesicles and calcium crystal deposition diseases. *Curr Opin Rheumatol* 2016;28:127-32. DOI PubMed PMC
123. Scotchford CA, Vickers M, Ali SY. The isolation and characterization of magnesium whitlockite crystals from human articular cartilage. *Osteoarthr Cartil* 1995;3:79-94. PubMed
124. Lee RS, Kayser MV, Ali SY. Calcium phosphate microcrystal deposition in the human intervertebral disc. *J Anat* 2006;208:13-9. DOI PubMed PMC
125. Hayes CW, Conway WF. Calcium hydroxyapatite deposition disease. *Radiographics* 1990;10:1031-48. DOI PubMed
126. Ulthoff HK, Loehr JW. Calcific tendinopathy of the rotator cuff: pathogenesis, diagnosis, and management. *J Am Acad Orthop Surg* 1997;5:183-91. DOI PubMed
127. Landis WJ. A study of calcification in the leg tendons from the domestic turkey. *J Ultrastruct Mol Struct Res* 1986;94:217-38. DOI
128. Oliva F, Via AG, Maffulli N. Physiopathology of intratendinous calcific deposition. *BMC Med* 2012;10:95. DOI PubMed PMC
129. McCarty DJ Jr, Gatter RA. Recurrent acute inflammation associated with focal apatite crystal deposition. *Arthritis Rheum* 1966;9:804-19. DOI PubMed
130. Gärtner J, Simons B. Analysis of calcific deposits in calcifying tendinitis. *Clin Orthop Relat Res* 1990;254:111-20. PubMed
131. Riley GP, Harrall RL, Constant CR, Cawston TE, Hazleman BL. Prevalence and possible pathological significance of calcium phosphate salt accumulation in tendon matrix degeneration. *Ann Rheum Dis* 1996;55:109-15. DOI PubMed PMC
132. Penel G, Leroy G, Rey C, Bres E. MicroRaman spectral study of the PO₄ and CO₃ vibrational modes in synthetic and biological apatites. *Calcif Tissue Int* 1998;63:475-81. DOI PubMed
133. Barron MJ, McDonnell ST, Mackie I, Dixon MJ. Hereditary dentine disorders: dentinogenesis imperfecta and dentine dysplasia. *Orphanet J Rare Dis* 2008;3:31. DOI PubMed PMC
134. Jin Y, Yip HK. Supragingival calculus: formation and control. *Crit Rev Oral Biol Med* 2002;13:426-41. DOI PubMed
135. White DJ. Dental calculus: recent insights into occurrence, formation, prevention, removal and oral health effects of supragingival and subgingival deposits. *Eur J Oral Sci* 1997;105:508-22. DOI PubMed
136. Sakae T, Yamamoto H, Hirai G. Mode of occurrence of brushite and whitlockite in a sialolith. *J Dent Res* 1981;60:842-4. DOI
137. Anneroth G, Eneroth CM, Isacson G. Crystalline structure of salivary calculi. a microradiographic and microdiffractometric study. *J Oral Pathol* 1975;4:266-72. DOI PubMed
138. Burnstein LS, Boskey AL, Tannenbaum PJ, Posner AS, Mandel ID. The crystal chemistry of submandibular and parotid salivary gland stones. *J Oral Pathol* 1979;8:284-91. DOI PubMed
139. Boskey AL, Burnstein LS, Mandel ID. Phospholipids associated with human parotid gland sialoliths. *Arch Oral Biol* 1983;28:655-7. DOI PubMed
140. Nicoll R, Henein MY. The predictive value of arterial and valvular calcification for mortality and cardiovascular events. *Int J Cardiol Heart Vessel* 2014;3:1-5. DOI PubMed PMC
141. Higgins CL, Marvel SA, Morrisett JD. Quantification of calcification in atherosclerotic lesions. *Arterioscler Thromb Vasc Biol* 2005;25:1567-76. DOI PubMed
142. Reid JD, Andersen ME. Medial calcification (whitlockite) in the aorta. *Atherosclerosis* 1993;101:213-24. DOI PubMed

143. Sage AP, Tintut Y, Demer LL. Regulatory mechanisms in vascular calcification. *Nat Rev Cardiol* 2010;7:528-36. DOI PubMed PMC
144. You AYE, Bergholt MS, St-Pierre JP, et al. Raman spectroscopy imaging reveals interplay between atherosclerosis and medial calcification in the human aorta. *Sci Adv* 2017;3:e1701156. DOI PubMed PMC
145. Chow B, Rabkin SW. The relationship between arterial stiffness and heart failure with preserved ejection fraction: a systemic meta-analysis. *Heart Fail Rev* 2015;20:291-303. DOI PubMed
146. Barasch E, Gottdiener JS, Marino Larsen EK, Chaves PH, Newman AB. Cardiovascular morbidity and mortality in community-dwelling elderly individuals with calcification of the fibrous skeleton of the base of the heart and aortosclerosis (The Cardiovascular Health Study). *Am J Cardiol* 2006;97:1281-6. DOI PubMed
147. Aikawa E, Nahrendorf M, Figueiredo JL, et al. Osteogenesis associates with inflammation in early-stage atherosclerosis evaluated by molecular imaging in vivo. *Circulation* 2007;116:2841-50. DOI
148. Wick G, Grundtman C. Inflammation and atherosclerosis. Boston: Springer Science & Business Media; 2011. DOI
149. Saita A, Bonaccorsi A, Motta M. Stone composition: where do we stand? *Urol Int* 2007;79 Suppl 1:16-9. DOI PubMed
150. Evan AP, Coe FL, Rittling SR, et al. Apatite plaque particles in inner medulla of kidneys of calcium oxalate stone formers: osteopontin localization. *Kidney Int* 2005;68:145-54. DOI PubMed
151. He JY, Deng SP, Ouyang JM. Morphology, particle size distribution, aggregation, and crystal phase of nanocrystallites in the urine of healthy persons and lithogenic patients. *IEEE Trans Nanobiosci* 2010;9:156-63. DOI PubMed
152. Alelign T, Petros B. Kidney stone disease: an update on current concepts. *Adv Urol* 2018;2018:3068365. DOI PubMed PMC
153. Chaudhary A, Singla SK, Tandon C. In vitro evaluation of terminalia arjuna on calcium phosphate and calcium oxalate crystallization. *Indian J Pharm Sci* 2010;72:340-5. PubMed PMC
154. Bensatal A, Ouahrani MR. Inhibition of crystallization of calcium oxalate by the extraction of *Tamarix gallica* L. *Urol Res* 2008;36:283-7. DOI PubMed
155. Griffith DP. Struvite stones. *Kidney Int* 1978;13:372-82. DOI PubMed
156. Luigia M, Summ V. A review of pathological biomineral analysis techniques and classification schemes. In: Aydinalp C, editor. An introduction to the study of mineralogy. London: InTech; 2012. DOI
157. Coe FL, Evan A, Worcester E. Kidney stone disease. *J Clin Invest* 2005;115:2598-608. DOI
158. Aggarwal KP, Narula S, Kakkar M, Tandon C. Nephrolithiasis: molecular mechanism of renal stone formation and the critical role played by modulators. *Biomed Res Int* 2013;2013:292953. DOI PubMed PMC
159. Coe FL, Parks JH, Asplin JR. The pathogenesis and treatment of kidney stones. *N Engl J Med* 1992;327:1141-52. DOI PubMed
160. Fleisch H. Inhibitors and promoters of stone formation. *Kidney Int* 1978;13:361-71. DOI PubMed
161. Ebrahimpour A, Perez L, Nancollas GH. Induced crystal growth of calcium oxalate monohydrate at hydroxyapatite surfaces. the influence of human serum albumin, citrate, and magnesium. *Langmuir* 1991;7:577-83. DOI
162. Asplin JR, Arsenault D, Parks JH, Coe FL, Hoyer JR. Contribution of human uropontin to inhibition of calcium oxalate crystallization. *Kidney Int* 1998;53:194-9. DOI PubMed
163. Stapleton A, Ryall U. Blood coagulation proteins and urolithiasis are linked: crystal matrix protein is the F1 activation peptide of human prothrombin. *Br J Urol* 1995;75:712-9. DOI
164. Pillay SN, Asplin JR, Coe FL. Evidence that calgranulin is produced by kidney cells and is an inhibitor of calcium oxalate crystallization. *Am J Physiol* 1998;275:F255-61. DOI PubMed
165. Loeb JA, Sohrab SA, Huq M, Fuerst DR. Brain calcifications induce neurological dysfunction that can be reversed by a bone drug. *J Neurol Sci* 2006;243:77-81. DOI PubMed
166. Smeyers-Verbeke J, Michotte Y, Pelsmaeckers J, et al. The chemical composition of idiopathic nonarteriosclerotic cerebral calcifications. *Neurology* 1975;25:48-57. DOI
167. Oliveira JR, Oliveira MF. Primary brain calcification in patients undergoing treatment with the bisphosphonate alendronate. *Sci Rep* 2016;6:22961. DOI PubMed PMC
168. Lemos RR, Ferreira JBMM, Keasey MP, Oliveira JRM. Chapter Fourteen - an update on primary familial brain calcification. In: Bhatia KP, Schneider SA, editors. International review of neurobiology. Cambridge: Academic Press. 2013; pp. 349-71. DOI
169. Jankovic J. Searching for a relationship between manganese and welding and Parkinson's disease. *Neurology* 2005;64:2021-8. DOI PubMed
170. Bekiesinska-Figatowska M, Mierzevska H, Jurkiewicz E. Basal ganglia lesions in children and adults. *Eur J Radiol* 2013;82:837-49. DOI PubMed
171. Simoni M, Pantoni L, Pracucci G, et al. Prevalence of CT-detected cerebral abnormalities in an elderly Swedish population sample. *Acta Neurol Scand* 2008;118:260-7. DOI
172. Yamada M, Asano T, Okamoto K, et al. High frequency of calcification in basal ganglia on brain computed tomography images in Japanese older adults. *Geriatr Gerontol Int* 2013;13:706-10. DOI
173. Deng H, Zheng W, Jankovic J. Genetics and molecular biology of brain calcification. *Ageing Res Rev* 2015;22:20-38. DOI
174. Anderson SB, de Souza RF, Hofmann-Rummelt C, Seitz B. Corneal calcification after amniotic membrane transplantation. *Br J Ophthalmol* 2003;87:587-91. DOI PubMed PMC
175. Nicholson BP, Lystad LD, Emch TM, Singh AD. Idiopathic dural optic nerve sheath calcification. *Br J Ophthalmol* 2011;95:290, 299. DOI PubMed

176. Russell SR, Mullins RF, Schneider BL, Hageman GS. Location, substructure, and composition of basal laminar drusen compared with drusen associated with aging and age-related macular degeneration. *Am J Ophthalmol* 2000;129:205-14. DOI PubMed
177. Hageman GS, Anderson DH, Johnson LV, et al. A common haplotype in the complement regulatory gene factor H (HF1/CFH) predisposes individuals to age-related macular degeneration. *Proc Natl Acad Sci USA* 2005;102:7227-32. DOI
178. Castellanos MR, Paramanathan K, El-Sayegh S, Forte F, Buchbinder S, Kleiner M. Breast cancer screening in women with chronic kidney disease: the unrecognized effects of metastatic soft-tissue calcification. *Nat Clin Pract Nephrol* 2008;4:337-41. DOI PubMed
179. Yildiz S, Toprak H, Aydin S, et al. The association of breast arterial calcification and metabolic syndrome. *Clinics* 2014;69:841-6. DOI PubMed PMC
180. Scimeca M, Giannini E, Antonacci C, Pistolese CA, Spagnoli LG, Bonanno E. Microcalcifications in breast cancer: an active phenomenon mediated by epithelial cells with mesenchymal characteristics. *BMC Cancer* 2014;14:286. DOI PubMed PMC
181. Scimeca M, Antonacci C, Colombo D, Bonfiglio R, Buonomo OC, Bonanno E. Emerging prognostic markers related to mesenchymal characteristics of poorly differentiated breast cancers. *Tumour Biol* 2016;37:5427-35. DOI PubMed
182. Hassler O. Microradiographic investigations of calcifications of the female breast. *Cancer* 1969;23:1103-9. DOI PubMed
183. Scott R, Stone N, Kendall C, Geraki K, Rogers K. Relationships between pathology and crystal structure in breast calcifications: an in situ X-ray diffraction study in histological sections. *NPJ Breast Cancer* 2016;2:16029. DOI PubMed PMC
184. Kunitake JAMR, Choi S, Nguyen KX, et al. Correlative imaging reveals physicochemical heterogeneity of microcalcifications in human breast carcinomas. *J Struct Biol* 2018;202:25-34. DOI PubMed PMC
185. Lakhdar A, Daudon M, Mathieu M, Kellum A, Balleyguier C, Bazin D. Underlining the complexity of the structural and chemical characteristics of ectopic calcifications in breast tissues through FE-SEM and μ FTIR spectroscopy. *Comptes Rendus Chimie* 2016;19:1610-24. DOI
186. Haka AS, Shafer-Peltier KE, Fitzmaurice M, et al. Identifying microcalcifications in benign and malignant breast lesions by probing differences in their chemical composition using raman spectroscopy. *Cancer Res* 2002;62:5375-80. PubMed
187. Scott R, Kendall C, Stone N, Rogers K. Elemental vs. phase composition of breast calcifications. *Sci Rep* 2017;7:136. DOI PubMed PMC
188. Tandan M, Talukdar R, Reddy DN. Management of pancreatic calculi: an update. *Gut Liver* 2016;10:873-80. DOI PubMed PMC
189. Narasimhulu KV, Gopal NO, Rao JL, et al. Structural studies of the biomineralized species of calcified pancreatic stones in patients suffering from chronic pancreatitis. *Biophys Chem* 2005;114:137-47. DOI
190. Pitchumoni CS, Viswanathan KV, Gee Varghese PJ, Banks PA. Ultrastructure and elemental composition of human pancreatic calculi. *Pancreas* 1987;2:152-8. DOI PubMed
191. Klimas R, Bennett B, Gardner WA Jr. Prostatic calculi: a review. *Prostate* 1985;7:91-6. DOI PubMed
192. Sutor DJ, Wooley SE. The crystalline composition of prostatic calculi. *Br J Urol* 1974;46:533-5. DOI PubMed
193. Hyun JS. Clinical significance of prostatic calculi: a review. *World J Mens Health* 2018;36:15-21. DOI PubMed PMC
194. Wallingford MC, Benson C, Chavkin NW, Chin MT, Frasch MG. Placental vascular calcification and cardiovascular health: it is time to determine how much of maternal and offspring health is written in stone. *Front Physiol* 2018;9:1044. DOI PubMed PMC
195. Poggi SH, Bostrom KI, Demer LL, Skinner HC, Koos BJ. Placental calcification: a metastatic process? *Placenta* 2001;22:591-6. DOI PubMed
196. Chen KH, Chen LR, Lee YH. Exploring the relationship between preterm placental calcification and adverse maternal and fetal outcome. *Ultrasound Obstet Gynecol* 2011;37:328-34. DOI PubMed
197. Marchiori E, Hochegger B, Zanetti G. Lymph node calcifications. *J Bras Pneumol* 2018;44:83. DOI PubMed PMC
198. Sakae T, Yamamoto H. Crystals and calcification patterns in two lymph node calcifications. *J Oral Pathol* 1987;16:456-62. DOI PubMed
199. Kim MH, Kim HJ, Kim NN, Yoon HS, Ahn SH. A rotational ablation tool for calcified atherosclerotic plaque removal. *Biomed Microdevices* 2011;13:963-71. DOI PubMed
200. Kaul A, Dhalla PS, Bapatla A, et al. Current treatment modalities for calcified coronary artery disease: a review article comparing novel intravascular lithotripsy and traditional rotational atherectomy. *Cureus* 2020;12:e10922. DOI PubMed PMC
201. Jahnhen-Dechent W, Schäfer C, Ketteler M, McKee MD. Mineral chaperones: a role for fetuin-A and osteopontin in the inhibition and regression of pathologic calcification. *J Mol Med* 2008;86:379-89. DOI PubMed
202. Schibler D, Russell RG, Fleisch H. Inhibition by pyrophosphate and polyphosphate of aortic calcification induced by vitamin D3 in rats. *Clin Sci* 1968;35:363-72. PubMed
203. O'Neill WC, Lomashvili KA, Malluche HH, Faugere MC, Riser BL. Treatment with pyrophosphate inhibits uremic vascular calcification. *Kidney Int* 2011;79:512-7. DOI PubMed PMC
204. Wu M, Rementer C, Giachelli CM. Vascular calcification: an update on mechanisms and challenges in treatment. *Calcif Tissue Int* 2013;93:365-73. DOI PubMed PMC
205. Schinke T, Amendt C, Trindl A, Pöschke O, Müller-Esterl W, Jahnhen-Dechent W. The serum protein alpha2-HS glycoprotein/fetuin inhibits apatite formation in vitro and in mineralizing calvaria cells. A possible role in mineralization and calcium homeostasis. *J Biol Chem* 1996;271:20789-96. DOI
206. Heiss A, Jahnhen-Dechent W, Endo H, Schwahn D. Structural dynamics of a colloidal protein-mineral complex bestowing on calcium phosphate a high solubility in biological fluids. *Biointerphases* 2007;2:16-20. DOI PubMed
207. Heiss A, DuChesne A, Denecke B, et al. Structural basis of calcification inhibition by alpha 2-HS glycoprotein/fetuin-A. Formation

- of colloidal calciprotein particles. *J Biol Chem* 2003;278:13333-41. DOI
208. Jahnen-Dechent W, Heiss A, Schäfer C, Ketteler M. Fetuin-A regulation of calcified matrix metabolism. *Circ Res* 2011;108:1494-509. DOI PubMed
209. Zebboudj AF, Imura M, Boström K. Matrix GLA protein, a regulatory protein for bone morphogenetic protein-2. *J Biol Chem* 2002;277:4388-94. DOI PubMed
210. Hruska KA, Mathew S, Saab G. Bone morphogenetic proteins in vascular calcification. *Circ Res* 2005;97:105-14. DOI PubMed
211. Mckee M, Nanci A. Osteopontin at mineralized tissue interfaces in bone, teeth, and osseointegrated implants: Ultrastructural distribution and implications for mineralized tissue formation, turnover, and repair. *Microsc Res Tech* 1996;33:141-64. PubMed
212. McKee MD, Nanci A. Osteopontin: an interfacial extracellular matrix protein in mineralized tissues. *Connect Tissue Res* 1996;35:197-205. DOI PubMed
213. Oikonomaki T, Papisotiriou M, Ntriniias T, et al. The effect of vitamin K2 supplementation on vascular calcification in haemodialysis patients: a 1-year follow-up randomized trial. *Int Urol Nephrol* 2019;51:2037-44. DOI
214. Eastell R, Walsh JS, Watts NB, Siris E. Bisphosphonates for postmenopausal osteoporosis. *Bone* 2011;49:82-8. DOI PubMed
215. Francis MD, Russell RG, Fleisch H. Diphosphonates inhibit formation of calcium phosphate crystals in vitro and pathological calcification in vivo. *Science* 1969;165:1264-6. DOI PubMed
216. der Sluis IM, Boot AM, Vernooij M, Meradji M, Kroon AA. Idiopathic infantile arterial calcification: clinical presentation, therapy and long-term follow-up. *Eur J Pediatr* 2006;165:590-3. DOI PubMed
217. Persy V, De Broe M, Ketteler M. Bisphosphonates prevent experimental vascular calcification: treat the bone to cure the vessels? *Kidney Int* 2006;70:1537-8. DOI PubMed
218. Shiraishi N, Kitamura K, Miyoshi T, et al. Successful treatment of a patient with severe calcific uremic arteriolopathy (calciophylaxis) by etidronate disodium. *Am J Kidney Dis* 2006;48:151-4. DOI
219. Jansen RS, Duijst S, Mahakena S, et al. ABCC6-mediated ATP secretion by the liver is the main source of the mineralization inhibitor inorganic pyrophosphate in the systemic circulation-brief report. *Arterioscler Thromb Vasc Biol* 2014;34:1985-9. DOI PubMed PMC
220. Li Q, Huang J, Pinkerton AB, et al. Inhibition of tissue-nonspecific alkaline phosphatase attenuates ectopic mineralization in the Abcc6(-/-) mouse model of PXE but not in the enpp1 mutant mouse models of GACI. *J Invest Dermatol* 2019;139:360-8. DOI PubMed PMC
221. Pomozi V, Brampton C, van de Wetering K, et al. Pyrophosphate supplementation prevents chronic and acute calcification in ABCC6-deficient mice. *Am J Pathol* 2017;187:1258-72. DOI PubMed PMC
222. Zhao J, Kingman J, Sundberg JP, Uitto J, Li Q. Plasma PPI deficiency is the major, but not the exclusive, cause of ectopic mineralization in an Abcc6(-/-) mouse model of PXE. *J Invest Dermatol* 2017;137:2336-43. DOI PubMed PMC
223. Garti N, Tibika F, Sarig S, Perlberg S. The inhibitory effect of polymeric carboxylic amino-acids and urine on calcium oxalate crystallization. *Biochem Biophys Res Commun* 1980;97:1154-62. DOI PubMed
224. Kleinman JG, Alatalo LJ, Beshensky AM, Wesson JA. Acidic polyanion poly(acrylic acid) prevents calcium oxalate crystal deposition. *Kidney Int* 2008;74:919-24. DOI PubMed PMC
225. Worcester EM, Blumenthal SS, Beshensky AM, Lewand DL. The calcium oxalate crystal growth inhibitor protein produced by mouse kidney cortical cells in culture is osteopontin. *J Bone Miner Res* 1992;7:1029-36. DOI PubMed
226. Wesson JA, Johnson RJ, Mazzali M, et al. Osteopontin is a critical inhibitor of calcium oxalate crystal formation and retention in renal tubules. *J Am Soc Nephrol* 2003;14:139-47. DOI
227. Cohen GF, Vyas NS. Sodium thiosulfate in the treatment of calciophylaxis. *J Clin Aesthet Dermatol* 2013;6:41-4. PubMed PMC
228. Guerra G, Shah RC, Ross EA. Rapid resolution of calciophylaxis with intravenous sodium thiosulfate and continuous venovenous haemofiltration using low calcium replacement fluid: case report. *Nephrol Dial Transplant* 2005;20:1260-2. DOI PubMed
229. Cicone JS, Petronis JB, Embert CD, Spector DA. Successful treatment of calciophylaxis with intravenous sodium thiosulfate. *Am J Kidney Dis* 2004;43:1104-8. DOI PubMed
230. Yatzidis H. Successful sodium thiosulphate treatment for recurrent calcium urolithiasis. *Clin Nephrol* 1985;23:63-7. PubMed
231. Sun XY, Xu M, Ouyang JM. Effect of crystal shape and aggregation of calcium oxalate monohydrate on cellular toxicity in renal epithelial cells. *ACS Omega* 2017;2:6039-52. DOI PubMed PMC
232. Bazin D, Chevallier P, Matzen G, Jungers P, Daudon M. Heavy elements in urinary stones. *Urol Res* 2007;35:179-84. DOI PubMed
233. Meyer J, Angino E. The role of trace metals in calcium urolithiasis. *Invest Urol* 1977;14:347-50. PubMed
234. Muñoz JA, Valiente M. Effects of trace metals on the inhibition of calcium oxalate crystallization. *Urol Res* 2005;33:267-72. DOI PubMed
235. Atakan IH, Kaplan M, Seren G, Aktöz T, Gül H, İnci O. Serum, urinary and stone zinc, iron, magnesium and copper levels in idiopathic calcium oxalate stone patients. *Int Urol Nephrol* 2007;39:351-6. DOI
236. Levy RJ, Schoen FJ, Flowers WB, Staelin ST. Initiation of mineralization in bioprosthetic heart valves: studies of alkaline phosphatase activity and its inhibition by AlCl₃ or FeCl₃ preincubations. *J Biomed Mater Res* 1991;25:905-35. DOI PubMed
237. Ali SY. Apatite-type crystal deposition in arthritic cartilage. *Scan Electron Microsc* 1985;Pt 4:1555-66. PubMed
238. Usai D, Maritan L, Dal Sasso G, et al. Late pleistocene/early holocene evidence of prostatic stones at Al khiday cemetery, central sudan. *PLoS One* 2017;12:e0169524. DOI PubMed PMC

Review

Open Access



Constructing and regulating nanochannels in two-dimensional-material-based membranes for specified separation applications

Chao Xing^{1,2,#}, Mengchen Zhang^{1,#}, Lingfeng Liu¹, Zehua Zheng¹, Ming Zhou², Shanqing Zhang² , Changyu Liu¹ 

¹School of Biotechnology and Health Sciences, Wuyi University, Jiangmen 529020, Guangdong, China.

²Centre for Catalysis and Clean Energy, School of Environment and Science, Gold Coast Campus, Griffith University, Queensland, QLD 4222, Australia.

[#]Authors contributed equally to this work.

Correspondence to: Prof. Shanqing Zhang, Centre for Catalysis and Clean Energy, School of Environment and Science, Gold Coast Campus, Griffith University, Queensland, QLD 4222, Australia. E-mail: s.zhang@griffith.edu.au; Dr. Ming Zhou, Centre for Catalysis and Clean Energy, School of Environment and Science, Gold Coast Campus, Griffith University, QLD 4222, Queensland, Australia. E-mail: ming.zhou@griffith.edu.au; Prof. Changyu Liu, School of Biotechnology and Health Sciences, Wuyi University, Jiangmen 529020, Guangdong China. E-mail: wyuchemistry@126.com

How to cite this article: Xing C, Zhang M, Liu L, Zheng Z, Zhou M, Zhang S, Liu C. Constructing and regulating nanochannels in two-dimensional-material-based membranes for specified separation applications. *Microstructures* 2023;3:2023031. <https://dx.doi.org/10.20517/microstructures.2023.11>

Received: 26 Feb 2023 **First Decision:** 19 Apr 2023 **Revised:** 26 May 2023 **Accepted:** 2 Jun 2023 **Published:** 10 Jul 2023

Academic Editors: Shujun Zhang, Yi Du **Copy Editor:** Fangyuan Liu **Production Editor:** Fangyuan Liu

Abstract

The two-dimensional (2D) materials offer atomic-level thickness and unique physical and chemical properties for the preparation of a new class of membranes, i.e., nanochannel membranes. The nanochannel membranes have been utilized in a broad spectrum of new separation applications. However, the instability of the nanochannels, interfacial instability of 2D materials, and the swelling problem could damage the membrane performance, such as permeability, selectivity, and service lifetime. Innovative strategies for constructing and regulating the nanochannels are enthusiastically explored to address these challenges. Along this line, in this work, we first provide insight into the mechanisms of the nanochannel construction, the separation mechanism, and the effect of nanochannels on the separation performance. Then, the strategies developed in the literature, in particular, the strategies for the preparation of ideal 2D nanosheets, the strategies for constructing nanochannels, and the strategies for regulating the characteristics of nanochannels (channel size, channel length, channel morphology, and channel surface physicochemical properties) are systematically summarized. After that, we briefly introduce the application of 2D-material-based nanochannel membranes and outline the current challenges and provide an



© The Author(s) 2023. **Open Access** This article is licensed under a Creative Commons Attribution 4.0 International License (<https://creativecommons.org/licenses/by/4.0/>), which permits unrestricted use, sharing, adaptation, distribution and reproduction in any medium or format, for any purpose, even commercially, as long as you give appropriate credit to the original author(s) and the source, provide a link to the Creative Commons license, and indicate if changes were made.



outlook in the further exploration of separation mechanism, large-scale manufacturing, and the eventual commercialization of the membranes.

Keywords: 2D nanosheet, nanochannel, membrane, separation, regulation, construction

INTRODUCTION

Membrane separation technologies have become revolutionized various industries by offering numerous benefits, such as low cost, high efficiency, and environmental sustainability. These technologies utilize thin membrane barriers that separate specific substances based on variations in size, charge, or other properties. Membranes can be roughly categorized into macrochannel membranes, microchannel membranes, and nanochannel membranes, depending on the size of the channels and their characteristic scale. Macrochannel membranes possess larger channel dimensions, typically in the millimeter to centimeter range. They are designed for applications involving larger particles or higher flow rates and are commonly used in pre-treatment processes in various industries, including chemical, environmental, pharmaceutical, mining, and more. Microchannel membranes have smaller channel dimensions than macrochannels but are still relatively large when compared to nanochannels. Typically, their channel sizes range from tens to hundreds of microns in diameter. They find a variety of applications in areas such as microfluidics, chemical synthesis, and biomedical devices. Nanochannel membranes feature channels with dimensions typically in the nanometer range. These membranes are engineered with extremely small channel sizes to precisely control molecular or ion transport. They are extensively used in diverse applications such as water treatment, ion selectivity, gas separation, DNA sequencing, protein analysis, drug delivery systems, *etc.* Each scale of the membrane has its own strengths and weaknesses (as shown in [Table 1](#) below), and the choice of the membrane depends on the specific separation requirements, target molecules or ions, and operating conditions^[1-7].

Compared with other membranes, nanochannel membranes have unique advantages due to their extremely small channel size, offering the potential for highly selective separations, reduced sample consumption, and single-molecule analysis. These properties make nanochannel membranes particularly suitable for applications that require precise control of molecular transport and analysis and have received increasing attention from the scientific and engineering communities^[8-14]. To meet specific requirements, ultrathin nanochannel membranes can be directly assembled from a variety of inorganic or organic materials. Two-dimensional (2D) materials are of particular interest in the field of nanochannel engineering due to their unique physical and chemical properties, including atomic-level thickness, hydrophilicity, and ductility. A diverse range of 2D materials are currently under investigation, such as graphene^[15], graphene oxide (GO)^[16], transition metal carbides/nitrides (MXenes)^[17], hexagonal boron nitride (h-BN)^[18], graphitic carbon nitride (g-C₃N₄)^[19], transition metal dichalcogenides (TMDs)^[20,21], layered double hydroxides (LDHs)^[22], 2D zeolites^[23], 2D metal-organic frameworks (2D MOFs)^[24], 2D covalent organic frameworks (2D COFs)^[25], and beyond. These materials offer a wealth of possibilities for creating high-performance 2D-material-based nanochannel membranes. The superb separation performance achieved by nanochannel membranes based on 2D materials is mainly attributed to the unique properties and structural characteristics of the materials. The atomic-level thickness of 2D materials allows the formation of nanochannels with precise dimensions, which can effectively restrict the passage of certain molecules or ions depending on their size. In addition, the layer spacing and surface chemistry of the nanochannels can be modulated by introducing functional groups or modifying the surface, further affecting the selectivity of the membrane. In addition, the high aspect ratio and large surface area of 2D materials provide abundant active sites for interaction with the target material, thus enabling molecular sieving and preferential ion transport. In addition, the ordered arrangement of nanosheets in the membrane structure facilitates the formation of continuous and uniform

Table 1. Key characteristics of macrochannel, microchannel, and nanochannel membranes

Membrane type	Channel size (typical range)	Key features	Applications
Macrochannel	> 100 μm	Large channel size, low surface-to-volume ratio, turbulent flow regime, and reduced resistance to flow	Pre-treatment processes in chemical, environmental, pharmaceutical, mining, and other industries
Microchannel	1-100 μm	Intermediate channel size, moderate surface-to-volume ratio, laminar flow regime, and diffusion dominates	Microfluidics, lab-on-a-chip devices, chemical synthesis, and separation processes
Nanochannel	< 100 nm	Very small channel size, high surface-to-volume ratio, molecular selectivity, and electrostatic interactions dominate	Water treatment, ion selectivity, gas separation, DNA sequencing, single-molecule analysis, nanofluidics, and biosensors

nanochannels, which improves permeation efficiency. Overall, the combination of these factors allows 2D-material-based nanochannel membranes to achieve selective separations by exploiting the size, charge, and interaction-based properties of the target species.

To comprehensively assess the performance of the membranes, several formulas can be utilized, including the rejection coefficient, separation factor, permeability, flux, rejection, fouling index, and interlayer spacing. By quantifying these parameters, researchers can better understand the potential benefits of using 2D materials with densely packed nanochannels for nanoscale separation applications.

The rejection coefficient (R) is determined by equation (1), where C_{feed} is the solute concentration in the feed, and $C_{permeate}$ is the solute concentration in the permeate.

$$R = \frac{C_{feed} - C_{permeate}}{C_{feed}} \quad (1)$$

The separation factor (α) is defined as the ratio of the rejection coefficients of two different solutes, A and B, which is determined by equation (2).

$$\alpha = \frac{R_A}{R_B} \quad (2)$$

Permeability (P) measures the ease with which a solvent flow through a porous material and is calculated using the formula (3), where Q is the permeate volume, A is the effective membrane area, and ΔP is the transmembrane pressure.

$$P = \frac{Q}{(A \times \Delta P)} \quad (3)$$

Flux (J) represents the volume of permeate that passes through the membrane per unit area per unit of time and is calculated using the formula (4), where Δt is the time.

$$J = \frac{Q}{A \times \Delta t} \quad (4)$$

Rejection (Re_j) is defined as the ratio of the solute concentration in the feed to the solute concentration in the permeate and is calculated using the formula (5).

$$Rej = 1 - \frac{C_{permeate}}{C_{feed}} \quad (5)$$

The fouling index (*FI*) is calculated using the formula (6), where J_{clean} is the flux of the clean membrane, and J_{fouled} is the flux of the fouled membrane.

$$FI = \frac{J_{clean} - J_{fouled}}{J_{clean} \times 100\%} \quad (6)$$

The interlayer spacing of the 2D-material-based nanochannel membranes can be calculated using the Bragg equation for X-ray diffraction (XRD), which is given by formula (7), where d is the interlayer spacing, λ is the wavelength of the X-ray, and θ is the diffraction angle.

$$d = \frac{\lambda}{2 \sin \theta} \quad (7)$$

Through a comprehensive analysis of membrane performance using the equations outlined above, valuable insights can be gained into the potential of nanochannel membranes based on 2D materials with densely packed channel arrays. These membranes are anticipated to offer several distinct advantages for nanoscale separation applications, including the following: (1) The membranes possess simple and tunable nanochannels that facilitate quantitative modeling and probing of nanofluids transport mechanisms; (2) The membranes allow flexible modification of nanochannels with favorable functionality to meet various application requirements; (3) The membranes enable ultra-thin structures down to single-atom thickness and ultra-high throughput by simple and scalable methods; and (4) The membranes can provide nanochannels with specific sizes, and the size can be precisely controlled from tens of nanometers to sub-nanometer scale to achieve high selectivity^[5,26,27].

Although their numerous theoretical advantages, 2D-material-based nanochannel membranes still face many practical challenges. One such challenge is that most 2D materials, including GO and MXene, contain numerous hydroxyl groups, carboxyl groups, Ti-O, and other hydrophilic functional groups on their surfaces, which can lead to severe swelling problems and thus reduce the selectivity of the membranes^[28]. Additionally, interfacial instability of 2D materials makes membrane structures very prone to collapse, resulting in generally shorter membrane lifespans that cannot meet practical needs^[29]. Besides, high operating pressures are still required for some membranes to achieve high permeability, which leads to increased energy consumption, and other issues such as poor anti-fouling ability and relatively expensive construction costs must be addressed^[30]. Given these challenges, there is no consensus on whether developing innovative, large-scale reproducible strategies for constructing and regulating nanochannels is a top priority for solving the aforementioned problems and ultimately enabling the widespread use of membranes in industrial applications. Most of the reviews in the literature focus more on the intricate details of membrane construction, regulation, and the role of nanochannels in separation performance. In contrast, this work seamlessly links the separation mechanisms, addressing the nanochannel separation and collapsing issues, selection of suitable membranes, and various practical applications.

This comprehensive review delves into the intricate details of membrane construction and regulation, highlighting the critical role of nanochannels in separation performance. This insight into the mechanism behind nanochannel collapse also provides invaluable insight into choosing the most suitable membrane for a particular application. As the fundamental building “bricks” of membrane construction, obtaining the ideal 2D material is a crucial starting step for achieving high-performance membranes. Therefore, the

review begins with a comprehensive description of 2D-material preparation strategies, including “top-down” and “bottom-up” approaches. Nanochannel properties directly impact separation performances, such as permeability and selectivity, and as such, the review outlines 2D nanosheet perforation methods (i.e., drilling out-of-plane nanochannels, similar to creating “porous bricks”) and membrane assembly methods (similar to building “house”) for obtaining in-plane nanochannels. Nanochannel regulation is similar to “renovating a house”, giving the membrane improved structural and functional properties. Thus, four aspects of such modification are briefly discussed (i.e., channel size, channel length, channel morphology, and surface chemistry). Laboratory-scale application attempts are the first step towards industrial applications (similar to “trial residence”), which are also reviewed. Afterward, to give readers a more intuitive picture, the review also categorizes various representative application scenarios and describes their specific needs for membranes, such as liquid molecular separation, gas separation, and ion sieving. A visual summary of the main elements described above is provided in [Figure 1](#). In the final section, we conclude with a discussion of current challenges and an outlook on the eventual commercialization of membranes. Overall, this comprehensive review presents readers with a detailed roadmap of the entire process of membrane preparation and regulation from raw materials to final applications (“clay” to “bricks” to “furnished houses”) and highlights the corresponding strategies employed in each step. By providing clear and concise information, this review aims to inspire future research and the development of new and innovative membrane preparation and regulation strategies, ultimately leading to the realization of highly efficient and effective membrane technologies.

CONSTRUCTING NANOCHANNELS WITH 2D NANOSHEETS

2D nanosheets refer to a class of materials that consists of only one or a few atomic layers, exhibiting an ultrathin sheet-like geometry beyond the nanoscale^[31]. These materials are characterized by strong interlayer covalent bonds and weak interlayer van der Waals bonds and exhibit excellent electrical, optical, and mechanical properties compared to their bulk counterparts, making them extremely attractive in the fields of physics, materials science, and chemistry^[32]. The successful isolation of monolayer graphene by Novoselov *et al.* in 2004 paved the way for the exploration of many other 2D materials, which have become ideal building blocks for the development of membranes with nanochannels due to their atomic thickness and unique physicochemical properties^[30,33].

When 2D materials are engineered into membranes, two basic forms of nanochannels can be created: out-of-plane nanochannels and in-plane nanochannels. Out-of-plane nanochannels can be formed by utilizing 2D nanosheets with intrinsically porous or perforating intrinsically nonporous 2D materials. In-plane nanochannels can be fabricated from 2D layered membranes in which several or multiple layers of nanosheets are aligned parallel to form well-defined nanochannels. This section describes typical construction strategies for creating nanochannels from 2D materials, including synthetic methods for intrinsic nanopores by multilayer peeling or monolayer growth, perforation approaches for artificial nanopores through physical and chemical etching, and various membrane assembly methods, including van der Waals assembly of individual nanochannels through nanosheet extraction, solution-assisted assembly of dense nanochannels by pressure/vacuum filtration, spin/spray coating, and other techniques.

Synthesis of 2D nanosheets

2D nanosheets serve as the foundational materials for constructing nanochannels from 2D materials. The synthesis of 2D nanosheets can be generally classified as “top-down” and “bottom-up” strategies, as shown in [Figures 2 and 3](#).

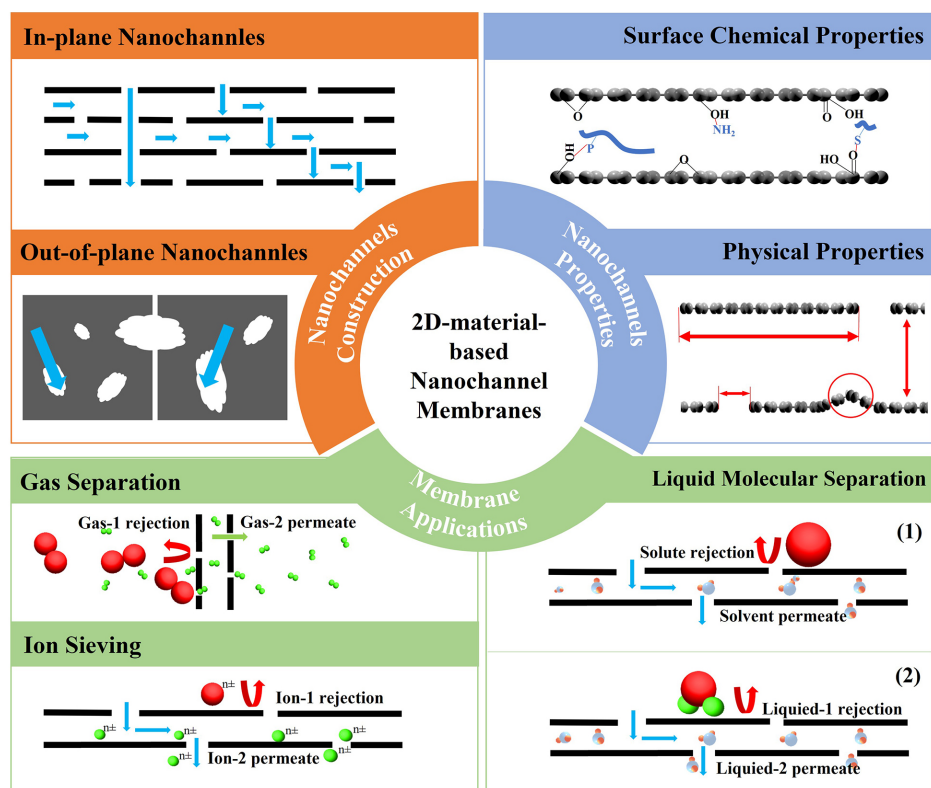


Figure 1. Strategies for constructing nanochannels, regulating nanochannels, and applications of 2D-material-based nanochannel membranes.

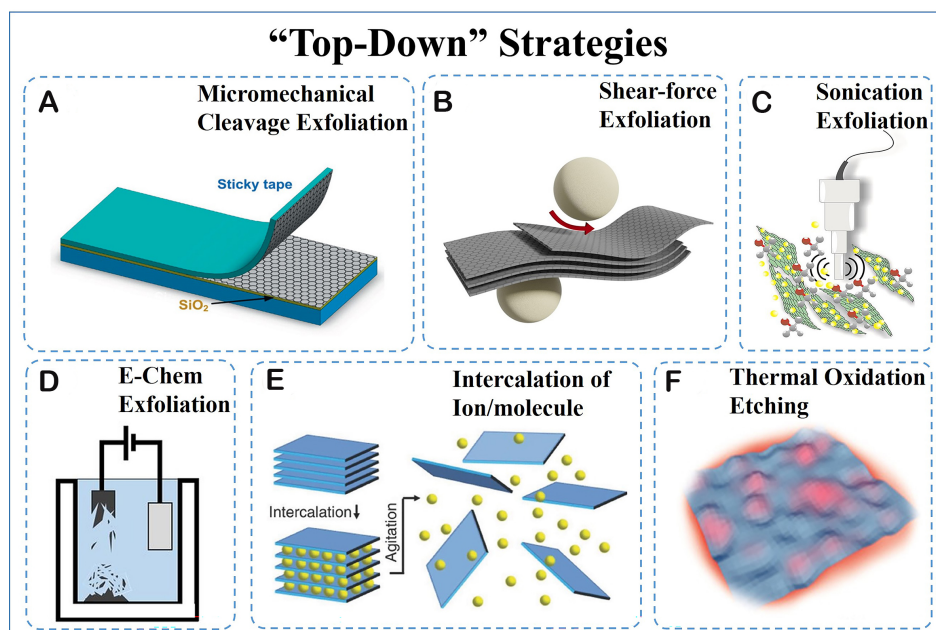


Figure 2. Schematics of the main “top-down” synthesis strategies of 2D nanosheets. (A) Micromechanical cleavage exfoliation^[171]. Copyright 2012, Elsevier Ltd. (B) Ball milling shear-force exfoliation. (C) Sonication exfoliation^[172]. Copyright 2018, Elsevier B.V. (D) Electrochemical (E-Chem) exfoliation^[38]. Copyright 2018, Springer Nature. (E) Ion/molecule intercalation^[173]. Copyright 2017, John Wiley & Sons, Inc. (F) Thermal oxidation etching^[47]. Copyright 2021, John Wiley & Sons, Inc.

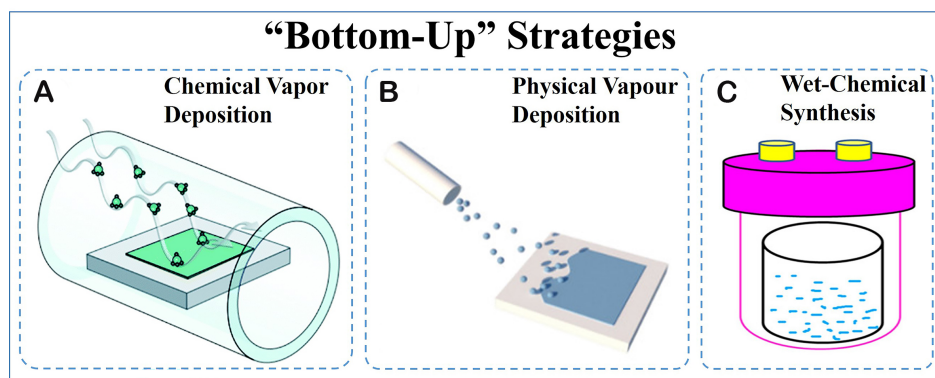


Figure 3. Schematics of the main “bottom-up” synthesis strategies of 2D nanosheets. (A) Chemical vapor deposition^[174]. Copyright 2017, Springer Nature. (B) Physical vapor deposition^[47]. Copyright 2021, John Wiley & Sons, Inc. (C) Wet-chemical synthesis^[175]. Copyright 2021, American Chemical Society.

The “top-down” strategy involves the exfoliation of 2D nanosheets from bulk-layered materials by breaking weak interlayer van der Waals, π - π stacking, and/or hydrogen bonding interactions [Figure 2]. Novoselov *et al.* pioneeringly achieved a single layer of graphite using the micromechanical cleavage method [Figure 2A], which enables the preparation of a variety of 2D nanosheets with a clean surface and high quality on a macroscopic scale^[33,34]. However, it is worth noting that this method has the drawback of low efficiency. Paton *et al.* took the lead in conducting shear force-assisted^[35] [Figure 2B] and sonication-assisted^[36] [Figure 2C] exfoliations in liquids, where bulk graphene and TMDs crystals can be efficiently dispersed in common solvents to obtain large quantities of mono- and few-layer nanosheets. Another representative shear force-assisted and sonication-assisted mixed work is demonstrated by Peng *et al.*, who developed a soft-physical process of preparing 2D MOF nanosheets with large lateral sizes by low-energy wet ball milling coupled with ultrasonication in methanol/propanol mixtures^[37]. Electrochemical (E-Chem) exfoliation [Figure 2D] is a promising bulk method for producing graphene from graphite, where an applied voltage drives ionic species to intercalate into graphite, forming gaseous species that expand and exfoliate individual graphene sheets. Achee *et al.* reported a method for sustained graphene output within a permeable and expandable containment system, indicating both high yield (65%) and extraordinarily large lateral size ($> 30 \mu\text{m}$) of graphene^[38].

The use of specific ions or molecules intercalation [Figure 2E] to weaken interactions within the layers by exchanging or reacting can further enhance the efficiency of liquid-phase exfoliations, which have been widely employed for preparing various types of 2D nanosheets such as GO, MXene, TMDs, and LDHs^[39-42]. Notably, these intrinsically nonporous 2D nanosheets still require a subsequent perforation process to fabricate nanochannels (as discussed in the next section). For example, intrinsically porous 2D nanosheets can be exfoliated from their related layered materials with high purity via melt blending with a polymer matrix, as demonstrated by Varoon *et al.*^[43]. And the synthesis of $g\text{-C}_3\text{N}_4$ nanosheets can be achieved by thermal oxidation [Figure 2F] with long-time heating and etching, which was shown by Ren *et al.*, to produce a series of $g\text{-C}_3\text{N}_4$ nanosheets with a thinner layer thickness, larger BET surface area, and higher graphitic nitrogen ratio^[44]. They proposed that the higher activity of the $g\text{-C}_3\text{N}_4$ from long-time thermal oxidative etching might be ascribed to the enlarged specific surface, pore volume, and higher graphitic nitrogen ratio with the loose and soft laminar morphology^[44].

However, it should be noted that the “top-down” strategy for exfoliation is limited by the availability of layered materials, which may result in incidental structural deterioration and morphological damage during

the exfoliation process. Such issues may hinder the obtainment of ideal 2D nanosheets.

The “bottom-up” strategy [Figure 3] involves synthesizing 2D nanosheets through chemical reactions from specific precursors under given conditions, which is theoretically feasible for all types of 2D nanosheets. Chemical vapor deposition (CVD) [Figure 3A] growth and physical vapor deposition (PVD) [Figure 3B] growth are reliable routes for synthesizing highly crystalline 2D nanosheets such as graphene, MXene, h-BN, TMDs, and others, with large-area uniformity^[45-47]. However, transferring the crack-free as-prepared 2D nanosheets from the substrate remains challenging^[48-50]. As an alternative, wet-chemical synthesis [Figure 3C] is widely employed due to its good controllability, reproducibility, and scalability, especially for preparing those crystalline porous materials made from predesigned skeletons such as zeolites, MOFs, and COFs. Jeon *et al.* successfully produced high-aspect-ratio MFI-type zeolite nanosheets using a nanocrystal-seeded growth method that was triggered by a single rotational intergrowth^[51]. These highly oriented MFI nanosheets with straight vertical micropores allow the secondary growth of thin and defect-free MFI membranes with extraordinary performance for separating xylene isomers^[51]. Makiura *et al.* reported a procedure for the rational modular assembly of MOF nanosheets with perfect orientation on a solid substrate by integrating the layer-by-layer growth and the Langmuir-Blodgett methods^[52]. Similarly, Rodenas *et al.*^[53] presented a new approach to produce self-standing intact MOF nanosheets that relied on the diffusion-mediated modulation of the MOF growth kinetics. The synthesis medium involves three vertically arranged liquid layers, where a topmost solution of cations and a bottom solution of linker precursors diffuse into the intermediate solvent layer, causing a slow supply of the MOF nutrients to form MOF nanosheets in a highly diluted medium. On the other hand, COF nanosheets can either grow on various substrates under solvothermal conditions or at solid-liquid/liquid-liquid/air-liquid interfaces via interfacial polymerizations^[54,55]. An excellent representative work was done by Kandambeth *et al.*, who successfully demonstrated the fabrication of various flexible, continuous, and defect-free COFs by casting and baking the mixed solution containing organic linkers and co-reagents^[56]. In addition, the “bottom-up” approach can also be used to directly fabricate porous graphene with a well-defined pore structure by selecting appropriate rigid molecular building blocks as monomers for the organic synthesis^[57].

Perforation on 2D nanosheets

Unlike intrinsically porous 2D nanosheets, the perfect monolayer nonporous 2D nanosheets are almost impermeable, requiring the artificial drilling of out-of-plane nanoscale holes to serve as nanochannels. Continuous experimental endeavors have been made to develop various perforation techniques to realize this goal, including physical and chemical methods such as focused electron beam, bombardment/focused ion beam, oxygen plasma etching, ultraviolet-induced oxidative etching, and chemical etching [Figure 4]. For example, Fischbein *et al.* showed that graphene nanosheets could be controllably nano-sculpted using the focused electron beam ablation technique with few nanometer precisions [Figure 4A]^[58]. Similarly, Koenig *et al.* utilized ultraviolet-induced oxidative etching [Figure 4B] to create angstrom-sized pores in the pristine graphene membrane, which were used as molecular sieves and exhibited selective gas transport capabilities^[59].

The focused ion beam perforation method is another effective technique [Figure 4C], which was successfully employed by Celebi *et al.* to produce narrowly-distributed pore sizes ranging from < 10 nm to 1 μm in free-standing graphene^[60]. Later, Russo *et al.* created pore nucleation sites on graphene using an argon ion beam followed by edge-selective electron recoil sputtering, yielding graphene nanopores with radii as small as 3 \AA , all without the use of focused beams^[61]. However, the effective areas of these nanoporous graphenes are limited to the micrometer scale. To overcome this limitation, O'Hern *et al.* introduced isolated and reactive defects into the graphene lattice through ion bombardment, which were then enlarged by oxidative etching to produce permeable pores with diameters of 0.40 ± 0.24 nm and

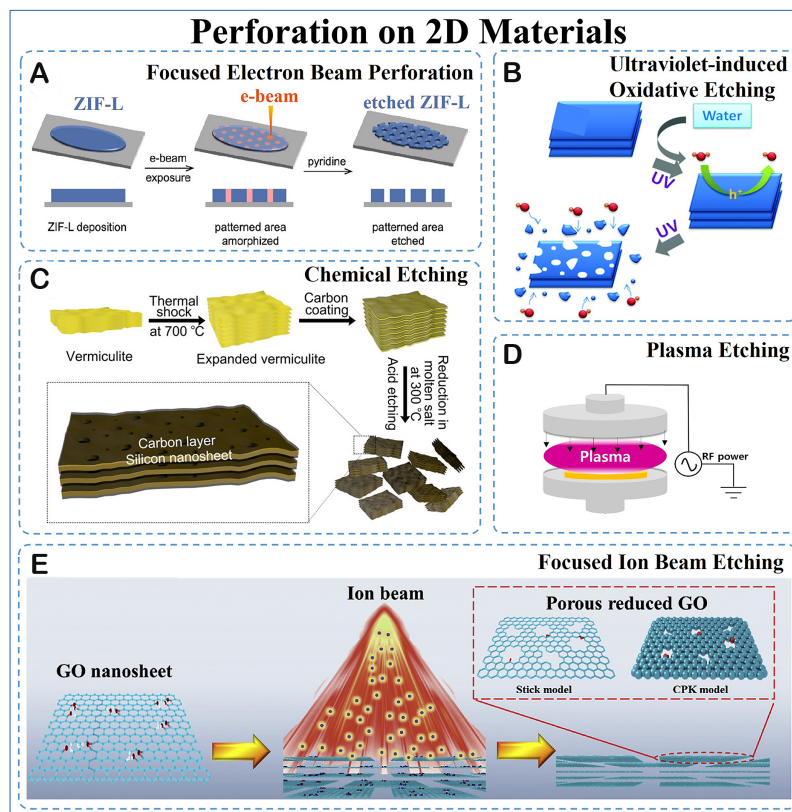


Figure 4. Schematics of perforation on 2D materials. (A) Low-dose e-beam patterning of ZIF-L with pyridine as an etchant^[176]. Copyright 2021, American Chemical Society. (B) UV irradiation etching of MoS₂/WS₂ nanosheets^[177]. Copyright 2016, Royal Society of Chemistry. (C) Focused ion beam etching process on GO^[178]. Copyright 2019, Elsevier Ltd. (D) Plasma etching process^[179]. Copyright 2020, MDPI. (E) The synthesis of porous Si/C composite nanosheets by chemical etching^[180]. Copyright 2019, American Chemical Society.

densities exceeding 10^{12} cm^{-2} ^[62]. In another approach, Surwade *et al.* employed an oxygen plasma etching process [Figure 4D] to produce nanopores with tunable diameters on a graphene monolayer, which exhibited rapid water transport and excellent salt rejection^[15]. Despite the success of these methods in achieving tailored pore sizes and densities, they can be relatively expensive due to the use of specialized instruments.

Generally, physical etching is an effective method to prepare arrays of monodisperse nanopores with a precise and tunable pore size distribution, whereas chemical etching [Figure 4E] is relatively easy and low-cost to produce nanopores in the graphene plane on a large scale. KOH, HNO₃, and others are commonly used to prepare porous graphene. Zhu *et al.* reported simple activations with KOH to generate nanoscale pores on the exfoliated GO nanosheets^[63]. The result in highly conductive, free-standing, and flexible porous GO paper possessed a very high specific surface area with excellent electrical conductivity and yielded outstanding performance, making it ideal for high-power energy storage^[61,63,64]. Zhao *et al.* introduced carbon vacancy pores into graphene nanosheets using a facile solution method that the HNO₃ reacted with the coordinatively unsaturated carbon atoms to partial detachment and removal of carbon atoms from the nanosheet^[65]. Wang *et al.* prepared porous graphene nanosheets by refluxing reduced GO (rGO) nanosheets in a concentrated HNO₃ solution^[66]. The diameters of nanopores can be readily modulated from several to hundreds of nanometers by varying the acid treatment time^[66]. Besides, H₂O₂^[67] and metal oxides^[68] can also be applied as chemical reagents to etch graphene.

In addition to graphene, other porous 2D nanosheets, such as h-BN^[69], MoS₂^[70,71], and g-C₃N₄^[19], can be obtained through artificial perforation approaches. The atomically thin 2D nanosheets hosting either intrinsic or artificial nanopores impart outstanding molecular transporting and sieving capabilities, making them promising materials for the direct fabrication of selectively permeable membranes with abundant nanofluidic channels.

Nanochannel membrane assembly strategies

In-plane parallel capillaries^[72] are another type of nanochannels that can be constructed by assembling isolated atomic planes of 2D nanosheets into van der Waals heterostructures made layer by layer in a precisely chosen sequence, namely van der Waals assembly [Figure 5A]. A typical stacking procedure starts by isolating micrometer-sized 2D nanosheets on top of a thin supporting film as one brick for the Lego wall, which are then put face-down onto a chosen target with the supporting film removed or dissolved. This process is repeated until the desired stack is assembled. While covalent solid bonds provide in-plane stability of 2D nanosheets, relatively weak, van der Waals-like forces are sufficient to keep the stack together. Radha has made outstanding contributions to this technique, having fabricated narrow and smooth capillaries through van der Waals assembly, with atomically flat graphene sheets at the top and bottom separated by spacers with a precisely controlled number of layers^[73]. They found that the water transport through the channels created by this method was characterized by an exceptionally fast flow that can be attributed to high capillary pressures and large slip lengths and can be associated with the structural ordering degree of nanoconfined water. They also investigated hydrated ion transport through ultimately narrow slits with dimensions approaching the size of small ions and water molecules^[74]. The ions with hydrated diameters larger than the slit size can still permeate through by distortions of their hydration shells. The mobility of ions under angstrom-scale confinement showed a notable dependence on the electric charges inside channels or at their entries. Using the same method, 2D channels made from graphene, MXene, and h-BN allowed helium gas flow that is orders of magnitude faster than expected from theory, whereas similar 2D channels made from MoS₂ exhibited much slower permeation that remains well described by Knudsen diffusion^[75]. It demonstrated the ballistic molecular transport effect that surface scattering could be either diffuse or specular, dependent on the fine details of the atomic landscape of the surface. The van der Waals assembly technique opens up an avenue to making capillaries with channel sizes tunable to angstrom precision and controllable transport properties through a wide choice of available 2D materials as channel walls. These series of 2D nanochannels in the forms of in-plane parallel capillaries provide an ideal experimental platform for offering a new understanding of many excellent nanofluidic observations, such as the unexpectedly high transport of thermal protons^[76,77], the qualitatively different coordination of square ice^[78], the anomalously low dielectric constant of confined water^[79], and the transistor-like electrohydrodynamic effect of hydrated ions^[80].

The assembly of uniform 2D layered films from well-dispersed 2D nanosheets provides an ideal platform for constructing densely packed nanochannels for nanofluidic transport due to the large aspect ratio with atomic thickness and micron lateral dimension. Furthermore, the spaces, including in-plane slits (or defects) and plane-to-plane interlayer galleries within the 2D laminates, create numerous channels for nanofluidic transport. Among various feasible strategies, solution-assisted assembly offers a general, facile, and scalable way for high-throughput constructing densely packed nanochannels from 2D materials. The internal forces, such as electrostatic and van der Waals attractive interactions that are existed inside the 2D laminate, together with external forces, such as compressive, centrifugal, and shear forces that are applied outside the 2D laminate, are largely responsible for tuning the 2D building blocks into the ordered 2D laminar membranes^[81]. Predominantly used solution-assisted assembly methods include pressure/vacuum filtrating, coating, and layer-by-layer assembling.

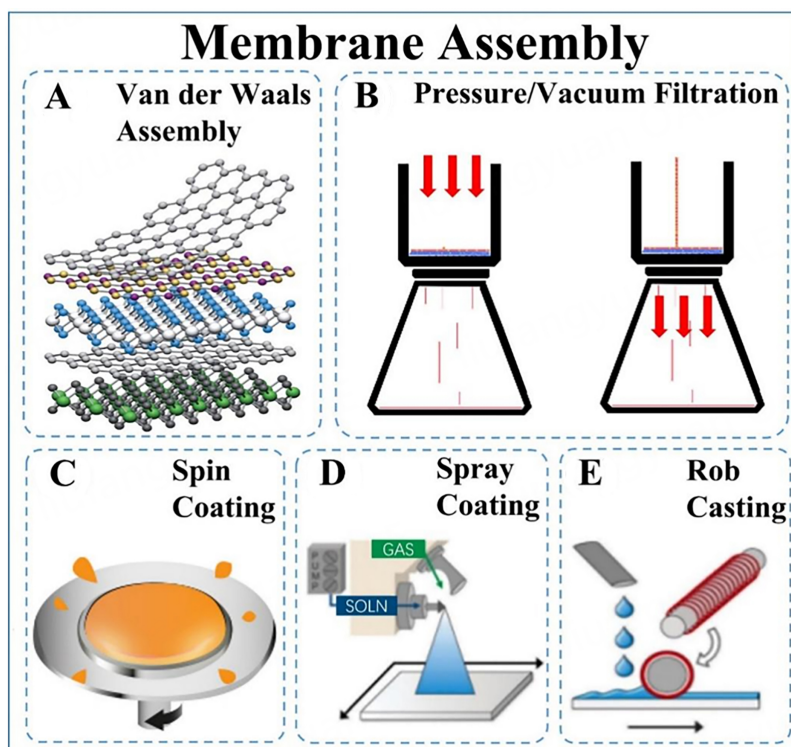


Figure 5. Schematics of the main assembly methods for 2D-material-based nanochannel membranes. (A) Building van der Waals heterostructures^[72]. Copyright 2013, Springer Nature Limited. (B) Pressure/Vacuum filtration. (C) Spin-coating. (D) Spray coating^[181]. Copyright 2011, Royal Society of Chemistry. (E) Rob casting^[181]. Copyright 2011, Royal Society of Chemistry.

The pressure/vacuum filtrating method [Figure 5B] is the most widely adopted to stack 2D laminar membranes. The thicknesses of the membrane can be straightforwardly controlled by altering the loading amount of 2D nanosheets via pressure control. For instance, Dikin *et al.* first reported the preparation of a free-standing GO membrane with macroscopic flexibility and stiffness by vacuum filtration of colloidal dispersions of individual GO nanosheets^[82]. The X-ray spectrum of a typical GO membrane showed a peak corresponding to a layer-to-layer distance (d -spacing) of about 0.83 nm, which can be attributed to an approximately one molecule-thick layer of water that is presumably hydrogen-bonded between the interlocked GO nanosheets within the laminates. Preparation parameters such as driving force, deposition rate, and substrate effect play critical roles in determining the structural formation of 2D laminar membranes. For example, Tsou *et al.* induced the assembly of GO membranes with different laminar microstructures ranging from highly ordered to highly random utilizing pressure, vacuum, and evaporation filtrating techniques^[83].

It is crucial to mention that due to the extremely thin feature, 2D laminates are usually supported by a porous substrate to form practical membranes. The differences in substrate properties also lead to a distinct assembly structure of resulting 2D laminar membranes with uneven performance. An example can be found in the study carried out by Zhang *et al.*, who investigated the effect of substrate on GO membrane formation and separation^[84]. The surface morphology and chemical structure of substrates induced the assembly of GO and determined its adhesion. Furthermore, the bulk pore structure of substrates dominated the whole transport resistance of the GO membrane.

Besides filtrating, various coating methods, such as spin-coating, spray-coating, and casting, have been reported to assemble 2D laminar membranes. During the spin-coating process [Figure 5C], a solution containing 2D materials to be deposited is spread out uniformly over the substrate under centrifugal force, forming the ultrathin and laminar membranes. Kim *et al.* demonstrated two different spin-coating methods to prepare GO membranes on polymeric substrates^[85]. When contacting the substrate surface to the air-liquid interface of the GO solution followed by spin-coating, the repulsive edge-to-edge electrostatic interactions lead to an island-like assembly of GO nanosheets, resulting in a relatively heterogeneous GO stacking structure. In contrast, when contacting the substrate surface to GO solution only during spin-coating, the face-to-face attractive capillary forces created by the spin-coating overcome the repulsive interactions between GO edges, leading to a considerably dense GO laminar deposition. Chi *et al.* found that a speed balance between deposition and solvent (water) evaporation is crucial to obtain smooth GO membranes with uniformly aligned GO nanosheets via spin coating^[86]. Faster deposition may lead to overflow of the solution, while more rapid evaporation will cause uneven distribution of nanosheets. By matching up deposition and evaporation speeds, they obtained a uniform ultrathin GO membrane with a thickness of 20 nm that grants high gas fluxes for efficient gas separation. For spray-coating [Figure 5D], Guan *et al.* carefully controlled spraying times and evaporating rates to achieve facile structure manipulation of GO membrane from disordered-to-ordered and porous-to-compact^[87]. Ibrahim *et al.* further verified that using dilute concentration GO suspensions in spray-coating can help minimize the edge-to-edge interactions and reduce extrinsic wrinkles formation^[88]. Casting [Figure 5E] also belongs to coating methods that allow the continuous production of large-scale membranes. Akbari *et al.* utilized the flow properties of a nematic GO fluid in developing an industrially adaptable process to produce GO membranes with large in-plane order and stacking periodicity by shear-induced alignment of liquid crystals of GO^[89]. Zhong *et al.* showcased a universal, scalable, efficient continuous centrifugal casting method to produce highly aligned and compact 2D laminar membranes with impressive performances^[90]. Fluid mechanics analyses indicated that the simultaneous generation of shear force and centrifugal force during the continuous centrifugal casting process could be responsible for the alignment and compaction of 2D nanosheets, respectively.

Layer-by-layer assembly is a flexible construction process involving alternate deposition of different materials, often using one or more of the previously described methods. Such a flexible layer-by-layer construction process enables precise control over the thickness of the selective layer by varying the number of deposition cycles and is beneficial for introducing various interlayer stabilizing forces, including covalent, electrostatic, or hydrogen bindings between adjacent 2D nanosheets, thereby producing membranes with robust and ordered laminar structures^[81]. Hu *et al.* reported a 1,3,5-benzenetricarbonyl trichloride cross-linked GO membrane made via layer-by-layer deposition^[91]. The covalent cross-linking enhanced the stability of the stacked GO nanosheets, overcoming their inherent dispensability in the water environment while fine-tuning their charges, functionality, and spacing^[91]. In addition, layer-by-layer assembly has been used to create stable GO membranes through the electrostatic bonding of negatively charged GO nanosheets and positively charged polyallylamine hydrochloride^[92]. These methods provide a gateway to rationally design the charge properties and other functionalities of interlayer nanochannels of 2D laminar membranes by carefully choosing the intercalated molecules, polyelectrolytes, or nanomaterials. For instance, Song *et al.* developed both positively charged polyallylamine hydrochloride@GO and negatively charged polystyrene sulfonate@GO, which they alternately deposited on polycarbonate substrates by the layer-by-layer assembly, producing polyelectrolyte intercalated GO membranes with tunable charge-gating ion exclusion effects^[93]. Apart from a single interaction, Zhao *et al.* fabricated GO-based hybrid membranes via layer-by-layer self-assembly of gelatin molecules and GO nanosheets driven by multiple interactions, including electrostatic attraction, hydrogen bond, and hydrophobic interaction^[94]. Electrostatic attractions were formed between ionized carboxyl groups on GO and protonated amino groups on gelatin, hydrogen

bonds between various polar groups on gelatin and GO, and hydrophobic interactions between the hydrophobic carbon backbone of GO and hydrophobic amino acid side chains on gelatin. These multiple interactions may contribute to the formation of highly ordered 2D laminar membranes with finely tuned 2D nanochannels for nanofluidic transport.

In summary, the structural properties of nanochannels in nanochannel films based on 2D materials, including layer thickness, stacking order, defects and grain boundaries, surface functionalization, embedding of additives or polymers, and nanosheet alignment and orientation, largely affect the overall filtration performance of the membrane. Controlling these factors can tune the interlayer spacing, pore size distribution, surface interactions, and flow dynamics within nanochannels, leading to membranes with higher selectivity, permeability, and fouling resistance. The choice of synthesis and assembly method depends on the desired material, application, scalability, and desired quality of 2D nanosheets. Each method has its advantages and limitations. Further studies to understand and optimize these structural properties will facilitate the development of more efficient and tailored nanochannel membranes for various separation applications.

Characterization methods

Characterization techniques are essential for understanding the properties of 2D materials. Various techniques allow for a thorough examination of these materials. XRD is used to determine the crystal structure and orientation of 2D materials. It involves directing X-rays onto the material and measuring the resulting diffraction pattern. XRD can provide information about lattice parameters, crystal symmetry, and the presence of specific crystalline phases. In addition, the layer spacing is calculated using XRD data according to Bragg's law. Optical spectroscopy techniques such as UV-Vis absorption spectroscopy and photoluminescence spectroscopy are used to study the optical properties of 2D materials. They can reveal information about the material band gap, exciton properties, and light-matter interactions. X-ray photoelectron spectroscopy (XPS) is used to analyze the chemical composition and electronic states of 2D materials. It involves irradiating the surface of a material with X-rays and measuring the energy of the emitted electrons. XPS can provide information about elemental composition, chemical bonding, and the presence of impurities or functional groups. Raman spectroscopy is used to analyze the vibrational modes of 2D materials. It involves shining a laser on the material and measuring the scattering spectrum. Raman spectroscopy provides insight into the crystal structure, composition, and strain of material and identifies different types of 2D materials. Atomic Force Microscopy (AFM) is a powerful technique for imaging the morphology and surface properties of 2D materials. It uses a sharp probe to scan the entire surface of a material, detecting force changes between the probe and the sample. AFM can provide information about the height, roughness, and mechanical properties of a material at high spatial resolution. Scanning electron microscopy (SEM) provides high-resolution images of the surface/sectional morphology of 2D materials. It uses a focused electron beam to scan the surface of a material, generating detailed images that reveal features such as the size, shape, and arrangement of thin sheets or layers of material. Transmission electron microscopy (TEM) is used to study the internal structure and atomic-level features of 2D materials. It involves the transmission of an electron beam through a thin sample to image the atomic structure and defects of the material. TEM can provide information about crystal structure, grain boundaries, stacking sequences, and even individual atomic arrangements.

Among other things, these characterization techniques allow researchers to gain a comprehensive understanding of the structural, morphological, chemical, and optical properties of 2D materials. By combining multiple techniques, a complete characterization of 2D materials can be achieved, facilitating their optimization and utilization in a variety of applications. The development of advanced characterization techniques, such as cryoelectron microscopy and *in-situ* Raman, will provide researchers

with more reliable means and opportunities to explore the deeper mechanisms of structure and separation and purification of 2D-material-based membranes^[95-98].

REGULATING NANOCHANNELS

The transport of nanofluids through nanochannel membranes based on 2D materials predominantly takes place within the interlayer space. It is within this space that the transport behavior is influenced by various physical and chemical factors. Moreover, addressing issues such as nanochannel instability, instability at the 2D-material interface, and swelling can be effectively tackled by adjusting the physicochemical factors of the 2D-material-based nanochannels. Therefore, rational regulation of the nanochannels is of utmost importance. Controlling the physical factors of channel size, channel length, and channel morphology can primarily modulate nanofluidic transport by achieving precise sieving, shortening the transport distance, and reducing the transport resistance. Regulating the chemical factors of the surface chemistry effects can specifically facilitate nanofluidic transport through various permeant-channel interactions. Many efforts have been devoted to carefully designing precise geometries and favorable chemical features of nanochannels for realizing fast and selective molecular/ionic transportation. This section presents typical provisions for the physicochemical properties of nanochannels in 2D-material-based membranes. Based on experimental and theoretical studies, various effects and in-depth structure-property relationships of nanofluid transport are also discussed.

Regulating size of nanochannels

In 2D-material-based nanochannel membranes, nanofluidic transport occurs in interlayer capillaries and wrinkles formed by adjacent 2D nanosheets and inter-edge gaps and intrinsic pores formed on planar 2D nanosheets interconnect with each other to create numerous nanochannels. Firstly, the channel size [Figure 6], one of the most prominent characteristics of nanochannels, firmly decides the entry of nanofluids. Joshi *et al.* found that the interlayer spacing of a GO membrane was ~ 0.9 nm^[16], allowing any ion or molecule with a hydrated radius of 0.45 nm or less to enter the nanochannels and permeate at a speed order of magnitude faster than would occur through simple diffusion, while all species larger than this are sieved out. Such sharp size cutoff determined by the interlayer spacing has significant implications on a myriad of occasions. By adjusting the channel size through diverse methods, such as confinement, reduction, cross-linking, and intercalation, a broad range of different-sized nanochannels can be designed to sieve target ions and molecules from the bulk solution precisely.

Due to the inevitable swelling effect when immersed, hydration would increase the size of nanochannels and deprive their sieving capability. Achieving a small channel size for the 2D laminates immersed in solvents has been a challenging task. Abraham *et al.* described a physical confinement method [Figure 6A] to control the interlayer spacing from ~ 9.8 Å to ~ 6.4 Å to obtain accurate and tunable ion sieving^[99]. GO laminates were stored at different relative humidities to yield controllable interlayer spacing attributed to incorporating water molecules into various sites between GO nanosheets. Subsequently, epoxy was used to encapsulate stacked GO laminates for preparing physically confined GO membranes since the epoxy mechanically restricts laminate swelling upon water exposure. As ions and water permeate along the GO nanochannel, the permeation rate for Na⁺ and K⁺ showed an exponential dependence, decreasing by two orders of magnitude as interlayer spacing decreased from 9.8 Å to 7.4 Å. However, the water permeation rate showed only a slight variation, reducing by a factor of ~ 2 within the same range of interlayer spacing. The former is related to the partial clogging of graphene capillaries, and the latter is attributed to a low barrier and a large slip length for water in graphene capillaries. Similarly, Li *et al.* reported an external pressure regulation method for controlling the interlayer spacing of GO laminates against swelling^[100].

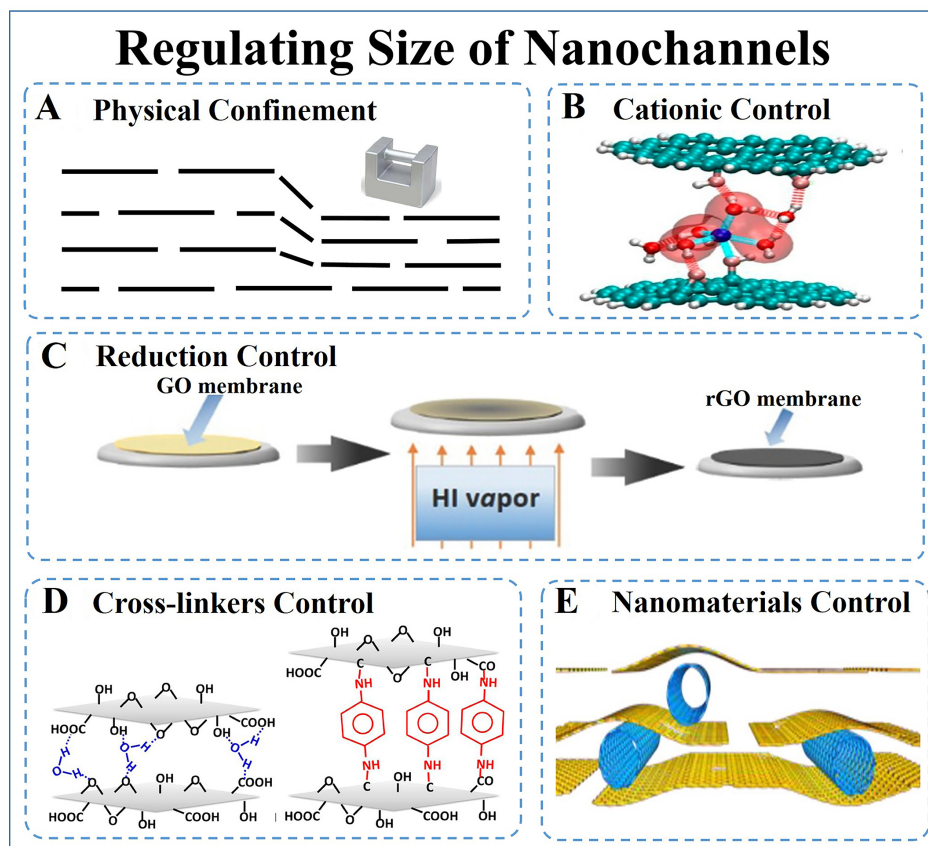


Figure 6. Regulating the size of nanochannels. (A) Physical confinement. (B) The stable, optimized geometries of $\text{Na}^+(\text{H}_2\text{O})_6$ @GO clusters from density functional theory computation^[101]. Copyright 2017, Springer Nature. (C) The fabrication procedure of free-standing rGO membranes using reduction control^[104]. Copyright 2015, John Wiley & Sons, Inc. (D) Original GO membrane (left) and the composite GO-framework prepared by *p*-phenylenediamine cross-linking GO membrane (right)^[105]. Copyright 2014, American Chemical Society. (E) Graphene/carbon nanotube composite membranes are prepared by assembling refluxed GO (rGO) and multi-walled carbon nanotubes^[120]. Copyright 2015, American Chemical Society.

Apart from channel size regulation based on external forces, cationic control is a representative method of channel size regulation based on internal forces. Chen *et al.* demonstrated cationic control of the interlayer spacing of GO membranes with angstrom precision using K^+ , Na^+ , Li^+ , Ca^{2+} , or Mg^{2+} ions [Figure 6B]^[101]. The confinement of interlayer spacing is mainly due to the interaction between hydrated cations and aromatic rings (cation- π interactions) on the GO nanosheet and the interaction between hydrated cations and the oxygenated groups on the GO nanosheet. As a result, the interlayer spacing controlled by one type of cation can efficiently and selectively exclude other cations with larger hydrated volumes. Especially the K^+ -controlled GO membranes can even reject K^+ itself owing to the comparable interaction energy between K^+ and GO nanosheets concerning the dehydration energy of K^+ .

Reduction is another effective method to control the small channel size for the solvated 2D laminates. These 2D nanosheets possess abundant functional oxygenated groups that open the interlayer spacing between adjacent nanosheets and allow solvent molecules to intercalate into 2D laminates. Partially removing these oxygenated functional groups through various thermal or chemical reductions can enhance interlayer π - π interactions, thereby producing narrowed and stabilized nanochannels. Qiu *et al.* reported that hydrothermal treatment could readily control the reduction of GO nanosheets in water^[102]. Meanwhile, Han *et al.* obtained an rGO dispersion by base-refluxing to generate moderate holes and create a large number of

permeation “gates”, ultimately increasing the permeability of the rGO membrane^[103]. However, the pre-treatment of reduction may lead to the worse dispersion of nanosheets that is not conducive to uniformly assembling them into well-stacked laminates. Liu *et al.* prepared a GO membrane beforehand and placed it above a hydrogen iodide (HI) solution [Figure 6C]^[104]. The HI steam acts as a reducing agent, which reduces GO and triggers the initial delamination between the rGO membrane and substrate. Fumagalli *et al.* found that GO laminates reduced using thermal, HI, and VC reductions are highly impermeable to strong chemicals and salt solutions, owing to a high degree of graphitization of the laminates, causing nanochannels collapse during the reduction process^[79].

The enlarged channel size can be achieved by cross-linking or intercalating cross-linkers, such as specific molecules, polyelectrolytes, or nanomaterials, to reinforce transport efficiency. The most commonly used cross-linkers for GO membranes are diamines^[105], including ethylenediamine (EDA), butylenediamine (BDA), and phenylenediamine (PDA), which can chemically bond with adjacent GO nanosheets through condensation and nucleophilic addition reactions [Figure 6D]. The spatial configuration of amine monomers primarily determines the channel size of cross-linked GO membranes in a dry state, whereas the bonding strength of amine monomers within the GO laminate likely determines their channel size in a wet state^[106]. Other molecules holding characteristic terminal groups, such as dicarboxylic acids^[107], tannic acid^[108], borate^[109], isophorone diisocyanate^[110], porphyrins^[111], and polybenzimidazole^[112], have also been proved to cross-link 2D-material membranes to address 2D channel size control chemically. Yang *et al.* demonstrated the preparation of thiourea covalently linked GO membrane where thiourea bridged GO laminates periodically through the reactions of amino and thiocarbonyl groups with the functional groups of GO, leading to mechanically stable and structurally well-defined 2D channels^[113]. These molecule cross-linkers usually yield covalent bonds through a limited number of active sites. In contrast, polyelectrolytes possess long polymer chains with abundant functional groups, which can serve as polymer cross-linkers to be incorporated into 2D laminates through sufficient active sites to produce a dense composite structure. The commonly used polymer cross-linkers are polyvinyl amine (PEI)^[114,115], polyvinyl alcohol (PVA)^[116], polyethylene glycol (PEG)^[117], and so on. Ran *et al.* utilized imidazolium-functionalized brominated poly (2,6-dimethyl-1,4-phenylene oxide) (Im-PPO) and sulfonated poly (2,6-dimethyl-1,4-phenylene oxide) (S-PPO) to connect neighboring GO nanosheets via non-covalent π - π , electrostatic, and hydrogen bonding interactions^[118]. These cross-linking strategies may pave the way to access highly stable and efficient transport of 2D lamellar membranes.

Besides cross-linking, intercalating nanomaterials of specific sizes is another means to significantly improve the permeability of 2D-material membranes, as it effectively creates large amounts of broadened pathways for nanofluidic transport. Carbon-based nanomaterials, metal oxide nanoparticles, MOFs, and COFs are among the representative intercalated nanomaterials. By embedding carbon nanodots of controllable sizes, Wang *et al.* were able to tune the permeability of GO membranes^[119]. Han *et al.* expanded the interlayer spacing of GO membranes by intercalating multi-walled carbon nanotubes (CNTs) [Figure 6E]^[120]. Goh *et al.* further proposed that intercalating of CNTs of different diameters can effectively inhibit the restacking (or aggregation) of GO nanosheets and thus create plenty of nanochannels for water transport while retaining the molecular sieving capability of the ensuing membranes. Moreover, CNTs can also act as anchors to interact and interconnect with the adjacent GO nanosheets due to the perfect compatibility of carbon-based materials to reinforce the membrane stability^[121]. Intercalation of metal oxide nanoparticles is another general and scalable approach to expand 2D nanochannels significantly. Zhang *et al.* prepared nanoparticles@GO membranes using a simple *in-situ* solvothermal synthesis method, where size- and density-controllable nanoparticles were uniformly grown on GO nanosheets through coordination^[122]. Compared to the membrane produced by filtering GO solutions mixed directly with nanoparticles, the *in-*

situ fabricated nanoparticles@GO membrane uniformly introduced nanoparticles within GO laminates without damaging their initial ordered stacking structures and hence exhibited ultrahigh water permeance and excellent rejections for various solutes in water, as well as good stability under high pressure and cross-flow operation. This general concept of intercalation can also be demonstrated by several kinds of nanoparticles such as TiO₂^[123], silica^[124], and hydroxy sodalite nanocrystals^[125], endowing nanoparticles intercalated GO membranes with additional multifunctions. Compared with nonporous metal oxide nanoparticles, intrinsically porous nanocrystals are more beneficial for fast nanofluidic transport when they are intercalated into 2D nanochannels. By incorporating MOFs^[126,127], COFs^[128,129], and biomimetic water channels^[130] with extra internal pathways through sub-nano-sized apertures as the microporous fillers into 2D laminates, both the size and the number of nanochannels are increased, leading to greatly enhanced nanofluidic transport performance. Li *et al.* described a route for fabricating MOFs channeled graphene composite membranes with molecular sieving properties using *in-situ* crystallization. A series of MOFs, including ZIF-8, ZIF-7, CuBTC, and MIL-100, were showcased to be impregnated into interlayers of GO laminates, which firmly anchored and bolstered up GO laminates by coordination bonds to form a highly porous architecture with uniform nanochannels^[127].

Khan *et al.* created a hybrid laminar membrane by assembling COFs and GO nanosheets^[128]. The incorporation of COFs nanosheets provides a large number of pores that shorten the transport pathway while retaining the interlayer distance. Similarly, Sui *et al.* also intercalated rigid 2D COFs into GO laminates to realize a robust GO/COF laminar membrane^[129]. The atomically thin 2D COFs with pores serve as a nano spacer to increase the interlayer spacing between GO nanosheets and provide direct transfer channels, thereby reducing water transfer resistance. On the other hand, the COFs enhance the self-supporting capacity of GO networks on a substrate with large pores. As a result, this strategy led to a significant increase in the water permeance of the optimized GO/COF laminate membrane compared to the pristine GO membrane without compromising its rejection rates to organic dyes. Mao *et al.* embedded imidazole-ureido bola-amphiphile-imidazole compound as biomimetic imidazole-quartet water channels into assembled GO laminates to enhance water transport selectivity over butanol benefiting from the hydrophilic water-preferential nanochannels along the imidazole-ureido molecular scaffolds^[130].

As the GO membrane is a showpiece that provides flexible platforms for developing versatile novel 2D-material membranes, the methods mentioned above for regulating channel size are adaptable for other 2D-material membranes. For example, Wang *et al.* related the performance of MoS₂ membranes to the size of their nanochannels in different hydration states^[131]. They found that the water-impermeable behavior of the dry MoS₂ nanochannel, which has a 0.62 nm interlayer spacing, is caused by the irreversible nanosheet restacking during a drying process. In comparison, the fully hydrated MoS₂ membrane possesses a stable 1.2 nm interlayer spacing, leading to high water permeability and moderate-to-high ionic and molecular rejection. Meanwhile, the MoS₂ nanochannel has a much stronger van der Waals attraction force than the GO nanochannel, which prevents the interlayer spacing from increasing, thereby ensuring the aqueous stability of MoS₂ membranes. Inspired by the structural characteristics of GO membranes, where oxidized zones act as spacers to provide a relatively large interlayer distance to accommodate water molecules, Ran *et al.* incorporated appropriate acid spacers between g-C₃N₄ interlayers to enlarge the width of the 2D channels^[132]. The intercalation molecules successfully break up the tightly stacked structure of g-C₃N₄ laminates. Accordingly, the modified g-C₃N₄ membranes give rise to two orders of magnitude higher water permeance without sacrificing the separation efficiency. In a similar route, Wang *et al.* devised a method to partially exfoliate dg-C₃N₄ nanosheets with artificial nanopores and unstripped fragments as self-supporting spacers and assemble them into 2D laminar membranes for water purification^[133]. The artificial nanopores and the spacers between the partially exfoliated g-C₃N₄ nanosheets provide numerous nanochannels for

nanofluidic transport with ultralow friction while effectively retaining larger molecules. Wang *et al.* also demonstrated a strategy for stabilizing the $Ti_3C_2T_x$ laminar architecture by alginate hydrogel pillars formed between the adjacent nanosheets^[133]. After pillared by different alginate hydrogel pillars, the nanochannel diameters are effectively fixed at ~ 7.4 Å, and the resulting membrane exhibited significantly enhanced the ion-sieving property with distinct ions permeation cutoff depending on the multivalent cations cross-linked with alginate molecules.

Regulating the length of nanochannels

Another physical factor influencing nanofluidic transport through 2D-material-based nanochannel membranes is channel length, which largely depends on the membrane thickness and porosity. Nanoporous 2D materials of single- or few-atom thickness are the ultimate building blocks for constructing ultrathin membranes with minimal resistance to maximize permeance.

As a straightforward way to shorten the channel length, many theoretical and experimental studies have demonstrated the ultrafast permeation performance of ultrathin 2D-material membranes. For example, Cohen-Tanugi *et al.* predicted that ultrathin nanoporous graphene membrane could have water permeability several orders of magnitude higher than conventional membranes thanks to the chemical functionalization, which may have a valuable role to play in water purification [Figure 7A]^[134]. Han *et al.* fabricated ultrathin (~ 22 -53 nm) graphene nanofiltration membranes on microporous substrates for efficient water purification^[103]. Liu *et al.* prepared free-standing ultrathin rGO membranes with thickness down to ~ 20 nm by HI vapor and water-assisted delamination^[104]. Yang *et al.* reported highly laminated GO membranes of only several layers in thickness (~ 8 nm), exhibiting outstanding sieving properties accompanied by ultrafast solvent permeation^[135]. Li *et al.* described a reproducible facile filtration method to produce ultrathin GO membranes down to 1.8 nm in thickness, which exhibited superior gas separation performance^[136]. Furthermore, single-layer 2D-material membranes for practical use have also been attempted. For example, Heiranian *et al.* showed that a single-layer nanoporous MoS_2 effectively allowed water transport at a high rate associated with permeation coefficients, energy barriers, water density, and velocity distributions in the pores [Figure 7B]^[137].

Although the ultrathin 2D-material membranes exhibit exceptional permeation performances, the limited mechanical strength of these membranes over large areas remains a hindrance to their widespread use. To overcome this limitation, Yang *et al.* reported the production of an atomically thin nanoporous membrane with a single-layer graphene nanomesh (GNM) supported by an interwoven network of single-walled carbon nanotubes (SWNT)^[138]. The monolayer GNM featuring high-density subnanometer pores [Figure 7C] allows efficient transport of water molecules with minimum resistance while effectively blocking solute ions or molecules to enable size-selective separation. The mechanically strong, interconnected SWNT network, acting as the microscopic framework, separates the GNM into micro-sized islands, thus ensuring the structural integrity of the atomically thin GNM. The resulting large-area, ultrathin GNM/SWNT hybrid membrane showed high water permeance and excellent size selectivity combined with excellent anti-fouling characteristics, making it highly attractive for energy-efficient and robust water treatment.

Regulating morphology of nanochannels

The morphology of the channel in ultrathin 2D-material membranes plays a crucial role in determining the distance traveled by nanofluids. Inter-edge gaps [Figure 8A] and intrinsic pores [Figure 8B] are crucial elements that influence this distance^[135,136]. Ibrahim *et al.* proposed using nanofluidic pathways in laminar GO membranes, where permeation occurs through pinholes within GO flakes and capillaries between them^[139]. Utilizing small and porous nanosheets to assemble membranes can efficiently introduce more

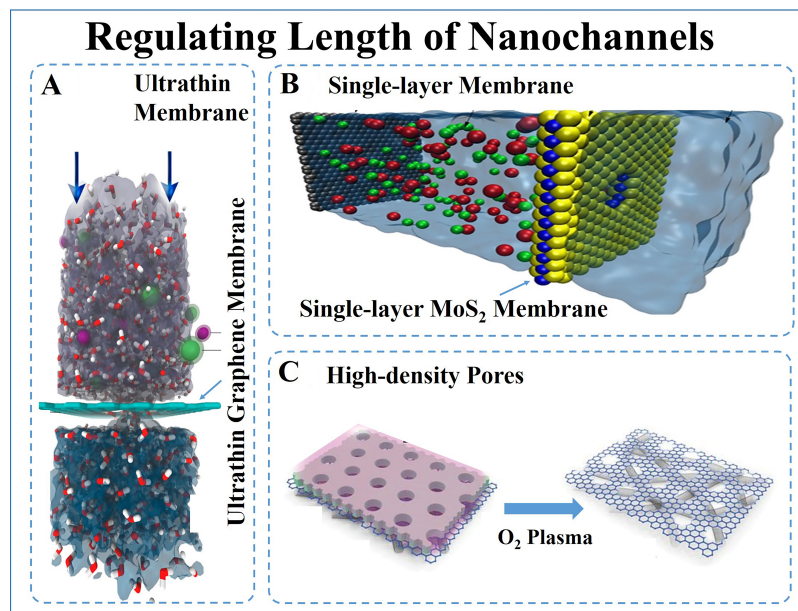


Figure 7. Regulating length of nanochannels. (A) side view of the computational system of ultrathin graphene membrane in the desalination process^[134]. Copyright 2012, American Chemical Society. (B) The simulation box consists of a single-layer MoS₂ sheet (molybdenum in blue and sulfur in yellow), water (transparent blue), ions (in red and green), and a graphene sheet (in gray)^[137]. Copyright 2015, Springer Nature. (C) The fabrication process of density pores on graphene-nanomesh/carbon-nanotube hybrid membranes using O₂ plasma^[138]. Copyright 2019, Science Publishing Group.

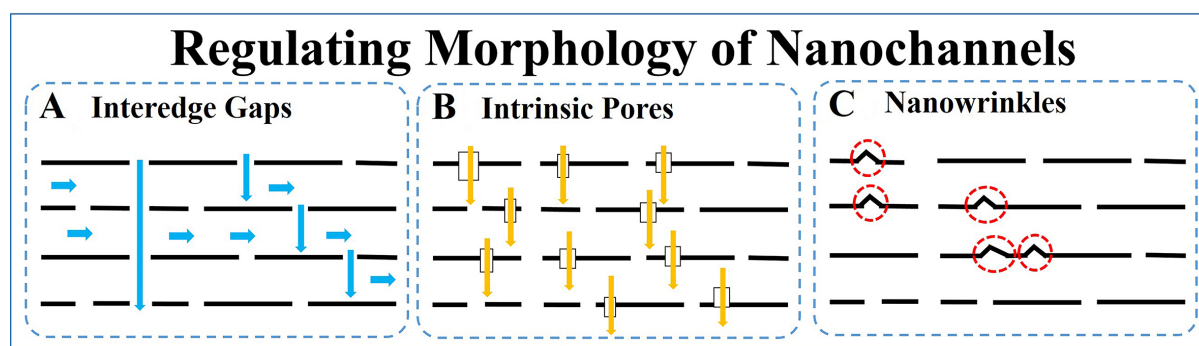


Figure 8. Regulating morphology of nanochannels: inter-edge gaps (A), intrinsic pores (B), and nanowrinkles (C).

inter-edge gaps and intrinsic pores, enabling nanofluids to take shortcuts to perform ultrafast transport. A few works have developed simple methods for the lateral size fractionation of 2D nanosheets using techniques such as sonication^[140], filtrations^[141], differential centrifugation^[142], and controlled directional freezing^[143]. It is found that when the dimension of nanosheets within the membrane is changed from microsize to nanosize, the amount of nanofluidic pathways formed within the GO membrane is increased significantly, resulting in the enhancement of trans-membrane transportation in the case of nanosized 2D-material membranes^[144]. Nie *et al.* exploited this concept of lateral dimension control to engineer shorter and less tortuous transport pathways for solvent molecules, leading to the development of small-flake GO membranes that achieved ultrafast selective molecular transport^[145]. The methanol permeance in these membranes reached up to 2.9-fold higher than its large-flake GO counterpart, with high selectivity towards organic dyes^[145]. Section 2.2 has described various perforation techniques to produce nanopores on 2D

nanosheets^[15,19,58-71]. The creation of nanopores can provide a greater number of transport nanochannels for nanofluids and sharply reduce the average transport distances. Ying *et al.* reported GO membranes with introduced in-plane mesopores by a reoxidation process, demonstrating 2-3 folds enhancement of water permeance as that of the pristine GO membranes^[146]. Li *et al.* also proposed thermally reduced nanoporous GO membranes through a combination of mild H₂O₂ oxidation and moderate thermal treatment, increasing the water permeability by 26 times^[147]. Those intrinsically porous 2D materials are more attractive as building blocks to assemble 2D laminar membranes. Their uniform nanopores consisting of angstrom-sized windows and nanometer-sized cavities can provide numerous cross-layer shortcuts and ensure precise size exclusions. Peng *et al.* reported ultra-permeable and super selective molecular sieve membranes made of 2D MOF nanosheets, which achieved H₂ permeance of up to several thousand GPU with H₂/CO₂ selectivity greater than 200^[37,148]. Shinde *et al.* demonstrated ultrathin 2D COF membranes with a well-defined ordered porous structure^[149]. These membranes displayed remarkable permeabilities for polar and nonpolar organic solvents, which were approximately 100 times higher than the amorphous polymer membranes^[149].

Besides the tortuous transport pathways through internal nanochannels of 2D laminar membranes extending in horizontal and vertical directions, nanowrinkled morphologies [Figure 8C] also exist in 2D laminar membranes, whose effects in transmembrane transport should not be neglected. Xi *et al.* proposed an rGO membrane with 2D nanochannels uniformly confined with a space size of $\sim 8 \text{ \AA}$ ^[150]. The mild reduction avoids the hydrothermal corrugation of GO nanosheets and thus enables the creation of highly parallel 2D nanochannels for precise sieving of mono-/multi-valent metal ions^[150]. Li *et al.* also demonstrated a mild-thermal annealing for preparing rGO membrane for nanofiltration since the mild reduction condition might favor the formation of a more ordered and better-controlled transport nanochannel^[151]. Contrary to these efforts to eliminate nanowrinkles, Saraswat *et al.* hypothesized that the imperfect stacking in the 2D laminates could lead to voids, wrinkles, and disordered microstructures that could provide alternative non-ideal transport pathways for nanofluids, resulting in a higher effective permeance^[152]. Kang *et al.* further revealed the roles of nanowrinkles in mass transport across GO membranes^[153]. They found nanowrinkles by themselves serve as fast transporting ways while their connection with narrow interlayer channels can form a selective network^[153]. Huang *et al.* developed a nanostrand-channeled GO membrane, whose permeance offered a 10-fold enhancement without sacrificing the rejection rate compared with that of pristine GO membrane, attributing to the generation of more nanofluidic channel networks in the membrane^[154]. The nanostrand-channeled concept is also extendable to other 2D laminar membranes, such as MXene^[17] and WS₂ membranes^[155], for increased permeability. These findings corroborate that nanowrinkles serve as fast tracks for nanofluids to enhance membrane permeability. Considering nanowrinkles broadly existing within flexible 2D nanosheets, they are expected to show critical transportcontrolling effects in nanofluidic transport in 2D-material membranes.

Regulating surface physicochemical properties of nanochannels

The 2D-material nanosheets have abundant functional groups. During the filtration process, the 2D material-based membrane is prone to swelling effect, resulting in the collapse of nanochannels and loss of sieving performance. Targeted modification of 2D-material surfaces is, therefore, significant, and a number of methods have been developed for modifying the chemical properties of membrane surfaces [Figure 9]. One commonly used strategy is the Chemical intercalation of cross-linking agents (e.g., ions, small molecules, or macromolecules), which enhances the interlayer force and improves the mechanical stability of 2D nanosheet membranes. At the same time, this strategy modulates the affinity of water/ions to the nanosheet surfaces, thereby regulating their mobility as they pass through the channels.

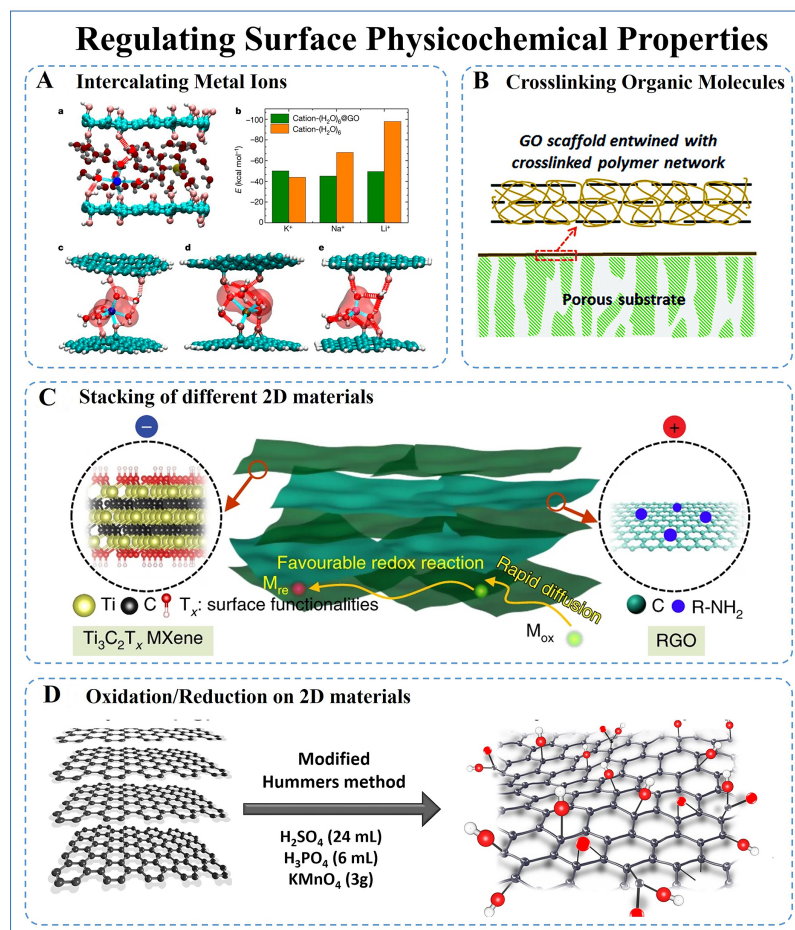


Figure 9. Regulating surface physicochemical properties of nanochannels. (A) Intercalating metal ions. [a] A snapshot of the ab initio molecular dynamics simulation at 27 ps. [b] The interaction energy between hydrated cations and graphene oxide sheets [labeled cation-(H₂O)₆@GO] and the hydration energy of the cation [labeled cation-(H₂O)₆]. [c–e] The most stable optimized geometries of cation-(H₂O)₆@GO clusters from density functional theory computation, where the cations are Na⁺, K⁺, and Li⁺^[101]. Copyright 2017, Springer Nature. (B) A GO polymer cross-linked network composite membrane for forward osmosis desalination^[158]. Copyright 2017, The Royal Society of Chemistry. (C) Restacked Ti₃C₂T_x-based membrane by introducing reduced GO as the spacer^[160]. Copyright 2019, Springer Nature. (D) Oxidation process from graphite to graphene oxide^[161]. Copyright 2021, MDPI.

Modifying the surface of 2D materials with a small number of metal ions, such as Mg²⁺ and Ca²⁺, is considered an effective strategy to improve the membrane performance significantly. This enhancement is mainly due to the electrostatic bonding between metal ions and functional groups on the surface of 2D materials^[156]. To further understand this mechanism, Chen *et al.* modified the GO membrane with hydrated Na⁺ ions and found, through DFT calculations, that the hydrated ions were adsorbed through hydrogen bonds in the region where the oxidized groups and aromatic rings coexisted, effectively adjusting and fixing the interlayer distance^[101]. The interlayer distance is proportional to the hydration radius of the corresponding Li⁺ > Na⁺ > K⁺ class ions [Figure 9A]. Ding *et al.* effectively reduced the d-spacing to ~ 1.5 nm. They effectively suppressed the swelling effect by intercalating Al³⁺ into the Ti₃C₂T_x MXene film combined with abundant surface termini (such as ¼O, eOH, and eF functional groups) within the nanosheets^[157]. Cross-linking 2D materials by organic molecules is another effective strategy to tune and fix the interlayer distance in layered films. Epoxy, a commonly used chemical raw material, is employed to modify the surface of 2D-material nanosheets. This strategy successfully prevented the swelling of GO and produced nearly 97% NaCl repulsion^[99]. Hung *et al.* cross-linked GO with EDA monomer to make the

nucleophilic substitution condensation reaction between the oxygen-containing groups of amine and GO to form a CeN covalent bond, which effectively suppressed the swelling effect^[105]. *In-situ* polymerization on the surface of 2D materials to generate twins is also a commonly used strategy^[72-75]. Kim *et al.* using N,N'-methylenebisacrylamide (MBA) as the cross-linking agent, N-isopropylacrylamide (NIPAM) as the monomer, and then ammonium persulfate (APS) as the initiator, successfully synthesized the GO@polymer twins^[158]. The prepared membranes have excellent anti-swelling properties and desalination ability^[158,159] [Figure 9B].

The potential interaction of functional groups on the surfaces of different 2D materials makes the superimposition of different 2D materials a possible strategy for modifying the surface chemistry of materials [Figure 9C]. Xie *et al.* reported a $Ti_3C_2T_x$ MXene-based membrane whose microstructure was optimized by inserting rGO between the layers^[160]. The surface of the membrane was progressively hydroxylated to increase the accessibility of $Ti_3C_2T_x$, thus improving the wettability of the film and enhancing the adsorption and reduction of heavy metal ions.

Oxidation and reduction processes are commonly used to modify and prepare 2D materials, so surface properties are often modified during the preparation process. For example, using a modified Hummers method (i.e., oxidation procedures), Alkhouzaam *et al.*^[161] prepared a GO membrane with more active surface properties than a graphene membrane, which facilitates its functionalization to meet the request [Figure 9D].

The properties of nanochannel membranes based on 2D materials, including swelling resistance and water permeability and retention, are closely related to the transport control effects of nanochannels and the interleaving of surface properties. These factors play a key role in determining the overall performance and functionality of the membranes. Therefore, it becomes imperative to thoroughly evaluate and consider the effects of various modification methods on the nanochannels. This careful evaluation enables researchers to select and optimize the most suitable 2D-material-based membranes for specific applications. By understanding and exploiting the complex relationship between nanochannels and surface properties, researchers can unlock the full potential of these membranes in areas as diverse as water purification to energy storage.

APPLICATIONS OF 2D-MATERIAL-BASED NANOCANNEL MEMBRANES

By rationalizing the structural and functional characteristics, 2D-material-based nanochannel membranes can achieve many features, such as ultrafast transmission, selective sieving, sensitive sensing, controlled gating, and rectification, among others. This section summarizes typical developments in liquid molecular separation, gas separation, and ion sieving using state-of-the-art 2D-material-based nanochannel membranes [Figure 10].

Liquid molecular separation

Membranes are highly susceptible to swelling effects when applied in liquid environments (i.e., liquid molecular separations, including liquid solvent-molecular solute separations and liquid-liquid separations), leading to the collapse of nanochannels, reduced selectivity, and shortened membrane lifespan. Therefore, it is imperative to improve the swelling resistance of membranes in liquid environments compared to membranes in other conditions.

A series of anti-swelling MXene nanochannel membranes were synthesized by Xing *et al.* using the interaction forces generated by introducing negatively charged polymers into positively charged MXene

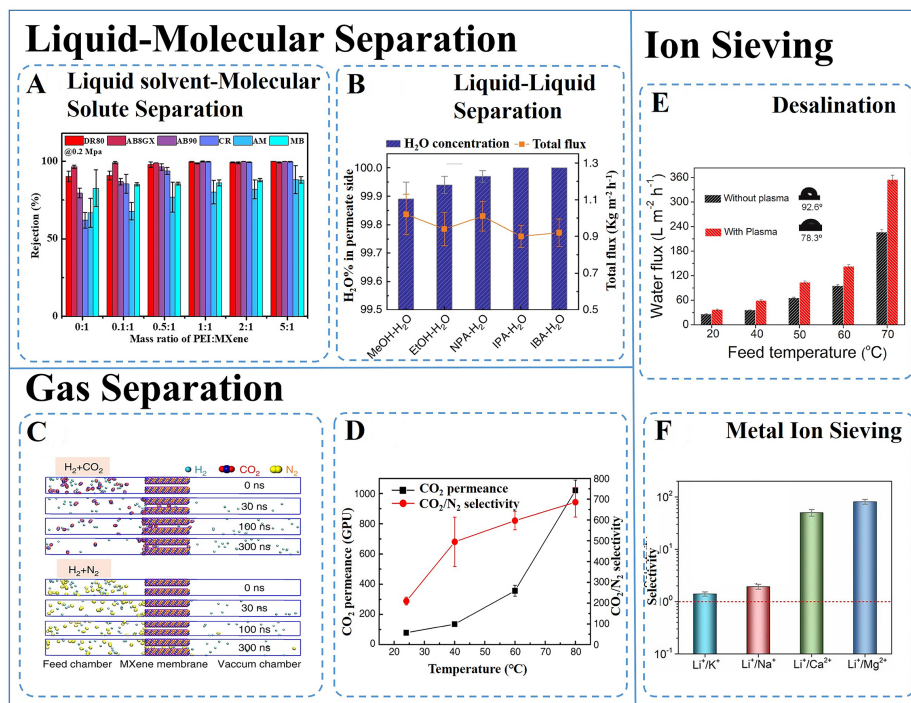


Figure 10. Liquid-molecule separation performance in representative applications. (A) Rejection rates of various dyes (i.e., Liquid solvent-Molecular solute separation) on an anti-swelling MXene-based membrane^[162]. Copyright 2022, John Wiley & Sons, Inc. (B) Separation performance of various alcohols to H₂O (i.e., Liquid-liquid separation) on a 2D-interspacing-narrowed graphene oxide membrane^[163]. Copyright 2017, Springer Nature. Gas separation performance in representative applications. (C) Simulation diagram of highly efficient gas separation on MXene molecular sieving membranes^[164]. Copyright 2018, Springer Nature. (D) Highly efficient CO₂ capture performance on ultrathin graphene oxide-based hollow fiber membranes with brush-like CO₂-philic agent^[165]. Copyright 2017, Springer Nature. Ion sieving performance in representative applications. (E) Ultrafast water flux of a graphene desalination membrane with 99.99% NaCl rejection rate at different feed temperatures^[167]. Copyright 2021, Elsevier B.V. (F) Fast and selective lithium-ion transport performance on an oriented UiO-67 Metal-Organic Framework membrane^[170]. Copyright 2022, John Wiley & Sons, Inc.

membranes^[162]. And by tuning the ratio of polymer and MXene, different sizes of nanochannels can be obtained for separating different hydrated molecules [Figure 10A]. Xing *et al.* reported a separation membrane that can adjust the size of nanochannels by operating pressure, which can retain 99.9% of hydrated dye molecules under a small operating pressure and 51.8% of the hydrated ions under a large operating pressure^[14]. Liquid-liquid separation plays a pivotal role in chemical production. Qi *et al.* reported a GO-based nanochannel membrane with an interlayer channel size between water and methanol molecules, which can effectively separate methanol-water mixtures with a high separation efficiency of 99.89 wt.% [Figure 10B]^[163]. For a better comparison of related membranes, a summary of liquid molecular separation membranes is shown in Table 2.

Gas separation

Unlike other separations, gas separation is more sensitive to adsorption and desorption on membrane surfaces, requiring smaller nanochannels than other separation systems used throughout many industries, such as methane reforming, CO₂ capture, and hydrogen purification. Therefore, Controlling the nanochannel size and modifying the surface is essential.

The preparation of high-performance hydrogen purification membranes has become critical for constraining hydrogen exchange to replace fossil dyes in catalytic hydrogen production processes. Ding *et al.* prepared a two-position separation membrane with a nanochannel size ~ 0.35 nm, which possesses H₂

Table 2. Summary of liquid molecular separation membranes

Membrane	Base material	Assembly method	Interlayer spacing	Molecular	Dye rejection (%)	Permeate flux (L·m ⁻² ·h ⁻¹ ·bar ⁻¹)
uGNMs ^[103]	Graphene	Vacuum filtration	sub-1-nm	DR 8,	> 99	21.8
PRGO/HNTs ^[182]	Graphene oxide	Solvent evaporation	8.87 Å	RB 5,	97.9	11.3
GO(120) NFM ^s ^[183]	Graphene oxide	Electro spraying	0.818 nm	EB,	99.99	11.13
c-GO/PAN ^[14]	Graphene oxide	Vacuum filtration	7.6/7.15 Å	DR 80,	> 99	78.5-117.2
MCM0.6-75 ^[184]	MXene	Suction filtration	1.41 nm	Methylene blue,	100	44.97
HGM30 ^[185]	Graphene oxide	Vacuum filtration	0.77 nm	rhodamine B (RhB),	99.30	89.6
MXene/GO-B ^[186]	MXene & graphene oxide	Vacuum filtration	5 Å	Brilliant blue,	100	0.23
GO/MXene ^[187]	Graphene oxide & MXene	Filtration	7.3 Å-14.5 Å	Chrysoidine G,	- 97	71.9
MXene/GO ^[188]	MXene & graphene oxide	Vacuum filtration	12.7 Å	Methylene blue,	98.56	16.69
10%MXene@CA ^[189]	MXene)/cellulose acetate	Casting	~ 6.68 Å	Rhodamine B,	92	256
21% Ag@MXene ^[190]	MXene	Vacuum filtration	2.1 Å	Rhodamine B,	79.93	420

permeability of > 2,200 Barrer and H₂/CO₂ selectivity of > 160, demonstrating excellent eventual commercialization potential [Figure 10C]^[164]. Carbon neutrality has become a hot topic in recent years. The separation of CO₂/N₂ is a prerequisite for CO₂ capture, leading to the successful synthesis of organic matter from CO₂. Zhou *et al.* cross-linked piperazine with GO, resulting in a membrane with a high affinity for CO₂, thus significantly improving the separation efficiency of CO₂/N₂ [Figure 10D]^[165]. The separation of hydrogen isotopes is vital for medical diagnosis and treatment. Lozada-Hidalgo *et al.* reported that graphene monolayers and BN membranes could separate hydrogen ion isotopes with a separation factor of about 10^[166]. For a better comparison of related membranes, a summary of gas separation membranes is shown in Table 3.

Ion sieving

Recently, researchers have paid increasing attention to high-performance ion sieve membranes in addition to traditional separation methods. Membranes with various properties are required to meet the different needs of ion sieve membranes for applications such as water desalination, microcurrent, hydrogen production, and energy storage.

In seawater desalination, stringent channel dimensions are necessary, with nanochannels often needing to be sub-nanometers in size to achieve ultra-high desalination efficiency. Chen *et al.* reported a graphene desalination membrane with sub-nanopores that achieved 99.99% NaCl rejection with an ultrafast water flux combined with evaporation methods [Figure 10E]^[167]. In energy storage applications, ion sieve membranes are often used as diaphragms, where excellent ionic conductivity and electrical insulation are required. Ghazi *et al.* synthesize a MoS₂/celgard separator with outstanding lithium ion passage and polysulfide retention capacity, which can effectively inhibit the shuttle effect in lithium-sulfur batteries, significantly improving the battery performance^[168].

Table 3. Summary of gas separation membranes

Membrane	Base material	Assembly method	Pore size	Gas	Selectivity
Graphene/NPC/MWNT ^[191]	Graphene	Spin-coating	20-30 nm	H ₂ /CH ₄	11-23
pCN ^[192]	Carbon nitride	Low-pressure chemical vapor deposition	N/A	H ₂ /CO ₂	6.58
Zn/Co-HDS ^[193]	Bimetallic MOF nanosheet	Vapor phase transformation	0.21 nm	H ₂ /CO ₂	54.1
β-ketoenamine-type COF membrane ^[194]	β-ketoenamine-type COF	Hot-drop coating	0.6 nm	H ₂ /CO ₂	22
(LDH/FAS)n-PDMS hybrid membranes	LDHs	Vacuum filtration/layer-by-layer assembly	N/A	H ₂ /CO ₂	43
BN membrane ^[195]	Boron nitride	Vacuum filtration	0.33 nm	Ethylene/Ethane	128
Printed GO-based membranes ^[196]	GO	Printing	0.89 nm	CO ₂ /N ₂	70

Yang *et al.* prepared a metal-organic framework as a multifunctional ionic sieve membrane for aqueous zinc-iodide batteries, greatly extending the battery lifespan^[169]. The recovery of rare metals has become increasingly popular due to the rising popularity of electric vehicles and electronic products. Efficient screening of metal ions is the key to recovering rare metals. Xu *et al.* developed a special lithium ion sieving UiO-67/AAO membrane, which achieved an ultra-high Li⁺ permeability of 27.01 mol m⁻² h⁻¹ and a Li⁺/Mg²⁺ selectivity of up to 159.4 [Figure 10F]^[170]. For a better comparison of related membranes, a summary of ion sieving membranes is shown in Table 4.

Important factors to consider when selecting a 2D nanochannel membrane for separation are the object to be separated, expected performance, ideal structure, cost-effectiveness, and environmental impact. In various application scenarios, choosing the appropriate membrane fabrication and modification process is the precondition for the membrane to ensure the ideal performance. Taking these factors into account can lead to the successful development of efficient and environmentally friendly separation processes.

CONCLUSION AND OUTLOOK

In summary, the emergence of a family of 2D materials with atomic-level thickness and excellent physical and chemical properties has brought significant development opportunities to nanochannel membranes. Over decades of development, 2D-materials-based membranes have made a preliminary breakthrough from raw materials to laboratory-level applications.

As outlined in Figure 11, this review summarized in detail strategies for constructing nanochannels in section CONSTRUCTING NANOCHANNELS WITH 2D NANOSHEETS. The extensive research on the swelling mechanism of 2D-material-based membranes has provided effective guidance for researchers to synthesize 2D nanosheets with ideal properties *via* “top-down” and “bottom-up” strategies, i.e., from a “clay” to “bricks” process. The appearance of various types of perforation methods (e.g., focused ion beam, plasma etching, chemical etching, *etc.*) has facilitated the transition from “bricks” to “porous bricks”, providing more options for the next step of nanochannel formation. The membrane assembly process is analogous

Table 4. Summary of ion sieving membranes

Membrane	Base material	Assembly method	Pore size	Ion/Ion	Selectivity
COF (TpBDMe ₂) membrane ^[197]	COF	Interfacial growth strategy	1.4 nm	K ⁺ /Mg ²⁺	765
COF-300/PS membrane ^[198]	COF-300 and polystyrene (PS)	N/A	1 nm	K ⁺ /Li ⁺	31.5
GOM ^[199]	GO	Vacuum filtration	13.9 Å	Lanthanides/actinides	~ 400
C@TM ^[200]	Ti ₃ C ₂ T _x	Suction-filtered	4.8 ± 0.1 Å	Li ⁺ /Mg ²⁺	30
EDA-GO ^[201]	GO	Vacuum filtration	5.82 Å-6.04 Å	K ⁺ /Na ⁺	1.5-5
s-MOF-801 polycrystalline ^[202]	MOF-801	Secondary growth method	6.2 Å	H ⁺ /V	194
COF-based membrane ^[203]	COF	Interfacial polymerization	2.34 nm	Li ⁺ /Mg ²⁺	64
GPETNC ^[204]	graphene	Asymmetric track-etching technique		K ⁺ /ions	4.6
KCl-controlled GO membranes ^[205]	GO	Vacuum filtration	10.7 Å	Na ⁺ /Mg ²⁺	30.6

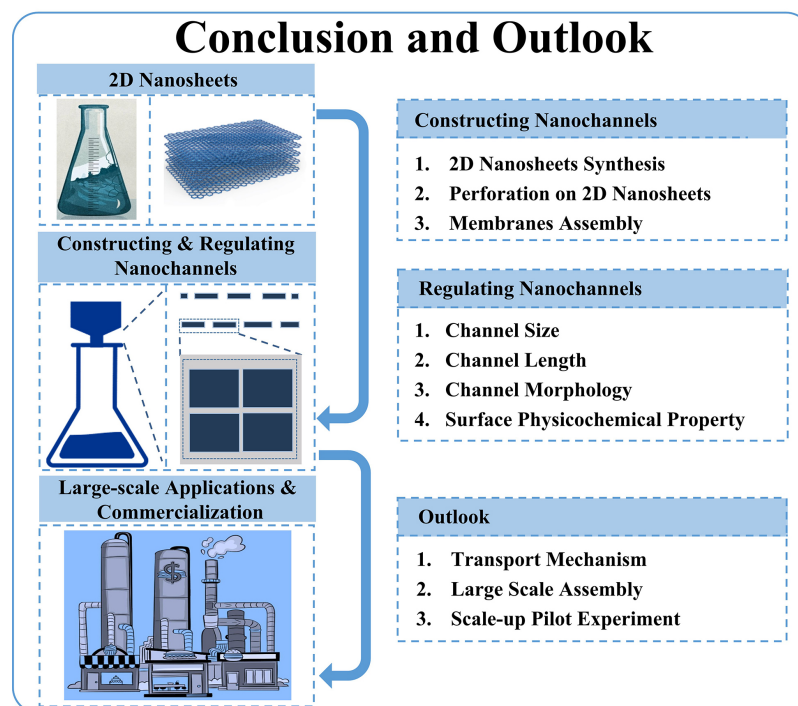


Figure 11. Conclusion and outlook of the development of the 2D-material-based membranes from the preparation of starting materials 2D nanosheets, the strategies of constructing nanochannels, the strategies of regulating the characteristics of nanochannels (channel size, channel length, channel morphology, and channel surface physicochemical properties), and the outlook to eventual commercialization.

to the process of “bricks” to “house”, and the selection of assembly strategy (e.g., pressure/vacuum filtration, spin coating, *etc.*) is crucial, as a suitable assembly method often leads to the right membrane.

A well-renovated and furnished “house” holds great value. Modifying the nanochannel of the membranes is similar to the “renovation” process. We comprehensively summarized the regulation strategies from four modifiable nanochannel properties, i.e., channel size, channel length, channel morphology, and the surface chemical property, in Section “REGULATING NANOCHANNELS”. The appropriate regulating strategy

allows the membrane to obtain the desired properties (e.g., defined size nanochannels, specific ionic or electronic conductivity, *etc.*) to meet the requirements for the corresponding applications.

Although researchers have tried a variety of membranes for liquid molecular separation, gas separation, and ion sieving applications (e.g., wastewater treatment, desalination, CO₂ capture, ion recovery, *etc.*), as we summarized in section APPLICATIONS OF 2D-MATERIAL-BASED NANOCHANNEL MEMBRANES, the vast majority of these applications are only at the laboratory level (“trial residence” stage), and the research and development of high-performance 2D-material-based nanochannel membranes are still at an early stage with both opportunities and challenges. To speed up the eventual commercialization of membranes and make them better serve the development of society, we propose an outlook on the future development of membranes from the following three aspects.

(1) Transport Mechanism. The current research has well explained the mechanism of the swelling problem and the construction and modification of nanochannels. Moreover, there is a large amount of work using theoretical calculations and simulations to try to make theoretical explanations for the differences in the filtration performance of various membranes. However, mechanisms during filtrations (e.g., the behavior mechanism of nanofluid in the channel, the rejection and passage mechanism of nanochannel to various filtrates, the force mechanism of nanochannel, the interaction mechanism between nanochannel and various filtrates, *etc.*) still need to be studied in depth. The emergence of various advanced characterization tools (e.g., cryoelectron microscopy, *in-situ* electron microscopy, *in-situ* Raman, *etc.*) provides new possibilities to investigate these mechanisms in depth. Mechanistic studies of the dynamic behavior of nanochannel membranes (including nanofluids and membranes themselves) will significantly advance mechanical innovation in the membrane field and accelerate the development of the new generation of high-performance membranes and industrial applications.

(2) Large-scale preparation. Rapid advances in chemistry and materials science have given rise to thousands of 2D materials. Yet, the mainstream “top-down” and “bottom-up” strategies are often only suitable for small-scale production in the laboratory. While there have been reports of kilogram-scale yields, this remains insufficient to meet the industrial demand of tens or even hundreds of kilograms. To overcome this challenge, it is crucial to develop new reliable methods for the preparation of 2D materials and reliable related manufacturing equipment. Notably, corresponding membrane assembly and modification technologies are also growing rapidly. Similarly, most methods, such as vacuum filtration, spin coating, and cross-linking, are more suitable for small-scale laboratory production and modification. Therefore, large-scale preparation is inevitable to apply advanced nanochannel membranes in the industry successfully. This calls for deep collaboration between the scientific and industrial communities to develop simple and scalable membrane fabrication methods, and relevant pilot experiments are necessary.

(3) Applications. Although almost all studies reported outstanding application performance, such as high selectivity, high permeability, and long membrane lifespan, these properties may be overestimated due to the limited membrane operating area, mild test conditions, and relatively short test durations in the laboratory. To truly reflect membrane capabilities, scaled-up application experiments under harsh conditions close to real-world applications (e.g., the effects of biochemical contaminants, sudden changes in water temperature and flow rate, *etc.*) are needed, which may pose additional challenges to researchers but will significantly facilitate the eventual commercialization of the membranes.

By addressing these challenges, the development of membranes with optimized nanochannels has the potential to transcend the limitations of traditional separation methods. Advances in membrane technology,

including selective ion, molecular, and particle transport, have important implications for energy-efficient operation, resource conservation, carbon capture, biogas purification, green hydrogen production, and energy storage. This avenue of research offers great promise for shaping a cleaner, more sustainable world.

DECLARATIONS

Authors' contributions

Draft writing, literature summary, picture production, language polishing, format adjustment: Xing C

Article frame writing, draft writing, literature summary: Zhang M

Literature summary, picture production: Liu L

Format adjustment: Zheng Z

Language polishing, format adjustment, literature summary: Zhou M

Financial support, article frame writing, language polishing: Liu C

Financial support, article frame writing, language polishing, supervision: Zhang S

Availability of data and materials

Not applicable.

Financial support and sponsorship

This research was supported by Griffith University Ph.D. Scholarship, the National Natural Science Foundation of China (Nos. 22274117 and 22008182), the Natural Science Foundation of Guangdong Province (No. 2021A1515010376), and the Education Department of Guangdong Province (No. 2020ZDZX2015).

Conflicts of interest

All authors declared that there are no conflicts of interest.

Ethical approval and consent to participate

Not applicable.

Consent for publication

Not applicable.

Copyright

© The Author(s) 2023.

REFERENCES

1. Wang F, Zhang Z, Shakir I, Yu C, Xu Y. 2D polymer nanosheets for membrane separation. *Adv Sci* 2022;9:e2103814. [DOI](#) [PubMed](#) [PMC](#)
2. Yuan S, Li X, Zhu J, Zhang G, Van Puyvelde P, Van der Bruggen B. Covalent organic frameworks for membrane separation. *Chem Soc Rev* 2019;48:2665-81. [DOI](#)
3. Li X, Liu Y, Wang J, Gascon J, Li J, Van der Bruggen B. Metal-organic frameworks based membranes for liquid separation. *Chem Soc Rev* 2017;46:7124-44. [DOI](#)
4. Park HB, Kamcev J, Robeson LM, Elimelech M, Freeman BD. Maximizing the right stuff: the trade-off between membrane permeability and selectivity. *Science* 2017;356:eaab0530. [DOI](#) [PubMed](#)
5. Wang S, Yang L, He G, et al. Two-dimensional nanochannel membranes for molecular and ionic separations. *Chem Soc Rev* 2020;49:1071-89. [DOI](#)
6. Kim JH, Choi Y, Kang J, et al. Shear-induced assembly of high-aspect-ratio graphene nanoribbon nanosheets in a confined microchannel: Membrane fabrication for ultrafast organic solvent nanofiltration. *Carbon* 2022;191:563-70. [DOI](#)
7. Pakulski D, Czepa W, Buffa SD, Ciesielski A, Samori P. Atom-thick membranes for water purification and blue energy harvesting. *Adv Funct Mater* 2020;30:1902394. [DOI](#)
8. Feng X, Peng D, Zhu J, Wang Y, Zhang Y. Recent advances of loose nanofiltration membranes for dye/salt separation. *Sep Purif*

- Technol* 2022;285:120228. DOI
9. Liu X, Jiang B, Yin X, Ma H, Hsiao BS. Highly permeable nanofibrous composite microfiltration membranes for removal of nanoparticles and heavy metal ions. *Sep Purif Technol* 2020;233:115976. DOI
 10. Ren Y, Ma Y, Min G, Zhang W, Lv L, Zhang W. A mini review of multifunctional ultrafiltration membranes for wastewater decontamination: additional functions of adsorption and catalytic oxidation. *Sci Total Environ* 2021;762:143083. DOI
 11. Zhao S, Liao Z, Fane A, et al. Engineering antifouling reverse osmosis membranes: a review. *Desalination* 2021;499:114857. DOI
 12. Xing C, Liu L, Guo X, et al. Efficient water purification using stabilized MXene nanofiltration membrane with controlled interlayer spacings. *Sep Purif Technol* 2023;317:123774. DOI
 13. Xing C, Liu C, Lai C, Zhang S. Tuning d-spacing of graphene oxide nanofiltration membrane for effective dye/salt separation. *Rare Met* 2023;42:418-29. DOI
 14. Xing C, Han J, Pei X, et al. Tunable graphene oxide nanofiltration membrane for effective dye/salt separation and desalination. *ACS Appl Mater Interfaces* 2021;13:55339-48. DOI
 15. Surwade SP, Smirnov SN, Vlassiuk IV, et al. Water desalination using nanoporous single-layer graphene. *Nat Nanotechnol* 2015;10:459-64. DOI
 16. Joshi RK, Carbone P, Wang FC, et al. Precise and ultrafast molecular sieving through graphene oxide membranes. *Science* 2014;343:752-4. DOI
 17. Ding L, Wei Y, Wang Y, Chen H, Caro J, Wang H. A two-dimensional lamellar membrane: MXene nanosheet stacks. *Angew Chem Int Ed* 2017;56:1825-9. DOI
 18. Caglar M, Silkina I, Brown BT, et al. Tunable anion-selective transport through monolayer graphene and hexagonal boron nitride. *ACS Nano* 2020;14:2729-38. DOI PubMed PMC
 19. Wang Y, Li L, Wei Y, et al. Water transport with ultralow friction through partially exfoliated g-C₃N₄ nanosheet membranes with self-supporting spacers. *Angew Chem Int Ed* 2017;56:8974-80. DOI
 20. Ries L, Petit E, Michel T, et al. Enhanced sieving from exfoliated MoS₂ membranes via covalent functionalization. *Nat Mater* 2019;18:1112-7. DOI
 21. Jia P, Wen Q, Liu D, et al. Highly efficient ionic photocurrent generation through WS₂-based 2D nanofluidic channels. *Small* 2019;15:e1905355. DOI
 22. Lu P, Liu Y, Zhou T, Wang Q, Li Y. Recent advances in layered double hydroxides (LDHs) as two-dimensional membrane materials for gas and liquid separations. *J Membr Sci* 2018;567:89-103. DOI
 23. Jiang Z, Liu H, Ahmed SA, et al. Insight into ion transfer through the sub-nanometer channels in zeolitic imidazolate frameworks. *Angew Chem Int Ed* 2017;129:4845-9. DOI
 24. Li X, Zhang H, Wang P, et al. Fast and selective fluoride ion conduction in sub-1-nanometer metal-organic framework channels. *Nat Commun* 2019;10:2490. DOI PubMed PMC
 25. Kuehl VA, Yin J, Duong PHH, et al. A highly ordered nanoporous, two-dimensional covalent organic framework with modifiable pores, and its application in water purification and ion sieving. *J Am Chem Soc* 2018;140:18200-7. DOI
 26. Danda G, Drndić M. Two-dimensional nanopores and nanoporous membranes for ion and molecule transport. *Curr Opin Biotechnol* 2019;55:124-33. DOI PubMed
 27. Prozorovska L, Kidambi PR. State-of-the-art and future prospects for atomically thin membranes from 2D materials. *Adv Mater* 2018;30:e1801179. DOI
 28. Kim S, Wang H, Lee YM. 2D Nanosheets and their composite membranes for water, gas, and ion separation. *Angew Chem Int Ed* 2019;131:17674-89. DOI
 29. Kang Y, Xia Y, Wang H, Zhang X. 2D laminar membranes for selective water and ion transport. *Adv Funct Mater* 2019;29:1902014. DOI
 30. Koltanow AR, Huang J. Two-dimensional nanofluidics. *Science* 2016;351:1395-6. DOI PubMed
 31. Tan C, Cao X, Wu XJ, et al. Recent advances in ultrathin two-dimensional nanomaterials. *Chem Rev* 2017;117:6225-331. DOI
 32. Nicolosi V, Chhowalla M, Kanatzidis MG, Strano MS, Coleman JN. Liquid exfoliation of layered materials. *Science* 2013;340:1226419. DOI
 33. Novoselov KS, Geim AK, Morozov SV, et al. Electric field effect in atomically thin carbon films. *Science* 2004;306:666-9. DOI
 34. Novoselov KS, Jiang D, Schedin F, et al. Two-dimensional atomic crystals. *Proc Natl Acad Sci USA* 2005;102:10451-3. DOI PubMed PMC
 35. Paton KR, Varrla E, Backes C, et al. Scalable production of large quantities of defect-free few-layer graphene by shear exfoliation in liquids. *Nat Mater* 2014;13:624-30. DOI
 36. Coleman JN, Lotya M, O'Neill A, et al. Two-dimensional nanosheets produced by liquid exfoliation of layered materials. *Science* 2011;331:568-71. DOI
 37. Peng Y, Li Y, Ban Y, et al. Metal-organic framework nanosheets as building blocks for molecular sieving membranes. *Science* 2014;346:1356-9. DOI
 38. Achee TC, Sun W, Hope JT, et al. High-yield scalable graphene nanosheet production from compressed graphite using electrochemical exfoliation. *Sci Rep* 2018;8:14525. DOI PubMed PMC
 39. Wang X, Narita A, Müllen K. Precision synthesis versus bulk-scale fabrication of graphenes. *Nat Rev Chem* 2018;2:0100. DOI
 40. Naguib M, Mashtalir O, Carle J, et al. Two-dimensional transition metal carbides. *ACS Nano* 2012;6:1322-31. DOI

41. Wang Q, O'Hare D. Recent advances in the synthesis and application of layered double hydroxide (LDH) nanosheets. *Chem Rev* 2012;112:4124-55. [DOI](#) [PubMed](#)
42. Ma R, Sasaki T. Two-dimensional oxide and hydroxide nanosheets: controllable high-quality exfoliation, molecular assembly, and exploration of functionality. *Acc Chem Res* 2015;48:136-43. [DOI](#) [PubMed](#)
43. Varoon K, Zhang X, Elyassi B, et al. Dispersible exfoliated zeolite nanosheets and their application as a selective membrane. *Science* 2011;334:72-5. [DOI](#)
44. Ren J, Liu X, Zhang L, Liu Q, Gao R, Dai W. Thermal oxidative etching method derived graphitic C₃N₄: highly efficient metal-free catalyst in the selective epoxidation of styrene. *RSC Adv* 2017;7:5340-8. [DOI](#)
45. Yu J, Li J, Zhang W, Chang H. Synthesis of high quality two-dimensional materials via chemical vapor deposition. *Chem Sci* 2015;6:6705-16. [DOI](#) [PubMed](#) [PMC](#)
46. Shi Y, Li H, Li LJ. Recent advances in controlled synthesis of two-dimensional transition metal dichalcogenides via vapour deposition techniques. *Chem Soc Rev* 2015;44:2744-56. [DOI](#)
47. Ou M, Wang X, Yu L, et al. The emergence and evolution of borophene. *Adv Sci* 2021;8:2001801. [DOI](#) [PubMed](#) [PMC](#)
48. Huang S, Dakhchoune M, Luo W, et al. Single-layer graphene membranes by crack-free transfer for gas mixture separation. *Nat Commun* 2018;9:2632. [DOI](#) [PubMed](#) [PMC](#)
49. Zhang J, Lin L, Sun L, et al. Clean transfer of large graphene single crystals for high-intactness suspended membranes and liquid cells. *Adv Mater* 2017;29:1700639. [DOI](#)
50. Chen Y, Gong XL, Gai JG. Progress and challenges in transfer of large-area graphene films. *Adv Sci* 2016;3:1500343. [DOI](#) [PubMed](#) [PMC](#)
51. Jeon MY, Kim D, Kumar P, et al. Ultra-selective high-flux membranes from directly synthesized zeolite nanosheets. *Nature* 2017;543:690-4. [DOI](#)
52. Makiura R, Motoyama S, Umemura Y, Yamanaka H, Sakata O, Kitagawa H. Surface nano-architecture of a metal-organic framework. *Nat Mater* 2010;9:565-71. [DOI](#) [PubMed](#)
53. Rodenas T, Luz I, Prieto G, et al. Metal-organic framework nanosheets in polymer composite materials for gas separation. *Nat Mater* 2015;14:48-55. [DOI](#) [PubMed](#) [PMC](#)
54. Feng X, Ding X, Jiang D. Covalent organic frameworks. *Chem Soc Rev* 2012;41:6010-22. [DOI](#) [PubMed](#)
55. Dai W, Shao F, Szczerbiński J, et al. Synthesis of a two-dimensional covalent organic monolayer through dynamic imine chemistry at the air/water interface. *Angew Chem Int Ed* 2016;128:221-5. [DOI](#)
56. Kandambeth S, Biswal BP, Chaudhari HD, et al. Selective molecular sieving in self-standing porous covalent-organic-framework membranes. *Adv Mater* 2017;29:1603945. [DOI](#)
57. Moreno C, Vilas-Varela M, Kretz B, et al. Bottom-up synthesis of multifunctional nanoporous graphene. *Science* 2018;360:199-203. [DOI](#)
58. Fischbein MD, Drndić M. Electron beam nanosculpting of suspended graphene sheets. *Appl Phys Lett* 2008;93:113107. [DOI](#)
59. Koenig SP, Wang L, Pellegrino J, Bunch JS. Selective molecular sieving through porous graphene. *Nat Nanotechnol* 2012;7:728-32. [DOI](#) [PubMed](#)
60. Celebi K, Buchheim J, Wyss RM, et al. Ultimate permeation across atomically thin porous graphene. *Science* 2014;344:289-92. [DOI](#)
61. Russo CJ, Golovchenko JA. Atom-by-atom nucleation and growth of graphene nanopores. *Proc Natl Acad Sci USA* 2012;109:5953-7. [DOI](#) [PubMed](#) [PMC](#)
62. O'Hern SC, Boutilier MS, Idrobo JC, et al. Selective ionic transport through tunable subnanometer pores in single-layer graphene membranes. *Nano Lett* 2014;14:1234-41. [DOI](#)
63. Zhu Y, Murali S, Stoller MD, et al. Carbon-based supercapacitors produced by activation of graphene. *Science* 2011;332:1537-41. [DOI](#)
64. Zhang LL, Zhao X, Stoller MD, et al. Highly conductive and porous activated reduced graphene oxide films for high-power supercapacitors. *Nano Lett* 2012;12:1806-12. [DOI](#)
65. Zhao X, Hayner CM, Kung MC, Kung HH. Flexible holey graphene paper electrodes with enhanced rate capability for energy storage applications. *ACS Nano* 2011;5:8739-49. [DOI](#) [PubMed](#)
66. Wang X, Jiao L, Sheng K, Li C, Dai L, Shi G. Solution-processable graphene nanomeshes with controlled pore structures. *Sci Rep* 2013;3:1996. [DOI](#) [PubMed](#) [PMC](#)
67. Palaniselvam T, Valappil MO, Illathvalappil R, Kurungot S. Nanoporous graphene by quantum dots removal from graphene and its conversion to a potential oxygen reduction electrocatalyst via nitrogen doping. *Energy Environ Sci* 2014;7:1059. [DOI](#)
68. Zhou D, Cui Y, Xiao PW, Jiang MY, Han BH. A general and scalable synthesis approach to porous graphene. *Nat Commun* 2014;5:4716. [DOI](#)
69. Gilbert SM, Dunn G, Azizi A, et al. Fabrication of subnanometer-precision nanopores in hexagonal boron nitride. *Sci Rep* 2017;7:15096. [DOI](#) [PubMed](#) [PMC](#)
70. Feng J, Graf M, Liu K, et al. Single-layer MoS₂ nanopores as nanopower generators. *Nature* 2016;536:197-200. [DOI](#)
71. Feng J, Liu K, Graf M, et al. Electrochemical reaction in single layer MoS₂: nanopores opened atom by atom. *Nano Lett* 2015;15:3431-8. [DOI](#)
72. Geim AK, Grigorieva IV. Van der Waals heterostructures. *Nature* 2013;499:419-25. [DOI](#)
73. Radha B, Esfandiari A, Wang FC, et al. Molecular transport through capillaries made with atomic-scale precision. *Nature*

- 2016;538:222-5. DOI
74. Esfandiar A, Radha B, Wang FC, et al. Size effect in ion transport through angstrom-scale slits. *Science* 2017;358:511-3. DOI
75. Keerthi A, Geim AK, Janardanan A, et al. Ballistic molecular transport through two-dimensional channels. *Nature* 2018;558:420-4. DOI
76. Hu S, Lozada-Hidalgo M, Wang FC, et al. Proton transport through one-atom-thick crystals. *Nature* 2014;516:227-30. DOI
77. Gopinadhan K, Hu S, Esfandiar A, et al. Complete steric exclusion of ions and proton transport through confined monolayer water. *Science* 2019;363:145-8. DOI
78. Algara-Siller G, Lehtinen O, Wang FC, et al. Square ice in graphene nanocapillaries. *Nature* 2015;519:443-5. DOI
79. Fumagalli L, Esfandiar A, Fabregas R, et al. Anomalously low dielectric constant of confined water. *Science* 2018;360:1339-42. DOI
80. Mouterde T, Keerthi A, Poggioli AR, et al. Molecular streaming and its voltage control in ångström-scale channels. *Nature* 2019;567:87-90. DOI
81. Shen J, Liu G, Huang K, Chu Z, Jin W, Xu N. Subnanometer two-dimensional graphene oxide channels for ultrafast gas sieving. *ACS Nano* 2016;10:3398-409. DOI
82. Dikin DA, Stankovich S, Zimney EJ, et al. Preparation and characterization of graphene oxide paper. *Nature* 2007;448:457-60. DOI
83. Tsou C, An Q, Lo S, et al. Effect of microstructure of graphene oxide fabricated through different self-assembly techniques on 1-butanol dehydration. *J Membr Sci* 2015;477:93-100. DOI
84. Zhang M, Sun J, Mao Y, Liu G, Jin W. Effect of substrate on formation and nanofiltration performance of graphene oxide membranes. *J Membr Sci* 2019;574:196-204. DOI
85. Kim HW, Yoon HW, Yoon SM, et al. Selective gas transport through few-layered graphene and graphene oxide membranes. *Science* 2013;342:91-5. DOI
86. Chi C, Wang X, Peng Y, et al. Facile preparation of graphene oxide membranes for gas separation. *Chem Mater* 2016;28:2921-7. DOI
87. Guan K, Shen J, Liu G, Zhao J, Zhou H, Jin W. Spray-evaporation assembled graphene oxide membranes for selective hydrogen transport. *Sep Purif Technol* 2017;174:126-35. DOI
88. Ibrahim AF, Lin Y. Synthesis of graphene oxide membranes on polyester substrate by spray coating for gas separation. *Chem Eng Sci* 2018;190:312-9. DOI
89. Akbari A, Sheath P, Martin ST, et al. Large-area graphene-based nanofiltration membranes by shear alignment of discotic nematic liquid crystals of graphene oxide. *Nat Commun* 2016;7:10891. DOI PubMed PMC
90. Zhong J, Sun W, Wei Q, Qian X, Cheng HM, Ren W. Efficient and scalable synthesis of highly aligned and compact two-dimensional nanosheet films with record performances. *Nat Commun* 2018;9:3484. DOI PubMed PMC
91. Hu M, Mi B. Enabling graphene oxide nanosheets as water separation membranes. *Environ Sci Technol* 2013;47:3715-23. DOI PubMed
92. Hu M, Mi B. Layer-by-layer assembly of graphene oxide membranes via electrostatic interaction. *J Membr Sci* 2014;469:80-7. DOI
93. Song X, Zambare RS, Qi S, et al. Charge-gated ion transport through polyelectrolyte intercalated amine reduced graphene oxide membranes. *ACS Appl Mater Interfaces* 2017;9:41482-95. DOI
94. Zhao J, Zhu Y, Pan F, et al. Fabricating graphene oxide-based ultrathin hybrid membrane for pervaporation dehydration via layer-by-layer self-assembly driven by multiple interactions. *J Membr Sci* 2015;487:162-72. DOI
95. Zhao D, Chen Z, Liao X. Microstructural evolution and ferroelectricity in HfO₂ films. *Microstructures* 2022;2:2022007. DOI
96. Chen Z, Liao X, Zhang S. The visible hand behind properties. *Microstructures* 2021;1:2021001. DOI
97. Xing C, Chen H, Qian S, et al. Regulating liquid and solid-state electrolytes for solid-phase conversion in Li-S batteries. *Chem* 2022;8:1201-30. DOI
98. Xing C, Chen H, Zhang S. Powering 10-Ah-level Li-S pouch cell via a smart “skin”. *Matter* 2022;5:2523-5. DOI
99. Abraham J, Vasu KS, Williams CD, et al. Tunable sieving of ions using graphene oxide membranes. *Nat Nanotechnol* 2017;12:546-50. DOI
100. Li W, Wu W, Li Z. Controlling interlayer spacing of graphene oxide membranes by external pressure regulation. *ACS Nano* 2018;12:9309-17. DOI
101. Chen L, Shi G, Shen J, et al. Ion sieving in graphene oxide membranes via cationic control of interlayer spacing. *Nature* 2017;550:380-3. DOI
102. Qiu L, Zhang X, Yang W, Wang Y, Simon GP, Li D. Controllable corrugation of chemically converted graphene sheets in water and potential application for nanofiltration. *Chem Commun* 2011;47:5810-2. DOI
103. Han Y, Xu Z, Gao C. Ultrathin graphene nanofiltration membrane for water purification. *Adv Funct Mater* 2013;23:3693-700. DOI
104. Liu H, Wang H, Zhang X. Facile fabrication of freestanding ultrathin reduced graphene oxide membranes for water purification. *Adv Mater* 2015;27:249-54. DOI
105. Hung W, Tsou C, De Guzman M, et al. Cross-linking with diamine monomers to prepare composite graphene oxide-framework membranes with varying *d*-spacing. *Chem Mater* 2014;26:2983-90. DOI
106. Zhang M, Mao Y, Liu G, Liu G, Fan Y, Jin W. Molecular bridges stabilize graphene oxide membranes in water. *Angew Chem Int Ed* 2020;59:1689-95. DOI PubMed
107. Jia Z, Shi W. Tailoring permeation channels of graphene oxide membranes for precise ion separation. *Carbon* 2016;101:290-5. DOI
108. Lim M, Choi Y, Kim J, et al. Cross-linked graphene oxide membrane having high ion selectivity and antibacterial activity prepared

- using tannic acid-functionalized graphene oxide and polyethyleneimine. *J Membr Sci* 2017;521:1-9. DOI
109. Wang S, Wu Y, Zhang N, et al. A highly permeable graphene oxide membrane with fast and selective transport nanochannels for efficient carbon capture. *Energy Environ Sci* 2016;9:3107-12. DOI
 110. Zhang P, Gong J, Zeng G, et al. Cross-linking to prepare composite graphene oxide-framework membranes with high-flux for dyes and heavy metal ions removal. *Chem Eng J* 2017;322:657-66. DOI
 111. Xu XL, Lin FW, Du Y, Zhang X, Wu J, Xu ZK. Graphene oxide nanofiltration membranes stabilized by cationic porphyrin for high salt rejection. *ACS Appl Mater Inter* 2016;8:12588-93. DOI
 112. Fei F, Cseri L, Szekely G, Blanford CF. Robust covalently cross-linked polybenzimidazole/graphene oxide membranes for high-flux organic solvent nanofiltration. *ACS Appl Mater Inter* 2018;10:16140-7. DOI
 113. Yang J, Gong D, Li G, et al. Self-assembly of thiourea-crosslinked graphene oxide framework membranes toward separation of small molecules. *Adv Mater* 2018;30:e1705775. DOI
 114. Liu Y, Xu L, Liu J, et al. Graphene oxides cross-linked with hyperbranched polyethylenimines: preparation, characterization and their potential as recyclable and highly efficient adsorption materials for lead (II) ions. *Chem Eng J* 2016;285:698-708. DOI
 115. Nam YT, Choi J, Kang KM, Kim DW, Jung HT. Enhanced stability of laminated graphene oxide membranes for nanofiltration via interstitial amide bonding. *ACS Appl Mater Inter* 2016;8:27376-82. DOI
 116. Wang N, Ji S, Zhang G, Li J, Wang L. Self-assembly of graphene oxide and polyelectrolyte complex nano hybrid membranes for nanofiltration and pervaporation. *Chem Eng J* 2012;213:318-29. DOI
 117. Wang S, Xie Y, He G, et al. Graphene oxide membranes with heterogeneous nanodomains for efficient CO₂ separations. *Angew Chem Int Ed* 2017;56:14246-51. DOI
 118. Ran J, Chu C, Pan T, et al. Non-covalent cross-linking to boost the stability and permeability of graphene-oxide-based membranes. *J Mater Chem A* 2019;7:8085-91. DOI
 119. Wang W, Eftekhari E, Zhu G, Zhang X, Yan Z, Li Q. Graphene oxide membranes with tunable permeability due to embedded carbon dots. *Chem Commun* 2014;50:13089-92. DOI
 120. Han Y, Jiang Y, Gao C. High-flux graphene oxide nanofiltration membrane intercalated by carbon nanotubes. *ACS Appl Mater Inter* 2015;7:8147-55. DOI
 121. Goh K, Jiang W, Karahan HE, et al. All-carbon nanoarchitectures as high-performance separation membranes with superior stability. *Adv Funct Mater* 2015;25:7348-59. DOI
 122. Zhang M, Guan K, Shen J, Liu G, Fan Y, Jin W. Nanoparticles@rGO membrane enabling highly enhanced water permeability and structural stability with preserved selectivity. *AIChE J* 2017;63:5054-63. DOI
 123. Li C, Sun W, Lu Z, Ao X, Yang C, Li S. Systematic evaluation of TiO₂-GO-modified ceramic membranes for water treatment: retention properties and fouling mechanisms. *Chem Eng J* 2019;378:122138. DOI
 124. Wang S, Mahalingam D, Sutisna B, Nunes SP. 2D-dual-spacing channel membranes for high performance organic solvent nanofiltration. *J Mater Chem A* 2019;7:11673-82. DOI
 125. Guo H, Kong G, Yang G, et al. Cross-linking between sodalite nanoparticles and graphene oxide in composite membranes to trigger high gas permeance, selectivity, and stability in hydrogen separation. *Angew Chem Int Ed* 2020;132:6343-7. DOI
 126. Guan K, Zhao D, Zhang M, et al. 3D nanoporous crystals enabled 2D channels in graphene membrane with enhanced water purification performance. *J Membr Sci* 2017;542:41-51. DOI
 127. Li W, Zhang Y, Su P, et al. Metal-organic framework channelled graphene composite membranes for H₂/CO₂ separation. *J Mater Chem A* 2016;4:18747-52. DOI
 128. Khan NA, Yuan J, Wu H, et al. Mixed nanosheet membranes assembled from chemically grafted graphene oxide and covalent organic frameworks for ultra-high water flux. *ACS Appl Mater Inter* 2019;11:28978-86. DOI
 129. Sui X, Yuan Z, Liu C, et al. Graphene oxide laminates intercalated with 2D covalent-organic frameworks as a robust nanofiltration membrane. *J Mater Chem A* 2020;8:9713-25. DOI
 130. Mao Y, Zhang M, Cheng L, et al. Bola-amphiphile-imidazole embedded GO membrane with enhanced solvent dehydration properties. *J Membr Sci* 2020;595:117545. DOI
 131. Wang Z, Tu Q, Zheng S, Urban JJ, Li S, Mi B. Understanding the aqueous stability and filtration capability of MoS₂ membranes. *Nano Lett* 2017;17:7289-98. DOI PubMed
 132. Ran J, Pan T, Wu Y, et al. Endowing g-C₃N₄ membranes with superior permeability and stability by using acid spacers. *Angew Chem Int Ed* 2019;58:16463-8. DOI
 133. Wang J, Zhang Z, Zhu J, et al. Ion sieving by a two-dimensional Ti₃C₂T_x alginate lamellar membrane with stable interlayer spacing. *Nat Commun* 2020;11:3540. DOI PubMed PMC
 134. Cohen-Tanugi D, Grossman JC. Water desalination across nanoporous graphene. *Nano Lett* 2012;12:3602-8. DOI PubMed
 135. Yang Q, Su Y, Chi C, et al. Ultrathin graphene-based membrane with precise molecular sieving and ultrafast solvent permeation. *Nat Mater* 2017;16:1198-202. DOI
 136. Li H, Song Z, Zhang X, et al. Ultrathin, molecular-sieving graphene oxide membranes for selective hydrogen separation. *Science* 2013;342:95-8. DOI
 137. Heiraniyan M, Farimani AB, Aluru NR. Water desalination with a single-layer MoS₂ nanopore. *Nat Commun* 2015;6:8616. DOI PubMed PMC
 138. Yang Y, Yang X, Liang L, et al. Large-area graphene-nanomesh/carbon-nanotube hybrid membranes for ionic and molecular

- nanofiltration. *Science* 2019;364:1057-62. DOI
139. Ibrahim A, Lin Y. Gas permeation and separation properties of large-sheet stacked graphene oxide membranes. *J Membr Sci* 2018;550:238-45. DOI
 140. Amadei CA, Montessori A, Kadow JP, Succi S, Vecitis CD. Role of oxygen functionalities in graphene oxide architectural laminate subnanometer spacing and water transport. *Environ Sci Technol* 2017;51:4280-8. DOI PubMed
 141. Chen J, Li Y, Huang L, Jia N, Li C, Shi G. Size Fractionation of graphene oxide sheets via filtration through track-etched membranes. *Adv Mater* 2015;27:3654-60. DOI
 142. Shen J, Zhang M, Liu G, Guan K, Jin W. Size effects of graphene oxide on mixed matrix membranes for CO₂ separation. *AIChE J* 2016;62:2843-52. DOI
 143. Geng H, Yao B, Zhou J, et al. Size fractionation of graphene oxide nanosheets via controlled directional freezing. *J Am Chem Soc* 2017;139:12517-23. DOI
 144. Sun P, Zheng F, Zhu M, et al. Selective trans-membrane transport of alkali and alkaline earth cations through graphene oxide membranes based on cation- π interactions. *ACS Nano* 2014;8:850-9. DOI
 145. Nie L, Goh K, Wang Y, et al. Realizing small-flake graphene oxide membranes for ultrafast size-dependent organic solvent nanofiltration. *Sci Adv* 2020;6:eaa9184. DOI PubMed PMC
 146. Ying Y, Sun L, Wang Q, Fan Z, Peng X. In-plane mesoporous graphene oxide nanosheet assembled membranes for molecular separation. *RSC Adv* 2014;4:21425. DOI
 147. Li Y, Zhao W, Weyland M, et al. Thermally reduced nanoporous graphene oxide membrane for desalination. *Environ Sci Technol* 2019;53:8314-23. DOI
 148. Peng Y, Li Y, Ban Y, Yang W. Two-dimensional metal-organic framework nanosheets for membrane-based gas separation. *Angew Chem Int Ed* 2017;129:9889-93. DOI
 149. Shinde DB, Sheng G, Li X, et al. Crystalline 2D covalent organic framework membranes for high-flux organic solvent nanofiltration. *J Am Chem Soc* 2018;140:14342-9. DOI
 150. Xi Y, Liu Z, Ji J, et al. Graphene-based membranes with uniform 2D nanochannels for precise sieving of mono-/multi-valent metal ions. *J Membr Sci* 2018;550:208-18. DOI
 151. Li Y, Yuan S, Xia Y, et al. Mild annealing reduced graphene oxide membrane for nanofiltration. *J Membr Sci* 2020;601:117900. DOI
 152. Saraswat V, Jacobberger RM, Ostrander JS, et al. Invariance of water permeance through size-differentiated graphene oxide laminates. *ACS Nano* 2018;12:7855-65. DOI
 153. Kang Y, Qiu R, Jian M, et al. The role of nanowrinkles in mass transport across graphene-based membranes. *Adv Funct Mater* 2020;30:2003159. DOI
 154. Huang H, Song Z, Wei N, et al. Ultrafast viscous water flow through nanostrand-channelled graphene oxide membranes. *Nat Commun* 2013;4:2979. DOI
 155. Sun L, Ying Y, Huang H, et al. Ultrafast molecule separation through layered WS₂ nanosheet membranes. *ACS Nano* 2014;8:6304-11. DOI
 156. Park S, Lee KS, Bozoklu G, Cai W, Nguyen ST, Ruoff RS. Graphene oxide papers modified by divalent ions-enhancing mechanical properties via chemical cross-linking. *ACS Nano* 2008;2:572-8. DOI
 157. Ding L, Li L, Liu Y, et al. Effective ion sieving with Ti₃C₂T_x MXene membranes for production of drinking water from seawater. *Nat Sustain* 2020;3:296-302. DOI
 158. Kim S, Lin X, Ou R, et al. Highly crosslinked, chlorine tolerant polymer network entwined graphene oxide membrane for water desalination. *J Mater Chem A* 2017;5:1533-40. DOI
 159. Kim S, Ou R, Hu Y, et al. Non-swelling graphene oxide-polymer nanocomposite membrane for reverse osmosis desalination. *J Membr Sci* 2018;562:47-55. DOI
 160. Xie X, Chen C, Zhang N, Tang Z, Jiang J, Xu Y. Microstructure and surface control of MXene films for water purification. *Nat Sustain* 2019;2:856-62. DOI
 161. Alkhouzaam A, Qiblawey H, Khraisheh M. Polydopamine functionalized graphene oxide as membrane nanofiller: spectral and structural studies. *Membranes* 2021;11:86. DOI PubMed PMC
 162. Xing C, Zhang Y, Huang R, et al. Anti-swelling polyethyleneimine-modified MXene nanofiltration membranes for efficient and selective molecular separation. *EcoMat* 2023;5:e12300. DOI
 163. Qi B, He X, Zeng G, et al. Strict molecular sieving over electrodeposited 2D-interspace-narrowed graphene oxide membranes. *Nat Commun* 2017;8:825. DOI PubMed PMC
 164. Ding L, Wei Y, Li L, et al. MXene molecular sieving membranes for highly efficient gas separation. *Nat Commun* 2018;9:155. DOI PubMed PMC
 165. Zhou F, Tien HN, Xu WL, et al. Ultrathin graphene oxide-based hollow fiber membranes with brush-like CO₂-philic agent for highly efficient CO₂ capture. *Nat Commun* 2017;8:2107. DOI PubMed PMC
 166. Lozada-Hidalgo M, Hu S, Marshall O, et al. Sieving hydrogen isotopes through two-dimensional crystals. *Science* 2016;351:68-70. DOI
 167. Chen X, Zhu Y, Yu H, et al. Ultrafast water evaporation through graphene membranes with subnanometer pores for desalination. *J Membr Sci* 2021;621:118934. DOI

168. Ghazi ZA, He X, Khattak AM, et al. MoS₂/Celgard separator as efficient polysulfide barrier for long-life lithium-sulfur batteries. *Adv Mater* 2017;29:1606817. DOI
169. Yang H, Qiao Y, Chang Z, Deng H, He P, Zhou H. A metal-organic framework as a multifunctional ionic sieve membrane for long-life aqueous zinc-iodide batteries. *Adv Mater* 2020;32:e2004240. DOI
170. Xu R, Kang Y, Zhang W, Zhang X, Pan B. Oriented UiO-67 metal-organic framework membrane with fast and selective lithium-ion transport. *Angew Chem Int Ed* 2022;61:e202115443. DOI
171. Bonaccorso F, Lombardo A, Hasan T, Sun Z, Colombo L, Ferrari AC. Production and processing of graphene and 2D crystals. *Mater Today* 2012;15:564-89. DOI
172. Navik R, Gai Y, Wang W, Zhao Y. Curcumin-assisted ultrasound exfoliation of graphite to graphene in ethanol. *Ultrason Sonochem* 2018;48:96-102. DOI PubMed
173. Dhanabalan SC, Ponraj JS, Guo Z, Li S, Bao Q, Zhang H. Emerging trends in phosphorene fabrication towards next generation devices. *Adv Sci* 2017;4:1600305. DOI PubMed PMC
174. Batool S, Idrees M, Zhang SR, Han ST, Zhou Y. Novel charm of 2D materials engineering in memristor: when electronics encounter layered morphology. *Nanoscale Horiz* 2022;7:480-507. DOI
175. Duraisamy S, Ganguly A, Sharma PK, Benson J, Davis J, Papakonstantinou P. One-step hydrothermal synthesis of phase-engineered MoS₂/MoO₃ electrocatalysts for hydrogen evolution reaction. *ACS Appl Nano Mater* 2021;4:2642-56. DOI
176. Miao Y, Tsapatsis M. Electron beam patterning of metal-organic frameworks. *Chem Mater* 2021;33:754-60. DOI
177. Lu X, Wang R, Hao L, et al. Oxidative etching of MoS₂/WS₂ nanosheets to their QDs by facile UV irradiation. *Phys Chem Chem Phys* 2016;18:31211-6. DOI
178. Wei Y, Pastuovic Z, Shen C, Murphy T, Gore DB. Ion beam engineered graphene oxide membranes for mono-/di-valent metal ions separation. *Carbon* 2020;158:598-606. DOI
179. Kim B, Im S, Yoo G. Performance evaluation of CNN-based end-point detection using in-situ plasma etching data. *Electronics* 2021;10:49. DOI
180. Huang X, Cen D, Wei R, Fan H, Bao Z. Synthesis of porous Si/C composite nanosheets from vermiculite with a hierarchical structure as a high-performance anode for lithium-ion battery. *ACS Appl Mater Inter* 2019;11:26854-62. DOI
181. Pasquarelli RM, Ginley DS, O'Hayre R. Solution processing of transparent conductors: from flask to film. *Chem Soc Rev* 2011;40:5406-41. DOI PubMed
182. Zhu L, Wang H, Bai J, Liu J, Zhang Y. A porous graphene composite membrane intercalated by halloysite nanotubes for efficient dye desalination. *Desalination* 2017;420:145-57. DOI
183. Chen L, Moon J, Ma X, et al. High performance graphene oxide nanofiltration membrane prepared by electrospraying for wastewater purification. *Carbon* 2018;130:487-94. DOI
184. Zhang S, Liao S, Qi F, et al. Direct deposition of two-dimensional MXene nanosheets on commercially available filter for fast and efficient dye removal. *J Hazard Mater* 2020;384:121367. DOI
185. Han R, Wu P. High-performance graphene oxide nanofiltration membrane with continuous nanochannels prepared by the *in situ* oxidation of MXene. *J Mater Chem A* 2019;7:6475-81. DOI
186. Kang KM, Kim DW, Ren CE, et al. Selective molecular separation on Ti₃C₂T_x-graphene oxide membranes during pressure-driven filtration: comparison with graphene oxide and MXenes. *ACS Appl Mater Inter* 2017;9:44687-94. DOI
187. Liu T, Liu X, Graham N, Yu W, Sun K. Two-dimensional MXene incorporated graphene oxide composite membrane with enhanced water purification performance. *J Membr Sci* 2020;593:117431. DOI
188. Wei S, Xie Y, Xing Y, et al. Two-dimensional graphene Oxide/MXene composite lamellar membranes for efficient solvent permeation and molecular separation. *J Membr Sci* 2019;582:414-22. DOI
189. Pandey RP, Rasheed PA, Gomez T, Azam RS, Mahmoud KA. A fouling-resistant mixed-matrix nanofiltration membrane based on covalently cross-linked Ti₃C₂T_x (MXene)/cellulose acetate. *J Membr Sci* 2020;607:118139. DOI
190. Pandey RP, Rasool K, Madhavan VE, Aïssa B, Gogotsi Y, Mahmoud KA. Ultrahigh-flux and fouling-resistant membranes based on layered silver/MXene (Ti₃C₂T_x) nanosheets. *J Mater Chem A* 2018;6:3522-33. DOI
191. Lee W, Bondaz L, Huang S, He G, Dakhchoune M, Agrawal KV. Centimeter-scale gas-sieving nanoporous single-layer graphene membrane. *J Membr Sci* 2021;618:118745. DOI
192. Ashirov T, Siena JS, Zhang M, Ozgur Yazaydin A, Antonietti M, Coskun A. Fast light-switchable polymeric carbon nitride membranes for tunable gas separation. *Nat Commun* 2022;13:7299. DOI PubMed PMC
193. Ma C, Gao G, Liu H, Liu Y, Zhang X. Fabrication of 2D bimetallic metal-organic framework ultrathin membranes by vapor phase transformation of hydroxy double salts. *J Membr Sci* 2022;644:120167. DOI
194. Wang P, Peng Y, Zhu C, et al. Single-phase covalent organic framework staggered stacking nanosheet membrane for CO₂-selective separation. *Angew Chem Int Ed* 2021;60:19047-52. DOI
195. Dou H, Jiang B, Xu M, et al. Boron nitride membranes with a distinct nanoconfinement effect for efficient ethylene/ethane separation. *Angew Chem Int Ed* 2019;131:14107-13. DOI
196. Zhou F, Dong Q, Chen J, et al. Printed graphene oxide-based membranes for gas separation and carbon capture. *Chem Eng J* 2022;430:132942. DOI
197. Sheng F, Wu B, Li X, et al. Efficient ion sieving in covalent organic framework membranes with sub-2-nanometer channels. *Adv Mater* 2021;33:e2104404. DOI

198. Niu B, Xin W, Qian Y, Kong XY, Jiang L, Wen L. Covalent organic frameworks embedded in polystyrene membranes for ion sieving. *Chem Commun* 2022;58:5403-6. [DOI](#) [PubMed](#)
199. Wang Z, Huang L, Dong X, et al. Ion sieving in graphene oxide membrane enables efficient actinides/lanthanides separation. *Nat Commun* 2023;14:261. [DOI](#) [PubMed](#) [PMC](#)
200. He M, Liu Z, Wang L, et al. Carboxymethylcellulose (CMC)/glutaraldehyde (GA)-modified $Ti_3C_2T_x$ membrane and its efficient ion sieving performance. *J Membr Sci* 2023;675:121541. [DOI](#)
201. Leong ZY, Han Z, Wang G, Li D, Yang SA, Yang HY. Electric field modulated ion-sieving effects of graphene oxide membranes. *J Mater Chem A* 2021;9:244-53. [DOI](#)
202. Cao H, Xia Y, Lu Y, et al. MOF-801 polycrystalline membrane with sub-10 nm polymeric assembly layer for ion sieving and flow battery storage. *AIChE J* 2022;68:e17657. [DOI](#)
203. Bing S, Xian W, Chen S, et al. Bio-inspired construction of ion conductive pathway in covalent organic framework membranes for efficient lithium extraction. *Matter* 2021;4:2027-38. [DOI](#)
204. Su S, Zhang Y, Peng S, et al. Multifunctional graphene heterogeneous nanochannel with voltage-tunable ion selectivity. *Nat Commun* 2022;13:4894. [DOI](#) [PubMed](#) [PMC](#)
205. Liang S, Wang S, Chen L, Fang H. Controlling interlayer spacings of graphene oxide membranes with cationic for precise sieving of mono-/multi-valent ions. *Sep Purif Technol* 2020;241:116738. [DOI](#)

Review

Open Access



Synthesis strategies of metal-organic frameworks for CO₂ capture

Meng Sun, Xiaokang Wang^{ID}, Fei Gao, Mingming Xu, Weidong Fan, Ben Xu, Daofeng Sun

State Key Laboratory of Heavy Oil Processing, School of Materials Science and Engineering, China University of Petroleum (East China), Qingdao 266580, Shandong, China.

Correspondence to: Prof. Weidong Fan, School of Materials Science and Engineering, China University of Petroleum (East China), Qingdao 266580, Shandong, China. E-mail: wdfan@upc.edu.cn; Prof. Ben Xu, School of Materials Science and Engineering, China University of Petroleum (East China), Qingdao 266580, Shandong, China. E-mail: benxu@upc.edu.cn

How to cite this article: Sun M, Wang X, Gao F, Xu M, Fan W, Xu B, Sun D. Synthesis strategies of metal-organic frameworks for CO₂ capture. *Microstructures* 2023;3:2023032. <https://dx.doi.org/10.20517/microstructures.2023.32>

Received: 13 Jun 2023 **First Decision:** 7 Jul 2023 **Revised:** 19 Jul 2023 **Accepted:** 31 Jul 2023 **Published:** 10 Aug 2023

Academic Editor: Zhanxi Fan **Copy Editor:** Fangyuan Liu **Production Editor:** Fangyuan Liu

Abstract

The high consumption of fossil energy has led to increasing concentrations of carbon dioxide (CO₂) in the atmosphere, making carbon capture and separation a research hotspot in this century. As novel porous materials, metal-organic frameworks (MOFs) are widely used for CO₂ capture due to their unique structures and tunable properties. Currently, several relatively mature strategies have been applied to synthesize MOFs for CO₂ capture. Herein, we investigate strategies for tuning the pore windows, pore sizes, open metal sites, and post-synthesis or pre-synthesis modifications of MOFs from the perspective of CO₂ capture performance. Furthermore, we summarize the relevant CO₂ capture technologies and research advances and describe the application of different strategies in the synthesis of CO₂ capture-oriented MOFs.

Keywords: Metal-organic frameworks, carbon capture and separation, CO₂ capture strategy

INTRODUCTION

Since the Industrial Revolution, the extraction and consumption of fossil fuels have caused a remarkable expansion of greenhouse gases in the atmosphere. The Earth's climate is undergoing major changes characterized by global warming, according to numerous authoritative studies^[1-4]. Compared to other greenhouse gases, carbon dioxide (CO₂) has a weaker greenhouse effect, but it has the highest proportion in



© The Author(s) 2023. **Open Access** This article is licensed under a Creative Commons Attribution 4.0 International License (<https://creativecommons.org/licenses/by/4.0/>), which permits unrestricted use, sharing, adaptation, distribution and reproduction in any medium or format, for any purpose, even commercially, as long as you give appropriate credit to the original author(s) and the source, provide a link to the Creative Commons license, and indicate if changes were made.



the atmosphere, with its warming effect accounting for about 60% of the total warming effect among all greenhouse gases^[5,6]. Therefore, it is urgent to work out an environment-friendly CO₂ capture technology to alleviate the greenhouse effect^[7,8].

In recent years, the development of carbon capture and separation (CCS) technology has attracted social attention. Adsorbents that can be used for CO₂ capture include activated carbon, zeolite, alumina, metal oxides (CaO, MgO, K₂O, Li₂O), metal-organic frameworks (MOFs), and other surface-modified porous media^[9-12]. Compared to traditional inorganic porous materials, MOFs have many advantages and show great application potential in CO₂ adsorption and sequestration. One is the modifiability of its secondary building units (SBUs) and organic ligands. Through the modification of inorganic/organic nodes on functionality groups, the fine-tuning of the pore size and channel environment in MOFs can be precisely achieved, and then MOFs oriented to CO₂ capture can be synthesized^[13-15]. On the other hand, due to their high density of active sites, high stability, and rich topological structures, MOFs have distinct advantages, such as mild reaction conditions and easy adsorption and sequestration of CO₂^[16-18].

A large number of relevant papers and reviews have been published^[19,20]. In contrast to the published reviews, this paper presents the current CO₂ capture technology and related adsorbents. Then, the parameters for evaluating the performance of CO₂ capture adsorbents are presented to achieve the best capture capacity and reduce costs and energy expenditure. In addition, recent advances in MOF-based CO₂ capture methods and ways to improve the capture performance of the materials are explored. The strategies and methods described in this review will not only provide new propositions for the construction of CO₂-oriented capture MOFs but also contribute to the mitigation of industrial consumption to achieve carbon neutrality and thus slow down the process of global warming.

CO₂ CAPTURE

In September 2020, the “Address at the General Debate of the 75th Session of the United Nations General Assembly” and the “Address at the United Nations Biodiversity Summit” proposed that China should aim to achieve CO₂ peak emissions by 2030 and carbon neutrality by 2060. In addition, many countries around the world have enacted policies or legislation to advance the goal of carbon neutrality. So far, 29 countries and regions have pledged to be carbon neutral^[21]. The prevailing view is that CCS may be the cheapest technology to reduce emissions in the long term and will gain time to develop new technologies such as alternative energy sources^[22,23].

CO₂ capture technology

CCS technology refers to the separation of CO₂ from industrial and energy-related production activities and its long-term sequestration in natural underground reservoirs in order to reduce CO₂ emissions to the atmosphere^[24,25]. There are three main components to CCS technology: (1) CO₂ capture from fixed carbon sources (e.g., power plants); (2) CO₂ compression and transport; and (3) CO₂ storage.

In terms of the capture process, there are three main types of CO₂ capture technologies: pre-combustion capture, post-combustion capture, and oxy-fuel combustion^[26] [Figure 1]. Pre-combustion capture uses new gasification technology to convert fossil fuels into H₂ and CO₂, which are then captured before combustion. Compared with direct coal combustion, this technology has higher fossil fuel utilization, less waste disposal, and less water consumption. In addition, due to high CO₂/H₂ gas pressure and CO₂ concentration, the energy consumption of pre-combustion CO₂ capture is only 10%-16% of the total energy consumption, which is about half of the energy consumption of post-combustion capture. However, the high energy consumption of the fuel conversion step limits its further development^[27-29]. Oxy-fuel combustion is based

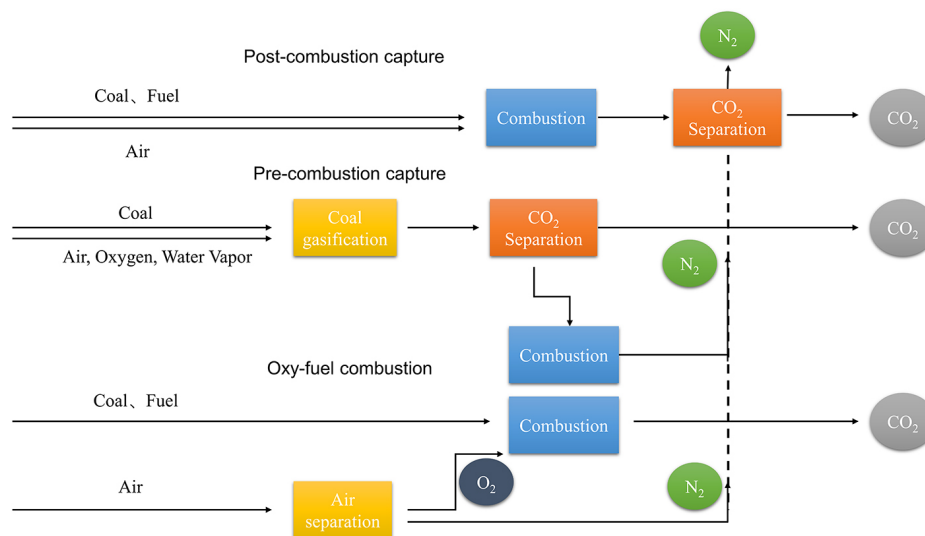


Figure 1. Three basic routes (post-combustion capture, pre-combustion capture, and oxy-fuel combustion) of CO₂ capture in industry.

on burning fossil fuels in oxygen-rich gases to obtain high concentrations of CO₂, which is direct sequestration and utilization. Due to the removal of N₂ in the air, the volume of combustion gas is reduced, so the volume of flue gas produced after combustion is reduced to 1/5-1/3 of that of conventional coal-fired boilers. Meanwhile, the concentration of CO₂ in the flue gas is high, making the cost of capturing CO₂ lower. However, this technology is not ideal for CO₂ capture due to its high energy consumption and investment costs^[30,31]. Post-combustion capture means capturing CO₂ in the flue gas from the combustion emissions. Since the partial pressure of CO₂ after capture is low, it is necessary to pressurize the CO₂ before storage, which increases the operating cost. Even so, post-combustion capture has the following advantages over other capture techniques: (1) A wide range of applications. Post-combustion capture technology can not only separate CO₂ from flue gas but also capture NO_x and SO_x to achieve the purpose of denitrification and desulfurization; (2) Strong applicability. The trapping device is installed in the flue gas tail of the power plant, which has no influence on the existing power generation equipment and; (3) Relatively mature development and flexible operation^[32-34]. Therefore, post-combustion capture is a common CO₂ capture technology.

In addition, CO₂ capture technology can be classified based on different capture methods, including chemical absorption^[35], membrane separation^[36-38], biological immobilization^[39], adsorption^[40-43], and other approaches. Among them, the adsorption method is the most competitive CO₂ capture technique.

CO₂ capture adsorbent

Adsorption is the uptake of molecules or ions from the surrounding liquid or gas by the surface of a solid substance. The adsorption method has been widely studied by scholars for its advantages of low cost and simple operation^[44]. However, its practical application requires the design and synthesis of an easily regenerated and durable adsorbent material. Generally speaking, a suitable CO₂ adsorbent needs to have high selectivity and adsorption capacity, adequate adsorption/desorption kinetics, stability after several adsorption/desorption cycles, and good chemical and mechanical stability.

Among many CO₂ adsorbents, porous solid adsorbents have good application prospects because of their low adsorption enthalpy and easy recycling. The traditional porous adsorbents for CO₂ capture mainly include activated carbon, zeolite, silica gel, activated alumina, and so on^[45-48]. Zeolite, a common solid adsorbent, is a

porous silica-aluminate material with a pore size between 5 Å and 12 Å^[49-51]. Among them, zeolite 13X is the most widely studied adsorbent, with a specific surface area of 726 m² g⁻¹, a pore volume of 0.25 cm³ g⁻¹, and a CO₂ adsorption capacity of 16.4 wt% (0.8 bar) at room temperature, which can be used as a benchmark for solid adsorbents^[52,53].

Another class of solid adsorbents is carbon-based adsorbents, including activated carbon, carbon molecular sieves, and carbon nanotubes, which have been used for different forms of CO₂ separation. The common activated carbon has an inorganic porous structure, high surface area, and high CO₂ adsorption capacity, and it can be generated through resin and other pyrolysis processes, which is a low-cost and highly available adsorbent^[54,55]. Even in an environment with water vapor, activated carbon can maintain its structure without being destroyed and has high adsorption stability. However, activated carbon has lower CO₂ adsorption capacity at low pressures and poor adsorption selectivity for different gases due to the absence of an electric field generated by cations on the activated carbon surface. To sum up, these traditional adsorption technologies and adsorbents need to be further improved to enhance their ability of CO₂ capture and separation.

MOFs are the most representative new porous materials and promising adsorbents, which have attracted extensive attention in gas separation applications^[56,57]. As a porous adsorbent with a framework structure formed by organic ligands bridging metal ion nodes, the MOF has a very high surface area, ultra-high porosity, flexibility of the porous structure, and diversity of surface functional groups due to the presence of organic ligands and is easy to be chemically modified. These advantages make MOFs exhibit great potential for CO₂ capture and storage^[58-60].

CO₂ capture performance parameters

Compared with other solid materials, the greatest advantage of MOFs lies in their ability to precisely fine-tune their pore size through the modulation of ligand size. At the same time, the pore environment can be modified by modifying the functional groups on the metal ions (clusters) or ligands to enhance the interaction force with the guest molecules, thus achieving the separation of different gas molecules^[61-64]. There have been several reviews on MOFs for gas separation applications, and they have made great progress in adsorptive separation applications in the past few years. However, there are still some limitations. To address the limitations of MOFs, a series of studies have been conducted in recent years on improving their adsorption and separation capacities, expanding new structures, novel functionalization pathways, and adopting hybrid systems and techniques^[65]. In addition, studies exploring the adsorption mechanism of MOFs and the improvement of their adsorption capacity in moist environments have gradually become the focus of attention^[14,66]. An adsorbent suitable for capturing CO₂ from flue gas should consider the following performance parameters.

The adsorption capacity of CO₂

This is a key criterion for evaluating the performance of solid sorbents and represents the quantity of sorbent required for a given load, as well as the adsorbent bed size, which is deemed to be a key factor in determining the energy requirement in the regeneration step. In addition, the amount of CO₂ adsorbed is related to its partial pressure in the gas phase. The specific adsorption of CO₂ indicates the ability of the MOF material to adsorb CO₂.

The selectivity of CO₂

It represents the adsorption ratio of the adsorbent for CO₂ to other gases (usually used for post-combustion capture and natural gas upgrading). The sorption selectivity of a gas mixture for CO₂ can be estimated

quantitatively by means of a single-component gas sorption isotherm or ideal adsorption solution theory (IAST). The CO₂ selectivity of materials is primarily due to the following aspects (the relevant parameters are shown in Table 1): (1) Selectivity based on pore size screening (molecular sieve effect). Due to the different kinetic diameters of gas molecules of each component in the gas mixture, CO₂ can be effectively separated from the gas mixture by precisely adjusting the pore size of the material; (2) Selectivity based on adsorption (thermodynamic separation), i.e., separation based on the interaction forces between different gas molecules and the material surface and; (3) Selectivity based on diffusion effects, i.e., to separate the gas mixture according to the different diffusion rates of different gases in the material^[5,67].

The adsorption enthalpy of CO₂

Adsorption enthalpy is another key parameter for evaluating the performance of the storage of CO₂ by physical adsorption. It represents the strength of the interaction between the adsorbent and the adsorbate molecules. Moreover, it is an indicator of the energy required to regenerate a solid adsorbent, and the magnitude of the adsorption enthalpy clearly affects the cost of the adsorbent regeneration process. If the adsorption enthalpy is too high, the material binds CO₂ too strongly, requiring a large amount of energy to break the framework-CO₂ interaction, thereby increasing the regeneration cost. Conversely, very low adsorption enthalpy is undesirable. While regeneration costs will be lower, the captured CO₂ will be less pure, resulting in lower adsorption selectivity and a larger adsorption bed size^[68-70]. Typically, the adsorption enthalpy of MOFs is in the range of 20-50 kJ mol⁻¹, which is comparable to other physical adsorbents (such as zeolites). Table 2 shown some MOF-based sorbents with their CO₂ uptake capacity and Q_{st}.

The experimental adsorption enthalpy (Q_{st}) was applied to assess the strength of the bond between the adsorbent and the adsorbate and was defined as:

$$Q_{st} = RT^2 \left(\frac{\partial \ln p}{\partial T} \right)$$

The adsorption enthalpy, Q_{st}, is determined using the pure component isotherm fits using the Clausius-Capeyron equation, where T(K) is the temperature, p(kPa) is the pressure, and R is the gas constant.

The stability of the CO₂ adsorbent

In order to reduce operating costs and operational difficulties, solid adsorbents must be able to be used in a wide range of industrial environments and show good stability under fume conditions, under adsorption operating conditions, and during multi-cycle adsorption regeneration. Particular attention must be paid to the stability of the adsorbent in the presence of water vapor. In addition, chemical and mechanical stability are equally important^[71].

The adsorption/desorption kinetics of CO₂

Sorption-regeneration cycle times are largely dependent on the kinetic properties of the CO₂ adsorption-desorption curves measured in breakthrough experiments. The ability to effectively reduce the cycle time and the amount of adsorbent, thereby lowering the cost of CO₂ separation, is the first parameter to be considered in selecting the CO₂ adsorbent. Adsorbents that adsorb and desorb CO₂ in a relatively short period of time become the preferred choice.

The cost of adsorbent material

This is an essential ingredient in choosing an adsorbent material. Owing to the high preparation cost, many adsorbents with excellent adsorption properties are not successfully used in industry. Therefore, the preparation of materials with good adsorption properties at low cost is considered to be the main goal of researchers in the field of CO₂ capture.

Table 1. Physical properties of common gas molecules coexisting with CO₂

Gas molecules	Dynamic diameter (Å)	Size (Å)	Boiling point (K)	Polarity (10 ⁻²⁵ cm ³)
N ₂	3.64	-	77.35	15.3
H ₂	2.89	-	20.38	-
H ₂ O	2.65	-	373	14.8
CO ₂	3.3	3.18 × 3.33 × 5.36	194.75	29.11
C ₂ H ₂	3.3	3.32 × 3.34 × 5.70	188.4	33.3-39.3
CH ₄	3.76	3.83 × 3.94 × 4.10	111.6	25.93

Table 2. MOF-based sorbent and related CO₂ uptake capacity at 298 K

Materials	BET surface area (m ² /g)	Pressure (bar)	Capacity (mmol g ⁻¹)	Q _{st} (kJ mol ⁻¹)	Ref.
Fe-dbai	1,280	1	6.4	23.5	[100]
Cu(adci)-2	805	0.15	2.01	27.5	[110]
NKU-521	1,100	1	6.21	41	[119]
MUF-16(Mn)	214	1	2.31	37	[113]
MUF-16(Ni)	204	1	2.25	32	[113]
ZnDatzBdc	303	1	2.05	-	[125]
NJU-Bai52	1,908	0.0004	0.013	18.1	[128]
NJU-Bai53	1,844	0.0004	0.64	17.5	[128]

Based on the above elaboration of CO₂ capture performance parameters, the quantitative assessment of the CO₂ capture capacity of adsorbents mainly refers to the following data: (1) The adsorption capacity of CO₂ at 15 kPa is greater than 50 STP cm³ g⁻¹; (2) IAST selectivity (CO₂/N₂ = 15/85) is greater than 500; (3) Good thermal stability, the structure will not collapse before the temperature is higher than 300 °C; (4) Good chemical stability, the structure remains stable in most organic solvents; (5) Q_{st} < 40 kJ mol⁻¹.

Research progress of MOFs for CO₂ capture

As novel porous materials, MOFs were initially proposed by Prof. Omar M. Yaghi and have been extensively researched by scientists^[72-77]. They are formed from inorganic metal ions or clusters and organic ligands that are connected through coordination bonds with varying degrees of connectivity. In contrast to conventional inorganic porous materials, such as porous silicates and molecular sieves, MOFs possess a remarkably adaptable structure. Different structures and characteristics of MOFs are built by choosing metal nodes with varying activities and a diverse range of organic ligands^[78-80]. Furthermore, they enable specific function-oriented compositions. By utilizing various trapping mechanisms, including molecular sieve separation, host-guest interaction, and kinetic diffusion, MOFs with distinct pore sizes ranging from micropore to mesopore can be conveniently synthesized by modifying the length of ligands or functionalizing inorganic nodes and ligands, resulting in MOFs with unique properties. As novel crystalline porous materials, MOFs possess significantly higher specific surface area and porosity compared to other porous materials (with a specific surface area of up to 10,000 m² g⁻¹ and porosity of 90%), providing substantial scope for the development in gas storage^[81,82], adsorption and separation^[83], catalysis^[84], sensor^[85], and other areas.

The ability of MOFs to capture CO₂ from varying gas mixtures depends on their inherent properties and the attributes of the gas mixtures. Over the past two decades, diverse topological structures and function-oriented MOFs have been synthesized, leading to the formation of various branches of materials, including iso-reticular MOFs (IRMOFs), zeolitic imidazolate frameworks (ZIFs), materials of institute Lavoisier frameworks (MILs), and porous coordination networks (PCNs), *etc.*^[86-89]. Different branches possess specific characteristics to cater to distinct applications. Currently, several relatively mature strategies [Figure 2] have been applied to synthesize CO₂ capture-oriented MOFs^[90-92].

Functionalized modification strategy

The -NH₂ functional group is widely utilized in various adsorbent materials due to its strong attraction of CO₂ to the amine group, which gives the amine molecule higher adsorption and selectivity for CO₂. Moreover, numerous polar functional groups, including halogen atoms, hydroxyl, carboxyl, cyano, and nitro, have been demonstrated to influence the adsorption ability of CO₂ in MOFs^[93-95].

Diamine-functionalized MOFs in the form of diamine-Mg₂(dobpdc) (dobpdc⁴⁻ = 4,4'-dioxidobiphenyl-3,3'-dicarboxylate) offer the most potential for carbon capture applications due to their adjustable, stair-like profiles for CO₂ adsorption. In view of this, Dinakar *et al.* reported that MOFs containing dmen-Mg₂(dobpdc) (dobpdc = 1,2-diamino-2-methylpropane) composition [Figure 3] can capture CO₂ from coal-fired flue gas at moderate pressure^[96]. Further, using Mg₂(pc-dobpdc) (pc-dobpdc = 3,3'-dioxobiphenyl-4,4'-dicarboxylate) with higher structural symmetry to avoid sub-stability during CO₂ adsorption, dmen-Mg₂(pc-dobpdc) demonstrates carbon capture capabilities under similar conditions in a simulated coal-fired power plant, achieving a complete CO₂ adsorption effect.

It has been shown that some specific sites of MOFs can effectively capture CO₂, including unsaturated metal sites (UMSs) and Lewis base sites (LBSs), such as amines, pyridines, sulfones, and amides. UMSs are capable of establishing potent electrostatic interactions with CO₂ and have a high CO₂ capture capacity. However, the ubiquitous water molecules tend to coordinate with UMSs in a competitive manner, resulting in a significant reduction in the ability of CO₂ adsorption. Regarding LBSs, compared with -NH₂, the amide functional group exhibits a robust attraction towards CO₂ due to the existence of two binding sites, carbonyl (CO-) and amine (NH-), leading to superior CO₂ adsorption and selectivity^[97-99]. In addition, MOFs modified by amide functional groups tend to be more stable.

Fe-dbai (dbai = 5-(3,5-Dicarboxybenzoylamino) isophthalic acid) combines two specific functional sites, UMSs and amide functional groups. Its CO₂ adsorption capacity is measured at 6.4 mmol g⁻¹, while its CO₂/N₂ selectivity is 64 (298 K, 1 bar), surpassing multiple other reported MOFs^[100]. Importantly, in the breakthrough experiments, the CO₂ adsorption capacity of Fe-dbai at 60% RH (Relative Humidity: the percentage of water vapor pressure in air to the saturated water vapor pressure at the same temperature) was able to maintain 94% of its capacity under dry conditions. Molecular simulation results showed that the amide CO-group, with its electronegative properties, exhibits a strong affinity towards CO₂ and enhances the interaction between Fe-UMS and CO₂ [Figure 4]. The outstanding CO₂ capture efficiency of Fe-dbai suggests its potential suitability for real-world implementation of CO₂ capture.

Amino acid (AA)-modified MOFs also show great potential for CO₂ capture applications. Modification of MOF-808 with 11 different AAs resulted in a series of MOF-808-AA structures [Figure 5]. Under fume conditions, MOF-808 functionalized with glycine and DL-lysine (MOF-808-Gly and MOF-808-DL-Lys) was observed to exhibit the greatest CO₂ adsorption capacity. The increased CO₂ capture efficiency in the presence of water was detected and analyzed by single-component adsorption isotherms, CO₂/H₂O

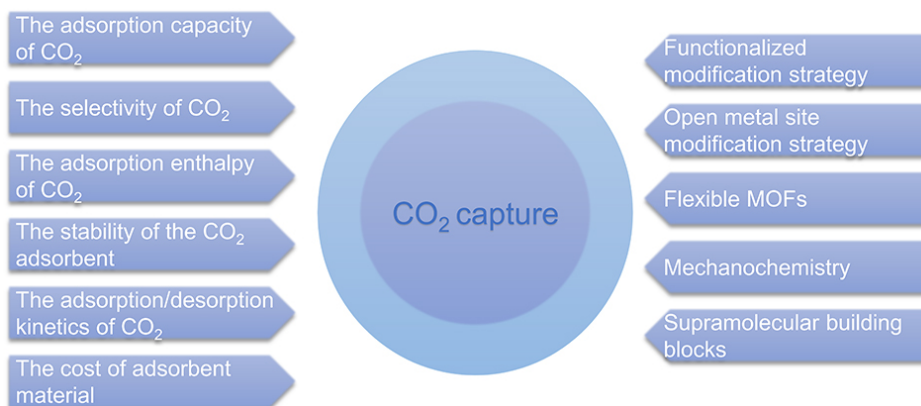


Figure 2. Schematic representation of MOF performance parameters and state-of-the-art CO₂ capture strategies.

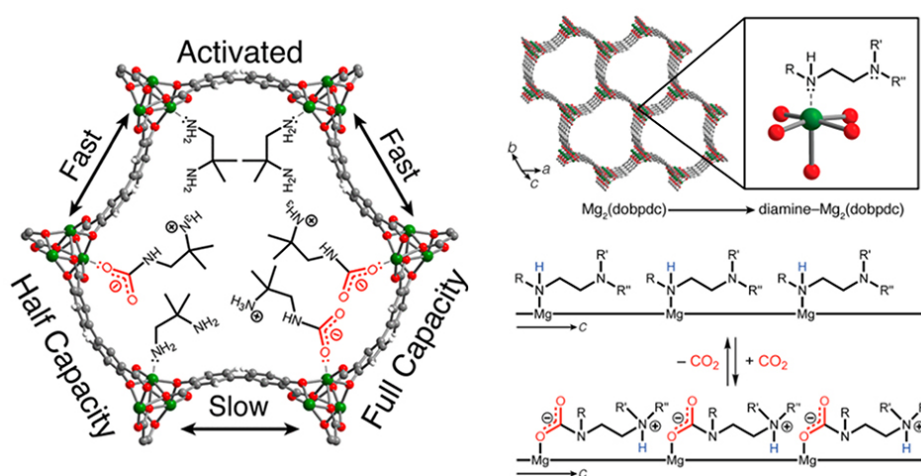


Figure 3. Depiction of the formation of ammonium carbamate chains in diamine-Mg₂(dobpdc) upon cooperative CO₂ adsorption. Reproduced with permission from Dinakar et al.^[96]. Copyright 2021 American Chemical Society.

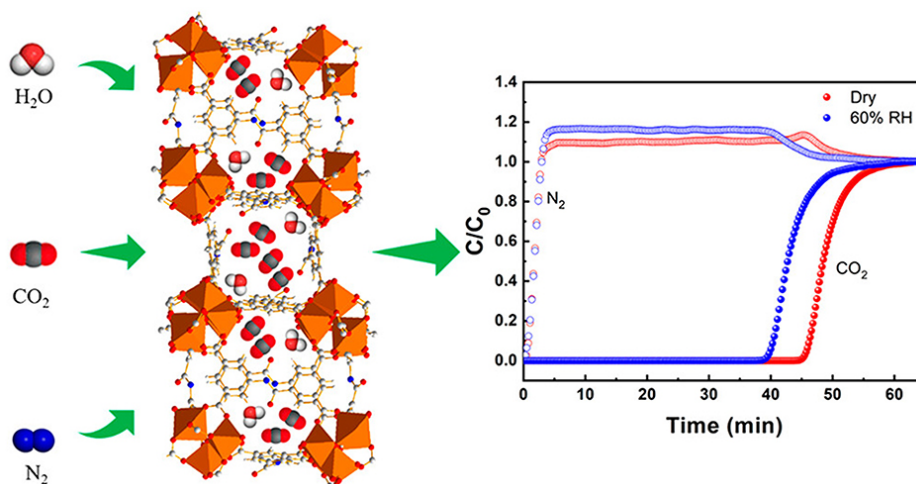


Figure 4. Adsorption behavior and experimental column breakthrough curves of Fe-dbai. Reproduced with permission from Tu et al.^[100]. Copyright 2023 American Chemical Society.

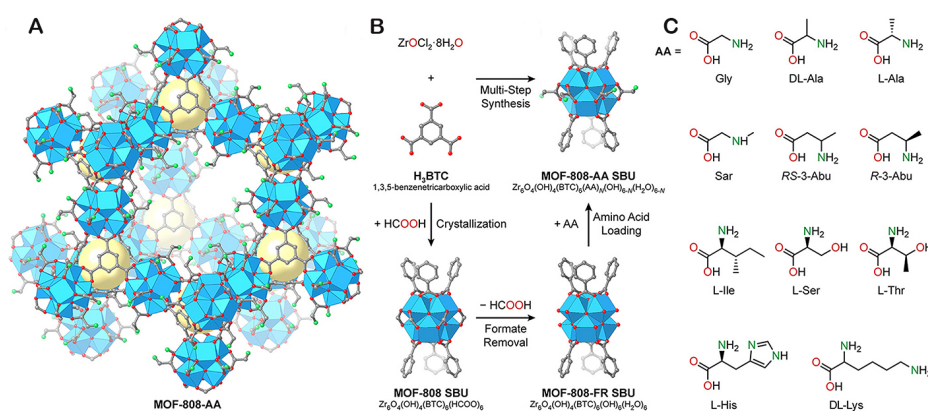


Figure 5. Structure of MOF-808-AA and structural schemes of the coordinatively loaded amino acids. Reproduced with permission from Lyu *et al.*^[101]. Copyright 2022 American Chemical Society.

dichotomy isotherms, and dynamic breakthrough measurements. This study enhances our comprehension of CO₂ capture in MOFs by uncovering the mechanism in which amine groups, firmly attached to the MOF structure, generate molecules within the pores that facilitate the adsorption and desorption of CO₂ at relatively low temperatures without requiring any heating^[101].

Among physisorption materials, anion-functionalized MOFs are novel porous materials composed of metal moieties, organic linkers, and inorganic anions^[102,103]. In recent years, anionic-functionalized MOFs have gradually made their presence felt in the field of CO₂ capture. The reticular design approach can effectively regulate the pore chemistry of anionic-functionalized MOFs by utilizing molecular building units. As previously reported by Bhatt *et al.*, NbOFFIVE-1-Ni and SIFSIX-3-Cu exhibit CO₂ adsorption capacities of 1.3 and 1.2 mmol g⁻¹ at a low concentration of 400 ppm and 298 K, respectively^[104]. Their study also shows that reducing the pore size of the porous adsorbent facilitates enhanced interaction between the CO₂ molecules and the main framework, resulting in high CO₂ uptake at lower pressures.

ZU-16-Co is an anion-functionalized MOF with fine-tuned pore chemistry featuring one-dimensional (1D) pores modified by enriched F atoms that can effectively trap CO₂ at concentrations of 400-10,000 ppm. Highly organized Lewis basic sites of anions limited to the ultramicroporous pores substantially enhance the ability to bind CO₂ [Figure 6]. This work clarifies the structure-function relationship of ZU-16-Co in capturing CO₂ and demonstrates its suitability for decarbonization at low concentrations^[105].

Two polar sulfonated oxygen-rich 3D MOFs, {[Zn₂(TPOM)(3,7-DBTDC)₂]·7H₂O·DMA}_n (1) and {[Cd₂(TPOM)(3,7-DBTDC)₂]·6H₂O·3DMF}_n (2) (TPOM = tetrakis(4-pyridyloxymethylene)-methane), were synthesized by a solvothermal approach by Chakraborty *et al.*^[106]. Structural diversity was achieved by changing the metal centers. Due to the strong quadrupole interaction between the sulfone moiety and CO₂ molecules, the adsorption of CO₂ on 1 and 2 is highly selective over the adsorption of N₂ and CH₄^[106,107]. Furthermore, both frameworks exhibit high chemical and water stability and cyclic regeneration [Figure 7]. This work provides an effective route for the development of functionalized MOFs with high selectivity for CO₂ capture.

The pore windows and pore sizes of MOFs are made up of both organic and inorganic structural blocks. Therefore, the pore size of MOFs can be adjusted by changing the type of organic and inorganic structural blocks, allowing the pore structure of MOFs to vary considerably in size, which is one of the key reasons for

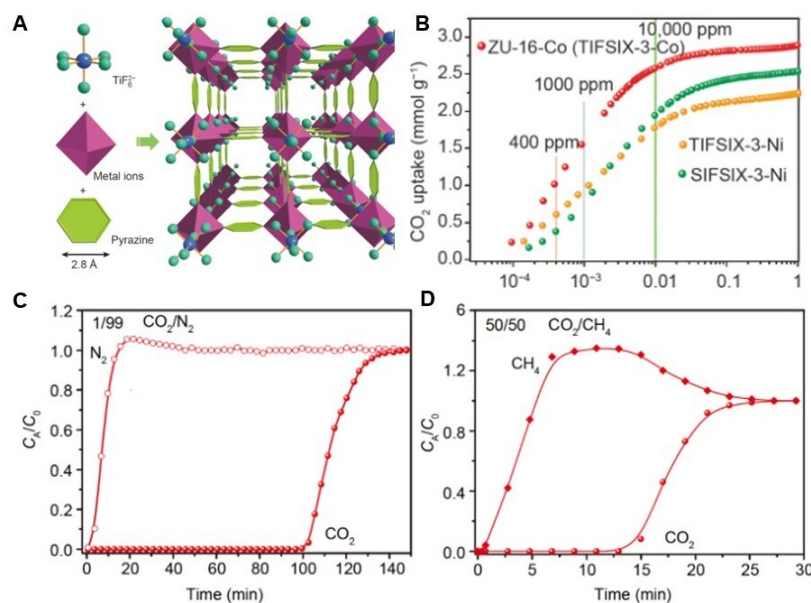


Figure 6. (A) Schematic representation of the construction and the pore structure of ZU-16 (TIFSIX-3) materials with pyrazine linker; (B) CO₂ adsorption isotherms on various anion-functionalized ultramicroporous materials at 298 K; (C and D) CO₂/N₂ (1/99, flow rate: 5 mL min⁻¹) and CO₂/CH₄ (50/50, flow rate: 4 mL min⁻¹) conducted on ZU-16-Co. Reproduced with permission from Zhang *et al.*^[105]. Copyright 2021 Science China Press and Springer-Verlag GmbH Germany, part of Springer Nature.

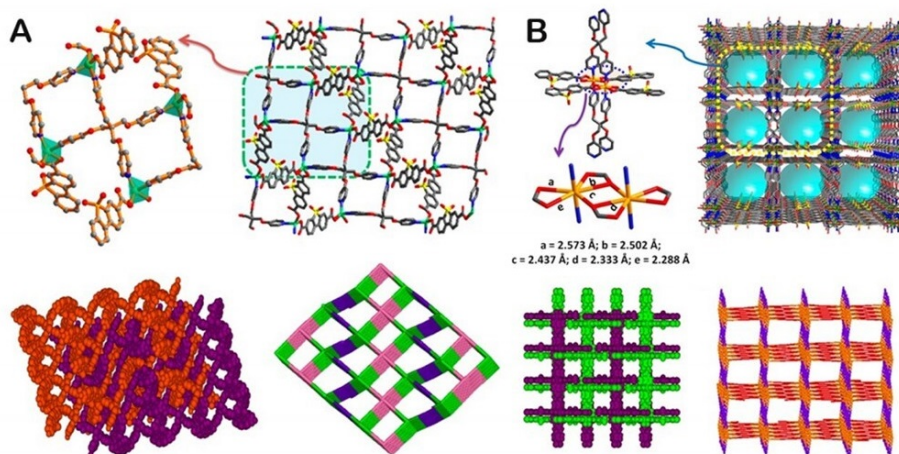


Figure 7. Single-crystal X-ray structure of 1 (A) and 2 (B). Reproduced with permission from Chakraborty *et al.*^[106]. Copyright 2020 American Chemical Society.

the wide variety of MOF materials currently available. Due to the wide range of pore sizes of MOFs, they show great potential for different kinds of gas capture applications^[108,109]. Selective adsorption of CO₂ can be achieved by using large linkers, short ligands, interpenetrating networks, and smaller metal molecules.

A novel copper-based ultramicroporous MOF, Cu(adci)-2 (adci = 2-amino-4,5-dicyanoimidazole), was proposed by Jo *et al.*^[110]. This MOF is a CO₂ capture-oriented physical adsorbent synthesized by two strategies: performing aromatic amine functionalization and introducing ultramicropores. The Cu(adci)-2 structure has one-dimensional square channels where all of the auxiliary ligands, particularly the NH₂ group

at the 2 position of the imidazole ring, are oriented in the identical direction in each channel so that pairs of NH₂ groups face away from each other along contrary sides of the channel walls. Cu(adci)-2 shows higher CO₂ adsorption capacity (2.01 mmol at 298 K and 15 kPa g⁻¹) but a lower adsorption enthalpy at zero coverage (27.5 kJ mol⁻¹). It showed good selectivity and easy regeneration under both dry and humid conditions [Figure 8].

CALF-20 consists of 1,2,4-triazole-bridged zinc(II) ion layers supported by oxalate ionic pillars forming a 3D lattice and a 3D pore structure [Figure 9]. The crystallographically unique zinc center is five-coordinate with a distorted triangular bipyramidal geometry. The competitive separation on CALF-20 shows not only preferential physisorption of CO₂ below 40% RH but also inhibition of water adsorption by CO₂, which is confirmed by computational modeling. Furthermore, CALF-20 facilitates industrial-scale CO₂ capture in a cost-effective and reliable manner^[111]. This shows that the reasonable addition of anionic column bracing can effectively inhibit water adsorption, which, in turn, makes the adsorbent exhibit an excellent CO₂ capture capacity.

Efficient and sustainable CO₂ capture can be achieved by porous physical adsorbents with high void fraction whose sizes and electrostatic potentials complementary to CO₂ molecules^[112]. Qazvini *et al.* proposed a strong, recoverable, and affordable adsorbent called MUF-16 [Figure 10]^[113]. MUF-16(Co), MUF-16(Ni), and MUF-16(Mn) were prepared by mixing 5-amino-*m-m*-phthalic acid (H₂aip), a cheap, commercially available ligand, with cobalt (II), nickel (II), or manganese (II) salts in methanol. Through static adsorption curves, IAST, and density functional theory calculations, it is determined that the one-dimensional channel of MUF-16 can capture CO₂ with high affinity while demonstrating weaker affinities for other competitive gases such as CH₄, C₂H₂, C₂H₄, C₂H₆, C₃H₆, and C₃H₈. Therefore, MUF-16 has high CO₂ adsorption selectivity. The selectivity of MUF-16 to CO₂/CH₄ and CO₂/C₂H₂ is measured at 6,690 and 510, respectively.

Open metal site modification strategy

Besides the functionalization of MOFs, metal sites have an important impact on enhancing the capacity and selectivity of CO₂ relative to other gases. UMSs are usually partially positively charged, and these sites show an affinity for larger quadrupole moments and greater polarizability for CO₂ compared to N₂. It is these open sites that lead to high CO₂ uptake. Furthermore, the difference in intensity between CO₂ and other gas molecules is the driving force for CO₂ capture^[114-116].

MIL-101 has two dissimilar mesopores and distinct metal sites in a single local pore. Shin *et al.* demonstrated by adsorption isotherm combined with in situ crystallographic analysis that substrate-adsorbate interactions influence the initial adsorption and pore coalescence steps^[117].

Unsaturated alkali metal sites have been reported to be anchored in MOFs by tetrazolium-based patterning to improve gas affinity^[118]. In NKU-521 (NKU denotes Nankai University), Li *et al.* effectively embedded K⁺ cations into the trinuclear Co²⁺-tetrazolium coordination pattern^[119]. The embedded K⁺ sites were exposed in the pores of NKU-521 by dehydration, and the Q_{st} of CO₂ increased to 41 kJ mol⁻¹. The K⁺ cations actually act as gas traps and increase the CO₂-framework affinity, as measured by the Q_{st} , by 24%. Furthermore, the effect of unsaturated alkali metal sites in MOFs on hydrocarbon separation was investigated. IAST calculations and breakthrough experiments showed that the exposed K⁺ sites greatly improved the CO₂ capture and separation performance of this MOF [Figure 11].

UMSs and adsorbent polarity play an important role in CO₂ adsorption. MIL-88 was selected as the prototyping framework to verify the above strategy^[120]. By introducing the C₃ symmetry of the second

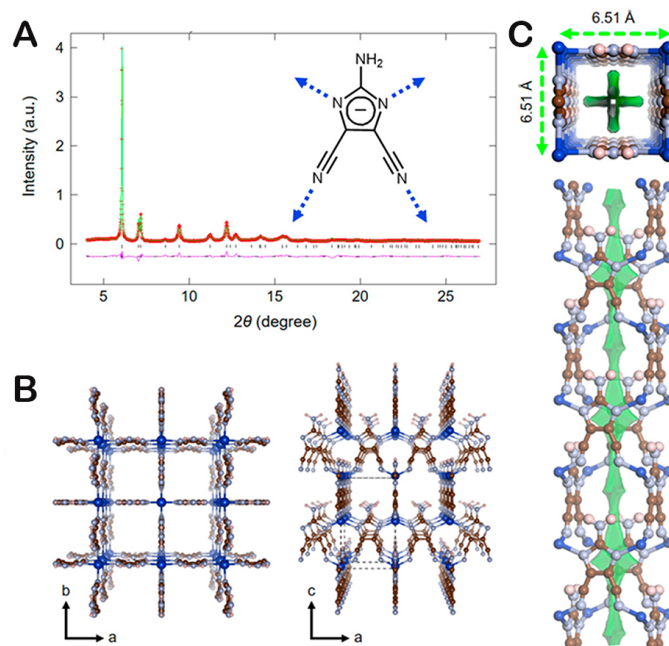


Figure 8. (A) Rietveld plot of desolvated Cu(adci)-2; (B) Perspective views of the refined structure of Cu(adci)-2 along the c (left) and b (right) axes; (C) Top and side views of a 1D channel of Cu(adci)-2. Reproduced with permission from Jo *et al.*^[110]. Copyright 2022 American Chemical Society.

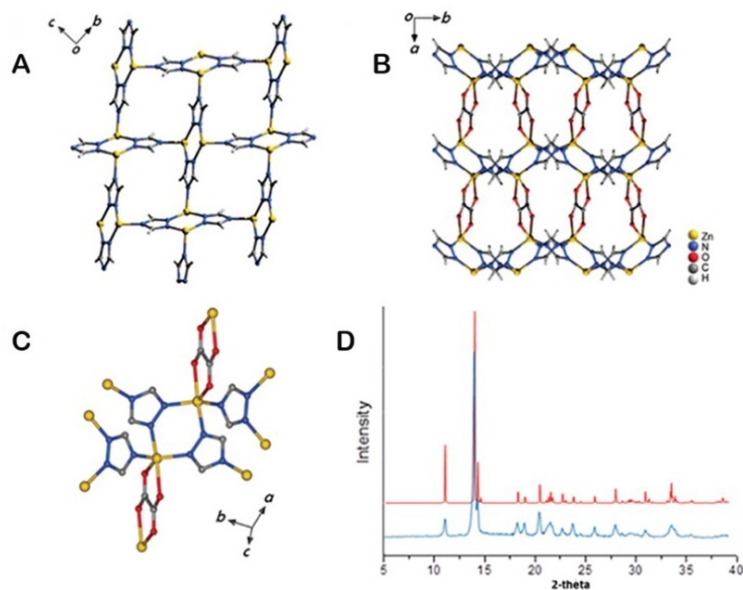


Figure 9. (A-C) Single-crystal structure of CALF-20; (D) Powder X-ray pattern simulated from the single-crystal structure (top) and obtained experimentally. Reproduced with permission from Lin *et al.*^[111]. Copyright 2021 American Association for the Advancement of Science.

ligand 2,4,6-tri(4-pyridyl)-1,3,5-triazine (tpt), the initial hexagonal 1D pore of the MIL-88 is split into numerous hexagonal cages of a certain length. As a direct result, MIL-88 loses metal vacancies and is replaced by split ligands. Moreover, the framework becomes more rigid, and there is no respiration effect

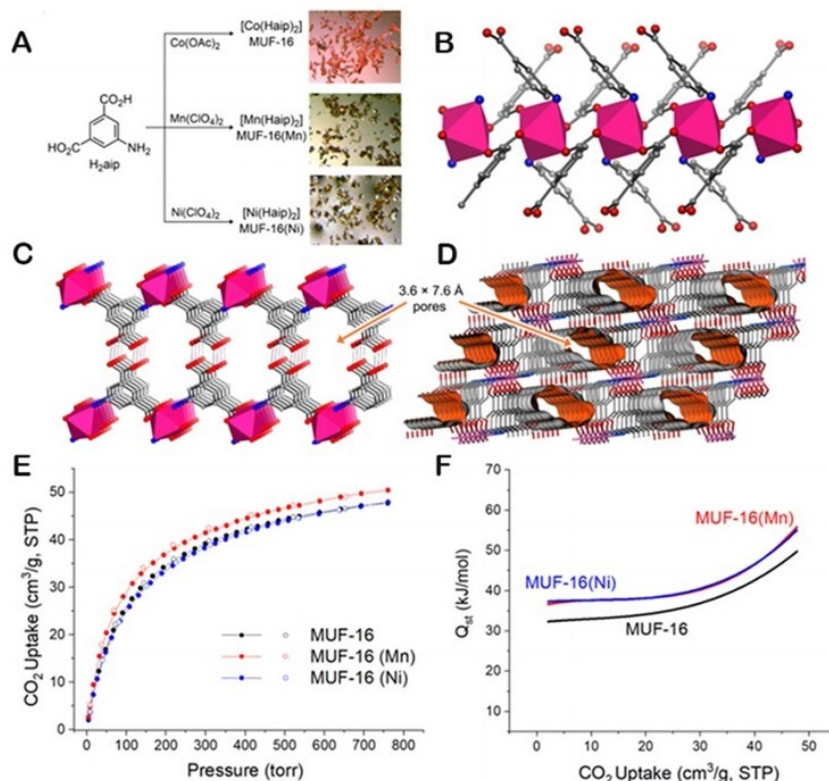


Figure 10. (A-D) Synthesis and structure of MUF-16 materials; (E) Volumetric adsorption (filled circles) and desorption (open circles) isotherms of CO₂ at 293 K and for MUF-16 (black), MUF-16(Mn) (red), and MUF-16(Ni) (blue); (F) Adsorption enthalpy (Q_{st}) calculated for CO₂ binding to MUF-16 (black), MUF-16(Mn) (red), and MUF-16(Ni) (blue) as a function of CO₂ uptake. Reproduced with permission from Qazvini et al.^[113]. Copyright 2021 Springer Nature.

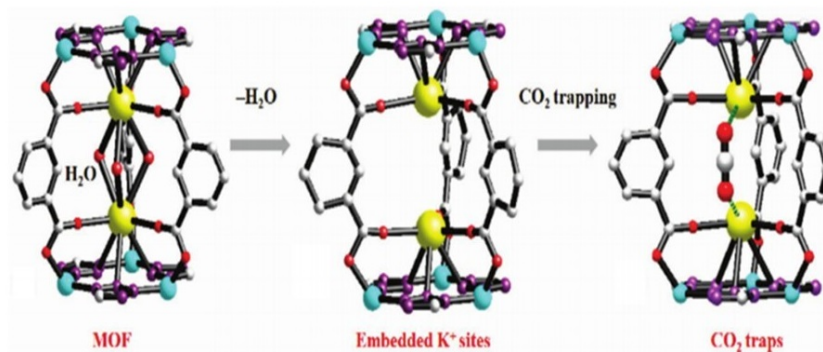


Figure 11. Structural change of the embedded K⁺ from H₂O coordinated state to the exposed state as CO₂ traps for the preferential binding of CO₂. Reproduced with permission from Li et al.^[119]. Copyright 2019 Wiley-VCH Verlag GmbH & Co. KGaA, Weinheim.

before and after gas adsorption. The introduction of the second ligand (tpt) not only provides more action sites but also enhances the interaction area between objects. In addition, the group also modifies the terephthalic acid that constitutes the framework, introduces -OH and -NH₂ groups, and increases the interaction sites between gas molecules and the framework. The CO₂ adsorption test shows that CPM-33b with tpt and -OH introduced has the highest CO₂ adsorption value compared to the existing MOFs without metal vacancies, which is comparable to the adsorption effect of MOF-74-Ni [Figure 12]. This study

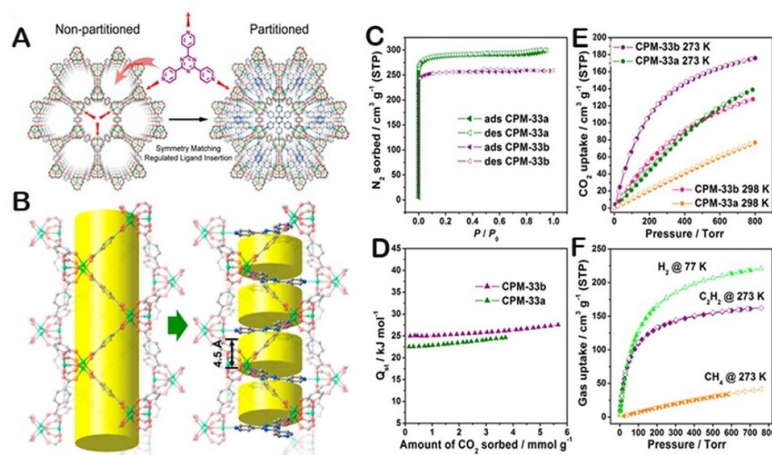


Figure 12. (A and B) Illustration of pore space partition through symmetry-matching regulated ligand insertion; (C-F) Gas sorption study on compounds CPM-33a and CPM-33b. Reproduced with permission from Zhao *et al.*^[120]. Copyright 2015 American Chemical Society.

provides a new idea for MOFs to improve gas adsorption performance and is expected to achieve greater breakthroughs in fuel molecule adsorption.

Other functionalization

In addition to these common CO₂ capture strategies, scientists have also explored other ways to efficiently capture CO₂. In a typical Langmuir-type isotherm, bulk CO₂ adsorbents cannot be regenerated during desorption because the adsorption gain decreases with increasing temperatures. Instead, adsorbents with S-shaped CO₂ isotherms are preferable. Some flexible MOFs can display such S-shaped CO₂ equivalent due to the structural switch from the CP (close-phase) state to the OP (open-phase) state^[121-123]. Furthermore, as an individual guest molecule has its own gate opening pressure, this difference allows for high selectivity in gas mixtures, i.e., the target molecule can open the gate while others cannot^[124]. Therefore, flexible MOFs with S-shaped isotherms can be used as potential carbon capture adsorbents with good operability and high selectivity for CO₂.

ZnDatzBdc (Datz = 3,5-diamine-1,2,4-triazolate, Bdc = 1,4-benzenedicarboxylate) is a flexible MOF for highly selective capture of CO₂ [Figure 13]. X-ray diffraction studies confirmed a convertible structure conversion between its OP and CP states. Importantly, ZnDatzBdc exhibits an S-shaped CO₂ isotherm, yielding appreciable CO₂ workability of 94.9 cm³ cm⁻³ under typical PVSA operations at 273 K, superior to most reported flexible MOFs^[125].

Mechanochemistry at the chemical reaction level mainly refers to the application of mechanical energy to condensed substances, such as solids and liquids, by means of shear, abrasion, impact, and extrusion to induce changes in their structure and physicochemical properties and to induce chemical reactions. Unlike ordinary thermochemical reactions, mechanization, the driving force of the reaction, is mechanical energy rather than thermal energy; thus, the reaction can be completed without high temperature, high pressure, and other harsh conditions. It has been developing rapidly. This approach not only provides a green and energy-efficient route for chemical transformations but also offers more possibilities for the expanded preparation of materials^[126]. Ultramicroporous MOFs with negatively charged anionic columns, such as SiF₆²⁻ and TiF₆²⁻, often exhibit promising applications in gas separation and CO₂ capture. As shown in Figure 14, a GeF₆²⁻ pillared ultramicroporous MOF, ZU-36-Ni (also known as GeFSIX-3-Ni,

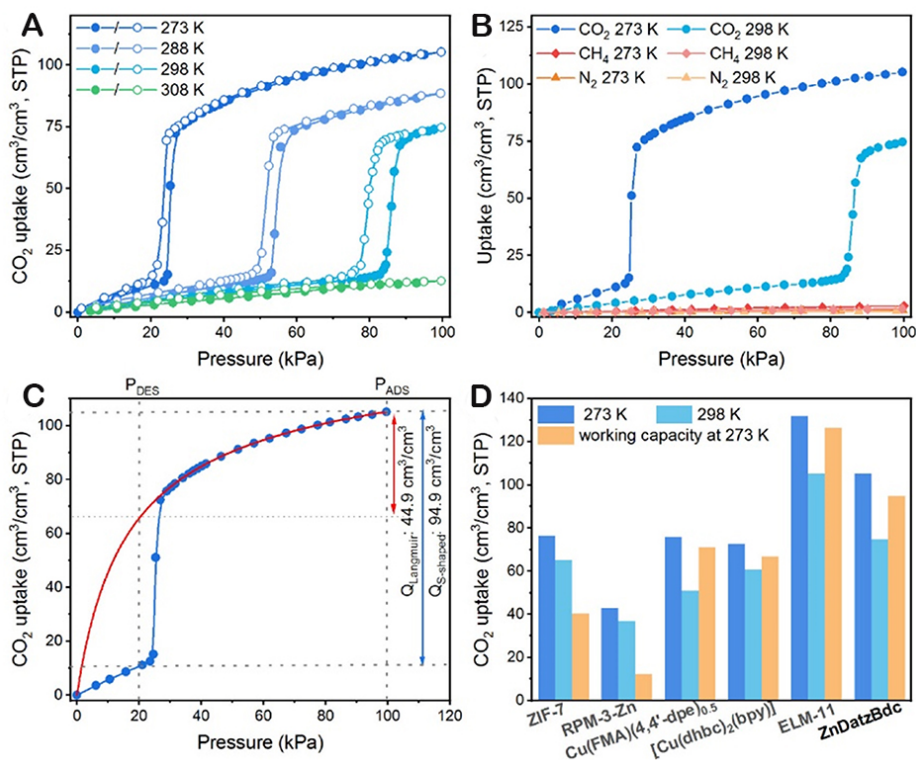


Figure 13. (A) Single-component CO₂ isotherms on ZnDatzBdc up to 100 kPa and varied temperatures; (B) adsorption isotherms of CO₂, N₂, and CH₄ up to 100 kPa at 273 and 298 K; (C) CO₂ working capacities for the step-shaped isotherm of ZnDatzBdc and the simulated Langmuir isotherm from the CO₂ adsorption data in the open phase, for a cycle of adsorption at 100 kPa and desorption at 20 kPa (273 K); (D) comparison of CO₂ uptakes and working capacities of ZnDatzBdc and other flexible MOFs with S-shaped CO₂ isotherms. Reproduced with permission from Peng *et al.*^[125]. Copyright 2022 American Chemical Society.

GeFSIX = GeF₆²⁻), was prepared for the first time by sphere mill auxiliary conversion methodology by Zhang *et al.*^[102]. The strong binding affinity of GeF₆²⁻ and the comparatively long Ge-F bond distance (1.83 Å) lead to increased electronegativity and pore size contraction, resulting in high capacity and enhanced selectivity for trapping trace amounts of CO₂ (1.07 mmol g⁻¹ at 400 ppm).

A winning path to high levels of connectivity MOFs was proposed by Cairns *et al.* in 2007 by using metal-organic polyhedra (MOPs) as supramolecular building blocks (SBBs)^[127]. NJU-Bai52 and NJU-Bai53, prepared by a pure-supramolecular-linker (PSL) approach, are two kinds of high-connected isomeric MOFs with a rare (3,3,6,6)-c topology^[128]. Among them, TPBTM acts as a 12-connected supramolecular linker connected by the M₃O cluster, forming two height-connected linkers. The equilibrium charge on these M₃O clusters was delicately tuned from Cl⁻ ions to monodentate hydroxide anions, resulting in a significant ~50-fold increase in the CO₂ uptake for NJU-Bai53 (2.74 wt%) compared to NJU-Bai52 (0.74 wt%) at 298 K and 0.4 mbar. At 298 K and 0.15 bar, the CO₂ uptake of NJU-Bai53 (7.67 wt%) was greatly increased compared to NJU-Bai52 (0.057 wt%), which is the highest among the reported amide-functionalized MOFs (AFMOFs). In addition, NJU-Bai53 exhibited higher selectivity and chemical stability [Figure 15].

CONCLUSIONS

In conclusion, a great deal of CO₂ capture research has been performed on MOFs in the past few decades. This is due to their special properties, such as large pore volume, high surface area, maintainability, structural diversity, *etc.* This review systematically describes several strategies that can be applied to design

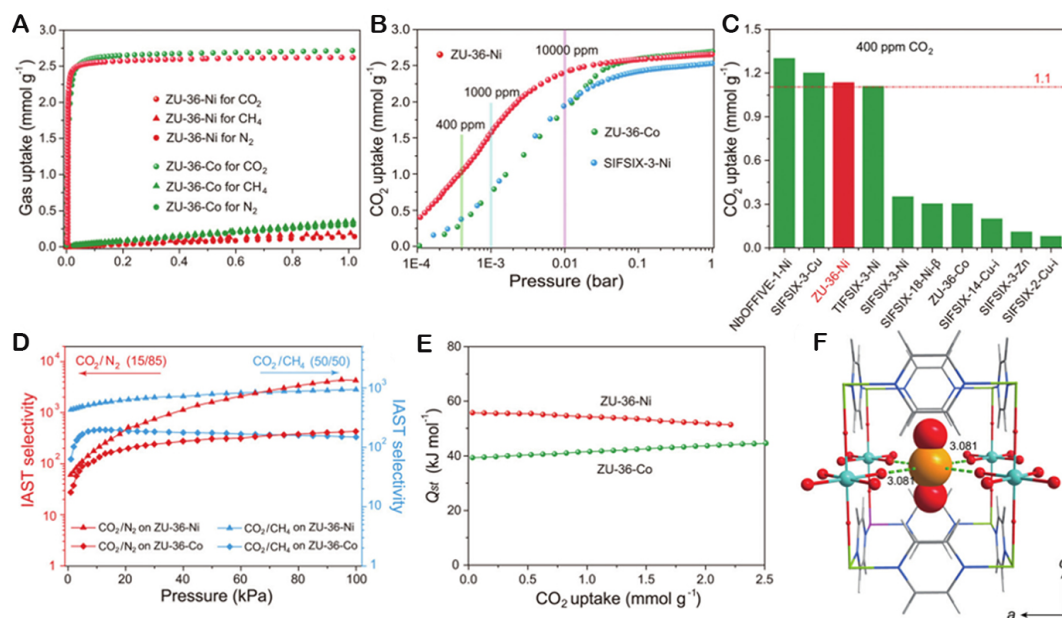


Figure 14. (A and B) Adsorption isotherms of CO₂, CH₄, and N₂ on ZU-36 materials at 298 K. (C) Comparison of the CO₂ uptake on various materials at 400 ppm. (D) IAST selectivity of CO₂/N₂ (15/85) and CO₂/CH₄ (50/50) on ZU-36 materials; (E) Q_{st} value of CO₂ on ZU-36 materials. (F) DFT calculated binding site of CO₂ in ZU-36-Ni. Reproduced with permission from Zhang et al.^[102]. Copyright 2020 Royal Society of Chemistry.

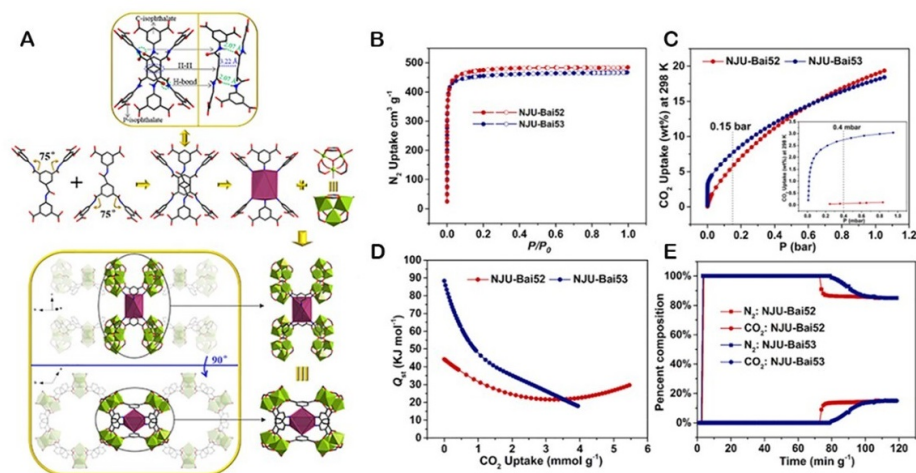


Figure 15. (A) TPBTM⁶⁻ ligand self-assembles into PSL by strong π - π stacking and H-bonds, together with Fe₃O clusters to construct NJU-Bai52, in which the P-isophthalates form metallamacrocycles and the C-isophthalates bridge these metallamacrocycles; (B) N₂ adsorption and desorption isotherms at 77 K of NJU-Bai52 and NJU-Bai53; (C) CO₂ adsorption isotherms at 298 K of NJU-Bai52 and NJU-Bai53; (D) CO₂ adsorption enthalpies of NJU-Bai52 and NJU-Bai53; (E) breakthrough curves at 298 K of NJU-Bai52 and NJU-Bai53. Reproduced with permission from Song et al.^[128]. Copyright 2019 American Chemical Society.

and synthesize CO₂ capture-oriented MOFs, such as tuning the pore size window, functional group modification, and active site insertion. The emergence of these synthetic strategies offers enormous possibilities for the use of MOFs in practical applications in the area of CO₂ capture and separation. Regardless of these strategies, it is imperative that certain characteristics of the original MOF are considered during the design phase, including the original functional groups, crystal structures, and acid and base properties of the MOF.

DECLARATIONS

Authors' contributions

Conceptualization, investigation, and writing-original draft: Sun M

Editing: Wang X, Gao F, Xu M

Writing-review & editing, supervision, and funding acquisition: Fan W, Xu B, Sun D

Availability of data and materials

Not applicable.

Financial support and sponsorship

This work was supported by the National Natural Science Foundation of China (NSFC, Grant Nos. 22201305, 22275210), the Fundamental Research Funds for the Central Universities (22CX06024A, 23CX04001A), and the Outstanding Youth Science Fund Projects of Shandong Province (2022HWYQ-070).

Conflicts of interest

All authors declared that there are no conflicts of interest.

Ethical approval and consent to participate

Not applicable.

Consent for publication

Not applicable.

Copyright

© The Author(s) 2023.

REFERENCES

1. Sejas SA, Taylor PC, Cai M. Unmasking the negative greenhouse effect over the antarctic plateau. *NPJ Clim Atmos Sci* 2018;1:17. [DOI](#) [PubMed](#) [PMC](#)
2. Dong K, Dong X, Jiang Q, Zhao J. Assessing energy resilience and its greenhouse effect: a global perspective. *Energy Econ* 2021;104:105659. [DOI](#)
3. Sullivan I, Goryachev A, Digdaya IA, et al. Coupling electrochemical CO₂ conversion with CO₂ capture. *Nat Catal* 2021;4:952-8. [DOI](#)
4. Friedlingstein P, O'sullivan M, Jones MW, et al. Global carbon budget 2022. *Earth Syst Sci Data* 2022;14:4811-900. [DOI](#)
5. Parekh A, Chaturvedi G, Dutta A. Sustainability analyses of CO₂ sequestration and CO₂ utilization as competing options for mitigating CO₂ emissions. *Sustain Energy Technol Assess* 2023;55:102942. [DOI](#)
6. Obama B. The irreversible momentum of clean energy. *Science* 2017;355:126-9. [DOI](#) [PubMed](#)
7. Horike S, Kishida K, Watanabe Y, et al. Dense coordination network capable of selective CO₂ capture from C1 and C2 hydrocarbons. *J Am Chem Soc* 2012;134:9852-5. [DOI](#)
8. Wang Q, Bai J, Lu Z, Pan Y, You X. Finely tuning MOFs towards high-performance post-combustion CO₂ capture materials. *Chem Commun* 2016;52:443-52. [DOI](#)
9. Eddaoudi M, Sava DF, Eubank JF, Adil K, Guillerme V. Zeolite-like metal-organic frameworks (ZMOFs): design, synthesis, and properties. *Chem Soc Rev* 2015;44:228-49. [DOI](#) [PubMed](#)
10. Wang S, Belmabkhout Y, Cairns AJ, et al. Tuning gas adsorption properties of zeolite-like supramolecular assemblies with gis topology via functionalization of isorecticular metal-organic squares. *ACS Appl Mater Interfaces* 2017;9:33521-7. [DOI](#)
11. Zhou HC, Kitagawa S. Metal-organic frameworks (MOFs). *Chem Soc Rev* 2014;43:5415-8. [DOI](#) [PubMed](#)
12. Guo B, Zhang J, Wang Y, Qiao X, Xiang J, Jin Y. Study on CO₂ adsorption capacity and kinetic mechanism of CO₂ adsorbent prepared from fly ash. *Energy* 2023;263:125764. [DOI](#)
13. Pei J, Wang J, Shao K, et al. Engineering microporous ethane-trapping metal-organic frameworks for boosting ethane/ethylene separation. *J Mater Chem A* 2020;8:3613-20. [DOI](#)
14. Gu XW, Wang JX, Wu E, et al. Immobilization of lewis basic sites into a stable ethane-selective MOF enabling one-step separation of ethylene from a ternary mixture. *J Am Chem Soc* 2022;144:2614-23. [DOI](#)
15. Lv XL, Feng L, Xie LH, et al. Linker desymmetrization: access to a series of rare-earth tetracarboxylate frameworks with eight-connected hexanuclear nodes. *J Am Chem Soc* 2021;143:2784-91. [DOI](#)

16. Lei Z, Xue Y, Chen W, et al. MOFs-based heterogeneous catalysts: new opportunities for energy-related CO₂ conversion. *Adv Energy Mater* 2018;8:1801587. DOI
17. Cui X, Chen K, Xing H, et al. Pore chemistry and size control in hybrid porous materials for acetylene capture from ethylene. *Science* 2016;353:141-4. DOI
18. Fu HR, Jiang YY, Luo JH, Li T. A robust heterometallic Cd(II)/Ba(II)-organic framework with exposed amino group and active sites exhibiting excellent CO₂/CH₄ and C₂H₂/CH₄ Separation. *Chin J Struct Chem* 2022;41:2203287-92. Available from: <https://www.sciencedirect.com/science/article/abs/pii/S0254586123002180> [Last accessed on 11 Aug 2023].
19. Usman M, Iqbal N, Noor T, et al. Advanced strategies in metal-organic frameworks for CO₂ capture and separation. *Chem Rec* 2022;22:e202100230. DOI
20. Zhang X, Wang X, Fan W, Sun D. Pore-environment engineering in multifunctional metal-organic frameworks. *Chin J Chem* 2020;38:509-24. DOI
21. Bhardwaj A, Kaur J, Wuest M, Wuest F. In situ click chemistry generation of cyclooxygenase-2 inhibitors. *Nat Commun* 2017;8:1. DOI PubMed PMC
22. Palluet A, Lique F. Fine-structure excitation of CCS by He: potential energy surface and scattering calculations. *J Chem Phys* 2023;158:044303. DOI PubMed
23. Harvey S, Hopkins J, Kuehl H, O'brien S, Mateeva A. Quest CCS facility: time-lapse seismic campaigns. *Int J Greenh Gas Control* 2022;117:103665. DOI
24. Li J, Ma Y, Mccarthy MC, et al. Carbon dioxide capture-related gas adsorption and separation in metal-organic frameworks. *Coord Chem Rev* 2011;255:1791-823. DOI
25. D'Alessandro DM, Smit B, Long JR. Carbon dioxide capture: prospects for new materials. *Angew Chem Int Ed* 2010;49:6058-82. DOI PubMed
26. Fominykh S, Stankovski S, Markovic VM, Petrovic D, Osmanović S. Analysis of CO₂ migration in horizontal saline aquifers during carbon capture and storage process. *Sustain* 2023;15:8912. DOI
27. Kirchon A, Feng L, Drake HF, Joseph EA, Zhou HC. From fundamentals to applications: a toolbox for robust and multifunctional MOF materials. *Chem Soc Rev* 2018;47:8611-38. DOI PubMed
28. Jansen D, Gazzani M, Manzolini G, Dijk EV, Carbo M. Pre-combustion CO₂ capture. *Int J Greenh Gas Control* 2015;40:167-87. DOI
29. Kheirnik M, Ahmed S, Rahmanian N. Comparative techno-economic analysis of carbon capture processes: pre-combustion, post-combustion, and oxy-fuel combustion operations. *Sustain* 2021;13:13567. DOI
30. Maffei T, Khatami R, Pierucci S, Faravelli T, Ranzi E, Leventis YA. Experimental and modeling study of single coal particle combustion in O₂/N₂ and oxy-fuel (O₂/CO₂) atmospheres. *Combust Flame* 2013;160:2559-72. DOI
31. Cau G, Tola V, Ferrara F, Porcu A, Pettinau A. CO₂-free coal-fired power generation by partial oxy-fuel and post-combustion CO₂ capture: techno-economic analysis. *Fuel* 2018;214:423-35. DOI
32. Sircar S, Golden TC. Purification of hydrogen by pressure swing adsorption. *Sep Sci Technol* 2000;35:667-87. DOI
33. Chao C, Deng Y, Dewil R, Baeyens J, Fan X. Post-combustion carbon capture. *Renew Sustain Energ* 2021;138:110490. DOI
34. Dinca C, Slavu N, Badea A. Benchmarking of the pre/post-combustion chemical absorption for the CO₂ capture. *J Energy Inst* 2018;91:445-56. DOI
35. Na S, Hwang SJ, Kim H, Baek I, Lee KS. Modeling of CO₂ solubility of an aqueous polyamine solvent for CO₂ capture. *Chem Eng Sci* 2019;204:140-50. DOI
36. Kárászová M, Zach B, Petrusová Z, et al. Post-combustion carbon capture by membrane separation, review. *Sep Purif Technol* 2020;238:116448. DOI
37. Liu M, Nothling MD, Webley PA, Jin J, Fu Q, Qiao GG. High-throughput CO₂ capture using PIM-1@MOF based thin film composite membranes. *Chem Eng J* 2020;396:125328. DOI
38. Wang Z, Ren H, Zhang S, Zhang F, Jin J. Polymers of intrinsic microporosity/metal-organic framework hybrid membranes with improved interfacial interaction for high-performance CO₂ separation. *J Mater Chem A* 2017;5:10968-77. DOI
39. Witt A, Pozzi R, Diesch S, Hädicke O, Grammel H. New light on ancient enzymes - *in vitro* CO₂ fixation by pyruvate synthase of *Desulfotribium africanus* and *Sulfolobus acidocaldarius*. *FEBS J* 2019;286:4494-508. DOI PubMed
40. Hefti M, Joss L, Bjelobrk Z, Mazzotti M. On the potential of phase-change adsorbents for CO₂ capture by temperature swing adsorption. *Faraday Discuss* 2016;192:153-79. DOI PubMed
41. Mesfer MK, Danish M, Fahmy YM, Rashid MM. Post-combustion CO₂ capture with activated carbons using fixed bed adsorption. *Heat Mass Transfer* 2018;54:2715-24. DOI
42. Gutierrez-ortega A, Nomen R, Sempere J, Parra J, Montes-morán M, Gonzalez-olmos R. A fast methodology to rank adsorbents for CO₂ capture with temperature swing adsorption. *Chem Eng J* 2022;435:134703. DOI
43. Rehman A, Farrukh S, Hussain A, Fan X, Pervaiz E. Adsorption of CO₂ on amine-functionalized green metal-organic framework: an interaction between amine and CO₂ molecules. *Environ Sci Pollut Res Int* 2019;26:36214-25. DOI PubMed
44. Choi S, Drese JH, Jones CW. Adsorbent materials for carbon dioxide capture from large anthropogenic point sources. *ChemSusChem* 2009;2:796-854. DOI PubMed
45. Yi H, Li F, Ning P, et al. Adsorption separation of CO₂, CH₄, and N₂ on microwave activated carbon. *Chem Eng J* 2013;215:635-42. DOI

46. Jung Y, Ko YG, Nah IW, Choi US. Designing large-sized and spherical CO₂ adsorbents for highly reversible CO₂ capture and low pressure drop. *Chem Eng J* 2022;427:131781. DOI
47. Wahby A, Silvestre-albero J, Sepúlveda-escrignano A, Rodríguez-reinoso F. CO₂ adsorption on carbon molecular sieves. *Microporous Mesoporous Mater* 2012;164:280-7. DOI
48. Li S, Gallucci F. CO₂ capture and activation with a plasma-sorbent system. *Chem Eng J* 2022;430:132979. DOI
49. Zhang Q, Gao S, Yu J. Metal sites in zeolites: synthesis, characterization, and catalysis. *Chem Rev* 2023;123:6039-106. DOI
50. Su F, Lu C. CO₂ capture from gas stream by zeolite 13X using a dual-column temperature/vacuum swing adsorption. *Energy Environ Sci* 2012;5:9021. DOI
51. Hong SH, Jang MS, Cho SJ, Ahn WS. Chabazite and zeolite 13X for CO₂ capture under high pressure and moderate temperature conditions. *Chem Commun* 2014;50:4927-30. DOI PubMed
52. Shang J, Li G, Singh R, Xiao P, Liu JZ, Webley PA. Determination of composition range for “molecular trapdoor” effect in chabazite zeolite. *J Phys Chem C* 2013;117:12841-7. DOI
53. Remy T, Peter SA, Van Tendeloo L, et al. Adsorption and separation of CO₂ on KFI zeolites: effect of cation type and Si/Al ratio on equilibrium and kinetic properties. *Langmuir* 2013;29:4998-5012. DOI
54. Fiuzza RA Jr, Medeiros de Jesus Neto R, Correia LB, Carvalho Andrade HM. Preparation of granular activated carbons from yellow mombin fruit stones for CO₂ adsorption. *J Environ Manage* 2015;161:198-205. DOI PubMed
55. Xu D, Xiao P, Zhang J, et al. Effects of water vapour on CO₂ capture with vacuum swing adsorption using activated carbon. *Chem Eng J* 2013;230:64-72. DOI
56. Ghazvini M, Vahedi M, Najafi Nobar S, Sabouri F. Investigation of the MOF adsorbents and the gas adsorptive separation mechanisms. *J Environ Chem Eng* 2021;9:104790. DOI
57. Liu J, Thallapally PK, McGrail BP, Brown DR, Liu J. Progress in adsorption-based CO₂ capture by metal-organic frameworks. *Chem Soc Rev* 2012;41:2308-22. DOI PubMed
58. Zheng D, Yu Q, Heng Y, Cheng PL. Recent advances in C₂ gases separation and purification by metal-organic frameworks. *Chin J Struct Chem* 2022;41:2211031-44. Available from: <https://www.sciencedirect.com/science/article/abs/pii/S0254586123002441> [Last accessed on 11 Aug 2023].
59. Wong-Foy AG, Matzger AJ, Yaghi OM. Exceptional H₂ saturation uptake in microporous metal-organic frameworks. *J Am Chem Soc* 2006;128:3494-5. DOI PubMed
60. Eddaoudi M, Kim J, Rosi N, et al. Systematic design of pore size and functionality in isorecticular MOFs and their application in methane storage. *Science* 2002;295:469-72. DOI
61. Salahuddin U, Iqbal N, Noor T, et al. ZIF-67 Derived MnO₂ doped electrocatalyst for oxygen reduction reaction. *Catalysts* 2021;11:92. DOI
62. Zhu C, Zhao B, Takata M, Aoki Y, Habazaki H. Biomass derived porous carbon for superior electrocatalysts for oxygen reduction reaction. *J Appl Electrochem* 2023;53:1379-88. DOI
63. Yaqoob L, Noor T, Iqbal N, Nasir H, Mumtaz A. Electrocatalytic performance of NiNH₂BDC MOF based composites with rGO for methanol oxidation reaction. *Sci Rep* 2021;11:13402. DOI PubMed PMC
64. Usman M, Ali M, Al-Maythaly BA, et al. Highly efficient permeation and separation of gases with metal-organic frameworks confined in polymeric nanochannels. *ACS Appl Mater Interfaces* 2020;12:49992-50001. DOI
65. Jiang H, Jia J, Shkurenko A, et al. Enriching the reticular chemistry repertoire: merged nets approach for the rational design of intricate mixed-linker metal-organic framework platforms. *J Am Chem Soc* 2018;140:8858-67. DOI
66. Ming Y, Purewal J, Yang J, et al. Kinetic stability of MOF-5 in humid environments: impact of powder densification, humidity level, and exposure time. *Langmuir* 2015;31:4988-95. DOI
67. Gu Y, Wang Y, Zhao S, et al. N-donating and water-resistant Zn-carboxylate frameworks for humid carbon dioxide capture from flue gas. *Fuel* 2023;336:126793. DOI
68. Li JR, Sculley J, Zhou HC. Metal-organic frameworks for separations. *Chem Rev* 2012;112:869-932. DOI PubMed
69. Zhang Z, Yao Z, Xiang S, Chen B. Perspective of microporous metal-organic frameworks for CO₂ capture and separation. *Energy Environ Sci* 2014;7:2868. DOI
70. Samanta A, Zhao A, Shimizu GKH, Sarkar P, Gupta R. Post-combustion CO₂ capture using solid sorbents: a review. *Ind Eng Chem Res* 2012;51:1438-63. DOI
71. Zhang J, Singh R, Webley PA. Alkali and alkaline-earth cation exchanged chabazite zeolites for adsorption based CO₂ capture. *Microporous Mesoporous Mater* 2008;111:478-87. DOI
72. Zhou C, Li H, Qin H, et al. Defective UiO-66-NH₂ monoliths for optimizing CO₂ capture performance. *Chem Eng J* 2023;467:143394. DOI
73. Patel HA, Byun J, Yavuz CT. Carbon dioxide capture adsorbents: chemistry and methods. *ChemSusChem* 2017;10:1303-17. DOI PubMed
74. Yu H, Li B, Liu S, et al. Three new copper(II) coordination polymers constructed from isomeric sulfo-functionalized phthalate tectonics: synthesis, crystal structure, photocatalytic and proton conduction properties. *J Solid State Chem* 2021;294:121860. DOI
75. O’Keeffe M, Yaghi OM. Deconstructing the crystal structures of metal-organic frameworks and related materials into their underlying nets. *Chem Rev* 2012;112:675-702. DOI PubMed
76. Stock N, Biswas S. Synthesis of metal-organic frameworks (MOFs): routes to various MOF topologies, morphologies, and composites. *Chem Rev* 2012;112:933-69. DOI PubMed

77. Zhu QL, Xu Q. Metal-organic framework composites. *Chem Soc Rev* 2014;43:5468-512. DOI PubMed
78. Bai Y, Dou Y, Xie LH, Rutledge W, Li JR, Zhou HC. Zr-based metal-organic frameworks: design, synthesis, structure, and applications. *Chem Soc Rev* 2016;45:2327-67. DOI
79. Kalmutzki MJ, Hanikel N, Yaghi OM. Secondary building units as the turning point in the development of the reticular chemistry of MOFs. *Sci Adv* 2018;4:eaat9180. DOI PubMed PMC
80. Moghadam PZ, Li A, Wiggin SB, et al. Development of a cambridge structural database subset: a collection of metal-organic frameworks for past, present, and future. *Chem Mater* 2017;29:2618-25. DOI
81. Farrusseng D, Aguado S, Pinel C. Metal-organic frameworks: opportunities for catalysis. *Angew Chem Int Ed* 2009;48:7502-13. DOI PubMed
82. Morris RV, Ruff SW, Gellert R, et al. Identification of carbonate-rich outcrops on Mars by the Spirit rover. *Science* 2010;329:421-4. DOI
83. Suh MP, Park HJ, Prasad TK, Lim DW. Hydrogen storage in metal-organic frameworks. *Chem Rev* 2012;112:782-835. DOI PubMed
84. He Y, Zhou W, Qian G, Chen B. Methane storage in metal-organic frameworks. *Chem Soc Rev* 2014;43:5657-78. DOI PubMed
85. Masoomi MY, Morsali A, Dhakshinamoorthy A, Garcia H. Mixed-metal MOFs: unique opportunities in metal-organic framework (MOF) functionality and design. *Angew Chem Int Ed* 2019;58:15188-205. DOI PubMed
86. Ahmad A, Khan S, Tariq S, Luque R, Verpoort F. Self-sacrifice MOFs for heterogeneous catalysis: synthesis mechanisms and future perspectives. *Mater Today* 2022;55:137-69. DOI
87. Small LJ, Henkelis SE, Rademacher DX, et al. Near-zero power MOF-based sensors for NO₂ detection. *Adv Funct Mater* 2020;30:2006598. DOI
88. Hausdorf S, Baitalov F, Böhle T, Rafaja D, Mertens FO. Main-group and transition-element IRMOF homologues. *J Am Chem Soc* 2010;132:10978-81. DOI PubMed
89. Titi HM, Marrett JM, Dayaker G, et al. Hypergolic zeolitic imidazolate frameworks (ZIFs) as next-generation solid fuels: unlocking the latent energetic behavior of ZIFs. *Sci Adv* 2019;5:eaav9044. DOI PubMed PMC
90. Yang S, Li X, Zeng G, et al. Materials Institute Lavoisier (MIL) based materials for photocatalytic applications. *Coord Chem Rev* 2021;438:213874. DOI
91. Yang J, Yang K, Zhu X, et al. Band engineering of non-metal modified polymeric carbon nitride with broad spectral response for enhancing photocatalytic CO₂ reduction. *Chem Eng J* 2023;461:141841. DOI
92. Zhang G, Wei G, Liu Z, Oliver SRJ, Fei H. A robust sulfonate-based metal-organic framework with permanent porosity for efficient CO₂ capture and conversion. *Chem Mater* 2016;28:6276-81. DOI
93. Liu Y, Wang ZU, Zhou H. Recent advances in carbon dioxide capture with metal-organic frameworks. *Greenhouse Gas Sci Technol* 2012;2:239-59. DOI
94. Quílez-bermejo J, Melle-franco M, San-fabián E, Morallón E, Cazorla-amorós D. Towards understanding the active sites for the ORR in N-doped carbon materials through fine-tuning of nitrogen functionalities: an experimental and computational approach. *J Mater Chem A* 2019;7:24239-50. DOI
95. Serra-crespo P, Ramos-fernandez EV, Gascon J, Kapteijn F. Synthesis and characterization of an amino functionalized MIL-101(Al): separation and catalytic properties. *Chem Mater* 2011;23:2565-72. DOI
96. Dinakar B, Forse AC, Jiang HZH, et al. Overcoming metastable CO₂ adsorption in a bulky diamine-appended metal-organic framework. *J Am Chem Soc* 2021;143:15258-70. DOI
97. Lu W, Sculley JP, Yuan D, Krishna R, Wei Z, Zhou H. Polyamine-tethered porous polymer networks for carbon dioxide capture from flue gas. *Angew Chem Int Ed* 2012;51:7480-4. DOI PubMed
98. Khan J, Iqbal N, Asghar A, Noor T. Novel amine functionalized metal organic framework synthesis for enhanced carbon dioxide capture. *Mater Res Express* 2019;6:105539. DOI
99. McDonald TM, D'alessandro DM, Krishna R, Long JR. Enhanced carbon dioxide capture upon incorporation of N,N'-dimethylethylenediamine in the metal-organic framework CuBTri. *Chem Sci* 2011;2:2022-8. DOI
100. Tu S, Yu L, Liu J, et al. Efficient CO₂ capture under humid conditions on a novel amide-functionalized Fe-soc metal-organic framework. *ACS Appl Mater Interfaces* 2023;15:12240-7. DOI
101. Lyu H, Chen OI, Hanikel N, et al. Carbon dioxide capture chemistry of amino acid functionalized metal-organic frameworks in humid flue gas. *J Am Chem Soc* 2022;144:2387-96. DOI
102. Zhang Z, Ding Q, Peh SB, et al. Mechano-assisted synthesis of an ultramicroporous metal-organic framework for trace CO₂ capture. *Chem Commun* 2020;56:7726-9. DOI
103. Peng YL, Pham T, Li P, et al. Robust ultramicroporous metal-organic frameworks with benchmark affinity for acetylene. *Angew Chem Int Ed* 2018;57:10971-5. DOI
104. Bhatt PM, Belmabkhout Y, Cadiau A, et al. A fine-tuned fluorinated MOF addresses the needs for trace CO₂ removal and air capture using physisorption. *J Am Chem Soc* 2016;138:9301-7. DOI
105. Zhang Z, Ding Q, Cui J, Cui X, Xing H. High and selective capture of low-concentration CO₂ with an anion-functionalized ultramicroporous metal-organic framework. *Sci China Mater* 2021;64:691-7. DOI
106. Chakraborty G, Das P, Mandal SK. Polar sulfone-functionalized oxygen-rich metal-organic frameworks for highly selective CO₂ capture and sensitive detection of acetylacetone at ppb level. *ACS Appl Mater Interfaces* 2020;12:11724-36. DOI PubMed

107. Lin RB, Chen D, Lin YY, Zhang JP, Chen XM. A zeolite-like zinc triazolate framework with high gas adsorption and separation performance. *Inorg Chem* 2012;51:9950-5. [DOI](#) [PubMed](#)
108. Lin R, Xiang S, Zhou W, Chen B. Microporous metal-organic framework materials for gas separation. *Chem* 2020;6:337-63. [DOI](#)
109. Fan W, Wang X, Zhang X, et al. Fine-tuning the pore environment of the microporous Cu-MOF for high propylene storage and efficient separation of light hydrocarbons. *ACS Cent Sci* 2019;5:1261-8. [DOI](#) [PubMed](#) [PMC](#)
110. Jo D, Lee SK, Cho KH, Yoon JW, Lee UH. An Amine-functionalized ultramicroporous metal-organic framework for postcombustion CO₂ capture. *ACS Appl Mater Interfaces* 2022;14:56707-14. [DOI](#) [PubMed](#)
111. Lin JB, Nguyen TTT, Vaidhyanathan R, et al. A scalable metal-organic framework as a durable physisorbent for carbon dioxide capture. *Science* 2021;374:1464-9. [DOI](#)
112. Oschatz M, Antonietti M. A search for selectivity to enable CO₂ capture with porous adsorbents. *Energy Environ Sci* 2018;11:57-70. [DOI](#)
113. Qazvini OT, Babarao R, Telfer SG. Selective capture of carbon dioxide from hydrocarbons using a metal-organic framework. *Nat Commun* 2021;12:197. [DOI](#) [PubMed](#) [PMC](#)
114. Chowdhury P, Mekala S, Dreisbach F, Gumma S. Adsorption of CO, CO₂ and CH₄ on Cu-BTC and MIL-101 metal organic frameworks: Effect of open metal sites and adsorbate polarity. *Microporous Mesoporous Mater* 2012;152:246-52. [DOI](#)
115. Kökçam-Demir Ü, Goldman A, Esrafilı L, et al. Coordinatively unsaturated metal sites (open metal sites) in metal-organic frameworks: design and applications. *Chem Soc Rev* 2020;49:2751-98. [DOI](#)
116. Lim D, Chyun SA, Suh MP. Hydrogen storage in a potassium-ion-bound metal-organic framework incorporating crown ether struts as specific cation binding sites. *Angew Chem Int Ed* 2014;126:7953-6. [DOI](#)
117. Shin SR, Cho HS, Lee Y, et al. In Situ mapping and local negative uptake behavior of adsorbates in individual pores of metal-organic frameworks. *J Am Chem Soc* 2021;143:20747-57. [DOI](#)
118. Chen K, Kang YS, Zhao Y, Yang JM, Lu Y, Sun WY. Cucurbit[6]uril-based supramolecular assemblies: possible application in radioactive cesium cation capture. *J Am Chem Soc* 2014;136:16744-7. [DOI](#)
119. Li N, Chang Z, Huang H, et al. Specific K⁺ binding sites as CO₂ traps in a porous MOF for enhanced CO₂ selective sorption. *Small* 2019;15:e1900426. [DOI](#)
120. Zhao X, Bu X, Zhai QG, Tran H, Feng P. Pore space partition by symmetry-matching regulated ligand insertion and dramatic tuning on carbon dioxide uptake. *J Am Chem Soc* 2015;137:1396-9. [DOI](#) [PubMed](#)
121. Oh JM, Venters CC, Di C, et al. U1 snRNP regulates cancer cell migration and invasion *in vitro*. *Nat Commun* 2020;11:1. [DOI](#) [PubMed](#) [PMC](#)
122. Balogun HA, Bahamon D, Almenhali S, Vega LF, Alhajaj A. Are we missing something when evaluating adsorbents for CO₂ capture at the system level? *Energy Environ Sci* 2021;14:6360-80. [DOI](#)
123. Wang Q, Ke T, Yang L, et al. Cover picture: separation of Xe from Kr with record selectivity and productivity in anion-pillared ultramicroporous materials by inverse size-sieving. *Angew Chem Int Ed* 2020;59:3341. [DOI](#)
124. Chen Y, Qiao Z, Lv D, et al. Efficient adsorptive separation of C₃H₆ over C₃H₈ on flexible and thermoresponsive CPL-1. *Chem Eng J* 2017;328:360-7. [DOI](#)
125. Peng J, Liu Z, Wu Y, Xian S, Li Z. High-performance selective CO₂ capture on a stable and flexible metal-organic framework via discriminatory gate-opening effect. *ACS Appl Mater Interfaces* 2022;14:21089-97. [DOI](#)
126. Jiang Y, Tan P, Qi S, et al. Cover picture: metal-organic frameworks with target-specific active sites switched by photoresponsive motifs: efficient adsorbents for tailorable CO₂ capture. *Angew Chem Int Ed* 2019;58:6457. [DOI](#)
127. Cairns AJ, Perman JA, Wojtas L, et al. Supermolecular building blocks (SBBs) and crystal design: 12-connected open frameworks based on a molecular cubohemioctahedron. *J Am Chem Soc* 2008;130:1560-1. [DOI](#)
128. Song X, Zhang M, Chen C, et al. Pure-supramolecular-linker approach to highly connected metal-organic frameworks for CO₂ capture. *J Am Chem Soc* 2019;141:14539-43. [DOI](#)

Research Article

Open Access



Influence of kinks on the interaction energy between ferroelastic domain walls in membranes and thin films

Guangming Lu¹, Kimura Hideo¹, Xiangdong Ding², Zhijun Xu¹, Ruiqing Chu¹, Guillaume F. Nataf³, Ekhard K. H. Salje⁴

¹School of Environmental and Materials Engineering, Yantai University, Yantai 264005, Shandong, China.

²State Key Laboratory for Mechanical Behavior of Materials, Xi'an Jiaotong University, Xi'an 710049, Shaanxi, China.

³GREMAN UMR7347, CNRS, University of Tours, INSA Centre Val de Loire, Tours 37000, France.

⁴Department of Earth Sciences, University of Cambridge, Cambridge CB2 3EQ, UK.

Correspondence to: Dr. Guangming Lu, School of Environmental and Materials Engineering, Yantai University, Yantai 264005, Shandong, China. E-mail: luguangming1990@ytu.edu.cn; Prof. Ekhard K. H. Salje, Department of Earth Sciences, University of Cambridge, Cambridge CB2 3EQ, UK. E-mail: ekhard@esc.cam.ac.uk

How to cite this article: Lu G, Hideo K, Ding X, Xu Z, Chu R, Nataf GF, Salje EKH. Influence of kinks on the interaction energy between ferroelastic domain walls in membranes and thin films. *Microstructures* 2023;3:2023033.
<https://dx.doi.org/10.20517/microstructures.2023.28>

Received: 30 May 2023 **First Decision:** 17 Jul 2023 **Revised:** 28 Jul 2023 **Accepted:** 5 Aug 2023 **Published:** 11 Aug 2023

Academic Editors: Shujun Zhang, Alexei Gruverman **Copy Editor:** Fangling Lan **Production Editor:** Fangling Lan

Abstract

In thin samples, such as membranes, kinks inside ferroelastic domain walls interact through “dipolar” interactions following a $1/d^2$ decay, where d is the distance between the walls. Simultaneously, the samples relax by bending. Bending is not possible in thick samples or can be suppressed in thin films deposited on a rigid substrate. In these cases, wall-wall interactions decay as $1/d$, as monopoles would do. In free-standing samples, we show a wide crossover regime between “dipolar” $1/d^2$ interactions and “monopolar” $1/d$ interactions. The surfaces of all samples show characteristic relaxation patterns near the kink, which consists of ridges and valleys. We identify the sample bending as the relevant image force that emanates from kinks inside walls in thin samples. When samples are prevented from bending by being attached to a substrate, the dipolar force is replaced by “monopolar” forces, even in thin samples. These results are important for transmission electron microscopy imaging, where the typical sample size is in the dipolar range while it is in the monopolar range for the bulk.

Keywords: Kink interactions, Crossover regime for kink interactions, Ferroelectricity, Finite size dependent scaling



© The Author(s) 2023. **Open Access** This article is licensed under a Creative Commons Attribution 4.0 International License (<https://creativecommons.org/licenses/by/4.0/>), which permits unrestricted use, sharing, adaptation, distribution and reproduction in any medium or format, for any purpose, even commercially, as long as you give appropriate credit to the original author(s) and the source, provide a link to the Creative Commons license, and indicate if changes were made.



INTRODUCTION

Ferroelectric and ferroelastic materials spontaneously split into domains where the order parameter (spontaneous polarisation or spontaneous strain, respectively) is uniform. The boundaries between these domains are called domain walls. They move in response to an applied external field (electric field or stress field)^[1-6]. They also exhibit emergent properties that do not exist in bulk, such as a spontaneous polarisation in ferroelastics^[7] or anomalous electrical conductivity in ferroelectrics^[8-11].

Landau theory predicts that domain walls are smooth with a hyperbolic tangent profile. However, experimental observations demonstrate a different behaviour, showing that domain walls can exhibit complex profiles with meanders and atomic steps called kinks^[12-15]. This phenomenon is particularly evident in various materials such as membranes^[16], ceramics^[17,18] and thin films^[19]. This internal structure has direct consequences on the emergent properties of domain walls. In lithium niobate, scanning transmission electron microscopy images on a lamella cut from a bulk single crystal revealed kinks and antikinks (i.e., atomic steps in the opposite direction compared to kinks) at domain walls. It was proposed that these kinks and antikinks lead to localised electric charges that influence the dielectric response of the material^[20].

Kinks are also essential elements that form during switching under an applied external field^[21-23]. Clear experimental evidence supports the notion that kink formation and local bending constitute the first stage of domain wall motion^[24]. As such, the collective motion of domain walls in avalanche-like processes is triggered by kinks^[25]. Kinks seem to play an even more important role in switching along non-polar directions or in non-polar materials. In lithium niobate, switching on non-polar cuts is governed by the generation and propagation of charged kinks^[13]. Simulations also indicate that kink movements dominate the switching mechanism of polar domain walls in non-polar ferroelastic^[26]. In addition, the movement of kinks has been predicted to be supersonic, opening possibilities for materials applications at GHz frequencies^[27].

In samples with high densities of domain walls, interactions between walls are governed by their junctions^[28,29]. In simpler but not uncommon configurations of parallel domain walls separated by distances larger than the boundary thickness, the interactions may arise from kinks^[30] that are known to lead to enhanced areas of strain^[18]. For nanoscopic sizes, the interaction energy between domain walls was found to be dipolar, i.e., to decay as $1/d^2$ where d is the distance between the walls^[30], which agrees well with the energy decay of surface steps^[31,32]. For large samples, the interaction energy was found to decay as $1/d^{3/2}$ ^[33].

In this work, using reasonable interatomic potentials, we show that a crossover between “dipolar” $1/d^2$ interactions and “monopolar” $1/d$ interactions in free-standing samples occurs at lateral sizes in the order of 1,000 l.u. (l.u. = lattice unit), which corresponds to around 0.5 μm for a unit cell parameter of 0.5 nm. This behaviour changes greatly if the sample is clamped on one side, such as in thin films, since we find that the kink-kink interactions stay monopolar even for very thin films (~ 100 l.u.). Our findings are important for understanding the organisation of domain walls and their response to an applied external field in membranes, transmission electron microscopy lamellae, ceramics, and thin films.

METHODS

Ferroelastic domains and confined atomic kinks residing inside domain walls are described by a model for ferroelastic transitions based on a Landau-type double-well potential^[34], as schematically shown in [Supplementary Figure 1](#). The potential energy $U(r)$ contains three terms: the harmonic first nearest atomic interactions $U(r) = 20(r - 1)^2$ (black springs), the anharmonic second-nearest interactions $U(r) = -25(r - \sqrt{2})^2 + 20,000(r - \sqrt{2})^4$ (yellow springs) along diagonals in the lattice unit and the fourth-order third-nearest

interactions $U(r) = 8(r - 2)^4$ (green springs), where r is the distance between atoms. The first- and third-nearest interactions are related to the elastic interactions and constitute the elastic background in ferroelastic materials. The model parameters are inspired by SrTiO₃ with the energy scale determined by $T_c = 105$ K and typical ferroelastic shear angle of 2° . The atomic mass is $M = 50$ amu. The relevant strain components ϵ_{xx} , ϵ_{yy} , and ϵ_{xy} are calculated from the appropriate interatomic distances relative to those of the monodomain. The sample was relaxed for ca. 10^5 computational steps. All simulations were performed using the LAMMPS program^[35], which minimises the potential energy of the total system. Although our formulated interatomic potential is simple, the main elastic properties of ferroelastic materials have been considered such that the simulated results can successfully reveal the elastic interactions between kinks, which would also be predicted by advanced methods, such as analytical potentials^[36] and DFT calculations, where more parameters and physical processes are considered. Two different boundary conditions are used in our simulations. The first one is the open or Dirichlet boundary condition applied in both x and y directions, where sample relaxations, including shape changes and rotations, are allowed. The initial lattice parameters in x and y directions are set to $a = 1$ l.u. and relax to 1.0001297 l.u. and 0.9995027 l.u. in x and y directions, respectively. A single domain wall with a kink residing at its centre was constructed to investigate the size dependence of tilt angles and self-energies of the kink [Figure 1A and B]. Two parallel domain walls containing one kink in each wall, i.e., a kink-kink pair and a kink-antikink pair [Figure 1A] with various separations [Figure 1C] were constructed to investigate the effect of the sample size on the kink interactions.

The second boundary condition was constructed with the bottom layer fixed while all other surfaces were free to relax. This configuration represents an extreme case of hard interfacial bonding without any lattice defect between the sample and the substrate. This situation is encountered in thin films on “hard” substrates. All other parameters were identical to the first case of open boundary conditions. The kinks were initially created inside domain walls, and the system was then relaxed using a conjugate gradient method followed by 5×10^6 (5×10^3 ps) molecular dynamics (MD) simulation steps to obtain the full ferroelastic domain structure. Ferroelastic domain structures were obtained by averaging structural snapshots every 1,000 MD steps (1 ps). To avoid the movement of kinks in the domain wall, the temperature was kept very low at $T = 0.001$ K using a Nosé-Hoover thermostat^[37]. All simulations were performed using the LAMMPS code. The atomic configurations were displayed using the OVTIO software^[38].

RESULTS AND DISCUSSION

Free standing sample (membrane, lamella)

We first construct a single domain wall with a stable kink located at the centre within a cell with open boundary conditions with a constant lateral size (L_x) of 1,601 l.u. in the x direction and variable vertical sizes (L_y) between 101 l.u. and 1,601 l.u. in the y direction (sample thickness indicated by Δ in Figure 2A). The kink-induced distortion is observed in the strain ϵ_{xx} map, as shown in Figure 2A. The strain fields generated by the kinks manifest obvious compressive and tensile regimes on the top and bottom of the kink, similar to those of dislocations^[39]. A local bending near the kink, together with a macroscopic tilt of the domain wall on the left and right sides of this kink, is observed in Figure 2A and B. Such local bending can also be discussed under the framework of the Helfrich model^[40]. The tilt angle is defined as the macroscopic angle between the domain wall and the horizontal direction, with the angles θ_1 and θ_2 shown in Figure 2B. All atomic layers from the bottom (green lines in Figure 2A) to the top surface (blue lines in Figure 2A) show similar tilt angles. Figure 2C shows the tilt angles as a function of the sample thickness. Both θ_1 and θ_2 decrease as the system thickness increases, following $\theta \sim \Delta^{-1}$. All these results are in agreement with our previous results on kink interactions^[30].

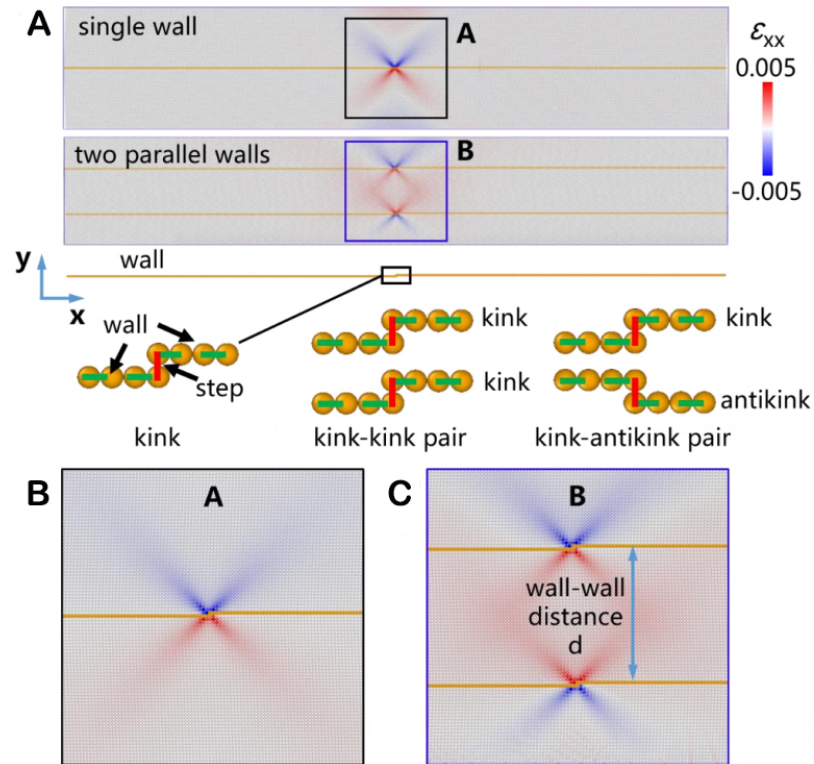


Figure 1. Domain wall configurations for kink interactions. (A) Domain wall configurations containing one or two kinks. The structural details of the atomic kinks, kink pairs and strain fields near the kinks are shown in (B and C). The strain maps in (A-C) are colour-coded by the atomic-level strain: ϵ_{xx} . Green dashed lines in (A) indicate the position of domain walls. Red solid lines in (A) indicate the atomic steps of the kink structures.

We then calculate the self-energy of kinks in domain walls with different sample thicknesses. The self-energy of kinks is calculated as the energy difference between samples with and without kinks inside the wall. The self-energy is dependent on the sample thickness, as shown in Figure 2D. In analogy with dislocations, the self-energy of kinks consists of two components, namely the core energy of the kink and the elastic energy around the core. The core energy is found to be 0.17 eV, similar to values found for kinks in dislocations in silicon (~ 0.12 eV)^[41]. The evolution of the total energy with the sample thickness Δ follows a logarithmic size dependence for thicknesses $> 1,000$ l.u. [Figure 2D]. At lower distances, the energy is lower and follows a power law $E_{\text{kink}} = E_{\text{core}} - A/\Delta$ with $E_{\text{core}} = 0.17$ eV and $A = 6$ eV l.u. The kink energy per unit cell is defined as E_{kink} divided by the total number of unit cells in the sample and decays with a power law dependence from 10^{-7} eV/unit cell in the smallest sample with $\Delta = 150$ l.u. to 2×10^{-8} eV/unit cell for a sample with a thickness of $\Delta = 1,601$ l.u.

The size dependence of kink-kink and kink-antikink pair interactions is then investigated. Two parallel domain walls with one kink or one antikink in each wall are created [Figure 1A and C]. The two walls were initialised at symmetric positions with respect to centre of the sample, with a kink (or an antikink) at the centre of each wall. The samples range from small ($L_x = 201$ l.u., $L_y = 200$ l.u.) to large sizes ($L_x = 1,601$ l.u., $L_y = 1,600$ l.u.). To calculate the interaction energy of the kink-kink configuration, the total potential energy is reduced by the potential energy of two noninteracting kinks $E_{\text{kink-kink}} = E_{\text{total}} - 2E_{\text{kink}}$. Figure 3 shows the sample size dependence of kink-kink interactions. For small sample sizes, the kink-kink interaction energies (black symbols and fitted lines in Supplementary Figure 2) are similar to Lu *et al.*, and the wall-wall interaction shows an atypical “dipolar” character with a scaling exponent of -2 [Figure 3A]^[30]. As the sample

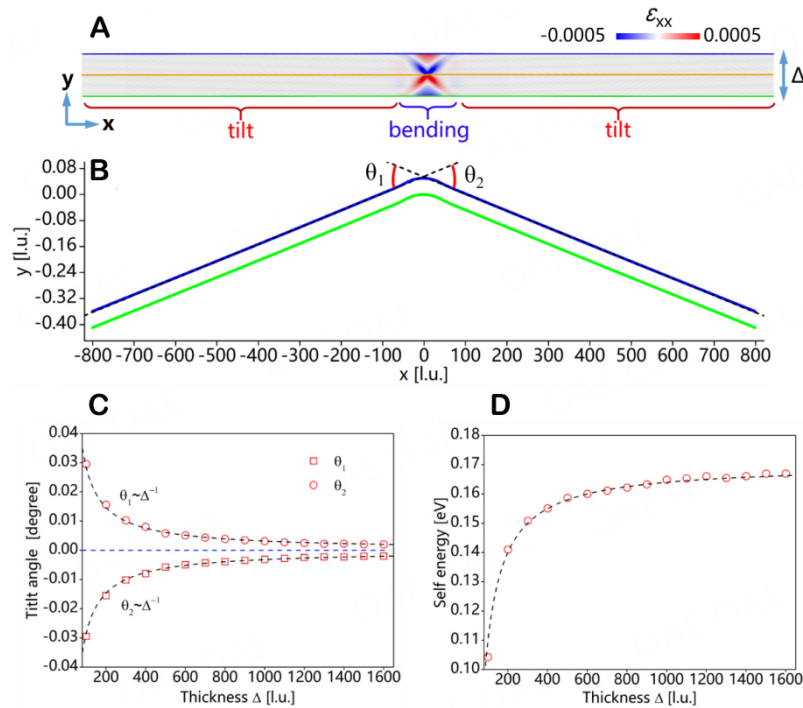


Figure 2. Dependence of the kink-induced wall tilt and kink self-energy on the sample thickness Δ . (A) Strain distribution induced by the kink for a sample with a thickness Δ of 101 l.u. (B) Bending of the local lattice with tilt angles θ_1 and θ_2 . The green and blue lines indicate the bottom and top surfaces, respectively. (C) The variation of macroscopic tilt angles as a function of sample thickness Δ . The data points in (C) are fitted by $\theta = a + b \times \Delta^c$ with $a = 0$ for θ_1 and θ_2 , $b = 2.246$ for θ_1 and $b = -2.246$ for θ_2 , and $c = -1$ for θ_1 and θ_2 . The fitted line in (C) shows the scaling exponent of -1 between the sample thickness and the tilt. (D) Relationship between kink self-energy and sample thickness Δ . The data points in (D) are fitted by $E_{\text{kink}} = E_{\text{core}} - A \times \Delta^B$ with $E_{\text{core}} = 0.17$ eV, $A = 6$ eV l.u. and $B = -1$. The fitted line in (D) shows a scaling of $-1/\Delta$ while logarithmic scaling equally fits the data for thicknesses $> 1,000$ l.u.

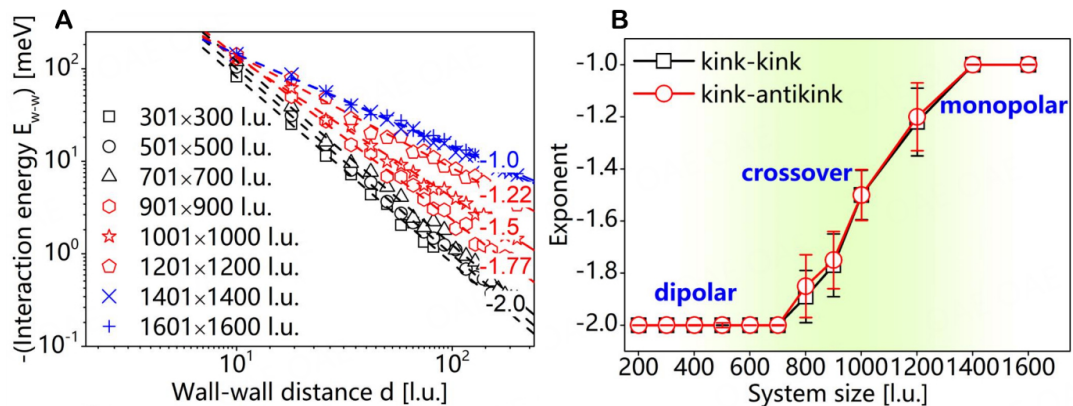


Figure 3. Interaction energies of kink-kink configurations residing inside two parallel walls as a function of the wall-wall distance d . (A) Interaction energy on logarithmic scales with the fitted scaling exponents. (B) Scaling exponents as a function of sample sizes. The thickness scaling changes from d^2 for thin samples to d^{-1} for thick samples.

size increases, the scaling exponents decrease and “monopolar” interactions with an exponent of -1 are reached when the sample size is larger than 1,001 l.u. This “monopolar” wall-wall interaction is consistent with previous theoretical predictions^[42]. Our energy scaling for the sample thickness reveals a wide crossover regimen, which had not been found before, that occurs near thicknesses of 1,000 l.u. [Figure 3B]. To explore further the physical processes leading to this crossover, lattice profiles [Figure 4A-D] and strain

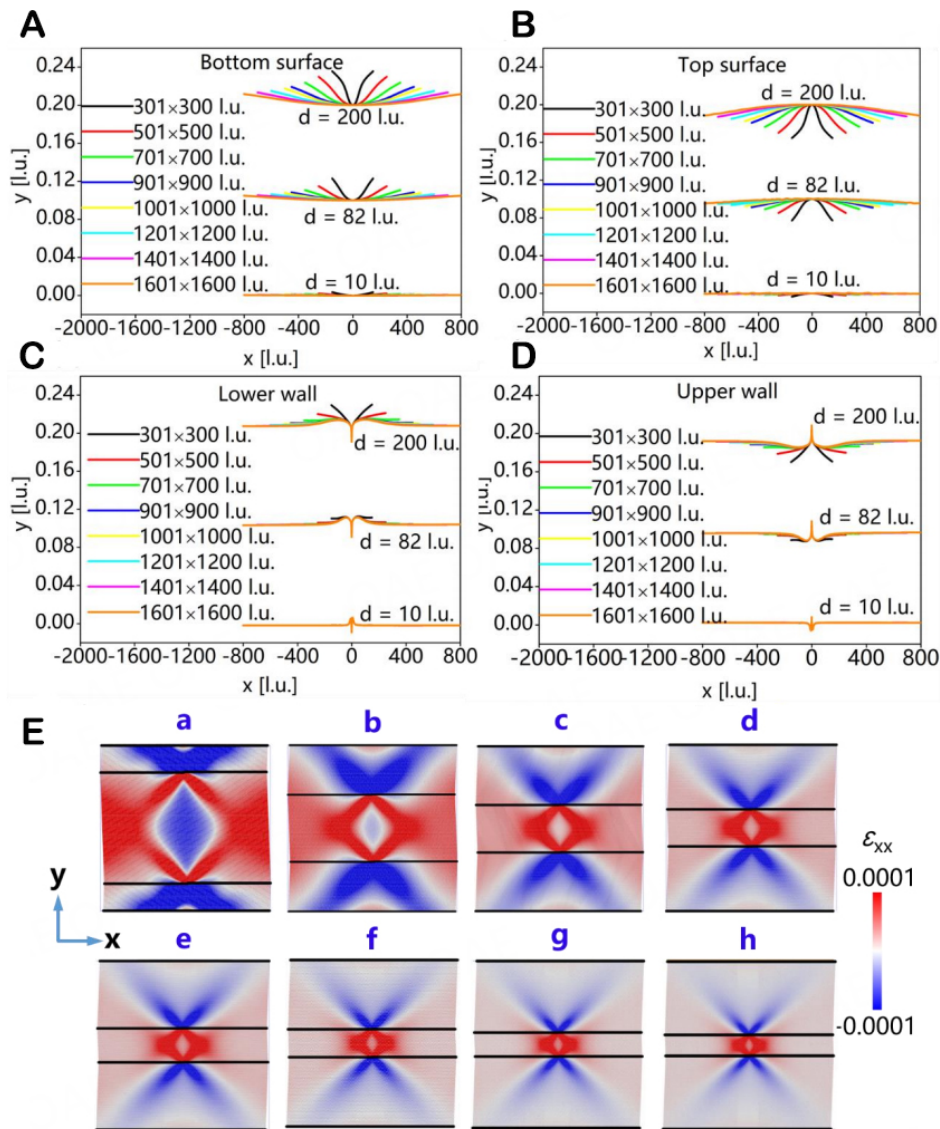


Figure 4. Lattice profiles and strain maps of kink-kink configurations with different system sizes and wall-wall distance d . (A-D) Lattice profiles for the bottom surfaces, top surfaces, lower walls and upper walls of samples with $d = 10$ l.u., 82 l.u. and 200 l.u. Strain maps in (E) are colour-coded according to the atomic-level normal strain: ϵ_{xx} with a wall-wall distance of $d = 200$ l.u. The sample sizes for (A-D) are 301 l.u. \times 300 l.u., 501 l.u. \times 500 l.u., 701 l.u. \times 700 l.u., 901 l.u. \times 900 l.u., 1,001 l.u. \times 1,000 l.u., 1,201 l.u. \times 1,200 l.u., 1,401 l.u. \times 1,400 l.u., and 1,601 l.u. \times 1,600 l.u. The black lines indicate the bottom surface, lower wall, upper wall, and top surface.

maps [Figure 4E] are analysed. Strong strain deformations observed near the surfaces of small-sized sample [Figure 4E(a-c)] decay when the system size increases [Figure 4E(d-f)] and almost disappear when the size is over 1,400 l.u [Figure 4E(g and h)]. The simulated energies as a function of the wall-wall distances are power laws for all thicknesses. They do not represent superpositions of two power laws of more complex functions, which could have represented the intermediate range between the surface-dominated and bulk-dominated interactions. The evolution of this size-dependent surface strain is, thus, seen as the change of exponents of the wall-wall interaction in Figure 3B. The top layers bend nearly parabolically in opposite directions so that the negative displacement of the bottom layer [Figure 4A] is the same as the positive bending of the top layer [Figure 4B]. Small samples bend very strongly, while thick samples are more rigid. The lower and upper domain walls show more local deformations at the kink positions. The same thickness

dependence is found for interactions between kinks and antikinks [Supplementary Figure 3].

The change of the interaction energy exponent from -2 for small samples to -1 for thick samples extends over an interval of sample thicknesses between 700 l.u. and 1,400 l.u. In real materials, the interval extends from 350 nm to 700 nm for a lattice unit of 0.5 nm. The weaker wall-wall interactions could lead to a higher concentration of domain walls.

Sample on a substrate (thin film)

A thin film on a substrate cannot bend on the fixed surface but can relax the free surface. To explore the effect of a fixed boundary on the kink interactions, we simulate this scenario by clamping the lower surface in the limit of hard interfaces with no lattice misfit. The model has a sample size of 601 l.u. in the x direction and 100 l.u. in the y direction [Figure 5A]. Similar to the cases of samples with free boundaries, the two parallel domain walls are symmetric with respect to the centre of the sample, and the kink is stabilised at the centre of each domain wall. We then relaxed the entire sample. The resultant strain fields are shown in Figure 5A. The strain fields do not extend to the bottom surface, while strain fields deform the top surface. Figure 5B shows the local displacements of the fixed bottom surface, lower wall, upper wall and top surface of samples with wall-wall distances of $d = 10$ l.u., 22 l.u., and 42 l.u. The bottom surface remains flat, while the top surface shows local ridge-and-valley deformations. These local deformations are in the order of 0.02 l.u. or 2% strain for $d = 42$ l.u. The local deformations of the domain walls are of the same order of magnitude, with a sharp singularity at the kinks. The upper wall exhibits a larger deformation than the lower wall.

The fundamental difference between the clamped and the free samples is that no macroscopic bending can occur under clamping conditions, while the local deformations are visible in both cases. The decay of the valley structure away from the centre is exponential and extends over some 50 l.u. The decay resembles the deformation caused by intersections between domain walls and surfaces^[43,44].

The interaction between the two kinks, and hence between the walls, is shown in Figure 5C. The scaling function is a power law with an exponent of -1 [Figure 5D]. In straight samples without any macroscopic bending, the scaling $E \sim d^{-1}$ holds even though only one surface is clamped and the opposite surface is free to deform. Similar results were found for the kink-antikink interactions, as shown in Supplementary Figure 4.

CONCLUSIONS

Kink-kink interactions in bulk samples interact as “monopoles” with a d^{-1} dependence when they are separated by the distance d . As the sample size decreases, the interaction for thin samples decays following a characteristic d^{-2} trend similar to that of dipoles. This behaviour of any singularity (dielectric, dislocations, interstitials, etc.) is commonly described analytically by the concept of “image force”. The construction is based on the calculation of the surface relaxation as having the same energy as if a fictitious image force was placed outside the sample. Such image forces have also been used to describe the dynamics of dislocation movements^[45]. Our results clarify the role of the crossover regime near $d = 1,000$ l.u., which is rather wide.

Detailed investigations of wall profiles are often attempted by transmission electron microscopy where the typical sample thickness is 50 l.u., well within the “dipolar” range. We demonstrate the role of image forces that are responsible for the dipolar relaxation by comparing the relaxation patterns of free-standing samples and thin films. They are closely related to the bending of the sample and much less to the bulging of the surface to form ridge-and-valley structures. This corresponds not only to substrate effects but also to thin

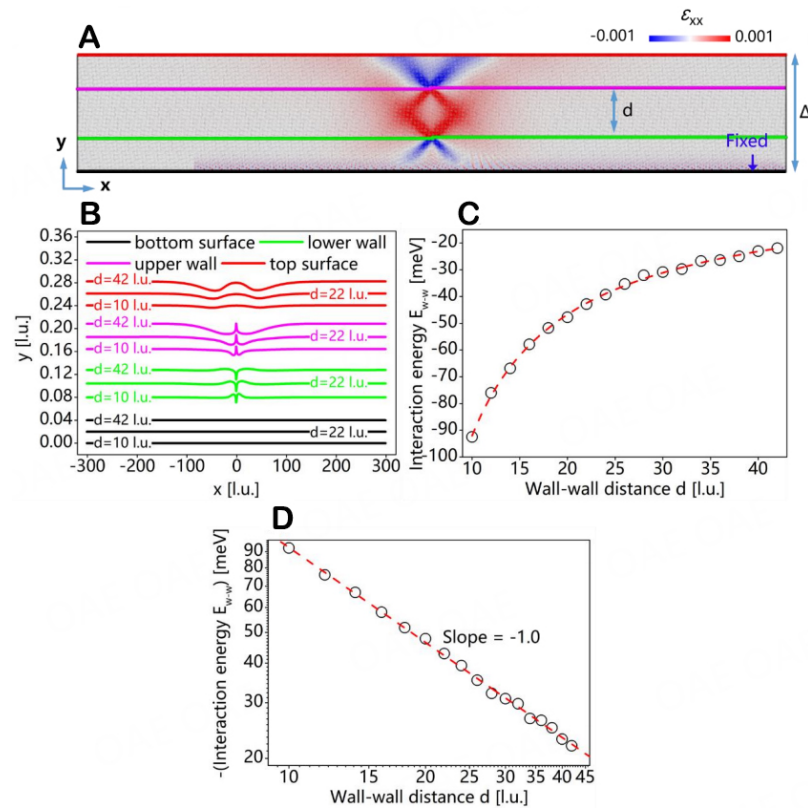


Figure 5. Interaction energies of kink-kink configurations with a clamped bottom surface. (A) Strain fields of the thin film with a thickness of $\Delta = 100$ l.u. and wall-wall distances of $d = 42$ l.u. The strain map was colour-coded according to the atomic-level strain ϵ_{xx} . (B) Lattice displacements of fixed bottom surface, lower wall, upper wall, and top surface due to the kink-kink interactions. (C) The variation of interaction energies as a function of wall-wall distance. The data points in (C) are fitted by using the equation $E_{\text{kink-kink}} = E_0 - A \times d^B$ with $E_0 \sim 0$ (noninteracting kinks), $A = 0.832$ eV l.u. and $B = -1$. The scaling exponent of -1 is shown in (D).

wedges in transmission electron microscopy investigations where the imaged part of the sample is very thin but constrained by the thicker part of the specimen. Still, even in clamped samples, such as thin films on rigid substrates, rather large surface structures, such as ridges and valleys, are observed in our simulation and could be detected experimentally.

Our simulated results provide a comprehensive understanding of the elastic interactions between kinks in ferroelastic and ferroelectric domain walls. The existence of a wide crossover regime in free-standing samples indicate that their domain structures should organise differently and exhibit abnormal behaviours in response to external fields, leading to unusual functionalities (e.g., superelasticity). Future research on membranes with *in-situ* TEM or dynamic piezoresponse force microscopy should provide valuable insights and investigations on novel nanomaterials.

DECLARATIONS

Authors' contributions

Conceptualization and performance of molecular dynamic simulations; data curation; writing original draft preparation: Lu G

Writing, review, and editing: Lu G, Nataf GF, Salje EKH

Review and discussion: Lu G, Hideo K, Ding X, Xu Z, Chu R, Nataf GF, Salje EKH

Supervision: Lu G, Salje EKH

Funding acquisition: Lu G, Ding X, ESalje EKH

All authors have read and agreed to the published version of the manuscript.

Availability of data and materials

The data that support the findings of this study are available from the corresponding author upon reasonable request.

Financial support and sponsorship

This work was supported by the National Key Research and Development Program of China (2019YFA0307900). Guangming Lu is grateful for the financial support from the Doctoral Starting Fund of Yantai University (Grant No. 1115-2222006). EKHS is grateful to EPSRC (EP/P024904/1) and the EU's Horizon 2020 programme under the Marie Skłodowska-Curie Grant (861153).

Conflicts of interest

All authors declared that there are no conflicts of interest.

Ethical approval and consent to participate

Not applicable.

Consent for publication

Not applicable.

Copyright

© The Author(s) 2023.

REFERENCES

1. Bassiri-Gharb N, Fujii I, Hong E, Trolier-McKinstry S, Taylor DV, Damjanovic D. Domain wall contributions to the properties of piezoelectric thin films. *J Electroceram* 2007;19:49. [DOI](#)
2. Ishibashi Y, Takagi Y. Note on ferroelectric domain switching. *J Phys Soc Jpn* 1971;31:506-10. [DOI](#)
3. Li S, Bismayer U, Ding X, Salje EKH. Ferroelastic shear bands in $\text{Pb}_3(\text{PO}_4)_2$. *Appl Phys Lett* 2016;108:022901. [DOI](#)
4. Lu G, Li S, Ding X, Sun J, Salje EKH. Electrically driven ferroelastic domain walls, domain wall interactions, and moving needle domains. *Phys Rev Mater* 2019;3:114405. [DOI](#)
5. Nataf GF, Salje EKH. Avalanches in ferroelectric, ferroelastic and coelastic materials: phase transition, domain switching and propagation. *Ferroelectrics* 2020;569:82-107. [DOI](#)
6. He X, Li S, Ding X, Sun J, Kustov S, Salje EK. Internal friction in complex ferroelastic twin patterns. *Acta Mater* 2022;228:117787. [DOI](#)
7. Lu G, Li S, Ding X, Sun J, Salje EKH. Enhanced piezoelectricity in twinned ferroelastics with nanocavities. *Phys Rev Mater* 2020;4:074410. [DOI](#)
8. Salje EKH. Multiferroic domain boundaries as active memory devices: trajectories towards domain boundary engineering. *ChemPhysChem* 2010;11:940-50. [DOI](#) [PubMed](#)
9. Catalan G, Seidel J, Ramesh R, Scott JF. Domain wall nanoelectronics. *Rev Mod Phys* 2012;84:119-56. [DOI](#)
10. Nataf GF, Guennou M, Gregg JM, et al. Domain-wall engineering and topological defects in ferroelectric and ferroelastic materials. *Nat Rev Phys* 2020;2:634-48. [DOI](#)
11. Meier D, Selbach SM. Ferroelectric domain walls for nanotechnology. *Nat Rev Mater* 2022;7:157-73. [DOI](#)
12. Gonnissen J, Batuk D, Nataf GF, et al. Direct observation of ferroelectric domain walls in LiNbO_3 : wall-meanders, kinks, and local electric charges. *Adv Funct Mater* 2016;26:7599-604. [DOI](#)
13. Shur VY, Pelegova EV, Turygin AP, Kosobokov MS, Alikin YM. Forward growth of ferroelectric domains with charged domain walls. local switching on non-polar cuts. *J Appl Phys* 2021;129:044103. [DOI](#)
14. Gopalan V, Dierolf V, Scrymgeour DA. Defect-domain wall interactions in trigonal ferroelectrics. *Annu Rev Mater Res* 2007;37:449-89. [DOI](#)
15. Zhang L, Li S, Ding X, Sun J, Salje EKH. Statistical analysis of emission, interaction and annihilation of phonons by kink motion in ferroelastic materials. *Appl Phys Lett* 2020;116:102902. [DOI](#)

16. Dong G, Li S, Yao M, et al. Super-elastic ferroelectric single-crystal membrane with continuous electric dipole rotation. *Science* 2019;366:475-9. DOI
17. Condurache O, Dražić G, Sakamoto N, Rojac T, Benčan A. Atomically resolved structure of step-like uncharged and charged domain walls in polycrystalline BiFeO₃. *J Appl Phys* 2021;129:054102. DOI
18. Simons H, Haugen AB, Jakobsen AC, et al. Long-range symmetry breaking in embedded ferroelectrics. *Nat Mater* 2018;17:814-9. DOI
19. Jia C, Mi S, Urban K, Vrejoiu I, Alexe M, Hesse D. Atomic-scale study of electric dipoles near charged and uncharged domain walls in ferroelectric films. *Nat Mater* 2008;7:57-61. DOI PubMed
20. Nataf GF, Aktas O, Granzow T, Salje EKH. Influence of defects and domain walls on dielectric and mechanical resonances in LiNbO₃. *J Phys Condens Matter* 2016;28:015901. DOI PubMed
21. Miller RC, Weinreich G. Mechanism for the sidewise motion of 180° domain walls in barium titanate. *Phys Rev* 1960;117:1460-6. DOI
22. Shin Y, Grinberg I, Chen I, Rappe AM. Nucleation and growth mechanism of ferroelectric domain-wall motion. *Nature* 2007;449:881-4. DOI PubMed
23. Maerten L, Bojahr A, Gohlke M, Rössle M, Bargheer M. Coupling of GHz phonons to ferroelastic domain walls in SrTiO₃. *Phys Rev Lett* 2015;114:047401. DOI PubMed
24. Anbusathaiah V, Nagarajan V, Aggarwal S. Nanoscale polarization relaxation kinetics in polycrystalline ferroelectric thin films. *J Appl Phys* 2007;101:084104. DOI
25. Casals B, Nataf GF, Salje EKH. Avalanche criticality during ferroelectric/ferroelastic switching. *Nat Commun* 2021;12:345. DOI PubMed PMC
26. Lu G, Li S, Ding X, Sun J, Salje EKH. Ferroelectric switching in ferroelastic materials with rough surfaces. *Sci Rep* 2019;9:15834. DOI PubMed PMC
27. Salje EKH, Wang X, Ding X, Scott JF. Ultrafast switching in avalanche-driven ferroelectrics by supersonic kink movements. *Adv Funct Mater* 2017;27:1700367. DOI
28. Salje EKH, Ishibashi Y. Mesoscopic structures in ferroelastic crystals: needle twins and right-angled domains. *J Phys Condens Matter* 1996;8:8477. DOI
29. Lee K, Baik S. Ferroelastic domain structure and switching in epitaxial ferroelectric thin films. *Annu Rev Mater Res* 2006;36:81-116. DOI
30. Lu G, Ding X, Sun J, Salje EKH. Wall-wall and kink-kink interactions in ferroelastic materials. *Phys Rev B* 2022;106. DOI
31. Shilkrot LE, Srolovitz DJ. Elastic field of a surface step: atomistic simulations and anisotropic elastic theory. *Phys Rev B* 1996;53:11120. DOI
32. Andreev AF, Kosevich YK. Capillary phenomena in the theory of elasticity. *J Exp Theor Phys* 1981;54:761. Available from: <http://jetp.ras.ru/cgi-bin/e/index/e/54/4/p761?a=list> [Last accessed on 9 August 2023]
33. Pertsev NA, Novak J, Salje EKH. Long-range elastic interactions and equilibrium shapes of curved ferroelastic domain walls in crystals. *Philos Mag A* 2000;80:2201-13. DOI
34. Salje EKH, Ding X, Zhao Z, Lookman T, Saxena A. Thermally activated avalanches: jamming and the progression of needle domains. *Phys Rev B* 2011;83:104109. DOI
35. Lu G, Li S, Ding X, Salje EKH. Piezoelectricity and electrostriction in ferroelastic materials with polar twin boundaries and domain junctions. *Appl Phys Lett* 2019;114:202901. DOI
36. Ferrando R, Jellinek J, Johnston RL. Nanoalloys: from theory to applications of alloy clusters and nanoparticles. *Chem Rev* 2008;108:845-910. DOI PubMed
37. Nosé S. A unified formulation of the constant temperature molecular dynamics methods. *J Chem Phys* 1984;81:511-9. DOI
38. Stukowski A. Visualization and analysis of atomistic simulation data with OVITO-the open visualization tool. *Model Simul Mater Sci Eng* 2010;18:015012. DOI
39. Shima H, Umeno Y, Sumigawa T. Analytic formulation of elastic field around edge dislocation adjacent to slanted free surface. *R Soc Open Sci* 2022;9:220151. DOI PubMed PMC
40. Seifert U. Configurations of fluid membranes and vesicles. *Adv Phys* 1997;46:13-137. DOI
41. Nunes RW, Bennetto J, Vanderbilt D. Atomic structure of dislocation kinks in silicon. *Phys Rev B* 1998;57:10388-97. DOI
42. He X, Li S, Ding X, Sun J, Selbach SM, Salje EK. The interaction between vacancies and twin walls, junctions, and kinks, and their mechanical properties in ferroelastic materials. *Acta Mater* 2019;178:26-35. DOI
43. Novak J, Salje EKH. Surface structure of domain walls. *J Phys Condens Matter* 1998;10:L359-66. DOI
44. Conti S, Salje EKH. Surface structure of ferroelastic domain walls: a continuum elasticity approach. *J Phys Condens Matter* 2001;13:L847-54. DOI
45. Gurrutxaga-Lerma B, Balint DS, Dini D, Sutton AP. Elastodynamic image forces on dislocations. *Proc R Soc A* 2015;471:20150433. DOI PubMed PMC

Research Article

Open Access



Optimizing the energy storage performance of NaNbO_3 ceramics by rare-earth-based composite perovskite $\text{Sm}(\text{Mg}_{0.5}\text{Zr}_{0.5})\text{O}_3$ modification

Mingzhao Xu, Dafu Zeng, Xiang Wang, Peng Nong, Yue Pan, Qinpeng Dong, Jiaming Wang, Huanfu Zhou, Xiuli Chen

Key Laboratory of Nonferrous Materials and New Processing Technology, Ministry of Education, School of Materials Science and Engineering, Guilin University of Technology, Guilin 541004, Guangxi, China.

Correspondence to: Prof. Huanfu Zhou, Key Laboratory of Nonferrous Materials and New Processing Technology, Ministry of Education, School of Materials Science and Engineering, Guilin University of Technology, Guilin 541004, Guangxi, China. E-mail: zhouhuanfu@163.com; Prof. Xiuli Chen, Key Laboratory of Nonferrous Materials and New Processing Technology, Ministry of Education, School of Materials Science and Engineering, Guilin University of Technology, Guilin 541004, Guangxi, China. E-mail: cxlnwpu@163.com

How to cite this article: Xu M, Zeng D, Wang X, Nong P, Pan Y, Dong Q, Wang J, Zhou H, Chen X. Optimizing the energy storage performance of NaNbO_3 ceramics by rare-earth-based composite perovskite $\text{Sm}(\text{Mg}_{0.5}\text{Zr}_{0.5})\text{O}_3$ modification. *Microstructures* 2023;3:2023034. <https://dx.doi.org/10.20517/microstructures.2023.19>

Received: 20 Apr 2023 **First Decision:** 13 Jul 2023 **Revised:** 9 Aug 2023 **Accepted:** 17 Aug 2023 **Published:** 1 Sep 2023

Academic Editor: Shujun Zhang **Copy Editor:** Fangyuan Liu **Production Editor:** Fangyuan Liu

Abstract

Researchers often improve the energy storage performance of NaNbO_3 ceramics through doping with Bi-based composites. Recent studies have shown that rare-earth elements, such as La and Sm, can suppress remanent polarization. In this study, a $(1-x)\text{NaNbO}_3\text{-}x\text{Sm}(\text{Mg}_{0.5}\text{Zr}_{0.5})\text{O}_3$ ceramic system was designed. Doping with $\text{Sm}(\text{Mg}_{0.5}\text{Zr}_{0.5})\text{O}_3$ (SMZ) increases the resistance, activation energy, and bandgap of NaNbO_3 ceramics, improves the breakdown field strength, and optimizes the energy storage efficiency of NaNbO_3 ceramics. In this study, $0.92\text{NaNbO}_3\text{-}0.08\text{SMZ}$ achieved an energy storage density of $4.3/\text{cm}^3$ and an energy storage efficiency of 85.6% at 560 kV/cm. When $x = 0.15$, the sample exhibited an ultrahigh breakdown field strength and energy storage efficiency (720 kV/cm and 91%, respectively). In addition, the 0.08 SMZ sample had an ultrafast release rate of $t_{0.9}$ (57 ns), high current density ($777.1\text{ A}/\text{cm}^2$), and high power density ($69.93\text{ MW}/\text{cm}^3$). It has practical application prospects in high-performance energy storage capacitors.

Keywords: NaNbO_3 , energy storage density, rare-earth modification



© The Author(s) 2023. **Open Access** This article is licensed under a Creative Commons Attribution 4.0 International License (<https://creativecommons.org/licenses/by/4.0/>), which permits unrestricted use, sharing, adaptation, distribution and reproduction in any medium or format, for any purpose, even commercially, as long as you give appropriate credit to the original author(s) and the source, provide a link to the Creative Commons license, and indicate if changes were made.



INTRODUCTION

NaNbO₃-based energy storage dielectric ceramics have excellent electrical properties, such as antiferroelectric (AFE) properties, high polarization strength, and relative breakdown resistance. They are lightweight and have a wide working temperature range, which is beneficial for practical applications and has attracted the attention of many researchers^[1,2]. By using NaNbO₃ as the base and adding a variety of structural compounds to form solid solutions with different properties, energy storage dielectric ceramics with excellent performance can be obtained^[3,4]. However, as an AFE material, NaNbO₃ decreases the energy storage efficiency owing to the large polarization hysteresis caused by the inevitable field-induced AFE-relaxor ferroelectric (FE) phase transition while obtaining a high energy density^[5,6].

Researchers often adjust the relaxation behavior of ceramics, reduce the average grain size, stabilize the AFE type, and delay the AFE-FE transition by incorporating doping Bi-based composite perovskites to improve the energy storage performance of NaNbO₃-based ceramics. For instance, NaNbO₃ doped with Bi(Ni_{0.5}Zr_{0.5})O₃ exhibits a breakdown field strength of 500 kV/cm, an energy storage density of 4.90 kV/cm³, and an efficiency of 73%^[7]. An energy storage density of 3.70 J/cm³ and an energy storage efficiency of 77% were obtained through doping with Bi(Mg_{2/3}Nb_{1/3})O₃ ceramics with a breakdown field strength of 460 kV/cm^[1]. Good results have been achieved, but the challenge of achieving low energy storage efficiencies persists. Notably, there is still a lack of research on rare-earth-based composite perovskites.

Ye studied 0.96Na_{0.88}La_{0.12}NbO₃-0.04CaSnO₃^[8], and a 2.1 J/cm³ recoverable energy storage density (W_{rec}) and 62% energy storage efficiency (η) were obtained. Although the energy storage performance was general, doping with La inhibited P_r . The ceramics doped with La(Mg_{0.5}Zr_{0.5})O₃ in a Sr_{0.7}Bi_{0.2}TiO₃ matrix studied by Chen achieved an energy storage density of 1.22 J/cm³ and an ultrahigh energy storage efficiency of 98.2%^[9]. The energy storage density was low, but η was high. Yang^[10] obtained a 6.5 J/cm³ W_{rec} and 96% η by adding Sm³⁺ and Ti⁴⁺ to NaNbO₃. This shows that the energy storage efficiency of the matrix can be changed by doping with rare-earth elements.

In studies of NaNbO₃, BaTiO₃, and Sr_{0.7}Bi_{0.2}TiO₃ ceramics, doping with Bi (Mg_{0.5}Zr_{0.5})O₃ helped maintain good performance stability^[9,11,12]. Based on the above research, Sm(Mg_{0.5}Zr_{0.5})O₃ (SMZ) was introduced into a NaNbO₃ matrix, and (1-x)NaNbO₃-xSm(Mg_{0.5}Zr_{0.5})O₃ ($x = 0.05, 0.08, 0.12, \text{ and } 0.15$) (NN-SMZ) ceramics were designed. The electrical properties, such as energy storage performance, temperature stability, frequency stability, and resistance, were analyzed and studied. It is concluded that the energy storage performance of the matrix can be improved by doping Sm³⁺ ions at the A site of the perovskite structure, and the performance stability of the ceramics can be improved.

EXPERIMENTAL PROCEDURE

NN-SMZ was prepared using a conventional solid-state reaction. Na₂CO₃ (99.8%), Nb₂O₅ (99%), Sm₂O₃ (99.99%), ZrO₂ (99%), and MgO (98.5%) were stoichiometrically weighed and ball-milled with Zr balls in ethanol for 5 h. After drying, the mixed powders were calcined at 900 °C for 5 h and ball-milled again for 5 h. Polyvinyl alcohol (5%) was added as a binder to press the dried powder into a disk with a diameter of 8 mm and thickness of 1 mm. The disks were calcined at 550 °C for 4 h for glue extrusion. Finally, the samples were embedded in a precursor powder of the same composition and sintered at 1,340 °C for 2 h. The test instrument information during the experiment is added to the support material. The thicknesses and silver electrode areas of the samples used for P-E testing are listed in [Supplementary Table 1](#).

RESULTS AND DISCUSSION

The X-Ray diffraction analysis (XRD) patterns of the NN-SMZ ceramics are shown in [Figure 1A](#). Enlarging the characteristic peak clearly shows that with the addition of SMZ, the (200) characteristic peak shifts to a lower angle, indicating that the sample lattice has expanded^[13,14]. After doping with SMZ, Sm^{3+} (1.24 Å) partially replaces Na^+ (1.39 Å) at the A site, and Mg^{2+} (0.72 Å) and Zr^{4+} (0.72 Å) replace the smaller Nb^{5+} (0.64 Å) at the B site^[15]. The results show that the lattice expansion of the sample was mainly affected by the introduction of Mg^{2+} and Zr^{4+} at the B site^[7]. To explore the reason for this phenomenon, the NN-SMZ component samples were refined. The refined results are shown in [Figure 1B-E](#) and [Supplementary Figure 1](#). The NaNbO_3 ceramic exhibited an orthorhombic phase at room temperature; with the increase in SMZ doping, the sample gradually changed from the orthorhombic phase (*Pnma*) to the pseudocubic phase (*Pm3m*). When $x = 0.05$ and 0.08 , the sample exhibited a two-phase coexistence phenomenon. [Supplementary Figure 2](#) shows the refinement results for the NN-SMZ at 35° - 45° . The refinement result for the sample was good. As the sample gradually changed to the pseudocubic phase, the intensity of the superlattice diffraction peak gradually decreased.

The Raman spectra of each component sample are shown in [Figure 2A](#). The gradually widened peak width and gradually decreased peak intensity indicate that the complexity of the sample and the disorder of ions increased owing to the nonequivalent substitution of ions with different radii at the A and B sites^[16,17]. To study further the effect of adding SMZ to the system, Peakfit software was used to analyze the Raman spectra of each component sample. The center position, peak intensity, and peak half-width of the vibration modes ν_1 and ν_5 fitted by each Raman component are shown in [Figure 2B](#) and [C](#). With an increase in the SMZ content, the peak intensities of vibration modes ν_1 and ν_5 gradually decreased, and the half-width and height gradually increased, which proved that the complexity of the sample and the disorder of the ions increased. The vibration mode ν_5 moved to a high-wavenumber position, and a blue shift occurred. The red shift of the vibration mode ν_1 may be caused by the phase transition of the sample, which corresponds to the XRD refinement results in this study^[18].

Scanning electron microscopy (SEM) images of the NN-SMZ components under the natural surface and the average grain size fitted by the Gaussian function are shown in [Figure 3A](#). The surfaces of the NN-SMZ ceramic component samples were dense and had no obvious defects, and the average grain size generally increased. The grain sizes of 0.08 SMZ and 0.12 SMZ significantly increased. According to the XRD refinement results, the appearance of the pseudo-cubic phase is one reason for this phenomenon. According to the formula $E_b \propto G^{-1/2}$, the grain size (G) is negatively correlated with the breakdown field strength (E_b). The grain size of each component is smaller than that of pure NaNbO_3 (generally tens of micrometers)^[19,20], which helps the samples obtain a higher E_b ^[21]. The energy dispersive spectrometry (EDS) mapping of the 0.08 SMZ ceramic is shown in [Figure 3B](#). Each element was uniformly distributed without enrichment, indicating that the SMZ was uniformly dissolved in the NN lattice^[22]. An atomic force microscopy analysis was performed on the samples after hot corrosion. The test results are shown in [Supplementary Figure 3](#). The surface of each component sample was dense, without obvious pores or defects. The sintering densities of the NN-SMZ samples are shown in [Supplementary Table 2](#). The incorporation of the SMZ reduced the sintering temperature, improved the density of the ceramics, and helped the samples obtain a higher breakdown field strength.

A Transmission Electron Microscope test can effectively observe the domain morphology and phase structure of FE materials. The domain morphology of pure NaNbO_3 ceramics is shown in [Figure 4A](#) and clearly shows the existence of a 180° domain. The domain morphology of the 0.08 SMZ sample is shown in [Figure 4B](#), and the larger domain cannot be clearly observed, which is related to the gradual transition of the

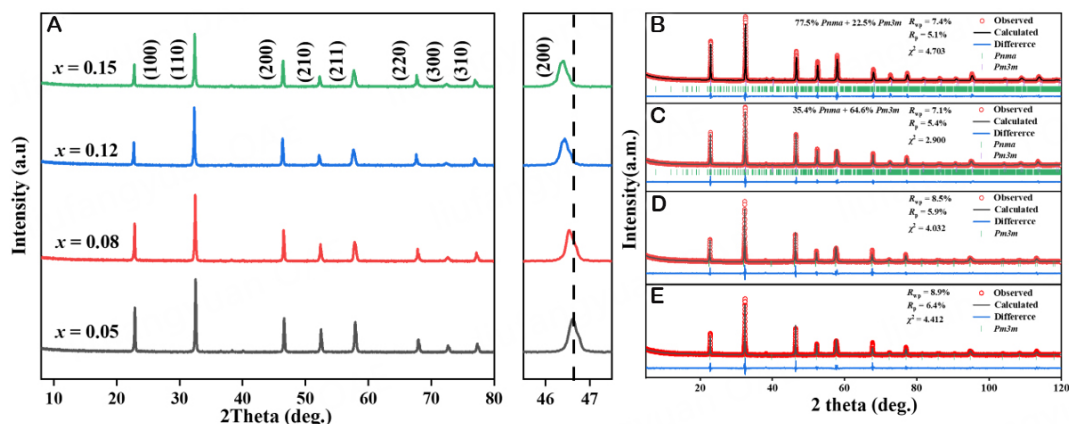


Figure 1. XRD patterns of $\text{NaNbO}_{3-x}\text{Sm}(\text{Mg}_{0.5}\text{Zr}_{0.5})\text{O}_3$ ceramics ($0.05 \leq x \leq 0.15$) (A), (B) XRD refinement of 0.05 SMZ component, (C) XRD refinement of 0.08 SMZ component, (D) XRD refinement of 0.12 SMZ component, and (E) XRD refinement of 0.15 SMZ component.

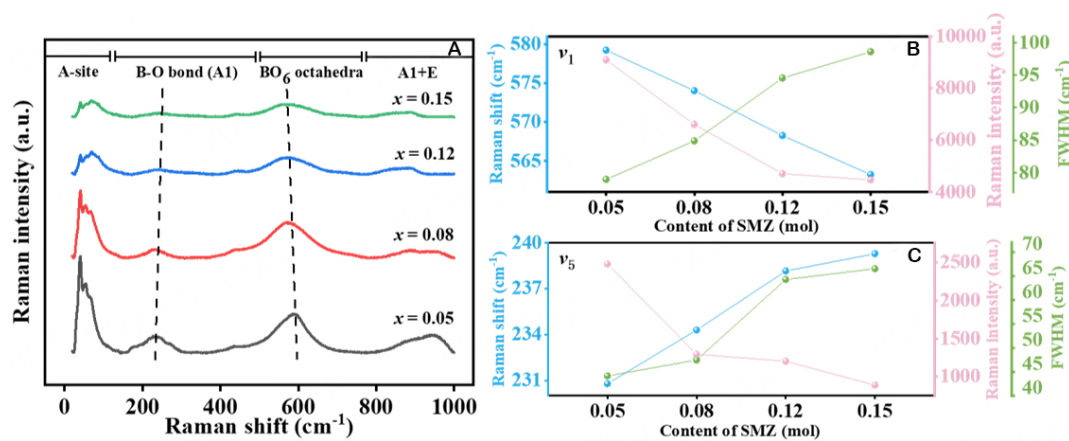


Figure 2. Raman Test Diagram of $\text{NaNbO}_{3-x}\text{Sm}(\text{Mg}_{0.5}\text{Zr}_{0.5})\text{O}_3$ ceramics ($0.05 \leq x \leq 0.15$) (A) and the Raman vibration modes ν_1 (B) and ν_5 (C) of NN-SMZ components are plotted.

phase structure of the sample to the weak polar pseudocubic phase^[23]. In NaNbO_3 ceramics, due to the presence of large-sized domains, when the polarization direction changes, the direction of the domain will be irreversible, which greatly deteriorates the energy storage performance of the ceramics. The domain sizes of the 0.08 SMZ ceramic sample were smaller, which was beneficial to the sample to obtain a faster polarization response in the charge and discharge test, reduced the polarization loss, and achieved the purpose of improving the energy storage performance of the sample^[24]. Figure 4C and D depicts selected area electron diffraction (SAED) images of 0.08 SMZ samples taken in the $[100]_c$ and $[111]_c$ directions. The presence of $(eoo)/2$ and $(oeo)/2$ in the $[100]_c$ direction and the presence of $(ooe)/2$ superlattice diffraction spots in the $[111]_c$ direction (o and e are odd and even, respectively) proved the existence of octahedral distortion, indicating that this was a commensurate modulation phase structure with two-fold unit cell. The SEAD images also proved the perovskite structure of the 0.08 SMZ sample again^[25].

To investigate the change in the dielectric constant of NN-SMZ ceramics with temperature, the dielectric constant of NN-SMZ was tested at -160 °C to 180 °C. The temperature spectra of the components are shown in Figure 5A-D, where the dielectric peaks of the components near 0 °C formed because of the

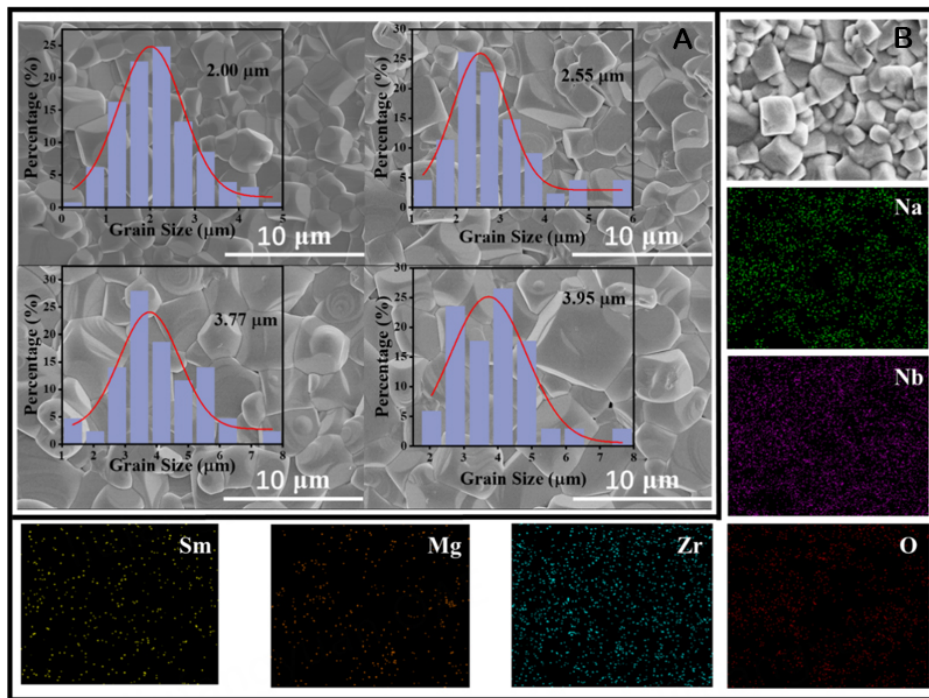


Figure 3. SEM images (A) and EDS mapping images of the NN-SMZ ceramic (B).

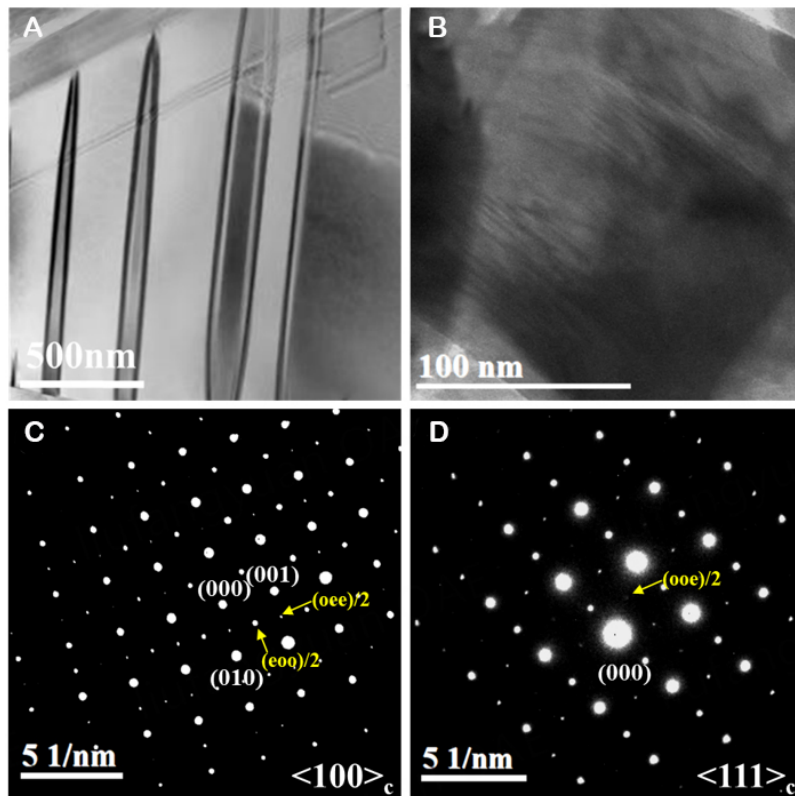


Figure 4. (A) Domain morphology of NN ceramics, (B) domain morphology of 0.08 SMZ ceramics. Lattice fringes and SAED patterns of 0.92 NN-0.08 SMZ ceramics along (C) $[100]_c$ and (D) $[111]_c$.

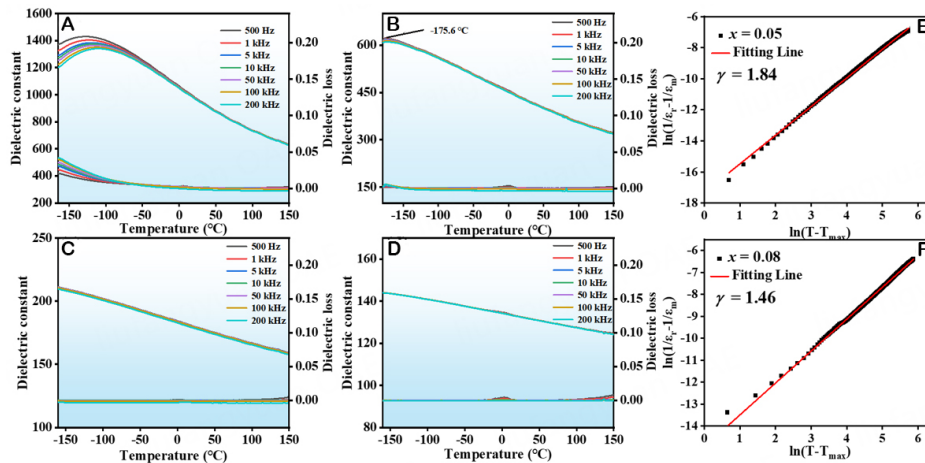


Figure 5. Temperature dependences of dielectric constant and loss of NN-SMZ ceramics: (A) $x = 0.05$, (B) $x = 0.08$, (C) $x = 0.12$, (D) $x = 0.15$. Fitting analysis of $\ln(1/\epsilon_r - 1/\epsilon_m)$ versus $\ln(T - T_m)$ for NN-SMZ ceramics at 500 kHz: (E) $x = 0.05$, (F) $x = 0.08$.

interference of ice during the temperature change. They are not phase transition peaks^[26]. The figure shows that the 0.05 SMZ sample had an obvious dielectric peak; the Curie temperature was near -120 °C, and the dielectric peak of the 0.08 SMZ sample appeared at -175.6 °C. The dielectric peaks of the 0.12 SMZ and 0.15 SMZ samples were not obtained in the test. This may have resulted from the addition of SMZ, which caused the dielectric peak of the sample to shift to a lower temperature. The Curie temperature of the 0.12 SMZ and 0.15 SMZ samples was lower than the test temperature. As the amount of SMZ doping increased, the dielectric peak of the material gradually disappeared. The $T - \epsilon_r$ curve of the material gradually becomes a flattened, somewhat straight line, showing the dielectric temperature spectrum characteristics of the linear dielectric material^[27].

The dispersion coefficients of 0.05 SMZ and 0.08 SMZ samples fitted according to the dielectric peak are shown in Figure 5E and F. The increase in the SMZ content reduces the dispersion coefficient of the sample. This means that the relaxation and the polar microregion of the sample are reduced, which is consistent with the Raman and XRD results. The frequency stability of the dielectric constant of the NN-SMZ ceramics is shown in Supplementary Figure 4. The samples of each component can maintain the stability of the dielectric constant over a wide frequency range of $10^3 - 10^6$ ^[28].

The $P - E$ curve obtained by the FE test of the sample provides direct evidence for evaluating the energy storage performance of the sample, and the relevant energy storage performance calculation formula is provided in the supporting materials^[6]. The test results for the NN-SMZ component samples at a field strength of 400 kV/cm are shown in Figure 6A-C. With an increase in x , the maximum polarization intensity P_{\max} of the sample decreased, the residual polarization intensity P_r decreased, and the obtained energy storage efficiency increased from 71.1% to 93.1%. This is because, with the incorporation of SMZ, the phase of the NN-SMZ sample gradually transformed into a weakly polar pseudocubic phase, which reduced the P_{\max} and P_r of the sample, leading to the gradual reduction of domains in the sample^[23]. The results are consistent with the results of the Raman test and dielectric-constant-frequency test, proving that the doping of rare-earth-based composite perovskites can significantly increase the energy storage efficiency of the sample. Figure 6D-F shows the maximum breakdown field strength FE test diagrams of the component samples of NN-SMZ. As the figure shows, the breakdown field strength of the sample increased with the increase in the ratio. When $x = 0.08$, the sample exhibited the best energy storage performance. The breakdown field strength of the sample was 560 kV/cm, the energy storage density was 4.3 J/cm³, and the

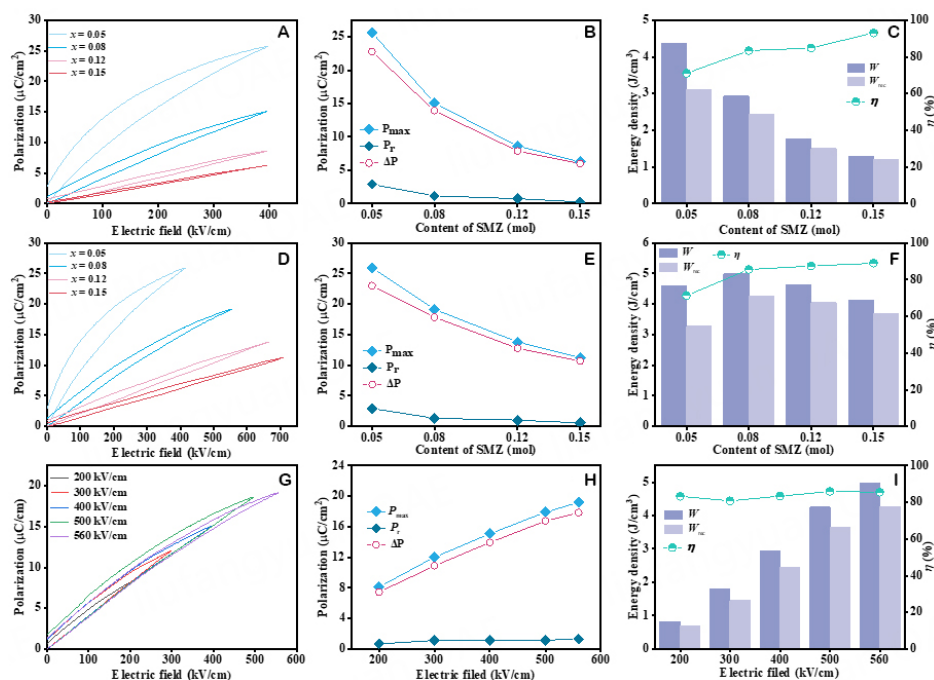


Figure 6. For NN-SMZ ceramics: at the electric field of 400 kV/cm: Unipolar P-E hysteresis loops (A), the corresponding energy storage properties (B) and polarization (C) at various content of SMZ. Unipolar P-E hysteresis loops (D), the corresponding energy storage properties (E), and polarization (F) at all content of SMZ. 0.08 SMZ unipolar P-E hysteresis loops (G), the corresponding energy storage properties (H) and polarization (I) at 0.08 SMZ.

energy storage efficiency was 85.6%. When $x = 0.15$, the breakdown field strength of the sample reached 720 kV/cm, indicating that the addition of SMZ significantly improved the E_b of the sample. Figure 6G-I shows the FE test results for the 0.08 SMZ samples under different field strengths. With an increase in the field strength, the P_{max} of the sample increased, and the number of domains that could not be flipped increased, resulting in an increase in P_r . In summary, the addition of the SMZ increased the energy storage efficiency and breakdown field strength of the samples^[29].

The frequency stability of the P-E curve of the 0.08 SMZ ceramics is shown in Figure 7A-C. At an electric field of 350 kV/cm and different frequencies, the 0.08 SMZ ceramics exhibited a stable energy storage density of 1.9 ± 0.02 J/cm³ and a stable energy storage efficiency. This shows that 0.08 SMZ ceramics have excellent frequency stability and practical application prospects^[30,31]. The temperature stability of the 0.08 SMZ ceramics is shown in Figure 7D-F. At a frequency of 10 Hz and an electric field of 350 kV/cm, the energy storage performance of the sample decreased with increasing temperature. The P_{max} and P_r of the samples increased with an increase in temperature, which may have been caused by the deterioration of the leakage current and boosted mobility of the domain walls at high temperatures^[23].

To study the intrinsic mechanism of high E_b in NN-SMZ ceramics, we discussed the non-intrinsic factors and intrinsic factors with the sample^[31]. We used the phase field method to simulate the electrical breakdown behavior of pure NaNbO₃ ceramics and 0.08 SMZ ceramic samples. The initial geometric model of the simulation was extracted from the SEM test results, and the simulation results of the final breakdown path are shown in Figure 8; the calculation formula used to simulate electrical breakdown has been provided in the support material^[32]. Figure 8A1-A3 is the simulation result of pure NaNbO₃ ceramics. There was almost no obvious electrical tree branch phenomenon observed. With the increase of time, pure NaNbO₃

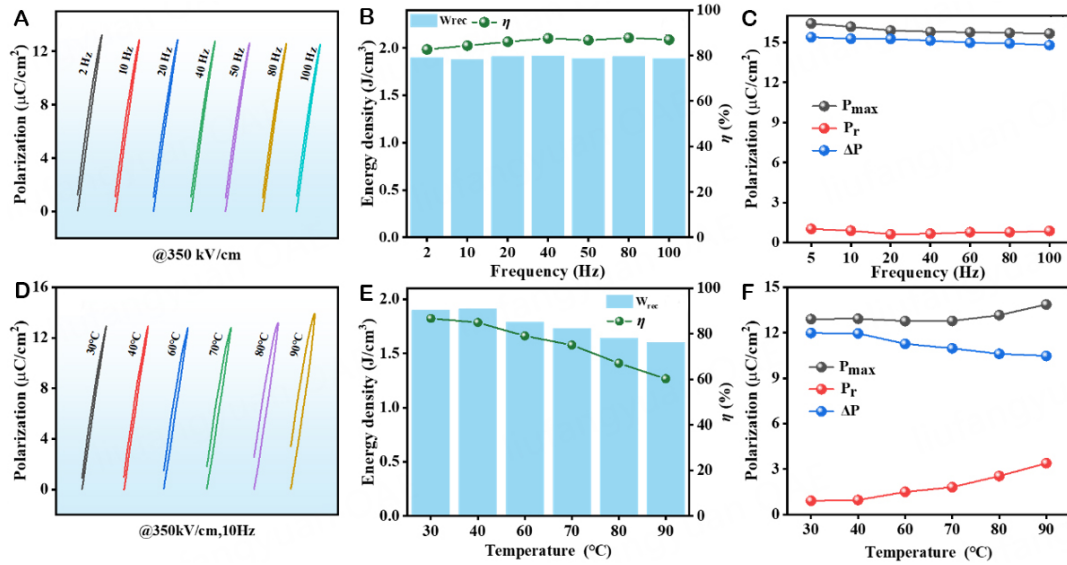


Figure 7. Unipolar P-E hysteresis loops (A and D), the corresponding energy storage properties (B and E), and P_{max} , ΔP , and P_r (C and F) for 0.08 SMZ ceramics at different frequencies and temperatures under different electric fields.

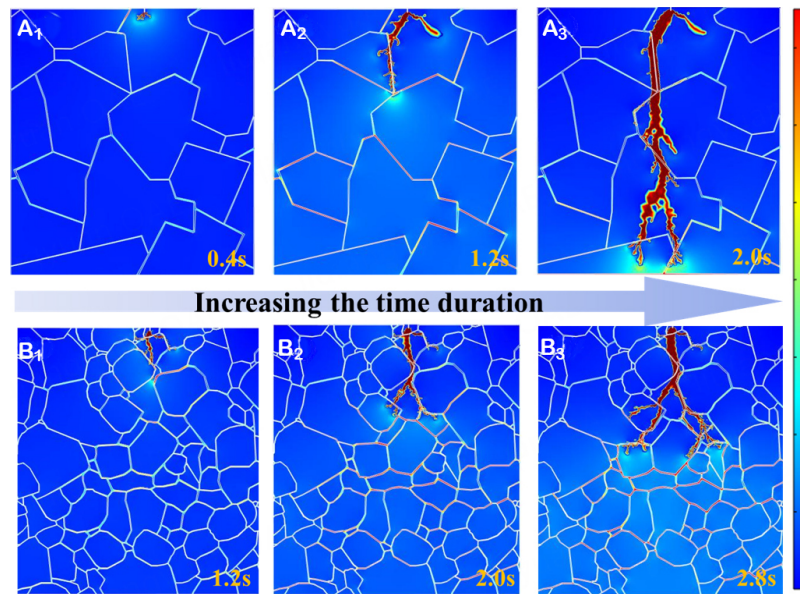


Figure 8. Breakdown paths for (1-x)NN-xSMZ samples under various times. x = 0: Figure 8A₁-A₃, x = 0.08: Figure 8B₁-B₃.

ceramics experienced a rapid electrical breakdown. The breakdown simulation of the 0.08 SMZ sample is shown in Figure 8B₁-B₃, and the electrical tree branch phenomenon of the sample can be clearly observed. The reason for this difference is that the average grain sizes of 0.08 SMZ ceramics were much smaller than those of pure NaNbO₃ ceramics. The smaller grain sizes were beneficial to generate more energy dissipation regions to suppress the breakdown behavior, which was manifested as the phenomenon of electrical tree branches. Usually, the more branches indicated that the material was more difficult to be broken down, which can also be proved by the marking time.

To understand further the intrinsic reason for the high E_b of the doped SMZ sample, impedance tests were conducted on the NN-SMZ sample. Because the impedance test pattern curve was semicircular and there was almost no difference between the grain boundary and the grain response, a set of RQC structures was used to fit the resistance of the NN-SMZ sample^[33,34]. The test and fitting results are shown in [Figure 9A-D](#). In [Supplementary Figure 5](#), the curve of the imaginary part changing with frequency has only a single peak, which also proves this point. [Supplementary Figure 6](#) shows the relationship between the AC conductivity of the NN-SMZ sample and the frequency change. The incorporation of SMZ reduced the conductivity of the sample, which was beneficial for obtaining a higher breakdown field strength.

[Figure 9E](#) shows that under the test condition of 560 °C, the resistance of the sample increased gradually with the incorporation of SMZ. When $x = 0.15$, the resistance of the sample reached a maximum value of 70,515 Ω . According to the activation energy calculation formula, the activation energy of each component is shown in [Figure 9G](#). The activation energy of the sample increases with increasing SMZ doping. In general, the higher the activation energy of the sample, the larger its energy barrier, the more energy it needs to break down, and the higher its breakdown field strength^[34,35]. To study the bandgap of the NN-SMZ ceramics further, ultraviolet test results of the samples are shown in [Figure 9F](#). The Tauc equation was used to estimate the E_g value^[36]. The E_g values of the NN-SMZ samples were 3.31, 3.37, 3.42, and 3.45 eV, which also indicated that the bandgap of the samples gradually increased^[37]. This may have been caused by the incorporation of Sm_2O_3 and ZrO_2 , which had large bandgaps. In summary, due to its significantly smaller grain size, the NN-SMZ sample obtained a higher breakdown field strength than the pure NN sample. Although the average grain sizes of each component increased with the increase of SMZ doping amount, the resistance and conductivity of each component increased. In terms of intrinsic factors, the band gap of the sample was increased, which helped the sample to obtain a high E_b .

The charge-discharge test of the sample was helpful for exploring its actual energy storage capacity. The data for the NN-SMZ samples under different electric fields at room temperature are shown in [Figure 10A](#) and [B](#). In the environment of 2-18 kV, the I_{\max} of the sample gradually increased to 54.9 A, the current density of the sample increased from 172.7 A/cm² to 777.1 A/cm², and the power density of the sample increased to 69.93 MW/cm³^[35,38]. The charge-discharge test of samples was performed in the range of 30 °C-100 °C under a field strength of 16 kV/mm. The results are shown in [Supplementary Figure 7](#). The I_{\max} value of the sample was 48.93 ± 3 A, the current power was 692 ± 40 A/cm², and the change rate of the test results was within 5%, indicating that NN-SMZ can maintain stable performance under working environments with different temperatures^[38,39].

To judge the feasibility of the practical application of the NN-SMZ ceramics, a 210- Ω resistor was connected to perform an overdamped charge-discharge test on the sample. As shown in [Figure 10C](#) and [D](#) and [Supplementary Figure 8A](#), when the applied electric field of the 0.08 SMZ sample gradually increased to 18 kV/cm at 30 °C, the current increased to 11.5 A, the discharge energy density W_d increased to 0.33 J/cm³, and an ultrafast stable discharge time ($t_{0.9}$) of 57 ± 5 ns was obtained. As shown in [Supplementary Figure 8B-D](#), when the temperature of the 0.08 SMZ sample increased from 30 °C to 100 °C under the condition of 16 kV/cm, the current remained at a stable value of $10.185 \text{ A} \pm 1\%$, and the value of $t_{0.9}$ was stable at 55 ± 3 ns. This shows that 0.08 SMZ can maintain stable performance under working conditions with different temperatures and meet the needs of actual pulse capacitors^[40-42].

CONCLUSION

In this study, NN-SMZ was prepared by solid-phase sintering. The crystal phase of NN-SMZ gradually changed from the orthorhombic phase ($Pnma$) to the pseudocubic phase ($Pm3m$) with increasing SMZ

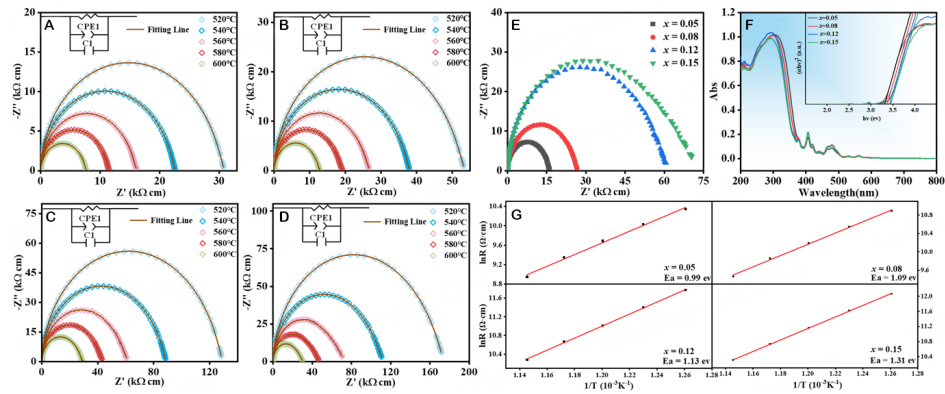


Figure 9. Impedance diagram of NN-SMZ ceramics. (A) $x = 0.05$, (B) $x = 0.08$, (C) $x = 0.12$, and (D) $x = 0.15$. (E) Impedance diagram of NN-SMZ components at 560 °C, (F) Band gap energy for NN-SMZ ceramics, (G) The fitted activation energy of NN-SMZ.

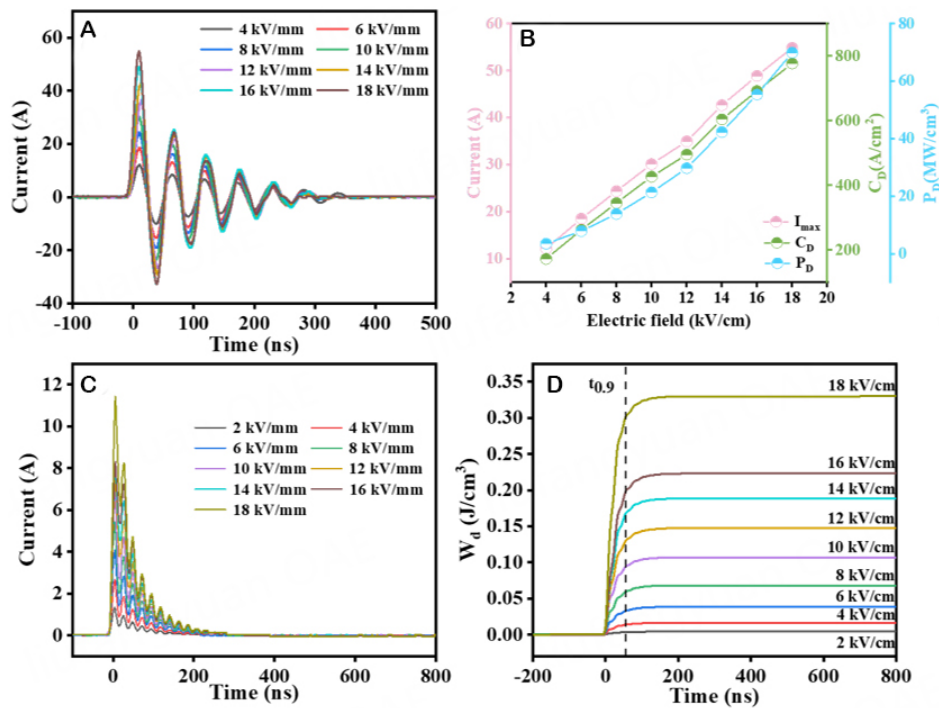


Figure 10. (A) Underdamped discharge waveform of 0.08 SMZ ceramics at room temperature. (B) The changes of I_{max} , C_D , and P_D at room temperature. (C) Over-damped discharge current curves of 0.08 SMZ ceramics at different temperatures. (D) The changes of I_{max} , C_D , and P_D under different conditions.

doping. Meanwhile, an increase in the SMZ significantly reduced the residual polarization intensity of the system and improved the breakdown field strength, resistance, and activation energy of the system. In addition, 0.92NaNbO₃-0.08 SMZ achieved a 4.3 J/cm³ energy storage density and 85.6% energy storage efficiency at 560 kV/cm. Finally, the 0.08 SMZ ceramics showed excellent dielectric stability in charge and discharge tests, indicating their potential for practical applications. In summary, rare-earth-based composite perovskites can be used to optimize the energy storage performance of NaNbO₃ ceramics.

DECLARATIONS

Authors' contributions

Writing original draft, Writing review and editing: Xu M

Conceptualization : Xu M, Zhou H, Chen X

Methodology: Xu M

Investigation and data curation: Xu M, Zeng D, Wang X, Nong P, Pan Y, Dong Q, Wang J

Supervision, project administration and funding acquisition: Zhou H, Chen X

Availability of data and materials

Not applicable.

Financial support and sponsorship

This work was supported by the Natural Science Foundation of China (No. 12064007, No. 11664008 and No. 61761015), Natural Science Foundation of Guangxi (No. 2018GXNSFFA050001, No. 2017GXNSFDA198027, and No. 2017GXNSFFA198011), and High-Level Innovation Team and Outstanding Scholar Program of Guangxi Institutes.

Conflicts of interest

All authors declared that there are no conflicts of interest.

Ethical approval and consent to participate

Not applicable.

Consent for publication

Not applicable.

Copyright

© The Author(s) 2023.

REFERENCES

1. Wang X, Dong Q, Pan Y, et al. Enhanced energy storage performances of Bi(Ni_{1/2}Sb_{2/3})O₃ added NaNbO₃ relaxor ferroelectric ceramics. *Ceram Int* 2022;48:13862-8. DOI
2. Wang W, Zhang L, Shi W, et al. Enhanced energy storage properties in lead-free (Na_{0.5}Bi_{0.5})_{0.7}Sr_{0.3}TiO₃-based relaxor ferroelectric ceramics through a cooperative optimization strategy. *ACS Appl Mater Interfaces* 2023;15:6990-7001. DOI
3. Pan Y, Wang X, Dong Q, et al. Enhanced energy storage properties of Bi(Ni_{2/3}Nb_{1/6}Ta_{1/6})O₃-NaNbO₃ solid solution lead-free ceramics. *Ceram Int* 2022;48:26466-75. DOI
4. Dong Q, Wang X, Wang J, et al. Enhanced energy storage performance in Na_(1-3x)BixNb_{0.85}Ta_{0.15}O₃ relaxor ferroelectric ceramics. *Ceram Int* 2022;48:776-83. DOI
5. Xie A, Qi H, Zuo R, Tian A, Chen J, Zhang S. An environmentally-benign NaNbO₃ based perovskite antiferroelectric alternative to traditional lead-based counterparts. *J Mater Chem C* 2019;7:15153-61. DOI
6. Xie A, Zuo R, Qiao Z, Fu Z, Hu T, Fei L. NaNbO₃-(Bi_{0.5}Li_{0.5})TiO₃ lead-free relaxor ferroelectric capacitors with superior energy-storage performances via multiple synergistic design. *Adv Energy Mater* 2021;11:2101378. DOI
7. Chen H, Chen X, Shi J, et al. Achieving ultrahigh energy storage density in NaNbO₃-Bi(Ni_{0.5}Zr_{0.5})O₃ solid solution by enhancing the breakdown electric field. *Ceram Int* 2020;46:28407-13. DOI
8. Ye J, Wang G, Chen X, Dong X. Effect of rare-earth doping on the dielectric property and polarization behavior of antiferroelectric sodium niobate-based ceramics. *J Mater* 2021;7:339-46. DOI
9. Chen J, Si F, Zhao P, Zhang S, Tang B. Novel lead-free (1-x)Sr_{0.7}Bi_{0.2}TiO_{3-x}La(Mg_{0.5}Zr_{0.5})O₃ energy storage ceramics with high charge-discharge and excellent temperature-stable dielectric properties. *Ceram Int* 2021;47:26215-23. DOI
10. Yang L, Qi J, Yang M, et al. High comprehensive energy storage properties in (Sm, Ti) co-doped sodium niobate ceramics. *Appl Phys Lett* 2023;122:192901. DOI
11. Qu N, Du H, Hao X. A new strategy to realize high comprehensive energy storage properties in lead-free bulk ceramics. *J Mater Chem C* 2019;7:7993-8002. DOI

12. Yuan Q, Li G, Yao F, et al. Simultaneously achieved temperature-insensitive high energy density and efficiency in domain engineered BaTiO₃-Bi(Mg_{0.5}Zr_{0.5})O₃ lead-free relaxor ferroelectrics. *Nano Energy* 2018;52:203-10. DOI
13. Zeng D, Dong Q, Nong P, et al. Achieving high energy storage density in BaTiO₃- (Bi_{0.5}Li_{0.5})(Ti_{0.5}Sn_{0.5})O₃ lead-free relaxor ferroelectric ceramics. *J Alloys Compd* 2023;937:168455. DOI
14. Dong X, Li X, Chen H, et al. Realizing enhanced energy storage and hardness performances in 0.90NaNbO₃-0.10Bi(Zn_{0.5}Sn_{0.5})O₃ ceramics. *J Adv Ceram* 2022;11:729-41. DOI
15. Shannon RD. Revised effective ionic radii and systematic studies of interatomic distances in halides and chalcogenides. *Acta Cryst A* 1976;32:751-67. DOI
16. Hreščak J, Dražić G, Deluca M, et al. Donor doping of K_{0.5}Na_{0.5}NbO₃ ceramics with strontium and its implications to grain size, phase composition and crystal structure. *J Eur Ceram Soc* 2017;37:2073-82. DOI
17. Schulz T, Veerapandiyar VK, Gindler T, Deluca M, Töpfer J. Hexavalent (Me - W/Mo)-modified (Ba,Ca)TiO₃-Bi(Mg,Me)O₃ perovskites for high-temperature dielectrics. *J Am Ceram Soc* 2020;103:6881-92. DOI
18. Chen H, Wang X, Dong X, et al. Adjusting the energy-storage characteristics of 0.95NaNbO₃-0.05Bi(Mg_{0.5}Sn_{0.5})O₃ ceramics by doping linear perovskite materials. *ACS Appl Mater Interfaces* 2022;14:25609-19. DOI
19. Shi J, Chen X, Sun C, et al. Superior thermal and frequency stability and decent fatigue endurance of high energy storage properties in NaNbO₃-based lead-free ceramics. *Ceram Int* 2020;46:25731-7. DOI
20. Xie A, Qi H, Zuo R. Achieving remarkable amplification of energy-storage density in two-step sintered NaNbO₃-SrTiO₃ antiferroelectric capacitors through dual adjustment of local heterogeneity and grain scale. *ACS Appl Mater Interfaces* 2020;12:19467-75. DOI PubMed
21. Dai Z, Xie J, Fan X, et al. Enhanced energy storage properties and stability of Sr(Sc_{0.5}Nb_{0.5})O₃ modified 0.65BaTiO₃-0.35Bi_{0.5}Na_{0.5}TiO₃ ceramics. *Chem Eng J* 2020;397:125520. DOI
22. Wang H, Yuan H, Li X, et al. Enhanced energy density and discharged efficiency of lead-free relaxor (1-x)[(Bi_{0.5}Na_{0.5})_{0.94}Ba_{0.06}La_{0.02}TiO_{3-x}KNb_{0.6}Ta_{0.4}O₃] ceramic capacitors. *Chem Eng J* 2020;394:124879. DOI
23. Li X, Xing J, Wang F, et al. Realizing high energy density and efficiency simultaneously in (Bi_{0.5}Na_{0.5})_{0.7}Sr_{0.3}TiO₃-based ceramics via introducing linear dielectric CaTiO₃. *J Mater Chem A* 2022;10:18343-53. DOI
24. Liu G, Chen L, Qi H. Energy storage properties of NaNbO₃-based lead-free superparaelectrics with large antiferrodistortion. *Microstructures* 2023;3:2023009. DOI
25. Xie A, Chen J, Zuo J, et al. Excellent energy-storage performance of (0.85 - x)NaNbO₃-xNaSbO₃-0.15(Na_{0.5}La_{0.5})TiO₃ antiferroelectric ceramics through B-site Sb⁵⁺ driven phase transition. *ACS Appl Mater Interfaces* 2023;15:22301-9. DOI
26. Pang F, Chen X, Shi J, et al. Bi(Mg_{0.5}Sn_{0.5})O₃-doped NaNbO₃ lead-free ceramics achieve excellent energy-storage and charge/discharge performances. *ACS Sustain Chem Eng* 2021;9:4863-71. DOI
27. Ding Y, Li P, He J, et al. Simultaneously achieving high energy-storage efficiency and density in Bi-modified SrTiO₃-based relaxor ferroelectrics by ion selective engineering. *Compos B Eng* 2022;230:109493. DOI
28. Zhou M, Liang R, Zhou Z, Dong X. Novel BaTiO₃-based lead-free ceramic capacitors featuring high energy storage density, high power density, and excellent stability. *J Mater Chem C* 2018;6:8528-37. DOI
29. Yadav AK, Fan H, Yan B, et al. High strain and high energy density of lead-free (Bi_{0.50}Na_{0.40}K_{0.10})_{0.94}Ba_{0.06}Ti_(1-x)(Al_{0.50}Ta_{0.50})_xO₃ perovskite ceramics. *J Mater Sci* 2020;55:11137-50. DOI
30. Li T, Chen P, Li F, Wang C. Energy storage performance of Na_{0.5}Bi_{0.5}TiO₃-SrTiO₃ lead-free relaxors modified by AgNb_{0.85}Ta_{0.15}O₃. *Chem Eng J* 2021;406:127151. DOI
31. Li X, Tan Z, Xing J, et al. Simultaneous enhancement of energy storage and hardness performances in (Na_{0.5}Bi_{0.5})_{0.7}Sr_{0.3}TiO₃-based relaxor ferroelectrics via multiscale regulation. *ACS Appl Mater Interfaces* 2022;14:42245-57. DOI
32. Cai Z, Wang X, Hong W, Luo B, Zhao Q, Li L. Grain-size-dependent dielectric properties in nanograin ferroelectrics. *J Am Ceram Soc* 2018;101:5487-96. DOI
33. Li F, Zhai J, Shen B, Zeng H, Jian X, Lu S. Multifunctionality of lead-free BiFeO₃-based ergodic relaxor ferroelectric ceramics: high energy storage performance and electrocaloric effect. *J Alloys Compd* 2019;803:185-92. DOI
34. Zhao N, Fan H, Li C, Huang F, Cao J, Li Z. Enhanced energy storage density and efficiency in Sm³⁺-doped ((Bi_{0.5}Na_{0.5})_{0.7}(Sr_{0.7}Bi_{0.2})_{0.3})TiO₃ ceramics. *J Mater Sci Mater Electron* 2021;32:24930-8. DOI
35. Zhang M, Yang H, Li D, Lin Y. Excellent energy density and power density achieved in K_{0.5}Na_{0.5}NbO₃-based ceramics with high optical transparency. *J Alloys Compd* 2020;829:154565. DOI
36. Pu Y, Wang W, Guo X, Shi R, Yang M, Li J. Enhancing the energy storage properties of Ca_{0.5}Sr_{0.5}TiO₃-based lead-free linear dielectric ceramics with excellent stability through regulating grain boundary defects. *J Mater Chem C* 2019;7:14384-93. DOI
37. Dong X, Li X, Chen X, Wu J, Zhou H. Simultaneous enhancement of polarization and breakdown strength in lead-free BaTiO₃-based ceramics. *Chem Eng J* 2021;409:128231. DOI
38. Tian A, Zuo R, Qi H, Shi M. Large energy-storage density in transition-metal oxide modified NaNbO₃-Bi(Mg_{0.5}Ti_{0.5})O₃ lead-free ceramics through regulating the antiferroelectric phase structure. *J Mater Chem A* 2020;8:8352-9. DOI
39. Muhammad R, Ali A, Camargo J, et al. Enhanced thermal stability in dielectric properties of NaNbO₃-modified BaTiO₃-BiMg_{1/2}Ti_{1/2}O₃ ceramics for X9R-MLCC applications. *Crystals* 2022;12:141. DOI
40. Xu M, Wang X, Nong P, et al. 0.90(0.88NaNbO₃-0.12Bi(Ni_{0.5}Zr_{0.5})O₃)-0.10CaTiO₃ lead-free dielectric ceramics with high energy storage properties. *ACS Appl Energy Mater* 2023;6:1630-8. DOI

41. Li X, Cheng Y, Wang F, et al. Enhancement of energy storage and hardness of $(\text{Na}_{0.5}\text{Bi}_{0.5})_{0.7}\text{Sr}_{0.3}\text{TiO}_3$ -based relaxor ferroelectrics via introducing $\text{Ba}(\text{Mg}_{1/3}\text{Nb}_{2/3})\text{O}_3$. *Chem Eng J* 2022;431:133441. DOI
42. Lin Y, Li D, Zhang M, Yang H. $(\text{Na}_{0.5}\text{Bi}_{0.5})_{0.7}\text{Sr}_{0.3}\text{TiO}_3$ modified by $\text{Bi}(\text{Mg}_{2/3}\text{Nb}_{1/3})\text{O}_3$ ceramics with high energy-storage properties and an ultrafast discharge rate. *J Mater Chem C* 2020;8:2258-64. DOI

Research Article

Open Access



Investigation of BiFeO₃-BaTiO₃ lead-free piezoelectric ceramics with nonstoichiometric bismuth

Hailan Qin^{1,2}, Jianwei Zhao², Xiaoxin Chen^{1,2}, Hongtian Li^{1,2}, Shenghao Wang², Yuxiao Du², Huanfu Zhou¹, Peifeng Li², Dawei Wang³

¹College of Materials Science and Engineering, Guilin University of Technology, Guilin 541004, Guangxi, China.

²Shenzhen Institute of Advanced Electronic Materials, Shenzhen Institute of Advanced Technology, Chinese Academy of Sciences, Shenzhen 518055, Guangdong, China.

³School of Instrumentation Science and Engineering, Harbin Institute of Technology, Harbin 150080, Heilongjiang, China.

Correspondence to: Prof. Huanfu Zhou, College of Materials Science and Engineering, Guilin University of Technology, Guilin 541004, Guangxi, China. E-mail: zhouhuanfu@163.com; Prof. Peifeng Li, Shenzhen Institute of Advanced Electronic Materials, Shenzhen Institute of Advanced Technology, Chinese Academy of Sciences, Shenzhen 518055, Guangdong, China. E-mail: pf.li1@siat.ac.cn; Prof. Dawei Wang, School of Instrumentation Science and Engineering, Harbin Institute of Technology, Harbin 150080, Heilongjiang, China. E-mail: wangdawei102@gmail.com

How to cite this article: Qin H, Zhao J, Chen X, Li H, Wang S, Du Y, Zhou H, Li P, Wang D. Investigation of BiFeO₃-BaTiO₃ lead-free piezoelectric ceramics with nonstoichiometric bismuth. *Microstructures* 2023;3:2023035. <https://dx.doi.org/10.20517/microstructures.2023.34>

Received: 28 Jun 2023 **First Decision:** 22 Aug 2023 **Revised:** 23 Aug 2023 **Accepted:** 25 Aug 2023 **Published:** 19 Sep 2023

Academic Editors: Mojca Otonicar, Xiaozhou Liao **Copy Editor:** Fangyuan Liu **Production Editor:** Fangyuan Liu

Abstract

BiFeO₃-BaTiO₃ (BF-BT)-based lead-free ceramics are promising piezoelectric materials exhibiting high Curie temperatures and excellent electrochemical properties. In this study, 0.70Bi_{1+x}FeO₃-0.30BaTiO₃ (Bi_{1+x}F-BT, x = -0.01, 0.00, 0.01, 0.02, 0.03, 0.04) lead-free piezoelectric ceramics were successfully fabricated via the conventional solid-phase reaction process. Crystallographic structure, microstructure, dielectric, impedance, ferroelectric, and piezoelectric properties among different compositions were comprehensively investigated. The X-ray diffraction analysis confirmed that all compositions exhibited a typical perovskite structure with a cubic-rhombohedral phase mixture. The grain size of ceramics tends to increase as the Bi₂O₃ content rises. In particular, the backscattered electron images and energy dispersive analysis revealed prominent core-shell microstructure within grains. Notably, the BF-BT ceramic containing 1% excess Bi displayed the maximum d_{33} ~217 pC/N and d_{33}^* ~243 pm/V accompanied by a high Curie temperature of 515 °C. The findings demonstrate the potential feasibility of BF-BT ceramics in the field of lead-free piezoelectric ceramics.

Keywords: Piezoelectric ceramics, lead-free, BF-BT, bismuth, nonstoichiometric



© The Author(s) 2023. **Open Access** This article is licensed under a Creative Commons Attribution 4.0 International License (<https://creativecommons.org/licenses/by/4.0/>), which permits unrestricted use, sharing, adaptation, distribution and reproduction in any medium or format, for any purpose, even commercially, as long as you give appropriate credit to the original author(s) and the source, provide a link to the Creative Commons license, and indicate if changes were made.

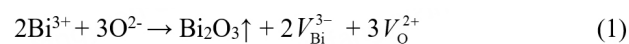


INTRODUCTION

Piezoelectric ceramics are extensively employed in electronic devices, such as sensors, actuators, filters, ultrasonic devices, *etc.*, which are realized through the mutual conversion between mechanical and electrical energies^[1-3]. Over decades, Pb(Zr_xTi_{1-x})O₃-based piezoelectric ceramics have been used dominantly in commercial devices. However, the toxicity of lead (Pb) can cause irreversible damage to human health and the environment, which promotes research hotspots on lead-free materials^[4-6]. Among the lead-free materials, (K,Na)NbO₃ (KNN)-based and Bi_{1/2}Na_{1/2}TiO₃ (BNT)-based piezoelectric ceramics are considered to be promising candidates for lead-based piezoelectric ceramics^[7-10]. Despite the high piezoelectric coefficient ($d_{33} > 500$ pC/N), KNN ceramics suffer from certain drawbacks, such as the K and Na volatilization, unstable phase structures near room temperature, and low Curie temperatures (T_C) ~ 200 °C^[11-13]. BNT-based ceramics used to exhibit high T_C , but the volatilization of Bi and Na elements leads to unstable chemical compositions and a high coercive field; consequently, superior polarization is difficult to achieve^[14-17].

In recent years, BiFeO₃- x BaTiO₃ (BF- x BT) piezoelectric ceramics have emerged as competitive candidates in lead-free materials^[2,18-20]. As a kind of multiferroic material, BF has a rhombohedral phase perovskite structure (ABO₃), which has attracted significant attention because of its high T_C (830 °C) and excellent spontaneous polarization ($P_s = 90-100$ $\mu\text{C}/\text{cm}^2$)^[21,22]. Recent studies of BF single crystal^[23-25], polycrystalline thin film^[26-29], and epitaxial thin film^[30-34] have also been conducted, which has given researchers additional ideas for exploring and application. However, the synthesis of pure BF is usually accompanied by the generation of impurities, where excess Fe₂O₃ exceeding 5 mol % leads to the formation of pyrochlore Bi₂Fe₄O₉ and gamma-Fe₂O₃^[35]. Additionally, the volatilization of Bi and the valence reduction of Fe³⁺ to Fe²⁺ at high temperatures cause high leakage currents, resulting in challenges for practical applications^[36-38]. BT is a traditional ferroelectric material exhibiting a tetragonal phase structure at room temperature and possesses a low T_C of ~ 120 °C^[39]. It has been found that the sintering of BF- x BT solid solution can effectively suppress the generation of secondary or impurity phases and reduce the leakage current. Specifically, a morphotropic phase boundary (MPB) can be constructed when x approaches 0.30 \sim 0.35, which contributes to enhanced dielectric, piezoelectric, and ferroelectric properties while maintaining a high T_C ^[40-42].

However, one of the notable disadvantages in BF- x BT-based piezoelectric ceramics is the Bi₂O₃ volatilization during the sintering process, resulting in poor electrical resistivity and piezoelectric performance. The volatilization of Bi₂O₃ can be described by the following defect Equation (1)^[43]



The volatilization of Bi₂O₃ leads to the generation of Bi vacancies (V_{Bi}^{3-}) and O vacancies (V_{O}^{2+}) within the ceramics. Various strategies have been attempted to solve the problem. One of the most common strategies is using nonstoichiometric (excess) Bi to compensate for the loss of Bi during high-temperature sintering, as listed in [Table 1](#).

In this study, a series of 0.70Bi_{1+x}F-0.30BT ($x = -0.01, 0, 0.01, 0.02, 0.03, 0.04$) ceramics were fabricated using the conventional solid-state reaction method. The influence of Bi₂O₃ compensation on the phase structure, microstructure, dielectric, ferroelectric, and piezoelectric properties of ceramics are systematically investigated.

Table 1. Summary of ferroelectric and piezoelectric properties of BF-BT system piezoelectric ceramics with excess Bi₂O₃

Composition	d_{33}/d_{33}^*	P_r ($\mu\text{C}/\text{cm}^2$)	T_c ($^\circ\text{C}$)	References
0.70Bi _{1.02} F-0.30BT	183 pC/N	21.38	480	[44]
0.69Bi _{1.04} F-0.31BT	207 pC/N	-	-	[45]
0.70Bi _{1.02} F-0.30BT	211 pm/V	19.6	421	[46]
0.65Bi _{1.05} F-0.35BT	270 pm/V	27.61	432	[47]
0.70Bi _{1.02} F-0.30BT	214 pC/N	19.61	528	[48]
0.54Bi _{1.01} F-0.36BT-0.10BZ	197 pC/N	20	445	[49]
0.70Bi _{1.02} FMT-0.30BT	198 pC/N	-	497	[50]
0.70Bi _{1.05} F-0.30BT	180 pC/N	-	506	[43]
0.75Bi _{1.01} F-0.25BT	114 pC/N	34.4	508	[51]
0.71Bi _{1.04} F-0.29BT	142 pC/N	-	452	[52]

MATERIALS AND METHODS

0.70Bi_{1+x}FeO₃-0.30BaTiO₃ (B_{1+x}F-BT, $x = -0.01, 0.00, 0.01, 0.02, 0.03, 0.04$) piezoelectric ceramics were fabricated using a solid-state reaction process. Bi₂O₃ (99%, Sinopharm, China), Fe₂O₃ (99.9%, Aladdin, China), BaCO₃ (99%, Sinopharm, China), and TiO₂ (98%, Sinopharm, China) powders were employed as raw materials. All powders were weighed according to stoichiometric ratios and ball-milled for 24 h using zirconia balls in ethanol. The mixed slurry was dried and calcined at 750 °C in a sealed alumina crucible for 2 h, followed by a secondary ball-milling process for 12 h. The calcined powder was mixed with a 10 wt% polyvinyl alcohol (PVA) binder, and the green pellets with a diameter of 10 mm were formed under a pressure of 127 MPa. The green pellets were kept at 600 °C for 2 h to burn out PVA and then sintered into ceramics at 1,010 °C for 3 h to obtain ceramics. Silver paste was sintered on parallel ceramic surfaces to form electrodes for electrical measurements.

The crystal structure and morphology were probed by the X-ray powder diffraction (XRD, D8 Advance X, Bruker, Germany) with Cu-K α radiation and the scanning electron microscope (SEM, Apreo 2, Thermo Scientific, United States) equipped with an energy-dispersive spectroscopy (EDS) detector, respectively. The dielectric and impedance properties were measured via a precision LCR meter (E4980A, Agilent Technologies, United States) connected to a high-temperature dielectric test system (DMS-1000, Balab Technology, China). The ferroelectric hysteresis (*PE*) loops and field-induced strain (*SE*) curves were collected by a ferroelectric tester station (PK-10E, PolyK Technologies, United States). The piezoelectric coefficient (d_{33}) is recorded by a quasi-static d_{33} meter (SA1303A, PolyK Technology, United States).

RESULTS AND DISCUSSION

The XRD results reveal that all B_{1+x}F-BT compositions exhibit a perovskite structure with a phase mixture consisting of cubic ($Pm\bar{3}m$) and rhombohedral ($R3c$) phases, as shown in Figure 1A. The impurity of Bi₂₅FeO₄₀, a common occurrence in the BF-BT system^[37], is appeared when $x \geq 0.03$. The enlarged (111) and (200) peaks show insignificant peak shifts with varying Bi₂O₃ content. The refined results for each component are displayed in Figure 1B and Table 2. The cubic phase gradually decreases as the Bi₂O₃ content increases and tends to stabilize at $x \geq 0.01$, according to this Table. This demonstrates that the phase structure changes from the Bi₂O₃-deficient to the Bi₂O₃-excess tends to change from the cubic phase to the rhombohedral phase, while the excess Bi₂O₃ phase structure has little effect, which is also reflected in the lattice parameter.

Table 2. The rietveld refinement data of the observed XRD patterns for $B_{1+x}F$ -BT ceramics

x	Phase fraction (%)		Rhombohedral			Cubic		R_{wp}	χ^2
	Rhombohedral (R3c)	Cubic ($Pm\bar{3}m$)	a (Å)	c (Å)	V (Å ³)	a (Å)	V (Å ³)		
-0.01	38	62	5.6454	13.8319	381.781	3.9989	63.948	8.0	1.41
0.00	54	46	5.6437	13.8376	381.704	3.9991	63.958	9.3	1.73
0.01	66	34	5.6393	13.8590	381.689	4.0045	64.281	8.8	1.49
0.02	65	35	5.6396	13.8614	381.805	4.0084	64.407	8.6	1.52
0.03	77	23	5.6389	13.8669	381.854	4.0063	64.303	9.5	1.74
0.04	74	26	5.6389	13.8654	381.812	4.0075	64.363	9.2	1.67

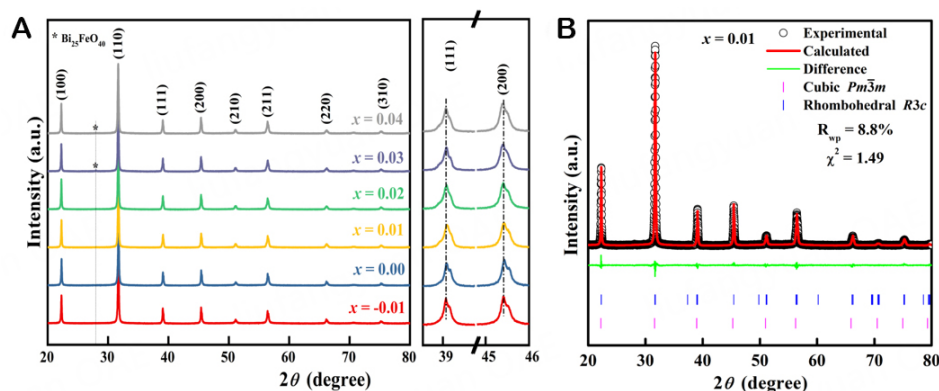
**Figure 1.** (A) XRD patterns of the $B_{1+x}F$ -BT ceramics, (B) the Rietveld refinement results for $x = 0.01$.

Figure 2 shows the surface morphology of the $B_{1+x}F$ -BT ceramics in different compositions. The ceramic surface exhibits a compact morphology with clear grain boundaries and seldom pores. The calculated relative density is higher than 95% for all compositions [Supplementary Figure 1], which is consistent with the observations from SEM results. Statistical analysis of the grain size distributions reveals that the grains tend to increase with enriching the Bi_2O_3 content. The ceramic grain size increases from 4.01 μm of $x = -0.01$ to 9.62 μm of $x = 0.04$. It is evident that the excess Bi_2O_3 not only compensates for volatilization but also acts as a sintering aid promoting grain growth, which is consistent with the literature^[46,47].

Figure 3 shows the backscattered electron (BSE) images of the polished surface of $B_{1+x}F$ -BT ceramics with the corresponding elemental mapping results by EDS. A BSE image is used to see the dark and bright contrast, showing the light and heavy element distributions to evidence the core-shell structure in grains, and EDS helps further identify the exact elements in the core and shell regions. The images reveal a non-uniform distribution of elements inside the ceramic, leading to a distinct core-shell microstructure, which is caused by immiscibility of the dominantly ionically bonded BT and covalently bonded BF phases and the microscopic segregation of elements that forms during the slow cooling process of sintering^[3,53-56]. Murakami *et al.* synthesized the $0.05BiScO_3-(0.95-x)BaTiO_3-xBiFeO_3$ ceramics without a discernible core-shell microstructure^[53]; it is proven that the BF-BT lattice can be replaced by dopants in the narrow range of the ionic radius ($R_{Sc^{3+}}: 0.745$; $R_{Ti^{4+}}: 0.605$; $R_{Fe^{3+}}: 0.645\text{\AA}$)/electronegativity ($E_{Sc^{3+}}: 1.3$; $E_{Ti^{4+}}: 1.5$; $E_{Fe^{3+}}: 1.8$) difference so as to prevent phase separation during slow cooling processes. Notably, there is a noticeable contrast between light and dark regions in Figure 3. The core, enriched with Bi and Fe, appears brighter, while the shell, enriched with Ba and Ti, appears relatively darker. In addition, the BSE images of $x = -0.01$ and $x = 0.03$ and the distribution of EDS elements are shown in Supplementary Figure 2 and Supplementary Figure 3.

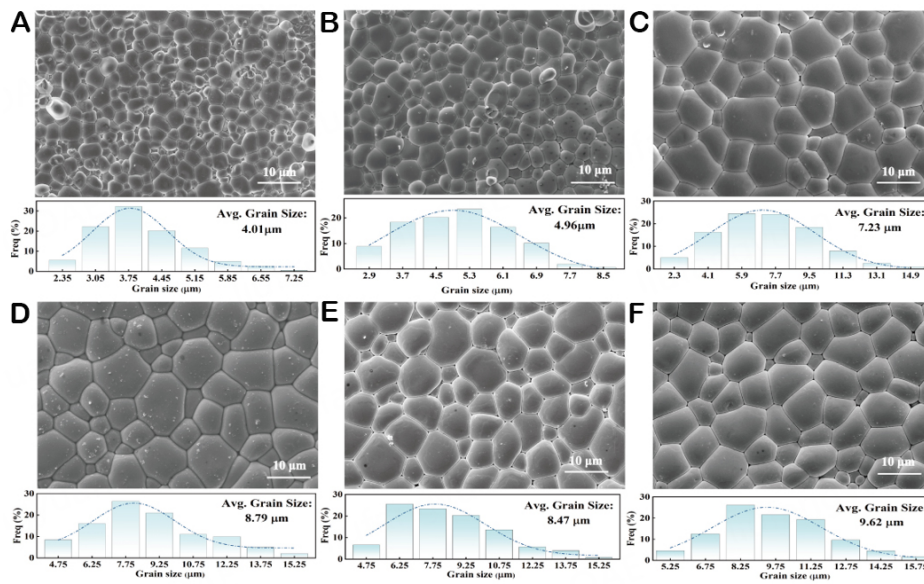


Figure 2. SEM images and grain size distribution in $B_{1+x}F$ -BT ceramics with $x =$ (A) -0.01, (B) 0.00, (C) 0.01, (D) 0.02, (E) 0.03, and (F) 0.04.

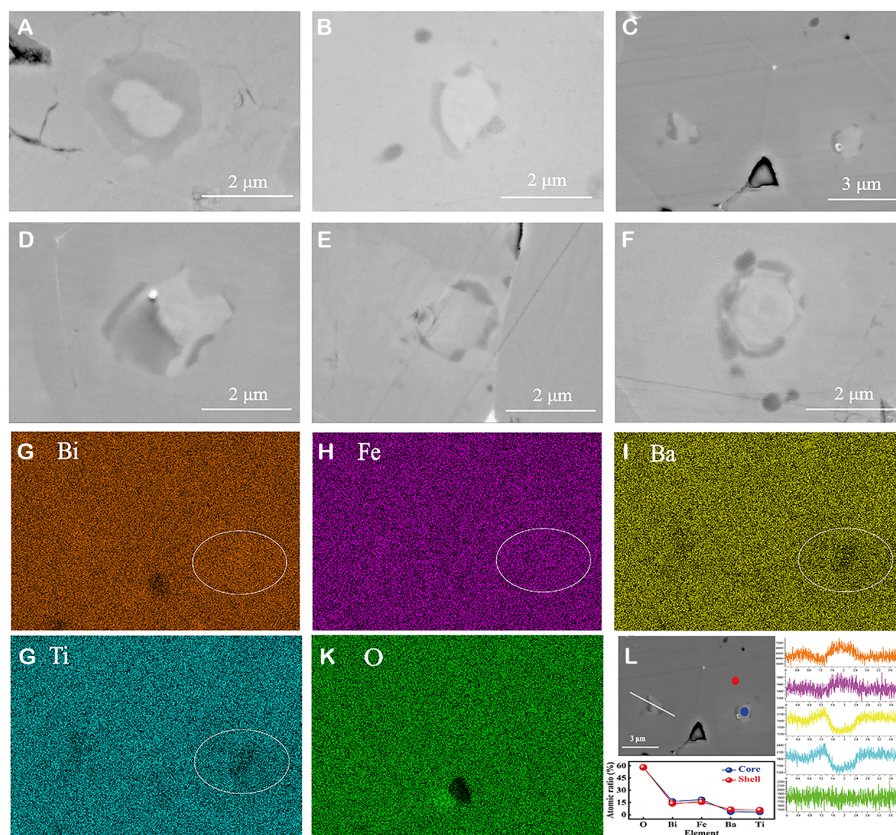


Figure 3. BSE images of $B_{1+x}F$ -BT ceramics: $x =$ (A) -0.01, (B) 0.00, (C) 0.01, (D) 0.02, (E) 0.03, (F) 0.04, and EDS elemental mapping results (G) Bi, (H) Fe, (I) Ba, (J) Ti, and (K) O, (L) the scanned points in a core and a shell region and scanned line, EDS data of points and line scan on the core-shell in $B_{1.01}F$ -BT ceramic.

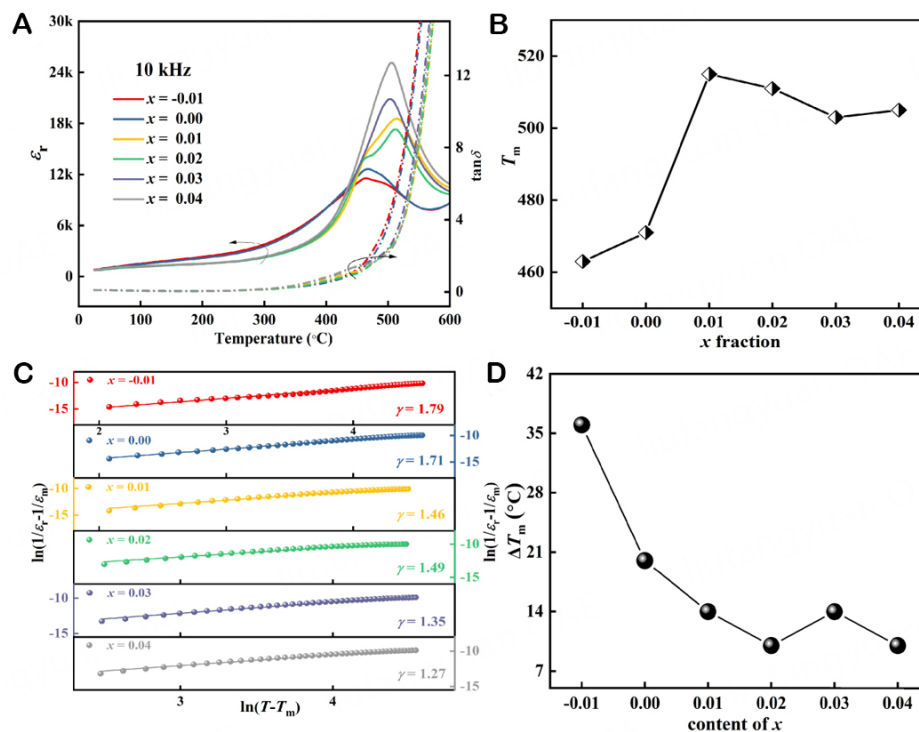
Figure 4A presents the temperature-dependent behavior of relative permittivity (ϵ_r) and dielectric loss ($\tan\delta$) at 10 kHz. It reveals that as the Bi_2O_3 content increases, the dielectric peak becomes narrower, and the maximum relative dielectric constant (ϵ_r) gradually increases, indicating a reduction of diffuse behavior. It is evident from the spectra that the dielectric peaks of the ceramics exhibit asymmetry, which is related to the presence of a core-shell structure within the ceramic grains. As plotted in Figure 4A, the $\tan\delta$ of ceramics exhibits an abrupt increase around the T_m (temperature exhibiting the maximum ϵ_r), suggesting that there is a transition from the diffuse ferroelectric to the paraelectric phase [Figure 4B]. Figure 4C illustrates the relaxation factor (γ) calculated at 10 kHz, which demonstrates that the value of γ decreases as the x content increases, ranging from $\gamma = 1.79$ at $x = -0.01$ to $\gamma = 1.27$ at $x = 0.04$. Figure 4D displays the variation of ΔT_m between 1 kHz and 1 MHz for each component in the temperature spectrum. It is evident that ΔT_m tends to decrease with increasing x content, which reveals that the ferroelectricity of the ceramic becomes more prominent, aligning with the decreasing γ depicted in Figure 4C.

The complex impedance (Z^*) plots of $\text{B}_{1+x}\text{F-BT}$ ceramics at 400 °C are shown in Figure 5A, where Z' and Z'' represent the real part and imaginary part of Z^* , respectively^[57]. At 400 °C, the total impedance initially increases from 36.5 k Ω -cm at $x = -0.01$ to 44.4 k Ω -cm at $x = 0.01$ and then decreases with incorporating more Bi_2O_3 content, which indicates that the composition of $x = 0.01$ is the most electrically resistive. The Z'' and M''/ϵ_0 plots of $x = 0.01$ at 300 °C are plotted in Figure 5B, illustrating the electrical heterogeneity associated with various conductive components. Three peaks are found in the plots corresponding to the three conductive components. Z'' exhibits a single peak related to the grain boundary response (component 1), while M''/ϵ_0 shows a strong peak in the low-frequency region and a weak peak in the high-frequency region, which is ascribed to the electrical heterogeneity from the core-shell structure. In this study, the strong peak represents the shell response (component 2), whereas the weaker peak is considered as the core response (component 3). The resistance (R) and capacitance (C) of all conductive components at 325 °C were calculated based on the peaks of Z'' and M''/ϵ_0 [Table 3]. The R values of components 1 and 2 reach the maximum in the composition of $x = 0.01$. However, the R value of component 3 did not change significantly with the increase of Bi_2O_3 content. Additionally, the resistance of components 1 and 2 is two orders of magnitude higher than that of component 3, which matches the frequency of the peaks of the three components in Figure 5B. It is worth noting that component 3 exhibits a capacitance that is an order of magnitude higher than components 1 and 2, indicating the formation of an electrically conducting core and a nonconductive shell. Figure 5C shows the Arrhenius plots of the grain shell, core, and boundary, and the calculated activation energy calculated by fitting is shown in Figure 5D. The activation energy of the shell (1.06-1.14 eV) is generally lower than that of the core (1.15-1.28 eV) and grain boundary (1.09-1.16 eV).

Figure 6A illustrates the PE loops of the $\text{B}_{1+x}\text{F-BT}$ ceramics at 60 kV/cm under a frequency of 1 Hz, and the corresponding P_r and E_C are plotted in Figure 6B. The PE loops show typical ferroelectric features without observations of leakage characteristics at high field amplitudes. However, when $x = -0.01, 0.00$, the loops demonstrate the phenomenon of leakage conduction, resulting in relatively high values of P_r and E_C , which is mainly attributed to the formation of Bi and O vacancies caused by the Bi_2O_3 volatilization^[43]. When $x \geq 0.01$, the leakage conductivity of BF-BT is significantly reduced, leading to stable values of P_r and E_C . The electric SE loops of ceramics measured at 60 kV/cm are shown in Figure 6C. It can be seen that the strain value increases as x increases from -0.01 to 0.01, reaching a maximum value of 0.146% at $x = 0.01$, and then the strain value decreases. The strains are calculated by averaging the positive strains obtained at ± 60 kV/cm and used for deriving the d_{33}^* values, as plotted in Figure 6D. Notably, the highest $d_{33}^* = 243$ pm/V and $d_{33} = 217$ pC/N are achieved at $x = 0.01$, evidencing that the suitable amount of compensation of Bi_2O_3 is effective in improving the piezoelectric properties of the BF-BT ceramics. In addition, the inset image of Figure 6D depicts the temperature dependence of d_{33} for $x = 0.01$. It demonstrates that the d_{33} value has a

Table 3. The values of R and C for each component at 325 °C derived based on the Z'' and M''/ϵ_0 peak values for $-0.01 \leq x \leq 0.04$

Composition	Component 1 (grain boundary)		Component 2 (shell)		Component 3 (core)	
	$R = 2 Z''$ (kΩ·cm)	$C = 1/(4\pi f Z'')$ (F cm ⁻¹)	$R = M''/(\epsilon_0 \pi f)$ (kΩ·cm)	$C = \epsilon_0/(2M'')$ (F cm ⁻¹)	$R = M''/(\epsilon_0 \pi f)$ (kΩ·cm)	$C = \epsilon_0/(2 M'')$ (F cm ⁻¹)
-0.01 (325 °C)	346	5.73×10^{-10}	281	4.65×10^{-10}	0.82	1.42×10^{-9}
0.00 (325 °C)	393	6.07×10^{-10}	315	4.77×10^{-10}	1.08	1.30×10^{-9}
0.01 (325 °C)	474	3.48×10^{-10}	378	2.88×10^{-10}	0.95	1.06×10^{-9}
0.02 (325 °C)	438	5.45×10^{-10}	329	4.16×10^{-10}	1.12	1.14×10^{-9}
0.03 (325 °C)	314	5.25×10^{-10}	230	3.93×10^{-10}	0.99	1.08×10^{-9}
0.04 (325 °C)	334	5.41×10^{-10}	245	4.03×10^{-10}	1.07	1.09×10^{-9}

**Figure 4.** Temperature-dependent ϵ'' and $\tan \delta$ of (A) $-0.01 \leq x \leq 0.04$ measured at 10 kHz, (B) the T_m at 10 kHz, (C) the relaxation coefficient γ at 10 kHz, (D) the ΔT_m from 1 kHz to 1 MHz for the $\text{Bi}_{1+x}\text{F-BT}$ ceramics.

great temperature sensitivity and decreases above 300 °C as a result of the gradual depolarization at high temperatures.

CONCLUSIONS

In this work, a series of $0.70\text{Bi}_{1+x}\text{F-0.30BT}$ -based lead-free piezoelectric ceramics were systematically studied. The addition of Bi_2O_3 to 0.70BF-BT ceramics plays a crucial role in compensating for the volatilization of Bi elements during high-temperature sintering, leading to enhanced dielectric and piezoelectric performance. The phase structure of the ceramics is barely influenced while varying the Bi_2O_3 content, where all compositions exhibit a typical perovskite structure with a rhombohedral-cubic phase mixture. The microscopy results indicate an increasing trend of grain size as more Bi_2O_3 content is incorporated into the composition. The BSE images and element mappings reveal core-shell microstructures in the ceramics, which are attributed to the segregation of elements during the sintering process. Moreover, the higher Bi_2O_3

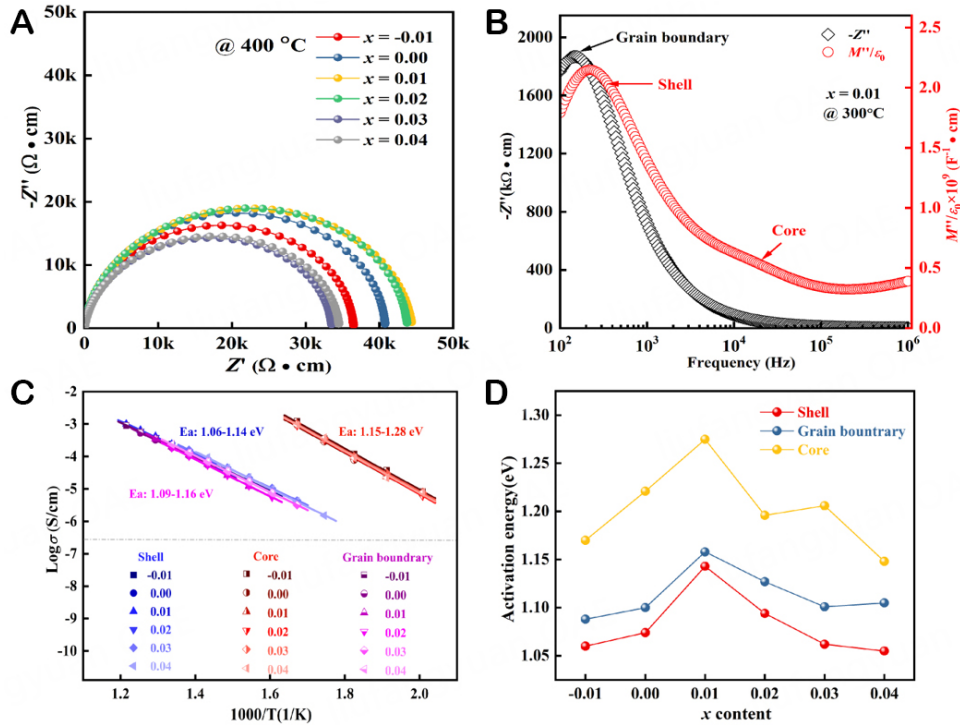


Figure 5. (A) Temperature-dependent Z'' plots for $B_{1+x}F$ -BT ceramics at 400 °C, (B) Combined Z'' and M''/ϵ_0 spectroscopic plots at 300 °C for $x = 0.01$, (C) Arrhenius plots and (D) the activation energy for the $B_{1+x}F$ -BT ceramics.

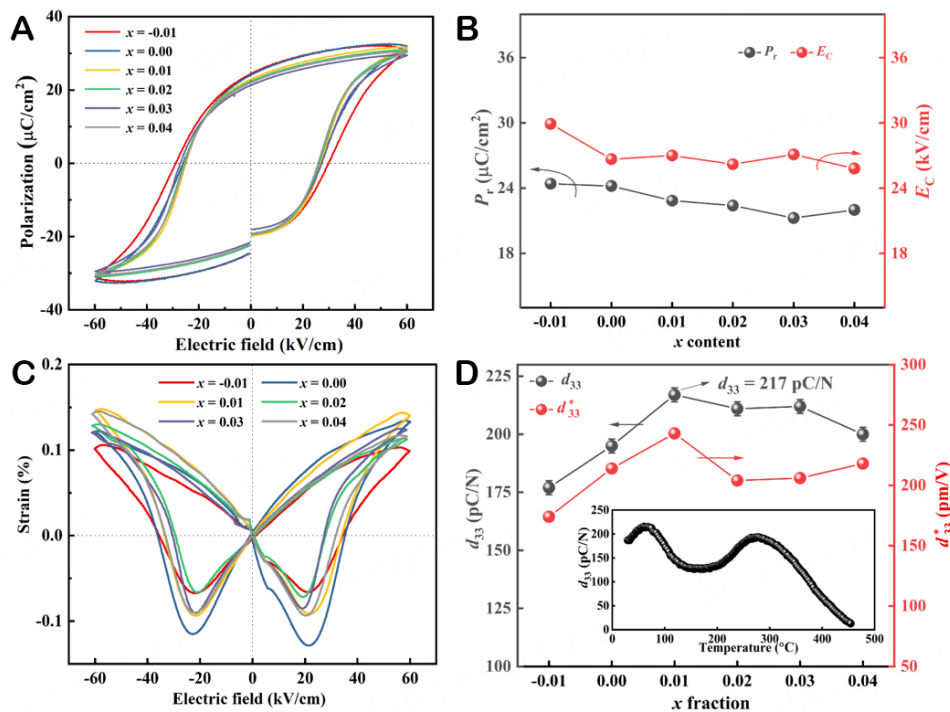


Figure 6. Ferroelectric properties of (A) PE loops at 60 kV/cm and associated (B) P_r and E_c of the $B_{1+x}F$ -BT ceramics. (C) SE loops at 60 kV/cm and (D) d_{33} and d_{33}^* as a function of x concentration for the $B_{1+x}F$ -BT ceramics; the inset image shows the temperature dependence of d_{33} for $x = 0.01$.

content leads to narrower dielectric peaks, higher maximum ϵ_r , and diminished relaxation factor, indicating a deteriorated relaxor behavior. The ferroelectric properties of the ceramics, as demonstrated by PE loops, show that the excess of Bi_2O_3 helps improve the leakage conductivity while stabilizing the P_r and E_C . The piezoelectric properties of the ceramics are optimized at $x = 0.01$ with $d_{33} \sim 217$ pC/N and $d_{33}^* \sim 243$ pm/V, but it has a great temperature sensitivity. The nonstoichiometric optimization of the Bi_2O_3 content in BF-BT was investigated in this work. The findings can be utilized as a foundation for further research into the BF-BT system.

DECLARATIONS

Authors' contributions

Synthesis and testing of materials, data collection, original manuscript writing: Qin H

Validation and original manuscript revision: Zhao J

Data analysis: Chen X, Li H

Data reduction: Wang S

Chart design: Du Y

Validation: Zhou H

Revision: Li P

Reviewing and editing: Wang D

Availability of data and materials

According to reasonable requirements, all of the data examined in this research can be obtained from the correspondents.

Financial support and sponsorship

This work is supported by the Science, Technology and Innovation Committee of Shenzhen Municipality (Grant No. JCYJ20220531095802005 and No. RCBS20210706092341001).

Conflicts of interest

All authors declared that there are no conflicts of interest.

Ethical approval and consent to participate

Not applicable.

Consent for publication

Not applicable.

Copyright

© The Author(s) 2023

REFERENCES

1. Saito Y, Takao H, Tani T, et al. Lead-free piezoceramics. *Nature* 2004;432:84-7. [DOI](#)
2. Wang D, Wang G, Murakami S, et al. $BiFeO_3$ - $BaTiO_3$: a new generation of lead-free electroceramics. *J Adv Dielect* 2018;8:1830004. [DOI](#)
3. Murakami S, Wang D, Mostaed A, et al. High strain (0.4%) $Bi(Mg_{2/3}Nb_{1/3})O_3$ - $BaTiO_3$ - $BiFeO_3$ lead-free piezoelectric ceramics and multilayers. *J Am Ceram Soc* 2018;101:5428-42. [DOI](#)
4. Panda PK, Sahoo B. PZT to Lead Free Piezo Ceramics: a review. *Ferroelectrics* 2015;474:128-43. [DOI](#)
5. Souza-Araujo J, Hussey NE, Hauser-Davis RA, Rosa AH, Lima MO, Giarrizzo T. Human risk assessment of toxic elements (As, Cd, Hg, Pb) in marine fish from the Amazon. *Chemosphere* 2022;301:134575. [DOI](#) [PubMed](#)
6. McFarland MJ, Hauer ME, Reuben A. Half of US population exposed to adverse lead levels in early childhood. *Proc Natl Acad Sci*

- USA 2022;119:e2118631119. DOI PubMed PMC
7. Liu K, Zhang Y, Marwat MA, et al. Large electrostrain in low-temperature sintered NBT-BT-0.025FN incipient piezoceramics. *J Am Ceram Soc* 2020;103:3739-47. DOI
 8. Zhang Y, Liu X, Wang G, et al. Enhanced mechanical energy harvesting capability in sodium bismuth titanate based lead-free piezoelectric. *J Alloys Compd* 2020;825:154020. DOI
 9. Wang D, Hussain F, Khesro A, et al. Composition and temperature dependence of structure and piezoelectricity in $(1-x)(K_{1-y}Na_y)NbO_3-x(Bi_{1/2}Na_{1/2})ZrO_3$ lead-free ceramics. *J Am Ceram Soc* 2017;100:627-37. DOI
 10. Khesro A, Wang D, Hussain F, et al. Temperature dependent piezoelectric properties of lead-free $(1-x)K_{0.6}Na_{0.4}NbO_3-xBiFeO_3$ ceramics. *Front Mater* 2020;7:140. DOI
 11. Zhang S, Kounga AB, Aulbach E, Ehrenberg H, Rödel J. Giant strain in lead-free piezoceramics $Bi_{0.5}Na_{0.5}TiO_3$ - $BaTiO_3$ - $K_{0.5}Na_{0.5}NbO_3$ system. *Appl Phys Lett* 2007;91:112906. DOI
 12. Zheng T, Wu J, Xiao D, Zhu J. Giant d_{33} in nonstoichiometric $(K,Na)NbO_3$ -based lead-free ceramics. *Scr Mater* 2015;94:25-7. DOI
 13. Shi H, Chen J, Wang R, Dong S. Full set of material constants of $(Na_{0.5}K_{0.5})NbO_3$ - $BaZrO_3$ - $(Bi_{0.5}Li_{0.5})TiO_3$ lead-free piezoelectric ceramics at the morphotropic phase boundary. *J Alloys Compd* 2016;655:290-5. DOI
 14. Bai W, Li P, Li L, Zhang J, Shen B, Zhai J. Structure evolution and large strain response in BNT-BT lead-free piezoceramics modified with $Bi(Ni_{0.5}Ti_{0.5})O_3$. *J Alloys Compd* 2015;649:772-81. DOI
 15. Hiruma Y, Nagata H, Takenaka T. Formation of morphotropic phase boundary and electrical properties of $(Bi_{1/2}Na_{1/2})TiO_3$ - $Ba(Al_{1/2}Nb_{1/2})O_3$ solid solution ceramics. *Jpn J Appl Phys* 2009;48:09KC08. DOI
 16. Dittmer R, Webber KG, Aulbach E, Jo W, Tan X, Rödel J. Electric-field-induced polarization and strain in $0.94(Bi_{1/2}Na_{1/2})TiO_3$ - $0.06BaTiO_3$ under uniaxial stress. *Acta Mater* 2013;61:1350-8. DOI
 17. Li T, Lou X, Ke X, et al. Giant strain with low hysteresis in A-site-deficient $(Bi_{0.5}Na_{0.5})TiO_3$ -based lead-free piezoceramics. *Acta Mater* 2017;128:337-44. DOI
 18. Wang G, Hu T, Zhu W, et al. Multiple local symmetries result in a common average polar axis in high-strain $BiFeO_3$ -based ceramics. *Phys Rev Lett* 2023;130:076801. DOI
 19. Lu Z, Wang G, Li L, et al. In situ poling X-ray diffraction studies of lead-free $BiFeO_3$ - $SrTiO_3$ ceramics. *Mater Today Phys* 2021;19:100426. DOI
 20. Wang G, Fan Z, Murakami S, et al. Origin of the large electrostrain in $BiFeO_3$ - $BaTiO_3$ based lead-free ceramics. *J Mater Chem A* 2019;7:21254-63. DOI
 21. Li Z, Hou Z, Song W, et al. Mg-substitution for promoting magnetic and ferroelectric properties of $BiFeO_3$ multiferroic nanoparticles. *Mater Lett* 2016;175:207-11. DOI
 22. Wang D, Wang M, Liu F, et al. Sol-gel synthesis of Nd-doped $BiFeO_3$ multiferroic and its characterization. *Ceram Int* 2015;41:8768-72. DOI
 23. Sono N, Kinoshita Y, Kida N, Ito T, Okamoto H, Miyamoto T. Terahertz-field-induced changes of electronic states associated with a polarization modulation in $BiFeO_3$. *J Phys Soc Jpn* 2021;90:033703. DOI
 24. Huang S, Hong F, Xia Z, et al. Multiferroic behavior from synergetic response of multiple ordering parameters in $BiFeO_3$ single crystal under high magnetic field up to 50 tesla. *J Appl Phys* 2020;127:044101. DOI
 25. Bialek M, Ito T, Rønnow H, Ansermet J. Terahertz-optical properties of a bismuth ferrite single crystal. *Phys Rev B* 2019;99. DOI
 26. Blázquez Martínez A, Gysan P, Girod S, et al. Strain engineering of the electro-optic effect in polycrystalline $BiFeO_3$ films [invited]. *Opt Mater Express* 2023;13:2061. DOI
 27. Yi J, Liu L, Shu L, Huang Y, Li JF. Outstanding ferroelectricity in Sol-gel-derived polycrystalline $BiFeO_3$ films within a wide thickness range. *ACS Appl Mater Interfaces* 2022;14:21696-704. DOI
 28. Zhou Y, Wang C, Tian S, et al. Switchable ferroelectric diode and photovoltaic effects in polycrystalline $BiFeO_3$ thin films grown on transparent substrates. *Thin Solid Films* 2020;698:137851. DOI
 29. Önal F, Maksutoglu M, Zarbali M, Mikailzade F. Magnetization and magnetic resonance in sol-gel derived polycrystalline $BiFeO_3$ film. *J Magn Magn Mater* 2019;477:92-8. DOI
 30. Song H, Son JY. Physical properties of Cr-doped epitaxial $BiFeO_3$ thin films influenced by ferroelectric domain structures. *J Phys Chem Solids* 2023;177:111306. DOI
 31. Ding J, Guo R, Hu J, et al. Switchable ferroelectric photovoltaic in the low bandgap cobalt-substituted $BiFeO_3$ epitaxial thin films. *Appl Surf Sci* 2022;606:154898. DOI
 32. Lee JY, Anoop G, Unithrattil S, et al. The role of intermediate S-polymorph towards high piezoelectricity in La-doped $BiFeO_3$ epitaxial thin films. *Acta Mater* 2021;207:116683. DOI
 33. Pei W, Chen J, You D, et al. Enhanced photovoltaic effect in Ca and Mn co-doped $BiFeO_3$ epitaxial thin films. *Appl Surf Sci* 2020;530:147194. DOI
 34. Zhou Z, Sun W, Liao Z, Ning S, Zhu J, Li J. Ferroelectric domains and phase transition of sol-gel processed epitaxial Sm-doped $BiFeO_3$ (001) thin films. *J Mater* 2018;4:27-34. DOI
 35. Lahmar A, Zhao K, Habouti S, Dietze M, Solterbeck C, Es-souni M. Off-stoichiometry effects on $BiFeO_3$ thin films. *Solid State Ionics* 2011;202:1-5. DOI
 36. Wang J, Neaton JB, Zheng H, et al. Epitaxial $BiFeO_3$ multiferroic thin film heterostructures. *Science* 2003;299:1719-22. DOI
 37. Rojac T, Bencan A, Malic B, et al. $BiFeO_3$ ceramics: processing, electrical, and electromechanical properties. *J Am Ceram Soc*

- 2014;97:1993-2011. DOI
38. Rojac T, Kosec M, Budic B, Setter N, Damjanovic D. Strong ferroelectric domain-wall pinning in BiFeO₃ ceramics. *J Appl Phys* 2010;108:074107. DOI
 39. Ismailzade IH, Ismailov RM, Alekberov AI, Salaev FM. Investigation of the magnetoelectric (ME)_H effect in solid solutions of the systems BiFeO₃-BaTiO₃ and BiFeO₃-PbTiO₃ and BiFeO₃-PbTiO₃. *Phys Status Solid* 1981;68:K81-5. DOI
 40. Wei Y, Wang X, Zhu J, Wang X, Jia J, Damjanovic D. Dielectric, ferroelectric, and piezoelectric properties of BiFeO₃-BaTiO₃ ceramics. *J Am Ceram Soc* 2013;96:3163-8. DOI
 41. Habib M, Lee MH, Kim DJ, et al. Phase evolution and origin of the high piezoelectric properties in lead-free BiFeO₃-BaTiO₃ ceramics. *Ceram Int* 2020;46:22239-52. DOI
 42. Kumar MM, Srinivas A, Suryanarayana SV. Structure property relations in BiFeO₃/BaTiO₃ solid solutions. *J Appl Phys* 2000;87:855-62. DOI
 43. Zheng T, Ding Y, Wu J. Bi nonstoichiometry and composition engineering in (1-x)Bi_{1+y}FeO_{3+3y/2}-xBaTiO₃ ceramics. *RSC Adv* 2016;6:90831-9. DOI
 44. Yang L, Chen C, Jiang X, Huang X, Nie X, Chang S. Enhanced ferroelectric and piezoelectric properties of BiFeO₃-BaTiO₃ lead-free ceramics by simultaneous optimization of Bi compensation and sintering conditions. *Ceram Int* 2022;48:12866-74. DOI
 45. Yi W, Lu Z, Liu X, et al. Excellent piezoelectric performance of Bi-compensated 0.69BiFeO₃-0.31BaTiO₃ lead-free piezoceramics. *J Mater Sci Mater Electron* 2021;32:22637-44. DOI
 46. Zhang G, Dai J, Lu Y. Phase structure and electrical properties of (1-x)Bi_{1+y}FeO₃-xBaTiO₃ lead-free ceramics with different Bi contents. *J Mater Sci Mater Electron* 2021;32:10289-98. DOI
 47. Ahmed T, Khan SA, Bae J, et al. Role of Bi chemical pressure on electrical properties of BiFeO₃-BaTiO₃-based ceramics. *Solid State Sci* 2021;114:106562. DOI
 48. Xun B, Wang N, Zhang B, et al. Enhanced piezoelectric properties of 0.7BiFeO₃-0.3BaTiO₃ lead-free piezoceramics with high Curie temperature by optimizing Bi self-compensation. *Ceram Int* 2019;45:24382-91. DOI
 49. Jian J, Peng R, Fu D, Chen J, Cheng J. Structure and enhanced electrical properties of high-temperature BiFeO₃-PbTiO₃-BaZrO₃ ceramics with bismuth excess. *Ceram Int* 2018;44:21774-8. DOI
 50. Zhu L, Zhang B, Li S, Zhao G. Large piezoelectric responses of Bi(Fe,Mg,Ti)O₃-BaTiO₃ lead-free piezoceramics near the morphotropic phase boundary. *J Alloys Compd* 2017;727:382-9. DOI
 51. Chen J, Cheng J. Enhanced thermal stability of lead-free high temperature 0.75BiFeO₃-0.25BaTiO₃ ceramics with excess Bi content. *J Alloys Compd* 2014;589:115-9. DOI
 52. Zhou C, Yang H, Zhou Q, Chen G, Li W, Wang H. Effects of Bi excess on the structure and electrical properties of high-temperature BiFeO₃-BaTiO₃ piezoelectric ceramics. *J Mater Sci Mater Electron* 2013;24:1685-9. DOI
 53. Murakami S, Ahmed NTA, Wang D, Feteira A, Sinclair DC, Reaney IM. Optimising dopants and properties in BiMeO₃ (Me = Al, Ga, Sc, Y, Mg_{2/3}Nb_{1/3}, Zn_{2/3}Nb_{1/3}, Zn_{1/2}Ti_{1/2}) lead-free BaTiO₃-BiFeO₃ based ceramics for actuator applications. *J Eur Ceram Soc* 2018;38:4220-31. DOI
 54. Calisir I, Hall DA. Chemical heterogeneity and approaches to its control in BiFeO₃-BaTiO₃ lead-free ferroelectrics. *J Mater Chem C* 2018;6:134-46. DOI
 55. Wang D, Fan Z, Li W, et al. High energy storage density and large strain in Bi(Zn_{2/3}Nb_{1/3})O₃-doped BiFeO₃-BaTiO₃ ceramics. *ACS Appl Energy Mater* 2018;1:4403-12. DOI
 56. Calisir I, Amirov AA, Kleppe AK, Hall DA. Optimisation of functional properties in lead-free BiFeO₃-BaTiO₃ ceramics through La³⁺ substitution strategy. *J Mater Chem A* 2018;6:5378-97. DOI
 57. Lu Z, Wang G, Bao W, et al. Superior energy density through tailored dopant strategies in multilayer ceramic capacitors. *Energy Environ Sci* 2020;13:2938-48. DOI

Research Article

Open Access



Improving orientation mapping by enhancing the diffraction signal using Auto-CLAHE in precession electron diffraction data

Ainiu L. Wang, Marcus H. Hansen, Yi-Cheng Lai, Jiaqi Dong, Kelvin Y. Xie 

Department of Materials Science and Engineering, Texas A&M University, College Station, TX 77843, USA.

Correspondence to: Prof. Kelvin Y. Xie, Department of Materials Science and Engineering, Texas A&M University, 575 Ross St., College Station, TX 77843, USA. E-mail: kelvin_xie@tamu.edu

How to cite this article: Wang AL, Hansen MH, Lai YC, Dong J, Xie KY. Improving orientation mapping by enhancing the diffraction signal using Auto-CLAHE in precession electron diffraction data. *Microstructures* 2023;3:2023034. <https://dx.doi.org/10.20517/microstructures.2023.27>

Received: 28 May 2023 **First Decision:** 7 Aug 2023 **Revised:** 7 Aug 2023 **Accepted:** 31 August 2023 **Published:** 7 Oct 2023

Academic Editor: Lin Gu **Copy Editor:** Fangyuan Liu **Production Editor:** Fangyuan Liu

Abstract

Precession electron diffraction (PED) is a powerful technique for revealing the crystallographic orientation of samples at the nanoscale. However, the quality of orientation indexing is strongly influenced by the quality of diffraction patterns. In this study, we have developed a novel algorithm called Auto-CLAHE (automatic contrast-limited adaptive histogram equalization), which automatically enhances low-intensity diffraction pattern signals using contrast-limited adaptive histogram equalization (CLAHE). The degree of enhancement is dynamically adjusted based on the overall intensity of the diffraction pattern, with greater enhancement applied to patterns with fewer spots (i.e., away from zone axes) and little or no enhancement applied to patterns with many spots (i.e., at a zone axis). By improving the visibility of low-intensity diffraction spots, Auto-CLAHE significantly improves the template matching between experimentally acquired and simulated diffraction patterns, leading to orientation maps with dramatically higher quality and lower noise. We anticipate that Auto-CLAHE provides an efficient and practical solution for preprocessing PED data, enabling higher-quality crystal orientation mapping to be routinely obtained.

Keywords: Precession electron diffraction (PED), orientation mapping, contrast-limited adaptive histogram equalization (CLAHE), magnesium, nanoindentation



© The Author(s) 2023. **Open Access** This article is licensed under a Creative Commons Attribution 4.0 International License (<https://creativecommons.org/licenses/by/4.0/>), which permits unrestricted use, sharing, adaptation, distribution and reproduction in any medium or format, for any purpose, even commercially, as long as you give appropriate credit to the original author(s) and the source, provide a link to the Creative Commons license, and indicate if changes were made.



INTRODUCTION

Precession electron diffraction (PED) is a powerful characterization technique used to obtain high-resolution crystal structure/orientation^[1-3] and elastic strain^[4-6] information about materials at the nanoscale level. Some notable PED applications include characterizing thin film microstructures^[7-10], nanocrystalline grain growth behavior^[11,12], material deformation behavior at large strains^[13,14], and submicron and nanoscale martensite variants^[15,16]. When applying PED, the electron beam in the transmission electron microscope (TEM) is converged to a small probe ($\sim 1-3$ nm) and rasters on the specimen. Precession (typically $0.3^\circ-0.8^\circ$) is applied to excite higher-order reflections and reduce the dynamical effect^[1,17,18]. The experimentally acquired diffraction patterns from each pixel are compared to the simulated diffraction patterns in a database to determine the crystal structure and orientation. The information is then used to create phase (crystal structure) and orientation maps. The PED-based orientation mapping is also termed automated crystal orientation mapping (ACOM)^[2,3,8,10]. Compared to electron backscatter diffraction (EBSD, another widely used orientation mapping technique, typical resolution $\sim 20-50$ nm), PED offers superior spatial resolution (~ 3 nm resolution in conventional field-emission gun TEM). In addition, PED offers a larger field of view compared to high-resolution TEM (HRTEM). HRTEM typically allows examination of lattice fringes to deduce crystal orientation in a field of view up to 50×50 nm², while PED can provide a field of view up to 6×6 μm^2 . Hence, the PED-based orientation mapping fills the length-scale gap between HRTEM and EBSD.

The quality of PED orientation mapping depends heavily on the quality of the diffraction pattern. Various factors can affect the diffraction pattern signal, including sample thickness and crystal orientation. Generally, thinner samples are preferred as longer rel-rods intersect with the Ewald sphere, resulting in more diffraction spots and accurate template matching between the experimentally acquired and simulated diffraction patterns^[19]. Diffraction patterns acquired at or close to zone axes are also preferable since they offer more diffraction spots for template matching. Conversely, diffraction patterns acquired far away from zone axes have fewer spots, and the intensity of the spots that are not at the exact Bragg condition diminishes rapidly, potentially leading to poor orientation indexing. While sample thickness can be controlled by the researcher, it is difficult to control the exact diffraction condition of individual grains in polycrystalline or deformed single-crystal samples. Therefore, there is a need for a robust and efficient algorithm to enhance diffraction spot information when it is not ideal for template matching.

Previous work from various research groups has reported that preprocessing PED data is critical to realizing the full potential of the subsequent algorithms. For example, Bergh *et al.* demonstrated the importance of binning and center beam alignment before background removal and diffraction spot identification to resolve overlapping diffraction patterns^[20]. Zhao *et al.* effectively reduced noise in PED raw data through various filters (e.g., Gaussian, non-local means, and Wiener) to enable precise diffraction spot position identification and strain mapping^[4]. Folastre *et al.* employed sub-pixel adaptive image processing and linear filtering to enhance pattern matching for crystal orientation determination and phase recognition^[21]. However, none of these data preprocessing techniques were specifically designed to amplify the signals of low-intensity diffraction spots.

In this study, we introduce a new algorithm called “Auto-CLAHE” for enhancing diffraction data in PED. The name is short for “automatic contrast-limited adaptive histogram equalization”. Auto-CLAHE is based on a popular image processing technique called CLAHE (contrast-limited adaptive histogram equalization)^[22-24], which applies histogram equalization to small regions of an image independently to prevent over-enhancement of local contrast. The amount of enhancement is controlled by a clip limit, with higher clip limits corresponding to greater enhancement. In our method, the clip limit for each diffraction

pattern is automatically assigned based on its average intensity. Our results show that Auto-CLAHE significantly improves the signal-to-noise ratio of low-intensity diffraction spots, particularly those from patterns acquired away from zone axes. This improvement in diffraction pattern quality enables better template matching, resulting in less noise and more accurate orientation mapping.

MATERIALS AND METHODS

An indented pure magnesium (Mg) TEM specimen was used as the model system to test the Auto-CLAHE algorithm. The bulk sample was a hot-rolled commercially pure Mg purchased from MetalMart International Inc. The sample was annealed at 500 °C for two hours under an argon flow atmosphere to homogenize the microstructure and remove most of the dislocations, then mechanically polished to 1,200 grit SiC abrasive sandpaper and chemically polished in a 10% nitric acid in methanol before nanoindentation. Nanoindentation was carried out using a KLA iMicro nanoindentation testing system (KLA Instruments) equipped with a Berkovich tip. Nanoindentation was performed on a grain close to the [0001] direction so the indentation is approximately parallel to the c-axis of the crystal. The indentation depth was 600 nm. The focused ion beam (FIB, Helios G4, ThermoFisher, 30 kV Ga⁺ beam) lift-out method was used to prepare the cross-sectional TEM specimen to investigate the microstructure under the indent impression. The TEM characterizations were performed in an FEI Tecnai TEM operated at 200 keV and equipped with a NanoMEGAS ASTAR system with a *Stingray* CCD camera for PED experiments. The precession angle was 0.3° and the step size was 20 nm when acquiring the map. The 0.3° precession angle was selected because it offers a good combination of reduction in the dynamical effect and retaining a decent beam spot size (~3 nm). One precession per pixel was used, and the diffraction pattern rate was approximately 0.06 s per pixel.

The Auto-CLAHE method was developed as a Python program, utilizing several scientific libraries to handle data. The source code can be found in our GitHub repository linked under the “Availability of data and materials” section. In the code, the HyperSpy and PixSTEM libraries are used to open and read the PED raw data .blo files. The average intensity of each diffraction pattern is calculated. The diffraction patterns are recorded as 8-bit images. The pixel intensity ranges from 0 (dark) to 255 (bright). Next, each diffraction pattern is processed with CLAHE (from the OpenCV library). The clip limit value is calculated using the equation:

$$\text{Clip limit} = \left(\frac{10}{\text{Average_intensity}} \right) + 1.$$

There is an inverse relationship between the clip limit value and the average intensity of the diffraction pattern. If the diffraction pattern is at or close to a zone axis, many diffraction spots are excited. The average intensity of the pattern is high, the clip limit is small, and little enhancement is required. In contrast, if the diffraction pattern is far away from zone axes, a few diffraction spots are excited. The average intensity of the pattern is low, the clip limit is large, and signal enhancement is applied. In the equation, the numerator coefficient of 10 in the Auto-CLAHE algorithm was determined by a combination of trial and error and visual inspection to ensure optimal quality of the enhanced diffraction patterns. It is worth noting that if the average intensity of a diffraction pattern is too high, the “10/Average_intensity” term may round down to 0. Using it alone as the clip limit can cause the CLAHE algorithm to default to non-CLAHE, which will produce erroneous results. To address this issue, another coefficient of 1 was introduced to help preserve image information when processing bright diffraction patterns. With this setup, we have successfully applied this approach to generate enhanced diffraction patterns in various datasets, but users can adjust the coefficients based on their own PED datasets.

The user interface of the algorithm is described as follows. First, the user selects a PED dataset. Next, an analysis window containing a virtual bright-field image of the selected dataset appears. The virtual bright-field image is created by taking the average intensity of the direct beam in the diffraction patterns of each pixel. The user can click on any point on the virtual bright-field (VBF) image to preview the raw and enhanced diffraction pattern at that pixel. Finally, the entire dataset is enhanced with Auto-CLAHE and exported as a new .blo file, which can be further analyzed using the NanoMEGAS commercial software.

RESULTS AND DISCUSSION

Figure 1 shows the cross-sectional VBF image of the indented Mg specimen as the model system. The indent impression is apparent at the top. The region under the indent impression is plastically deformed, and the diffraction contrast is complex. The plastic zone is tilted to the $[11\bar{2}0]$ zone axis. Since plastic deformation under the indent can change the crystal orientation^[25], the exact orientation will vary from pixel to pixel. Three diffraction patterns were selected within the dataset to represent various diffraction “quality levels”, which decrease going down the right-side column of the figure. Here, we consider diffraction patterns that contain more diffraction spots as good quality as they facilitate more accurate template matching. The first diffraction pattern (marked with a green dot) was taken at the $[11\bar{2}0]$ zone axis. It has many highly visible diffraction spots, and its average intensity is high. As a result, it does not require enhancement. The second diffraction pattern (marked with a blue dot) is slightly away from the $[11\bar{2}0]$ zone axis. It can be regarded as a medium-quality pattern, as many of the diffraction spots are obscured. However, some diffraction spots are clearly visible, and the crystal symmetry information is still retained. This type of diffraction pattern requires some enhancement for more diffraction spots to be visible. The third diffraction pattern (marked with a red dot) is regarded as a low-quality pattern. Nearly all diffraction spots aside from the center spot are obscured, and the average intensity is low. The pattern requires a high level of enhancement to properly reveal the diffraction spots. From these observations, it can be deduced that the level of image enhancement should have an inverse relationship with the original average intensity of the diffraction pattern.

Prior to investigating the effect of CLAHE, we first explored the use of conventional image processing techniques to enhance diffraction information, focusing on brightness, contrast, and gamma adjustment^[26] on selected diffraction patterns from the indented Mg dataset, as depicted in Figure 2. While brightness adjustment uniformly increases the intensity of each pixel and uncovers previously obscured spots, it also raises the brightness of the background and lowers contrast, making it less suitable for analysis. Contrast adjustment also uncovers obscured spots but creates excessive contrast between the spots, resulting in overcorrection of bright spots in the original diffraction patterns, which appear overly saturated and enlarged. Gamma correction performs better than the other techniques by revealing hidden diffraction spots while maintaining a dark background and consistent brightness between spots. However, the low-intensity spots are still a bit dim after the gamma correction, and it is challenging to further enhance them without making the diffraction patterns grainy. Moreover, gamma correction operates uniformly on the entire image, which means that it cannot adapt to local contrast variations^[26]. This can lead to suboptimal results in images with significant variations in contrast across different regions (e.g., bright direct beam spots vs. dim diffracted beam spots in the low “quality” diffraction patterns). Hence, a more advanced enhancement method is needed for more effective data processing.

The CLAHE algorithm demonstrated remarkable signal enhancement in the diffraction patterns, and the results of applying different clip limits to the selected Mg diffraction patterns are shown in Figure 3. Increasing the clip limit consistently improved the visibility of low-intensity diffraction spots across all

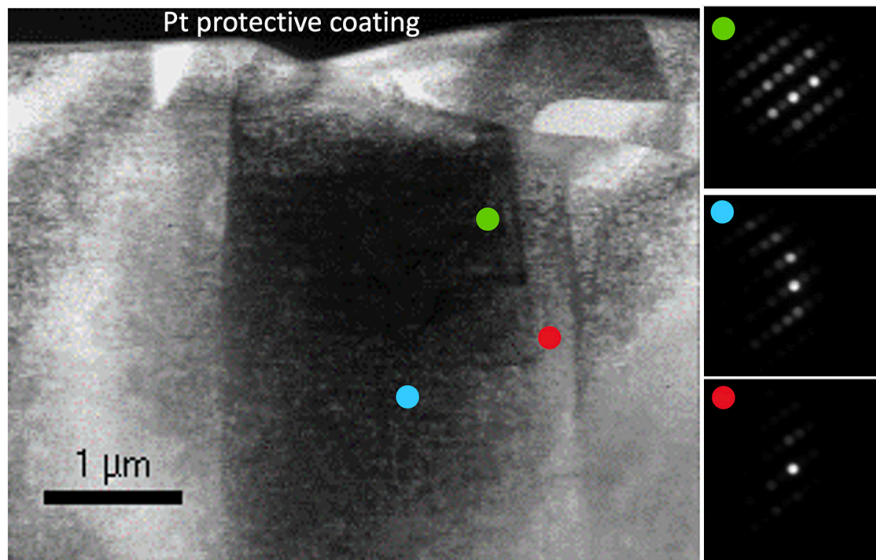


Figure 1. A virtual bright-field TEM image of the indented Mg specimen, along with the selected diffraction patterns. The patterns shown on the right generally decrease in “quality” going down the column.

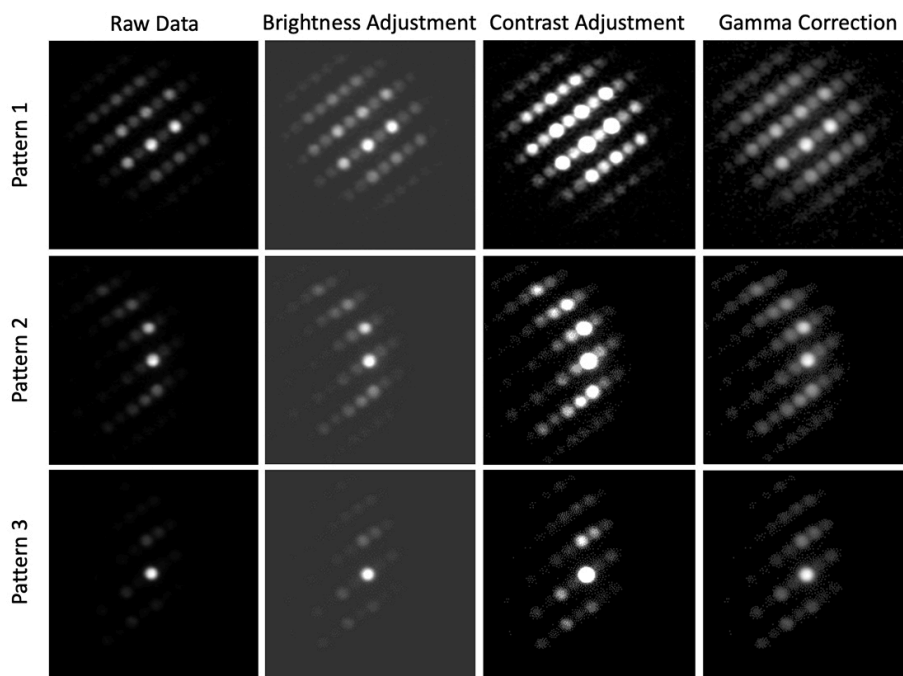


Figure 2. Selected diffraction patterns processed using brightness, contrast, and gamma adjustments.

patterns. However, as the clip limit increased, the radii of all diffraction spots also increased, including those with originally high intensity, which became even brighter. In comparison to conventional image processing techniques described in the previous paragraph, CLAHE better preserves a dark background and avoids over-saturation in the originally bright spots while allowing weak diffraction spots to be well-illuminated without sacrificing the overall quality of the diffraction pattern.

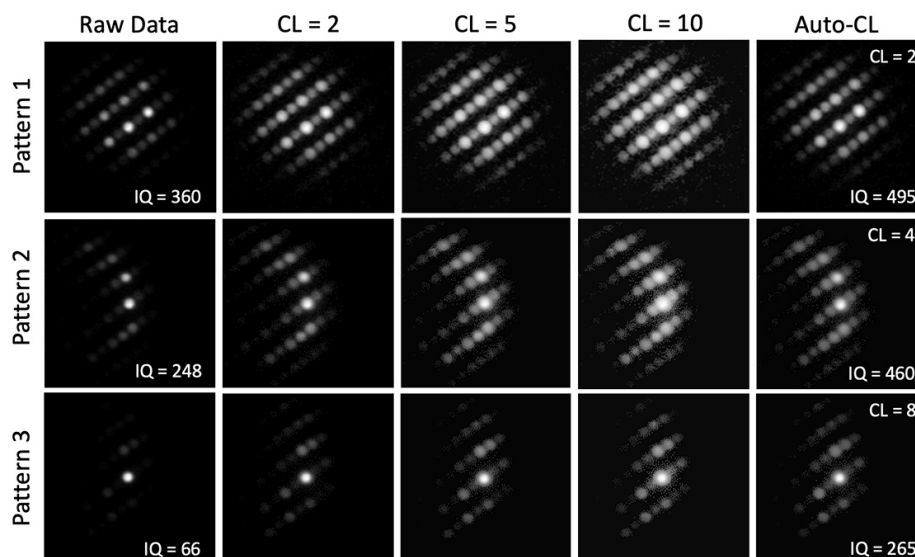


Figure 3. Selected diffraction patterns processed with CLAHE. Different clip limit (CL) values are applied. For Auto-CLAHE, the algorithm automatically selects the clip limit values. The orientation indexing quality (IQ) of the raw data and the Auto-CLAHE processed data is also shown in the figure.

The Auto-CLAHE algorithm automatically calculates the clip limit for each diffraction pattern, only applying necessary levels of signal enhancement for diffraction pattern indexing. For example, in Pattern 1 in the figure, CLAHE with the calculated clip limit of 2 produces a good result. Greater clip limit values tend to degrade the diffraction pattern quality by augmenting the size of diffraction spots and by leading to the merging of spots. In Pattern 2, a clip limit of 4 was calculated by the algorithm. Lower clip limit values (e.g., 2) may not bring out enough diffraction pattern signal, whereas higher clip limit (e.g., 10) results in excessive spot size augmentation. In Pattern 3, the calculated clip limit of 8 appears to produce a decent result in that many obscured spots are now visible and the crystal symmetry information is revealed. One unique advantage of using Auto-CLAHE to preprocess the PED data is that the signal enhancement is dynamic. For high-quality diffraction patterns, little correction is needed; thus, a lower clip limit is automatically selected. As the diffraction pattern “quality” and overall brightness decrease, a higher clip limit is applied, allowing hidden spots to be effectively revealed.

Next, we quantify the efficacy of Auto-CLAHE in improving the orientation indexing via template matching using the NanoMEGAS commercial software. It is important to note that the quality of template matching and, subsequently, the orientation indexing are affected by background noise and the excitation of the diffraction spots (e.g., intensity) in the experimental data. The challenge of high background noise can be overcome by preparing better quality (e.g., thinner) TEM foils. This leads to more electrons undergoing elastic scattering that forms diffraction spots rather than inelastic scattering that augments the background noise. In addition to matching the high-intensity diffraction spots, the Auto-CLAHE algorithm enhances the signal of low-intensity diffraction spots, which also contributes to the template matching to reach better indexing quality (IQ). The IQ (i.e., template matching quality) of the raw data and the Auto-CLAHE-processed data are shown in Figure 3. Indeed, after the Auto-CLAHE enhancement, all diffraction patterns, regardless of their initial quality, exhibit better IQ as calculated by the NanoMEGAS commercial software. For instance, the IQ of the high-quality diffraction pattern (Pattern 1) improves from 360 to 495, median-quality diffraction pattern (Pattern 2) from 248 to 460, and low-quality (Pattern 3) from 66 to 265.

We further inspected the local intensity information in the raw data and the Auto-CLAHE-processed data to evaluate the impact of signal enhancement on forbidden reflections and noise in diffraction patterns. [Figure 4](#) depicts the selected diffraction patterns before and after Auto-CLAHE processing, together with the intensity profile plotted along the [0002] direction, indicated by the dashed boxes. Mg has the hexagonal closed-packed (HCP) crystal structure; hence, the even-numbered reflections (e.g., 0002, 0004, *etc.*) are allowed, and the odd-numbered reflections (e.g., 0001, 0003, *etc.*) are forbidden. However, due to the TEM foil thickness and the limited 0.3° precession angle, some dynamical effects persist, making the forbidden reflections visible but with reduced intensity (grey curves in the intensity profiles for Patterns 1 and 3). Even after the Auto-CLAHE signal enhancement, the lower intensity of the forbidden reflection is retained (maroon curves in the intensity profiles for Patterns 1 and 3). For Pattern 2, due to the specific crystal orientation, the $000\bar{1}$ reflection has a higher intensity than the 0002 reflection in the raw data. This information is preserved in the Auto-CLAHE-processed diffraction pattern. The above observations indicate that although the CLAHE algorithm amplifies the weak signals more than the strong ones, it does not arbitrarily amplify weak spots to the detriment of crucial structural information, particularly regarding the relative diffraction spot intensities influenced by structure factors. One should bear in mind that with the signal enhancement, the background level in the vicinity of the diffraction spots can increase. The background is largely attributed to the overlapping of Gaussian profile tails of the diffraction spots, and its level can be assessed by the intensity at the troughs between the peaks. In all cases, the background levels are higher in the Auto-CLAHE processed diffraction patterns than in raw data. However, the adverse effect of the increased background level in diffraction patterns seems to be outweighed by the benefits gained from signal enhancement, which is evidenced by the increase in IQ after Auto-CLAHE processing, as shown in [Figure 3](#). It is also interesting to observe the preservation of very low noise/background levels from the regions in the raw data to the auto-CLAHE-enhanced data, indicated by the black arrows in the intensity profiles in Patterns 2 and 3 [[Figure 4](#)]. This provides assurance that the CLAHE algorithm does not introduce noise arbitrarily into areas of low noise in diffraction patterns.

To test the overall effectiveness of the Auto-CLAHE algorithm, crystal orientation maps were constructed using both raw and enhanced datasets. [Figure 5A](#) shows the raw data-constructed orientation maps along the X, Y, and Z directions overlaid with the index maps. The orientations map is created by comparing the experimentally acquired diffraction patterns with the simulated diffraction patterns via template matching. The index map is created by comparing the experimentally acquired diffraction patterns with the simulated ones, with better fits corresponding to brighter pixels. It is very similar to the band contrast map in EBSD. The quality of the orientation maps constructed from the raw data is acceptable. The maps reveal the overall deformed matrix and deformation twinning in the top right corner. (The very top layer is the Pt protective coating, and its indexing information should be discarded.) The deformed microstructure is expected as the plastic deformation of c-axis compressed Mg is predominantly accommodated by $\langle c+a \rangle$ dislocations^[27,28]. The complex stress state from nanoindentation also activated some deformation twinning^[29,30]. However, it is also apparent that regions of noise are present in both the matrix and the twin, as indicated by the white arrows. This noise is caused by a lack of clarity in the diffraction spots of the raw data. With the obscured diffraction spots, the commercial orientation indexing software is unable to accurately match the experimental data with the simulated ones, resulting in erroneous orientation assignments in several diffraction patterns. [Figure 5B](#) shows the Auto-CLAHE-enhanced orientation maps overlaid with the index maps. After preprocessing the dataset using Auto-CLAHE, a vast majority of the noise in the orientation maps is removed, as distinct diffraction spots are revealed in the diffraction patterns, allowing for accurate orientation indexing. Additionally, it is worth pointing out that there is a region in the raw data that appears to be a twin grain, as indicated by the black arrows in [Figure 5A](#). However, in the raw data, it is difficult to distinguish if it is actually present or merely an extension of the noise. In contrast, the filtered

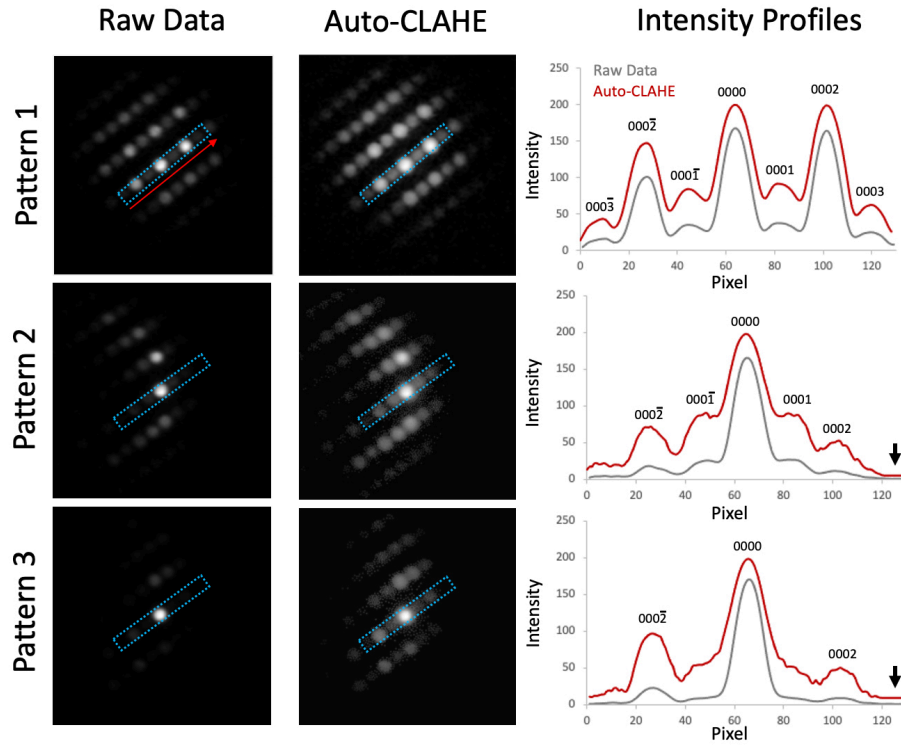


Figure 4. Selected diffraction patterns before and after the Auto-CLAHE processing, together with the diffraction pattern intensity profile along the [0002] direction. The dashed boxes indicate where the intensity profiles are generated. The red arrow in the first diffraction pattern indicates the intensity signal plotting direction.

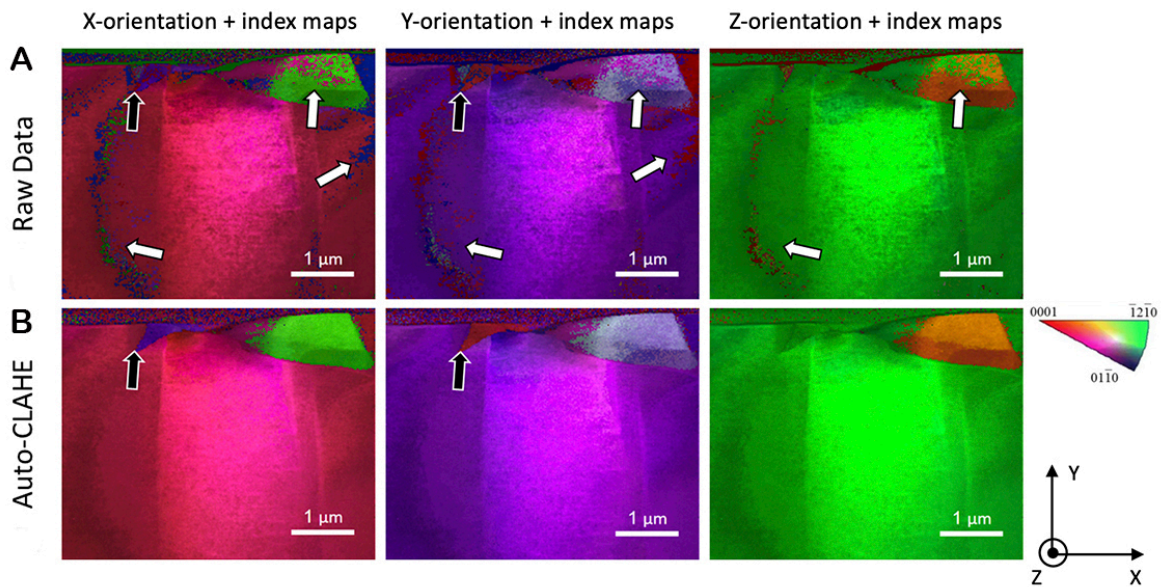


Figure 5. Crystal orientation maps overlapped with index maps with (A) raw data and (B) data processed using Auto-CLAHE.

data clearly reveals a twin grain in the sample, reducing the uncertainty of the feature identification in the dataset. Based on these results, Auto-CLAHE dramatically improves orientation mapping on the PED raw datasets.

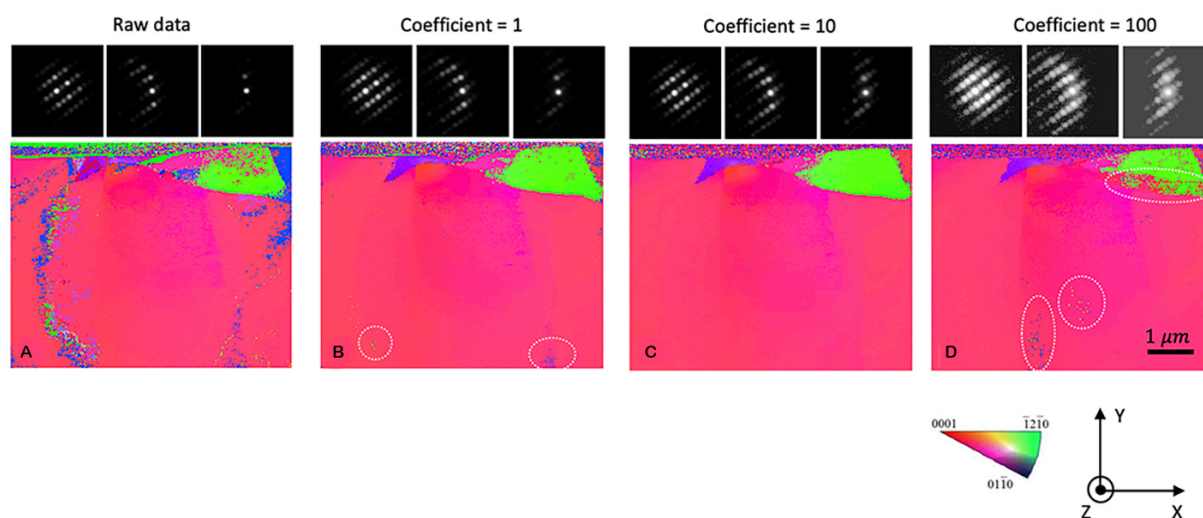


Figure 6. Selected diffraction patterns and reconstructed x-direction orientation maps using the (A) raw data and Auto-CLAHE algorithm-processed data with (B) 1, (C) 10, and (D) 100 numerator coefficients.

It is worth noting that determination of the clip limit using the inverse relationship in the equation $Clip\ limit = \left(\frac{10}{Average_intensity} \right) + 1$ is based on empirical considerations. Here, we explore the effect of changing the numerator coefficient on the qualities of diffraction patterns and orientation maps. [Figure 6A](#) depicts the selected diffraction patterns and the corresponding orientation map from the raw data. Noise is apparent in both the matrix and the twin, as previously described. In contrast, all Auto-CLAHE-processed data demonstrate much reduced noise in the respective orientation maps compared to the raw data. When choosing 1 as the numerator coefficient, some visible enhancements of the diffraction pattern were observed, and most noise in the orientation map was removed [[Figure 6B](#)]. However, low noise level persists in the matrix and the twin (some indicated by the white dashed circles). Increasing the numerator coefficient to 10 (the one we adopted in our algorithm) further enhances the diffraction pattern signals and leads to a near-noise-free orientation map [[Figure 6C](#)]. Further increasing the numerator coefficient to 100 results in over-saturation of the diffraction spots and a noisier orientation map [[Figure 6D](#)]. The most notable noise is the misidentification of the twinned region as the matrix in the top right part of the map; some noise also appears in the matrix (indicated by the white circles). This is caused by the poorer indexing from the diffraction spot supersaturation, diffraction spots merging, and arbitrarily augmented background. Taken together, these observations are encouraging, suggesting that the Auto-CLAHE algorithm is relatively robust - improved orientation maps can be generated with a wide range selection of the numerator coefficients. However, carefully selecting the numerator coefficient is critical to creating orientation maps with high confidence and low noise. Moreover, we encourage the users to try different numerator coefficients or even different inverse relationships (e.g., $Clip\ limit = e^{-\alpha(Average_intensity)}$) based on the diffraction quality to achieve optimal indexing results.

Furthermore, we point out that the NanoMEGAS ASTAR commercial software offers the flexibility of adjusting brightness, contrast, and gamma settings after data acquisition before data reconstruction. However, an equal degree of enhancement (determined by the user) is uniformly applied to all acquired diffraction patterns. For instance, a 50% increase in brightness can effectively enhance faint diffraction spots

in certain pixels. Yet, this same enhancement level might cause oversaturation and compromise indexing accuracy in pixels containing intense diffraction patterns. In contrast, the auto-CLAHE algorithm employs a dynamic approach to signal enhancement. It selectively applies signal amplification to pixels that contain diffraction patterns with low intensity. This ensures that pixel-specific enhancements are tailored to the actual signal characteristics.

CONCLUSIONS

TEM-based crystal orientation mapping at the nanoscale using PED is a useful tool that can reveal microstructural information that has been inaccessible to SEM-based EBSD. In this work, we present a new algorithm named Auto-CLAHE, which automatically amplifies signals of low-intensity diffraction patterns. The degree of enhancement is tailored dynamically based on the overall intensity of the pattern. The algorithm applies greater enhancement to patterns with fewer spots located away from zone axes, while little or no enhancement is used for patterns with many spots located at a zone axis. By enhancing the visibility of low-intensity diffraction spots, Auto-CLAHE remarkably improves template matching between experimentally obtained and simulated diffraction patterns, leading to orientation maps with considerably higher quality and lower noise. Our findings suggest that Auto-CLAHE offers a convenient and efficient solution for preprocessing PED data. The scientific significance of this work is two-fold. First, our method improves the diffraction signal, enabling nanoscale orientation mapping in previously challenging systems with pixels that contain low-intensity diffraction spots. Second, considering that many microscopists are not trained in digital image processing, our technique serves as an example of successful cross-disciplinary implementation, demonstrating how knowledge from other research areas can advance electron microscopy characterization. We anticipate the Auto-CLAHE approach can be routinely applied to all PED datasets and potentially be extended to enhance the diffraction signal in 4D-STEM datasets^[31] to achieve further improved analyses.

DECLARATIONS

Acknowledgments

The authors would like to express their gratitude to Dr. Yuwei Zhang and Professor George Pharr for their invaluable support and guidance on nanoindentation. Additionally, the authors acknowledge the instrumental and technical support from the Microscopy & Imaging Center (MIC) at Texas A&M University.

Authors' contributions

Designing the Auto-CLAHE algorithm and performing data analysis: Wang AL, Hansen MH

Performing sample prep, PED data acquisition, and data analysis: Lai YC, Dong J

Designing the experiment: Xie KY

All authors participated in the writing of the manuscript.

Availability of data and materials

Our source code can be found at <https://github.com/lukewang05/Auto-CLAHE>. A tutorial on how to use our code can be found on YouTube: <https://www.youtube.com/watch?v=OmUV1fHHfbE>.

Financial support and sponsorship

This work was supported by the National Science Foundation (NSF-DMR, grant number 2144973, Program Manager: Dr. Jonathan Madison).

Conflicts of interest

All authors declared that there are no conflicts of interest.

Ethical approval and consent to participate

Not applicable.

Consent for publication

Not applicable.

Copyright

© The Author(s) 2023.

REFERENCES

1. Rauch EF, Portillo J, Nicolopoulos S, Bultreys D, Rouvimov S, Moeck P. Automated nanocrystal orientation and phase mapping in the transmission electron microscope on the basis of precession electron diffraction. *Z Kristallogr* 2010;225:103-9. DOI
2. Kobler A, Kübel C. Towards 3D crystal orientation reconstruction using automated crystal orientation mapping transmission electron microscopy (ACOM-TEM). *Beilstein J Nanotech* 2018;9:602-7. DOI PubMed PMC
3. Rauch E, Véron M. Automated crystal orientation and phase mapping in TEM. *Mater Charact* 2014;98:1-9. DOI
4. Zhao D, Patel A, Barbosa A, et al. A reference-area-free strain mapping method using precession electron diffraction data. *Ultramicroscopy* 2023;247:113700. DOI
5. Ozdol VB, Gammer C, Jin XG, et al. Strain mapping at nanometer resolution using advanced nano-beam electron diffraction. *Appl Phys Lett* 2015;106:253107. DOI
6. Rouviere J, Béché A, Martin Y, Denneulin T, Cooper D. Improved strain precision with high spatial resolution using nanobeam precession electron diffraction. *Appl Phys Lett* 2013;103:241913. DOI
7. Yadav D, Zhao D, Baldwin JK, Devaraj A, Demkowicz MJ, Xie KY. Persistence of crystal orientations across sub-micron-scale “super-grains” in self-organized Cu-W nanocomposites. *Scr Mater* 2021;194:113677. DOI
8. Kobler A, Kübel C. Challenges in quantitative crystallographic characterization of 3D thin films by ACOM-TEM. *Ultramicroscopy* 2017;173:84-94. DOI PubMed
9. Mompiau F, Legros M, Boé A, Coulombier M, Raskin J, Pardoën T. Inter- and intragranular plasticity mechanisms in ultrafine-grained Al thin films: an in situ TEM study. *Acta Materialia* 2013;61:205-16. DOI
10. Kobler A, Kashiwar A, Hahn H, Kübel C. Combination of in situ straining and ACOM TEM: a novel method for analysis of plastic deformation of nanocrystalline metals. *Ultramicroscopy* 2013;128:68-81. DOI PubMed
11. Rottmann PF, Hemker KJ. Experimental observations of twin formation during thermal annealing of nanocrystalline copper films using orientation mapping. *Scr Mater* 2017;141:76-9. DOI
12. Mompiau F, Legros M. Quantitative grain growth and rotation probed by in-situ TEM straining and orientation mapping in small grained Al thin films. *Scr Mater* 2015;99:5-8. DOI
13. Ma X, Zhao D, Yadav S, Sagapuram D, Xie KY. Grain-subdivision-dominated microstructure evolution in shear bands at high rates. *Mater Res Lett* 2020;8:328-34. DOI
14. Xiang S, Ma L, Yang B, et al. Tuning the deformation mechanisms of boron carbide via silicon doping. *Sci Adv* 2019;5:eaay0352. DOI PubMed PMC
15. Dong J, Umale T, Young B, Karaman I, Xie KY. Structure and substructure characterization of solution-treated Ni_{50.3}Ti_{29.7}Hf₂₀ high-temperature shape memory alloy. *Scr Mater* 2022;219:114888. DOI
16. Hansen M. Crystallographic variant mapping using precession electron diffraction data. *Microstructures* 2023;3:2023029. DOI
17. Portillo J, Rauch EF, Nicolopoulos S, Gemmi M, Bultreys D. Precession electron diffraction assisted orientation mapping in the transmission electron microscope. *Mater Sci Forum* 2010;644:1-7. DOI
18. Wu G, Zaeferrer S. Advances in TEM orientation microscopy by combination of dark-field conical scanning and improved image matching. *Ultramicroscopy* 2009;109:1317-25. DOI PubMed
19. Williams DB, Carter CB. Transmission electron microscopy: basics, diffraction, imaging, and spectrometry. Berlin: Springer; 2009.
20. Bergh T, Johnstone DN, Crout P, et al. Nanocrystal segmentation in scanning precession electron diffraction data. *J Microsc* 2020;279:158-67. DOI
21. Folastré N, Cao J, Oney G, et al. Adaptive Diffraction image registration for 4D-STEM to optimize ACOM pattern matching. Available from: <https://arxiv.org/abs/2305.02124> [Last accessed on 5 Sep 2023].
22. Reza AM. Realization of the contrast limited adaptive histogram equalization (CLAHE) for real-time image enhancement. *J VLSI Signal Process Sys* 2004;38:35-44. DOI
23. Pizer SM, Amburn EP, Austin JD, et al. Adaptive histogram equalization and its variations. *Comput Vis Grap Image Process* 1987;39:355-68. DOI

24. Zuiderveld K. Contrast limited adaptive histogram equalization. In: Heckbert PS, editor. *Graphics gems IV*. US: Academic Press Professional; 1994. pp. 474-85. [DOI](#)
25. Ma X, Higgins W, Liang Z, Zhao D, Pharr GM, Xie KY. Exploring the origins of the indentation size effect at submicron scales. *Proc Natl Acad Sci USA* 2021;118. [DOI](#) [PubMed](#) [PMC](#)
26. Gonzalez RC. *Digital image processing*. London: Pearson; 2009.
27. Obara T, Yoshinga H, Morozumi S. {1122} <1123> slip system in magnesium. *Acta Metallurgica* 1973;21:845-53. [DOI](#)
28. Xie KY, Reddy KM, Ma L, Caffee A, Chen M, Hemker KJ. Experimental observations of the mechanisms associated with the high hardening and low strain to failure of magnesium. *Materialia* 2019;8:100504. [DOI](#)
29. Barnett M. Twinning and the ductility of magnesium alloys. *Mater Sci Eng A* 2007;464:1-7. [DOI](#)
30. Shin J, Kim S, Ha T, Oh K, Choi I, Han H. Nanoindentation study for deformation twinning of magnesium single crystal. *Scr Mater* 2013;68:483-6. [DOI](#)
31. Ophus C. Four-dimensional scanning transmission electron microscopy (4D-STEM): from scanning nanodiffraction to ptychography and beyond. *Microsc Microanal* 2019;25:563-82. [DOI](#) [PubMed](#)

Review

Open Access



Machine learning assisted intelligent design of meta structures: a review

Liangshu He¹, Yan Li¹, Daniel Torrent², Xiaoying Zhuang^{3,4} , Timon Rabczuk⁵ , Yabin Jin¹

¹School of Aerospace Engineering and Applied Mechanics, Tongji University, Shanghai 200092, China.

²GROC-UJI, Institut de Noves Tecnologies de la Imatge, Universitat Jaume I, Castello 12080, Spain.

³College of Civil Engineering, Tongji University, Shanghai 200092, China.

⁴Institute of Photonics, Department of Mathematics and Physics, Leibniz University Hannover, Hannover 30167, Germany.

⁵Institute of Structural Mechanics, Bauhaus-Universitat Weimar, Weimar 99423, Germany.

Correspondence to: Prof./Dr. Yan Li, School of Aerospace Engineering and Applied Mechanics, Tongji University, 100 Zhangwu Road, Shanghai 200092, China. E-mail: liyan@tongji.edu.cn; Prof./Dr. Xiaoying Zhuang, College of Civil Engineering, Tongji University, 1239, Siping Road, Shanghai 200092, China. E-mail: xiaoyingzhuang@tongji.edu.cn; Prof./Dr. Yabin Jin, School of Aerospace Engineering and Applied Mechanics, Tongji University, 100 Zhangwu Road, Shanghai 200092, China. E-mail: 083623jinyabin@tongji.edu.cn

How to cite this article: He L, Li Y, Torrent D, Zhuang X, Rabczuk T, Jin Y. Machine learning assisted intelligent design of meta structures: a review. *Microstructures* 2023;3:2023034. <https://dx.doi.org/10.20517/microstructures.2023.29>

Received: 1 Jun 2023 **First Decision:** 13 Jul 2023 **Revised:** 27 Jul 2023 **Accepted:** 4 Aug 2023 **Published:** 9 Oct 2023

Academic Editor: Jiamian Hu **Copy Editor:** Fangyuan Liu **Production Editor:** Fangyuan Liu

Abstract

In recent years, the rapid development of machine learning (ML) based on data-driven or environment interaction has injected new vitality into the field of meta-structure design. As a supplement to the traditional analysis methods based on physical formulas and rules, the involvement of ML has greatly accelerated the pace of performance exploration and optimization for meta-structures. In this review, we focus on the latest progress of ML in acoustic, elastic, and mechanical meta-structures from the aspects of band structures, wave propagation characteristics, and static characteristics. We finally summarize and envisage some potential research directions of ML in the field of meta-structures.

Keywords: Meta-structure, inverse design, machine learning, continuous fiber reinforced composite meta-structure, additive manufacture

INTRODUCTION

Meta-structures^[1] are artificially designed functional structures that meet specific performance requirements



© The Author(s) 2023. **Open Access** This article is licensed under a Creative Commons Attribution 4.0 International License (<https://creativecommons.org/licenses/by/4.0/>), which permits unrestricted use, sharing, adaptation, distribution and reproduction in any medium or format, for any purpose, even commercially, as long as you give appropriate credit to the original author(s) and the source, provide a link to the Creative Commons license, and indicate if changes were made.



and possess physical properties beyond the capabilities of natural materials. Based on different disciplines, acoustic meta-structures^[2], mechanical meta-structures^[3], electromagnetic meta-structures^[4], and other types can be distinguished. Acoustic meta-structures^[5], including phononic crystals, acoustic metamaterials, and acoustic metasurfaces, have emerged as an elegant means of manipulating acoustic and elastic waves. Through special structural designs, researchers can achieve dynamic characteristics that are not found in natural materials, enabling novel operations such as mechanical wave blocking^[6], absorption^[7,8], focusing^[9,10], robust energy harvesting^[11,12], negative refraction^[13], invisibility^[14,15], topological transmission^[16], and more. The significant advancement in the field of acoustic meta-structures can be attributed primarily to the extensive research conducted on electronic crystals and photonic crystals. Matter waves and electromagnetic waves exhibit band structures separated by bandgaps under the action of Bloch periodic potential fields formed by the above structures. Bandgap formation is attributed to the Bragg scattering mechanism, which results from destructive interference between scattered waves caused by periodic structures. Phononic crystals^[17,18], which are formed by the periodic distribution of materials or structures in space, can exhibit bandgaps that effectively block or attenuate the propagation of mechanical waves as an extension of the aforementioned concept. The subsequent development of localized resonant phononic crystals enables the formation of low-frequency hybridization bandgaps through scatterer resonance, independent of the periodicity of the structure itself^[19]. The local resonance mechanism has triggered a revolutionary innovation in the realm of acoustic metamaterials^[20]. On the one hand, the bandgap frequency is determined by the resonant unit frequency, providing theoretical support for developing compact structures with vibration and noise reduction functions in limited space requirements. On the other hand, it has been proven to possess new physical properties with locally resonant parameters, resulting in equivalent exotic properties. This has stimulated extensive research on negative mass density^[21], negative bulk modulus^[22,23], and double-negative parameters^[24,25].

In the past decade, guided by the goal of achieving efficient regulation of low-frequency acoustic/elastic waves through thin and lightweight structures, researchers have developed acoustic metasurfaces by designing subwavelength functional unit arrays to form phase gradients based on the generalized Snell's law^[26]. Acoustic metasurfaces^[27] include reflective, absorptive, and transmissive types, which can achieve functions such as acoustic/elastic wave focusing^[28], cloaking^[29,30], low-frequency perfect absorption^[31,32], asymmetric transmission^[33], self-bending^[34], and so forth. Compared with phononic crystals and acoustic metamaterials, acoustic metasurfaces have the characteristics of ultra-thin, planar, low loss, and strong designability, which make it possible to develop extremely miniaturized acoustic functional devices.

Recently, the concept of topological insulators in condensed matter physics has been added to the design of acoustic meta-structures for regulating mechanical waves^[35-39]. Due to the existence of bandgaps, mechanical waves within specific frequency ranges are not allowed to propagate. In these bandgaps, acoustic meta-structures can be considered as insulators of mechanical waves. The topological properties of bandgaps can be characterized by calculating topological invariants and can generally be classified as topological trivial and topological non-trivial bandgaps^[40,41]. On the structural boundaries with the above two bandgaps, certain frequencies of waves within the bandgap are allowed to propagate, which are the so-called topological edge states. Supported by topological mechanisms, topological edge states have robust transmission characteristics, such as defect immunity, unidirectional waveguides, and backscatter suppression effects^[42,43]. The in-depth studies of topological states have broadened the application prospects of acoustic meta-structures to a certain extent.

The research on mechanical meta-structures primarily centers around the three material parameters of elastic modulus, shear modulus, and Poisson's ratio in order to attain exceptional static performance^[3].

Natural solid materials typically exhibit positive elastic and shear moduli, which are related by Poisson's ratio, typically falling between 0 and 0.5. The mechanical meta-structures designed through origami and kirigami structures^[44], chiral structures^[45], lattice structures^[46], honeycomb structures^[47], and other methods can constrain and adjust the overall elastic deformation, thus exhibiting unconventional equivalent characteristics, such as negative stiffness, negative compression, negative Poisson's ratio, multi-stability, and so forth. Mechanical meta-structures greatly enrich the way of regulating static performance and provide support for the design and application of engineering vibration suppression, impact resistance, energy absorption, and structural protection devices.

The process of analyzing the wave or mechanical properties of a certain meta-structure is a forward problem, which can be easily realized through theoretical, experimental, or commercial software analysis. However, designing structures with specific properties considering practical application backgrounds can essentially be attributed to inverse problems^[48]. The traditional strategy for solving inverse problems usually relies on trial and error supported by experimental and computational modeling techniques, which require a significant amount of time and resource costs. Subsequently, some heuristic optimization methods that relied on global search were developed, such as genetic algorithms (GA)^[49], simulated annealing algorithms^[50], particle swarm optimization algorithms^[51], and so forth. These methods can effectively identify the meta-structure parameters corresponding to the target property and can be modified to adapt to different goals. However, their performance generally depends on the specific problem, usually lacking stability and being prone to falling into local optima.

With the deepening of artificial intelligence (AI) research, the improvement of computer hardware performance, and the emergence of open-source deep learning frameworks, machine learning (ML) algorithms have been rapidly developed and widely applied, and advanced methods, such as deep neural networks (DNNs) and reinforcement learning (RL), have emerged. The development of ML has shown a strong ability to circumvent the shortcomings of traditional methods, leading to an interdisciplinary revolution, including biology^[52], finance^[53], materials science^[54], computational chemistry^[55], computational mechanics^[56], *etc.* Certainly, the meta-structure design scheme based on intelligent algorithms has become an important core to break through the bottleneck of inverse problems and promote the development of the field. In the past several years, some review articles have introduced the latest progress of ML-enabled meta-structure design from different aspects, for instance, the progress of ML-enabled nanophotonics and photonic devices in an all-round way^[57-66]. Furthermore, Khatib *et al.* introduced the progress in the field of designing electromagnetic meta-structures by ML^[67]. Jiao *et al.* discussed the advent and prospects of ML in the field of mechanical meta-structures^[68]. Jin *et al.* introduced some basic ML algorithm principles and reviewed intelligent on-demand design of phononic metamaterials^[69]. Subsequently, Muhammad *et al.* and Liu *et al.* successively updated the progress of ML in phononic crystals and metamaterial^[70,71]. From the works in recent years, the field of integrating ML in the design of acoustic, elastic, and mechanical meta-structures has developed rapidly, but there is still a lack of comprehensive review that directly takes design objectives as the classification standard, which is helpful to understand the latest progress of various inverse design problems in this field.

In this review, we draw attention to a series of recent results on ML inverse design of acoustic, elastic, and mechanical meta-structures from the perspective of design objectives. We first introduce the background of the development of ML and how basic algorithms can be combined with meta-structures for inverse design. Then, we summarize the latest progress from three aspects: design of band structure in infinite meta-structures, design of wave propagation characteristics in finite meta-structures, and design of static characteristics in mechanical meta-structures. Finally, we summarize the current status of this cutting-edge

cross-disciplinary field and discuss potential future development prospects.

BACKGROUND OF ML

AI is committed to enabling machines to acquire and expand human intelligence. The development of AI can be traced back to the proposal of this concept at the Dartmouth Conference in 1956, but related research has already begun earlier. It has gone through periods of symbolism, connectionism, and behaviorism^[72]. Early researchers constructed expert systems by feeding human experience into machines through programming, which is a symbolic approach. Although expert systems perform well in environments with strong logic, such as mathematical deduction, this approach cannot obtain new knowledge beyond input, and human intelligence is acquired through autonomous learning rather than direct input. Therefore, researchers turned to exploring ways to enable machines to autonomously acquire knowledge starting in the 1980s, a concept known as ML^[73]. At this time, connectionism represented by an artificial neural network (ANN) algorithm ushered in the peak of development. Artificial neurons were proposed in 1943^[74], followed by the development of a variable strength criterion for inter-unit connections, which led to the formation of a perceptron model^[75]. In 1986, the success of the back-propagation training algorithm enabled the multilayer perceptron (MLP) model to have nonlinear processing capability^[76]. On this basis, researchers began to explore the deepening of neural network models. Recurrent neural networks (RNN)^[77] with time series prediction function and convolutional neural networks (CNN)^[78] with image processing function were successively proposed. The deepening of the model has brought about an explosive increase in training difficulty, but this dilemma has been effectively overcome with the improvement of computer computing power. Since 2006, research on ANNs has entered the era of deep learning^[79], and the emergence of many open-source deep learning frameworks has greatly reduced the learning cost of algorithms. Over the past decade, a large number of DNN models have emerged, such as generative adversarial networks (GAN)^[80], condition GANs (CGAN)^[81], tandem neural networks (TNN)^[82], and so forth. RL, originating from behaviorism^[83], has gradually emerged in the context of the flourishing development of deep learning. The basic principle is that the agent takes different actions to change its own state and corrects its behavior based on environmental feedback, thereby selecting the optimal strategy to achieve the goal. RL is seen as the future development direction of AI and has achieved great success in fields such as Go programs^[84] and autonomous driving^[85].

The advantage of DNNs lies in their ability to learn potential laws implicitly from data, especially for nonlinear mapping problems with unclear or complex physical mechanisms, and the design of meta-structures belongs to such problems. Unlike the process of calculating property from structural parameters in a forward problem, inverse design, which involves extrapolating the property back to the structure, often finds it difficult to obtain analytical solutions based on clear functional relationships. However, with the nonlinear processing ability of data-driven neural networks, the design parameters of the structure can be quickly obtained by taking the target property as input.

For situations where high-dimensional data or image data are used as property inputs, CNNs are often used to reduce the number of connections between neurons, thereby reducing the computational complexity of the computer. Autoencoders (AE) can be used to extract features from high-dimensional property data for further wave or mechanical analysis. In the inverse design meta-structure paradigm, there may be a problem that one property corresponds to multiple sets of structural parameters, which leads to the convergence failure of neural network training.

The proposal of TNN effectively solves this problem by freezing the training parameters of the pre-trained forward network and cascading it after the inverse network^[82]. The subsequently developed probabilistic

TNN can obtain multiple reasonable structures as alternative solutions based on inputs. Additionally, in order to deal with the situation of only small-scale data, researchers introduced transfer learning into meta-structure design^[86,87]. Transfer the model trained from similar data sources to the target data for retraining, thereby reducing the demand for target data without affecting the training results.

Another solution is to rely on GAN^[80] and CGAN^[81]. In this solution, the generator of GAN takes random vectors as input, initiates the generation of a structure, and then sends the generated structure and real structure to the discriminator for authenticity discrimination to guide model updates. After adversarial training of the generator and discriminator, a generator model that can generate the target structure can be obtained. While inputting random vectors, the expected property can be input together to enable the generator to generate structures under this condition. The combination mode of RL and meta-structure inverse design is to regard structural parameters as agents. These agents execute the action of parameter changes, determine feedback based on the proximity of the altered property to the design goal, and finally explore a parameter path to achieve the goal.

As a summary, the overview diagram of ML in the field of meta-structure for forward performance prediction and inverse structure design is shown in [Figure 1](#). In addition, there are various types of ML algorithms, some of which may be simple and perform well when dealing with specific problems. For example, linear regression obtains sample distribution patterns by fitting data points as closely as possible. Logistic regression can compress samples to a specific range through nonlinear functions, thus realizing the classification of samples. A decision tree is a tree-structured classifier that classifies samples by representing branches of different attributes. Multiple groups of decision trees can form a random forest, which yields higher performance and prediction stability. However, the increase in the complexity of the model requires more computing time. Readers can refer to relevant literature for more information^[73,88,89].

The emergence of some deep learning open-source frameworks, such as TensorFlow^[90] and PyTorch^[91], helps beginners easily grasp the basic usage of ML. These frameworks are integrated through Python packages and can be easily called, eliminating the hassle of writing low-level computational code for neural networks. Researchers can use some shared ready-made datasets for training and learning, such as Handwritten Digit Dataset, CIFAR10, Fashion-MNIST, and so forth. In addition, the commercial software MATLAB also has a built-in toolbox for neural networks, which can be easily modeled through the user interface.

APPLICATION OF ML IN META-STRUCTURES

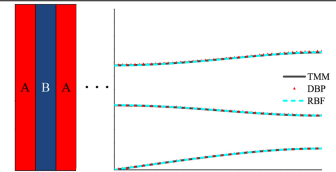
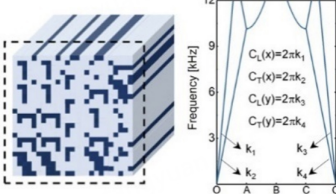
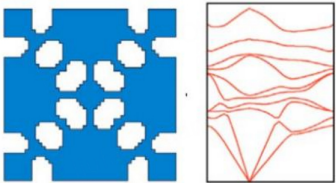
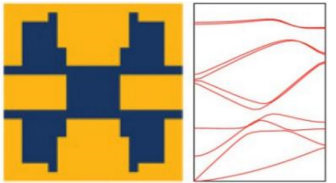
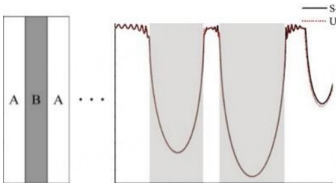
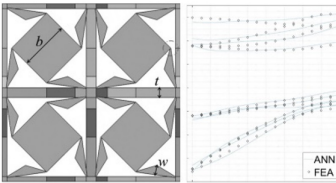
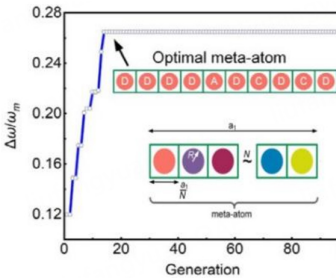
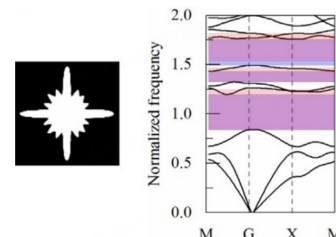
Design of band structure in infinite meta-structures

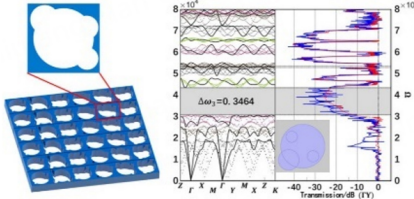
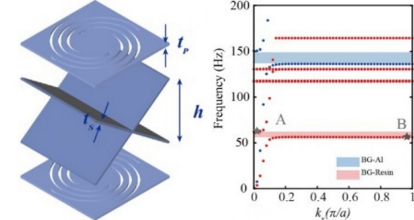
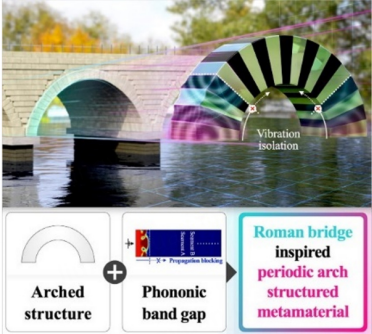
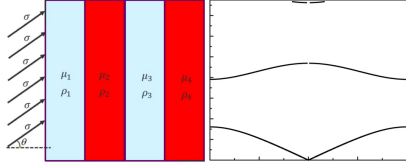
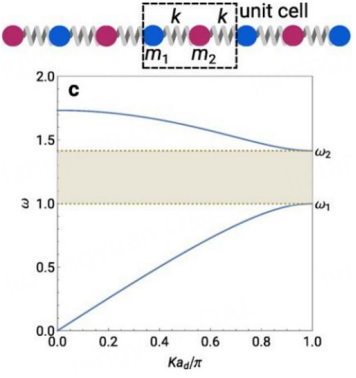
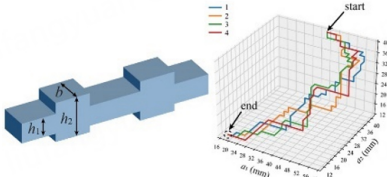
A band structure is the most basic way to describe the acoustic/elastic wave characteristics in meta-structure, so it is the most direct research idea to carry out the application of ML in meta-structure design around a band structure and the wave information it carries. With the maturity of deep learning algorithms and open-source frameworks, a large amount of design work has emerged around band structures, which can be mainly divided into two categories: design based on complete band structures and design based on bandgaps. [Table 1](#) provides a brief overview of ML for the design of band structures in infinite meta-structures.

Complete band structures

For the design of complete band structures, one type of work is to predict the corresponding band structure of a meta-structure from a forward perspective to replace the analytical process. Liu and Yu^[92] used MLP and radial basis function neural networks (RBF-NN) to predict the band structures of one-dimensional

Table 1. A brief overview of design based on band structures in infinite meta-structures

Design type	Algorithm	Meta-structure and performance	Description	Year
Complete band structures	MLP RBF-NN		RBF is suitable for single parameter prediction, while MLP can meet multi-parameter prediction ^[92]	2019
	CNN		Construct digital structure genomes through forward prediction. Thus, the target property structures can be quickly extracted from the genomes ^[93]	2021
Tailoring bandgaps	GAN CNN		Generate optimal structure based on customized dispersion and accelerate design processes ^[94]	2022
	GAN CNN		Generate and screen structures with excellent attenuation performance. The dataset is generated through secondary mirroring, which lacks flexibility ^[95]	2022
Tailoring bandgaps	MLP TNN		Compared to MLP, TNN can solve the problem of data inconsistency and is suitable for multi-parameter inverse design ^[96]	2019
	GA MLP		The model is insufficient to provide accurate predictions beyond the training data range and only performs well within local data points ^[97]	2020
	GA MLP		The model can obtain the target modular metamaterial but cannot find the configuration beyond the dataset ^[98]	2020
Tailoring bandgaps	AE MLP		Can accurately process data beyond the dataset. Only a relatively small region of the design space in RVE is explored using a nine-parameter analytical function ^[99]	2020

GA MLP		Fast forward search to obtain the maximum bandgap structure. Performed well in both single-objective and multi-objective optimization designs ^[100]	2021
MLP		Flexible design of meta-structures based on target bandgap for vibration isolation. The designed structure has been experimentally verified ^[101]	2022
TNN		Arch-shaped vibration isolation structure inspired by the Roman Bridge. The TNN model can design structure accurately based on target bandgaps and verified through experiments ^[102]	2022
RL		Efficient interactive inverse design for layered phononic crystals. For the same model, simply changing the objective function can easily achieve different designs ^[103]	2020
RL GA		Designing one-dimensional diatomic and hexatomic lattice chains based on RL. The rate of convergence is much faster than the baseline GA ^[104]	2021
RL		Designing a one-dimensional phononic beam based on RL. The model still maintains an efficient and stable exploration ability in the huge parameter space ^[105]	2022

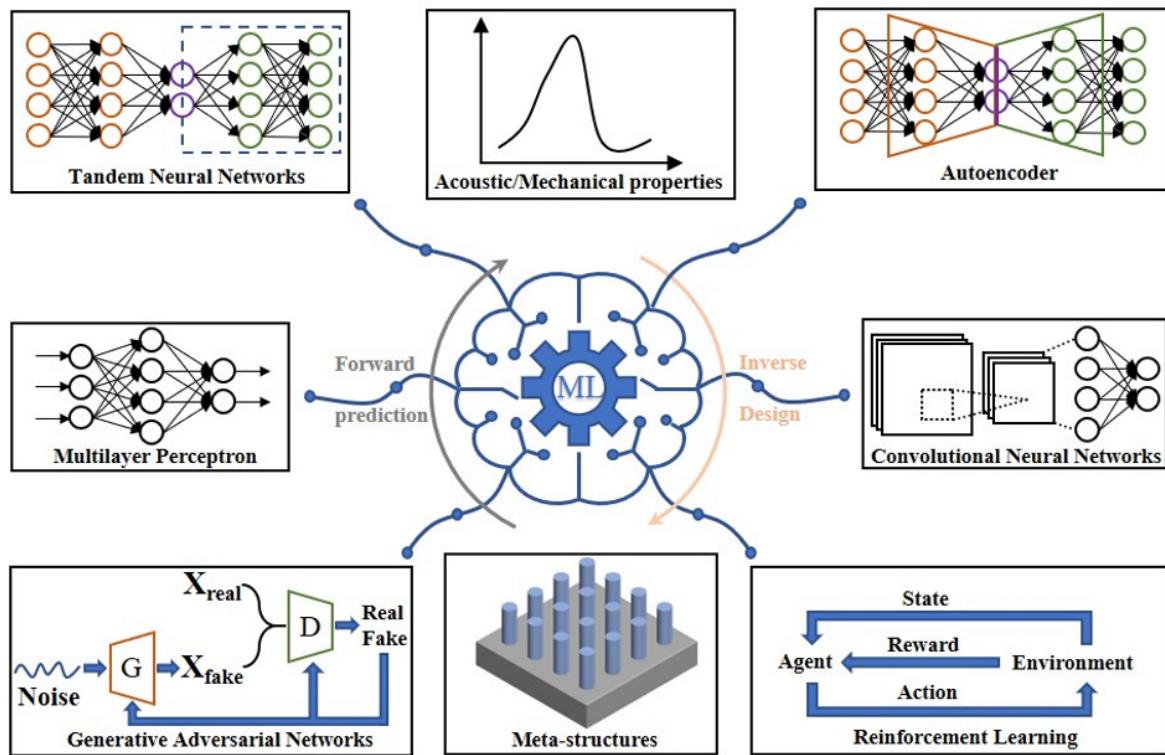


Figure 1. ML in solving the problem of properties prediction and inverse design for meta-structures.

layered phononic crystals and compared their efficiency and accuracy. The input parameters of the neural networks are one to three selected from the filling fraction, mass density ratio, and shear-designed structure. The accuracy in predicting band structures is achieved using a single parameter (fill fraction), while in the case of multiple parameters, MLP outperforms RBF-NN.

Another type of work is to use trained forward models to assist in the selection of alternative structures after inverse design. Zhang *et al.* constructed a digital structural genome using CNN to achieve structural screening with specified elastic wave properties^[93]. For representative volume elements (RVEs) of size 5×5 , each unit has two coding forms, with a total of 2^{25} possible configurations, which makes it difficult to find configurations with target elastic wave properties. Their approach is to calculate the band structures of a small portion of RVEs using a finite element method and extract wave properties to construct a dataset. Then, by using data-driven CNN to predict the elastic wave properties of all possible configurations, a digitally structured genome is constructed. For a set of target elastic wave properties, the corresponding structure can be found in the genome. Jiang *et al.* proposed a novel way to inverse design similar digitally coded metamaterials, as shown in Figure 2A^[94]. This work can be divided into three steps: first, train CNN to predict the band structures; second, train GAN to generate digitally coded metamaterials from band structures; and finally, take out the generator of GAN and connect it with CNN. The overall workflow is as follows: the generator takes random noise and target band structures as inputs, generating a series of alternative structures. Predict the corresponding band structures of all candidate structures through CNN and then compare them with the target band structure to screen the best structure. Almost at the same time, Han *et al.* employed the same design process to realize inverse design of digitally coded metamaterials with

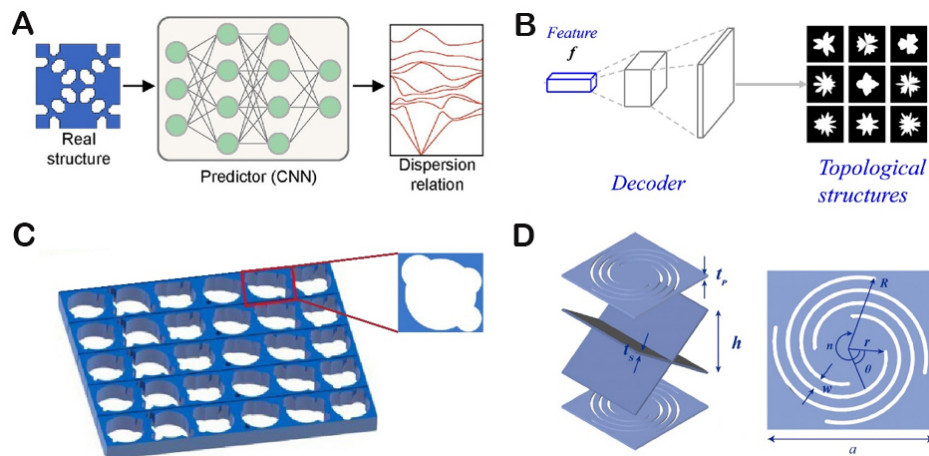


Figure 2. ML for the design of band structure in infinite meta-structures. (A) Combining GAN and CNN to realize inverse design of digitally coded metamaterials with anticipated band structures^[94]. Reproduced with the permission of Ref.^[94] Copyright 2022, Elsevier. (B) Design phononic crystals with anticipated bandgaps by combining AE and MLP^[99]. Reproduced with the permission of Ref.^[99] Copyright 2020, Elsevier. (C) Design phononic crystals with anticipated bandgaps by combining GA and MLP^[100]. Reproduced with the permission of Ref.^[100] Copyright 2023, Taylor & Francis. (D) Employ MLP to design lightweight meta-structures with low-frequency broadband vibration isolation functions^[101].

optimal wave attenuation^[95]. It is worth noting that this work characterizes the wave attenuation ability of the structure through complex band structures. Although the design process focuses on the real part of the band structures, the final screening process from alternative structures is achieved by comparing the imaginary part of band structures.

Tailoring bandgaps

From an application perspective, it is usually not necessary to determine the complete band structures but only focuses on the wave information provided by the bandgaps in the band structures. In contrast, the design based on bandgaps simplifies the difficulty of model training and has a stronger design purpose, so a lot of work has been carried out in this area.

Liu *et al.* employed MLP and TNN to achieve inverse design from bandgaps to structures for the layered phononic crystals^[96]. The basic conclusion is that for inverse design with single (filling fraction) or dual (shear modulus ratio and mass density ratio) parameters, MLP and TNN perform equally. However, for inverse design with three parameters, TNN has obvious advantages, while MLP has difficulty in convergence. This is due to the increase in the number of design parameters deepens the nonlinearity of the mapping, leading to the gradual exposure of data inconsistency issues. As mentioned in the introduction, TNN can effectively solve this training bottleneck. Dong *et al.* proposed using GA to optimize MLP architecture for fast prediction of bandgap width^[97]. The starting point of this study is to serve as an efficient means to avoid the significant computational costs required for repeated finite element analysis of elastic meta-structures. Wu *et al.* explored a design and optimization scheme of modular metamaterial using ML^[98]. In their work, modular metamaterials are composed of a certain number of four candidate materials through different configurations to form phononic crystals. By using GA and MLP, they realize the optimal configuration design of one-dimensional and two-dimensional (2D) modular metamaterial according to the bandgap target. Li *et al.* combined an AE with MLP to achieve 2D phononic crystal design with anticipated bandgaps, as shown in Figure 2B^[99]. The RVE of phononic crystals is generated through random functions, and the band structure data are obtained through a finite element method. The implementation of this design consists of three steps. Firstly, the AE is trained to extract the topological features of the RVE

configuration. Secondly, an MLP model is trained to describe the relationship between the anticipated bandgap and topological features. Finally, the encoder in the AE is replaced with MLP. Miao *et al.* conducted another study on the design of 2D phononic crystals described by random functions, as shown in [Figure 2C](#)^[100]. In this work, they first employed MLP to predict the bandgap and then used MLP combined with GA to achieve the inverse design of the structure. In the inverse design scheme, GA is taken as the main body, and the fitness function is constructed with the predicted bandgap of MLP and the target bandgap in the iterative process, and the optimal individual that can adapt to the target bandgap is obtained through iteration.

In terms of meta-structure design with high-quality vibration reduction function, Jin *et al.* employed MLP to inverse design the Archimedes spiral meta-structure with deep subwavelength vibration isolation function, as shown in [Figure 2D](#)^[101]. The double-layer corrugated core sandwiched structure between two spiral plates can provide low-frequency bandgaps through a local resonance mechanism. However, it is difficult to analyze the relationship between the bandgap and the parameters of the spiral plate. The trained MLP model avoided the analytical process of inverse design and obtained a structure with low-frequency broadband vibration isolation performance, which showed good consistency with the experiment. On *et al.* modified the TNN architecture and realized the design of arch meta-structure with anticipated bandgap vibration reduction function^[102]. Specifically, they inverted the pre-trained forward network and inverse design network in traditional TNN, where the input is a structural parameter, while the intermediate layer outputs the bandgap frequency. After training, preserving the inverse network of the backend can achieve the design of bandgap frequencies to structures.

The application of RL in band structures is mainly to maximize the bandgap width or optimize the specific range and focuses on one-dimensional structures with analytical dispersion relation. According to the analytical dispersion relation of layered phononic crystals, Luo *et al.* used RL to optimize the component widths and realized two functions: maximizing the bandgap width and customizing the bandgap range^[103]. Wu *et al.* employed RL to optimize the masses of one-dimensional atomic chains to achieve custom bandgaps^[104]. He *et al.* analyzed the longitudinal wave dispersion of periodically variable cross-section beams and optimized three length parameters using RL to achieve maximum bandgap width^[105].

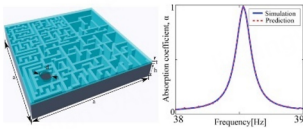
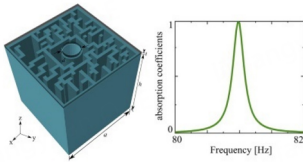
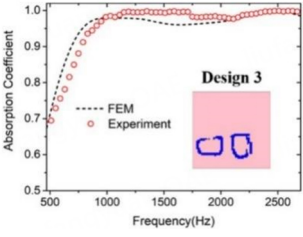
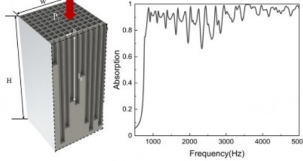
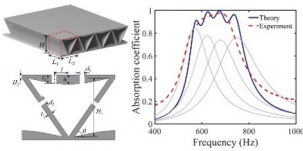
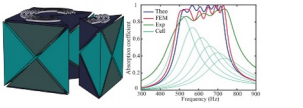
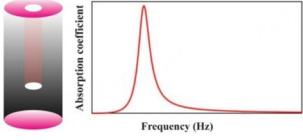
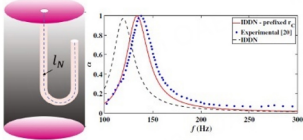
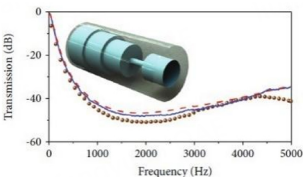
Design of wave propagation characteristics in finite meta-structures

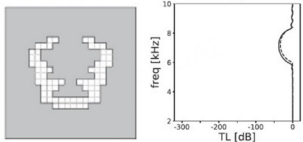
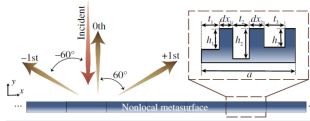
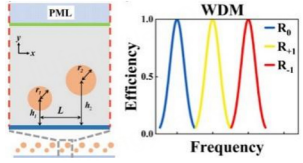
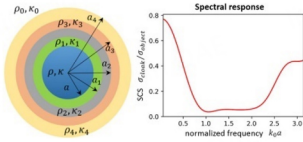
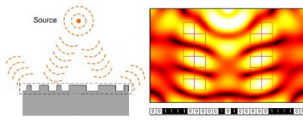
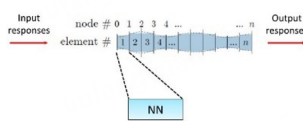
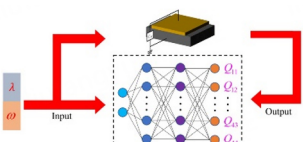
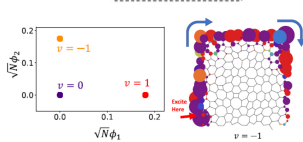
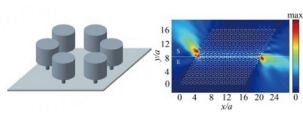
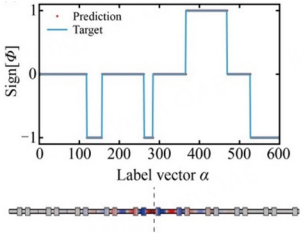
Different from the ideal infinite period meta-structures, the meta-structures in practical engineering can only be composed of periodic or aperiodic finite distributions. Analyzing the propagation characteristics of acoustic/elastic waves in finite meta-structures is an important step toward achieving practical engineering applications for meta-structures. In this section, we review the finite meta-structure design works around propagation characteristics. [Table 2](#) provides a brief overview of ML for the design of wave propagation characteristics in finite meta-structures.

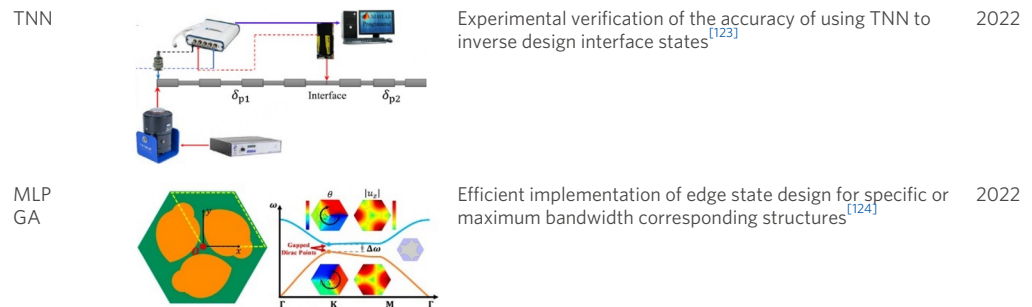
Enhancing noise reduction

Arranging sound absorption structures is one of the main methods for controlling environmental noise, which can be divided into porous sound absorption structures, resonant sound absorption structures, and special sound absorption structures, and has been widely used. The ability of a structure to absorb sound energy is usually characterized by calculating its sound absorption coefficient. Due to the complexity and diversity of the structure, design is an important step to meet practical needs. Researchers have conducted extensive explorations in this area using ML. For example, Donda *et al.* employed CNN to characterize the acoustic absorption performance of acoustic absorbing metasurfaces^[106]. Subsequently, they implemented the inverse design of the metasurface using CGAN^[107]. Zhang *et al.* realized the accelerated topological

Table 2. A brief overview of design based on wave propagation characteristics in infinite meta-structures

Design type	Algorithm	Meta-structure and performance	Description	Year
Enhancing noise reduction	CNN		Predicted the absorption spectra of metasurfaces based on CNN and conducted experimental verification ^[106]	2021
	CNN CGAN		Prediction of sound absorption spectra of absorbers based on CNN and inverse design based on CGAN ^[107]	2022
	GAN		The generated structures can have completely new configurations and rich local features. They can be in good agreement with experimental results ^[108]	2021
	TNN		Overcoming the data inconsistency caused by the complex coupling effect between Fabry Perot channels, the experimental results are in good agreement ^[109]	2022
	RL		Exploring deep subwavelength broadband sound absorption meta-structures based on RL, replacing the artificial selection of structural parameters. The accuracy of the design was verified through sound absorption experiments ^[110]	2022
	RL		Employing RL to optimize the huge parameter space with nine aperture parameters to design broadband sound absorption meta-structures, and further validated through experimentation ^[111]	2023
	CNN		Inverse design of the absorber based on the target absorption spectrum by employing a one-dimensional CNN model. The difficulty lies in the selection of neural network structure and hyperparameters ^[112]	2021
	TNN		Inverse design of the absorber based on the target absorption spectrum by employing TNN. The model uses fewer hyperparameters and has higher accuracy and efficiency than traditional CNN ^[113]	2023
	MLP gaussian sampling		The inverse design incorporating probability sampling can obtain all possible structures. The transmission spectrum measured in the experiment is highly consistent with the predicted results, and the accuracy of the report is better than models such as ANN and GAN ^[114]	2020

	CGAN		Applying CGAN to generate sound insulation structure. The generated structure may not fully conform to physical laws, and the dataset may have a few duplicate samples ^[115]	2021
Advanced control of wave propagation characteristics	TNN		TNN effectively handles the increase in non-inconsistency of the dataset caused by non-local coupling effects ^[116]	2021
	TNN gaussian sampling		Introducing probability sampling in the middle layer of TNN, the design parameters have high flexibility, diversity, and robustness ^[117]	2022
	TNN gaussian sampling		A probabilistic model is a powerful tool to solve data inconsistency and has strong robustness to sensitive parameter design ^[118]	2021
	CNN GA		Employing CNN to achieve inverse design of metasurfaces based on multi-point sound pressure and the accuracy report is better than GA ^[119]	2021
	MLP		Replace the physical unit with MLP and transfer the input response, material properties, and output response of the whole system through the connection between MLPs ^[104]	2021
	MLP		MLP captures the relationship between the input and output wave responses of physical units to construct the overall structure and replace the time-consuming numerical simulation process ^[120]	2022
Optimizing topological states	Clustering		Through clustering algorithms, topological classification is carried out according to the real characteristics of the system, without prior knowledge and calculation of topological invariant ^[121]	2020
	MLP		Inverse design of phononic plate with anticipated bandgap width and topological property Using MLP. The quality of the edge state can be freely controlled through the preset bandgap width ^[122]	2021
	TNN		TNN overcomes data inconsistency and supports inverse design structures based on topological properties to achieve custom interface states ^[105]	2022



design of metaporous materials with broadband sound absorption performance by GAN^[108]. Liu *et al.* used cascaded inverse and forwarded CNN to achieve the inverse design of acoustic absorbing devices with coiled Fabry-Perot channels, which is based on the same principle as a fully connected TNN architecture^[109]. Jin *et al.* used RL to optimize a lightweight sound absorption multi-function integrated meta-structure with perforated fish-belly panels^[110]. Subsequently, they used this method to optimize a spiral plate sandwich structure that integrates lightweight, vibration reduction, and sound absorption functions^[111]. Mahesh *et al.* proposed a one-dimensional CNN inverse design scheme for low-frequency Helmholtz resonate sound absorber^[112]. Afterward, they further constructed a TNN architecture using inverse and forward one-dimensional CNNs for inverse design of a similar sound-absorbing structure^[113].

Sound insulation is another method of controlling noise, with the objective of blocking or attenuating the transmission of acoustic waves. It typically relies on the transmission coefficient to characterize the performance of the sound insulation structure in blocking sound energy. For the design enabled by ML in sound insulation meta-structures, Luo *et al.* provided a paradigm of fuzzy design to overcome the problem of data inconsistency, as shown in Figure 3A^[114]. Specifically, they combine MLP with mixed Gaussian sampling, mapping a target transmission spectrum to multiple sets of Gaussian sampling parameters through MLP and then linearly overlaying these Gaussian distributions to obtain a mixed Gaussian distribution. All acoustic meta-structures corresponding to the local maximum values are alternative structures that meet the target transmission frequency spectrum. Gurbuz *et al.* used a random algorithm to generate binary images of units composed of fluid elements and solid elements and obtained the transmission loss spectra through the finite element method^[115]. Then, by training CGAN to capture the potential relationship between transmission loss spectrum and unit geometry, they carried out inverse design of the structural units to achieve the required sound insulation purpose.

Advanced control of wave propagation characteristics

Subwavelength scale metasurfaces may experience significant losses due to the presence of viscous friction and narrow acoustic channels. The diffraction acoustic meta-grating designed based on diffraction theory can improve the control efficiency of the acoustic metasurface. Ding *et al.* employed the TNN model to achieve inverse design of non-local metasurfaces for acoustic wave diffraction characteristics^[116]. They explored the coupling effect between all subunits rather than nearest-neighbor coupling, demonstrating the ability of non-local metasurfaces to reshape the acoustic field. Meanwhile, the implementation of this work effectively demonstrates the ability of TNN to support the design of non-local coupled metasurfaces, especially in the face of complex coupling effects that greatly increase the degree of nonlinearity. In another work, Du *et al.* designed acoustic meta-grating wavelength division multiplexing by using an improved TNN architecture^[117]. Specifically, they introduced probability sampling in the TNN architecture, which divides the design space into two layers instead of the traditional one layer for design parameters. Among them, the latter layer is the design parameters of the structure, obtained by sampling from the Gaussian

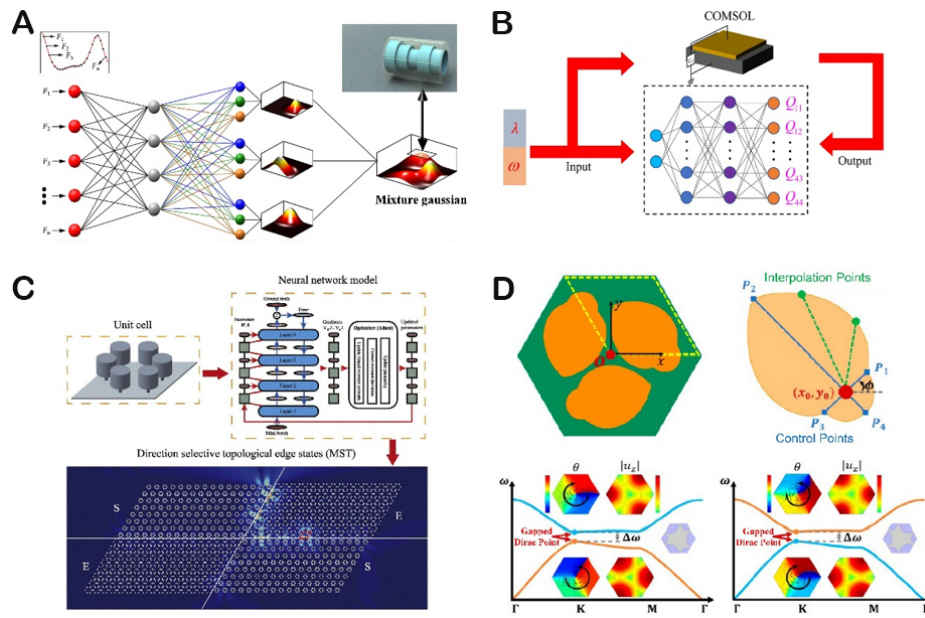


Figure 3. ML for the design of wave propagation characteristics in finite meta-structures. (A) Fuzzy design of acoustic meta-structures by combining MLP with Gaussian mixture sampling^[114]. (B) Employ MLP to realize global transfer matrix prediction of active metabeams^[120]. Reproduced with the permission of Ref.^[120] Copyright 2020, Elsevier. (C) Employ MLP to realize the design of metaplates with robust edge states^[122]. (D) Design of Valley Hall acoustic topological insulator by combining MLP and GA^[124].

distribution parameters of the previous layer. The probabilistic TNN model has a strong generalization ability, greatly reducing the design cost of acoustic meta-grating wavelength division multiplexing. It demonstrates the flexibility, diversity, and robustness of design parameters.

The acoustic cloak technology aims to reduce the sound signals generated by objects in order to reduce the detectability of the sound detection system and achieve the effect of stealth. Ahmed *et al.* implemented a design of a multilayer core-shell acoustic cloak using probabilistic TNN architecture, demonstrating its effectiveness in solving the problem of high sensitivity of stealth cloaks to design parameters^[118]. Stealth requirements weaken or even eliminate the disturbance of objects to the sound field, while in some practical needs, it is desired to freely weaken or enhance the sound field in certain specific areas. In this aspect, Zhao *et al.* proposed a CNN-based inverse design of metasurface phase gradient to achieve the regional control of sound field enhancement or attenuation^[119].

In addition, research has attempted to enable MLP to learn the physical mechanisms of a single unit and then use it to construct a functional analysis of wave propagation in the overall structure. For example, Wu *et al.* used MLP to learn the input-output relationship of longitudinal waves in non-uniform thin rod elements and then assembled multiple MLP elements to construct a non-uniform overall structure^[104]. A series of cascaded MLP units describe the input-output relationship of the overall structure and then use optimization algorithms to determine the design parameters of each individual unit. Similarly, Chen *et al.* used MLP for transfer matrix prediction of active metabeam elements, as shown in Figure 3B^[120]. In their work, the metabeam unit is constructed by affixing a piezoelectric material on the main beam and connecting a negative capacitance circuit. By using COMSOL software to obtain transfer matrices for different capacitance values and frequencies, a dataset is constructed and used for MLP training. The global transfer matrix of the array elements can be obtained by connecting multiple groups of MLP in sequence, then the output and input signals of the whole metabeam can be connected.

Optimizing topological states

A topological state is also an important form of wave characteristics in finite structures. We now turn to focus on some recent design works on topological states. Generally speaking, topological invariants can characterize topological properties of structures, but their definition and calculation are often difficult. In essence, topological properties certainly exist in structural features, so exploring topological properties from actual structures instead of relying on topological invariants is another idea for topological classification. Long *et al.* demonstrated an unsupervised clustering algorithm for extracting topological features of phononic crystals, thereby classifying topological properties^[121]. He *et al.* achieved the inverse design of phononic crystal thin plates with anticipated bandgap width and topological property based on MLP, as shown in [Figure 3C](#)^[122]. By designing two units with a broadband common bandgap, they constructed a highly robust localized edge state for bending wave transmission. This group subsequently proposed using TNN to achieve the inverse design of phononic beams from topological properties to structure^[105]. The topological properties of the bandgap were characterized by the reflection phase, and the interface states of one-dimensional phononic beams were predicted and constructed using TNN. Afterward, Muhammad *et al.* also completed a similar work^[123]. Du *et al.* realized the inverse design of Valley Hall acoustic topological insulator by combining MLP and GA, as shown in [Figure 3D](#)^[124]. Specifically, they first trained regression neural networks and classification neural networks for predicting bandgap and topological properties, respectively. Then, two neural networks are put into the optimization process of GA to obtain two structures with opposite topological properties under a common bandgap for constructing edge states.

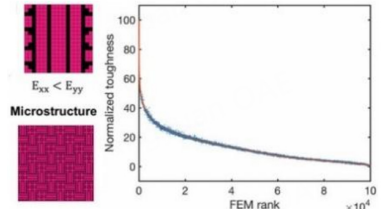
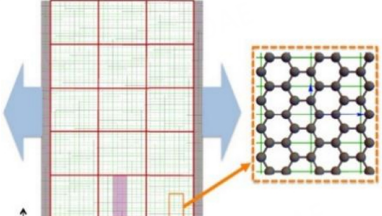
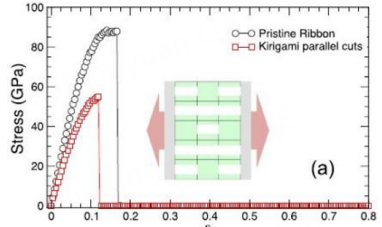
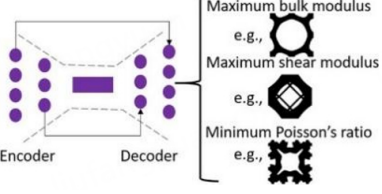

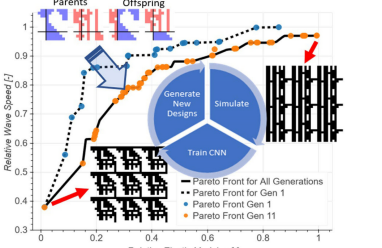

The application of ML in Hermitian systems mentioned above is still in the initial stage, and more achievements need to be further expanded. At the same time, we have also found that ML has recently made some attempts in non-Hermitian systems. Yu *et al.* used diffusion maps to unsupervised manifold learning of topological phases in non-Hermitian systems^[125]. Different from the unsupervised method, there are also some works that demonstrate training ANNs for supervised prediction of non-Hermitian topological invariants^[126-128]. The essential difference between unsupervised and supervised is that the former does not need labels and directly extracts topological invariant from the on-site elements of the model, while the latter relies on the calculated topological invariant as labels to construct data sets. In non-Hermitian systems, an exception point (EP) is an important feature that represents the critical point at which the system transitions from a real eigen-spectrum to a complex eigen-spectrum^[129]. In the latest work, Reja *et al.* introduced neural networks for the characterization of EP^[130]. They proposed a method called summed phase rigidity (SPR) to characterize the order of EPs in different models. Then, they trained MLP models to realize the prediction of EPs for two-site and four-site gain and loss models.

Design of static characteristics in mechanical meta-structures

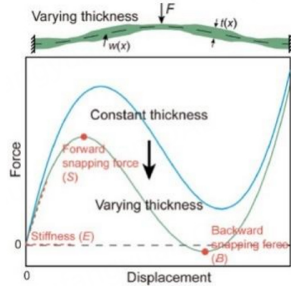
Mechanical meta-structures have become an emerging growth point in the field of ML-enabling design due to their extreme static performance. Combined with ML, meta-structures with excellent mechanical properties can be obtained through design optimization by adding, deleting, or changing. [Table 3](#) provides a brief overview of ML for the design of static characteristics in mechanical meta-structures.

A lot of work has been carried out around the 2D mechanical meta-structures. These structures are usually designed and optimized on a plane to obtain specific shapes or material compositions with specific mechanical properties. CNN, as a high-quality model for image feature extraction, is widely used in the design of 2D mechanical meta-structures. Gu *et al.* proposed a self-learning CNN model to search for high-performance hierarchical mechanical structures^[131]. This model can continuously learn patterns from high-performance structures, ultimately achieving design results superior to the training set. Hanakata *et al.* reported a design study on stretchable graphene kirigami, as shown in [Figure 4A](#)^[132]. The cutting density and

Table 3. A brief overview of design based on static characteristics in mechanical meta-structures

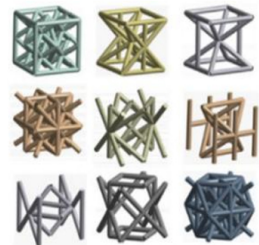
Design Type	Algorithm	Meta-structure and Performance	Description	Year
2D structure	CNN		The inverse design of high toughness hierarchical structures based on CNN greatly saves computational time compared to traditional finite element methods ^[131] .	2018
	CNN		Effectively searching for the optimal cutting mode for stretchable graphene kirigami structures under given yield strain and stress conditions based on CNN models ^[132] .	2018
Supervised AE	AE		Generate the structure by passing potential variables to the decoder. It is expected to find new structures, but the prediction of mechanics performance beyond the dataset may be biased ^[133] .	2020
	CNN		CNN for predicting 2D metamaterials with the best mechanical properties. The model exhibits robustness in terms of accuracy and inference time ^[134] .	2020
DCGAN CNN	DCGAN CNN		Combine DCGAN and CNN for designing microstructures. The model has high efficiency and can flexibly control geometric constraints ^[135] .	2019
CNN GA	CNN GA		Combining CNN and GA can find Pareto's optimal structural design using a relatively small dataset, even with complex nonlinear constraints ^[136] .	2021
CNN GAN	CNN GAN		Inverse design of 2D metamaterial based on predefined Poisson's ratio. The model can generate structures beyond the dataset and exhibit responses similar to real structures ^[137] .	2022

1D/3D structure MLP



Realize accurate prediction of variable thickness curved beams and their properties. Efficient and accurate optimization design results were obtained with different optimization objectives^[138]. 2020

GAN



Generate lightweight and high load-bearing performance lattice structures using GAN and conduct experimental verification^[139]. 2021

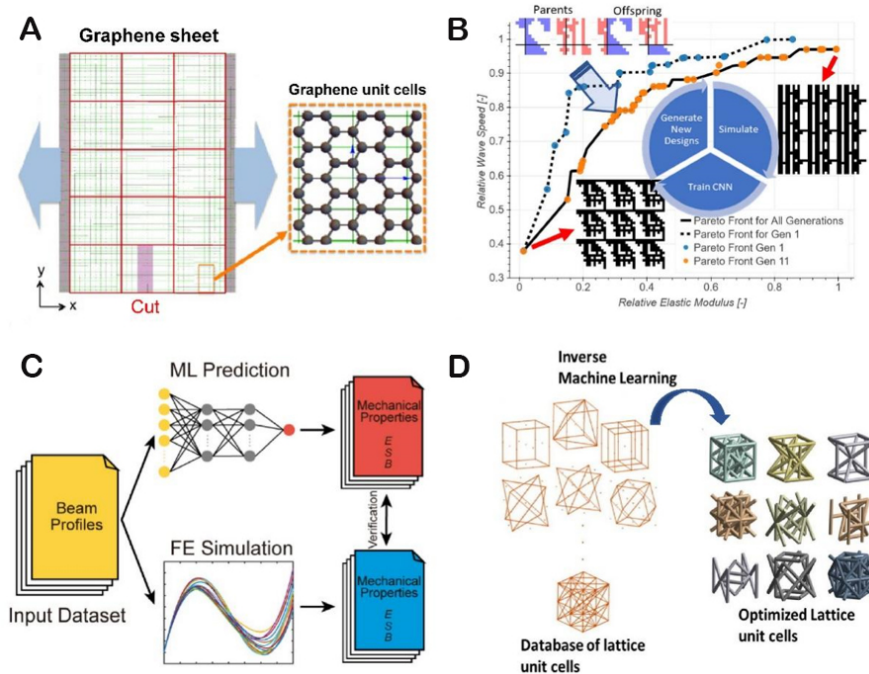


Figure 4. ML for the design of static characteristics in mechanical meta-structures. (A) Searching for the graphene kirigami with the best stretching performance through gradual training of CNN^[132]. Reproduced with the permission of Ref.^[132] Copyright 2018, the American Physical Society. (B) Combining CNN and GA to realize lattice metamaterial design satisfying additive manufacturing constraints^[136]. (C) Design of curved beams with best mechanical properties based on MLP and optimization methods^[138]. Reproduced with the permission of Ref.^[138] Copyright 2020, Elsevier. (D) Design of lightweight lattice structures by GAN-based inverse design framework^[139].

cutting position control the elastic stretchability of graphene kirigami. They first trained CNN through supervision to predict the stretchability of graphene kirigami expressed by yield strain. Then, in the inverse design, the CNN is trained using the dataset obtained from molecular dynamics calculations, and the model is gradually trained using the best performance predicted by the CNN. In subsequent research^[133], they proposed a supervised AE to design graphene kirigami. Kollmann *et al.* reported the 2D metamaterial

design with either maximum bulk modulus, maximum shear modulus, or minimum Poisson's ratio using CNN^[134]. The dataset of their work is generated by the topology optimization framework based on the energy homogenization method and periodic boundary conditions.

To optimize the structure to obtain a 2D structure with the best mechanical properties, CNN is often combined with GAN or GA. Tan *et al.* reported a model in which deep convolutional GANs (DCGAN) are used to generate candidates adhering to geometric constraints, while CNN associates microstructures with properties^[135]. After training, combine the two models for inverse design microstructural materials with specific mechanical properties. Garland *et al.* demonstrated the design of structural lattice metamaterial combining CNN and GA to meet the constraints of additive manufacturing, as shown in Figure 4B^[136]. In addition, Wang *et al.* and Chang *et al.* also used this design paradigm to realize the inverse design of shell-based mechanical metamaterial and auxetic metamaterial with zero Poisson's ratio, respectively^[140,141]. Tian *et al.* proposed the combination of CNN and GAN to achieve customized Poisson's ratio meta-structure design^[137]. CNN is trained to predict the global Poisson's ratio response of a given meta-structure, while GAN realizes the structural inverse design of the anticipated Poisson's ratio response through adversarial training.

In addition, some works have been done to design and optimize specific mechanical properties of one-dimensional or three-dimensional (3D) meta-structures. Liu *et al.* demonstrated a design work of curved beams based on MLP and optimization methods, as shown in Figure 4C^[138]. The mechanical properties of curved beams are characterized by stiffness, forward snapping force, and backward snapping force and are controlled by thickness distributions. They first trained MLP to predict the mechanical properties of curved beams with variable thickness and then put the trained MLP model into the optimization cycle proposed by Gu *et al.*, as mentioned above, to optimize the thickness distribution with the best mechanical properties^[131]. Challapalli *et al.* demonstrated the GAN-based inverse design framework for optimizing lightweight lattice structures, as shown in Figure 4D^[139]. The basic idea of this framework is to add initial conditions, boundary conditions, and forward regression to the real data distinguished by discriminators to obtain structural units with excellent performance. The new dataset is then used for GAN training, and the process is iterated repeatedly to obtain the structure with the best mechanical performance.

CONCLUSION AND OUTLOOK

In this review, we have discussed the combination and synchronous development of ML and meta-structure and reviewed the recent flexible applications of ML algorithms in the fields of acoustics, elastic, and mechanical meta-structures from the aspects of band structures, wave propagation characteristics, and static characteristics. Through analysis, we have come to the following main conclusions:

(1) The forward performance prediction of meta-structures can usually rely on analytical formulas or simulation software. The purpose of introducing ML is to save time and computing resources or to provide a forward computing part for some combined inverse design schemes. The inverse design of meta-structures is difficult to deal with analytically. DNNs with strong nonlinear modeling capabilities effectively solve this problem and can directly serve as alternative models for inverse problems. In addition, RL can also serve as an inverse design algorithm in meta-structures to explore structures that meet customized performance goals in the parameter space.

(2) A crucial issue in the inverse design process is how to alleviate data inconsistency. There are two main ideas. One approach is based on deterministic strategies, with representative approaches being: 1. TNN architecture with inverse and forward network concatenation. 2. Combining MLP (or CNN) with an AE.

The former achieves mapping from performance to features, while the latter achieves structure reconstruction from features. 3. Combining MLP (or CNN) with GA. The former achieves performance prediction through pre-training and then adds it to the iterative process of the latter. Another approach is based on probabilistic strategies; the main approach is to use Gaussian sampling after the data passes through the neural network rather than directly mapping to the structure or introducing Gaussian sampling in the middle design layer of the TNN architecture. Compared to deterministic strategies, probabilistic strategies have more diverse design choices.

(3) As the functional requirements of meta-structures become more critical, the design of meta-structures based on specific goals becomes more and more complex, which makes many advanced algorithms constantly develop and combine to meet the requirements. The support of an open-source framework makes the development of relevant algorithms for meta-structure design easier, even for the researchers without professional backgrounds in ML, which is an important reason for this field in a period of vigorous development and growth.

Although the research on the combination of ML and meta-structures has aroused great interest and attention in recent years, and many research achievements have been made, there are still many problems that restrict further development. The main problems and future directions can be summarized as follows:

(1) Obtaining data is often difficult, especially for problems without analytical solutions or high numerical calculation costs. Therefore, it is necessary to develop algorithms that only need small dataset training, such as reducing the demand for source data by transfer learning. Additionally, there is currently a lack of commonly used datasets in the field of meta-structure design. If researchers can share some datasets of conventional meta-structures, it will be easy to achieve data migration and fusion in the future.

(2) ANNs are often seen as black boxes, wherein the input of a set of structural parameters naturally results in the output of a corresponding set of performance parameters. Exploring what changes the data has undergone in the process of layer-by-layer transmission, in other words, how the structural parameters change step by step toward the performance parameters after each layer of operation, is important research to uncover the interpretability application of neural networks in the field of meta-structures.

(3) The research on some new physical concepts, such as non-Hermit smart phononic crystals, is in full swing in the field of meta-structures. What role ML can play in these new physical mechanisms is a question that can be deeply explored at present.

(4) The research of meta-structure mainly involves design and manufacturing. ML can theoretically provide excellent design results for various acoustic or mechanical requirements of targets, but most current research lacks manufacturing and experimental verification after design. Therefore, more consideration of manufacturing and verification is an important prerequisite for the application of this field.

(5) Multifunctional integration is an important direction of the development of meta-structures at present, which may involve the coupling of multiple physical fields, such as acoustics, mechanics, electromagnetism, and heat. Developing ML algorithms for multifunctional meta-structure design with multi-physical field characteristics is not only a challenge but also a promising direction. The path planning problem of multifunctional integrated composite meta-structure configuration in 3D printing containing continuous fibers is one of the important reasons currently restricting the manufacturing of complex composite structures. By introducing ML algorithms to optimize the fiber distribution direction field of continuous

fiber path planning, a collaborative optimization scheme between continuous fiber path and functional structure configuration can be achieved, which is expected to become an important means for the manufacturing of complex composite meta-structures in the future.

DECLARATIONS

Authors' contributions

Supervision, conceptualization, validation, project administration, funding acquisition: Jin Y, Li Y, Zhuang X

Original draft preparation, reviewing, and editing: He L, Li Y, Torrent D, Zhuang X, Rabczuk T, Jin Y

Availability of data and materials

Not applicable.

Financial support and sponsorship

This work was supported by the National Key R&D Program of China (Grant No. 2022YFB4602000), the National Natural Science Foundation of China (No.12272267 and No. 52278411), the Young Elite Scientists Sponsorship Program by CAST (2021QNR001), the Shanghai Science and Technology Committee (No. 22JC1404100 and No. 21JC1405600), the Fundamental Research Funds for the Central Universities. This publication is part of Project No. PID2021-124814NB-C22, funded by MCIN/AEI/10.13039/501100011033, "FEDER, A way of making Europe".

Conflicts of interest

All authors declared that there are no conflicts of interest.

Ethical approval and consent to participate

Not applicable.

Consent for publication

Not applicable.

Copyright

© The Author(s) 2023.

REFERENCES

1. Kumar R, Kumar M, Chohan JS, Kumar S. Overview on metamaterial: history, types and applications. *Mater Today Proc* 2022;56:3016-24. [DOI](#)
2. Ma G, Sheng P. Acoustic metamaterials: from local resonances to broad horizons. *Sci Adv* 2016;2:e1501595. [DOI](#) [PubMed](#) [PMC](#)
3. Yu X, Zhou J, Liang H, Jiang Z, Wu L. Mechanical metamaterials associated with stiffness, rigidity and compressibility: a brief review. *Prog Mater Sci* 2018;94:114-73. [DOI](#)
4. Cui T. Electromagnetic metamaterials - from effective media to field programmable systems. *Sci Sin Inf* 2020;50:1427. [DOI](#)
5. Jin Y, Pennec Y, Bonello B, et al. Physics of surface vibrational resonances: pillared phononic crystals, metamaterials, and metasurfaces. *Rep Prog Phys* 2021;84:086502. [DOI](#)
6. Wu X, Wen Z, Jin Y, Rabczuk T, Zhuang X, Djafari-rouhani B. Broadband rayleigh wave attenuation by gradient metamaterials. *Int J Mech Sci* 2021;205:106592. [DOI](#)
7. Cao L, Yang Z, Xu Y, et al. Flexural wave absorption by lossy gradient elastic metasurface. *J Mech Phys Solids* 2020;143:104052. [DOI](#)
8. Huang S, Zhou Z, Li D, et al. Compact broadband acoustic sink with coherently coupled weak resonances. *Sci Bull* 2020;65:373-9. [DOI](#)
9. Jin Y, Wang W, Khelif A, Djafari-rouhani B. Elastic metasurfaces for deep and robust subwavelength focusing and imaging. *Phys Rev Appl* 2021;15:024005. [DOI](#)
10. Wang W, Iglesias J, Jin Y, Djafari-rouhani B, Khelif A. Experimental realization of a pillared metasurface for flexural wave focusing.

- APL Mater* 2021;9:051125. DOI
11. Wen Z, Jin Y, Gao P, Zhuang X, Rabczuk T, Djafari-rouhani B. Topological cavities in phononic plates for robust energy harvesting. *Mech Syst Signal Process* 2022;162:108047. DOI
 12. Wen Z, Wang W, Khelif A, Djafari-rouhani B, Jin Y. A perspective on elastic metastructures for energy harvesting. *Appl Phys Lett* 2022;120:020501. DOI
 13. He H, Qiu C, Ye L, et al. Topological negative refraction of surface acoustic waves in a Weyl phononic crystal. *Nature* 2018;560:61-4. DOI
 14. Jin Y, Fang X, Li Y, Torrent D. Engineered diffraction gratings for acoustic cloaking. *Phys Rev Appl* 2019;11:011004. DOI
 15. Zhou H, Fu W, Wang Y, Wang Y, Laude V, Zhang C. Ultra-broadband passive acoustic metasurface for wide-angle carpet cloaking. *Mater Des* 2021;199:109414. DOI
 16. Zhang X, Xiao M, Cheng Y, Lu M, Christensen J. Topological sound. *Commun Phys* 2018;1:97. DOI
 17. Kushwaha MS, Halevi P, Dobrzynski L, Djafari-Rouhani B. Acoustic band structure of periodic elastic composites. *Phys Rev Lett* 1993;71:2022-5. DOI PubMed
 18. Martínez-sala R, Sancho J, Sánchez JV, Gómez V, Llinares J, Meseguer F. Sound attenuation by sculpture. *Nature* 1995;378:241. DOI
 19. Liu Z, Zhang X, Mao Y, et al. Locally resonant sonic materials. *Science* 2000;289:1734-6. DOI
 20. Liao G, Luan C, Wang Z, Liu J, Yao X, Fu J. Acoustic metamaterials: a review of theories, structures, fabrication approaches, and applications. *Adv Mater Technol* 2021;6:2000787. DOI
 21. Yang Z, Mei J, Yang M, Chan NH, Sheng P. Membrane-type acoustic metamaterial with negative dynamic mass. *Phys Rev Lett* 2008;101:204301. DOI PubMed
 22. Fang N, Xi D, Xu J, et al. Ultrasonic metamaterials with negative modulus. *Nat Mater* 2006;5:452-6. DOI
 23. Ding C, Hao L, Zhao X. Two-dimensional acoustic metamaterial with negative modulus. *J Appl Phys* 2010;108:074911. DOI
 24. Lee SH, Park CM, Seo YM, Wang ZG, Kim CK. Composite acoustic medium with simultaneously negative density and modulus. *Phys Rev Lett* 2010;104:054301. DOI PubMed
 25. Li J, Chan CT. Double-negative acoustic metamaterial. *Phys Rev E* 2004;70:055602. DOI
 26. Yu N, Genevet P, Kats MA, et al. Light propagation with phase discontinuities: generalized laws of reflection and refraction. *Science* 2011;334:333-7. DOI
 27. Assouar B, Liang B, Wu Y, Li Y, Cheng J, Jing Y. Acoustic metasurfaces. *Nat Rev Mater* 2018;3:460-72. DOI
 28. Qi S, Li Y, Assouar B. Acoustic focusing and energy confinement based on multilateral metasurfaces. *Phys Rev Appl* 2017;7:054006. DOI
 29. Faure C, Richoux O, Félix S, Pagneux V. Experiments on metasurface carpet cloaking for audible acoustics. *Appl Phys Lett* 2016;108:064103. DOI
 30. Sounas DL, Fleury R, Alù A. Unidirectional cloaking based on metasurfaces with balanced loss and gain. *Phys Rev Appl* 2015;4:014005. DOI
 31. Huang S, Fang X, Wang X, Assouar B, Cheng Q, Li Y. Acoustic perfect absorbers via spiral metasurfaces with embedded apertures. *Appl Phys Lett* 2018;113:233501. DOI
 32. Ji J, Li D, Li Y, Jing Y. Low-frequency broadband acoustic metasurface absorbing panels. *Front Mech Eng* 2020;6:586249. DOI
 33. Li Y, Shen C, Xie Y, et al. Tunable asymmetric transmission via lossy acoustic metasurfaces. *Phys Rev Lett* 2017;119:035501. DOI
 34. Fang X, Wang X, Li Y. Acoustic splitting and bending with compact coding metasurfaces. *Phys Rev Appl* 2019;11:064033. DOI
 35. Wang P, Lu L, Bertoldi K. Topological phononic crystals with one-way elastic edge waves. *Phys Rev Lett* 2015;115:104302. DOI PubMed
 36. Torrent D, Mayou D, Sánchez-dehesa J. Elastic analog of graphene: dirac cones and edge states for flexural waves in thin plates. *Phys Rev B* 2013;87:115143. DOI
 37. Lera N, Torrent D, San-jose P, Christensen J, Alvarez JV. Valley hall phases in kagome lattices. *Phys Rev B* 2019;99:134102. DOI
 38. Chaunsali R, Chen C, Yang J. Subwavelength and directional control of flexural waves in zone-folding induced topological plates. *Phys Rev B* 2018;97:054307. DOI
 39. Lu J, Qiu C, Ye L, et al. Observation of topological valley transport of sound in sonic crystals. *Nat Phys* 2017;13:369-74. DOI
 40. Wang H, Guo G, Jiang J. Band topology in classical waves: wilson-loop approach to topological numbers and fragile topology. *New J Phys* 2019;21:093029. DOI
 41. Fukui T, Hatsugai Y, Suzuki H. Chern numbers in discretized brillouin zone: efficient method of computing (spin) hall conductances. *J Phys Soc Jpn* 2005;74:1674-7. DOI
 42. Huo SY, Chen JJ, Huang HB. Topologically protected edge states for out-of-plane and in-plane bulk elastic waves. *J Phys Condens Matter* 2018;30:145403. DOI PubMed
 43. He C, Ni X, Ge H, et al. Acoustic topological insulator and robust one-way sound transport. *Nat Phys* 2016;12:1124-9. DOI
 44. Zhai Z, Wu L, Jiang H. Mechanical metamaterials based on origami and kirigami. *Appl Phys Rev* 2021;8:041319. DOI
 45. Wu W, Hu W, Qian G, Liao H, Xu X, Berto F. Mechanical design and multifunctional applications of chiral mechanical metamaterials: a review. *Mater Des* 2019;180:107950. DOI
 46. Zheng X, Lee H, Weisgraber TH, et al. Ultralight, ultrastiff mechanical metamaterials. *Science* 2014;344:1373-7. DOI
 47. Ingrole A, Hao A, Liang R. Design and modeling of auxetic and hybrid honeycomb structures for in-plane property enhancement.

- Mater Des* 2017;117:72-83. DOI
48. Molesky S, Lin Z, Piggott AY, Jin W, Vucković J, Rodriguez AW. Inverse design in nanophotonics. *Nat Photon* 2018;12:659-70. DOI
 49. Goldberg DE, Holland JH. Genetic algorithms and machine learning. *Mach Learn* 1988;3:95-9. DOI
 50. Zhao Y, Cao X, Gao J, et al. Broadband diffusion metasurface based on a single anisotropic element and optimized by the simulated annealing algorithm. *Sci Rep* 2016;6:23896. DOI PubMed PMC
 51. Robinson J, Rahmat-Samii Y. Particle swarm optimization in electromagnetics. *IEEE Trans Antennas Propag* 2004;52:397-407. DOI
 52. Greener JG, Kandathil SM, Moffat L, Jones DT. A guide to machine learning for biologists. *Nat Rev Mol Cell Biol* 2022;23:40-55. DOI PubMed
 53. Fischer T, Krauss C. Deep learning with long short-term memory networks for financial market predictions. *Eur J Oper Res* 2018;270:654-69. DOI
 54. Li W, Chen P, Xiong B, et al. Deep learning modeling strategy for material science: from natural materials to metamaterials. *J Phys Mater* 2022;5:014003. DOI
 55. Goh GB, Hodas NO, Vishnu A. deep learning for computational chemistry. *J Comput Chem* 2017;38:1291-307. DOI PubMed
 56. Oishi A, Yagawa G. Computational mechanics enhanced by deep learning. *Comput Methods Appl Mech Eng* 2017;327:327-51. DOI
 57. Yao K, Unni R, Zheng Y. Intelligent nanophotonics: merging photonics and artificial intelligence at the nanoscale. *Nanophotonics* 2019;8:339-66. DOI PubMed PMC
 58. Ma W, Liu Z, Kudyshev ZA, Boltasseva A, Cai W, Liu Y. Deep learning for the design of photonic structures. *Nat Photonics* 2021;15:77-90. DOI
 59. Jiang J, Chen M, Fan JA. Deep neural networks for the evaluation and design of photonic devices. *Nat Rev Mater* 2021;6:679-700. DOI
 60. Wang N, Yan W, Qu Y, Ma S, Li SZ, Qiu M. Intelligent designs in nanophotonics: from optimization towards inverse creation. *Photonix* 2021;2:22. DOI
 61. Piccinotti D, MacDonald KF, A Gregory S, Youngs I, Zheludev NI. Artificial intelligence for photonics and photonic materials. *Rep Prog Phys* 2021;84:012401. DOI PubMed
 62. Chen J, Hu S, Zhu S, Li T. Metamaterials: from fundamental physics to intelligent design. *Interdiscip Mater* 2023;2:5-29. DOI
 63. Zhang Q, Yu H, Barbiero M, Wang B, Gu M. Artificial neural networks enabled by nanophotonics. *Light Sci Appl* 2019;8:42. DOI PubMed PMC
 64. Xu Y, Zhang X, Fu Y, Liu Y. Interfacing photonics with artificial intelligence: an innovative design strategy for photonic structures and devices based on artificial neural networks. *Photon Res* 2021;9:B135-52. DOI
 65. Wiecha PR, Arbouet A, Girard C, Muskens OL. Deep learning in nano-photonics: inverse design and beyond. *Photon Res* 2021;9:B182-200. DOI
 66. So S, Badloe T, Noh J, Bravo-abad J, Rho J. Deep learning enabled inverse design in nanophotonics. *Nanophotonics* 2020;9:1041-57. DOI
 67. Khatib O, Ren S, Malof J, Padilla WJ. Deep learning the electromagnetic properties of metamaterials - a comprehensive review. *Adv Funct Mater* 2021;31:2101748. DOI
 68. Jiao P, Alavi AH. Artificial intelligence-enabled smart mechanical metamaterials: advent and future trends. *Int Mater Rev* 2021;66:365-93. DOI
 69. Jin Y, He L, Wen Z, et al. Intelligent on-demand design of phononic metamaterials. *Nanophotonics* 2022;11:439-60. DOI
 70. Muhammad, Kennedy J, Lim C. Machine learning and deep learning in phononic crystals and metamaterials - a review. *Mater Today Commun* 2022;33:104606. DOI
 71. Liu C, Yu G. Deep learning for the design of phononic crystals and elastic metamaterials. *J Computat Des Eng* 2023;10:602-14. DOI
 72. Russell S, Norvig P. Artificial intelligence: a modern approach, 4th US ed. Prentice Hall 2009. Available from: <http://aima.cs.berkeley.edu/index.html> [Last accessed on 14 Aug 2023].
 73. Jordan MI, Mitchell TM. Machine learning: trends, perspectives, and prospects. *Science* 2015;349:255-60. DOI PubMed
 74. McCulloch WS, Pitts W. A logical calculus of the ideas immanent in nervous activity. *Bull Math Biophys* 1943;5:115-33. DOI
 75. Rosenblatt F. The perceptron: a probabilistic model for information storage and organization in the brain. *Psychol Rev* 1958;65:386-408. DOI PubMed
 76. Rumelhart DE, Hinton GE, Williams RJ. Learning representations by back-propagating errors. *Nature* 1986;323:533-6. DOI
 77. Elman J. Finding structure in time. *Cogn Sci* 1990;14:179-211. DOI
 78. LeCun Y, Bottou L, Bengio Y, Haffner P. Gradient-based learning applied to document recognition. *Proc IEEE* 1998;86:2278-324. DOI
 79. Hinton GE, Osindero S, Teh YW. A fast learning algorithm for deep belief nets. *Neural Comput* 2006;18:1527-54. DOI PubMed
 80. Goodfellow I, Pouget-Abadie J, Mirza M, et al. Generative adversarial nets. In: Ghahramani Z, Welling M, Cortes C, Lawrence ND, Weinberger KQ editors. In Proceedings of the 27th International Conference on Neural Information Processing Systems; 2014 Dec 8-13; Montreal, Canada. Cambridge: MIT Press; 2014. pp. 2672-80.
 81. Mirza M, Osindero S. Conditional generative adversarial nets. Available from: <https://arxiv.org/abs/1411.1784> [Last accessed on 14 Aug 2023].

82. Liu D, Tan Y, Khoram E, Yu Z. Training deep neural networks for the inverse design of nanophotonic structures. *ACS Photonics* 2018;5:1365-9. DOI
83. Kaelbling LP, Littman ML, Moore AW. Reinforcement learning: a survey. *J Artif Intell Res* 1996;4:237-85. Available from: <https://arxiv.org/abs/cs/9605103> [Last accessed on 14 Aug 2023].
84. Silver D, Schrittwieser J, Simonyan K, et al. Mastering the game of go without human knowledge. *Nature* 2017;550:354-9. DOI
85. Kiran BR, Sobh I, Talpaert V, et al. Deep reinforcement learning for autonomous driving: a survey. *IEEE Trans Intell Transport Syst* 2022;23:4909-26. DOI
86. Zhu R, Qiu T, Wang J, et al. Phase-to-pattern inverse design paradigm for fast realization of functional metasurfaces via transfer learning. *Nat Commun* 2021;12:2974. DOI PubMed PMC
87. Kim Y, Kim Y, Yang C, Park K, Gu GX, Ryu S. Deep learning framework for material design space exploration using active transfer learning and data augmentation. *NPJ Comput Mater* 2021;140:7. DOI
88. Alzubi J, Nayyar A, Kumar A. Machine learning from theory to algorithms: an overview. *J Phys Conf Ser* 2018;1142:012012. DOI
89. Mahesh B. Machine learning algorithms - a review. *Int J Sci Res* 2020;9:381-6. Available from: <https://www.ijsr.net/getabstract.php?paperid=ART20203995> [Last accessed on 9 Oct 2023].
90. Abadi M, Agarwal A, Barham P, et al. TensorFlow: large-scale machine learning on heterogeneous distributed systems. Available from: <https://arxiv.org/abs/1603.04467> [Last accessed on 14 Aug 2023].
91. Paszke A, Gross S, Massa F, et al. PyTorch: an imperative style, high-performance deep learning library. Available from: <https://arxiv.org/abs/1912.01703> [Last accessed on 14 Aug 2023].
92. Liu CX, Yu GL. Predicting the dispersion relations of one-dimensional phononic crystals by neural networks. *Sci Rep* 2019;9:15322. DOI PubMed PMC
93. Zhang J, Li Y, Zhao T, Zhang Q, Zuo L, Zhang K. Machine-learning based design of digital materials for elastic wave control. *Extreme Mech Lett* 2021;48:101372. DOI
94. Jiang W, Zhu Y, Yin G, Lu H, Xie L, Yin M. Dispersion relation prediction and structure inverse design of elastic metamaterials via deep learning. *Mater Today Phys* 2022;22:100616. DOI
95. Han S, Han Q, Li C. Deep-learning-based inverse design of phononic crystals for anticipated wave attenuation. *J Appl Phys* 2022;132:154901. DOI
96. Liu C, Yu G, Zhao G. Neural networks for inverse design of phononic crystals. *AIP Adv* 2019;9:085223. DOI
97. Dong J, Qin Q, Xiao Y. Nelder-mead optimization of elastic metamaterials via machine-learning-aided surrogate modeling. *Int J Appl Mech* 2020;12:2050011. DOI
98. Wu L, Liu L, Wang Y, et al. A machine learning-based method to design modular metamaterials. *Extreme Mech Lett* 2020;36:100657. DOI
99. Li X, Ning S, Liu Z, Yan Z, Luo C, Zhuang Z. Designing phononic crystal with anticipated band gap through a deep learning based data-driven method. *Comput Methods Appl Mech Eng* 2020;361:112737. DOI
100. Miao X, Dong HW, Wang Y. Deep learning of dispersion engineering in two-dimensional phononic crystals. *Eng Optim* 2023;55:125-39. DOI
101. Jin Y, Zeng S, Wen Z, He L, Li Y, Li Y. Deep-subwavelength lightweight metastructures for low-frequency vibration isolation. *Mater Des* 2022;215:110499. DOI
102. On S, Moon H, Yeon Park S, et al. Design of periodic arched structures integrating the structural nonlinearity and band gap effect for vibration isolation. *Mater Des* 2022;224:111397. DOI
103. Luo C, Ning S, Liu Z, Zhuang Z. Interactive inverse design of layered phononic crystals based on reinforcement learning. *Extreme Mech Lett* 2020;36:100651. DOI
104. Wu R, Liu T, Jahanshahi MR, Semperlotti F. Design of one-dimensional acoustic metamaterials using machine learning and cell concatenation. *Struct Multidisc Optim* 2021;63:2399-423. DOI
105. He L, Guo H, Jin Y, Zhuang X, Rabczuk T, Li Y. Machine-learning-driven on-demand design of phononic beams. *Sci China Phys Mech Astron* 2022;65:214612. DOI
106. Donda K, Zhu Y, Merkel A, et al. Ultrathin acoustic absorbing metasurface based on deep learning approach. *Smart Mater Struct* 2021;30:085003. DOI
107. Donda K, Zhu Y, Merkel A, Wan S, Assour B. Deep learning approach for designing acoustic absorbing metasurfaces with high degrees of freedom. *Extreme Mech Lett* 2022;56:101879. DOI
108. Zhang H, Wang Y, Zhao H, Lu K, Yu D, Wen J. Accelerated topological design of metaporous materials of broadband sound absorption performance by generative adversarial networks. *Mater Des* 2021;207:109855. DOI
109. Liu L, Xie L, Huang W, Zhang XJ, Lu M, Chen Y. Broadband acoustic absorbing metamaterial via deep learning approach. *Appl Phys Lett* 2022;120:251701. DOI
110. Jin Y, Yang Y, Wen Z, et al. Lightweight sound-absorbing metastructures with perforated fish-belly panels. *Int J Mech Sci* 2022;226:107396. DOI
111. Gu T, Wen Z, He L, et al. A lightweight metastructure for simultaneous low-frequency broadband sound absorption and vibration isolation. *J Acoust Soc Am* 2023;153:96-104. DOI
112. Mahesh K, Kumar Ranjith S, Mini RS. Inverse design of a Helmholtz resonator based low-frequency acoustic absorber using deep neural network. *J Appl Phys* 2021;129:174901. DOI

113. Mahesh K, Ranjith SK, Mini RS. A deep autoencoder based approach for the inverse design of an acoustic-absorber. *Eng Comput* 2023. DOI
114. Luo YT, Li PQ, Li DT, et al. Probability-density-based deep learning paradigm for the fuzzy design of functional metastructures. *Research* 2020;2020:8757403. DOI PubMed PMC
115. Gurbuz C, Kronowetter F, Dietz C, Eser M, Schmid J, Marburg S. Generative adversarial networks for the design of acoustic metamaterials. *J Acoust Soc Am* 2021;149:1162. DOI PubMed
116. Ding H, Fang X, Jia B, Wang N, Cheng Q, Li Y. Deep learning enables accurate sound redistribution via nonlocal metasurfaces. *Phys Rev Appl* 2021;16:064035. DOI
117. Du Z, Mei J. Metagrating-based acoustic wavelength division multiplexing enabled by deterministic and probabilistic deep learning models. *Phys Rev Res* 2022;4:033165. DOI
118. Ahmed WW, Farhat M, Zhang X, Wu Y. Deterministic and probabilistic deep learning models for inverse design of broadband acoustic cloak. *Phys Rev Res* 2021;3:013142. DOI
119. Zhao T, Li Y, Zuo L, Zhang K. Machine-learning optimized method for regional control of sound fields. *Extreme Mech Lett* 2021;45:101297. DOI
120. Chen J, Chen Y, Xu X, Zhou W, Huang G. A physics-guided machine learning for multifunctional wave control in active metabeams. *Extreme Mech Lett* 2022;55:101827. DOI
121. Long Y, Ren J, Chen H. Unsupervised manifold clustering of topological phononics. *Phys Rev Lett* 2020;124:185501. DOI PubMed
122. He L, Wen Z, Jin Y, Torrent D, Zhuang X, Rabczuk T. Inverse design of topological metaplates for flexural waves with machine learning. *Mater Des* 2021;199:109390. DOI
123. Muhammad, Ogun O, Kennedy J. Inverse design of a topological phononic beam with interface modes. *J Phys D Appl Phys* 2022;56:015106. DOI
124. Du Z, Ding X, Chen H, et al. Optimal design of topological waveguides by machine learning. *Front Mater* 2022;9:1075073. DOI
125. Yu LW, Deng DL. Unsupervised learning of non-Hermitian topological phases. *Phys Rev Lett* 2021;126:240402. DOI PubMed
126. Cheng Z, Yu Z. Supervised machine learning topological states of one-dimensional non-Hermitian systems. *Chin Phys Lett* 2021;38:070302. DOI
127. Narayan B, Narayan A. Machine learning non-Hermitian topological phases. *Phys Rev B* 2021;103:035413. DOI
128. Zhang L, Tang L, Huang Z, Zhang G, Huang W, Zhang D. Machine learning topological invariants of non-Hermitian systems. *Phys Rev A* 2021;103:012419. DOI
129. Miri MA, Alù A. Exceptional points in optics and photonics. *Science* 2019;363:eaar7709. DOI PubMed
130. Reja MA, Narayan A. Characterizing exceptional points using neural networks. Available from: <https://arxiv.org/abs/2305.00776> [Last accessed on 14 Aug 2023].
131. Gu GX, Chen C, Richmond DJ, Buehler MJ. Bioinspired hierarchical composite design using machine learning: simulation, additive manufacturing, and experiment. *Mater Horiz* 2018;5:939-45. DOI
132. Hanakata PZ, Cubuk ED, Campbell DK, Park HS. Accelerated search and design of stretchable graphene kirigami using machine learning. *Phys Rev Lett* 2018;121:255304. DOI
133. Hanakata PZ, Cubuk ED, Campbell DK, Park HS. Forward and inverse design of kirigami via supervised autoencoder. *Phys Rev Res* 2020;2:042006. DOI
134. Kollmann HT, Abueidda DW, Koric S, Guleryuz E, Sobh NA. Deep learning for topology optimization of 2D metamaterials. *Mater Des* 2020;196:109098. DOI
135. Tan RK, Zhang NL, Ye W. A deep learning - based method for the design of microstructural materials. *Struct Multidisc Optim* 2020;61:1417-38. DOI
136. Garland AP, White BC, Jensen SC, Boyce BL. Pragmatic generative optimization of novel structural lattice metamaterials with machine learning. *Mater Des* 2021;203:109632. DOI
137. Tian J, Tang K, Chen X, Wang X. Machine learning-based prediction and inverse design of 2D metamaterial structures with tunable deformation-dependent Poisson's ratio. *Nanoscale* 2022;14:12677-91. DOI
138. Liu F, Jiang X, Wang X, Wang L. Machine learning-based design and optimization of curved beams for multistable structures and metamaterials. *Extreme Mech Lett* 2020;41:101002. DOI
139. Challapalli A, Patel D, Li G. Inverse machine learning framework for optimizing lightweight metamaterials. *Mater Des* 2021;208:109937. DOI
140. Wang Y, Zeng Q, Wang J, Li Y, Fang D. Inverse design of shell-based mechanical metamaterial with customized loading curves based on machine learning and genetic algorithm. *Comput Methods Appl Mech Eng* 2022;401:115571. DOI
141. Chang Y, Wang H, Dong Q. Machine learning-based inverse design of auxetic metamaterial with zero Poisson's ratio. *Mater Today Commun* 2022;30:103186. DOI

Review

Open Access



The concept, structure, and progress of seawater metal-air batteries

Yuanyuan Guo¹, Yanhui Cao², Junda Lu¹, Xuerong Zheng^{1,2}, Yida Deng^{1,2} 

¹State Key Laboratory of Marine Resource Utilization in the South China Sea, School of Materials Science and Engineering, Hainan University, Haikou 570228, Hainan, China.

²School of Materials Science and Engineering, Key Laboratory of Advanced Ceramics and Machining Technology of Ministry of Education, Tianjin University, Tianjin 300072, China.

Correspondence to: Prof. Xuerong Zheng, State Key Laboratory of Marine Resource Utilization in South China Sea, School of Materials Science and Engineering, Hainan University, Haikou 570228, Hainan, China. E-mail: xrzh@hainanu.edu.cn; Prof. Yida Deng, State Key Laboratory of Marine Resource Utilization in the South China Sea, School of Materials Science and Engineering, Hainan University, Haikou 570228, Hainan, China. E-mail: yd_deng@hainanu.edu.cn

How to cite this article: Guo Y, Cao Y, Lu J, Zheng X, Deng Y. The concept, structure, and progress of seawater metal-air batteries. *Microstructures* 2023;3:2023038. <https://dx.doi.org/10.20517/microstructures.2023.30>

Received: 5 Jun 2023 **First Decision:** 29 Jun 2023 **Revised:** 16 Jul 2023 **Accepted:** 31 Jul 2023 **Published:** 10 Oct 2023

Academic Editor: Zaiping Guo **Copy Editor:** Fangyuan Liu **Production Editor:** Fangyuan Liu

Abstract

Seawater metal-air batteries (SMABs) are promising energy storage technologies for their advantages of high energy density, intrinsic safety, and low cost. However, the presence of such chloride ions complex components in seawater inevitably has complex effects on the air electrode process, including oxygen reduction and oxygen evolution reactions (ORR and OER), which requires the development of highly-active chloride-resistant electrocatalysts. In this review, we first summarized the developing status of various types of SMABs, explaining their working principle and comparing the battery performance. Then, the reported chlorine-resistant electrocatalysts were classified. The composition and structural design strategies of high-efficient chlorine-resistant ORR/OER electrocatalysts in seawater electrolytes were comprehensively summarized. Finally, the main challenges to be overcome in the commercialization of SMABs were discussed.

Keywords: Seawater metal-air batteries, oxygen reduction reactions, oxygen evolution reactions, chloride-resistant

INTRODUCTION

Renewable energy resources, such as wind energy, solar energy, and wave energy, exist extensively,

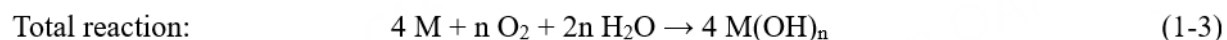
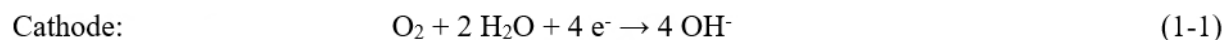


© The Author(s) 2023. **Open Access** This article is licensed under a Creative Commons Attribution 4.0 International License (<https://creativecommons.org/licenses/by/4.0/>), which permits unrestricted use, sharing, adaptation, distribution and reproduction in any medium or format, for any purpose, even commercially, as long as you give appropriate credit to the original author(s) and the source, provide a link to the Creative Commons license, and indicate if changes were made.



especially on the sea^[1,2]. Harvesting energy directly from the sea provides great potential for developing the marine economy and promoting marine research. Thus, developing renewable energy utilization techniques, such as wind power generation, photovoltaics, and hydroelectric generation, is highly demanded for providing green electricity to the marine equipment^[3-5]. However, the intermittent power supply property makes the clean energy sources difficult to be utilized efficiently. Moreover, traditional secondary batteries, such as Lithium (Li)-ion batteries and Lead-acid batteries, cannot meet the long-term and high-power density requirements of the equipment working in the deep and open sea^[6,7]. Therefore, harvesting energy directly from the ocean is critically demanded.

Seawater metal-air batteries (SMABs) are considered as extremely promising power sources for providing electricity for the equipment working on the sea or in the deep sea due to their high theoretical energy density, low cost, eco-friendly nature, *etc.*^[8,9]. During the discharge of SMABs, seawater is directly used as the electrolyte, the dissolved oxygen (O₂) in seawater is reduced on the cathode, and the metallic anode [Magnesium (Mg), Aluminum (Al), Sodium (Na), *etc.*] is oxidized^[10,11]. The working processes are summarized as follows:



The dissolved O₂ was harvested from seawater and subsequently reduced through the oxygen reduction reaction (ORR), while the metals (alloys) were oxidized, forming metallic hydroxides^[12,13]. Due to the open structure of SMABs, oxygen, as an active species, can infinitely diffuse to the cathode for ORR, which ensures the SMABs display high theoretical energy density^[14,15]. One critical issue is that the un-optimized electronic structure of metallic sites and the four reaction steps for the ORR process would result in sluggish catalytic kinetics^[16]. Although the OER is thermodynamically favored over the hypochlorite formation reaction in seawater (pH ≈ 8), both reactions were a balancing relationship during seawater catalysis owing to the slow catalytic kinetics in seawater^[17,18]. Currently, we consider OER to be the primary cathode reaction upon the charging of seawater batteries. Thus, designing and exploring efficient and low-cost electrocatalysts is an urgent task to enhance the battery performance. In the past few years, various types of electrocatalysts were designed to accelerate the ORR/OER catalytic kinetics in seawater, including noble metals of Pt, Ru, Ir, and their alloys^[19-21]. However, the noble metals are more easily being poisoned in seawater electrolytes. The non-noble metal electrocatalysts, such as Fe groups (Fe, Co, Ni) and carbon-based materials with abundant and inexpensive advantages, have been explored, displaying satisfying ORR performance and deserving further exploration as promising ORR/OER electrocatalysts in seawater conditions^[22-24]. At the same time, the circulating seawater electrolyte can promote the heat and charge transfer rate, thereby improving the intrinsic safety and cycle life of the SMABs^[25,26]. Therefore, the SMABs are particularly suitable as long-term power supply systems for the equipment working in the sea.

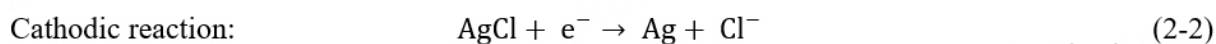
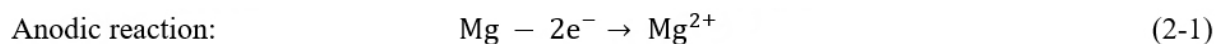
However, in comparison to the alkaline metal-air battery systems, the high content of chloride ions (Cl⁻) in seawater (19.345 g/kg) is easily absorbed on the surface of electrocatalysts. This absorption changes the electronic structure and poisons the metallic sites, thereby greatly reducing the power density of SMABs^[27,28]. Although some electrocatalysts display good ORR catalytic performance in conventional electrolytes, they cannot maintain active and stable in seawater electrolytes due to the poison of high concentration of Cl⁻^[29]. The recent results suggest that, on the one hand, the adsorption of Cl⁻ on the surface catalytic sites can hinder the breakage of O-O bonds and thus inducing the reaction pathway change from a four-electron to a sluggish two-electron pathway for the ORR process^[30,31]. Moreover, the adsorption of O₂ molecules would also be suppressed. On the other hand, due to competitive chlorine evolution reaction

(CIER) and chloride corrosion, the oxygen evolution reaction (OER) performance of the catalysts in seawater electrolytes decays rapidly during charging^[32]. Therefore, it remains a great challenge for the development of efficient chlorine-resistant ORR/OER electrocatalysts for their application in seawater electrolytes for SMABs.

In order to put forward the wide application of SMABs in the field of marine techniques, three key issues need to be solved urgently: (i) The poisoning mechanism of Cl⁻ on ORR/OER processes in seawater electrolytes should be clarified, thus providing guidance for designing high-efficient chlorine-resistant catalysts; (ii) The electronic structure of noble metal catalysts should be optimized to enhance the electrocatalytic activity and stability in seawater electrolytes. Specifically, this can be achieved through several strategies. Firstly, by modifying the ligands or surface modifiers, the electronic structure of the catalyst can be adjusted. This influences the distribution of electron density and the reactivity of the active sites, leading to improved electrocatalytic performance. Secondly, introducing suitable elements into the noble metal catalyst can modify its electronic structure. This alters the binding strength of reactants and intermediates, facilitating the desired electrochemical reactions and enhancing catalytic activity and stability. Thirdly, modifying the surface of the catalyst through techniques such as surface deposition or functionalization can regulate its electronic structure. This can enhance the interaction with reactants and ions in the electrolyte, improving catalytic activity and stability. At the same time, chlorine-resistant non-noble metal-based electrocatalysts with excellent ORR/OER performance should be developed to broaden the types of catalysts and reduce the cost of catalysts; and (iii) The integrated structure of SMABs should be optimized to improve the power density and stability of batteries. Based on the above consideration, this review presents the progress in the development of chlorine-resistant cathode electrocatalysts for SMABs. In this review, we first summarized the development of various types of SMABs to understand their working principle and battery performance [Figure 1]. Subsequently, the poisoning mechanism of Cl⁻ on cathode electrocatalysts during charging and discharging was studied and summarized. Then, we classified the reported chlorine-resistant electrocatalysts and comprehensively summarized the composition and structural designing strategies of high-efficient chlorine-resistant ORR/OER electrocatalysts in seawater electrolytes. Finally, the main challenges to be addressed in the commercialization of SMABs were discussed.

THE DEVELOPING HISTORY OF SEAWATER METAL-AIR BATTERIES

The SMABs were developed through three stages, starting from seawater-activated batteries (SABs) to primary SMABs (P-SMABs), and further evolving into rechargeable SMABs (R-SMABs)^[33]. The SAB was originally developed in the 1940s by Bell Telephone Laboratories to meet the requirement for high energy density, prolonged shelf-life, and outstanding low temperature performance. It was mainly used as a power source for military torpedoes. The SAB, which used magnesium as the anode, silver chloride (AgCl) as the cathode, and flowing seawater as the electrolyte, was first commercialized in 1943, as shown in Figure 2A. The battery can be stored for up to five years in a dry condition and can be activated by the addition of seawater when being used, thus being called SAB. During the discharge, the following reactions occur^[34]:



The above reaction possesses fast catalytic kinetics. For discharging, the AgCl on the cathode of the battery is reduced to Ag, leading to an increase in conductivity as the process proceeds. However, the discharge voltage would drop dramatically when AgCl is reduced to Ag completely. Moreover, another advantage of the Mg-AgCl battery system is that the device can keep working efficiently in wide temperature ranges. The

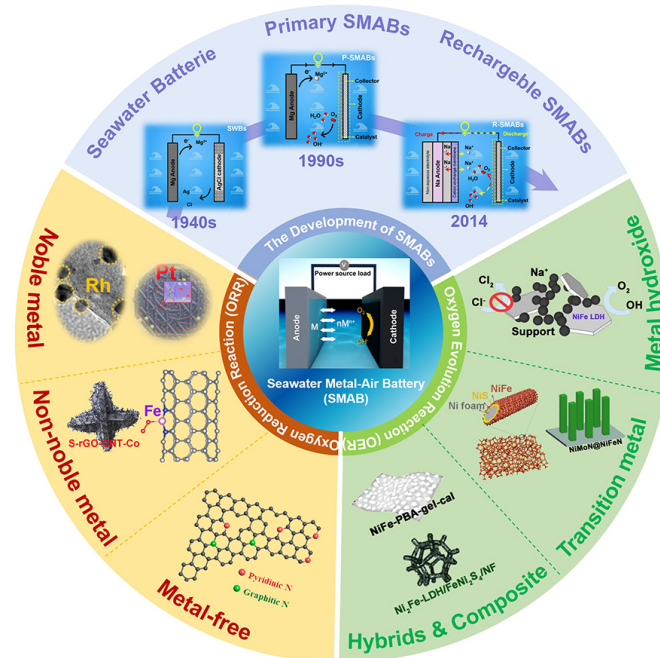


Figure 1. Schematic diagram of the classification of SMABs and ORR/OER electrocatalysts. (Reproduced with permission^[91]. Copyright 2021, Elsevier; Reproduced with permission^[92]. Copyright 2011, Wiley-VCH; Reproduced with permission^[97]. Copyright 2017, Elsevier; Reproduced with permission^[99]. Copyright 2021, Wiley-VCH; Reproduced with permission^[104]. Copyright 2020, American Chemical Society; Reproduced with permission^[128]. Copyright 2022, WILEY-VCH; Reproduced with permission^[127]. Copyright 2022, WILEY-VCH; Reproduced with permission^[121]. Copyright 2019, PNAS; Reproduced with permission^[120]. Copyright 2019, Springer Nature; Reproduced with permission^[114]. Copyright 2016, Wiley-VCH).

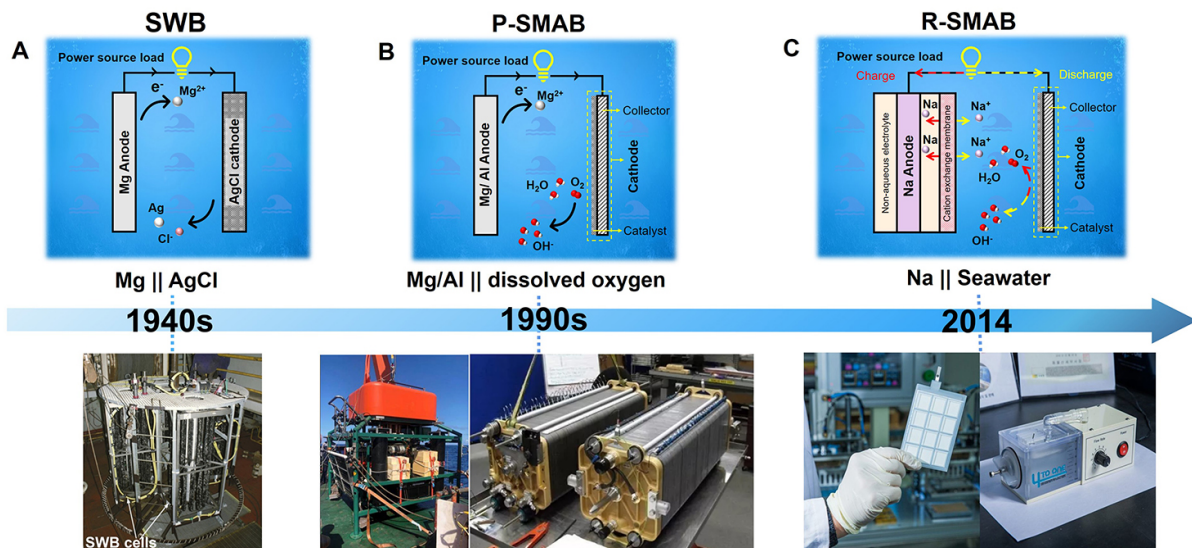
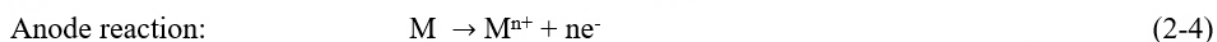
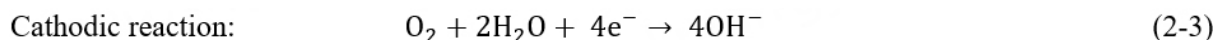


Figure 2. Timeline of the development of seawater-based batteries from SWBs to rechargeable SMABs.

discharge voltage can remain stable when the temperature changes from 219 K to 369 K, and the output power density has no obvious change. Therefore, the SAB generally displays remarkable advantages of steady discharge voltages, high discharge current densities, and high output powers of up to 70 kW. Up to now, the maximum discharge current density and voltage of SABs reached 2 A cm⁻² at about 1.32 V.

However, due to the large amount of consumption of precious silver and the resulting high cost, the SAB was only being used in the military area. Recently, many efforts have been devoted to reducing the battery manufacturing cost and to further increase the total power. For instance, a variety of Mg, Al, zinc (Zn), and Na alloys have been explored for being used as the anodes^[35-48], while the cuprous chloride^[34], cuprous iodide^[49,50], lead chloride^[51] and mercurous chloride^[52] have been explored as the cathodes of SABs. However, up to now, none of these systems can completely replace the Mg/AgCl system.

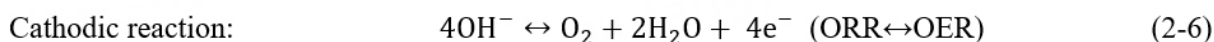
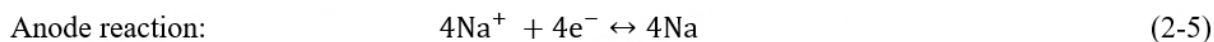
In the 1990s, the primary metal-air batteries driven by dissolved O₂ in seawater attracted attention due to their high theoretical energy density. The devices of P-SMABs mainly use Zn, Mg, and Al as anodes. The cathodic and anode electrochemical reactions for P-SMABs are as follows^[53]:



However, due to the slight solubility of oxygen in seawater, the battery performance is limited by the oxygen concentration and diffusion, thus leading to relatively low current density and operating voltage (1.0 V to 1.8 V). The P-SMABs, as a type of semi-fuel cells, have attracted tremendous attention due to their environmental friendliness and low cost. The geometrical structure of P-SMABs is similar to that of SABs. The key difference lies in the cathode materials and the related reduction reaction that occurred on cathodes.

The electrocatalysts on the cathode, such as graphite electrodes and carbonized fibers, play a critical role in accelerating ORR processes, as shown in [Figure 2B](#). The unsatisfying battery performance of P-SMABs makes it difficult to meet the requirements of underwater equipment for high power density, and thus, most P-SMABs are mainly being used in some long-endurance, low-power underwater equipment^[53-55]. Recently, Shinohara *et al.* installed a seafloor borehole broadband seismic observatory in the northwestern Pacific basin, where the water depth is 5,577 m^[54]. The observatory is powered by a system of four P-SMAB systems connected in series. The battery system can effectively power the monitoring system (the average power consumption is 6 W) and the Data Logger for at least five years. To enhance the current density and power density, one strategy is to develop efficient electrocatalysts with exposure to large active sites and higher intrinsic catalytic kinetics. This accelerates the ORR process while ensuring robust chlorine-corrosion resistance in natural seawater electrolytes.

To endow seawater batteries with the capability of storing electrical energy, Hwang *et al.* proposed and patented R-SMABs with half-opening structures in 2014^[33]. In this system, seawater not only serves as an electrolyte and provides the reactant for the cathode but also as a supplier of anode material. In the R-SMABs, sodium was used as the anode, electrocatalysts connected to the current collector as the cathode, and solid-state electrolytes as channels for transporting sodium ions and flowing seawater, as shown in [Figure 2C](#). During the charging process of R-SMABs, the anodes capture sodium ions from seawater in non-aqueous anolytes, while the cathode undergoes OER. During the discharging process, the sodium in the anode dissolves into sodium ions and is transferred to seawater, and the cathode reacts in the same way as the P-SMABs [Equations 5 and 6]. The half-cell reaction equations of the charging and discharging processes for R-SMABs are listed as follows^[51]:



The theoretical voltage of the R-SMABs can reach 3.48 V. However, due to the sluggish catalytic kinetics of electrocatalysts in cathodes, the Cl⁻ corrosion on both cathodes and anodes, and the competing relationship between the two electrodes, the battery system is still far from reaching its theoretical properties^[56-60]. To put forward the practical application of SMABs, such as the typical sodium-based seawater batteries, the power density, capacity, and stability of the SMABs should be further optimized. The SMABs can be divided into small (< 1 kWh), medium (1-10 kWh), and large-scale (> 1 MWh) power sources according to their discharging capacity. Some low-power seawater-based metal-air battery prototypes have been utilized for underwater observation and ocean buoys. Medium-power seawater batteries can be used for exploratory unmanned aerial vehicles and maritime search and rescue operations. The stability of large-scale seawater batteries should be further optimized for their large-scale application in the future.

THE COMPONENTS AND EVALUATION OF SEAWATER METAL-AIR BATTERY

The large-scale commercialization of efficient and stable SMABs remains a significant challenge, which requires the optimization of all individual components in the battery. As discussed above, SMABs feature an open structure. The essential components in the battery contain electrode materials (cathodes and anodes), electrolytes (anolytes, catholytes), current collectors, ceramic solid electrolytes, electrocatalysts, and the general cell type, depending on different categories of SMABs.

Electrocatalysts and electrode materials

SMABs are basically composed of anodes and cathodes with current collectors. The electrocatalysts were mixed with binders and were pasted onto the current collectors for preparing electrodes^[61,62]. Highly efficient SMABs require electrodes (both anodes and cathodes) with optimized electronic conductivity, porous density, and wettability^[63,64]. The electrodes should meet several prerequisites for developing efficient and stable SMAB devices [Figure 3A]. Developing anode materials should meet the following requirements: (i) avoid the side reactions that may lead to cell swelling and failure; (ii) possess good electronic conductivity and excellent stability in seawater conditions; and (iii) narrow voltage window, low-cost and low toxicity. At present, SMABs with anodes consisting of Li, Na, Mg, Al, Zn, and their alloys have been systematically studied^[65,66]. Among various types of SMABs, seawater lithium-air batteries theoretically possess the highest energy density, reaching up to 11,140 Wh·kg⁻¹. On the other hand, metals such as Zn, Mg, and Al display the advantages of environmental friendliness, abundance in the Earth's crust, low cost, and intrinsic safety. In addition, Al is readily available for recycling in massive amounts and has a high energy density of 8,100 Wh·kg⁻¹ and a significant theoretical voltage of 2.7 V^[67]. As a result, seawater aluminum-air batteries are considered as the most promising systems for developing SMABs.

The air cathode is composed of a gas diffusion layer (GDL), electrocatalyst, and current collector. As mentioned above, the OER and ORR occur in the cathodes when seawater batteries are charged and discharged, respectively^[68]. Therefore, an efficient air electrode should possess strong oxygen adsorption capacity, fast oxygen diffusion, and high electrochemical activity for oxygen redox reactions in SMABs. The electrocatalyst layer in the cathode has a significant influence on the performance of SMABs. The electrocatalysts on the cathodes may be noble metals, transition metals (TM), and non-metallic materials. Moreover, the electrocatalysts should not only display efficient ORR and OER activity and stability but also possess strong Cl⁻ corrosion resistance with stable physical structures in seawater conditions. The Cl⁻ in seawater can easily destroy the oxide thin film on the surface of the electrocatalysts and form complexes with metal ions, resulting in corrosion of metallic sites in seawater^[63,69]. The electrocatalysts can be divided into the following three categories: (1) noble metals and their alloys, such as Pt as ORR electrocatalysts while IrO_x and RuO_x as OER electrocatalysts; (2) non-noble metal-based catalysts, such as metal-supported carbon materials and metal oxides and sulfides; and (3) metal-free electrocatalysts, such as nitrogen (N) doping

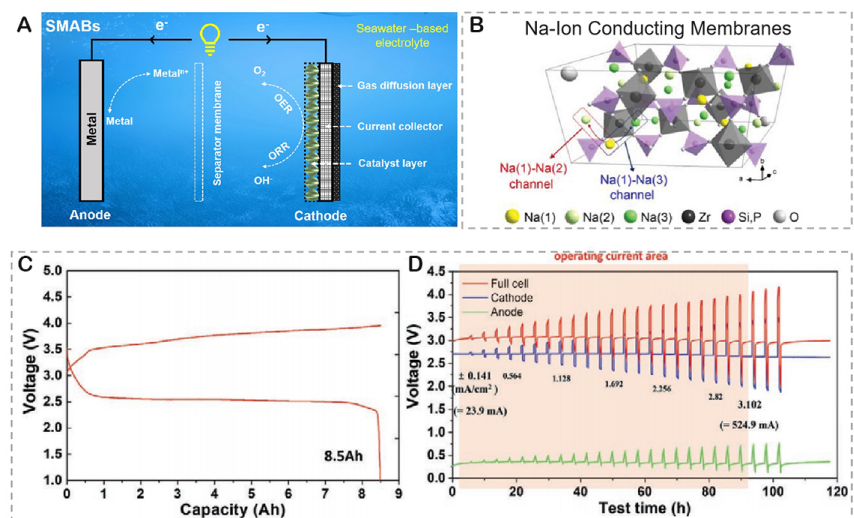


Figure 3. (A) a schematic illustration of the basic components. (B) Schematic of monoclinic structures of Na-Ion Conducting Membranes (Solid Electrolytes). (Reproduced with permission^[33]. Copyright 2018, Wiley-VCH) Parameters of performance evaluation. (C) Capacity and (D) efficiency. (Reproduced with permission^[61]. Copyright 2022, Wiley-VCH).

carbon. Currently, carbon-based functional materials have been recognized as promising electrocatalysts for their high corrosion resistance and are thus being utilized in the SMAB^[70,71]. Generally, carbon-based materials can be divided into carbon cloth, conductive carbon paper, and graphitic fiber. The GDL undertakes multiple tasks in the electrodes. It acts as a connector between the air and the catalyst, allowing oxygen to diffuse from the air atmosphere to the surface and further to the inner of an electrode, or in other words, it absorbs oxygen from the surrounding environment for OER and ORR catalysis. The GDL in the cathodes should have the following characteristics: hydrophobicity, lightness, thinness, and high porosity. It is often composed of electrocatalysts and hydrophobic binders, such as polytetrafluoroethylene (PTFE)^[72].

Electrolyte

SMABs are chemical power sources with seawater as electrolytes. Seawater is a naturally available, abundant, and renewable resource, accounting for about 70% of the Earth's surface. According to the seawater data, the salt content per liter of water reaches about 35 g. In addition to the main components of sodium chloride (NaCl), there are many other cations and anions in seawater, such as calcium, magnesium, sulfates, bicarbonates, and fluorides^[53,73]. The dissolved salt ions in seawater contribute to its high ionic conductivity of about 50 mS cm^{-1} (at $20 \text{ }^\circ\text{C}$). Therefore, seawater is considered as the electrolyte for electrochemical cells. Furthermore, seawater contains not only dissolved salt ions but also dissolved gases, such as oxygen, which can act as cathode-oxidants to react with H_2O molecules on cathode current collectors. However, the composition of seawater varies based on factors such as location, depth, time, climate, and environmental conditions.

Natural seawater contains abundant calcium ions and impurities, which can lead to calcium deposits and deactivation of the active materials, thus hindering effective contact between the electrode and electrolyte. In addition, the impurities in seawater may undergo side reactions with the anode and cathode, resulting in performance degradation or irreversible damage to the battery. To avoid the impurity ions in natural seawater, the simulated seawater and artificial seawater were also employed as electrolytes for the rechargeable metal-air batteries. The simulated and artificial seawater typically contains the following components: (i) salts such as NaCl, magnesium sulfate (MgSO_4), calcium sulfate (CaSO_4), etc.; (ii) pH adjusters such as sodium hydroxide (NaOH) or sulfuric acid (H_2SO_4) to adjust the pH value of the electrolyte; and (iii) dissolved organic compounds and trace elements, such as dissolved O_2 , silicates, iron,

manganese, *etc.* The specific composition and ratio of the simulated seawater electrolyte can be adjusted and optimized according to the specific research purposes and experimental requirements. In addition, the organic electrolytes containing NaCl were also being developed for their application in R-SMABs. This is because the organic electrolyte possesses good ion conductivity and fewer side reactions for charging and discharging. Commonly used organic electrolytes include ethylene glycol dimethyl ether (EGDME), acrylonitrile (AN), and propylene glycol (PG), which have good solubility and high ion conductivity.

Current collector

Although there is no solid electrode in this battery system, a current collector is still needed. It facilitates the transport of electrons released from the anode part during the deintercalation/dealloying process. Moreover, the current collector carries cathodic reactions (OER and ORR), which are necessary for related charge transport. Compared to the typical organic batteries with solid cathodes, current collectors usually require special properties, such as stability in saltwater^[74].

In the cathode chamber, the role of the current collector is to support the active materials and collect and transfer the electrons to the external circuit. In order to effectively promote the sluggish oxygen reaction kinetics, the current collector on the cathode should possess the advantages of high electronic conductivity, good electrochemical and mechanical stability, and large specific surface area.

In the anode chamber, the current collector should remain stable and work well with the anode materials (such as Mg, Al, and their alloys) and the electrolytes in the batteries. During working, the current collector should ensure the electrons transfer stably from electrolytes to the anode active materials. The commonly used current collectors are generally porous metal foams, such as nickel foam, copper foil, stainless steel, *etc.* Recently, newly developed carbon-based collectors are commonly used in seawater batteries, which could not only offer catalytic sites for the ORR and OER processes but also ensure an efficient charge transferring rate^[74,75].

Separator membrane

Sodium-ion-conducting membranes are widely used as separators to separate the anode and cathode compartments in R-SMABs [Figure 3B]^[33,76]. Such membrane materials are commonly used as solid electrolytes in solid-state batteries. The stability of the membrane in different types of liquid electrolytes should be stable to ensure the stability of the entire battery in both organic and aqueous solutions, especially for some SMABs that should work under high current density and voltage conditions. Therefore, the separator membrane should remain stable in a relatively wide electrochemical potential window to keep the battery working for long-term utilization. In addition, the solid electrolyte as the separator for seawater batteries also needs to have high sodium ion conductivity, good mechanical properties, and ultra-low porosity to avoid electrolyte penetration.

Criteria for evaluating the seawater metal-air battery performance

The SMABs should be assembled into a package before testing, and they generally contain three parts: an organic anode chamber, a seawater cathode chamber, and a separator. These three parts were sealed to avoid the electrolyte linkage. The distance between an anode, cathode, and separator should be kept constant to evaluate the performance of different SMABs. To evaluate the battery performance, the open circuit voltage, discharging capacity, power density, and other indexes were systematically tested. Typically, the capacity is one of the most important performance indexes to measure seawater battery performance, which describes the charge storage capacity of the SMAB (the amount of charge Q that a battery can provide or store) [Figure 3C], usually expressed as ampere-hour (Ah) and normalized to mass (Ah g^{-1}) or volume (Ah cm^{-3}). The value of battery capacity can be influenced by the discharge rate, discharge current,

discharge voltage, temperature, geometry dimension of the anode and cathode, and the mass loading of active materials^[77]. Generally, it is difficult to reach the theoretical capacity in practical applications due to the polarization effects and the side reactions during charging and discharging. Therefore, increasing the capacity of seawater batteries requires not only performance improvement of cathode/anode materials but also the optimization of the structure of the whole device.

Coulombic and energy efficiencies are typical parameters in electrochemical systems of R-SMABs, which represent the ratio of the amount of charge (Q) flowing through the battery and the voltage ratio between charging and discharging, respectively [Figure 3D]. A coulomb efficiency is usually used as a comparative value to determine the capacity loss for each cycle in the rechargeable battery systems, which is an important parameter to predict the remaining life of the battery^[78,79]. However, the performance of coulombic and energy efficiencies can be influenced by many factors, such as the environmental temperature, the humidity, and the uniformity of each package and electrode. Therefore, to precisely evaluate the key factors and the mechanisms that influence enhanced battery performance, the standard experimental procedure should be established.

Stability and safety are key parameters in assessing the performance of SMABs. The stability of positive electrodes in the seawater medium is one of the biggest factors for determining the long-term performance of the whole battery^[61]. Due to the existence of Cl⁻ in seawater electrolytes, more surface metallic sites would be attacked, thus decreasing the exposure of metallic sites. Moreover, the Cl⁻ adsorption would change the reaction pathway. For instance, the ORR pathway would be transferred from 4e⁻ in alkaline electrolytes to 2e⁻ in seawater electrolytes^[80]. As a result, it is a critical challenge to develop Cl⁻ corrosion-resistant electrocatalysts to enhance the stability of cathodes and the whole SMAB devices. Moreover, because seawater was employed as the electrolyte without the use of any organic additives, the SMABs possess highly intrinsic safety and are eco-friendly^[81-83]. In addition, the seawater battery is a semi-open or fully open electrochemical system, which is beneficial for gas release and temperature diffusion, thus keeping the system working in relatively low temperature conditions (generally lower than 60 °C).

ORR ELECTROCATALYSTS IN SEAWATER ELECTROLYTE

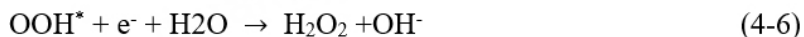
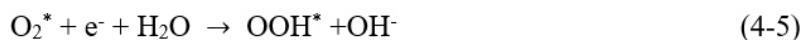
The oxygen electrocatalytic process in seawater is considered as a complicated pathway, which may involve the simultaneous occurrence of oxygen reduction and chlorine corrosion, depending on the condition of pH values, oxygen/chlorine concentration, temperature, *etc.*^[83-85]. The adsorption and corrosion of Cl⁻ play a critical role in enhancing the catalytic efficiency and stability of the catalysts, thus affecting the battery performance. In this section, we discussed the development of ORR electrocatalysts and the influence behavior of Cl⁻ toward the ORR process^[86].

ORR mechanism and Cl⁻-resistance mechanism in seawater batteries

The ORR mechanism in seawater involves the reduction of dissolved O₂ by a four-electron process to hydroxide ions (OH⁻) or by a two-electron process to form hydrogen peroxide (H₂O₂) on the cathode electrocatalysts. In the four-electron process, each oxygen molecule (O₂) accepts four electrons and undergoes a complete reduction to form OH⁻. This is the most favorable pathway for ORR as it does not produce any intermediate reactive species. The reaction process can be represented as follows:



In the two-electron process, each dissolved O₂ molecule accepts only two electrons, resulting in the formation of H₂O₂. This pathway is less desirable as it can lead to the generation of reactive oxygen species and undesirable byproducts. The overall reaction can be represented as follows:



Cl⁻ is among the most abundant ions in seawater electrolytes. However, due to the specific Cl⁻ blocking effect, the Cl⁻ tends to adsorb on the surface catalytic sites of the cathodes. The adsorption of Cl⁻ would cause several serious results: (1) the active site exposure would be reduced, thus causing the decrease of ORR current density; (2) the electronic structure of surface metallic sites would be changed, thus causing the poison of catalytic sites^[52,86]; and (3) the local bonding environment of active sites would be tuned in the catalysts and cause the dissolution of metal atoms, thus worsening the stability of cathodes. Currently, the reversibility of Cl⁻ adsorption is still debatable. Along with the blocking effect, Cl⁻ adsorption behavior would affect the breakage of O-O bonds during ORR processes, thus changing the ORR pathway from a four-electron to a two-electron mechanism, leading to the generation of H₂O₂. More importantly, the existence of H₂O₂ at the three-phase interface (gas-solution-solid) will produce free radicals that can attack the metal anodes or/and electrocatalysts, thus resulting in the reduction of durability^[87,88]. In order to overcome the bad influence of Cl⁻ on the catalytic process in seawater, the ORR electrocatalyst generally should possess the prerequisites of high electronic conductivity and electrochemical stability in saltwater electrolytes. In addition, other criteria such as large specific surface area, high intrinsic catalytic activity, and low mass loading are also should be considered^[88]. Based on the related reports, ORR electrocatalysts can be classified into three categories: noble metal-based materials, non-noble metal-based electrocatalysts, and metal-free electrocatalysts. This section will summarize the research efforts that have focused on enhancing the catalytic performance of different electrocatalysts in SMABs.

Noble metal-based ORR electrocatalysts

Noble metal-based ORR electrocatalysts, especially Pt-based catalysts, usually have high ORR efficiency, but they are expensive and can be easily destroyed by a large amount of Cl⁻ in seawater. Besides, the formation of soluble chlorine complexes (such as PtCl₄²⁻) can also lead to the dissolution of platinum and the surface passivation of metallic sites, which adversely affects the stability of ORR^[89,90]. Recently, Ryu *et al.* designed a Pt-Co alloy electrocatalyst using carbothermal shock (CTS) for use in high-performance seawater batteries^[91]. The authors prepared single and blended aqueous solutions of H₂PtCl₆·6H₂O and CoCl₂ precursors with different ratios to synthesize the Pt-Co alloy on heated carbon felt (HCF) within 10 s [Figure 4A and B]. Figure 4C enabled us to observe that the peak at q = 2.77 A⁻¹ shifted to a higher value, indicating that the formation of Pt-Co alloy leads to lattice contraction. Moreover, the Pt 4f XPS spectra of the samples mentioned above show that the peaks of Pt 4f_{5/2} and Pt 4f_{7/2} shift to high binding energy, mainly due to the loss of 5d electrons in Pt-based alloys, indicating the formation of Pt-Co alloys. As shown in Figure 4D, the catalyst with Pt:Co = 2:1 achieved high current density and low overpotential in the ORR process for the synergistic effect between the Pt and Co metallic sites. Moreover, the Pt-Co alloy electrocatalyst can remain stable in the seawater catholyte, and thus, the seawater batteries using Pt-Co alloys as cathodes exhibit excellent cycling stability with no obvious degradation [Figure 4E]. Compared to the SMAB using pristine HCF as a current collector, the battery using a composition of Pt-Co nanoparticle (NP)-decorated CF can be cycled at 0.3 mA cm⁻² for up to 500 h without substantial performance deterioration. In addition, Jin *et al.* reported well-dispersed Rh₁₇S₁₅ NPs supported on carbon nanotube (CNT) substrates^[92]. The diameter of the embedded particles was evenly about 8 nm, and the mass loading of Rh reaches 25 wt% when pyrolyzed at 650 °C. The ORR catalytic activity of the nanocomposites is highly active under Cl⁻ electrolysis conditions, which could exhibit considerable stability in the chloride environment.

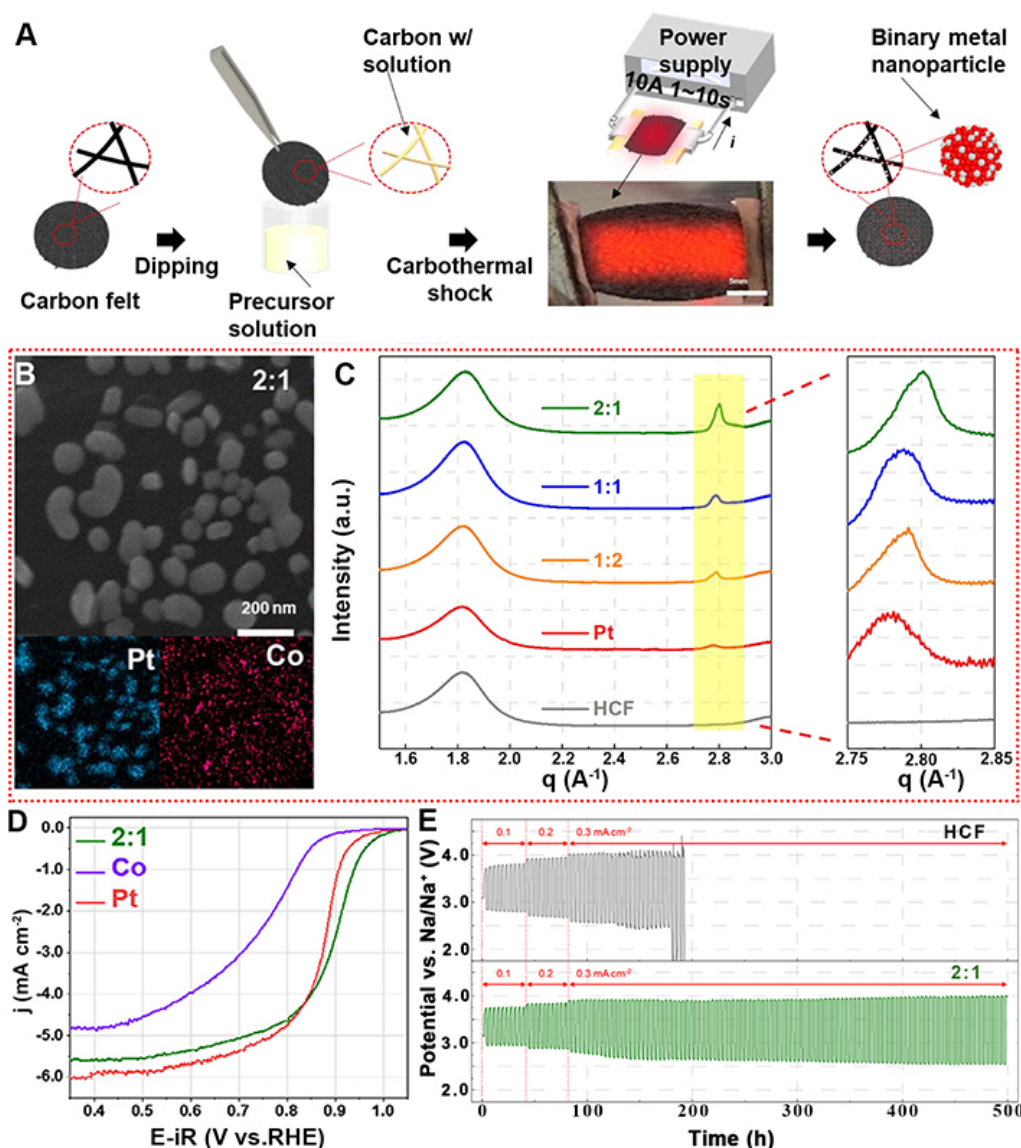


Figure 4. (A) Schematic diagram of the synthesis of Pt-Co alloy induced by CTS. (B) SEM image and EDX elemental distribution of Pt and Co in Pt-Co alloys (Pt:Co = 2:1). (C) Grazing incidence X-ray diffraction (GIXD) patterns of HCF, Pt, and Pt-Co alloys with different ratios. (D) ORR performance of the corresponding samples tested in 1.0 M KOH solutions. (E) Galvanostatic charge/discharge curves of seawater batteries with/without Pt-Co alloys on HCF at different current densities. (Reproduced with permission^[91]. Copyright 2021, Elsevier).

In general, although the chlorine resistance of noble metal-based catalysts is enhanced and the ORR performance in seawater is improved, the relatively high charging potential and the low power density of the as-developed seawater battery deny its inherent advantages. Therefore, numerous studies have been devoted to the development of non-noble metals or metal-free ORR electrocatalysts as alternatives.

Non-noble metal-based ORR electrocatalysts

With advantages such as low cost, excellent corrosion resistance, high conductivity, high surface area, and good mechanical properties, TM-based electrocatalysts were highly developed as the cathode materials for being utilized in SMABs^[93-96]. Particularly noteworthy is the design and synthesis of the TM composites with functional carbon materials to tune the intrinsic activity and stability of active sites. In the composited

structure, TMs can increase the degree of graphitization of carbon materials during carbonization. At the same time, encapsulating carbon materials on the surface of metal sites can effectively prevent metal agglomeration and promote electron transfer. Suh *et al.* designed a graphene-nanotube-cobalt hybrid electrocatalyst (S-rGO-CNT-Co) as a highly active seawater cathode catalyst [Figure 5A]^[97]. The reported S-rGO-CNT-Co is composed of tubular CNTs and partially anchored 10-30 nm Co NPs [Figure 5B]. The composite nanostructure of the Co-C and graphene protective layer prevents the adsorption of Cl⁻ on the cobalt and enhances the catalytic activity and stability of ORR. The S-rGO-CNT-Co sample was used as an electrocatalyst for the air cathode for SMABs. At a current density of 0.01 mA cm⁻², the charging voltage was 3.42 V, and the discharge voltage was 3.0 V. [Figure 5C]. Although the as-prepared electrocatalysts exhibit excellent performance, the discharge performance is still lower than that of 20 wt% Pt/C catalysts in SMABs [Figure 5D]. S-rGO-CNT-Co degraded rapidly in SMABs, even at a low current, and the cathode catalyst still suffered rapid Cl⁻ corrosion. Therefore, it is necessary to further modify the graphene-coated cobalt catalysts to improve their catalytic activity and stability in seawater electrolytes.

Wu *et al.* have developed a three-step method to construct defect-rich Fe-doped Co NPs coated by N-doped hierarchical carbon (D-FeCo@NHC) [Figure 6A]^[98]. The as-prepared D-FeCo@NHC has a typical core-shell structure with metal NPs encapsulated in carbon, which can promote the electrical conductivity and corrosion resistance of catalysts [Figure 6B]. Besides, Fe doping can not only promote the formation of metal defects but also adjust the electronic structure of D-FeCo@NHC. Meanwhile, DFT theoretical calculations show that the combination of metal and carbon defect synergistically optimized the d-band center of the sample and thus boosted the ORR activity [Figure 6C]. As shown in Figure 6D and E, the D-FeCo@NHC exhibits a high E_{1/2} of 0.874 V in alkaline seawater electrolytes, and the as-assembled battery shows a high peak power density and long cycling stability.

In addition, TM-based single-atom electrocatalysts have been widely employed, which show promising potential for being utilized as ORR electrocatalysts. Typically, Fe-N moieties on carbon matrix (Fe-N-C) catalysts show excellent ORR activity in alkaline and acidic electrolytes. Furthermore, compared with Pt/C and other noble metal-based catalysts, the Fe-N-C catalysts generally show excellent resistance to chlorine poisoning. Based on the mentioned above, Fe-N-C catalysts have the potential as cathode materials in the SMABs. However, up to now, little attention has been paid to its practical application in real seawater environments. Gao *et al.* reported a microwave heating method and synthesized the atomically dispersed Fe-N-G/CNT catalyst in a short time, which possesses high activity and a strong oxygen-philic interface between graphene and CNTs [Figure 7A]^[99]. In addition, DFT calculations and experimental results indicate that the high oxygen affinity of the catalyst is caused by the double adsorption sites on the G/CNT interface, and the high activity of Fe-N₄ active sites is due to charge separation [Figure 7B-E]. The Fe-N-G/CNT shows an excellent ORR performance in both O₂-saturated alkaline solution and seawater with E_{1/2} of 0.929 and 0.704 V, respectively, which are much better than commercial Pt/C [Figure 7F]. In addition, the SMAB with Fe-N-G/CNT as the cathode exhibits good battery performance in oxygen-poor seawater (≈ 0.4 mg L⁻¹), where the discharge voltage at 10 mA cm⁻² is 1.18 V [Figure 7G].

Although big progress has been made in the development and the application of Fe-N-C as the ORR electrocatalysts in seawater batteries, the catalytic influencing mechanism of the Cl⁻ resistance of Fe-N-C catalysts is still unclear and remains a challenge. Zhan *et al.* prepared an atomic electrocatalyst by anchoring Fe-N_x sites on N-doped activated carbon substrates (Fe-N_x/NAC) to explore the effect of Cl⁻ on Fe-N_x/NAC ORR performance^[100]. The isolated single Fe atom is well dispersed and embedded on porous NAC, and the Fe, C, N, and O elements are uniformly distributed throughout the active carbon matrix [Figure 8A and B]. Benefiting from the abundance of Fe-N_x active sites, high surface area of activated carbon, and good

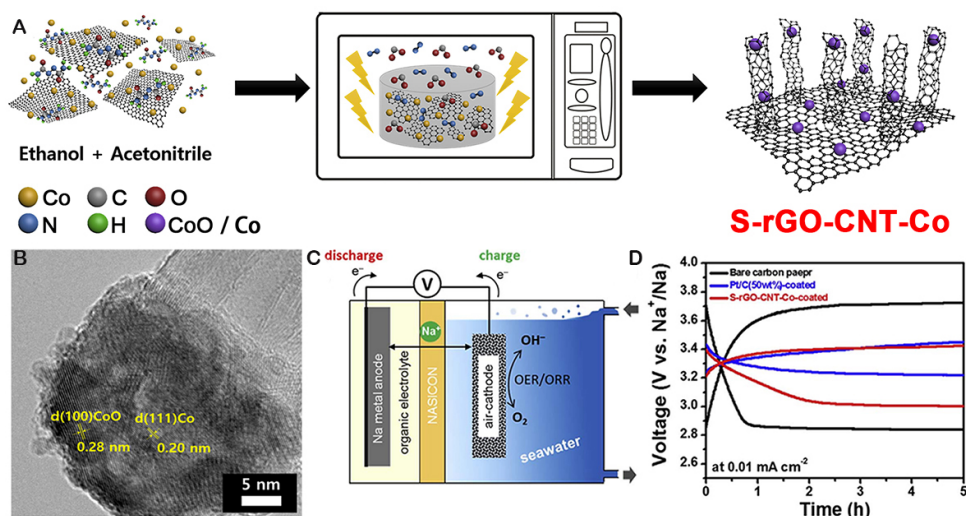


Figure 5. (A) The schematic diagram shows the microwave synthesis process of S-rGO-CNT-Co. (B) HRTEM image of the S-rGO-CNT-Co. (C) Structure diagram of seawater flow batteries. (D) The first charge-discharge voltage diagram of seawater flow batteries with different electrocatalysts. (Reproduced with permission^[97]. Copyright 2017, Elsevier).

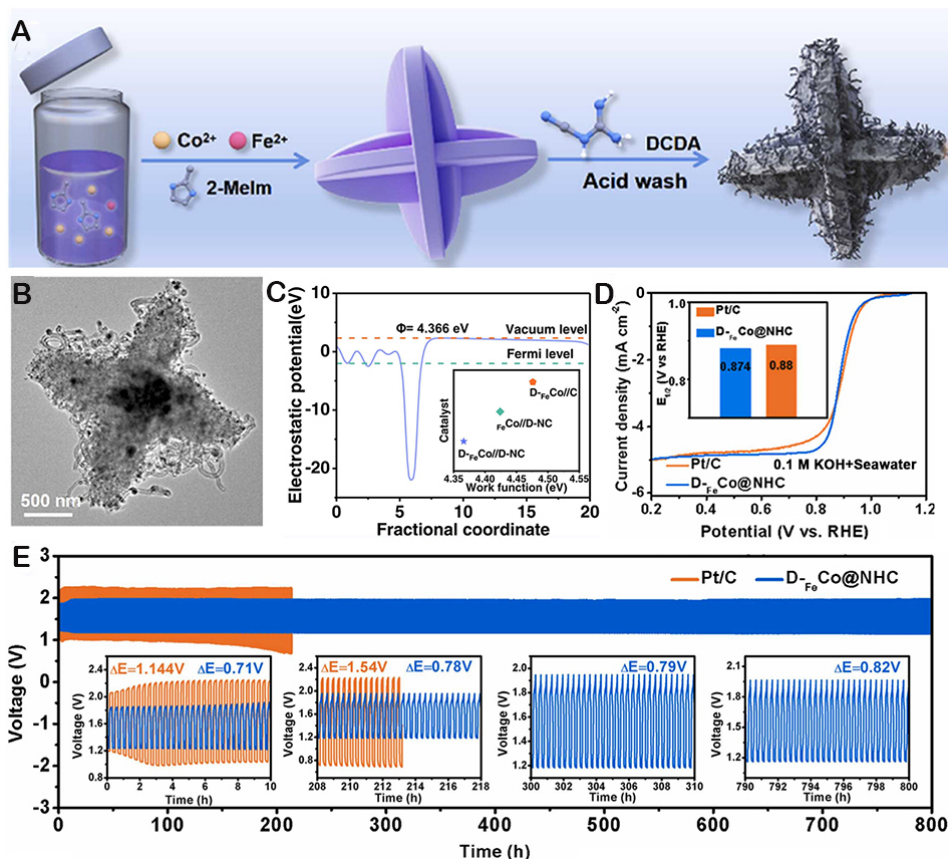


Figure 6. (A) The synthesis route diagram of D-FeCo@NHC. (B) HRTEM images of S-rGO-CNT-Co. (C) LSV curves of D-FeCo@NHC and Pt/C catalyst for ORR in 0.1 M KOH + seawater. (D) Computed work functions of D-FeCo//D-NC. (E) Galvanostatic discharge-charge cycling stability of liquid ZAB. (Reproduced with permission^[98]. Copyright 2023, Elsevier).

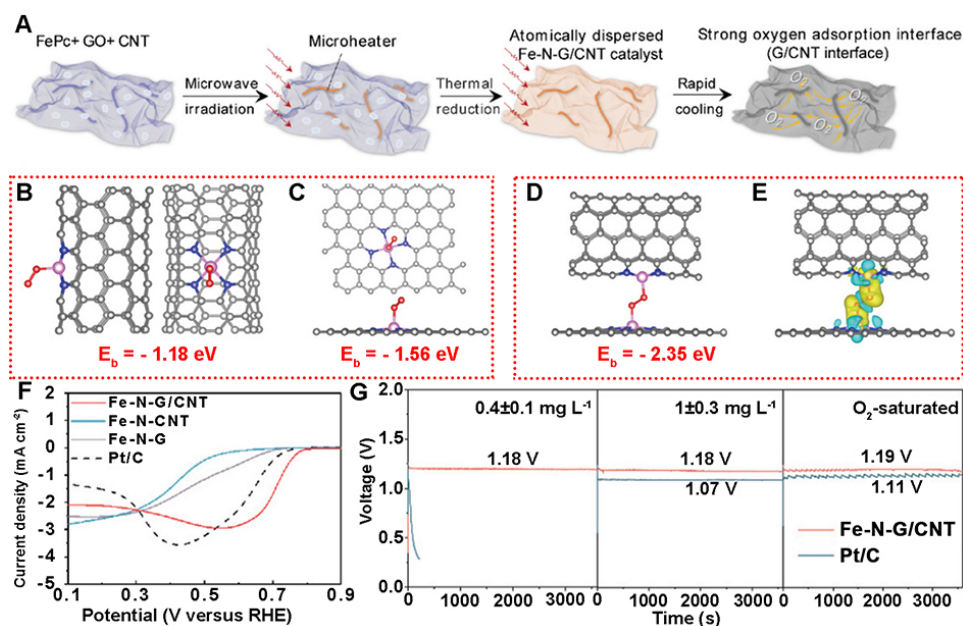


Figure 7. (A) Schematic illustration of the synthesis of Fe-N-G/CNT. (B-D) Geometry of the O_2 adsorption mechanism on (B) Fe-N-CNT; (C) Fe-N-G; and (D) Fe-N-G/CNT and the corresponding O_2 adsorption binding energies. (E) The three-dimensional charge density distribution of Fe-N-G/CNT absorbed O_2 . (F) LSV curves of the corresponding electrocatalysts in O_2 -saturated artificial seawater. (G) Discharge curves for different oxygen contents. (Reproduced with permission^[99]. Copyright 2021, Wiley-VCH).

resistance to Cl^- adsorption, Fe-N_x/NAC exhibits good ORR catalytic activity and high stability in 3.5 wt% NaCl solution, which exceeds the performance of Pt/C. In addition, the effect of Cl^- concentration on Fe-N_x/NAC activity was also studied. As shown in Figure 8C-E, with the increase in NaCl concentration, no significant activity change was observed. For composition, Pt, NAC, and FeO_x/AC were all poisoned by the strong Cl^- adsorption. However, Fe-N_x/NAC was not affected by Cl^- adsorption to some extent, and the ORR activity can remain stable. Moreover, to investigate the Cl^- poisoning resistance of Fe-N_x and Pt (111) sites, the reaction-free energies of OH^- and Cl^- desorption were calculated, respectively. The adsorption sites of the pyrrole(C) of Fe-N_x/NAC are demonstrated in Figure 8F by the structures of OH^- and Cl^- adsorption. As shown in Figure 8G, When the reaction Gibbs free energy, ΔG_r , O_2 of O_2 adsorption were investigated, it was found that the steps strongly related to ORR activity in alkaline and neutral solutions showed that the C site was not the main reaction center of ORR. As shown in Figure 8H, The calculation was performed on Fe sites in Fe-N_x/NACs at 0 V and 0.6 V. The reaction-free energy of OH^- and Cl^- desorption is more positive than that on Pt (111), which indicates that the adsorption energy of anions on Fe-N_x/NAC is stronger. This corrected desorption-free energy is consistent with the fact that Fe atoms are positively charged (Fe-pyridine is +1.34, Fe-pyrrole is +1.41) and easily attract anions. On the contrary, the Pt atom on Pt (111) is almost neutral (-0.04), so it is less attractive to anions. Although the Fe reaction center was blocked, the Fe-pyrroline-C site remained unblocked due to the discovery that Cl^- could not be bonded to the carbon atom of the electrocatalysts.

TM oxides also show promising ORR catalytic activity in seawater conditions^[101]. Kim *et al.* developed cobalt manganese oxide (CMO) as cathode electrocatalysts for rechargeable seawater batteries^[84]. The porous CMO NPs exhibit good bifunctional electrocatalytic activities for the ORR and OER processes, with stable cycle performance and high round-trip efficiencies (up to 85% at a current density of 0.01 mA cm⁻²). In addition, with a hard carbon electrode as the anode and the CMO as the electrocatalyst, the Na-free seawater batteries display excellent cycle performance. After 100 cycles, the average discharge voltage is

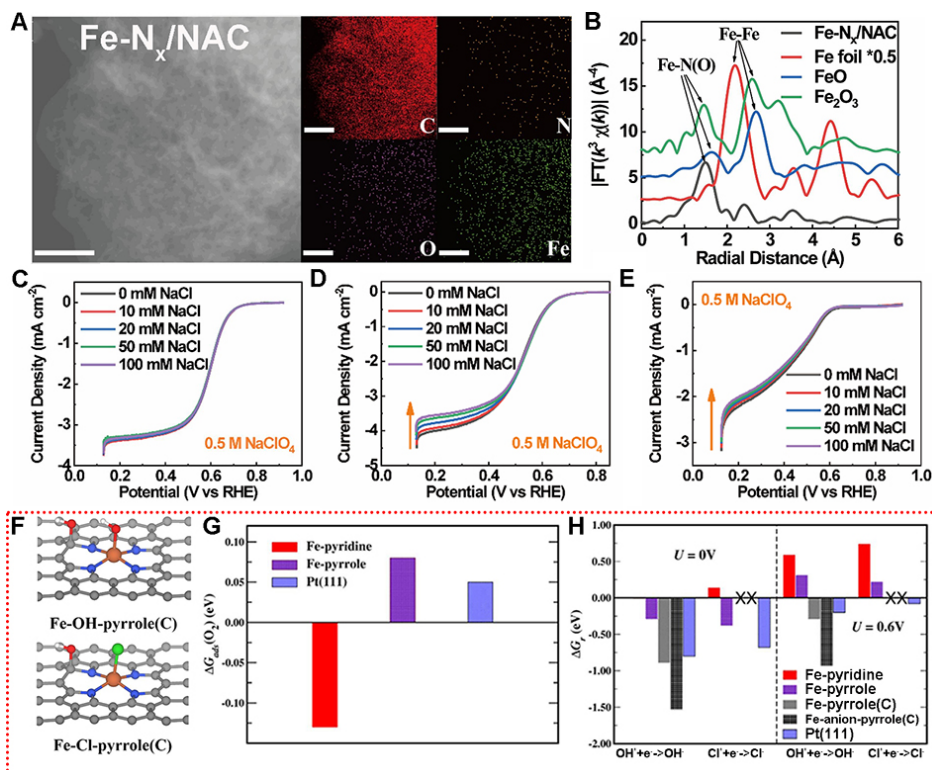


Figure 8. (A) The element maps and (B) Fe K-edge XANES spectra of Fe-N_x/NAC. LSV polarization curves of (C) Fe-N_x/NAC, (D) NAC, and (E) FeO_x/AC in 0.5 M NaClO₄ with different NaCl concentrations at 1,600 rpm. (F) The structure of Fe-N_x/NAC adsorbing O₂, OH⁻, and Cl⁻ calculated by DFT (H: white; O: red; Cl: green). (G) DFT calculation results of adsorption free energy of O₂ on Pt (111) and Fe-N_x/NAC. (H) The reaction-free energies of Cl⁻ desorption and OH⁻ desorption from Pt (111) phase and Fe-N_x/NAC at α(Cl⁻) = 0.5 mol L⁻¹ and pH = 7. (Reproduced with permission^[100]. Copyright 2022, Elsevier).

≤2.7 V, the coulombic efficiency is as high as 96%, and the energy efficiency is up to 74%-79%. Moreover, Son *et al.* fabricated a sacrificial electrocatalyst with Pt NP-modified 1T-MoS₂ layers by a CTS strategy [Figure 9A]^[102]. The HRTEM image clearly shows that the Pt NPs are uniformly anchored on the MoS₂ layer [Figure 9B]. Furthermore, the deconvolution region of the Pt 4f and Mo 3d XPS spectra show that electron transfer from Pt to MoS₂ layers, which increased the proportion of the 1T-MoS₂ phase in CTS-Pt@MoS₂ than that in CTS-MoS₂ [Figure 9C and D]. Besides, compared to those of the CTS-MoS₂ electrode, the introduction of Pt NPs improves the ORR activity of the CTS-MoS₂ electrode during the discharge process and further reduces the potential [Figure 9E]. The CTS-Pt@MoS₂ catalyst significantly improves the electrochemical performance of the fabricated seawater battery, achieving a high-power density of 6.56 mW cm⁻², a low discharge/charge potential gap of Δ0.39 V, and excellent long-term cycle stability of up to 400 h at a low charge potential (3.39-3.6 V) [Figure 9F]. Due to slight oxidation of the edges of the MoS₂ layer after 450 h of cycling, there is an increase in the voltage gap during charging and discharging. However, it can still work for at least 350 h at 4.0-2.6 V.

Metal-free ORR electrocatalysts

The study of metal-free catalysts, especially N-doped functional carbon materials, has attracted more attention for their application in seawater batteries. Zhang *et al.* fabricated a three-dimensional (3D) microporous carbon sponge by the simple pyrolysis of the formaldehyde-melamine-sodium bisulfite copolymer, which shows superior electrocatalytic activity and stability^[103]. The excellent electrocatalytic performance can be attributed to the following three parts. Firstly, the as-prepared 3D macroporous carbon

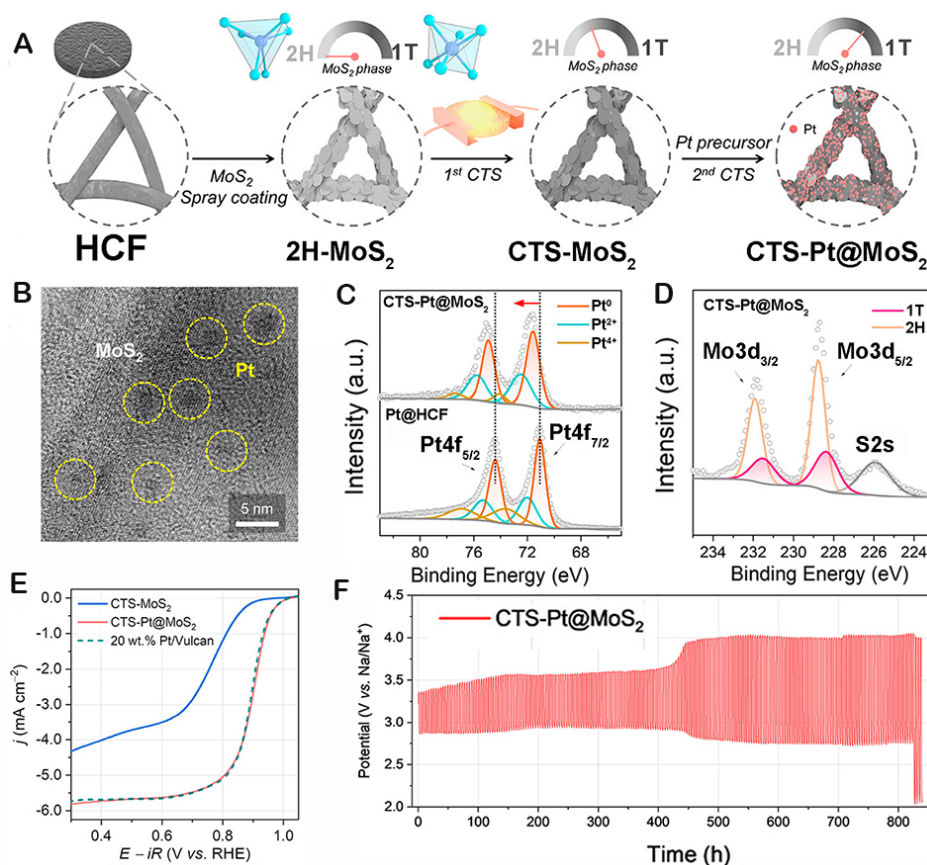


Figure 9. (A) Synthesis schematic of the Pt nanoparticle-modified 1T-MoS₂ sacrificial catalyst (1T: trigonal antiprismatic phase; 2H: hexagonal prismatic phase). (B) HRTEM image of CTS-Pt@MoS₂. (C) Pt 4f XPS profiles of pristine Pt@HCF and CTS-Pt@MoS₂. (D) Mo 3d XPS profiles of CTS-Pt@MoS₂. (E) LSV curves for determining the ORR activities of CTS-MoS₂, CTS-Pt@MoS₂, and 20 wt% Pt/Vulcan electrodes. (F) Galvanostatic charge/discharge cycling behavior of the CTS-Pt@MoS₂ electrode. (Reproduced with permission^[102]. Copyright 2022, American Chemical Society).

sponge exhibits excellent electrocatalytic activity toward the OER/ORR in seawater. The fabricated hybrid sodium-seawater flow battery prepared with a 3D macroporous carbon sponge as the cathode exhibits excellent battery behavior, high discharging voltage and energy efficiency, excellent rechargeability, and long-term cycle stability. The incorporation of nitrogen- and oxygen-containing groups in carbon skeletons and the defective structure provide abundant electrocatalytic active sites for OER/ORR. Secondly, the microporous structure provides a large number of pathways for the efficient transportation of dissolved O₂, OH⁻, and H₂O, which greatly enhances the OER/ORR performance. Thirdly, graphitization and interconnected carbon scaffolds form a 3D conductive network with rapid electron transfer, which promotes electrochemical OER/ORR activity. Kha Tu *et al.* prepared a controllable N-doped high specific surface area carbon cloth by a simple thermal annealing process [Figure 10A]^[104]. The N-doped carbon cloth prepared at 700 °C contains a high density of pyridinic-nitrogen sites, which is beneficial to improving the ORR and OER activity [Figure 10B]. At a current density of 0.25 mA cm⁻², the pyridinic-nitrogen-dominated carbon cathode exhibits excellent SMAB performance, such as a low overpotential gap of 0.84 V and high-power density of 9.66 mW cm⁻² [Figure 10C]. Moreover, the ORR active sites of the N-doped carbon cloth were confirmed to be related to the adjacent carbon atoms of pyridinic-nitrogen located at the zigzag edge of the carbon structure or single vacancy defect [Figure 10D and E].

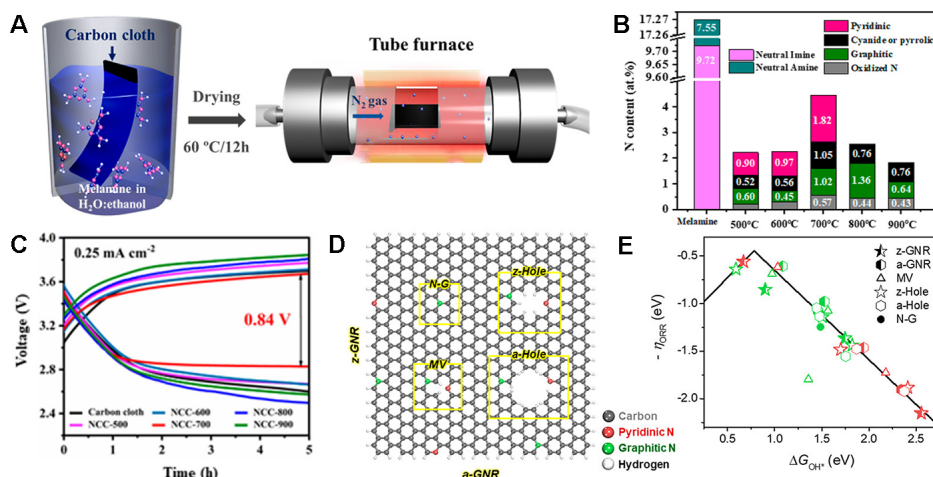


Figure 10. (A) Schematic illustration of the preparation of carbon cloths (CCs). (B) The type of nitrogen functional groups and atomic content in the melamine attached CC and N-doped CCs with increasing annealing temperature. (C) Constant current charge-discharge voltage curves. (D) Schematic presentation of N-doped configurations. zigzag (z-GNR), armchair (a-GNR) graphene nanoribbon; N-G: graphite nitrogen-substituted graphene base surface; MV: monovacancy defect; z-Hole: zigzag-terminated hole defect; a-Hole: armchair-terminated hole defect. (E) The ORR volcano plot for the active sites mentioned above as a function of the Gibbs formation energy of the OH^\ddagger intermediate from water ($\Delta G_{\text{OH}^\ddagger}$). (Reproduced with permission^[104]. Copyright 2020, American Chemical Society).

Generally, most of the current commercial electrocatalysts are noble metal-based, such as Pt- and Ru-based electrocatalysts, which are considered as the best electrocatalysts for the ORR catalysis in seawater electrolytes. However, the high cost and scarcity of noble metals hinder their widespread and large-scale applications. Developing non-noble metal-based or metal-free electrocatalysts is a preferred strategy to avoid Cl⁻ toxicity inhibition behavior. Generally, the ORR electrocatalysts should meet the requirements: (i) High active site exposure and intrinsic activity to achieve high onset potential and discharge current density toward ORR; (ii) Large surface area and enough porous structures are beneficial to effective mass transfer rates and enhanced electrocatalytic kinetics; (iii) A robust chemical and mechanical stability architecture for high durability in seawater conditions; and (iv) High mass and volume activity, and finally, abundant resources at low cost.

OER ELECTROCATALYSTS IN SEAWATER ELECTROLYTE

One of the biggest challenges for OER processes in seawater-based electrolytes is the competition from the oxidation of Cl⁻, including the hypochlorite formation reaction (HCFR) in an alkaline medium or the CLER in an acidic medium, which seriously affects the selectivity of electrocatalysts for OER^[105,106]. Furthermore, the absorbed Cl⁻ anions and the possible hypochlorite/chlorine byproducts could corrode the active sites of catalysts, and the resulting hydroxy-chloride could corrode and poison the metal active sites by means of coordination dissolution^[107,108]. Therefore, it is urgent to develop highly efficient and stable electrocatalysts for OER in seawater-based electrolytes. The outstanding OER electrocatalysts in the chlorine-containing electrolyte should be designed by the following aspects: (1) the excellent intrinsic OER catalytic activity; (2) the high electrochemical long-term stability and strong corrosion resistance to chlorides; (3) good conductivity; and (4) large active surface area and more exposed active sites. In this section, we discussed the development of OER electrocatalysts in the chlorine-containing electrolyte and the influence behavior of Cl⁻ toward the OER process.

Competition of chlorine oxidation in OER processes

Taking into the total concentration of Cl⁻ in seawater is approximately 0.54 M, Yu *et al.* plotted a simulated Pourbaix diagram of oxygen/chlorine electrochemistry in seawater to evaluate the relationship between the oxygen electrocatalytic reaction and the ClER during cycling, as shown in Figure 11^[53]. During charging, Cl⁻ in seawater may participate in the HCFR or ClER process, generating hypochlorite or chlorine byproducts. Among all pH ranges, OER is thermodynamically preferred over HCFR and ClER. Particularly, OER electrocatalysts functioning at an overpotential of 480 mV in 0.1 M KOH solution can block the HCFR process in seawater electrolytes, although this is difficult at relatively large current densities. Moreover, the potential difference between oxygen and chlorine becomes slightly less with a reduction of the pH value (< 7.4), where HClO replaces ClO⁻ as the main production. When the pH value is less than 2.9, the equilibrium potential is near to but still higher than the 100 ~ 200 mV required by OER criteria. Thus, the OER process has higher selectivity and feasibility in the electrolyte with the presence of Cl⁻.

The OER process would compete with the HCFR/ClER process in terms of reaction kinetics even though the OER process is thermodynamically superior to the HCFR/ClER during the charging process of SMABs^[109]. This is because HCFR/ClER is a 2e⁻ oxidation reaction involving only a single intermediate, whereas OER is based on a complex 4e⁻ pathway that requires the removal of four protons and involves three intermediates. Moreover, the two reaction routes would partially share similar active sites. By the theory calculations based on assumed mechanisms, Hansen *et al.* discovered a scaling relationship between the binding energies of ClER and OER intermediates^[110]. This indicates that electrocatalysts that easily bind oxygen-bound intermediates also tend to bind chloride-bound intermediates. The pH values, current density, and Cl⁻ content would also have significant impacts on this competition. Since HCFR cannot occur when the electrocatalysts provide a low overpotential, alkaline conditions are consequently preferable for selective OER in saltwater.

OER electrocatalysts in chlorine-containing electrolyte.

For the R-SMAB, the charging process depends on the OER catalysis on the air electrode. The four-electron reaction steps for the OER process would result in sluggish reaction kinetics, leading to large overpotentials; thus, the high charging voltage would restrain the performance of metal-air batteries in practice^[108,111]. In the complex seawater-based electrolyte, the main challenge is the HCFR process, competing with OER under near-neutral or alkaline conditions, together with the consequent electrocatalyst corrosion^[112,113]. Over the past decades, many OER electrocatalysts have been designed and prepared with excellent activity, selectivity, and stability in the chlorine-containing electrolyte, mainly including metal hydroxide-based electrocatalysts, TM compound-based electrocatalysts and hybrids, or compositing electrocatalysts. Furthermore, since the anode during seawater electrolysis also depends on the OER reaction, in order to comprehensively understand the impact of Cl⁻ on the OER reaction in seawater and the synthesis strategies for chloride-resistant OER electrocatalysts, this chapter will discuss the studies related to seawater electrolysis together.

Metal hydroxide-based electrocatalysts

Initiatively, Dionigi *et al.* established a general designing criterion for noble metal-free OER electrocatalysts, pointing out that the OER overpotential keeping smaller than 480 mV could achieve high selectivity in seawater in theory^[114]. The designing criterion is the only one and the most favorable condition to avoid HCFR from the air electrodes of seawater-based metal-air batteries. As shown in Figure 12A, a NiFe-layered double hydroxide (NiFe-LDH) catalyst was prepared, and the linear sweep voltammetry (LSV) curves of OER were measured in 0.1 M KOH and 0.3 M borate buffer solution with/without the addition of 0.5 M NaCl. The OER process was more likely to occur at pH = 13 than at pH = 9.2, and the overpotential increased by 110 mV at 1 mA cm⁻². Furthermore, the overpotential at 10 mA cm⁻² in pH = 13 reached 360 mV, which was not over 480 mV and satisfied the above criterion. Therefore, there were no changes for

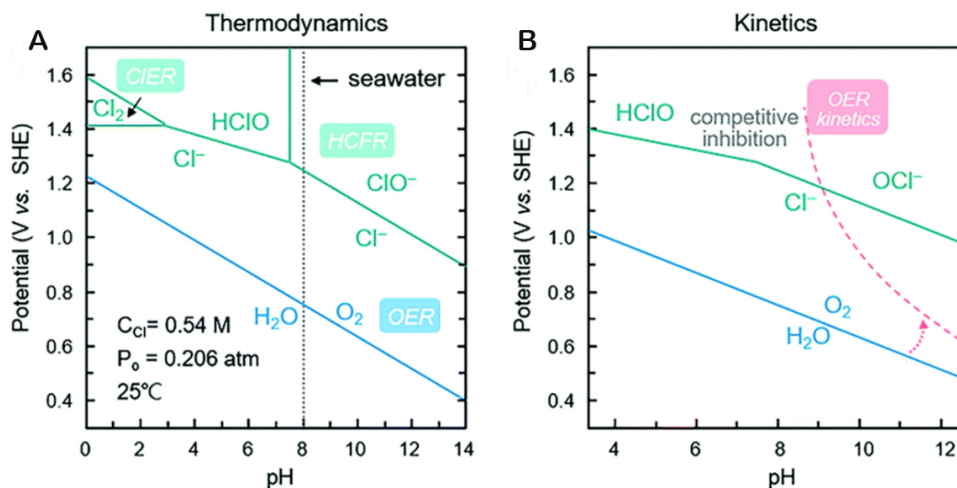


Figure 11. The Pourbaix diagram of seawater simulated according to (A) thermodynamics and (B) kinetics. (Reproduced with permission^[53]. Copyright 2000, The Royal Society of Chemistry).

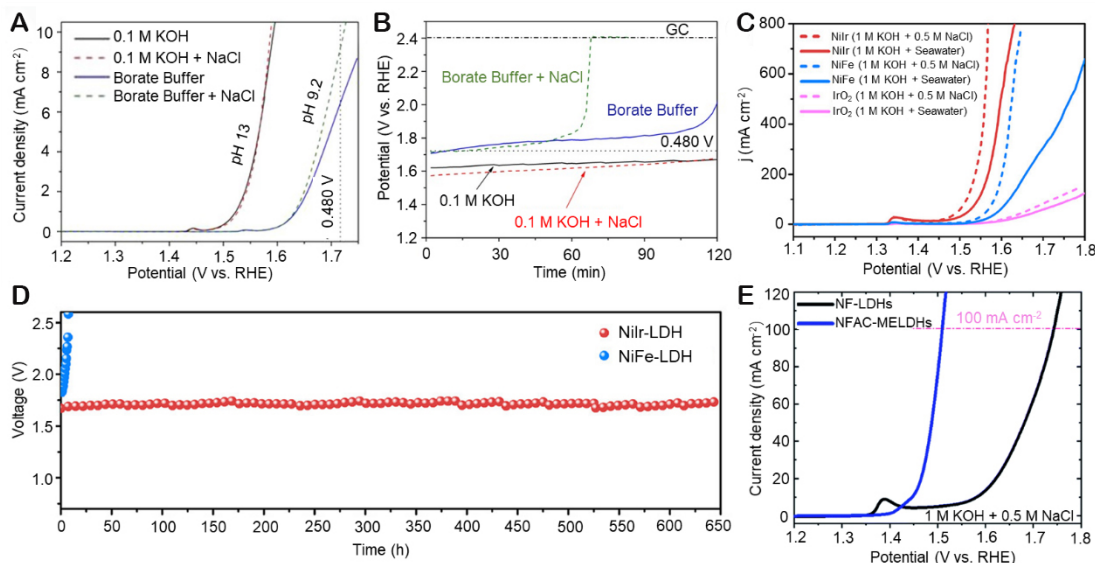


Figure 12. (A) The LSV curves of NiFe-LDH toward OER in different electrolytes. (B) Electrochemical stability of NiFe-LDH in different electrolytes at 10 mA cm⁻² and 1,600 rpm. (Reproduced with permission^[14]. Copyright 2016, Wiley-VCH). (C) OER LSV curves of NiIr-LDH, NiFe-LDH, and IrO₂ in two different electrolytes. (D) Durability tests of seawater catalysis (NiIr-LDH and NiFe-LDH) in 1 M KOH + seawater electrolyte at room temperature at 500 mA cm⁻². (Reproduced with permission^[15]. Copyright 2022, American Chemical Society). (E) Seawater OER catalytic activity test for NFAC-MELDHS. (Reproduced with permission^[16]. Copyright 2021, The Royal Society of Chemistry).

the overpotential with the addition of 0.5 M NaCl in 0.1 M KOH, which demonstrated the high OER selectivity. To evaluate the stability of the electrocatalysts in the electrolytes with different pH values, the NiFe-LDH catalyst was measured in the four electrolytes mentioned above by 2 h chronopotentiometry after 5 CV cycles, as shown in Figure 12B. It shows stable activity for 2 h in 0.1 M KOH, regardless of the addition of the Cl⁻. Conversely, the catalytic stability of NiFe-LDH in the borate buffer became worse, especially in the presence of Cl⁻. The potential rose sharply to 2.4 V after nearly 1 h at 10 mA cm⁻² in the near-neutral chlorine-containing electrolyte, which would give rise to the undesirable HCFR process.

Therefore, moderate current density and high pH values are the key conditions for catalysts to maintain excellent electrocatalytic activity, selectivity, and long-term stability for OER processes.

Ni-based LDH electrocatalysts are known as the best OER candidates in seawater electrolytes, and NiFe LDH, in particular, is considered to be the benchmark among noble metal-free catalysts. Furthermore, in view of the considerable stability of Ir metals for OER, You *et al.* introduced Ir to develop a monolayer NiIr-LDH as an OER catalyst for seawater electrocatalysis^[115]. The NiIr-LDH catalyst showed 313 mV and 361 mV overpotentials at 500 mA cm⁻² in artificial seawater (1 M potassium hydroxide + 0.5 M NaCl) and alkaline seawater (1 M potassium hydroxide + seawater), respectively, along with nearly 100% O₂ Faradaic efficiency in alkaline seawater [Figure 12C]. Impressively, the NiIr-LDH catalyst delivered excellent long-term stability, maintaining its performance for up to 650 h under an industrial 500 mA cm⁻² current density in alkaline seawater [Figure 12D]. Compared with the OER benchmark NiFe-LDH, both Ir and Ni are considered as the active sites for the OER in NiIr-LDH, and with the introduction of Ir, the Ni atom becomes more electrochemically active. The incorporation of Ir into the Ni(OH)₂ layer optimized the electron density of Ir and Ni sites and accelerated the rate-limiting step of the intermediate *O and *OOH generation on Ni and Ir sites. The synergistic effects of multi-component metallic sites are also one of the most effective strategies for constructing efficient and stable electrocatalysts in seawater conditions. Consequently, Enkhtuvshin *et al.* reported multi-metallic Ni-Fe-Al-Co-layered double hydroxides (NFAC-MELDHs) as OER catalysts (1.0 M KOH + 0.5 M NaCl), which showed an overpotential of 280 mV at a current density of 100 mA cm⁻² [Figure 12E]^[116]. The Fe sites are considered to be the real active sites for redox flexibility, which cooperate with the adjacent metals to stabilize the adsorption of oxygen intermediates while promoting charge transfer.

Transition metal-based electrocatalysts

In the past decades, TM compound-based electrocatalysts have been considered as the most promising alternatives for replacing noble metal-based electrocatalysts due to their earth-abundance, popular price, potential multi-catalytic performance, and adjustable crystal and electronic structures^[117-119]. Based on these advantages, strategies have been developed in recent reports to promote the OER performance of TM compound-based catalysts in seawater-based electrolytes. Accordingly, Yu *et al.* synthesized a 3D core-shell NiMoN@NiFeN OER catalyst for seawater catalysis^[120]. The seawater diffusion and gas releasing processes were facilitated, benefiting from the 3D core-shell structure with multiple levels of porosity. Therefore, on the one hand, the high conductivity and large surface area of interior NiMoN nanorods led to an efficient charge transfer rate and more active sites. On the other hand, thin amorphous NiFe oxy(hydroxide) layers in situ evolved from the outer NiFeN NPs under the OER-applied voltage, acting as the active species and effectively resisting the invasion of Cl⁻ [Figure 13A]. The NiMoN@NiFeN catalyst showed 368 mV and 398 mV OER overpotentials at industrial current densities of 500 mA cm⁻² and 1,000 mA cm⁻², respectively, in alkaline natural seawater, which are both below the 480 mV overpotential required to trigger the HCFR process [Figure 13B]. Kuang *et al.* designed a multilayer electrode NiFe/NiS_x-Ni as OER electrocatalysts in alkaline seawater [Figure 13C]^[121]. NiS_x was formed from the Ni foam by a solvothermal method, and NiFe hydroxide was prepared by electrodeposition using NiS_x-Ni foam as precursors. After anodic activation in an alkaline condition, the polyanion sulfate/carbonate-passivated NiFe/NiS_x-Ni foam anode was generated. After 1,000 h seawater catalysis in alkaline simulated seawater electrolyte (1 M KOH + 0.5 M NaCl), NiFe/NiS_x-Ni delivered an OER overpotential of 510 mV at the current density of 400 mA cm⁻², which could reach 300 mV at 400 mA cm⁻² after iR compensation and was below the 480 mV to limited the chloride oxidation to hypochlorite [Figure 13D]. Even under the condition of high temperature (80 °C), alkalinity (6 M KOH), and salinity (1.5 M NaCl), the catalyst still shows similar excellent activity. Generally, NiFe is a highly active and selective OER catalyst for seawater electrolysis, and the interior NiS_x layer is a conductive

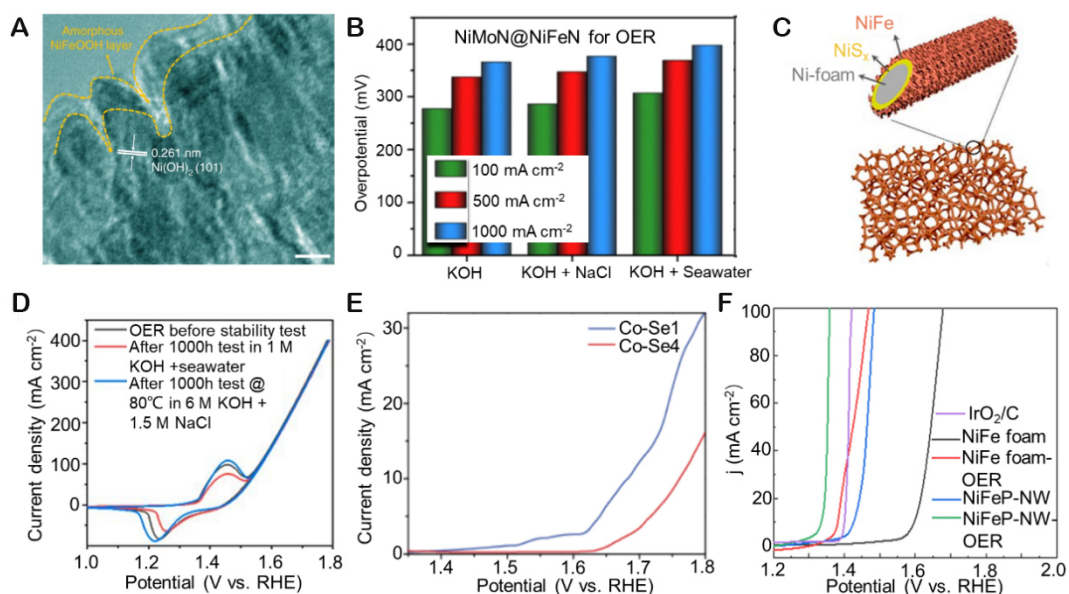


Figure 13. (A) HRTEM image of the NiMoN@NiFeN catalyst after OER tests. Scale bars: 5 nm. (B) Comparison of the OER overpotentials at 100, 500, and 1,000 mA cm⁻² for NiMoN@NiFeN in different electrolytes. (Reproduced with permission^[120]. Copyright 2019, Springer Nature). (C) Structure of the NiFe/NiS_x-Ni; (D) CV scans of a Ni³⁺ anode before and after 1,000 h seawater catalysis in an alkaline simulated seawater electrolyte. (Reproduced with permission^[121]. Copyright 2019, PNAS). (E) The OER polarization curves of Co-Se₁ and Co-Se₄ in seawater. (Reproduced with permission^[122]. Copyright 2018, WILEY-VCH). (F) OER activity of NiFe foam, NiFe foam-OER, NiFeP-NW, NiFeP-NW-OER, and IrO₂/C in alkaline simulated seawater. (Reproduced with permission^[123]. Copyright 2021, Elsevier).

medium. The anion-selective polyatomic anode could effectively inhibit the corrosion by repelling Cl⁻. Zhao *et al.* reported a 3D self-supporting cobalt selenide electrode by composing CoSe with Co₉Se₈ phases by regulating the Co³⁺/Co²⁺ ratio^[122]. Figure 13E shows that the combination of two cobalt selenide electrocatalysts of Co-Se₁ and Co-Se₄ with different Co ratios displays efficient OER performance in seawater electrolytes. The Co-Se₁ with a higher Co charge state reveals superior OER activity. Wang *et al.* prepared the amorphous NiFeP nanostructures as OER catalysts for overall seawater catalysis^[119]. The NiFeP catalyst shows a low overpotential of 129 mV for OER at 100 mA cm⁻² in alkaline simulated seawater electrolytes (1.0 M KOH + 0.01 M KHCO₃ + 1 M NaCl). The electronic states of NiFe sites are regulated by the ligand effect of the P element, which breaks the scaling relations for oxygen-containing intermediates and reduces the adsorption energy gap between HO* and HOO* from 3.08 eV to 2.62 eV [Figure 13F].

Hybrids and composite OER electrocatalysts

TM (hydr)oxides, sulfides, selenides, and phosphides have been developed to catalyze the OER process in alkaline and seawater-based electrolytes, and some of them show relatively outstanding activity and stability^[123-126]. Nevertheless, single-phase electrocatalysts generally possess some disadvantages, such as poor electrical conductivity, insufficient active site exposure, *etc.* Constructing rational heterostructures has been considered as a promising approach to combine the characteristics of materials and enhance the catalytic activity via synergistic effects and electron interactions. Accordingly, Tan *et al.* developed the Ni₂Fe-LDH/FeNi₂S₄/NF heterostructure electrocatalyst using a partial sulfidation strategy for OER in seawater^[127]. Furthermore, inspired by the perspective that sulfate layers could inhibit corrosion resistance by repelling Cl⁻, 2,000 CV cycles were performed to generate the sulfate anions before measuring the OER activity of Ni₂Fe-LDH/FeNi₂S₄/NF [Figure 14A]. As shown in Figure 14B, Ni₂Fe-LDH/FeNi₂S₄/NF after CVs (post-Ni₂Fe-LDH/FeNi₂S₄/NF) delivered the smallest overpotentials at 50 mA cm⁻² and 100 mA cm⁻², indicating its higher corrosion resistance to Cl⁻. The heterostructures provide abundant hydroxide/sulfide

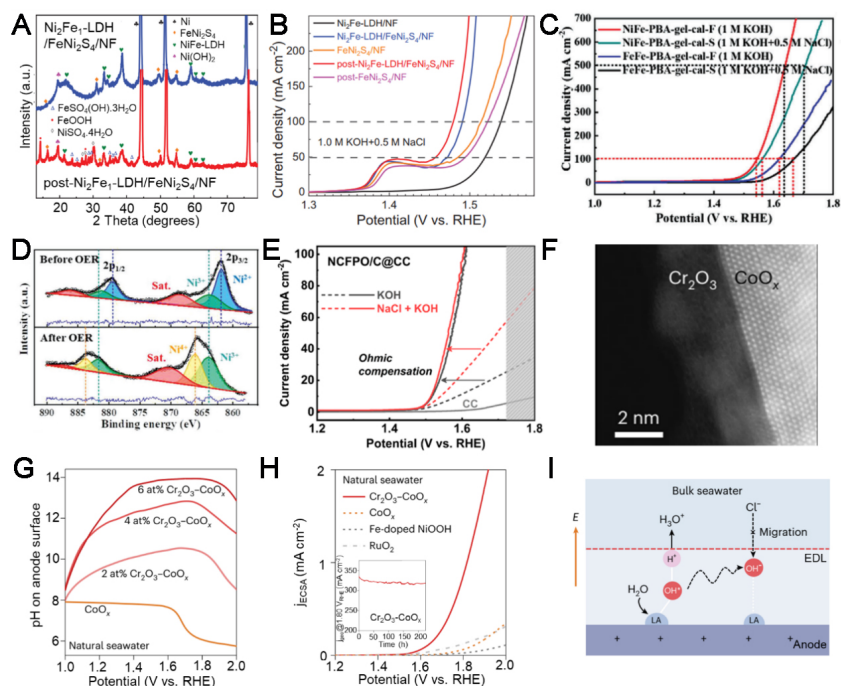


Figure 14. (A) XRD patterns of Ni₂Fe-LDH/FeNi₂S₄/NF and post-Ni₂Fe-LDH/FeNi₂S₄/NF. (B) The OER LSV curves of five different samples in 1.0 M KOH + 0.5 M NaCl. (Reproduced with permission^[127]. Copyright 2022, WILEY-VCH). (C) The OER polarization curves of NiFe-PBA-gel-cal and FeFe-PBA-gel-cal in alkaline freshwater and alkaline simulated seawater. (D) The XPS spectra of Ni 2p in NiFe-PBA-gel-cal before and after OER tests. (Reproduced with permission^[128]. Copyright 2022, WILEY-VCH). (E) Polarization curves of NCFPO/C@CC in the KOH and NaCl + KOH electrolytes. (Reproduced with permission^[129]. Copyright 2019, American Chemical Society). (F) HAADF-STEM image of Cr₂O₃-CoO_x. (G) Measured pH values on CoO_x and Cr₂O₃-CoO_x anode surfaces at different potentials. (H) OER LSV curves of 6 at% Cr₂O₃-CoO_x, CoO_x, Fe-doped NiOOH and RuO₂ catalysts in seawater. The inset shows the durability test of the 6 at% Cr₂O₃-CoO_x anode. (I) The Schematic diagram of local alkaline microenvironment generation of Lewis acid modified anode. (Reproduced with permission^[130]. Copyright 2023, Springer Nature).

interfaces and form a large number of active sites. Moreover, the excellent OER activity and stability also benefit from the large surface area, good electrical conductivity, rapid charge transfer, and mass transfer rates. To fully utilize the advantages of Ni-based and Fe-based compounds for catalyzing the OER process, Zhang *et al.* reported a TM oxide/TM carbide composite electrocatalyst with a two-step procedure^[128]. A Prussian blue analog (NiFe-PBA) precursor with 2D networks was prepared by a sol-gel method, and the precursor was further calcined in argon and air condition to continuously prepare NiFe-PBA with ultra-large surface area, which was composed of Fe₃O₄ and NiC_x. Figure 14C shows the OER activities of the catalysts in alkaline solution (1 M KOH) and alkaline artificial seawater (1 M KOH + 0.5 M NaCl). NiFe-PBA delivered enhanced OER activities in both alkaline solution and alkaline artificial seawater, which need 308 mV and 329 mV to achieve a current density of 100 mA cm⁻², respectively. The characterizations after OER measurement revealed that the Fe₃O₄ NPs were coated with amorphous NiOOH_{2-x} reconstructed from NiC_x, thus forming the core-shell structure. The high-valence ions and abundant oxygen defects formed along with the reconstruction process [Figure 14D]. DFT calculations and the ligand field theory uncovered that the *in-situ* generated high-valence Ni⁴⁺ leads to the formation of local O 2p electron holes as the electrophilic centers of the OER process. Furthermore, the OER process of NiFe-PBA follows the lattice oxygen oxidation mechanism pathway due to the existence of high valence Ni⁴⁺ and abundant oxygen defects, which exceeds the adsorption of oxygen-containing intermediates and is beneficial to the reaction kinetics. Song *et al.* reported the carbon-coated Na₂Co_{1-x}Fe_xP₂O₇ NPs (NCFPO/C NPs) as OER electrocatalysts for alkaline seawater electrolysis^[129]. The NCFPO/C NPs were dip-coated on the carbon cloth for OER measurement, which delivered an overpotential of 370 mV at a current density of

100 mA cm⁻² with the iR compensation in 0.1 M KOH + 0.5 M NaCl and showed similar LSV curves with that in 0.1 M KOH [Figure 14E]. The overpotential was less than 480 mV at 100 mA cm⁻², which demonstrated the high selectivity for OER electrocatalysis. No reactive chlorine species were detected after the OER test in the chlorine-containing electrolyte. Moreover, the excellent long-term stability of NCFPO/C NPs was tested by CV for 10,000 cycles and chronopotentiometry for 100 h at 10 mA cm⁻² and 50 mA cm⁻².

Up to now, most seawater electrolytes contain alkaline additives for seawater catalysis. The direct natural seawater catalysis without purification and alkali addition is an important technology in the future. A novel and efficient strategy is to create a favorable local reaction microenvironment on the surface of electrocatalysts for the direct natural seawater electrocatalysis. Guo *et al.* introduced a hard Lewis acid layer on the TM oxides to manipulate the local pH values for the direct seawater electrocatalysis [Figure 14F]^[130]. Due to the strong ability to water dissociation, a large amount of OH⁻ could be in situ generated on the surface of catalysts with the increased content of hard Lewis acid Cr₂O₃. In particular, the pH value on the 6 at% Cr₂O₃-CoO_x could approach 14.0 under the applied potential of 1.60 V (*vs.* RHE), which demonstrated that it was nearly in alkaline seawater [Figure 14G]. The normalized OER activity to the electrochemical surface area of 6 at% Cr₂O₃-CoO_x was much higher than those of CoO_x and benchmark Fe-doped NiOOH and RuO₂ [Figure 14H]. Furthermore, the Cr₂O₃-CoO_x could stably catalyze the natural seawater catalysis for more than 200 h at 1.8 V *vs.* RHE, higher than the potential required to trigger chloride oxidation. Most OH⁻ could participate in OER processes, and some residual OH⁻ could interact with the positive charge on the catalyst surface to constitute a stable electrical double layer (EDL) [Figure 14I]. The enrichment of OH⁻ prevents the diffusion and adsorption of Cl⁻ to the catalyst in seawater electrolytes, thus inhibiting the chlorine redox chemistry and the corrosion of the electrode. When the Cr₂O₃-CoO_x content is 6 at%, the current density of the as-developed flow type seawater electrolyzer at 1.87 V at 60 °C meets an industrial requirement of 1.0 A cm⁻², and it runs stably for 100 h at 500 mA cm⁻².

STUDY ON METAL ELECTRODES OF SMABS

Metal anodes, such as Na, Mg, Al, and Zn, play a critical role in determining the properties of cycling life, capacity, and energy density of the SMABs. Especially in R-SMABs, mainly the sodium-air batteries, where the anode is made of pure sodium or sodium alloys. During the discharge process, sodium ions are released from the negative electrode, generating electrical energy. During the charging process, sodium ions in the seawater at the negative electrode are reduced to metallic sodium. Sodium is abundantly available and is often used as anode material due to its high theoretical capacity of up to 1,166 mA g⁻¹. However, the uncontrolled growth of sodium dendrites hinders the safe operation of cells, damages the separator membrane, and shortens the device lifetime. Additionally, seawater-based sodium-air batteries still have a low coulombic efficiency and cell performance. Currently, the problem of sodium dendrites in seawater-based sodium-air batteries can be addressed through the following approaches: (i) Electrolyte optimization. By modifying the composition and concentration of the electrolyte, the formation of sodium dendrites can be reduced. Adding additives that inhibit the growth of sodium dendrites, such as polymers or ionic liquids, can effectively suppress their growth; (ii) Electrode coating. Applying a protective coating on the surface of the negative electrode can prevent the formation and growth of sodium dendrites. This coating can be a polymer or other materials that provide sufficient mechanical strength and chemical stability to prevent penetration and damage caused by dendrites; and (iii) Design optimization. By optimizing the structure and design of the battery, the formation of sodium dendrites can be minimized. For example, using porous electrode materials or nanostructures can provide more surface area and a more uniform distribution of sodium ions, reducing dendrite formation.

To investigate the growth of sodium dendrites on the surface of sodium electrodes, it is common to use *ex-situ* digital photos or SEM images to compare the changes in the surface of the negative electrode before and after reactions. For example, Kim *et al.* effectively alleviated the problem of sodium dendrite formation by designing a 1M NaBH₄/ether-based (glyme) electrolytes (NaBH₄/DEGDME and NaBH₄/TEGDME)^[131]. For control experiments, 1.0 M NaClO₄ in EC/PC + 5 wt% fluoroethylene carbonate (FEC) and 1M NaOTf in glyme electrolytes (denoted as NaClO₄ EC/PC + 5 wt% FEC and NaOTf/TEGDME) as reference electrolytes. As shown in Figure 15. NaClO₄ in carbonate solvents containing + 5 wt% FEC was rapidly decomposed upon reaction with sodium to form a solid-electrolyte interphase layer. This layer exhibited inhomogeneity, which facilitated dendrite growth. Therefore, porous and dendritic surfaces of sodium metal could be observed through SEM images and digital photos. [Figure 15A-C]. Although the sodium surface cycled by NaOTf/TEGDME is smoother and less porous than that cycled by NaClO₄ EC/PC + 5 wt% FEC electrolytes, a wrinkled surface with uneven local thickness was obtained [Figure 15D-F]. By contrast, it is observed that NaBH₄-based (glyme) electrolytes had a non-dendritic dense surface morphology, which proved that NaBH₄/glyme can be used as an effective strategy for ‘solid-electrolyte interphase layer reconstruction’ on sodium metals [Figure 15G-I].

PRACTICAL APPLICATIONS

The SMABs have promising applications in various fields, such as environmental detection, channel measuring, military operations, *etc.*^[132,133]. The discharging capacity of the package of SMABs can be controlled from small-scale (< 1 kWh) to medium-scale (1-10 kWh), even to large-scale (> 1 MWh) by connecting each unit pack together. For practical applications, for instance, the small-scale SMABs can be used in light buoys and detectors. Light buoys are floating devices that can be used for marking navigational channels, indicating hazards, or serving as reference points for marine activities. These buoys are designed to be easily deployed and controlled. They are often connected to a range of devices, such as lights, reflectors, and sensors, to provide visual and navigational information to vessels. The seawater battery in the light buoy can be charged by solar cells in the sunlight, thus providing more electricity to the LED lights.

The applications of medium-scale SMABs are aimed at providing electricity for various small autonomous machines, such as maritime exploration robots and drones. They are typically equipped with various sensors and cameras to monitor and search for targets in seawater, such as drifting vessels or people who have fallen overboard. These robots and drones can keep long-duration for the undersea operations using the seawater batteries. The high energy density and long lifespan of seawater batteries are being considered as ideal energy sources for maritime search and rescue robots or drones. By retrofitting and modifying existing robots or drones and integrating seawater batteries into their design, their endurance and operational efficiency can be enhanced, thereby better supporting the maritime search and rescue tasks. Moreover, there is great potential for the large-scale SMABs with energy capacities exceeding 1 MWh. These energy storage systems play a crucial role in providing electricity, stabilizing the grid, and integrating renewable energy sources into the power system. They can be utilized in various equipment, such as power plants, utility-scale renewable energy projects, industrial facilities, and large commercial buildings.

CONCLUSION AND OUTLOOK

SMABs directly utilize seawater as the electrolyte to achieve high energy density, long-term stability, and distributed, *in-situ* power supply systems, which possess broad application prospects. However, the application of OER/ORR catalysts as air cathodes is different from traditional alkaline metal-air batteries due to the influence of high content of Cl⁻ in seawater on the electrocatalytic processes. To improve the intrinsic OER/ORR electrocatalytic activity and stability, various electrocatalyst materials have been developed, such as noble metal-based, non-noble metal-based, and metal-free electrocatalysts. Some of these

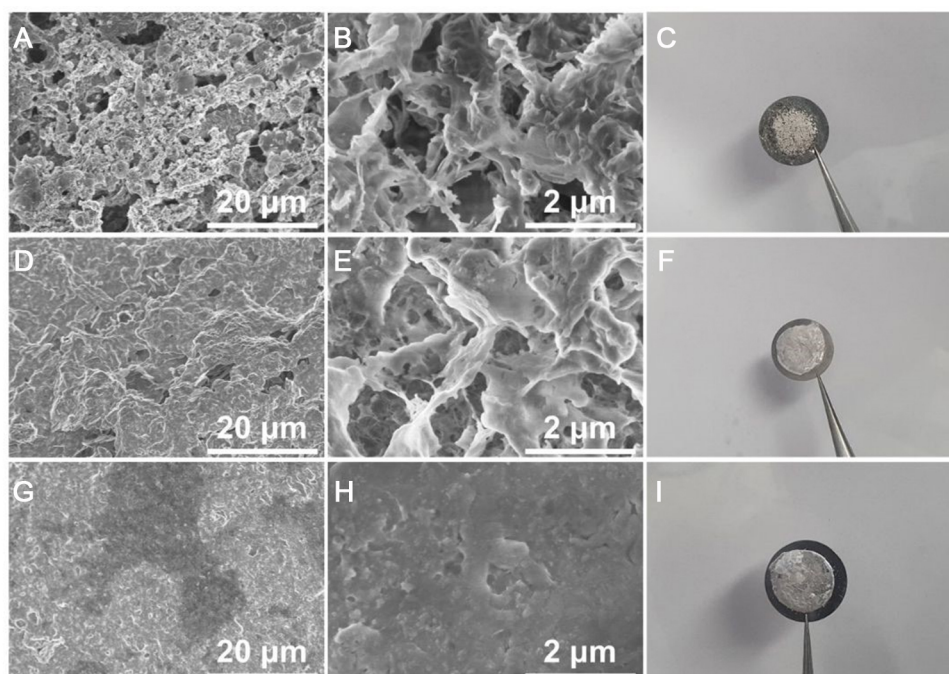


Figure 15. SEM images and digital photos for sodium metal electrodes of Na||Na symmetric cells after 50 cycles at 1 mA cm^{-2} , 1 mAh cm^{-2} . (A-C) NaClO_4 EC/PC + 5 wt% FEC, (D-F) NaOTf/TEGDME (G-I) NaBH_4 /DEGDME (Reproduced with permission^[31]). Copyright 2022, The Royal Society of Chemistry).

materials exhibit satisfactory OER/ORR activity, selectivity, and stability in the presence of Cl^- in seawater. As mentioned above, the intrinsic electrocatalytic ability can be improved by adjusting the electronic structure and atomic-scale surface-interface structure. It is believed that new insights into promoting the electrocatalytic processes of OER/ORR in chloride-containing and seawater electrolytes will lay the foundation for designing SMABs.

The further optimization of SMABs makes them possess promising applications as self-powering systems for the equipment working in the deep and open sea. In order to enhance the battery performance, several directions should be given more attention. Firstly, it is necessary to unveil the mechanism of Cl^- corrosion in the ORR process. The combination of theoretical calculations and *in-situ* experimental investigations is required to reveal the effect of Cl^- on ORR efficiency and stability. This will provide important theoretical and experimental foundations for the development of chlorine-resistant, efficient, and stable ORR/OER bifunctional oxygen electrocatalysts. Secondly, paying attention to the overall system design and integration is important to establish practical and scalable SMABs. This includes optimizing cell configurations, stack designs, and system components to maximize energy conversion efficiency and ensure long-term stability. Thirdly, more efforts should be devoted to the optimization of membranes to enhance the transfer rate of definite ions and improve the energy conversion efficiency and stability. When addressing these key issues, researchers may pave the way for the development of more efficient, stable, and environmentally friendly SMABs.

DECLARATIONS

Authors' Contributions

Conceptualization, investigation, and writing-original draft: Guo Y, Cao Y, Lu J

Writing-review & editing: Guo Y, Zheng X

Writing-review & editing, supervision, and funding acquisition: Zheng X, Deng Y

Availability of data and materials

Not applicable.

Financial support and sponsorship

This work was supported by the National Natural Science Foundation of China (52231008, 52177220) and the Key Research and Development Project of Hainan Province (ZDYF2022GXJS006).

Conflicts of interest

All authors declared that there are no conflicts of interest.

Ethical approval and consent to participate

Not applicable.

Consent for publication

Not applicable.

Copyright

© The Author(s) 2023.

REFERENCES

1. Helveston JP, He G, Davidson MR. Quantifying the cost savings of global solar photovoltaic supply chains. *Nature* 2022;612:83-7. DOI PubMed
2. Russo G. Renewable energy: wind power tests the waters. *Nature* 2014;513:478-80. DOI PubMed
3. Aziz MJ, Gayme DF, Johnson K, et al. A co-design framework for wind energy integrated with storage. *Joule* 2022;6:1995-2015. DOI
4. Almora O, Baran D, Bazan GC, et al. Device performance of emerging photovoltaic materials (version 1). *Adv Energy Mater* 2021;11:2002774. DOI
5. Zhang C, Wang H, Yu H, et al. Single-atom catalysts for hydrogen generation: rational design, recent advances, and perspectives. *Adv Energy Mater* 2022;12:e2200875. DOI
6. van Cresce A, Xu K. Aqueous lithium-ion batteries. *Carbon Energy* 2021;3:721-51. DOI
7. Lopes PP, Stamenkovic VR. Past, present, and future of lead-acid batteries. *Science* 2020;369:923-4. DOI PubMed
8. Kim J, Lee E, Kim H, Johnson C, Cho J, Kim Y. Rechargeable seawater battery and its electrochemical mechanism. *ChemElectroChem* 2015;2:328-32. DOI
9. Kim Y, Lee W. Secondary seawater batteries. In: *Seawater batteries. Green Energy and Technology*. Singapore: Springer; 2022. pp. 91-293. DOI
10. Mozaffari S, Nateghi MR. Recent advances in solar rechargeable seawater batteries based on semiconductor photoelectrodes. *Top Curr Chem* 2022;380:28. DOI PubMed
11. Khan Z, Park SO, Yang J, et al. Binary N,S-doped carbon nanospheres from bio-inspired artificial melanosomes: a route to efficient air electrodes for seawater batteries. *J Mater Chem A* 2018;6:24459-67. DOI
12. Sun Q, Dai L, Luo T, Wang L, Liang F, Liu S. Recent advances in solid-state metal-air batteries. *Carbon Energy* 2023;5:e276. DOI
13. Li Y, Lu J. Metal-air batteries: will they be the future electrochemical energy storage device of choice? *ACS Energy Lett* 2017;2:1370-7. DOI
14. Rahman MA, Wang X, Wen C. High energy density metal-air batteries: a review. *J Electrochem Soc* 2013;160:A1759-71. DOI
15. Zhang J, Zhang J, He F, et al. Defect and doping co-engineered non-metal nanocarbon ORR electrocatalyst. *Nanomicro Lett* 2021;13:65. DOI PubMed PMC
16. Chen Y, Xu J, He P, et al. Metal-air batteries: progress and perspective. *Sci Bull* 2022;67:2449-86. DOI
17. Galili N, Shemesh A, Yam R, et al. The geologic history of seawater oxygen isotopes from marine iron oxides. *Science* 2019;365:469-73. DOI
18. Gayen P, Saha S, Ramani V. Pyrochlores for advanced oxygen electrocatalysis. *ACC Chem Res* 2022;55:2191-200. DOI PubMed
19. Lv X, Wei W, Wang H, Huang B, Dai Y. Multifunctional electrocatalyst PtM with low Pt loading and high activity towards hydrogen and oxygen electrode reactions: a computational study. *Appl Catal B* 2019;255:117743. DOI

20. Cui X, Ren P, Ma C, et al. Robust interface Ru Centers for high-performance acidic oxygen evolution. *Adv Mater* 2020;32:e1908126. DOI
21. Kwon J, Sun S, Choi S, et al. Tailored electronic structure of Ir in high entropy alloy for highly active and durable bifunctional electrocatalyst for water splitting under an acidic environment. *Adv Mater* 2023;35:e2300091. DOI
22. Cai J, Zhang H, Zhang L, Xiong Y, Ouyang T, Liu ZQ. Hetero-anionic structure activated Co-S bonds promote oxygen electrocatalytic activity for high-efficiency zinc-air batteries. *Adv Mater* 2023;35:e2303488. DOI
23. Kim C, Min H, Kim J, Moon JH. Boosting electrochemical methane conversion by oxygen evolution reactions on Fe-N-C single atom catalysts. *Energy Environ Sci* 2023;16:3158-65. DOI
24. Gao FY, Gao MR. Nickel-based anode catalysts for efficient and affordable anion-exchange membrane fuel cells. *ACC Chem Res* 2023;56:1445-57. DOI PubMed
25. Wang L, Snihirova D, Deng M, et al. Sustainable aqueous metal-air batteries: an insight into electrolyte system. *Energy Stor Mater* 2022;52:573-97. DOI
26. Zhang W, Chang J, Wang G, et al. Surface oxygenation induced strong interaction between Pd catalyst and functional support for zinc-air batteries. *Energy Environ Sci* 2022;15:1573-84. DOI
27. Kim S, Ji S, Yang H, et al. Near surface electric field enhancement: pyridinic-N rich few-layer graphene encapsulating cobalt catalysts as highly active and stable bifunctional ORR/OER catalyst for seawater batteries. *Appl Catal B* 2022;310:121361. DOI
28. Zhu J, Chi J, Cui T, et al. F doping and P vacancy engineered FeCoP nanosheets for efficient and stable seawater electrolysis at large current density. *Appl Catal B* 2023;328:122487. DOI
29. Stamenkovic V, M. Markovic N, Ross P. Structure-relationships in electrocatalysis: oxygen reduction and hydrogen oxidation reactions on Pt(111) and Pt(100) in solutions containing chloride ions. *J Electroanal Chem* 2001;500:44-51. DOI
30. Liu K, Fu J, Lin Y, et al. Insights into the activity of single-atom Fe-N-C catalysts for oxygen reduction reaction. *Nat Commun* 2022;13:2075. DOI PubMed PMC
31. An L, Hu Y, Li J, et al. Tailoring oxygen reduction reaction pathway on spinel oxides via surficial geometrical-site occupation modification driven by the oxygen evolution reaction. *Adv Mater* 2022;34:e2202874. DOI
32. Wang N, Ou P, Hung SF, et al. Strong-proton-adsorption Co-based electrocatalysts achieve active and stable neutral seawater splitting. *Adv Mater* 2023;35:e2210057. DOI
33. Hwang SM, Park JS, Kim Y, et al. Rechargeable seawater batteries-from concept to applications. *Adv Mater* 2019;31:e1804936. DOI
34. Blake IC. Fiftieth anniversary: the anniversary issue on primary cell: silver chloride-magnesium reserve battery. *J Electrochem Soc* 1952;99:202C. DOI
35. Huang Q, Yu K, Yang S, Wen L, Dai Y, Qiao X. Effects of Al and Sn on electrochemical properties of Mg-6%Al-1%Sn (mass fraction) magnesium alloy as anode in 3.5%NaCl solution. *J Cent South Univ* 2014;21:4409-14. DOI
36. Wang N, Wang R, Peng C, Peng B, Feng Y, Hu C. Discharge behaviour of Mg-Al-Pb and Mg-Al-Pb-In alloys as anodes for Mg-air battery. *Electrochim Acta* 2014;149:193-205. DOI
37. Abdulrehman T, Yousif Z, Al-ameri S, Abdulkareem I, Abdulla A, Haik Y. Enhancing the performance of Mg-Al brine water batteries using conductive polymer-PEDOT:PSS. *Renew Energy* 2015;82:125-30. DOI
38. Yu K, Xiong H, Wen L, et al. Discharge behavior and electrochemical properties of Mg-Al-Sn alloy anode for seawater activated battery. *T Nonferr Metal Soc* 2015;25:1234-40. DOI
39. Yuasa M, Huang X, Suzuki K, Mabuchi M, Chino Y. Discharge properties of Mg-Al-Mn-Ca and Mg-Al-Mn alloys as anode materials for primary magnesium-air batteries. *J Power Sources* 2015;297:449-56. DOI
40. Shi Y, Peng C, Feng Y, Wang R, Wang N. Microstructure and electrochemical corrosion behavior of extruded Mg-Al-Pb-La alloy as anode for seawater-activated battery. *Mater Des* 2017;124:24-33. DOI
41. Shi Y, Peng C, Feng Y, Wang R, Wang N. Enhancement of discharge properties of an extruded Mg-Al-Pb anode for seawater-activated battery by lanthanum addition. *J Alloys Compd* 2017;721:392-404. DOI
42. Wang L, Wang R, Feng Y, Deng M, Wang N. Effect of heat treatment on electrochemical properties of Mg-9 wt.%Al-2.5 wt.%Pb alloy in sodium chloride solution. *JOM* 2017;69:2467-70. DOI
43. Xiong H, Li L, Zhang Y, et al. Microstructure and discharge behavior of Mg-Al-Sn-in anode alloys. *J Electrochem Soc* 2017;164:A1745-54. DOI
44. Wu J, Wang R, Feng Y, Peng C. Effect of hot rolling on the microstructure and discharge properties of Mg-1.6 wt%Hg-2 wt%Ga alloy anodes. *J Alloys Compd* 2018;765:736-46. DOI
45. Li J, Chen Z, Jing J, Hou J. Electrochemical behavior of Mg-Al-Zn-Ga-In alloy as the anode for seawater-activated battery. *J Mater Sci Technol* 2020;41:33-42. DOI
46. Wu Z, Zhang H, Zou J, et al. Effect of microstructure on discharge performance of Al-0.8Sn-0.05Ga-0.9Mg-1.0Zn (wt%) alloy as anode for seawater-activated battery. *Mater Corros* 2020;71:1680-90. DOI
47. Xie Q, Ma A, Jiang J, Liu H, Saleh B. Discharge properties of ECAP processed AZ31-Ca alloys as anodes for seawater-activated battery. *J Mater Res Technol* 2021;11:1031-44. DOI
48. Huang J, Liu H, Fang H, et al. Effects of intermetallic phases on electrochemical properties of powder metallurgy Mg-6%Al-5%Pb anode alloy used for seawater activated battery. *Mater Res Express* 2022;9:066504. DOI
49. Zhao C, Liu J, Yao N, et al. Low-temperature working feasibility of zinc-air batteries with noble metal-free electrocatalysts. *Renew Energy* 2023;1:73-80. DOI
50. Renuka R. Influence of allotropic modifications of sulphur on the cell voltage in Mg-CuI(S) seawater activated battery. *Mater Chem*

- Phys* 1999;59:42-8. DOI
51. Senthilkumar ST, Go W, Han J, et al. Emergence of rechargeable seawater batteries. *J Mater Chem A* 2019;7:22803-25. DOI
 52. Prasad K, Venkatakrishnan N, Mathur P. Preliminary report on the performance characteristics of the magnesium-mercurous chloride battery system. *J Power Sources* 1977;1:371-5. DOI
 53. Yu J, Li B, Zhao C, Zhang Q. Seawater electrolyte-based metal-air batteries: from strategies to applications. *Energy Environ Sci* 2020;13:3253-68. DOI
 54. Shinohara M, Araki E, Mochizuki M, Kanazawa T, Suyehiro K. Practical application of a sea-water battery in deep-sea basin and its performance. *J Power Sources* 2009;187:253-60. DOI
 55. Liu Q, Yan Z, Wang E, Wang S, Sun G. A high-specific-energy magnesium/water battery for full-depth ocean application. *Int J Hydrog Energy* 2017;42:23045-53. DOI
 56. Al-eggiely AH, Alguail AA, Gvozdenović MM, Jugović BZ, Grgur BN. Seawater zinc/polypyrrole-air cell possessing multifunctional charge-discharge characteristics. *J Solid State Electrochem* 2017;21:2769-77. DOI
 57. Jiao W, Fan Y, Huang C, Sanglin. Effect of modified polyacrylonitrile-based carbon fiber on the oxygen reduction reactions in seawater batteries. *Ionics* 2018;24:285-96. DOI
 58. Zhang Q, Zhou Y, Dai W, et al. Chloride ion as redox mediator in reducing charge overpotential of aprotic lithium-oxygen batteries. *Batteries Supercaps* 2021;4:232-9. DOI
 59. Kim Y, Kim G, Jeong S, et al. Large-scale stationary energy storage: seawater batteries with high rate and reversible performance. *Energy Stor Mater* 2019;16:56-64. DOI
 60. Kim Y, Kim H, Park S, Seo I, Kim Y. Na ion-conducting ceramic as solid electrolyte for rechargeable seawater batteries. *Electrochim Acta* 2016;191:1-7. DOI
 61. Kim Y, Shin K, Jung Y, Lee W, Kim Y. Development of prismatic cells for rechargeable seawater batteries. *Adv Sustain Syst* 2022;6:2100484. DOI
 62. Son M, Park S, Kim N, Angeles AT, Kim Y, Cho KH. Simultaneous energy storage and seawater desalination using rechargeable seawater battery: feasibility and future directions. *Adv Sci* 2021;8:e2101289. DOI PubMed PMC
 63. Kim Y, Jung J, Yu H, et al. Sodium biphenyl as anolyte for sodium-seawater batteries. *Adv Funct Mater* 2020;30:2001249. DOI
 64. Han J, Hwang SM, Go W, Senthilkumar S, Jeon D, Kim Y. Development of coin-type cell and engineering of its compartments for rechargeable seawater batteries. *J Power Sources* 2018;374:24-30. DOI
 65. Xu Y, Lv H, Lu H, et al. Mg/seawater batteries driven self-powered direct seawater electrolysis systems for hydrogen production. *Nano Energy* 2022;98:107295. DOI
 66. Yu J, Zhao C, Liu J, Li B, Tang C, Zhang Q. Seawater-based electrolyte for zinc-air batteries. *Green Chem Eng* 2020;1:117-23. DOI
 67. Wang C, Yu Y, Niu J, et al. Recent progress of metal-air batteries - a mini review. *App Sci* 2019;9:2787. DOI
 68. Zhang T, Tao Z, Chen J. Magnesium-air batteries: from principle to application. *Mater Horiz* 2014;1:196-206. DOI
 69. Park S, Ligaray M, Kim Y, Chon K, Son M, Cho KH. Investigating the influence of catholyte salinity on seawater battery desalination. *Desalination* 2021;506:115018. DOI
 70. Mamtani K, Jain D, Co AC, Ozkan US. Investigation of chloride poisoning resistance for nitrogen-doped carbon nanostructures as oxygen depolarized cathode catalysts in acidic media. *Catal Lett* 2017;147:2903-9. DOI
 71. Kim Y, Kim J, Vaalma C, et al. Optimized hard carbon derived from starch for rechargeable seawater batteries. *Carbon* 2018;129:564-71. DOI
 72. Jin Z, Li P, Meng Y, Fang Z, Xiao D, Yu G. Understanding the inter-site distance effect in single-atom catalysts for oxygen electroreduction. *Nat Catal* 2021;4:615-22. DOI
 73. Millero FJ, Feistel R, Wright DG, McDougall TJ. The composition of standard seawater and the definition of the reference-composition salinity scale. *Deep Sea Res Part I Oceanogr Res Pap* 2008;55:50-72. DOI
 74. Kim DH, Choi H, Hwang DY, et al. Reliable seawater battery anode: controlled sodium nucleation via deactivation of the current collector surface. *J Mater Chem A* 2018;6:19672-80. DOI
 75. Liu Q, Pan Z, Wang E, An L, Sun G. Aqueous metal-air batteries: fundamentals and applications. *Energy Stor Mater* 2020;27:478-505. DOI
 76. Kim D, Park J, Lee W, Choi Y, Kim Y. Development of rechargeable seawater battery module. *J Electrochem Soc* 2022;169:040508. DOI
 77. Arnold S, Wang L, Presser V. Dual-Use of seawater batteries for energy storage and water desalination. *Small* 2022;18:e2107913. DOI PubMed
 78. Kim K, Hwang SM, Park J, Han J, Kim J, Kim Y. Highly improved voltage efficiency of seawater battery by use of chloride ion capturing electrode. *J Power Sources* 2016;313:46-50. DOI
 79. Jung J, Hwang DY, Kristanto I, Kwak SK, Kang SJ. Deterministic growth of a sodium metal anode on a pre-patterned current collector for highly rechargeable seawater batteries. *J Mater Chem A* 2019;7:9773-81. DOI
 80. Lee C, Jeon D, Park J, et al. Tetraruthenium polyoxometalate as an atom-efficient bifunctional oxygen evolution reaction/oxygen reduction reaction catalyst and its application in seawater batteries. *ACS Appl Mater Interfaces* 2020;12:32689-97. DOI
 81. Kim J, Park J, Lee J, Lim W, Jo C, Lee J. Biomass-derived P, N self-doped hard carbon as bifunctional oxygen electrocatalyst and anode material for seawater batteries. *Adv Funct Mater* 2021;31:2010882. DOI
 82. Kim J, Mueller F, Kim H, et al. Rechargeable-hybrid-seawater fuel cell. *NPG Asia Mater* 2014;6:e144. DOI

83. Manikandan P, Kishor K, Han J, Kim Y. Advanced perspective on the synchronized bifunctional activities of P2-type materials to implement an interconnected voltage profile for seawater batteries. *J Mater Chem A* 2018;6:11012-21. DOI
84. Kim S, Yang H, Jeong S, et al. Negative surface charge-mediated Fe Quantum dots with N-doped graphene/Ti₃C₂T_x MXene as chlorine-resistance electrocatalysts for high performance seawater-based Al-air batteries. *J Power Sources* 2023;566:232923. DOI
85. Le Z, Li W, Dang Q, et al. A high-power seawater battery working in a wide temperature range enabled by an ultra-stable Prussian blue analogue cathode. *J Mater Chem A* 2021;9:8685-91. DOI
86. Guo Y, Yang M, Xie RC, Compton RG. The oxygen reduction reaction at silver electrodes in high chloride media and the implications for silver nanoparticle toxicity. *Chem Sci* 2020;12:397-406. DOI PubMed PMC
87. Hasvold Ø, Henriksen H, Melvåg E, et al. Sea-water battery for subsea control systems. *J Power Sources* 1997;65:253-61. DOI
88. Li J, Wang N, Liu K, Duan J, Hou B. Efficient electrocatalytic H₂O₂ production in simulated seawater on ZnO/reduced graphene oxide nanocomposite. *Colloids Surf A Physicochem Eng Asp* 2023;668:131446. DOI
89. Shao M, Chang Q, Dodelet JP, Chenitz R. Recent advances in electrocatalysts for oxygen reduction reaction. *Chem Rev* 2016;116:3594-657. DOI PubMed
90. Nie Y, Li L, Wei Z. Recent advancements in Pt and Pt-free catalysts for oxygen reduction reaction. *Chem Soc Rev* 2015;44:2168-201. DOI
91. Ryu JH, Park J, Park J, et al. Carbothermal shock-induced bifunctional Pt-Co alloy electrocatalysts for high-performance seawater batteries. *Energy Stor Mater* 2022;45:281-90. DOI
92. Jin C, Nagaiah TC, Xia W, Bron M, Schuhmann W, Muhler M. Polythiophene-assisted vapor phase synthesis of carbon nanotube-supported rhodium sulfide as oxygen reduction catalyst for HCl electrolysis. *ChemSusChem* 2011;4:927-30. DOI PubMed
93. Chen Y, Matanovic I, Weiler E, Atanassov P, Artyushkova K. Mechanism of oxygen reduction reaction on transition metal-nitrogen-carbon catalysts: establishing the role of nitrogen-containing active sites. *ACS Appl Energy Mater* 2018;1:5948-53. DOI
94. Gu W, Hu L, Li J, Wang E. Recent advancements in transition metal-nitrogen-carbon catalysts for oxygen reduction reaction. *Electroanalysis* 2018;30:1217-28. DOI
95. Zhao C, Ren D, Wang J, et al. Regeneration of single-atom catalysts deactivated under acid oxygen reduction reaction conditions. *J Energy Chem* 2022;73:478-84. DOI
96. Liu M, Li N, Cao S, et al. A “pre-constrained metal twins” strategy to prepare efficient dual-metal-atom catalysts for cooperative oxygen electrocatalysis. *Adv Mater* 2022;34:e2107421. DOI
97. Suh DH, Park SK, Nakhavivej P, Kim Y, Hwang SM, Park HS. Hierarchically structured graphene-carbon nanotube-cobalt hybrid electrocatalyst for seawater battery. *J Power Sources* 2017;372:31-7. DOI
98. Wu S, Liu X, Mao H, et al. Realizing high-efficient oxygen reduction reaction in alkaline seawater by tailoring defect-rich hierarchical heterogeneous assemblies. *Appl Catal B* 2023;330:122634. DOI
99. Gao Z, Yang Q, Qiu P, et al. p-type plastic inorganic thermoelectric materials. *Adv Energy Mater* 2021;11:2100883. DOI
100. Zhan Y, Ding Z, He F, et al. Active site switching of Fe-N-C as a chloride-poisoning resistant catalyst for efficient oxygen reduction in seawater-based electrolyte. *Chem Eng J* 2022;443:136456. DOI
101. Li H, Kelly S, Guevarra D, et al. Analysis of the limitations in the oxygen reduction activity of transition metal oxide surfaces. *Nat Catal* 2021;4:463-8. DOI
102. Son M, Park J, Im E, et al. Sacrificial catalyst of carbothermal-shock-synthesized 1T-MoS₂ layers for ultralong-lifespan seawater battery. *Nano Lett* 2023;23:344-52. DOI
103. Zhang Y, Park J, Senthikumar ST, Kim Y. A novel rechargeable hybrid Na-seawater flow battery using bifunctional electrocatalytic carbon sponge as cathode current collector. *J Power Sources* 2018;400:478-84. DOI
104. Tu NDK, Park SO, Park J, Kim Y, Kwak SK, Kang SJ. Pyridinic-nitrogen-containing carbon cathode: efficient electrocatalyst for seawater batteries. *ACS Appl Energy Mater* 2020;3:1602-8. DOI
105. Zhang F, Yu L, Wu L, Luo D, Ren Z. Rational design of oxygen evolution reaction catalysts for seawater electrolysis. *Trends Chem* 2021;3:485-98. DOI
106. Dresch S, Dionigi F, Klingenhof M, Strasser P. Direct electrolytic splitting of seawater: opportunities and challenges. *ACS Energy Lett* 2019;4:933-42. DOI
107. Vos JG, Wezendonk TA, Jeremiassi AW, Koper MTM. MnO_x/IrO_x as selective oxygen evolution electrocatalyst in acidic chloride solution. *J Am Chem Soc* 2018;140:10270-81. DOI PubMed PMC
108. Kim S, Lee T, Han S, Lee C, Kim C, Yoon J. Ir_{0.11}Fe_{0.25}O_{0.64} as a highly efficient electrode for electrochlorination in dilute chloride solutions. *J Ind Eng Chem* 2021;102:155-62. DOI
109. Kim Y, Harzandi AM, Lee J, Choi Y, Kim Y. Design of large-scale rectangular cells for rechargeable seawater batteries. *Adv Sustain Syst* 2021;5:2000106. DOI
110. Hansen HA, Man IC, Studt F, Abild-Pedersen F, Bligaard T, Rossmeisl J. Electrochemical chlorine evolution at rutile oxide (110) surfaces. *Phys Chem Chem Phys* 2010;12:283-90. DOI PubMed
111. Komiya H, Shinagawa T, Takanabe K. Electrolyte engineering for oxygen evolution reaction over non-noble metal electrodes achieving high current density in the presence of chloride ion. *ChemSusChem* 2022;15:e202201088. DOI PubMed PMC
112. Zhao X, Wang Y, Shi Y, et al. Exploiting interfacial Cl⁻/Cl⁰ redox for a 1.8-V voltage plateau aqueous electrochemical capacitor. *ACS Energy Lett* 2021;6:1134-40. DOI
113. Vos JG, Liu Z, Speck FD, et al. Selectivity trends between oxygen evolution and chlorine evolution on iridium-based double

- perovskites in acidic media. *ACS Catal* 2019;9:8561-74. DOI
114. Dionigi F, Reier T, Pawolek Z, Glied M, Strasser P. Design criteria, operating conditions, and nickel-iron hydroxide catalyst materials for selective seawater electrolysis. *ChemSusChem* 2016;9:962-72. DOI PubMed
115. You H, Wu D, Si D, et al. Monolayer NiIr-layered double hydroxide as a long-lived efficient oxygen evolution catalyst for seawater splitting. *J Am Chem Soc* 2022;144:9254-63. DOI
116. Enkhtuvshin E, Kim KM, Kim Y, et al. Stabilizing oxygen intermediates on redox-flexible active sites in multimetallic Ni-Fe-Al-Co layered double hydroxide anodes for excellent alkaline and seawater electrolysis. *J Mater Chem A* 2021;9:27332-46. DOI
117. Zhang K, Zou R. Advanced transition metal-based OER electrocatalysts: current status, opportunities, and challenges. *Small* 2021;17:e2100129. DOI PubMed
118. Ibrahim KB, Tsai M, Chala SA, et al. A review of transition metal-based bifunctional oxygen electrocatalysts. *J Chin Chem Soc* 2019;66:829-65. DOI
119. Wang J, Zhao C, Liu J, et al. Composing atomic transition metal sites for high-performance bifunctional oxygen electrocatalysis in rechargeable zinc-air batteries. *Particuology* 2023;77:146-52. DOI
120. Yu L, Zhu Q, Song S, et al. Non-noble metal-nitride based electrocatalysts for high-performance alkaline seawater electrolysis. *Nat Commun* 2019;10:5106. DOI PubMed PMC
121. Kuang Y, Kenney MJ, Meng Y, et al. Solar-driven, highly sustained splitting of seawater into hydrogen and oxygen fuels. *Proc Natl Acad Sci USA* 2019;116:6624-9. DOI PubMed PMC
122. Zhao Y, Jin B, Zheng Y, Jin H, Jiao Y, Qiao S. Charge state manipulation of cobalt selenide catalyst for overall seawater electrolysis. *Adv Energy Mater* 2018;8:1801926. DOI
123. Liu J, Liu X, Shi H, et al. Breaking the scaling relations of oxygen evolution reaction on amorphous NiFeP nanostructures with enhanced activity for overall seawater splitting. *Appl Catal B* 2022;302:120862. DOI
124. Song Y, Xu B, Liao T, Guo J, Wu Y, Sun Z. Electronic structure tuning of 2D metal (Hydr)oxides nanosheets for electrocatalysis. *Small* 2021;17:e2002240. DOI PubMed
125. Joo J, Kim T, Lee J, Choi SI, Lee K. Morphology-controlled metal sulfides and phosphides for electrochemical water splitting. *Adv Mater* 2019;31:e1806682. DOI PubMed
126. Dutta A, Pradhan N. Developments of metal phosphides as efficient OER precatalysts. *J Phys Chem Lett* 2017;8:144-52. DOI PubMed
127. Tan L, Yu J, Wang C, et al. Partial sulfidation strategy to NiFe-LDH@FeNi₂S₄ heterostructure enable high-performance water/seawater oxidation. *Adv Funct Mater* 2022;32:2200951. DOI
128. Zhang H, Geng S, Ouyang M, Yadegari H, Xie F, Riley DJ. A self-reconstructed bifunctional electrocatalyst of pseudo-amorphous nickel carbide@iron oxide network for seawater splitting. *Adv Sci* 2022;9:e2200146. DOI PubMed PMC
129. Song HJ, Yoon H, Ju B, Lee D, Kim D. Electrocatalytic selective oxygen evolution of carbon-coated Na₂Co_{1-x}Fe_xP₂O₇ nanoparticles for alkaline seawater electrolysis. *ACS Catal* 2020;10:702-9. DOI
130. Guo J, Zheng Y, Hu Z, et al. Direct seawater electrolysis by adjusting the local reaction environment of a catalyst. *Nat Energy* 2023;8:264-72. DOI
131. Kim J, Kim J, Jeong J, et al. Designing fluorine-free electrolytes for stable sodium metal anodes and high-power seawater batteries via SEI reconstruction. *Energy Environ Sci* 2022;15:4109-18. DOI
132. Bae H, Park J, Senthikumar S, Hwang SM, Kim Y. Hybrid seawater desalination-carbon capture using modified seawater battery system. *J Power Sources* 2019;410-11:99-105. DOI
133. Budde-meibes H, Drillkens J, Lunz B, et al. A review of current automotive battery technology and future prospects. *J Aut Eng* 2013;227:761-76. DOI

Review

Open Access



Metal-organic frameworks as promising flame retardants for polymeric materials

Boyoun Hou¹, Ye-Tang Pan¹, Pingan Song^{2,3}

¹National Engineering Research Center of Flame Retardant Materials, School of Materials Science & Engineering, Beijing Institute of Technology, Beijing 100081, China.

²Centre for Future Materials, University of Southern Queensland, Springfield 4300, Australia.

³School of Agriculture and Environmental Science, University of Southern Queensland, Springfield 4350, Australia.

Correspondence to: Assoc. Prof. Ye-Tang Pan, National Engineering Research Center of Flame Retardant Materials, School of Materials Science & Engineering, Beijing Institute of Technology, Beijing 100081, China. E-mail: pyt@bit.edu.cn; Prof. Pingan Song, Centre for Future Materials, University of Southern Queensland, Springfield 4300, Australia; School of Agriculture and Environmental Science, University of Southern Queensland, Springfield 4350, Australia. E-mail: pingan.song@usq.edu.au/pingansong@gmail.com

How to cite this article: Hou B, Pan YT, Song P. Metal-organic frameworks as promising flame retardants for polymeric materials. *Microstructures* 2023;3:2023039. <https://dx.doi.org/10.20517/microstructures.2023.37>

Received: 19 Jul 2023 **First Decision:** 10 Aug 2023 **Revised:** 24 Aug 2023 **Accepted:** 11 Sep 2023 **Published:** 10 Oct 2023

Academic Editor: Zhanxi Fan **Copy Editor:** Fangyuan Liu **Production Editor:** Fangyuan Liu

Abstract

This article presents a vision for advancing the development of next-generation flame-retardant materials through the utilization of metal-organic frameworks (MOFs). The proposed vision is centered on four key areas: industrialization, multifunctionality, ligand synthesis, and derivatives. By optimizing production processes, customizing MOFs for specific properties and applications, and developing novel ligands and derivatives, the effectiveness and versatility of MOFs as flame-retardant materials can be significantly enhanced. This vision represents a promising direction for the field that has the potential to address critical safety concerns across various industries.

Keywords: Microstructures, metal-organic frameworks, multifunction, industrialization, flame retardant

INTRODUCTION

Metal-organic frameworks (MOFs) are a type of porous material composed of metal ions or clusters linked by organic ligands. Their development can be traced back to the 1990s when researchers were exploring



© The Author(s) 2023. **Open Access** This article is licensed under a Creative Commons Attribution 4.0 International License (<https://creativecommons.org/licenses/by/4.0/>), which permits unrestricted use, sharing, adaptation, distribution and reproduction in any medium or format, for any purpose, even commercially, as long as you give appropriate credit to the original author(s) and the source, provide a link to the Creative Commons license, and indicate if changes were made.



novel approaches for synthesizing materials with large surface areas and high porosity. The initial MOF structure, designated as MOF-5, was synthesized in 1999 by researchers at the University of Michigan. This material comprised Zn^{2+} ions coordinated with 1,4-benzenedicarboxylate (H_2BDC) ligands and exhibited a remarkable surface area exceeding $2,900 \text{ m}^2/\text{g}$ ^[1]. In 2013, MOFs were introduced as fillers into the polymer matrix for the first time, thereby enhancing low-humidity proton conductivity^[2]. This breakthrough sparked a surge of interest in MOFs, prompting researchers to explore their potential for diverse applications such as gas storage, catalysis, and drug delivery. Since then, thousands of MOFs have been synthesized using various metal ions and ligands to create materials with distinct properties and functions. MOFs have garnered attention as potential flame retardants due to their high surface area, tunable pore size, thermal stability, abundance of transition metals, and flexible structure.

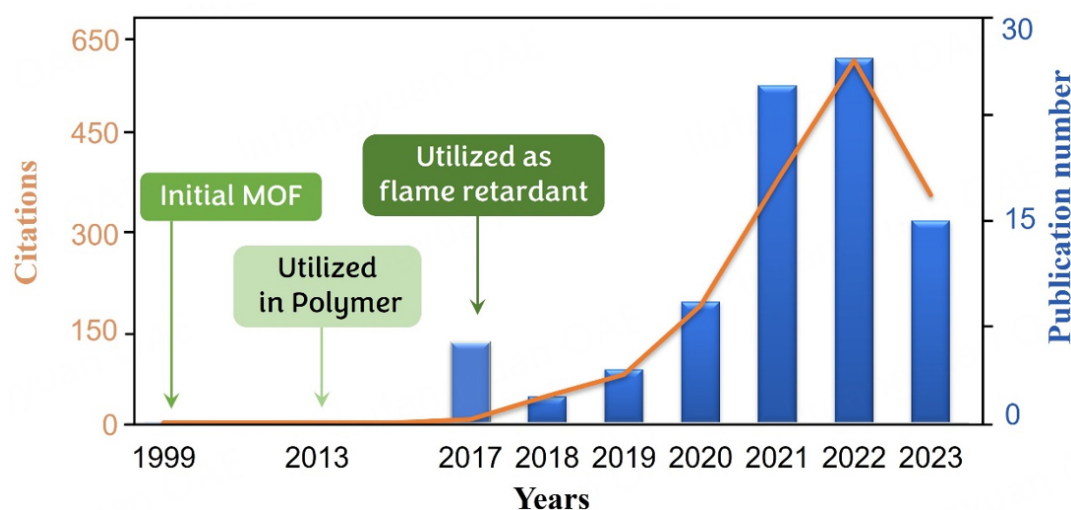
The application of MOFs as flame retardants can be traced back to research conducted in the late 2010s. In 2017, Hou *et al.* successfully synthesized iron-based and cobalt-based MOFs, which were subsequently incorporated into PS as flame retardants. The results demonstrated a significant improvement in both the thermostability and flame retardancy of the PS composites^[3]. Subsequently, researchers have investigated diverse categories of MOFs for their flame-retardant properties^[3-10]. Table 1 summarizes some MOF flame retardants for different polymer matrices^[11-23]. Recently, (zeolite imidazolate framework) ZIF series of MOFs have been intensively explored as potential flame retardants in various polymer matrices due to their ease of synthesis. MOFs contain flammable organic ligands in their structures, leading to limited efficiency, and therefore, modification or co-blending with other flame retardants is often required to boost their fire-retardant efficiency, e.g., performing better in UL-94 testing, especially at lower loading levels. It is accepted that MOFs usually reduce heat release rates and slow the combustion process of polymers via catalytic carbonization of transition metals within MOFs during combustion. However, there remain some unknowns on the impacts of structural compositions of MOFs on their catalyzing carbonization and modes of action. Additionally, they have explored the potential of incorporating MOFs as additives into existing flame-retardant materials to enhance their efficacy [Figure 1]. The use of MOFs as flame retardants is a relatively new and emerging area of research, and there are still ongoing debates regarding their cost-effectiveness compared to traditional flame retardants.

However, MOFs have several advantages over traditional flame retardants, such as their high porosity, high surface area, and tunable properties. These properties allow MOFs to be tailored to specific applications and offer superior flame-retardant performance. While MOFs may be relatively expensive compared to traditional flame retardants, their unique properties and superior flame-retardant performance may outweigh these costs in certain applications. The flame retardancy of MOFs is attributed to two primary mechanisms: gas-phase and condensed-phase. The gas-phase mechanism involves the liberation of non-flammable gases, such as water, carbon dioxide, and nitrogen. These gases can dilute the flammable gases and reduce the concentration of fuel and oxidizer in the flame zone^[24,25]. The condensed-phase mechanism involves the formation of a protective layer on the surface of the polymer, which acts as a physical barrier and reduces the combustion rate. This protective layer is formed by thermal decomposition of MOFs, releasing metal oxides or metal phosphates that react with the polymer to form a char layer. The char layer functions as an insulating layer, reducing heat transfer between flame and polymer and preventing fire spread^[26-29].

One may consider the potential benefits of utilizing MOFs as flame retardants, such as their capacity to enhance fire safety without adversely affecting the properties of the applied material. However, there are still some challenges associated with large-scale production and application of MOFs as flame retardants, as well as potential risks that come with using these materials. In this review, we aim to provide valuable guidance

Table 1. MOF-based flame retardants for different polymer matrices

Type of MOFs	Adding amount (%)	Matrix	UL-94	LOI (%)	pHRR reduction (%)	Reference
ZIF-8	1.0	PLA	V-2	26.0	-	[4]
UiO-66	5.0	PS	-	21.0	26.8	[5]
ZIF-8	0.91	PUF	-	18.8	50.6	[6]
Zr-MOF@CeHPP	2.0	PC	V-0	27.6	45.4	[11]
ZIF-67	2.0	EP	-	23.6	28.7	[12]
Ni-MOF	1.7 + 3.3 APP	PLA	V-0	31.0	26.9	[13]
ZIF-8	3 + 27 DDGS	PP	V-2	25.0	-	[14]
Fe-MOF	2.0	EP	-	-	18.6	[15]
Co-MOF	1.5 + 4.5 APP	TPU	V-0	28.2	81.1	[16]
ZIF-11	12.0	PUF	-	-	21.3	[17]
ZIF-8	0.75 + 2.25 EG	PUE	V-1	30.2	83.5	[18]
BP@MIL-53	1.0	PC	V-0	30.5	49.3	[19]
MIL-88B	1.0	PET	V-2	27.0	23.0	[20]
TEP@MIL-53	3.0	PS	-	-	24.7	[21]
ZIF-8/RGO	2.0	EP	V-1	26.8	49.66	[22]
Zr-MOF	4.0	PC	V-0	28.2	47.4	[23]

**Figure 1.** Data obtained with the keywords “MOF flame retard” or “MOF fire safety” in the Web of Science on August 14, 2023.

for researchers in this field by sharing our insights. One crucial aspect of MOFs is their adjustable structure, which enables precise manipulation of their physical and chemical properties. Ligand synthesis plays a pivotal role in fine-tuning the properties of MOFs, as ligands act as organic linkers that connect metal nodes and determine the framework structure. Therefore, the development of novel ligands and derivatives is imperative to enhance the versatility and performance of MOFs.

Furthermore, the industrialization of MOFs represents a crucial milestone toward their widespread commercial utilization. This entails scaling up the synthesis of MOFs, optimizing their properties for specific applications, and devising cost-effective production methods. Finally, the multifunctionality of MOFs is a key advantage that renders them suitable for a diverse range of applications. MOFs can be tailored to exhibit specific properties, such as antibacterial activity, gas storage capacity, and selective

adsorption.

The future of MOFs holds immense potential for innovation and impact across various industries. To advance the field of next-generation flame-retardant materials, we present a concise vision for industrialization, versatility, ligand synthesis, and MOF derivatives. This perspective is both timely and forward-looking, offering new insights and inspiration for senior researchers, deepening the understanding of young researchers, and providing guidance for those in related fields interested in the development of flame-retardant materials. Our work aims to provide valuable insights for a wide range of researchers and facilitate future advancements in this crucial field. We are confident that our article will make a significant contribution to the ongoing efforts toward developing safer and more sustainable materials for diverse applications.

INDUSTRIAL APPLICATION OF MOF-BASED FLAME RETARDANTS

Larger scale synthesis of MOF-based flame retardants

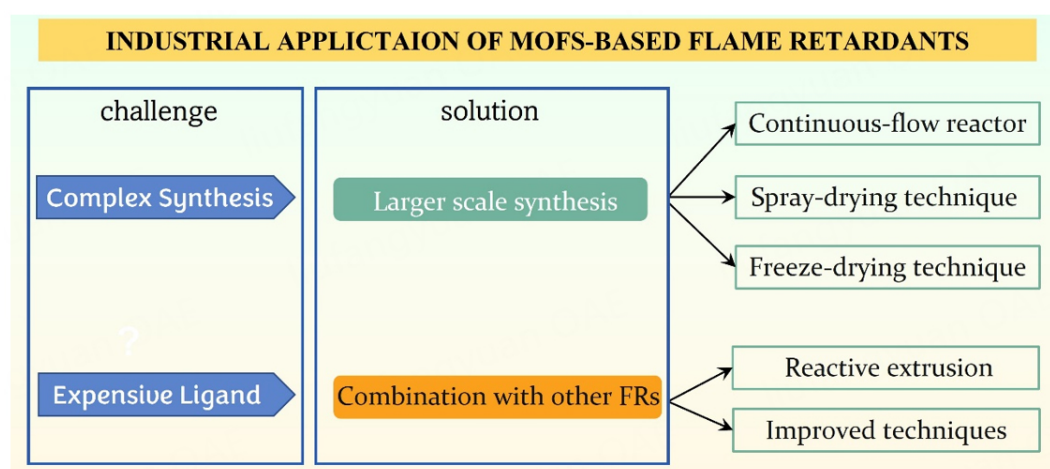
MOFs are typically synthesized in small quantities in a laboratory setting due to the intricate nature of their synthesis. For instance, the UIO and MIL series of MOFs necessitate a hydrothermal synthesis process followed by a high-temperature reaction in a reaction vessel^[30,31]. Achieving the desired MOF structure and properties requires meticulous control of reaction conditions, including temperature, pressure, and solvent composition. This process requires a significant amount of time. Even zeolite imidazolate skeleton materials (ZIFs), synthesized by facile methods, necessitate prolonged aging for the attainment of a flawless crystal structure^[32,33]. The aging process is essential for the formation of intermolecular hydrogen bonds between metal ions and ligands, which stabilize the MOF structure and prevent collapse. The duration of aging can vary from several hours to several days, depending on the specific MOF being synthesized and the desired crystal quality.

To achieve commercial viability, MOFs must be produced on a large scale [Table 2]. Despite the challenges associated with their synthesis, recent advances in synthetic methods have facilitated industrial production of MOFs, enabling scaling up to gram or even kilogram quantities [Figure 2]. Continuous-flow reactors are a commonly employed strategy for the large-scale synthesis of MOFs^[34-36]. In this approach, the reactants are continuously fed into the reactor and undergo controlled mixing and reaction, resulting in a steady-state production of MOFs. This method offers several benefits, including precise regulation of reaction parameters, rapid mixing, heat transfer, and continuous product output. A further approach is to employ the techniques of spray-drying or freeze-drying^[37-39]. The spray-drying technique involves the atomization of a liquid MOF precursor into small droplets, which are subsequently dried using a stream of hot air. As these droplets traverse through the drying chamber, the solvent evaporates, leaving behind solid MOF particles. The method is highly efficient in the production of MOF powders and can be readily scaled up for large-scale manufacturing.

Freeze-drying involves freezing a liquid MOF precursor and subsequently eliminating the solvent under vacuum conditions. The frozen specimen is then placed in a vacuum chamber where the solvent sublimates directly from the solid to the gas phase, resulting in a desiccated MOF powder. Freeze-drying is a more time-consuming process compared to spray-drying; however, it has the ability to maintain the crystalline structure of MOFs intact, which can prove crucial for certain applications. Both methods are capable of producing MOFs with high surface area, porosity, and thermal stability, rendering them highly versatile for a wide range of applications. Additionally, they facilitate the production of MOFs in powder form, which is more manageable and storable. Apart from that, the cost of MOFs can significantly affect large-scale production. Generally, the higher the cost of ligands, the greater the expense of producing MOFs. The price

Table 2. Industrial methods of MOF-based flame retardants

Method	Description	Example applications
Continuous flow reactors	MOFs are synthesized in a continuous flow system, where reactants are continuously pumped through a reactor	Large-scale production of MOFs
Spray-drying	A solution of MOF precursors is atomized into a hot drying gas, allowing rapid solvent evaporation and MOF formation in the form of dry powder	Production of MOF powders for various applications such as coatings and composites
Freeze-drying	MOF precursors are dissolved in a solvent, frozen, and then subjected to a vacuum, causing the solvent to sublime. The resulting solid is a porous MOF	Production of highly porous MOFs with preserved crystallinity

**Figure 2.** Industrial application of MOF-based flame retardants.

of MOF ligands can be influenced by a range of factors, such as the availability of raw materials used for synthesizing the ligands, the complexity involved in their synthesis, and the demand for MOF materials across various industries. With the advancement of novel and more efficient synthesis techniques, there is a possibility for a reduction in the cost of MOF ligands. As scientists have gained an enhanced comprehension of the structure and characteristics of MOFs, they have been able to optimize the production process of organic ligands that are utilized in creating these materials^[40,41]. This has resulted in more efficient and cost-effective approaches to synthesizing MOF ligands, thereby contributing to a reduction in their price. By reducing costs through economical synthesis and purification methods, MOFs can become more competitive with other materials, leading to increased adoption in industrial applications.

Combination of MOFs with other flame retardants

In this context, the commercial potential of incorporating MOFs as flame retardants into polymers has been demonstrated due to the decreasing cost of synthetic organic ligands. Recent unpublished work and conference papers have reported on MOFs acting as synergists with traditional flame retardants [Table 3]. MOFs can be added to other flame-retardant materials to enhance their performance^[18,42-48].

For example, MOFs can be added to intumescent coatings, which expand when exposed to heat, forming a protective layer that insulates the underlying material and delays its ignition. The thermal stability of the expanded coatings can be improved by adding MOFs; the coking property can be increased by transition metal catalysis, and the flame-retardant property can be enhanced. Shen *et al.* investigated the use of MOFs as a synergist for intumescent flame retardants in polypropylene (PP). The aim was to utilize ZIF-8 for enhancing char formation and improving fire retardancy of PP. It was discovered that the incorporation of ZIF-8 facilitated better char formation and reduced the emission of flammable gases during combustion^[42].

Table 3. Combination of MOFs with other flame retardants

MOF	Other flame retardants	Example applications
Ni-MOF ^[43]	Ammonium polyphosphate	Flame-retardant additives for polymers and textiles
MOF-Cu ^[44]	Ammonium polyphosphate	Flame-retardant additives for plastics and textiles
ZIF-67 ^[46]	Ammonium polyphosphate	Flame-retardant coatings and polymer formulations
ZIF-8 ^[47]	Phosphorus-based flame retardants	Flame-retardant coatings, textiles, and polymer matrices
UiO-66 ^[48]	Cyclotriphosphazene	Flame-retardant composites and polymer formulations

Xu *et al.* employed a solvothermal method to synthesize a specific type of MOF using cobalt ions and organic ligands, resulting in a porous material with high surface area and thermal stability. Subsequently, the Co-MOF was compounded with PP after being mixed with melamine polyphosphate (MPP), which is another flame retardant. The results indicate that the incorporation of Co-MOF into MPP/PP composite significantly enhances its flame retardancy, as compared to PP alone or with only MPP. This improvement is attributed to the release of water and gases from Co-MOF upon heating, which can effectively cool and dilute flames^[43]. Quan *et al.* explore the synergistic effects of ZIFs (ZIF-67 and ZIF-8) with different transition metals on intumescent flame-retarded PP composites^[49]. Overall, MOFs have the potential to be used as a synergist for intumescent flame retardants in polymers, which could lead to the development of more effective and efficient flame-retardant materials for a wide range of applications.

Escobar-Hernandez and Quan *et al.* provided valuable insights into the large-scale synthesis of MOFs^[50,51]. They present a promising method for the sustainable and efficient production of MOF-based polymer nanocomposites^[52]. The process utilized for the production of these materials is known as reactive extrusion, which involves blending MOF particles and polymers in an extruder. During this mixing procedure, chemical reactions take place between the MOFs and polymers, leading to the formation of robust chemical bonds between both materials. The sustainability and efficiency of this manufacturing process are emphasized by researchers. Reactive extrusion was utilized to produce MOF-based polymer nanocomposites with reduced energy consumption and waste generation compared to conventional methods for similar materials. Moreover, the incorporation of MOFs in these composites enhances their sustainability as they can be easily recycled and reused.

Despite their unique properties and potential for industrial applications, there are several challenges that must be overcome before MOFs can be widely adopted in the industry. MOFs are often susceptible to degradation or collapse when exposed to environmental factors such as moisture, heat, or mechanical stress. This can limit their long-term stability and durability, which is a crucial consideration for industrial applications. The cost of MOFs can be relatively high compared to traditional materials, which can limit their adoption in certain applications. Additionally, the cost of MOF synthesis and production can vary depending on the specific MOF and the synthesis method used, which can further complicate cost considerations. Addressing these challenges will require continued research and development in the synthesis, characterization, and integration of MOFs into industrial applications.

The industrialization of MOFs may follow a trajectory similar to that of graphene, which has demonstrated unique properties and potential for various industrial applications such as electronics, energy storage, and biomedical devices since its discovery in 2004^[53]. However, the slow pace of industrialization can be attributed to challenges in achieving mass production and cost-effective synthesis. Nevertheless, recent advancements in graphene research have resulted in the development of various scalable production methods, including chemical vapor deposition^[54], liquid-phase exfoliation^[55], and reduction of graphene oxide (GO)^[56]. These methods have enabled the production of high-quality graphene in large quantities at a

relatively low cost, making it possible for industries to incorporate graphene into their products. Furthermore, collaborations between academia and industry have facilitated the transfer of graphene research from the lab to the factory floor. Companies, including Samsung, Nokia, and IBM, have invested in graphene research and development, leading to the creation of new graphene-based products such as flexible displays, sensors, and batteries^[57]. In addition, the EU-funded Graphene Flagship project has played a crucial role in the industrialization of graphene^[58]. The project, launched in 2013, aims to accelerate the commercialization of graphene by bringing together over 150 academic and industrial partners from across Europe to develop new graphene-based technologies. Overall, the combination of advancements in research, scalable production methods, industry-academia collaborations, and funding initiatives has paved the way for the industrialization of graphene. Consequently, MOF-based products are increasingly prevalent across various industries, with expectations that MOFs will continue to play a significant role in future technology development.

MULTIFUNCTION OF MOF-BASED FLAME RETARDANTS

Due to the exorbitant cost of MOF-based flame retardants, their industrialization is still in its infancy. However, as a versatile material, it can also serve other purposes, such as wastewater adsorption, while retaining its flame-retardant properties [Figure 3]. This design has become a focal point of scholarly attention. Zhou *et al.* utilized MOF-derived layered double hydroxide (LDH) and 3-amino-propyl triethoxy-silane to modify hydroxylated boron nitride, resulting in polyurethane foam (PUF) composites with exceptional thermal stability, fire safety, and high absorption capacity. The incorporation of flame retardants significantly decreased the amount of combustible gas and toxic CO gas generated during PUF pyrolysis. The inhibition of smoke release was evidenced by a significant decrease in the emission of aromatic compounds. Moreover, the incorporation of 1 wt.% additive resulted in PUF composites with excellent pump oil adsorption capacity, achieving a removal rate of as high as 95%, which outperformed other PUF-based materials for oil and water separation^[59]. Piao *et al.* provided a growth site for ZIF-67 by *in-situ* polymerization of a polydopamine film on the surface of a polyurethane sponge. Then, ZIF-67 was etched with copper nitrate to form CuCo-LDH, and a high-performance oil-water separation flame retardant polyurethane sponge was obtained. The polyurethane composites demonstrate exceptional superhydrophobicity and superlipophilicity while also enhancing thermal stability, exhibiting excellent flame retardancy, and inhibiting the generation of toxic smoke. As such, they represent a highly efficient, sustainable, and safe material for emergency treatment of oil/organic solvent spills^[60].

Under the influence of this trend, we believe MOFs can be designed as a “one-pack” material with specific functionalities that allow them to serve multiple roles simultaneously. In the latest reports, MOFs can be functionalized with antimicrobial agents, ultraviolet (UV) stabilizers, or other additives to provide additional properties to the material. This can be particularly useful in applications where multiple properties are required, such as in the construction of buildings or in the aerospace industry. MOFs can exhibit antimicrobial activity through the release of metal ions. Besides, their high surface area and porous nature can facilitate contact between the MOFs and microorganisms, allowing for efficient antimicrobial action.

One example is the report by Zhao *et al.* on the synthesis of a novel antibacterial material based on silver nanoparticle-modified 2D MOF nanosheets. The authors first synthesized the MOF nanosheets using a solvothermal method and then modified them with silver nanoparticles using a simple deposition-reduction process. The resulting hybrid nanosheets exhibited excellent stability and could be easily dispersed in water. Then, they investigated the antibacterial properties of the hybrid nanosheets against *Escherichia coli* and *Staphylococcus aureus* and found that the nanosheets exhibited excellent antibacterial activity, which was

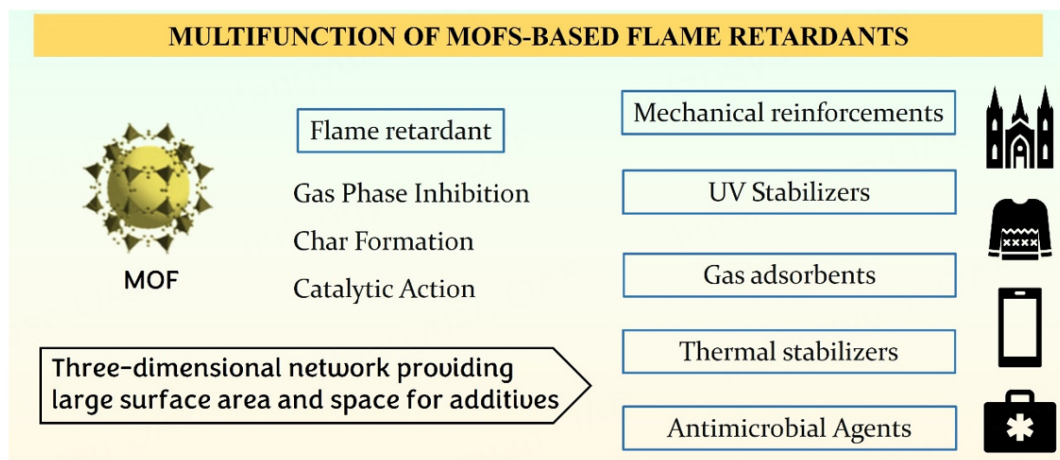


Figure 3. Multifunction of MOF-based flame retardants.

significantly enhanced under near-infrared light irradiation due to the photothermal effect of the silver nanoparticles. The authors also demonstrated that the antibacterial activity of the nanosheets could be further improved by increasing the silver content^[61]. This study provides a new strategy for the design and development of antibacterial materials based on 2D MOF nanosheets modified with silver nanoparticles. The use of near-infrared light to enhance the antibacterial activity of the material could have important implications for the development of new antibacterial therapies.

Another potential application of MOFs is as UV stabilizers. UV stabilizers are compounds that are added to polymers and plastics to protect them from the damaging effects of UV light, which can cause discoloration, degradation, and ultimately failure of the material. MOFs can be functionalized with UV stabilizers to improve their efficacy. Majidi *et al.* dispersed the GO nanoflakes in ethanol solvent and added the precursor solution of ZIF-7. The mixture was then stirred and sonicated to ensure that the ZIF-7 coated the surface of the GO nanoflakes. The resulting modified GO nanoflakes (GO-ZIF-7) were then incorporated into a polyurethane clear-coating^[62]. The researchers tested the weathering resistance and UV-shielding properties of the GO-ZIF-7-modified clear-coating and compared it to unmodified clear-coatings and coatings containing unmodified GO nanoflakes. The results showed that the GO-ZIF-7 modified clear-coating had significantly improved weathering resistance and UV-shielding properties compared to the other coatings. The MOF coating on the GO nanoflakes helped to absorb UV radiation, preventing it from penetrating the clear-coating and causing damage. Additionally, the MOF coating provided a barrier against other environmental factors, further improving the longevity of the clear coating. Therefore, the functional MOFs will continue to be developed in the future. In addition to their flame-retardant properties, MOF-based flame retardants can also influence specific functionalities to everyday applications.

MOF-derived carbon materials are synthesized by heating MOFs under controlled conditions in the absence of oxygen, resulting in the removal of the organic ligands and the formation of carbon structures^[63-66]. The resulting carbon materials inherit the unique properties of the original MOFs, such as high surface area, tunable pore size, and surface functionality. The prospect of MOF-derived carbon materials is significant due to their unique properties and potential applications. Some of the advantages of these materials include: (1) High surface area: MOF-derived carbon materials have a high surface area due to their porous nature, which makes them ideal for applications such as gas storage, catalysis, and energy storage; (2) Tunable properties: By controlling the composition and pyrolysis conditions, the properties of

the MOF-derived carbon materials can be tuned to meet specific application requirements; (3) Low cost: MOF-derived carbon materials can be synthesized from abundant and inexpensive precursors, making them cost-effective alternatives to other carbon materials and (4) Versatility: MOF-derived carbon materials can be synthesized in various forms, including powders, fibers, films, and monoliths, which makes them suitable for a wide range of applications.

In summary, the prospects for the multifunctionality of MOFs are very promising. Their unique properties make them highly versatile materials that can be tailored for a wide range of applications. We expect that future MOF-based flame retardants can show their functions in more aspects while ensuring fire safety. As research in this field continues, we can expect to see even more exciting applications of MOFs in the years to come.

LIGAND DESIGN OF MOF-BASED FLAME RETARDANTS

Traditional MOFs typically lack flame retardant properties due to the flammability of their organic components and the absence of other inherent flame-retardant elements, except for transition metals in metal frameworks. However, researchers have started to try to improve the flame-retardant properties of MOFs by different methods [Figure 4]. A commonly employed strategy involves the functionalization of ligand precursors with flame retardant moieties, such as phosphorus or nitrogen-containing groups, prior to their utilization in MOF synthesis^[67,68]. Phosphorus is an effective flame retardant because it can capture reactive radicals upon heating, which can dilute and quench the flame. Phosphorus-containing ligands, such as phosphonic acid and phosphonate derivatives, can act as flame retardant additives by releasing phosphoric acid and other phosphorus-containing species upon thermal decomposition, which promotes the formation of an expanded carbon layer. To achieve this, phosphonate or phosphonate groups can be incorporated into the organic linkers used to construct the MOF. In addition, transition metal ions that can coordinate with phosphorus-containing ligands can be used to enhance the flame-retardant properties of the MOF. Lu *et al.* synthesized an organic ligand containing P/N and combined it with Co to form a novel P-MOF^[69]. The researchers found that adding the P/N-treated cobalt MOFs to the lignin-based epoxy resins (EP) significantly improved their flame retardancy, as demonstrated by reduced peak heat release rates and decreased total heat release.

Bio-functional MOFs (Bio-MOFs) are biocompatible and biodegradable porous materials made from organic and inorganic building blocks with tunable porosity and high surface area. They can be functionalized with biological molecules to enhance selectivity and specificity, making them useful in biotechnology and environmental science^[70]. Nabipour *et al.* used adenine as an efficient adsorbent for *in situ* removal of zinc ions, resulting in the formation of a bio-MOF. The as-prepared bio-MOF was then added to the EP matrix to investigate its impact on the thermal stability, smoke suppression, and flame retardancy of the EP composites. The results showed that the addition of a boom improved the flame retardancy and smoke suppression properties of the EP composites^[71]. Zhou *et al.* present a study on a sustainable approach for simultaneously achieving flame retardancy, UV protection, and reinforcement in polylactic acid (PLA) composites using fully bio-based complexing couples. The authors used two bio-based complexing couples, tannin acid/ferric salt (TAF_e) and chitosan/phytic acid (CTSPA), to fabricate the composites. The thermal and burning properties of the composites were evaluated by various tests, including TGA, limiting oxygen index (LOI), UL-94 test, and cone calorimetry. The results showed that the composites with TAF_e and CTSPA had an earlier mass loss and higher char residue than pristine PLA. CTSPA also enhanced the LOI value of PLA from 19.6% to 30.5%. The study demonstrates a promising approach for developing sustainable composite materials with multiple desirable properties^[72].

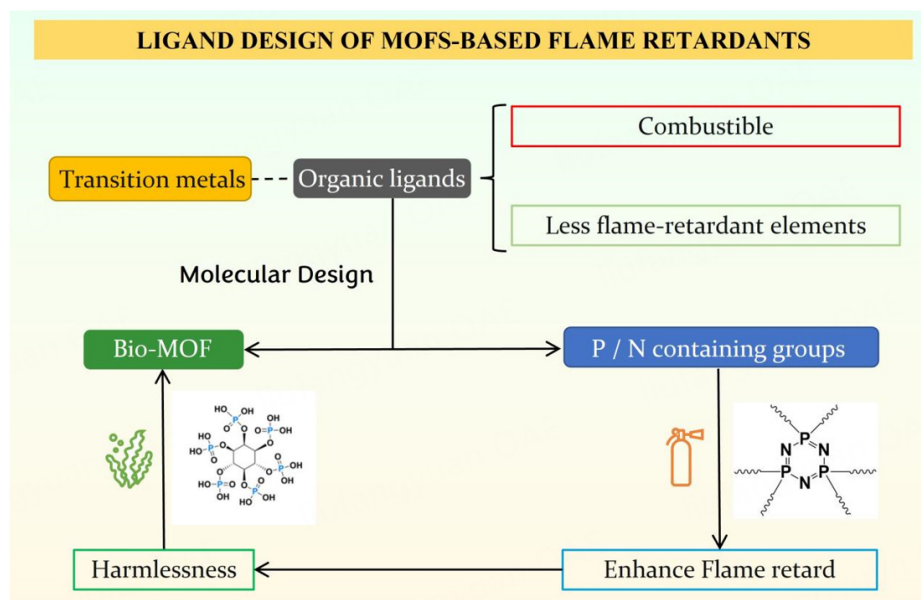


Figure 4. Ligand design of MOF-based flame retardants.

Harmlessness to the human body and environment-friendly recycling have become the prerequisites for the future development of flame retardants. Traditional flame retardants, such as halogenated compounds, have been found to be detrimental to both human health and the environment. Phosphorous flame retardants are commonly utilized in a diverse range of consumer goods, such as electronics, furniture, and construction materials, to mitigate the risk of fire. Nevertheless, these compounds have been associated with various potential hazards: (1) Phosphorus-based flame retardants have been found to accumulate in the environment, including soil, water, and air samples. They can also bioaccumulate in aquatic organisms and pose a toxic threat to fish and other wildlife; (2) Evidence suggests that exposure to certain phosphorus-based flame retardants may negatively impact human health. Therefore, developing effective ligands without the use of phosphorus or halogen presents a significant challenge. Overall, the utilization of biofunctional MOFs as flame retardants presents a promising avenue for research that could result in the development of safer and more environmentally sustainable materials. However, further investigation is necessary to comprehensively comprehend the properties and potential applications of these materials.

MOF DERIVATIVES TREATMENT AS FLAME RETARDANTS

As previously mentioned, the flammability of MOF ligands is a limiting factor in their inherent flame-retardant properties. Therefore, post-treatment techniques are often required to enhance their fire-resistant capabilities [Figure 5].

One common post-processing technique for MOFs involves the modification or removal of organic ligands. In MOFs, ligand removal can be achieved through an acid-base reaction between the MOF and solvent, which entails protonation of the organic ligand by a strong acid followed by detachment from the metal center. Generally, metal ions or clusters are linked by organic ligands in MOFs. These ligands usually contain carboxylic or amino functional groups that can serve as proton acceptors or donors, respectively. When a MOF is exposed to an acidic solution, the protons in the acid can interact with the functional groups on the ligands, resulting in protonation of the ligand. Subsequently, weakened affinity for metal centers allows easy detachment from metal ions or clusters. The liberated metal sites are then available for

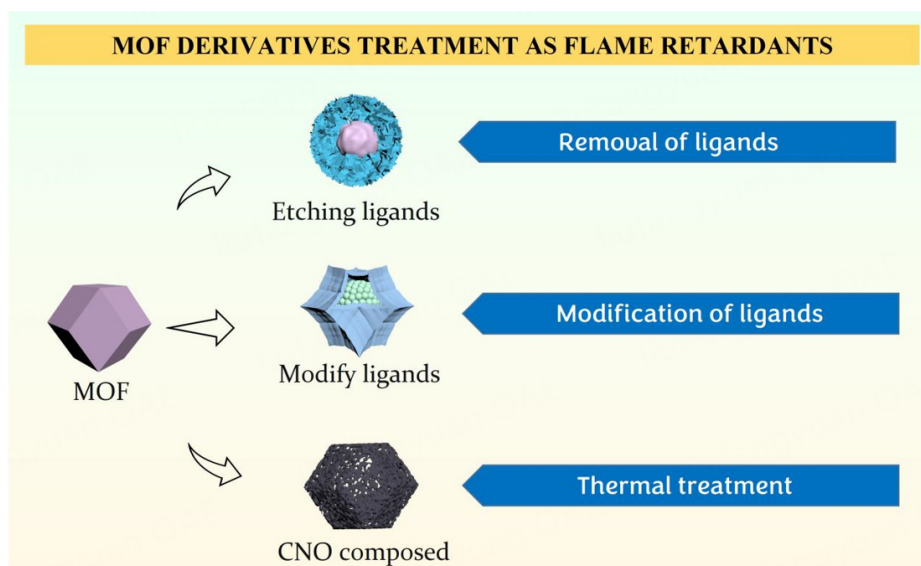


Figure 5. MOF derivatives treatment as flame retardants.

re-coordination with other ligands or functional groups, leading to a new MOF with altered properties^[73]. The acid-base theory of ligand removal in MOFs has found diverse applications, ranging from the synthesis of novel MOFs to the functionalization of existing ones with guest molecules and the recovery of metals from them^[74-76]. The judicious selection of acids and solvents can significantly impact both the extent and selectivity of ligand removal, rendering this approach highly versatile and tunable.

Previously, Pan's group have done a series of work to derive LDH by etching ZIF [Figure 6]^[77-82]. We incorporated mesoporous zinc hydroxystannate (ZHS) nanoparticles into NiCo-LDH nanocages that were derived from ZIF-67. The resulting composite material was then tested for its flame retardancy properties, and it was found that the LOI value of an epoxy composite containing 6 wt.% of these fillers increased to 27.2%. This improvement was significant enough to meet the UL-94 V-0 level, which is a widely recognized standard for flame retardancy. Subsequently, polyphosphazenes (PZS) is often used in modification and compounding of flame retardants because of its rich phosphorus and nitrogen, ZIF@LDH@PZS core-shell structures and LDH@PZS@NH trishell structures were synthesized through surface polycondensation on ZIF-67 using PZS, followed by ligand etching via nickel brine acidification. The interface of LDH was analyzed by adjusting the reaction time to enhance compatibility with the resin matrix. Recently, we have synthesized several hollow LDH nanocages with high thermal stability, featuring single-yolk shell nanostructures (s-CBC@LDH) and multi-yolk shell nanostructures (m-CBC@LDH). By incorporating phosphorus-based flame retardants, we have further enhanced their flame-retardant properties.

In the context of flame retardancy, LDHs are often used as additives to reduce the flammability of polymers. When LDHs are added to a polymer, they act as a physical barrier that prevents the diffusion of oxygen and other flammable gases to the surface of the material, thereby reducing the rate of combustion. One issue with the physical barrier effect of LDHs is that the thickness and width of the barrier layer are limited by the amount of the LDH that can be added to the polymer matrix without affecting its properties. Thicker barriers may be required to achieve adequate flame retardancy in some applications, but a small length-diameter ratio of LDH may not meet the flame-retardant demand. One of the main challenges in using LDHs as pure inorganic flame retardants is achieving proper dispersion in the polymer matrix. Inadequate dispersion can lead to the formation of voids or weak points in the barrier layer, which can compromise its

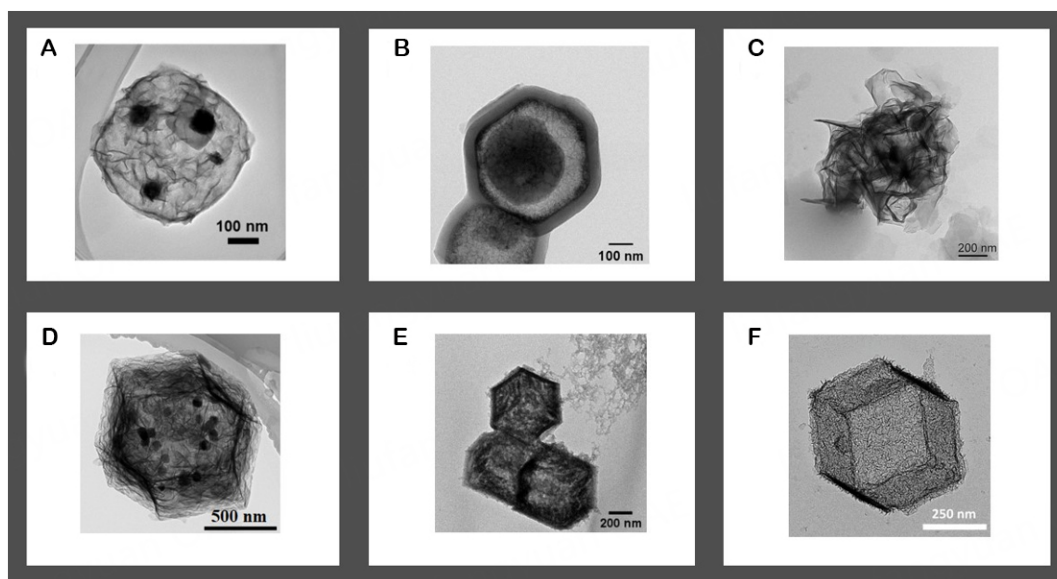


Figure 6. Microstructures of (A) ZHS@NCH (Reproduced with permission^[77]. Copyright 2019, American Chemical Society); (B) ZIF@LDH@PZS (Reproduced with permission^[78]. Copyright 2022, American Chemical Society); (C) m-CBC-P@LDH (Reproduced with permission^[79]. Copyright 2023, Elsevier); (D) m-CBC@LDH (Reproduced with permission^[80]. Copyright 2023, Elsevier); (E) MPOFs (Reproduced with permission^[81]. Copyright 2022, American Chemical Society); (F) ZNs-B/CP (Reproduced with permission^[82]. Copyright 2022, Elsevier).

effectiveness in preventing flame spread. Therefore, to enhance the compatibility of LDH, it is typically necessary to further modify or combine it with other flame retardants. Wang *et al.* modified LDH by toluene diisocyanate, 2-hydroxyethyl acrylate, and vinyl triethoxysilane (LDH-TDI-HEA-VTES) to improve its compatibility with organic matrix, resulting in better dispersion of modified LDH in matrix compared with LDH^[83]. The experimental results showed that with the increase of LDH-TDI-HEA-VTES content, the thermal stability, mechanical properties, flame retardant properties, and shear resistance of LDH-TDI-HEA-VTES-Acrylate composites were improved.

Moreover, acid etching can be employed to generate a novel ligand that substitutes the initial one. Wang *et al.* used a modified version of core-shell ZIF-67@ZIF-8, where phytic acid was added to the structure^[84]. The new phytate-metal ion hybrids are formed to improve the flame retardancy of EP. Our group also utilized carboxyl POSS to modify ZIF-67 and successfully synthesized Metal-POSS Organic Frameworks (MPOFs). Thioglycolic acid was employed to replace the original imidazole ligand and complex with metal ions. Additionally, We have synthesized hollow nanocage structures with a greater number of active sites by utilizing ZIF as a sacrificial template and employing stepwise etching in the sequence of phytic acid and boric acid. Another technique is thermal treatment. This involves exposing the MOF to high temperatures, which can cause structural changes that improve their ability to act as flame retardants. Hou *et al.* developed a method that involves utilizing HKUST-1, a MOF, as a sacrificial template to synthesize Oxygen-Rich Covalent C₂N (CNO) nanosheets through thermal treatment and chemical vapor deposition^[85].

In summary, conventional MOF ligands are often composed of organic compounds that possess flammability. Additionally, the limited presence of flame-retardant elements in MOFs may result in reduced flame-retardant effects and decreased practicality. The method of post-treatment MOFs is simple and controllable and has the following advantages: (1) Endowing MOFs with more flame-retardant elements: by

incorporating additional flame-retardant elements, such as phosphorus or nitrogen, into the MOF structure during post-treatment, their flame retardancy can be enhanced; (2) This method involves breaking the coordination bonds between the metal ions and the ligands in the MOF, which allows for the creation of a hybrid material that inherits some desirable properties of the original MOF, while also introducing new features; (3) Generating expanded pores: post-treatment of MOFs can create larger pores or expand existing ones, which can improve their ability to adsorb volatile organic compounds and harmful gases produced during polymer combustion. The expanded pores can be used as a carrier to load phosphorus-based flame retardants, which can further improve the flame retardancy of MOFs. Zhao *et al.* transformed the microporous structure of MIL-53 into macropores via ammonia water treatment under closed conditions, thereby enhancing its specific surface area and adsorption capacity^[21]. The excellent porous architecture was then utilized for triethyl phosphate (TEP) adsorption as a flame retardant in polystyrene and (4) Controlling morphology: multi-level pore structures can provide more active sites for catalytic reactions. Hollow structures can reduce the weight of flame retardants, which can improve their dispersion and increase the number of active sites available for flame retardancy. As a result, the flame-retardant efficiency has been significantly enhanced while minimizing any adverse effects on the mechanical properties of EP composites.

OUTLOOK

This perspective provides a concise overview of the latest research advances in MOF flame retardants and offers insights into their prospects. Compared to other commonly used fillers, such as platelet-like clay, carbon-based fillers, and silicates, MOFs offer several distinct advantages: In Gas-Phase, Certain MOFs containing nitrogen or phosphorus-containing organic ligands exhibit gas-phase action, effectively trapping active radicals and diluting combustible gases. This gas-phase action contributes to the overall flame retardancy of polymers by interrupting the combustion chain and reducing the availability of flammable gases. In the condensed phase, the metal ions or clusters present in MOFs act as catalytic centers, promoting char formation during combustion. This catalytic activity enhances the formation of a protective char layer, which acts as a barrier against heat and mass transfer, thereby improving the flame retardancy of the polymer. Furthermore, MOFs offer a high degree of tunability, allowing for the customization of their properties to suit specific applications. The pore size, surface area, and composition of MOFs can be tailored to optimize flame retardant performance and address specific requirements of the polymer matrix. These advantages position MOFs as promising alternatives to conventional flame-retardant fillers.

The cost outlook of MOF flame retardants is an important consideration for their widespread adoption in various industries. The cost of MOF flame retardants is influenced by several factors, including the cost of raw materials, the synthesis process, and the scale of production. One approach to reducing their cost is to optimize the synthesis process. The development of more efficient and scalable synthesis methods can reduce the cost of production and increase the yield of MOFs. Additionally, the use of cheaper starting materials and reagents can also lower the cost of MOF flame retardants. Another approach to improving the cost-effectiveness of MOF flame retardants is to increase their functionality and versatility. By designing MOFs with multiple functions, their value proposition can be increased, which can justify the higher cost. In addition to industrialization, researchers are also striving to develop multifunctional MOFs that can perform multiple tasks simultaneously. These types of MOFs can be engineered not only for flame retardants but also for gas absorption, antibacterial activity, or pollutant filtration. Ligand synthesis and derivatives are also important areas of research in the development of MOFs for flame retardant applications. By designing novel ligands and derivatives, researchers can precisely adjust the properties of MOFs to enhance their efficacy in fire suppression. Altering the structure of ligands or introducing new functional groups can elevate the thermal stability or augment the flame-retardant characteristics of MOFs.

The potential of MOFs in the field of flame retardancy is promising, with ongoing research expected to yield more effective and widely applicable flame-retardant materials that can address important safety concerns across a multitude of industries.

DECLARATIONS

Authors' contributions

Conceptual design and project supervision: Pan YT

Manuscript draft and revision: Song P, Hou B

Availability of data and materials

Not applicable.

Financial support and sponsorship

This work was supported by the National Natural Science Foundation of China (No.22005029) and the Australian Research Council (FT190100188; LP220100278).

Ethical approval and consent to participate

Not applicable.

Conflicts of interest

All authors declared that there are no conflicts of interest.

Consent for publication

Not applicable.

Copyright

© The Author(s) 2023.

REFERENCES

1. Li H, Eddaoudi M, O'keeffe M, Yaghi OM. Design and synthesis of an exceptionally stable and highly porous metal-organic framework. *Nature* 1999;402:276-9. [DOI](#)
2. Huo J, Marcello M, Garai A, Bradshaw D. MOF-polymer composite microcapsules derived from Pickering emulsions. *Adv Mater* 2013;25:2717-22. [DOI](#) [PubMed](#)
3. Hou Y, Hu W, Gui Z, Hu Y. Preparation of metal-organic frameworks and their application as flame retardants for polystyrene. *Ind Eng Chem Res* 2017;56:2036-45. [DOI](#)
4. Shi X, Dai X, Cao Y, Li J, Huo C, Wang X. Degradable poly(lactic acid)/metal-organic framework nanocomposites exhibiting good mechanical, flame retardant, and dielectric properties for the fabrication of disposable electronics. *Ind Eng Chem Res* 2017;56:3887-94. [DOI](#)
5. Chen W, Jiang Y, Qiu R, Xu W, Hou Y. Investigation of UiO-66 as flame retardant and its application in improving fire safety of polystyrene. *Macromol Res* 2020;28:42-50. [DOI](#)
6. Zhao S, Yin L, Zhou Q, Liu C, Zhou K. *In situ* self-assembly of zeolitic imidazolate frameworks on the surface of flexible polyurethane foam: towards for highly efficient oil spill cleanup and fire safety. *Appl Surf Sci* 2020;506:144700. [DOI](#)
7. Wang M, Song X, Jiang J, Xia J, Li M. Influence of zeolitic imidazolate framework-8 on the thermal stabilization of poly(vinyl chloride). *Polym Degrad Stab* 2018;149:112-8. [DOI](#)
8. Nabipour H, Nie S, Wang X, Song L, Hu Y. Highly flame retardant zeolitic imidazole framework-8@cellulose composite aerogels as absorption materials for organic pollutants. *Cellulose* 2020;27:2237-51. [DOI](#)
9. Nabipour H, Nie S, Wang X, Song L, Hu Y. Zeolitic imidazolate framework-8/polyvinyl alcohol hybrid aerogels with excellent flame retardancy. *Compos A Appl Sci Manuf* 2020;129:105720. [DOI](#)
10. Seidi F, Jouyandeh M, Taghizadeh M, et al. Metal-organic framework (MOF)/epoxy coatings: a review. *Materials* 2020;13:2881. [DOI](#) [PubMed](#) [PMC](#)
11. Sai T, Ran S, Guo Z, et al. Deposition growth of Zr-based MOFs on cerium phenylphosphonate lamella towards enhanced thermal stability and fire safety of polycarbonate. *Compos B Eng* 2020;197:108064. [DOI](#)

12. Li A, Xu W, Chen R, Liu Y, Li W. Fabrication of zeolitic imidazolate frameworks on layered double hydroxide nanosheets to improve the fire safety of epoxy resin. *Compos A Appl Sci Manuf* 2018;112:558-71. DOI
13. Wang X, Wang S, Wang W, et al. The flammability and mechanical properties of poly (lactic acid) composites containing Ni-MOF nanosheets with polyhydroxy groups. *Compos B Eng* 2020;183:107568. DOI
14. Xie J, Shi X, Zhang M, Dai X, Wang X. Improving the flame retardancy of polypropylene by nano metal-organic frameworks and bioethanol coproduct. *Fire Mater* 2019;43:373-80. DOI
15. Zheng Y, Lu Y, Zhou K. A novel exploration of metal-organic frameworks in flame-retardant epoxy composites. *J Therm Anal Calorim* 2019;138:905-14. DOI
16. Wang H, Qiao H, Guo J, et al. Preparation of cobalt-based metal organic framework and its application as synergistic flame retardant in thermoplastic polyurethane (TPU). *Compos B Eng* 2020;182:107498. DOI
17. Cheng J, Ma D, Li S, Qu W, Wang D. Preparation of zeolitic imidazolate frameworks and their application as flame retardant and smoke suppression agent for rigid polyurethane foams. *Polymers* 2020;12:347. DOI PubMed PMC
18. Wang G, Xu W, Chen R, Li W, Liu Y, Yang K. Synergistic effect between zeolitic imidazolate framework-8 and expandable graphite to improve the flame retardancy and smoke suppression of polyurethane elastomer. *J Appl Polymer Sci* 2020;137:48048. DOI
19. Qian Z, Zou B, Xiao Y, et al. Targeted modification of black phosphorus by MIL-53(Al) inspired by "Cannikin's Law" to achieve high thermal stability of flame retardant polycarbonate at ultra-low additions. *Compos B Eng* 2022;238:109943. DOI
20. Ma T, Wang W, Wang R. Thermal degradation and carbonization mechanism of Fe-based metal-organic frameworks onto flame-retardant polyethylene terephthalate. *Polymers* 2023;15:224. DOI PubMed PMC
21. Zhao H, Yuan B, Zhan Y, et al. Upgrading the pore-size scale of MIL-53 from microporous to macroporous for adsorbing triethyl phosphate and reducing the fire risk of polystyrene. *Compos A Appl Sci Manuf* 2022;159:107003. DOI
22. Xu B, Xu W, Wang G, Liu L, Xu J. Zeolitic imidazolate frameworks-8 modified graphene as a green flame retardant for reducing the fire risk of epoxy resin. *Polym Adv Techs* 2018;29:1733-43. DOI
23. Sai T, Ran S, Guo Z, Fang Z. A Zr-based metal organic frameworks towards improving fire safety and thermal stability of polycarbonate. *Compos B Eng* 2019;176:107198. DOI
24. Salmeia KA, Fage J, Liang S, Gaan S. An overview of mode of action and analytical methods for evaluation of gas phase activities of flame retardants. *Polymers* 2015;7:504-26. DOI
25. Molyneux S, Stec AA, Hull TR. The effect of gas phase flame retardants on fire effluent toxicity. *Polym Degrad Stab* 2014;106:36-46. DOI
26. Schartel B, Perret B, Dittrich B, et al. Flame retardancy of polymers: the role of specific reactions in the condensed phase. *Macromol Mater Eng* 2016;301:9-35. DOI
27. Bao C, Guo Y, Yuan B, Hu Y, Song L. Functionalized graphene oxide for fire safety applications of polymers: a combination of condensed phase flame retardant strategies. *J Mater Chem* 2012;22:23057-63. DOI
28. Xu Z, Xing W, Hou Y, et al. The combustion and pyrolysis process of flame-retardant polystyrene/cobalt-based metal organic frameworks (MOF) nanocomposite. *Combust Flame* 2021;226:108-16. DOI
29. Laoutid F, Bonnaud L, Alexandre M, Lopez-Cuesta JM, Dubois Ph. New prospects in flame retardant polymer materials: from fundamentals to nanocomposites. *Mater Sci Eng R Rep* 2009;63:100-25. DOI
30. Ru J, Wang X, Wang F, Cui X, Du X, Lu X. UiO series of metal-organic frameworks composites as advanced sorbents for the removal of heavy metal ions: synthesis, applications and adsorption mechanism. *Ecotoxicol Environ Saf* 2021;208:111577. DOI
31. Tomar S, Singh V. Review on synthesis and application of MIL-53. *Mater Today Proc* 2021;43:3291-6. DOI
32. Şahin F, Topuz B, Kalıpçılar H. Synthesis of ZIF-7, ZIF-8, ZIF-67 and ZIF-L from recycled mother liquors. *Microporous Mesoporous Mater* 2018;261:259-67. DOI
33. Lee Y, Jang M, Cho H, Kwon H, Kim S, Ahn W. ZIF-8: a comparison of synthesis methods. *Chem Eng J* 2015;271:276-80. DOI
34. Bagi SD, Myerson AS, Román-leshkov Y. Solvothermal crystallization kinetics and control of crystal size distribution of MOF-808 in a continuous flow reactor. *Cryst Growth Des* 2021;21:6529-36. DOI
35. Batten MP, Rubio-martinez M, Hadley T, et al. Continuous flow production of metal-organic frameworks. *Curr Opin Chem Eng* 2015;8:55-9. DOI
36. Dunne PW, Lester E, Walton RI. Towards scalable and controlled synthesis of metal-organic framework materials using continuous flow reactors. *React Chem Eng* 2016;1:352-60. DOI
37. Amery N, Abid H, Al-saadi S, Wang S, Liu S. Facile directions for synthesis, modification and activation of MOFs. *Mater Today Chem* 2020;17:100343. DOI
38. Liu X, Xie L, Wu Y. Recent advances in the shaping of metal-organic frameworks. *Inorg Chem Front* 2020;7:2840-66. DOI
39. Rubio-Martinez M, Aveci-Camur C, Thornton AW, Imaz I, Maspocho D, Hill MR. New synthetic routes towards MOF production at scale. *Chem Soc Rev* 2017;46:3453-80. DOI PubMed
40. Bagi S, Yuan S, Rojas-buzo S, Shao-horn Y, Román-leshkov Y. A continuous flow chemistry approach for the ultrafast and low-cost synthesis of MOF-808. *Green Chem* 2021;23:9982-91. DOI
41. Kochetygov I, Roth J, Espin J, et al. A simple, transition metal catalyst-free method for the design of complex organic building blocks used to construct porous metal-organic frameworks. *Angew Chem Int Ed Eng* 2023;62:e202215595. DOI
42. Shen R, Quan Y, Zhang Z, Ma R, Wang Q. Metal-organic framework as an efficient synergist for intumescent flame retardants against highly flammable polypropylene. *Ind Eng Chem Res* 2022;61:7292-302. DOI

43. Xu Y, Zhou R, Ma G, et al. Preparation of a cobalt metal-organic framework (Co-MOF) and its application as a polypropylene flame retardant by compounding with melamine polyphosphate. *Polym Test* 2022;116:107765. DOI
44. Chen X, Chen X, Li S, Jiao C. Copper metal-organic framework toward flame-retardant enhancement of thermoplastic polyurethane elastomer composites based on ammonium polyphosphate. *Polym Adv Technol* 2021;32:2829-42. DOI
45. Li H, Meng D, Qi P, et al. Fabrication of a hybrid from metal organic framework and sepiolite (ZIF-8@SEP) for reducing the fire hazards in thermoplastic polyurethane. *Appl Clay Sci* 2022;216:106376. DOI
46. Liu Q, Wang H, Li H, Sun J, Gu X, Zhang S. Constructing a novel synergistic flame retardant by hybridization of zeolitic imidazolate framework-67 and graphene oxide for thermoplastic polyurethane. *Poly Adv Technol* 2022;33:2374-85. DOI
47. Yue Z, Lin J, Yang D, et al. *In situ* growth of nano-MOFs on ammonium polyphosphate particles for boosting flame retardancy, smoke suppression and mechanical properties of epoxy. *J Mater Sci* 2022;57:20082-94. DOI
48. Jiang J, Huo S, Zheng Y, et al. A novel synergistic flame retardant of hexaphenoxycyclotriphosphazene for epoxy resin. *Polymers* 2021;13:3648. DOI PubMed PMC
49. Quan Y, Shen R, Schweizer C, et al. Synergistic effects of zeolitic imidazolate frameworks (ZIFs) with different transition metals on intumescent flame-retarded polypropylene composites: a comparative study. *J Mater Sci Technol* 2023;155:102-10. DOI
50. Escobar-hernandez HU, Shen R, Papadaki MI, Powell JA, Zhou H, Wang Q. Hazard evaluation of metal-organic framework synthesis and scale-up: a laboratory safety perspective. *ACS Chem Health Saf* 2021;28:358-68. DOI
51. Quan Y, Parker TF, Hua Y, Jeong H, Wang Q. Process elucidation and hazard analysis of the metal-organic framework scale-up synthesis: a case study of ZIF-8. *Ind Eng Chem Res* 2023;62:5035-41. DOI
52. Quan Y, Shen R, Ma R, Zhang Z, Wang Q. Sustainable and efficient manufacturing of metal-organic framework-based polymer nanocomposites by reactive extrusion. *ACS Sustain Chem Eng* 2022;10:7216-22. DOI
53. Novoselov KS, Geim AK, Morozov SV, et al. Electric field effect in atomically thin carbon films. *Science* 2004;306:666-9. DOI
54. Murdock AT, Koos A, Britton TB, et al. Controlling the orientation, edge geometry, and thickness of chemical vapor deposition graphene. *ACS Nano* 2013;7:1351-9. DOI
55. Hernandez Y, Nicolosi V, Lotya M, et al. High-yield production of graphene by liquid-phase exfoliation of graphite. *Nat Nanotechnol* 2008;3:563-8. DOI
56. Agarwal V, Zetterlund PB. Strategies for reduction of graphene oxide - a comprehensive review. *Chem Eng J* 2021;405:127018. DOI
57. Zurutuza A, Marinelli C. Challenges and opportunities in graphene commercialization. *Nat Nanotechnol* 2014;9:730-4. DOI PubMed
58. Milana S. The lab-to-fab journey of 2D materials. *Nat Nanotechnol* 2019;14:919-21. DOI
59. Zhou Y, Qiu S, Chu F, et al. High-performance flexible polyurethane foam based on hierarchical BN@MOF-LDH@APTES structure: enhanced adsorption, mechanical and fire safety properties. *J Colloid Interface Sci* 2022;609:794-806. DOI
60. Piao J, Lu M, Ren J, et al. MOF-derived LDH modified flame-retardant polyurethane sponge for high-performance oil-water separation: Interface engineering design based on bioinspiration. *J Hazard Mater* 2023;444:130398. DOI
61. Zhao X, Qiu H, Shao Y, et al. Silver nanoparticle-modified 2D MOF nanosheets for photothermally enhanced silver ion release antibacterial treatment. *Acta Physico Chimica Sinica* 2023;39:2211043. DOI
62. Majidi R, Keramatinia M, Ramezanzadeh B, Ramezanzadeh M. Weathering resistance (UV-shielding) improvement of a polyurethane automotive clear-coating applying metal-organic framework (MOF) modified GO nano-flakes (GO-ZIF-7). *Polym Degrad Stab* 2023;207:110211. DOI
63. Wang C, Kim J, Tang J, et al. New strategies for novel MOF-derived carbon materials based on nanoarchitectures. *Chem* 2020;6:19-40. DOI
64. Ren J, Huang Y, Zhu H, et al. Recent progress on MOF-derived carbon materials for energy storage. *Carbon Energy* 2020;2:176-202. DOI
65. Marpaung F, Kim M, Khan JH, et al. Metal-organic framework (MOF)-derived nanoporous carbon materials. *Chem Asian J* 2019;14:1331-43. DOI
66. Chaikittisilp W, Ariga K, Yamauchi Y. A new family of carbon materials: synthesis of MOF-derived nanoporous carbons and their promising applications. *J Mater Chem A* 2013;1:14-9. DOI
67. Hou Y, Xu Z, Chu F, et al. A review on metal-organic hybrids as flame retardants for enhancing fire safety of polymer composites. *Compos B Eng* 2021;221:109014. DOI
68. Sai T, Su Y, Shen H, et al. Fabrication and mechanism study of cerium-based P, N-containing complexes for reducing fire hazards of polycarbonate with superior thermostability and toughness. *ACS Appl Mater Interfaces* 2021;13:30061-75. DOI
69. Lu X, Lee AF, Gu X. Improving the flame retardancy of sustainable lignin-based epoxy resins using phosphorus/nitrogen treated cobalt metal-organic frameworks. *Mater Today Chem* 2022;26:101184. DOI
70. Zulys A, Yulia F, Muhadzib N, Nasruddin. Biological metal-organic frameworks (Bio-MOFs) for CO₂ capture. *Ind Eng Chem Res* 2021;60:37-51. DOI
71. Nabipour H, Qiu S, Wang X, Song L, Hu Y. Adenine as an efficient adsorbent for zinc ions removal from wastewater to *in situ* form bio-based metal-organic frameworks: a novel approach to preparing fire-safe polymers. *Compos A Appl Sci Manuf* 2022;161:107099. DOI
72. Zhou Y, Tawiah B, Noor N, et al. A facile and sustainable approach for simultaneously flame retarded, UV protective and reinforced poly(lactic acid) composites using fully bio-based complexing couples. *Compos B Eng* 2021;215:108833. DOI
73. Hamisu AM, Ariffin A, Wibowo AC. Cation exchange in metal-organic frameworks (MOFs): the hard-soft acid-base (HSAB)

- principle appraisal. *Inorganica Chim Acta* 2020;511:119801. DOI
74. Bao S, Li J, Guan B, Jia M, Terasaki O, Yu J. A green selective water-etching approach to MOF@mesoporous SiO₂ yolk-shell nanoreactors with enhanced catalytic stabilities. *Matter* 2020;3:498-508. DOI
 75. Lee S, Oh S, Oh M. Atypical hybrid metal-organic frameworks (MOFs): a combinative process for MOF-on-MOF growth, etching, and structure transformation. *Angew Chem* 2020;132:1343-9. DOI
 76. Narciso J, Ramos-fernandez EV, Delgado-marín JJ, Affolter CW, Olsbye U, Redekop EA. New route for the synthesis of Co-MOF from metal substrates. *Microporous Mesoporous Mater* 2021;324:111310. DOI
 77. Zhang Z, Li X, Yuan Y, Pan YT, Wang DY, Yang R. Confined dispersion of zinc hydroxystannate nanoparticles into layered bimetallic hydroxide nanocapsules and its application in flame-retardant epoxy nanocomposites. *ACS Appl Mater Interfaces* 2019;11:40951-60. DOI
 78. Hou B, Song K, Ur Rehman Z, et al. Precise control of a yolk-double shell metal-organic framework-based nanostructure provides enhanced fire safety for epoxy nanocomposites. *ACS Appl Mater Interfaces* 2022;14:14805-16. DOI
 79. Song K, Zhang H, Pan YT, et al. Metal-organic framework-derived bird's nest-like capsules for phosphorous small molecules towards flame retardant polyurea composites. *J Colloid Interface Sci* 2023;643:489-501. DOI
 80. Song K, Li X, Pan Y, et al. The influence on flame retardant epoxy composites by a bird's nest-like structure of Co-based isomers evolved from zeolitic imidazolate framework-67. *Polym Degrad Stab* 2023;211:110318. DOI
 81. Hou B, Zhang W, Lu H, et al. Multielement flame-retardant system constructed with metal POSS-organic frameworks for epoxy resin. *ACS Appl Mater Interfaces* 2022;14:49326-37. DOI
 82. Song K, Hou B, Ur Rehman Z, et al. "Sloughing" of metal-organic framework retaining nanodots via step-by-step carving and its flame-retardant effect in epoxy resin. *Chem Eng J* 2022;448:137666. DOI
 83. Wang X, Chen Q, Zheng Y, Hong M, Fu H. Study on novel flame retarded LDH-TDI-HEA-VTES-acrylate composites and their flame retardant mechanism. *React Funct Polym* 2020;147:104371. DOI
 84. Wang H, Li X, Su F, et al. Core-shell ZIF67@ZIF8 modified with phytic acid as an effective flame retardant for improving the fire safety of epoxy resins. *ACS Omega* 2022;7:21664-74. DOI PubMed PMC
 85. Hou Y, Chu F, Ma S, Hu Y, Hu W, Gui Z. Rapid synthesis of oxygen-rich covalent C₂N (CNO) nanosheets by sacrifice of HKUST-1: advanced metal-free nanofillers for polymers. *ACS Appl Mater Interfaces* 2018;10:32688-97. DOI

Perspective

Open Access



Scanning transmission electron microscopy for advanced characterization of ferroic materials

Matthew J. Cabral^{1,3} , Zibin Chen² , Xiaozhou Liao³ 

¹Department of Chemical Engineering, University of Rhode Island, Kingston, RI 02881, USA.

²Department of Industrial and Systems Engineering, Research Institute for Advanced Manufacturing, The Hong Kong Polytechnic University, Hong Kong, China.

³School of Aerospace, Mechanical and Mechatronic Engineering, The University of Sydney, Sydney, NSW 2006, Australia.

Correspondence to: Dr. Matthew J. Cabral, Department of Chemical Engineering, University of Rhode Island, 2 East Alumni Ave Room 084, Kingston, RI 02881, USA. E-mail: matthew.cabral@uri.edu

How to cite this article: Cabral MJ, Chen Z, Liao X. Scanning transmission electron microscopy for advanced characterization of ferroic materials. *Microstructures* 2023;3:2023040. <https://dx.doi.org/10.20517/microstructures.2023.39>

Received: 7 Aug 2023 **First Decision:** 23 Aug 2023 **Revised:** 29 Aug 2023 **Accepted:** 4 Sep 2023 **Published:** 16 Oct 2023

Academic Editor: Lin Gu **Copy Editor:** Fangling Lan **Production Editor:** Fangling Lan

Abstract

Scanning Transmission electron microscopy (STEM) technologies have undergone significant advancements in the last two decades. Advancements in aberration-correction technology, ultra-high energy resolution monochromators, and state-of-the-art detectors/cameras have established STEM as an essential tool for investigating material chemistry and structure from the micro to the atomic scale. This characterization technique has been invaluable for understanding and characterizing the origins of ferroic material properties in next-generation advanced materials. Many unique properties of engineering materials, such as ferroelectricity, piezoelectricity, and ferromagnetism, are intricately linked to their atomic-scale composition and structure. STEM enables direct observation of these structural characteristics, establishing a link with macroscopic properties. In this perspective, we provide an overview of the application of advanced STEM techniques in investigating the origin of ferroic material properties, along with discussions on potential opportunities for further utilization of STEM techniques.

Keywords: Scanning transmission electron microscopy, materials characterization, ferroic materials, aberration-correction, image analysis, atomic resolution imaging



© The Author(s) 2023. **Open Access** This article is licensed under a Creative Commons Attribution 4.0 International License (<https://creativecommons.org/licenses/by/4.0/>), which permits unrestricted use, sharing, adaptation, distribution and reproduction in any medium or format, for any purpose, even commercially, as long as you give appropriate credit to the original author(s) and the source, provide a link to the Creative Commons license, and indicate if changes were made.



INTRODUCTION

Ferroc materials constitute a crucial category of materials that possess a variety of unique properties, including ferroelectricity, ferromagnetism, and ferroelasticity, that are employed in numerous applications. These applications encompass areas such as energy harvesting, sensors, medical imaging, and consumer electronics^[1-5]. The properties and performance of these materials are intricately linked to their atomic-scale structures and chemistries. In certain instances, even a slight modification in composition can profoundly influence material performance. For instance, in both ceramics and single crystals, the piezoelectric coefficient of the relaxor ferroelectric PMN-PT can be nearly doubled by substituting < 1 mol% samarium (Sm) for lead (Pb) as demonstrated by Li *et al.*^[6,7]. Additionally, incorporating elements with varying valence states, ionic radii, electronegativities, and polarizabilities holds great potential in bolstering the piezoelectric and dielectric characteristics of ferroc materials, as demonstrated in the case of high-entropy alloys^[8]. Understanding the correlation between chemical distribution and structure becomes pivotal in comprehending the enhanced piezoelectric properties that arise in these materials. This understanding can be harnessed to design and engineer the next generation of high-performance ferroc materials.

Advanced scanning transmission electron microscopy (STEM) is an exceptionally powerful tool that enables direct visualization of atomic structure and chemistry in numerous materials. While electron microscopes have long provided nanometer-scale resolutions, the introduction of aberration-correction technology at the beginning of the 21st century has pushed the limits of resolution to sub-Angstrom length scales^[9-11]. This significant enhancement in imaging resolution, combined with improved accuracy and precision in STEM imaging, has ushered in a new era of electron microscopy applications. By harnessing the capabilities of an Angstrom-sized probe, it becomes possible to directly visualize atomic-scale chemistry and structure. For instance, annular dark-field (ADF) STEM imaging employs the mass contrast (*Z*) provided by the technique to identify individual dopant atoms within a bulk material^[12,13]. These techniques have further advanced, with electron ptychography achieving reported STEM resolutions as fine as 39 pm and capable of resolving interstitial atoms in a matrix^[14,15]. Moreover, imaging techniques in electron microscopes can readily integrate with spectroscopic methods, such as energy-dispersive X-ray spectroscopy (EDS) and electron energy loss spectroscopy (EELS), facilitating the examination of atomic-scale chemistry, electronic structure, and even vibrational modes^[16,17].

STEM continues to be a vital tool for studies of ferroc and other functional materials. These applications will continue to evolve with developments in electron optics, instrumentation, detectors, and *in-situ* capabilities^[18]. Techniques, such as electron ptychography^[14], 4D-STEM^[19], and ultra-high energy resolution EELS^[17], have allowed for the characterization of parameters, such as polarization, chemical/structural ordering, oxidation states, and electronic structure, at sub-nanometer length scales. Despite the technological advancements, increased accessibility, and user-friendliness of electron microscopes, which are now widely available in both industry and academia, a key challenge remains in bridging the gap between researchers specializing in electron microscopy technique development and materials researchers. Nonetheless, it is crucial for scientists in both domains to recognize the broad applicability of STEM for characterizing multifunctional materials. This perspective aims to provide insights into the latest developments in STEM instrumentation and techniques, emphasizing their broad utilization in ferroc materials research. Additionally, opportunities for in-depth data analysis to address materials-related questions will be discussed.

Basics of S/TEM

Aberration-correction technology has advanced the resolving power of conventional TEM and STEM from the nanometer to sub-Angstrom scales. High-resolution TEM (HRTEM) and STEM differ in electron optics

and image formation. HRTEM [Figure 1A] employs a broad, parallel electron beam that results in a coherent image that is affected by sample thickness and objective lens defocus. Interpreting HRTEM images requires image simulations to understand the impact of thickness and defocus on the resulting image^[20,21]. Conversely, STEM [Figure 1B], including a scanning electron microscope (SEM), uses a finely focused electron probe scanned pixel by pixel with electrons scattering in all directions. STEM imaging can be performed with conventional detectors or by using pixelated detectors for 4D-STEM [Figure 1C], which will be discussed in later sections. With higher voltages and aberration-correction, STEM significantly enhances resolving power. Compared to HRTEM, the incoherent image formation of STEM yields a contrast that is proportional to both atomic number and sample thickness. These directly interpretable images reveal atomic column positions and intensities corresponding to crystallographic locations and atomic numbers.

Atomic resolution imaging

Engineering ferroic materials involves multiple considerations. By manipulating chemistry at the atomic level, mixed phases, defect structures, and interfaces can be formed, significantly impacting material properties. STEM imaging is a valuable technique for directly observing these features and providing essential information. ADF imaging is commonly associated with STEM imaging. As a finely focused probe scans the sample, electrons undergo various forms of scattering during transmission. Rutherford scattering, characterized by elastic scattering due to Coulomb interaction, results in large-angle scattering (> 50 mrad), producing atom column intensities proportional to $\sim Z^{1.7}$ and sample thickness referred to as high-angle ADF (HAADF) imaging^[22,23]. By modifying the inner collection angle of a detector, such as to 25 mrad, the resulting image is low-angle ADF (LAADF) imaging, revealing strain contrast from inelastically scattered electrons^[24]. Figure 2A demonstrates the contrast variations between HAADF [Figure 2A(a)] and LAADF [Figure 2A(b and c)] STEM by modifying the detector inner collection angle for a low-angle twist grain boundary at a SrTiO₃/Nb:SrTiO₃ interface^[25]. Consequently, ADF-STEM allows for precise atomic column localization, contrast reflecting strain effects, and atom column contrast proportional to the chemical composition of the imaged structure based on the inner semi-angle of the detector.

With its sub-Angstrom spatial resolution and strong correlation between atomic number and contrast, HAADF-STEM is highly valuable for examining structures, characterizing interfaces, and studying defect structures in various piezoelectric materials. For instance, it is an effective tool for investigating chemical and structural order in materials, including A- and B-site ordered double perovskites such as NaLaMgWO₆ ceramics. These materials exhibit layered A-site ordering and B-site rock-salt ordering, which is attributed to a large energy barrier that results in non-switchable ferroelectric polarization^[26]. Using HAADF-STEM, this double perovskite structured ordered ceramic can be characterized by its structure and chemical distributions along various zone axes, as shown in Figure 2B. Cation ordering can be observed along the [111], [110], and [100] orientations by experiment [Figure 2B(a-c)] and confirmed by image simulation of the same orientations [Figure 2B(d-f)]. Although the cation ordering can be seen clearly due to the differences in Z-contrast of the constituent elements, the observations can be further confirmed by atomic resolution EDS mapping [Figure 2B(g-i)]^[26]. In addition to providing clear insights into chemical order, HAADF-STEM is also useful for quantifying polarization in ferroic materials. The positions of atomic columns can be utilized to quantify polarization in layered structures [Figure 2C], such as thin films of the multiferroic BiFeO₃ with varying doping profiles^[27]. These displacements can either be plotted directly on the ADF-STEM image [Figure 2C(a)] or averaged and plotted separately on a line-by-line basis [Figure 2C(b)]. These studies are particularly significant due to the emerging nature of these materials and the need to optimize their performance by structural modification for widespread applications.

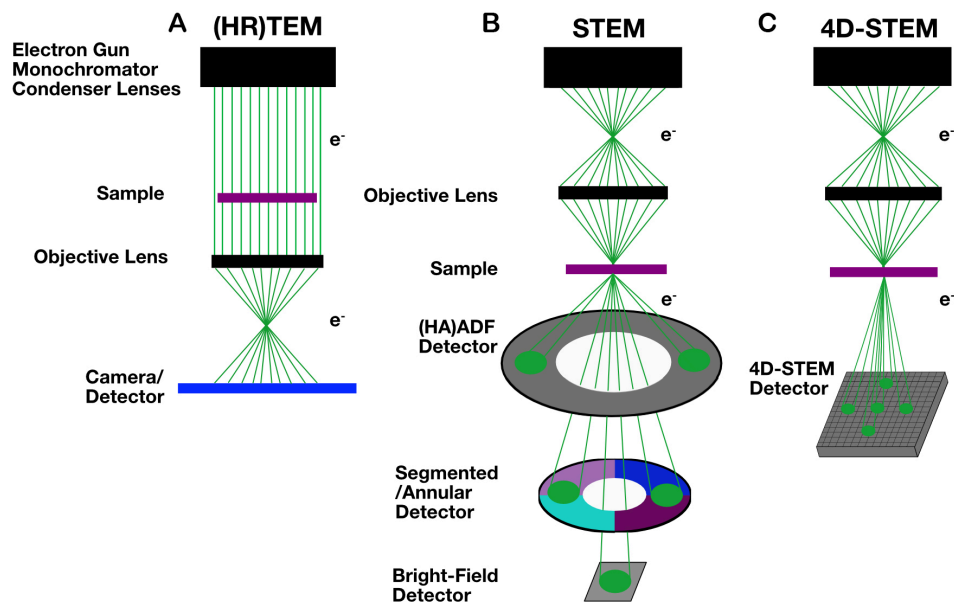


Figure 1. Schematic overview of (A) (HR)TEM, (B) STEM, and (C) 4D-STEM in electron microscopes.

Imaging atomic columns of light elements

Characterizing light elements is crucial in ferroic materials because their properties are often linked to the displacement of cations relative to anions. Elements such as oxygen ($Z = 8$) and lighter are typically described as light elements and generally occupy anion sites in ferroic materials. Moreover, materials may contain cations, anions, or dopants, such as H, O, N, or Li, or have light elements occupying cation sites, as seen in LiNbO_3 , a ferroelectric material widely used in non-linear optics and acoustic devices^[28]. Additional consideration should also be given to the difference between Z of the different elements. For example, in PMN-PT, there is a large difference in atomic numbers between Pb ($Z = 82$) and Mg ($Z = 12$), which can make it difficult to visualize Mg-rich atomic columns. HAADF-STEM, being strongly proportional to atomic number (Z), tends to emphasize heavier elements, making visualization of lighter elements challenging. To enhance the contrast of lighter elements, the collection angle of the annular detector can be reduced, as done in bright-field (BF) and annular BF (ABF) STEM imaging. BF-STEM uses a detector collection angle of approximately 0-20 mrad, while ABF-STEM collects scattered electrons in the range of 10-20 mrad^[29-31]. By narrowing the inner collection angle range in BF-STEM and ABF-STEM, the resulting images rely more on phase contrast rather than mass contrast, making them more sensitive to elements as light as hydrogen^[32]. Modern scanning/transmission electron microscopy (S/TEMs) are equipped with multiple annular detectors, enabling simultaneous collection of signals for BF, ABF, and ADF-STEM imaging. This simultaneous imaging capability has facilitated the observation of light elements, such as the oxygen anion in SrTiO_3 , as shown in [Figure 3A](#)^[33]. However, there are limitations to BF and ABF-STEM, including the requirement for ultrathin samples, a poor signal-to-noise ratio, a strong dependence on defocus, and the need for careful microscope alignment^[20].

An alternative to BF and ABF STEM image modes for imaging light elements is integrated differential phase contrast (iDPC) imaging, which utilizes a segmented ADF detector. This technique is an extension of differential phase contrast (DPC) imaging, initially introduced in the 1970s for imaging ferromagnetic samples by measuring changes in the center of mass (COM) of electron beams caused by the electric potential of samples^[18,36-38]. DPC proves particularly valuable for ferroelectric materials such as $\text{Pb}(\text{Zr}_{0.2}\text{Ti}_{0.8})\text{O}_3$ thin films, where the polar distortion of Ti cations results in visible contrast variations [[Figure 3B](#)]

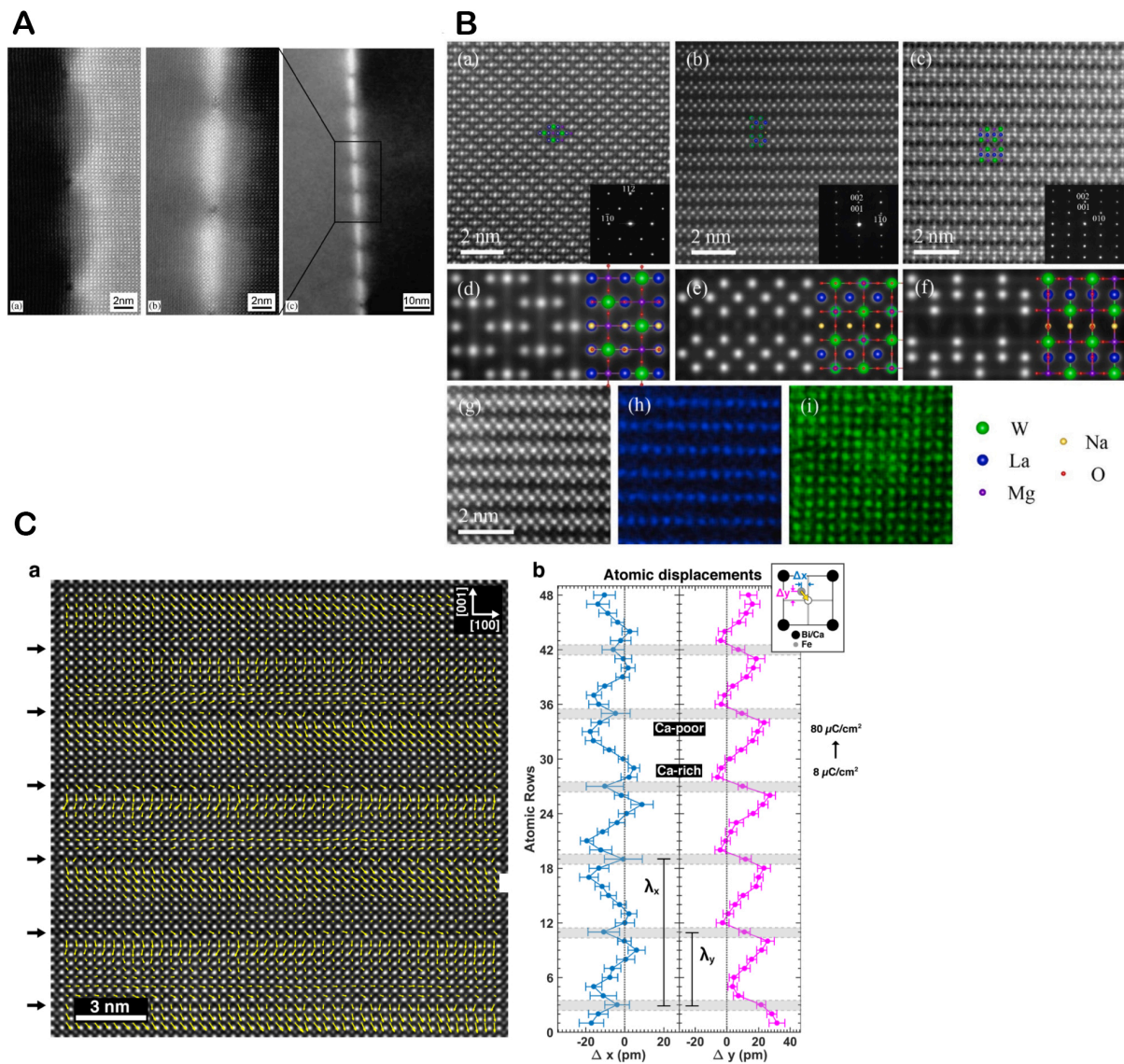


Figure 2. (A) HAADF-STEM (a) and LAADF-STEM (b and c) of a low-angle twist grain boundary between SrTiO₃ and Nb: SrTiO₃, demonstrating the effect of crystal orientation and strain fields for the respective imaging conditions. Reprinted with permission^[25]. Copyright © 2007 Elsevier. (B) HAADF-STEM images of NaLaMgWO₆ ceramics taken along the [111], [110], and [100] zone axes (a-c) confirmed by STEM image simulations for each zone (d-f). Chemical order further confirmed by atomic resolution EDS mapping (g-i). Reprinted with permission^[26]. Copyright © 2022 Elsevier. (C) Polarization map superimposed on HAADF-STEM image of Ca-doped BiFeO₃ thin films. Profiles of in-plane and out-of-plane displacement components are also displayed. Reprinted with permission^[27]. Copyright © 2018 American Chemical Society.

between ferroelectric domains^[34]. More recently, DPC has been implemented for atomic resolution STEM imaging using an ADF detector with between 2-16 segments. A 4-quadrant detector is commonly utilized where an acquired two-component vector image ($DPC_x = a-c$ and $DPC_y = b-d$) is subjected to 2D integration with the segmented detector, resulting in the iDPC image^[35,39]. Figure 3C showcases instances of iDPC imaging in gallium nitride (GaN) oriented along the $[11\bar{2}0]$ and $[10\bar{1}1]$ orientations, illustrating the remarkable resolving power of this technique^[35]. This imaging mode is sensitive to both light and heavy elements, less sensitive to defocus, and exhibits higher signal-to-noise ratios compared to other techniques for imaging light elements. However, iDPC requires extremely thin, flat, and contamination-free samples

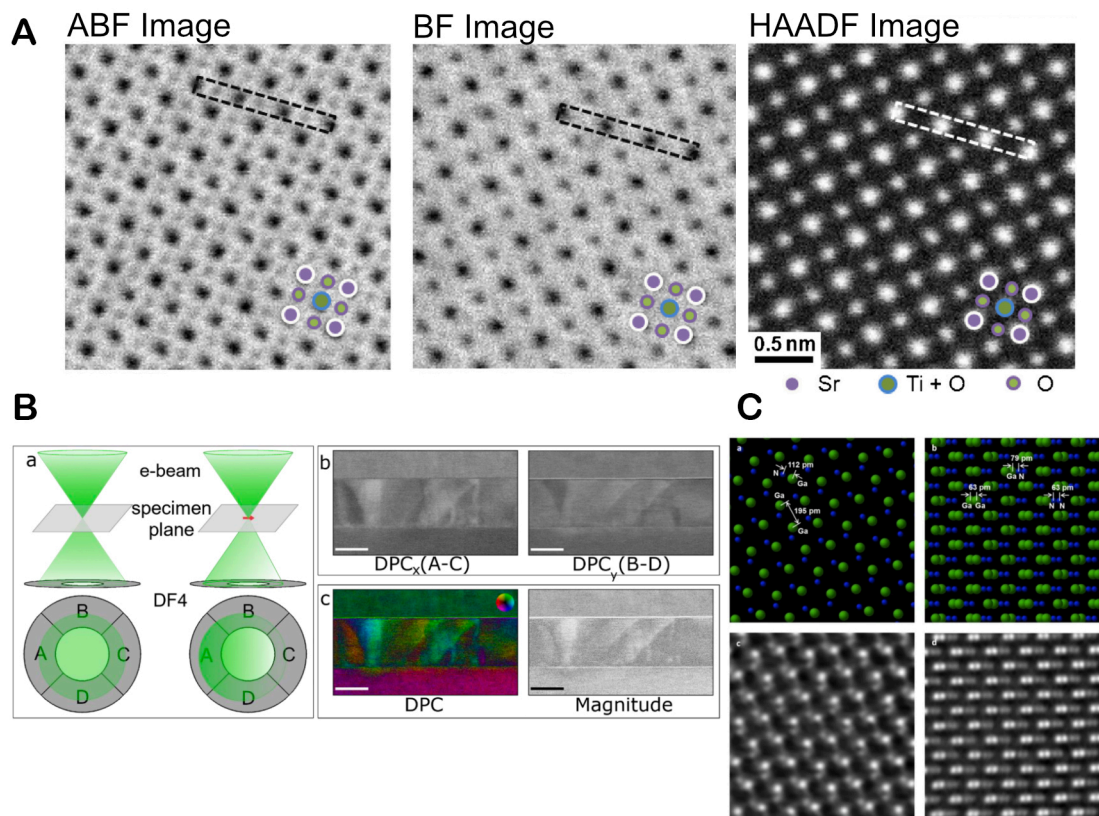


Figure 3. (A) Atomic resolution images of SrTiO₃ viewed along the [001] direction with ABF (11-22 mrad), BF (0-22 mrad), and ADF (90-170 mrad) STEM images. Adapted with permission^[33]. Copyright © 2012 Elsevier. (B) DPC detector configuration with accompanying A-C and B-D STEM images of the ferroelectric Pb(Zr_{0.2}Ti_{0.8})O₃ thin films. Contrast resulting from the ferroelectric domain structures in Pb(Zr_{0.2}Ti_{0.8})O₃ are visible. Reprinted with permission^[34]. Copyright © 2021 MDPI. (C) Atomic resolution iDPC images of gallium nitride (GaN) oriented along the [11̄0] and [101̄] orientations. Reprinted with permission^[35]. Copyright © 2018 Nature Publishing Group.

carefully tilted on a zone axis for optimal imaging^[20]. Despite the challenges involved in imaging light elements, the ability to do so simultaneously with other imaging modes, such as ADF imaging, offers a powerful method for characterizing atomic structures and chemistry at the atomic scale. For instance, simultaneous ADF and iDPC imaging were employed to investigate the atomic structure of the relaxor ferroelectric PMN-PT with varying Ti content. This allowed for a direct correlation of local chemistry with polarization, octahedral distortion, and octahedral tilting^[40]. These observations are crucial for understanding the origin of relaxor ferroelectricity and providing insights into how local structures can be engineered to optimize material properties.

Direct electron detectors and four-dimensional STEM

In the last decade, four-dimensional STEM (4D-STEM) has attracted significant research interest, given its plentiful prospects for material analysis. Conventional STEM detector technology converts the electrons collected at each pixel into a single value representing the contrast. While this number can be expanded upon by using segmented detectors, 4D-STEM refers to the recording of 2D images of the electron probe at each pixel in a 2D image, as illustrated in Figure 1C^[19,41,42]. Although there are numerous detector configurations that can be utilized for the collection of 4D-STEM, one of the most widely available detectors is the electron microscope pixel array detector (EMPAD), which is manufactured by ThermoFisher Scientific. The EMPAD is composed of a collection of photodiodes arranged on an integrated circuit that

collects electrons at each pixel position, converting them to a charge pulse. This charge pulse is integrated over time to produce a signal that is directly proportional to the number of electrons collected. This configuration results in a detection system that is sensitive to a single electron and yields a dynamic range of 1,000,000:1 with fast readout speeds^[19,43,44]. Although the number of pixels (128×128) in the EMPAD is comparatively small, collecting diffraction at each probe position enables extensive opportunities for analysis, including crystallographic orientation measurements, strain mapping, phase mapping, and other diffraction-based analyses. Moreover, the collection of the total electron diffraction pattern allows for the use of “virtual detectors”, which can be used to reconstruct any imaging mode, including HAADF, BF, DPC, *etc.*, through post processing.

Direct electron and pixelated detectors have enabled the development of advanced techniques such as electron ptychography. Although the resolution of conventional STEM imaging is limited by diffraction and the optics of the microscope, electron ptychography presents a way of overcoming these limits. By using a high-speed pixelated detector or direct electron detector that is sensitive to single electrons, the interference patterns of the scattered beams can be resolved and analyzed to determine the phase of the object. These patterns can then be used to reconstruct the image through post processing, thereby overcoming conventional diffraction limitations^[14,45]. Electron ptychography is a rapidly advancing technique that holds great promise due to its numerous applications, including applicability for biological imaging, imaging beam-sensitive materials, characterizing magnetic materials, and measuring strain in materials at sub-Angstrom length scales^[46,47].

Four-dimensional STEM presents numerous opportunities for advanced characterization of ferroic and other functional materials. The combined real space image with a corresponding diffraction pattern opens the opportunity to measure strain at material interfaces at atomic resolution by analyzing the distances between the diffraction disks^[48,49]. Further, diffraction patterns can be analyzed at each pixel in a 4D-STEM dataset to identify order/disorder nanostructures in ferroic materials. Nanobeam diffraction is highly sensitive to subtle changes in microstructure, enabling the identification of rhombohedral nanostructures in the tetragonal and orthorhombic phases of BaTiO_3 ^[50]. This study demonstrates the unique ability for local diffraction observations in an otherwise average technique as for neutron and x-ray diffraction. Four-dimensional STEM continues to see numerous applications, including many in piezoelectric and other functional materials, but data analysis remains a critical step to obtaining useful information.

***In-situ* S/TEM**

The structure, chemical distribution, and properties of ferroic materials, including ferroelectricity and ferromagnetism, are strongly linked to external stimuli such as temperature, electrical biasing, and strain. Understanding how ferroic materials respond to these stimuli is critical for understanding the fundamental mechanisms that result in their properties, including domain switching kinetics, domain growth, and phase transitions^[51]. To this end, the evolution of *in-situ* electron microscopy technology provides an extensive opportunity to study the dynamic processes of ferroic materials. While *in-situ* capabilities have been available in electron microscopes for decades, they have been limited by factors such as sample drift due to environmental changes. The combined improved stability of S/TEMs with innovative *in-situ* holder technology now enables direct observation of materials kinetics at sub-Angstrom resolution^[52].

The opportunities for *in-situ* S/TEMs are extensive and include liquid cell electron microscopy^[53,54], heating^[55,56], cooling^[51,57], biasing^[58,59], and mechanical stressing^[60-62]. While behaviors, such as domain wall motion and domain switching, can be observed using conventional TEM, the emergence of sub-Angstrom resolution, combined ADF/iDPC imaging, and 4D-STEM offer the opportunity for more in-depth

characterization and analysis. Although in-depth details of these techniques are beyond the scope of this perspective, comprehensive reviews are available that outline ongoing and future research directions of *in-situ* S/TEM^[63-65].

Analysis tools for electron microscopy data

With recent advancements in S/TEM instrumentation and technology, ease of use has increased dramatically. Many modern aberration-corrected microscopes are now equipped with software allowing for automatic tuning, greatly speeding up the process and ease of use for users. The coupled with improved microscope stability allows users to align the microscope and tune the corrector within a matter of minutes. Furthermore, many electron microscopes in shared user facilities are housed in carefully designed rooms that mitigate instabilities resulting from noise, temperature variations, mechanical vibrations, acoustical sources, and magnetic sources^[66]. With all these advancements, high-quality data collection can be performed much more efficiently, allowing for more time to perform post processing. In the following sections, we will detail various software tools that allow the correction of distortion in electron microscopy data and simplified post processing.

Correcting drift and distortion in STEM images

Despite significant improvements in the spatial resolution and stability of electron microscopes, sample drift and scanning distortion remain challenges for achieving accuracy and precision in STEM data. These issues arise from both intrinsic scanning distortion caused by the movement of the electron probe across the sample and external sources of drift^[67]. As a result, captured atomic resolution images may exhibit a combination of expansion, compression, and shearing, which hampers the accurate measurement of structural features such as lattice distances, atom column intensities, and polarization. Even the most stable microscopes can experience small quantities of drift over long acquisition times. To address these distortions, various techniques have been developed for correction in electron microscopy and other high spatial resolution techniques, such as scanning probe microscopy (SPM). One approach involves utilizing prior knowledge of the atomic features to correct distortions^[68]. However, this information may not be available when studying novel materials. Another method involves using a known standard sample (e.g., Si or SrTiO₃) to measure drift and distortion, which can then be applied to the samples of interest^[69]. In the case of beam-sensitive samples, a non-rigid image registration method can be employed using a series of images acquired at a low electron dose. This approach is particularly useful for noisy data, as it allows alignment of similar features from multiple images to a single image with a sufficient signal-to-noise ratio^[70-72]. These techniques offer effective ways to address sample drift and scanning distortion, enabling more accurate characterization of materials at the atomic scale.

One of the most frequently used techniques to correct sample drift and distortion is capturing a series of images and recombining them during post-processing. Many electron microscope user interfaces have tools built in for this approach, such as drift-corrected frame integration (DCFI) on Thermo Fisher Scientific instruments^[73], or they can be installed as plugins, such as those available for Digital Micrograph. However, although these tools are easy to use, they may not correct for non-linear drift and scan distortions. In such cases, other post-processing tools, including revolving STEM (RevSTEM), can be employed^[74]. RevSTEM captures a series of images with a short time/pixel dwell time and a 90° scan rotation between subsequent frames. By rotating the scanning system between successive frames, sample drift and distortion can be quantified and corrected through post-processing^[74]. Scanning distortion can also be corrected by quantifying it on a standard sample (such as Si or SrTiO₃) and mathematically applying it to the other images using an affine transformation. Another procedure for correcting non-linear drift distortion involves using orthogonal image pairs (90° rotation between images) to align the images by fitting contrast variations in the slow scan direction on a line-by-line basis^[67]. Although only two images are necessary for this process,

additional orthogonal images can be included in the correction. By applying such programs, STEM images free of artifacts resulting from sample drift or scanning distortions can be obtained for further quantification.

Identifying positions of atomic columns

Material properties often result from complex relationships between chemical distribution and structural distortions that occur at the atomic scale. To gain a better understanding of how these phenomena emerge at the macroscale, it is crucial to comprehend the connection between atomic structure and material properties. STEM imaging offers a valuable means of investigating both structure and chemistry at the atomic scale with accuracy and precision. Thanks to advancements in instrumentation and the elimination of artifacts in atomic resolution images, it is now possible to directly make accurate and reproducible crystallographic measurements in real space^[75]. In the following sections, we will introduce several tools that are available to extract and quantify useful information from atomic resolution images.

Before the widespread availability of aberration-corrected microscopes, advanced image analysis was mainly conducted by specialized electron microscopy research groups. Manual identification of thousands of atomic columns in atomic resolution images was a cumbersome and impractical process. As the technique became more popular, efforts focused on developing tools for rapid analysis of multiple images. Various approaches have been identified, including principal component analysis (PCA)^[76] and template matching^[77]. These techniques are particularly effective for detailed analysis of materials at length scales unattainable with other characterization methods. For example, in the case of a multiferroic BiFeO₃ thin film, initial guesses, followed by COM calculations, can determine the positions of cations and oxygen with PCA, which can then be applied to extract information on atomic column shape^[76]. Combining this data with STEM image simulations^[78-80] reveals octahedral tilting at domain walls, providing parameters applicable to theory. Such analyses are especially valuable for researchers investigating structure-property relationships in material design.

Numerous tools now facilitate rapid quantitative analysis of atomic resolution images. These tools include Atom Column Indexing (ACI)^[81], Atomap^[82], StatSTEM^[83], CalAtom^[84], and Oxygen octahedra picker^[85]. Most of these programs offer freely available source code online and utilize popular engineering software, such as MATLAB or Python. Additionally, software plugins such as DMPFIT can be installed on Digital Micrograph for atom column fitting and analysis^[86]. These programs employ various algorithms to identify and quantify atom column positions with sub-pixel precision. For example, ACI utilizes the image processing toolbox of MATLAB for normalized cross-correlation, Gaussian template matching, and 2D Gaussian fitting to determine column centers of mass, intensities, and shapes^[81]. ACI projects atom column positions onto non-collinear reference vectors, assigning each column an (i, j) matrix index, facilitating lattice analysis and quantitative calculations. In perovskite-structured oxides, matrix indices of atomic columns allow direct comparison of nearest neighbor distances and intensities, providing insights into the relationship between chemical distribution and structural distortion^[87]. Furthermore, direct analysis of atom-atom distances enables strain mapping over large areas, replacing conventional methods such as geometric phase analysis (GPA) or nanobeam electron diffraction^[88-90].

One of the best opportunities arising from recent developments in advanced electron microscope imaging and analysis software is the detailed study of oxygen structure in piezoelectric materials with perovskite or spinel structures. Many outstanding properties, such as antiferroelectricity, relaxor ferroelectricity, and magnetoelectric properties, result from the interplay of polarization and chemical ordering, which are evident in the tilting/distortion of oxygen octahedra^[76,91-94]. While BF and ABF-STEM have been widely

available for decades, the emergence of iDPC imaging provides an alternative means of imaging light elements with high contrast. Although these light element columns may be readily identifiable by visual inspection, difficulties may arise in extracting and segregating more than two atom column types, especially with a large contrast variation. Atomap, which is written in Python, is another freely available software package that facilitates the identification of multiple atom column types. Atomap has numerous advantages, including being programmed in Python, which is a free programming language (in contrast to MATLAB), has graphical user interface (GUI) functionality to assist with analysis, has well-developed documentation with examples, and is being expanded upon by other researchers to increase functionality. In common with many of the introduced programs, Atomap utilizes a model-based approach and 2D Gaussian fitting to first identify and locate the most intense atom column types. These intense columns can then be subtracted from the image, simplifying the process of extracting information from low-contrast sublattice sites^[82]. Since multiple STEM imaging modes can be performed simultaneously, this provides the opportunity to identify cation atom column positions in a HAADF image and subtract them from a BF/ABF/iDPC image to extract oxygen positions. With this approach, multiple atom column sublattice types can be extracted for individual analysis or determining relationships between them.

Quantification of atomic resolution data

Typically, the most challenging aspect of extracting quantitative information from electron microscopy images is locating and identifying all the atomic columns and storing this information in a format that can be easily manipulated. For example, distances between similar columns can be investigated using a projected pair distribution function [Figure 4A], which is analogous to the PDF techniques utilized in diffraction^[87]. In addition to locating atomic columns, Atomap offers numerous built-in functions that allow for a variety of analyses, such as measuring monolayer distances, calculating distances between different atom types [Figure 4B], drawing line profiles, determining polarization, and plotting pair distribution functions^[82].

The advantage of the open-source nature of many of these analysis tools is that it allows subsequent researchers to build upon previous work for their own applications. One such example of this is the open-source Python package TEMUL toolkit, which builds upon the Hyperspy^[96] and Atomap packages for quantification and visualization of STEM data^[97]. Within the TEMUL toolkit, the TopoTEM module can be used to further analyze lattice positions extracted by Atomap. Several additional functionalities are introduced, including the ability to average polarization vectors over several unit cells, varying the vector color with polarization angle, and contour plots, as illustrated in Figure 4C^[95].

With the improved user-friendliness of electron microscopy equipment and the availability of open-source software for image quantification, numerous opportunities arise for novel approaches to image analysis. Many properties of ferroic materials, such as relaxor ferroelectricity, result from short- to medium-range ordering of chemical composition or structural distortion^[40,98]. One innovative approach to analyzing the interplay of local structure and chemistry and its spatial variation in a relaxor ferroelectric is to utilize methods commonly applied to Geographic Information Systems (GIS). In this example, GIS analysis indicates a strong correlation between chemical and oxygen octahedral distortion ordering and a weak correlation between oxygen octahedral and tilt ordering^[99]. Such analyses can provide insights into important correlations between different types of short-range order in piezoelectric materials and in structural materials such as high-entropy alloys.

4D-STEM data analysis

While 4D-STEM presents tremendous opportunities for characterizing piezoelectric materials at the microscale to atomic resolution, the technique also presents unique challenges related to the size and scope

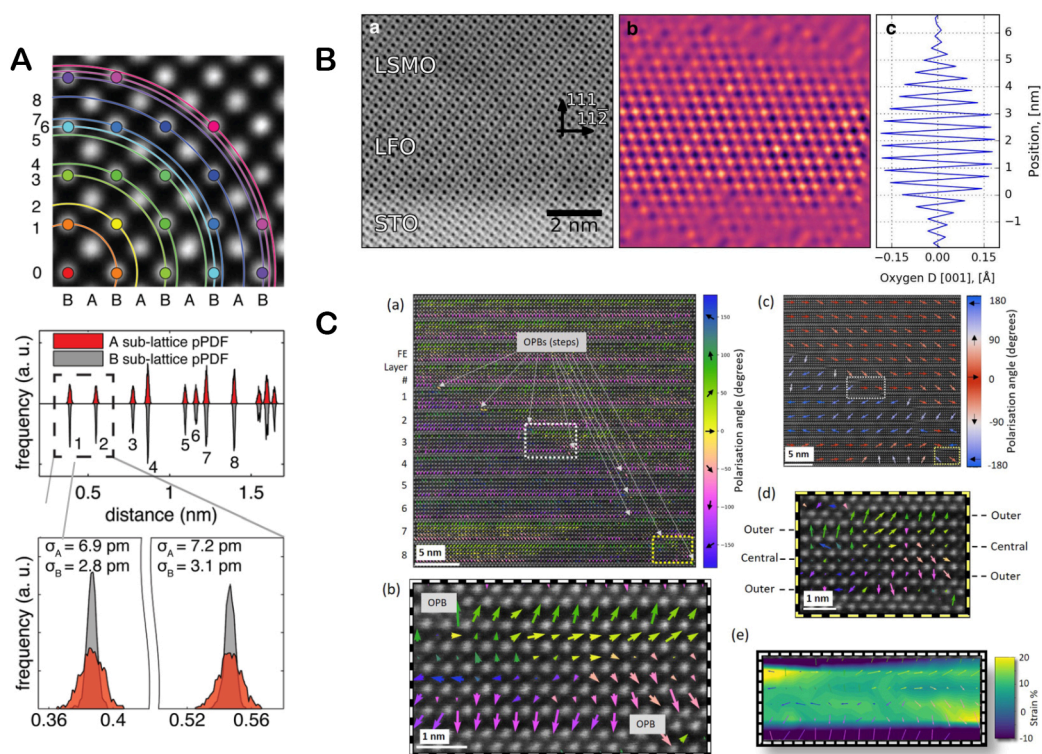


Figure 4. (A) Analyzing atom column positions to find the projected pair distribution functions of the A and B sublattices. Adapted with permission^[87]. Copyright © 2015 AIP Publishing. (B) Utilizing Atomap to find the displacement of oxygen columns in the [001] direction from an ABF-STEM image. Adapted with permission^[82]. Copyright © 2017 Springer. (C) Various polarization plots at domain walls for $\text{Bi}_6\text{Ti}_x\text{Fe}_y\text{Mn}_2\text{O}_{16}$ multiferroic thin films created with TopoTEM. Numerous plotting features, including angle-dependent vector colors, area-averaged polarization, and contour plots, are illustrated to highlight domain walls. Reprinted with permission^[95]. Copyright © 2022 American Chemical Society.

of the datasets. For example, a 128×128 pixel scan, with each position containing a 256×256 pixel diffraction pattern, produces a dataset that is several gigabytes in size. Increasing the number of pixels in either the 2D images or the 2D diffraction patterns can further expand the size of a single data set to hundreds of gigabytes or even several terabytes^[19]. Manually analyzing the vast quantity of data in even a small 4D-STEM data set is infeasible, making computational techniques critical for in-depth materials analysis. To facilitate material analysis with 4D-STEM, high computational power coupled with programmatic tools is essential. In the following section, we will outline some of the software available for analyzing 4D-STEM data.

To maximize the value of obtaining large 4D-STEM datasets, it is crucial to have tools available that enable researchers of various skill levels and backgrounds to extract meaningful data from these experiments. For instance, strain mapping requires measuring the spacing of diffraction disks, which is impractical to perform by manually identifying the disks and measuring their spacing. As discussed in previous sections, open-source software provides the best opportunity for widespread applications of these useful techniques.

One of the most valuable software packages for analyzing 4D-STEM data is py4DSTEM, an open-source Python package that facilitates data visualization and analysis^[100,101]. A good starting point for 4D-STEM data analysis is multimodal imaging, which allows for the observation of various imaging modes (e.g., BF, HAADF, DPC, etc.) from a single dataset. In this context, py4DSTEM employs a graphical user interface that can generate images by selecting the diffraction information included in the image via a “virtual

detector". Conversely, it allows the selection of a region of interest in the image to produce a Bragg Vector Map (BVM), which collapses the diffraction information into a single image^[100,101]. This information can be collected at various points in the image for further analysis, such as orientation mapping and strain mapping. Furthermore, py4DSTEM has built-in functionalities that enable users to locate diffraction disks and make quantitative measurements for parameters such as strain and polarization. This capability ensures that measurements can be standardized and repeated across a variety of datasets, facilitating repeatable analysis.

Although programs, such as py4DSTEM, provide a strong foundation for analyzing 4D-STEM datasets, there are cases where researchers need to develop custom tools for their specific applications. Automated analysis is the most practical approach for such analyses, but often, custom solutions need to be built. For instance, some datasets may contain noisy and complex features that require filtering and fitting algorithms. One recently introduced program is AutoDisk, a Python-based code that performs automated diffraction processing for strain mapping. Variations in diffraction patterns can arise due to various factors, including thickness gradients and low probe currents for beam-sensitive materials, which can complicate automated analysis. AutoDisk addresses these variations by utilizing cross-correlations, blob detection, edge refinements, and lattice fitting to identify diffraction disks^[102]. Once identified, this diffraction information can be used for various analyses, including characterizing phase, symmetry, and orientation. While there are many ways to analyze data, unique solutions may be necessary for analyzing specific datasets. There are numerous code repositories available for 4D-STEM data analysis, including py4DSTEM, HyperSpy, pyXem, LiberTEM, and Pycroscopy, which can serve as a basis for custom analysis^[19].

SUMMARY AND OUTLOOK

In conclusion, electron microscopy is a dynamic and continuously advancing technique with immense potential for the analysis of ferroic and other functional materials. Ferroic materials exhibit a wide range of unique properties that can be utilized in countless applications. These properties stem from chemical and structural inhomogeneities that occur at the atomic scale.

S/TEM offers a distinct advantage in probing these features in both real space and reciprocal space through electron diffraction measurements. Recent advancements in electron microscopy technology have improved the usability and enabled unprecedented resolution of these instruments. To fully harness the potential of S/TEM in the development of advanced materials, it is crucial to make data collection and analysis widely accessible to researchers. This accessibility will foster further exploration and utilization of S/TEM in material characterization. The field holds incredible potential, which can be further realized through ongoing advancements and the collaboration of researchers from various disciplines.

(1) Instrumentation availability and data analysis tools: STEM and TEM play a crucial role in the study of piezoelectric and other functional materials. While state-of-the-art instruments are not immediately available to all researchers, instruments are often accessible to external researchers at universities, national laboratories, and in industry. There are two aspects to make TEM and STEM available to more researchers:

a. Data collection: Modern S/TEM user interfaces are equipped with programmatic capabilities, enabling users to develop workflows to streamline data collection. S/TEMs can readily interface with Python code or support the user of custom scripts such as Gatan's Digital Micrograph. It is essential to promote the open-source nature of these programs so they can be utilized by researchers from various backgrounds. Simplifying data collection will allow researchers to allocate more time for analysis and characterization.

b. Data analysis: With the advancement in S/TEM instrumentation, the alignment and probe-correction processes have become more streamlined, allowing researchers to dedicate more time to data processing. Whether it involves HAADF or 4D-STEM imaging, data analysis remains a critical step in extracting meaningful information from images. To promote the widespread accessibility of advanced electron microscopy and analysis, it is crucial to make these tools readily available to all researchers. When publishing data, it is important to provide the associated analysis tools to ensure the repeatability of measurements and enable further development. By making analysis tools readily available, researchers can reproduce and validate the results obtained by their peers. Moreover, it allows for the exploration of alternative analysis techniques and the advancement of the field. This open sharing of analysis tools fosters collaboration, facilitates scientific progress, and maximizes the value of the obtained data.

(2) Development of 4D-STEM: Direct electron and pixelated detectors have opened new possibilities for advanced electron microscopy. Despite significant advancements in the last decade, there are many opportunities for additional applications. This includes the use of 4D-STEM with *in-situ* microscopy to characterize dynamic processes in materials. Although the data collection process for 4D-STEM is typically slower than with conventional detectors, the technique allows in-depth characterization of features such as domains and strain fields. The stability of modern *in-situ* systems makes this a promising direction for functional materials research.

Overall, electron microscopy holds tremendous potential for advanced characterization in the study of ferroic and the broader category of functional materials. The continuous development of instrumentation and data processing methods has allowed for deep insights into the characterization of advanced materials, which are crucial for understanding the intricate relationships between structure and properties. While there have been significant advancements in the field, it is important to recognize that there is still work to be done. Further efforts are needed to expand the scope of characterization techniques and enhance the accessibility of electron microscopy to researchers from diverse backgrounds. This includes developing new imaging modalities, improving data analysis tools, and making these resources widely available. By pushing the boundaries of electron microscopy, we can unlock discoveries and gain a deeper understanding of piezoelectric materials. Continuous advancements and the collaborative efforts of scientists across disciplines will play a crucial role in expanding the capabilities and accessibility of electron microscopy for the benefit of scientific research and technological advancements.

DECLARATIONS

Authors' contributions

Conceptual design and manuscript draft: Cabral MJ

Manuscript revision and project supervision: Chen Z, Liao X

Availability of data and materials

Not applicable.

Financial support and sponsorship

This research was partially financially supported by the Australian Research Council (ARC) through project DP190101155, the National Natural Science Youth Foundation of China (Grant No. 12204393), the Research Grant Council of Hong Kong SAR, China (Project No. PolyU25300022), and the Research Office of The Hong Kong Polytechnic University (Project Code: P0042733).

Conflicts of interest

All authors declared that there are no conflicts of interest.

Ethical approval and consent to participate

Not applicable.

Consent for publication

Not applicable.

Copyright

© The Author(s) 2023.

REFERENCES

1. Covaci C, Gontean A. Piezoelectric energy harvesting solutions: a review. *Sensors* 2020;20:3512. [DOI](#) [PubMed](#) [PMC](#)
2. Sezer N, Koç M. A comprehensive review on the state-of-the-art of piezoelectric energy harvesting. *Nano Energy* 2021;80:105567. [DOI](#)
3. Shung KK, Cannata JM, Zhou QF. Piezoelectric materials for high frequency medical imaging applications: a review. *J Electroceram* 2007;19:141-7. [DOI](#)
4. Sekhar MC, Veena E, Kumar NS, Naidu KCB, Mallikarjuna A, Basha DB. A review on piezoelectric materials and their applications. *Cryst Res Technol* 2023;58:2200130. [DOI](#)
5. Iqbal M, Nauman MM, Khan FU, et al. Vibration-based piezoelectric, electromagnetic, and hybrid energy harvesters for microsystems applications: a contributed review. *Int J Energy Res* 2021;45:65-102. [DOI](#)
6. Li F, Lin D, Chen Z, et al. Ultrahigh piezoelectricity in ferroelectric ceramics by design. *Nat Mater* 2018;17:349-54. [DOI](#)
7. Li F, Cabral MJ, Xu B, et al. Giant piezoelectricity of Sm-doped $\text{Pb}(\text{Mg}_{1/3}\text{Nb}_{2/3})\text{O}_3$ - PbTiO_3 single crystals. *Science* 2019;364:264-8. [DOI](#)
8. Zhang S. High entropy design: a new pathway to promote the piezoelectricity and dielectric energy storage in perovskite oxides. *Microstructures* 2022;3:2023003. [DOI](#)
9. Batson PE, Dellby N, Krivanek OL. Sub-angstrom resolution using aberration corrected electron optics. *Nature* 2002;418:617-20. [DOI](#)
10. Krivanek O, Dellby N, Lupini A. Towards sub-Å electron beams. *Ultramicroscopy* 1999;78:1-11. [DOI](#)
11. Hetherington C. Aberration correction for TEM. *Mater Today* 2004;7:50-5. [DOI](#)
12. Voyles PM, Muller DA, Grazul JL, Citrin PH, Gossmann HJ. Atomic-scale imaging of individual dopant atoms and clusters in highly n-type bulk Si. *Nature* 2002;416:826-9. [DOI](#) [PubMed](#)
13. Voyles PM, Grazul JL, Muller DA. Imaging individual atoms inside crystals with ADF-STEM. *Ultramicroscopy* 2003;96:251-73. [DOI](#) [PubMed](#)
14. Jiang Y, Chen Z, Han Y, et al. Electron ptychography of 2D materials to deep sub-ångström resolution. *Nature* 2018;559:343-9. [DOI](#)
15. Liu C, Cui J, Cheng Z, et al. Direct observation of oxygen atoms taking tetrahedral interstitial sites in medium-entropy body-centered-cubic solutions. *Adv Mater* 2023;35:e2209941. [DOI](#)
16. Close R, Chen Z, Shibata N, Findlay SD. Towards quantitative, atomic-resolution reconstruction of the electrostatic potential via differential phase contrast using electrons. *Ultramicroscopy* 2015;159 Pt 1:124-37. [DOI](#) [PubMed](#)
17. Krivanek OL, Lovejoy TC, Dellby N, et al. Vibrational spectroscopy in the electron microscope. *Nature* 2014;514:209-12. [DOI](#)
18. de la Mata M, Molina SI. STEM tools for semiconductor characterization: beyond high-resolution imaging. *Nanomaterials* 2022;12:337. [DOI](#) [PubMed](#) [PMC](#)
19. Ophus C. Four-dimensional scanning transmission electron microscopy (4D-STEM): from scanning nanodiffraction to ptychography and beyond. *Microsc Microanal* 2019;25:563-82. [DOI](#) [PubMed](#)
20. Lin Y, Zhou M, Tai X, Li H, Han X, Yu J. Analytical transmission electron microscopy for emerging advanced materials. *Matter* 2021;4:2309-39. [DOI](#)
21. Williams DB, Carter CB. Transmission electron microscopy. New York: Springer; 1996. [DOI](#)
22. Lebeau JM, Stemmer S. Experimental quantification of annular dark-field images in scanning transmission electron microscopy. *Ultramicroscopy* 2008;108:1653-8. [DOI](#) [PubMed](#)
23. LeBeau JM, Findlay SD, Allen LJ, Stemmer S. Quantitative atomic resolution scanning transmission electron microscopy. *Phys Rev Lett* 2008;100:206101. [DOI](#) [PubMed](#)
24. Muller DA, Nakagawa N, Ohtomo A, Grazul JL, Hwang HY. Atomic-scale imaging of nanoengineered oxygen vacancy profiles in SrTiO_3 . *Nature* 2004;430:657-61. [DOI](#) [PubMed](#)
25. Fitting L, Thiel S, Schmehl A, Mannhart J, Muller DA. Subtleties in ADF imaging and spatially resolved EELS: a case study of low-angle twist boundaries in SrTiO_3 . *Ultramicroscopy* 2006;106:1053-61. [DOI](#) [PubMed](#)

26. Zhang W, Zhang X, Xu P, et al. Structure domains induced nonswitchable ferroelectric polarization in polar doubly cation-ordered perovskites. *Ceram Int* 2022;48:30853-8. DOI
27. Campanini M, Erni R, Yang CH, Ramesh R, Rossell MD. Periodic giant polarization gradients in doped BiFeO₃ thin films. *Nano Lett* 2018;18:717-24. DOI PubMed
28. Shur VY, Akhmatkhanov AR, Baturin IS. Micro- and nano-domain engineering in lithium niobate. *App Phys Rev* 2015;2:040604. DOI
29. Okunishi E, Ishikawa I, Sawada H, Hosokawa F, Hori M, Kondo Y. Visualization of light elements at ultrahigh resolution by STEM annular bright field microscopy. *Microsc Microanal* 2009;15:164-5. DOI
30. Findlay SD, Shibata N, Sawada H, et al. Robust atomic resolution imaging of light elements using scanning transmission electron microscopy. *Appl Phys Lett* 2009;95:191913. DOI
31. Ge W, Beanland R, Alexe M, Ramasse Q, Sanchez AM. 180° head-to-head flat domain walls in single crystal BiFeO₃. *Microstructures* 2023;3:2023026. DOI
32. Ishikawa R, Okunishi E, Sawada H, Kondo Y, Hosokawa F, Abe E. Direct imaging of hydrogen-atom columns in a crystal by annular bright-field electron microscopy. *Nat Mater* 2011;10:278-81. DOI
33. Okunishi E, Sawada H, Kondo Y. Experimental study of annular bright field (ABF) imaging using aberration-corrected scanning transmission electron microscopy (STEM). *Micron* 2012;43:538-44. DOI
34. Vogel A, Sarott MF, Campanini M, Trassin M, Rossell MD. Monitoring electrical biasing of Pb(Zr_{0.2}Ti_{0.8})O₃ ferroelectric thin films in situ by DPC-stem imaging. *Materials* 2021;14:4749. DOI PubMed PMC
35. Yücelen E, Lazić I, Bosch EGT. Phase contrast scanning transmission electron microscopy imaging of light and heavy atoms at the limit of contrast and resolution. *Sci Rep* 2018;8:2676. DOI PubMed PMC
36. Rose H. Nonstandard imaging methods in electron microscopy. *Ultramicroscopy* 1977;2:251-67. DOI PubMed
37. Chapman JN, Batson PE, Waddell EM, Ferrier RP. The direct determination of magnetic domain wall profiles by differential phase contrast electron microscopy. *Ultramicroscopy* 1978;3:203-13. DOI
38. Shibata N, Findlay SD, Kohno Y, Sawada H, Kondo Y, Ikuhara Y. Differential phase-contrast microscopy at atomic resolution. *Nat Phys* 2012;8:611-5. DOI
39. Lazić I, Bosch EGT, Lazar S. Phase contrast STEM for thin samples: integrated differential phase contrast. *Ultramicroscopy* 2016;160:265-80. DOI PubMed
40. Kumar A, Baker JN, Bowes PC, et al. Atomic-resolution electron microscopy of nanoscale local structure in lead-based relaxor ferroelectrics. *Nat Mater* 2021;20:62-7. DOI
41. Pennycook TJ, Lupini AR, Yang H, Murfitt MF, Jones L, Nellist PD. Efficient phase contrast imaging in STEM using a pixelated detector. Part I: experimental demonstration at atomic resolution. *Ultramicroscopy* 2015;151:160-7. DOI PubMed
42. Yang H, Pennycook TJ, Nellist PD. Efficient phase contrast imaging in STEM using a pixelated detector. Part II: optimisation of imaging conditions. *Ultramicroscopy* 2015;151:232-9. DOI PubMed
43. Maclaren I, Macgregor TA, Allen CS, Kirkland AI. Detectors - the ongoing revolution in scanning transmission electron microscopy and why this important to material characterization. *APL Mater* 2020;8:110901. DOI
44. Tate MW, Purohit P, Chamberlain D, et al. High dynamic range pixel array detector for scanning transmission electron microscopy. *Microsc Microanal* 2016;22:237-49. DOI
45. Chen Z, Jiang Y, Shao YT, et al. Electron ptychography achieves atomic-resolution limits set by lattice vibrations. *Science* 2021;372:826-31. DOI
46. Lozano JG, Martinez GT, Jin L, Nellist PD, Bruce PG. Low-dose aberration-free imaging of Li-rich cathode materials at various states of charge using electron ptychography. *Nano Lett* 2018;18:6850-5. DOI PubMed
47. Chen Z, Odstrcil M, Jiang Y, et al. Mixed-state electron ptychography enables sub-Angstrom resolution imaging with picometer precision at low dose. *Nat Commun* 2020;11:2994. DOI PubMed PMC
48. Zeltmann SE, Müller A, Bustillo KC, et al. Patterned probes for high precision 4D-STEM bragg measurements. *Ultramicroscopy* 2020;209:112890. DOI
49. Mahr C, Müller-Caspary K, Grieb T, Krause FF, Schowalter M, Rosenauer A. Accurate measurement of strain at interfaces in 4D-STEM: a comparison of various methods. *Ultramicroscopy* 2021;221:113196. DOI PubMed
50. Tsuda K, Yasuhara A, Tanaka M. Two-dimensional mapping of polarizations of rhombohedral nanostructures in the tetragonal phase of BaTiO₃ by the combined use of the scanning transmission electron microscopy and convergent-beam electron diffraction methods. *Appl Phys Lett* 2013;103:082908. DOI
51. Mun J, Peng W, Roh CJ, et al. In situ cryogenic HAADF-STEM observation of spontaneous transition of ferroelectric polarization domain structures at low temperatures. *Nano Lett* 2021;21:8679-86. DOI
52. Zheng H, Zhu Y. Perspectives on in situ electron microscopy. *Ultramicroscopy* 2017;180:188-96. DOI
53. Ross FM. Opportunities and challenges in liquid cell electron microscopy. *Science* 2015;350:aaa9886. DOI PubMed
54. Schneider NM, Norton MM, Mendel BJ, Grogan JM, Ross FM, Bau HH. Electron-water interactions and implications for liquid cell electron microscopy. *J Phys Chem C* 2014;118:22373-82. DOI
55. Nukala P, Ahmadi M, Antoja-Ileonart J, et al. In situ heating studies on temperature-induced phase transitions in epitaxial Hf_{0.5}Zr_{0.5}O₂/La_{0.67}Sr_{0.33}MnO₃ heterostructures. *Appl Phys Lett* 2021;118:062901. DOI
56. Xu W, Bowes PC, Grimley ED, Irving DL, Lebeau JM. In-situ real-space imaging of single crystal surface reconstructions via

- electron microscopy. *Appl Phys Lett* 2016;109:201601. DOI
57. Zhu Y, Wang S, Li B, et al. Twist-to-untwist evolution and cation polarization behavior of hybrid halide perovskite nanoplatelets revealed by cryogenic transmission electron microscopy. *J Phys Chem Lett* 2021;12:12187-95. DOI
 58. Chen Z, Wang X, Ringer SP, Liao X. Manipulation of nanoscale domain switching using an electron beam with omnidirectional electric field distribution. *Phys Rev Lett* 2016;117:027601. DOI
 59. Chen Z, Li F, Huang Q, et al. Giant tuning of ferroelectricity in single crystals by thickness engineering. *Sci Adv* 2020;6:eabc7156. DOI PubMed PMC
 60. Chen Z, Huang Q, Wang F, Ringer SP, Luo H, Liao X. Stress-induced reversible and irreversible ferroelectric domain switching. *Appl Phys Lett* 2018;112:152901. DOI
 61. Chen Z, Hong L, Wang F, et al. Facilitation of ferroelectric switching via mechanical manipulation of hierarchical nanoscale domain structures. *Phys Rev Lett* 2017;118:017601. DOI
 62. Huang Q, Yang J, Chen Z, et al. Formation of head/tail-to-body charged domain walls by mechanical stress. *ACS Appl Mater Interfaces* 2023;15:2313-8. DOI
 63. Taheri ML, Stach EA, Arslan I, et al. Current status and future directions for in situ transmission electron microscopy. *Ultramicroscopy* 2016;170:86-95. DOI PubMed PMC
 64. Fan Z, Zhang L, Baumann D, et al. In situ transmission electron microscopy for energy materials and devices. *Adv Mater* 2019;31:e1900608. DOI
 65. Deng Y, Zhang R, Pekin TC, et al. Functional materials under stress: in situ TEM observations of structural evolution. *Adv Mater* 2020;32:e1906105. DOI
 66. Muller DA, Kirkland EJ, Thomas MG, Grazul JL, Fitting L, Weyland M. Room design for high-performance electron microscopy. *Ultramicroscopy* 2006;106:1033-40. DOI PubMed
 67. Ophus C, Ciston J, Nelson CT. Correcting nonlinear drift distortion of scanning probe and scanning transmission electron microscopies from image pairs with orthogonal scan directions. *Ultramicroscopy* 2016;162:1-9. DOI PubMed
 68. Jones L, Nellist PD. Identifying and correcting scan noise and drift in the scanning transmission electron microscope. *Microsc Microanal* 2013;19:1050-60. DOI PubMed
 69. Schnedler M, Weidlich PH, Portz V, Weber D, Dunin-Borkowski RE, Ebert P. Correction of nonlinear lateral distortions of scanning probe microscopy images. *Ultramicroscopy* 2014;136:86-90. DOI PubMed
 70. Berkels B, Binev P, Blom DA, Dahmen W, Sharpley RC, Vogt T. Optimized imaging using non-rigid registration. *Ultramicroscopy* 2014;138:46-56. DOI PubMed
 71. Berkels B, Liebscher CH. Joint non-rigid image registration and reconstruction for quantitative atomic resolution scanning transmission electron microscopy. *Ultramicroscopy* 2019;198:49-57. DOI PubMed
 72. Jones L, Yang H, Pennycook TJ, et al. Smart align - a new tool for robust non-rigid registration of scanning microscope data. *Adv Struct Chem Imaging* 2015;1:8. DOI
 73. Ihara S, Saito H, Yoshinaga M, Avala L, Murayama M. Deep learning-based noise filtering toward millisecond order imaging by using scanning transmission electron microscopy. *Sci Rep* 2022;12:13462. DOI PubMed PMC
 74. Sang X, LeBeau JM. Revolving scanning transmission electron microscopy: correcting sample drift distortion without prior knowledge. *Ultramicroscopy* 2014;138:28-35. DOI PubMed
 75. Dycus JH, Harris JS, Sang X, et al. Accurate nanoscale crystallography in real-space using scanning transmission electron microscopy. *Microsc Microanal* 2015;21:946-52. DOI
 76. Borisevich A, Ovchinnikov OS, Chang HJ, et al. Mapping octahedral tilts and polarization across a domain wall in BiFeO₃ from Z-contrast scanning transmission electron microscopy image atomic column shape analysis. *ACS Nano* 2010;4:6071-9. DOI
 77. Zuo JM, Shah AB, Kim H, Meng Y, Gao W, Rouvière JL. Lattice and strain analysis of atomic resolution Z-contrast images based on template matching. *Ultramicroscopy* 2014;136:50-60. DOI PubMed
 78. Kirkland EJ, Loane RF, Silcox J. Simulation of annular dark field stem images using a modified multislice method. *Ultramicroscopy* 1987;23:77-96. DOI
 79. Barthel J. Dr. Probe: A software for high-resolution STEM image simulation. *Ultramicroscopy* 2018;193:1-11. DOI PubMed
 80. Lazić I, Bosch EGT. Chapter three - analytical review of direct stem imaging techniques for thin samples. *Adv Imaging Electron Phys* 2017;199:75-184. DOI
 81. Sang X, Oni AA, LeBeau JM. Atom column indexing: atomic resolution image analysis through a matrix representation. *Microsc Microanal* 2014;20:1764-71. DOI PubMed
 82. Nord M, Vullum PE, MacLaren I, Tybell T, Holmestad R. Atomap: a new software tool for the automated analysis of atomic resolution images using two-dimensional Gaussian fitting. *Adv Struct Chem Imaging* 2017;3:9. DOI PubMed PMC
 83. Backer A, van den Bos KHW, Van den Broek W, Sijbers J, Van Aert S. StatSTEM: an efficient approach for accurate and precise model-based quantification of atomic resolution electron microscopy images. *Ultramicroscopy* 2016;171:104-16. DOI PubMed
 84. Zhang Q, Zhang LY, Jin CH, Wang YM, Lin F. CalAtom: a software for quantitatively analysing atomic columns in a transmission electron microscope image. *Ultramicroscopy* 2019;202:114-20. DOI
 85. Wang Y, Salzberger U, Sigle W, Eren Suyolcu Y, van Aken PA. Oxygen octahedra picker: a software tool to extract quantitative information from STEM images. *Ultramicroscopy* 2016;168:46-52. DOI
 86. Du H. DMPFIT: a tool for atomic-scale metrology via nonlinear least-squares fitting of peaks in atomic-resolution TEM images.

- Nanomanuf Metrol* 2022;5:101-11. DOI
87. Sang X, Grimley ED, Niu C, Irving DL, Lebeau JM. Direct observation of charge mediated lattice distortions in complex oxide solid solutions. *Appl Phys Lett* 2015;106:061913. DOI
 88. Oni AA, Sang X, Raju SV, et al. Large area strain analysis using scanning transmission electron microscopy across multiple images. *Appl Phys Lett* 2015;106:011601. DOI
 89. Hytch MJH, Snoeck E, Kilaas R. Quantitative measurement of displacement and strain fields from HREM micrographs. *Ultramicroscopy* 1998;74:131-46. DOI
 90. Rouviere J, Béché A, Martin Y, Denneulin T, Cooper D. Improved strain precision with high spatial resolution using nanobeam precession electron diffraction. *Appl Phys Lett* 2013;103:241913. DOI
 91. Zhao L, Liu Q, Gao J, Zhang S, Li JF. Lead-free antiferroelectric silver niobate tantalate with high energy storage performance. *Adv Mater* 2017;29:1701824. DOI
 92. Jeong IK, Darling TW, Lee JK, et al. Direct observation of the formation of polar nanoregions in $\text{Pb}(\text{Mg}_{1/3}\text{Nb}_{2/3})\text{O}_3$ using neutron pair distribution function analysis. *Phys Rev Lett* 2005;94:147602. DOI
 93. Wu H, Zhang Y, Wu J, Wang J, Pennycook SJ. Microstructural origins of high piezoelectric performance: a pathway to practical lead-free materials. *Adv Funct Mater* 2019;29:1902911. DOI
 94. Fiebig M. Revival of the magnetoelectric effect. *J Phys D Appl Phys* 2005;38:R123. DOI
 95. Moore K, O'Connell EN, Griffin SM, et al. Charged domain wall and polar vortex topologies in a room-temperature magnetoelectric multiferroic thin film. *ACS Appl Mater Interfaces* 2022;14:5525-36. DOI PubMed PMC
 96. de la Peña F, Prestat E, Fauske VT, et al. Hyperspy/hyperspy: release v1.7.3. 2022. DOI
 97. O'Connell EN, Moore K, McFall E, et al. TopoTEM: a python package for quantifying and visualizing scanning transmission electron microscopy data of polar topologies. *Microsc Microanal* 2022;28:1444-52. DOI
 98. Cabral MJ, Zhang S, Dickey EC, Lebeau JM. Gradient chemical order in the relaxor $\text{Pb}(\text{Mg}_{1/3}\text{Nb}_{2/3})\text{O}_3$. *Appl Phys Lett* 2018;112:082901. DOI
 99. Xu M, Kumar A, LeBeau JM. Correlating local chemical and structural order using geographic information systems-based spatial statistics. *Ultramicroscopy* 2023;243:113642. DOI PubMed
 100. Savitzky BH, Zeltmann SE, Hughes LA, et al. py4DSTEM: a software package for four-dimensional scanning transmission electron microscopy data analysis. *Microsc Microanal* 2021;27:712-43. DOI
 101. Savitzky BH, Hughes L, Bustillo KC, et al. py4DSTEM: open source software for 4D-STEM data analysis. *Microsc Microanal* 2019;25:124-5. DOI
 102. Wang S, Eldred TB, Smith JG, Gao W. AutoDisk: automated diffraction processing and strain mapping in 4D-STEM. *Ultramicroscopy* 2022;236:113513. DOI PubMed

Research Article

Open Access



What lies beneath? Investigations of atomic force microscopy-based nano-machining to reveal sub-surface ferroelectric domain configurations in ultrathin films

Lynette Keeney , Louise Colfer, Debismita Dutta, Michael Schmidt, Guannan Wei

Tyndall National Institute, University College Cork, Cork T12 R5CP, Ireland.

Correspondence to: Dr. Lynette Keeney, Tyndall National Institute, University College Cork, Lee Maltings Complex, Dyke Parade, Cork T12 R5CP, Ireland. E-mail: lynette.keeney@tyndall.ie

How to cite this article: Keeney L, Colfer L, Dutta D, Schmidt M, Wei G. What lies beneath? Investigations of atomic force microscopy-based nano-machining to reveal sub-surface ferroelectric domain configurations in ultrathin films. *Microstructures* 2023;3:2023041. <https://dx.doi.org/10.20517/microstructures.2023.41>

Received: 13 Aug 2023 **First Decision:** 24 Aug 2023 **Revised:** 31 Aug 2023 **Accepted:** 5 Sep 2023 **Published:** 20 Oct 2023

Academic Editor: Shujun Zhang **Copy Editor:** Fangyuan Liu **Production Editor:** Fangyuan Liu

Abstract

Multiferroic materials, encompassing simultaneous ferroelectric and ferromagnetic polarization states, are enticing multi-state materials for memory scaling beyond existing technologies. Aurivillius phase B6TFMO ($\text{Bi}_6\text{Ti}_x\text{Fe}_y\text{Mn}_z\text{O}_{18}$) is a unique room temperature multiferroic material that could ideally be suited to future production of revolutionary memory devices. As miniaturization of electronic devices continues, it is crucial to characterize ferroelectric domain configurations at very small (sub-10 nm) thickness. Direct liquid injection chemical vapor deposition allows for frontier development of ultrathin films at fundamental (close to unit cell) dimensions. However, layer-by-layer growth of ultrathin complex oxides is subject to the formation of surface contaminants and 2D islands and pits, which can obscure visualization of domain patterns using piezoresponse force microscopy (PFM). Herein, we apply force from a sufficiently stiff diamond cantilever while scanning over ultrathin films to perform atomic force microscopy (AFM)-based nano-machining of the surface layers. Subsequent lateral PFM imaging of sub-surface layers uncovers 45° orientated striped twin domains, entirely distinct from the randomly configured piezoresponse observed for the pristine film surface. Furthermore, our investigations indicate that these sub-surface domain structures persist along the in-plane directions throughout the film depth down to thicknesses of less than half of an Aurivillius phase unit cell (< 2.5 nm). Thus, AFM-based nano-machining in conjunction with PFM allows demonstration of stable in-plane ferroelectric domains at thicknesses lower than previously determined for multiferroic B6TFMO. These findings demonstrate the



© The Author(s) 2023. **Open Access** This article is licensed under a Creative Commons Attribution 4.0 International License (<https://creativecommons.org/licenses/by/4.0/>), which permits unrestricted use, sharing, adaptation, distribution and reproduction in any medium or format, for any purpose, even commercially, as long as you give appropriate credit to the original author(s) and the source, provide a link to the Creative Commons license, and indicate if changes were made.



technological potential of Aurivillius phase B6TFMO for future miniaturized memory storage devices. Next-generation devices based on ultrathin multiferroic tunnel junctions are projected.

Keywords: Scanning probe microscopy, piezoresponse force microscopy, ultrathin films, chemical vapor deposition, ferroelectrics, multiferroics, atomic force microscopy-based nano-machining, domains, domain walls

INTRODUCTION

As miniaturization of electronic devices continues, a key condition for materials in memory storage technologies is the extension of their functional properties to ultrathin (sub-10 nm) thicknesses. This is challenging for multiferroics and ferroelectrics, given that ferroelectricity is a collective effect between competing short-range covalent repulsions and long-range Coulomb interactions. These interactions will alter as the collective distortion of unit cells (u.c.) within the lattice is adjusted on decreased thickness, and the spontaneous ferroelectric polarization is projected only to be supported above a particular critical thickness^[1]. A consequence of fabricating low-dimensional ferroelectric nanostructures is an increase in surface area, which can result in enlarged depolarization field strengths (of magnitude inversely proportional to the thickness of the ferroelectric) if the surface charges are not completely screened. Below the critical thickness, out-of-plane ferroelectricity is destabilized, tending to a decline in performance and a lack of reproducibility. In 1997, this critical thickness was thought to be 20 nm^[2]; however, considerable advancements in thin film synthesis and characterization over the last two decades^[3] have enabled demonstration of stable out-of-plane ferroelectricity in high-quality ultrathin films at dimensions much thinner than this. Exploitation of epitaxial strain and confinement strain, along with effective screening of interface and surface charges, can counteract the opposing effects of thickness reduction and stabilize out-of-plane ferroelectricity at reduced dimensions. Out-of-plane ferroelectricity has been measured at a minimum thickness of 4 nm (10 u.c.) for Pb(Zr_{0.2}Ti_{0.8})O₃^[4], 1.2 nm (3 u.c.) for PbTiO₃^[5], 1 nm for BaTiO₃^[6], and 1 nm (2 u.c.) for Hf_{0.8}Zr_{0.2}O₂^[7].

Moreover, the problems pertaining to depolarization field effects are substantially diminished for in-plane polarization directions. Polarization is lateral to the surface for all in-plane directions and is, therefore, not impeded by contesting depolarization fields upon scaling down to ultrathin thicknesses^[8]. A family of materials possessing large in-plane spontaneous polarizations [P_s ($\approx 0.4 \text{ C m}^{-2}$)] are the Aurivillius phase materials described by the general formula Bi₂O₂(A_mB_mO_{3m+1})^[9-14]. They are a well-established group of ferroelectrics and a technologically important class of material. SrBi₂Ta₂O₉ ($m = 2$) and Bi_{3.25}La_{0.75}Ti₃O₁₂ ($m = 3$) thin films have been exploited for commercial use in ferroelectric random access memory devices^[15-18]. By intermixing differing types of A-site (Bi) and B-site (Ti, Mn, Fe) cations within the Aurivillius phase scaffold, the chemistries required for ferroelectricity and ferromagnetism can be combined in a single-phase to create the $m = 5$ B6TFMO(Bi₆Ti_xFe_yMn_zO₁₈) composition (where $x = 2.80$ to 3.04 ; $y = 1.32$ to 1.52 ; $z = 0.54$ to 0.64). B6TFMO is a valuable example of a single-phase room temperature (RT) multiferroic joining other innovatively designed multiferroics such as the compositionally controlled tilt-engineered perovskites^[19] and the 3D strained vertically aligned nanocomposites of polar and magnetic materials^[20,21]. B6TFMO displays saturation magnetization (M_s) values (215 emu/cm^3) two orders of magnitude larger than widely-studied BiFeO₃^[22] and demonstrates the reversible linear RT magnetoelectric switching necessary for practical applications in future high data-storage, multi-state memory storage devices^[23,24]. Furthermore, B6TFMO thin films are capable of hosting extraordinary polarization profiles, including charged domain walls and non-trivial polar vortex-type topologies. This further opens up technological prospects in nano-electronics, domain wall devices, and ultra-compact data storage^[25]. Aurivillius layer structures [Figure 1A] are innately two-dimensionally nanostructured with large c -axis lattice parameters (e.g., $c = 50.26 \text{ \AA}$ for B6TFMO)^[24]. Thus, they are ideal candidates for probing ferroelectric behavior close to the unit cell level^[26-30].

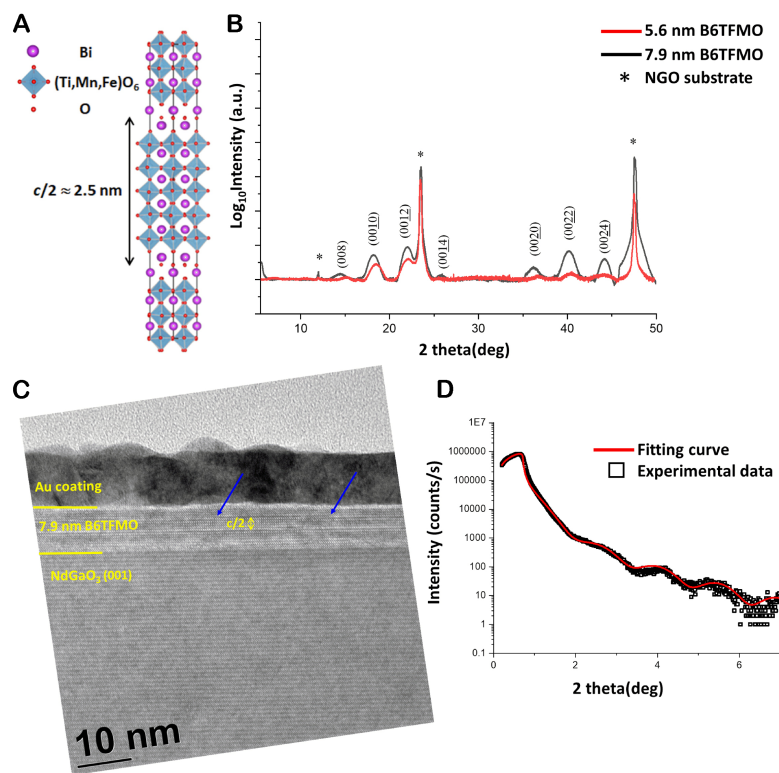


Figure 1. (A) Schematic of an $m = 5$ Aurivillius phase crystal structure (space group $B2eb$) projected down the $\langle 110 \rangle$ orientation^[43,59]. Half a u.c. ($c/2$) consists of five perovskite blocks between fluorite-type bismuth oxide layers. (B) Representative XRD patterns of 7.9 nm and 5.6 nm B6TFMO films on NGO (001). (C) Representative HR-TEM image demonstrating 7.9 nm thick B6TFMO films on NGO (001) substrates. (D) XRR plot used to extract the thickness value of the 5.6 nm B6TFMO film on NGO (001).

It is widely acknowledged^[31,32] that a ferroelectric domain structure is the initial governing factor in polarization switching behavior, influencing domain wall motion, evolution of existing ferroelectric domains, and the nucleation and development of further ferroelectric domains. The equilibrium domain configuration in a ferroelectric thin film arises from the minimization of the elastic and electrostatic energies in the crystal and is influenced by factors such as the film composition, growth mechanism, growth and cooling temperatures, underlying substrate, electrodes, and thin film thickness. Therefore, the characterization, understanding, and tailoring of ferroelectric domain structures in ultrathin films is imperative for controlling electromechanical properties and device applications. Piezoresponse force microscopy (PFM) is a powerful tool for probing ferroelectric phenomena at nanoscale and can reveal fundamental information on domain size, orientation, pattern, anisotropy/isotropy, and the nature of the domain walls that separate the ferroelectric domains. PFM experiments demonstrate that stable and switchable ferroelectricity persists in sub-8 nm Aurivillius B6TFMO films, initiating options for miniaturizing innovative multiferroic-based devices incorporating ultrathin tunnel junctions^[27,28]. However, because B6TFMO thin film synthesis tends to proceed by a 2D nucleation and layer-by-layer growth mechanism^[33], it can be difficult to control the formation of intermediary steps in the layer-by-layer growth mode, particularly at sub-10 nm film thickness. As a result, incomplete growth layers corresponding to heights of half of a unit cell of the Aurivillius phase (~ 2.5 nm thick) are visible on the film surface, complicating the surface PFM images and obscuring the ferroelectric domain configuration of the underlying B6TFMO film^[24,27].

In recent years, AFM tip-based nano-machining has been recognized as an emerging technology for machining nanostructures, nanometer-scale 3D imaging of material properties and photomask repair^[34-39]. In this contribution, we employ a commercially available probe to perform atomic force microscopy (AFM)-based nano-machining to remove surface artifacts and expose the underlying ferroelectric domain configuration of 7.9 nm (1.5 u.c.) and 5.6 nm (1 u.c.) B₆TFMO films. We perform PFM investigations as a function of milled depth (from surface to substrate) to investigate domain structures and persistence of ferroelectricity through the ultrathin B₆TFMO films.

MATERIALS AND METHODS

Ultrathin film synthesis

B₆TFMO thin films were fabricated using a horizontal flow AIXTRON AIX 200/4FE AVD direct liquid injection chemical vapor deposition (DLI-CVD) system using processes similar to those previously described by Keeney *et al.*^[27,28]. Bismuth, iron, and titanium precursor solutions [0.1 mol dm⁻³ solutions of Bi(thd)₃, Fe(thd)₃, and Ti(O-iPr)₂(thd)₂ (where thd = 2,2,6,6-tetramethyl 3,5-heptanedionate; O-iPr = isopropoxide) in toluene] were purchased from Epivalence Ltd. (The Wilton Centre, Redcar, Cleveland, TS10 4RF, United Kingdom) and were maintained under N₂(g) in stainless steel bubbler containers. 0.025 mol dm⁻³ manganese precursor was prepared by dissolving Mn(thd)₃ (99%, STREM chemicals) in anhydrous toluene (99.8%, Sigma-Aldrich) under N₂(g) and transferring to a stainless steel bubbler. The pressure of the growth chamber was 9 mbar, and the temperature of the susceptor [rotated with 60 sccm N₂(g)] heated substrate holder was maintained at 710 °C via an infra-red lamp assembly. The liquid precursors were injected using inert N₂(g) carrier gas into a vaporizer kept at 220 °C, using four individual injectors, one for each precursor source. The micro-liter injected precursor volumes were regulated by tuning the numbers of pulses [between 75 and 100 injections for each precursor, depending on desired film thickness (between 5 nm and 8 nm)] and the opening time of the injectors (between 1.3 and 11.3 ms) during a continuous injection mode (frequency of 1 Hz). The net volumetric precursor ratios were approximately 2.9:1.5:0.6 for Ti(O-iPr)₂(thd)₂, Mn(thd)₃, and Fe(thd)₃, respectively. Between 5 and 8% excess of Bi(thd)₃ was utilized to mitigate bismuth migration during deposition. The total N₂(g)/O₂(g) flow in the growth chamber was 3,000 sccm, of which O₂(g) flow was 1,000 sccm. The substrates used in this study were single-side polished (001)-orientated NdGaO₃ (NGO) with average dimensions 10 mm × 10 mm × 0.5 mm (Crystal GmbH, Ostendstraße 25, D-12459 Berlin, Germany). The substrates were cleaned with isopropyl alcohol followed by distilled water and dried using N₂(g).

Physical characterization

The crystallographic structure of the films was determined using a Panalytical MRD X-Pert Pro X-ray diffraction (XRD) system with a filtered Cu K radiation source ($\lambda = 0.1541876$ nm). The setup included a vertical magnetic strip mount, a 2 mm mask, and a divergence slit of 0.5°. Scans were conducted over a 2 θ (2 theta) range of 5° to 50°, employing a precise step size of 0.006°. Each step was captured within 0.5 s, resulting in a total of 7,500 data points collected across the scan. To ensure accurate intensity comparisons, a uniform baseline correction was applied to both spectra using the second derivative method. Full Width at Half Maximum (FWHM) values for the peaks were established by integrating the peaks using a Gaussian function in the Origin software. The X-ray reflectivity (XRR) method was used to determine the film thickness of the B₆TFMO film deposited using 75 injections. The same XRD system was used to detect the reflectometry on the ultrathin film and substrate. 2Theta-Omega scans were performed over an angular 2 θ range of 0.2° to 7° with an angular $\Delta\theta$ step of 0.005°. A parabolic mirror was used as the incident optics, while a parallel plate collimator with a 0.09° slit was used as the diffracted optics. The XRR data was then analyzed through automatic fitting procedures implemented in the Panalytical XRR software package, where the number of layers, the density of each layer, their thickness, and the interface or surface roughness can be adjusted within a reasonable user-defined range. During the simulation, three layers were assumed:

the NGO substrate, the B₆TFMO sample layer, and an extra oxidation layer on top (which is deemed reasonable, as the sample had been kept in the air after deposition). The initial density value inputted for the NGO substrate was taken from the datasheet provided by the substrate manufacturer (Crystal GmbH, Ostendstraße 25, D-12459 Berlin, Germany), and that for the B₆TFMO sample was taken from that reported by Bartkowska *et al.* on the $m = 5$ Aurivillius phase compositions^[40]. The deviation between the experimental data curve and the fitted curve was calculated to be 2.37%. The thickness values obtained from the XRR measurements were consistent with measurements obtained by transmission electron microscopy (TEM) imaging of previous samples prepared under similar DLI-CVD conditions^[27,28]. Micro-structural analysis was performed by high-resolution TEM (HR-TEM) on a JEOL 2100 TEM, operated at 200 kV. To enable HR-TEM imaging, the samples were coated with gold to counteract charging, followed by coating with platinum to enable focused ion beam (FIB) cross sectioning. Cross-section lamellae were made using a FEI Helios Nanolab 600i DualBeam FIB-scanning electron microscope (FIB-SEM) (final thinning settings: 93 pA current at 30 kV, final polish settings: 47 pA current at 5 kV). Thickness analysis of the B₆TFMO film deposited using 100 injections was performed from 55 measurements across a 7.6 μm wide lamella. The standard deviation (SD) variability of the dataset was ± 0.4 nm. An atomic force microscope (AFM), Bruker Dimension Icon in PeakForce Tapping mode (with Bruker SCANASYST-AIR probes, Al reflex coated, 2 nm tip radius, 70 kHz resonant frequency) was used for topography analysis of the films. Film surface roughness and surface impurity volume fraction measurements were accomplished by carrying out AFM measurements (1 $\mu\text{m} \times 1 \mu\text{m}$ scan area) over five different areas of the sample surface. Average root mean square (RMS) roughness (nm) figures are provided, along with the SD variability of the dataset. Average volume fraction (vol.%) quantities were determined from impurity particle count area as a proportion of the scan area.

AFM-based nano-machining and PFM experiments

AFM-based nano-machining of the surfaces of the ultrathin B₆TFMO films was achieved using an Asylum Research MFP-3D™ AFM by applying force from a sufficiently stiff diamond cantilever. NM-RC (single crystal diamond, Au reflex coated, < 10 nm tip radius, 486 kHz resonant frequency, boron-doped) probes, commercially available from Adama Innovations (c/o Republic of Work, 12 South Mall, Cork, T12 RD43, Ireland), were used for the AFM-based nano-machining studies. The normal loading force, F (N), was calculated using Hookes law, $F = kz$, where k is the spring constant (N/m), and z (m) is determined by multiplying the calibrated deflection sensitivity (m/V) by the setpoint (V) (the difference between photodiode signal when the cantilever is far from the surface and when it is at setpoint). The spring constant [1.89×10^2 ($\pm 8.39\%$) N/m] was calibrated via the Sader method^[41] by performing a thermal tune (1,000 samples) in free air to measure the resonance frequency and the quality factor of the cantilever. Loading forces of between 1.86 μN and 5.59 μN were utilized for each scan in this work. Successive scans were performed over 8 $\mu\text{m} \times 8 \mu\text{m}$ areas at a scan frequency of 0.75 Hz to progressively machine through the sample from the film surface until the substrate was reached. A machining scan angle of 90° was utilized unless otherwise specified. The depths of the nano-machined areas were measured by performing line section height profiles of imaged areas. The measured RMS roughness values for the nano-machined areas of the 7.9 nm B₆TFMO sample were, in general, rougher [values of 0.52 nm (SD = ± 0.42 nm), 0.46 nm (SD = ± 0.38 nm), 0.50 nm (SD = ± 0.42 nm), and 0.57 nm (SD = ± 0.48 nm) for depths of 0.7 nm, 2.0 nm, 3.8 nm, and 6.2 nm, respectively] compared with roughness values for the pristine B₆TFMO surface [0.29 nm (SD = ± 0.23 nm)], which may be due to fluctuations in composition, structures, and structural defects in the underlying film. Whereas, the measured RMS roughness values for the nano-machined areas of the 5.6 nm B₆TFMO sample were, as expected, in general smoother [values of 0.66 nm (SD = ± 0.51 nm), 0.09 nm (SD = ± 0.07 nm), 0.08 nm (SD = ± 0.07 nm), and 0.12 nm (SD = ± 0.09 nm) for depths of 0.4 nm, 3.7 nm, 4.6 nm, and 5.3 nm, respectively] compared with roughness values for the pristine B₆TFMO surface [0.37 nm (SD = ± 0.27 nm)]. The roughness values for when nano-machining reached the underlying NGO

substrate were 0.09 nm (SD = ± 0.07 nm) and 0.12 nm (SD = ± 0.10 nm) for NGO underneath the 7.9 nm film and 5.6 nm film, respectively. Nanoscale electromechanical properties of the ultrathin films were evaluated by PFM using an Asylum Research MFP-3D™ AFM in contact mode in conjunction with a HVA220 Amplifier and a cantilever scan angle of 90°. The Dual AC (alternating current) Resonance Tracking PFM (DART-PFM) mode was utilized to amplify both the vertical and lateral piezo signals. Apex Super Sharp conductive diamond probes AD-2.8-SS (boron doped, Au reflex coated, < 5 nm tip radius, 75 kHz resonant frequency) were purchased from Adama Innovations (c/o Republic of Work, 12 South Mall, Cork, T12 RD43, Ireland) and used to image piezoelectric domains over $1 \mu\text{m} \times 1 \mu\text{m}$ scan areas. Imaging of the same sample area by vertical PFM (Vert PFM) and lateral PFM (Lat PFM) enables corresponding measurements of the normal component of the piezoresponse vector (out-of-plane direction) and the transversal component of the in-plane piezoresponse (perpendicular to the cantilever axis), respectively^[42]. The Lat PFM measurements were conducted by a comparable method to the Vert PFM measurements, except the “InFast” option was set to “Lateral” as opposed to “AC Deflection”, respectively. The drive frequencies were operated near contact resonance for lateral (480 to 520 kHz) and vertical (250 to 280 kHz) modes. PFM measurements were operated at AC drive amplitudes (V_{AC}) of $4.0 V_{AC}$ and below.

RESULTS AND DISCUSSION

Characterization of structure, surface morphology, and surface piezo-configurations of as-prepared ultrathin B6TFMO films

Two different thicknesses of B6TFMO films were synthesized on (001)-orientated NGO substrates by pulsing either 75 injections or 100 injections of each precursor during the DLI-CVD process. The pseudo-cubic lattice parameter (a_p) of the perovskite-type layer in B6TFMO is 3.89 Å and a_p' is 3.858 Å for NGO; therefore, the lattice mismatch = -0.82%^[27]. Out-of-plane XRD profiles, as shown in Figure 1B, are consistent with epitaxial films of an orthorhombic Aurivillius phase with five perovskite layers per half unit cell ($m = 5$) interleaved by bismuth oxide interfaces, as depicted schematically in Figure 1A^[43]. Both B6TFMO films demonstrate a preference for orientating along the c -axis of the structure, with only (00 l) Bragg reflections visible in the diffractograms. The broadening of the peaks [e.g., FWHM values for the (0010), (0012), and (0020) peaks are 1.721°, 0.400°, and 2.114° and are 1.534°, 0.389° and 1.186° for B6TFMO deposited with 75 injections and 100 injections, respectively] is due to grain size effects and due to the fact that the X-ray beam is scattering from only three, or less, half-unit cell repeat entities^[44]. Comparative XRD patterns obtained from B6TFMO films deposited with 75 injections and 100 injections demonstrate that the intensities of the film deposited using 75 injections [e.g., the \log_{10} intensity of the (0010), (0012), and (0020) peaks are: 0.461, 0.616, and 0.130 counts] are lower than the intensities of the film deposited using 100 injections [e.g., the \log_{10} intensity of the (0010), (0012), and (0020) peaks are: 0.717, 0.951, and 0.371 counts], corresponding to a decreased film thickness for the film deposited using 75 injections. HR-TEM imaging [Figure 1C] confirms that the films have an $m = 5$ Aurivillius phase structure, displaying some regions with out-of-phase boundary defects and associated stacking faults (indicated by the blue arrows), typically observed for layered Aurivillius materials. This structural disorder within the samples would also contribute to peak broadening observed in the XRD profiles and might explain why there are additional variations in peak broadening between the 7.9 nm and 5.6 nm B6TFMO films [e.g., the FWHM value for the (008) reflection of the 7.9 nm film (1.079°) indicates that it is broader compared to the 5.6 nm film (0.970°)]. Contributions to the broadening of the asymmetric peaks may also result from segregation of secondary phases or crystal twinning, which will be discussed later. HR-TEM and XRR [Figure 1D] and [Supplementary Table 1] measurements yield average thickness values of 7.9 nm and 5.6 nm for B6TFMO films deposited using 100 injections and 75 injections, respectively. The former equates to a thickness of approximately 1.5 unit cells, and the latter equates to a thickness of approximately 1 unit cell of the $m = 5$ Aurivillius phase. These thickness measurements are consistent with previous TEM measurements of B6TFMO films prepared on different substrates under similar growth DLI-CVD conditions^[27,28].

Epitaxial growth of layered Aurivillius phases under high supersaturation conditions is inclined to proceed via a 2D nucleation and layer-by-layer (Frank-Van der Merwe) growth mode^[27-30,33,45], as illustrated in [Figure 2A](#). Laterally grown layers with heights consistent with the lattice parameter of half of a u.c. of the Aurivillius structure evolve and increasingly merge and condense to form a complete (flat) layer prior to the nucleation of subsequent half-unit cell-thick layers. Each complete growth layer is ~2.5 nm in thickness for B6TFMO. Depending on the level of saturation during intermediary steps in the layer-by-layer growth mode, either 2D islands or pits (holes) can be seen on the film surface. The pits are referred to as “lochkeime” (hole-nuclei), which are “negative” 2D islands^[33]. These types of 2D islands and pits are visible in the HR-TEM images in [Figure 2B](#) and the AFM image in [Figure 2C](#) for the 7.9 nm (1.5 u.c.) and 5.6 (1 u.c.) nm B6TFMO films. The coalescence of the laterally grown layers can be seen in [Figure 2C](#), where the majority of the incomplete surface is covered by the growing 2-D layer, with darker regions in between corresponding to the underlying layer beneath (“negative” 2D islands). The height (depth) of these Aurivillius phase 2D islands (pits) is approximately 2.5 nm, corresponding to half a unit cell ($c/2$) of the $m = 5$ B6TFMO structure. AFM imaging with a sharp (2 nm tip radius) probe exposes other island-type surface contaminants present at a volume fraction of 6.7 vol.%. These surface features, encircled in red in [Figure 2C](#), appear to be spherical in nature and are < 20 nm in diameter. While the HR-TEM imaging and XRD analysis in this work could not identify the spherical surface features, it is possible that they correspond to spinel-type secondary phases identified in previous reports for films of this type^[27,28]. Note that we have previously shown that these features can be reduced/eliminated by careful control of bismuth excess to counteract its volatility during growth^[28].

DART-PFM imaging [[Figure 2D](#)] and [[Supplementary Figure 1](#)] utilizing a conducting diamond probe with an apex super sharp tip (radius < 5 nm) demonstrates that a random mixture of piezoresponse with indiscriminate orientation is exhibited for measurements of the pristine surface of the 7.9 nm (1.5 u.c.) thick B6TFMO film. 180 phase contrast is displayed for oppositely polarized domains, separated by curved domain walls. Lateral PFM imaging [[Figure 2D](#)] and [[Supplementary Figure 1A-C](#)] enables measurement of the in-plane polarization components^[42], whereas vertical PFM images [[Supplementary Figure 1D and E](#)] provide information on the out-of-plane component. Average surface in-plane domain sizes of 440 nm² (SD = 1.6×10^3 nm²) and out-of-plane domain sizes of 378 nm² (SD = 488 nm²) are observed. Crystal symmetry of the $m = 5$ B6TFMO Aurivillius phase with an *odd* m number of perovskite layers determines that the major polarization vector primarily lies along the a -axis (in-plane, lateral direction). Only minor polarization is expected along the c -axis (out-of-plane, vertical direction)^[46]; therefore, a relatively weaker piezoresponse (pm) is observed in the corresponding out-of-plane directed domains (Vert PFM images, [[Supplementary Figure 1D and E](#)]). The presence of non-ferroelectric spinel-type impurities did not seem to impact the local ferroelectric signal measured. However, these surface contaminants, in conjunction with surface Aurivillius phase 2D islands and pits, may have the effect of introducing varying tip-sample contact areas and obscuring orientated domain configurations corresponding to the underlying epitaxial B6TFMO film during surface PFM measurements.

Investigations of ferroelectric domain configuration in ultrathin B6TFMO as a function of AFM-based nano-machined depth

Progress in the miniaturization of semi-conductor processes has created an increased demand for AFM-based nanomachining to satisfy the role of defect removal with nano-meter level accuracy during photomask repair^[37-39]. In this work, we apply the AFM-based nano-machining approach to remove surface contaminants from the ultra-thin B6TFMO films to uncover a complete Aurivillius phase surface layer. Successive scanning allows progressive nano-machining of the film at increased depths with nanometer-level control. A sufficiently stiff, commercially available diamond probe was used with a removal rate of between 0.13 nm/scan and 0.41 nm/scan.

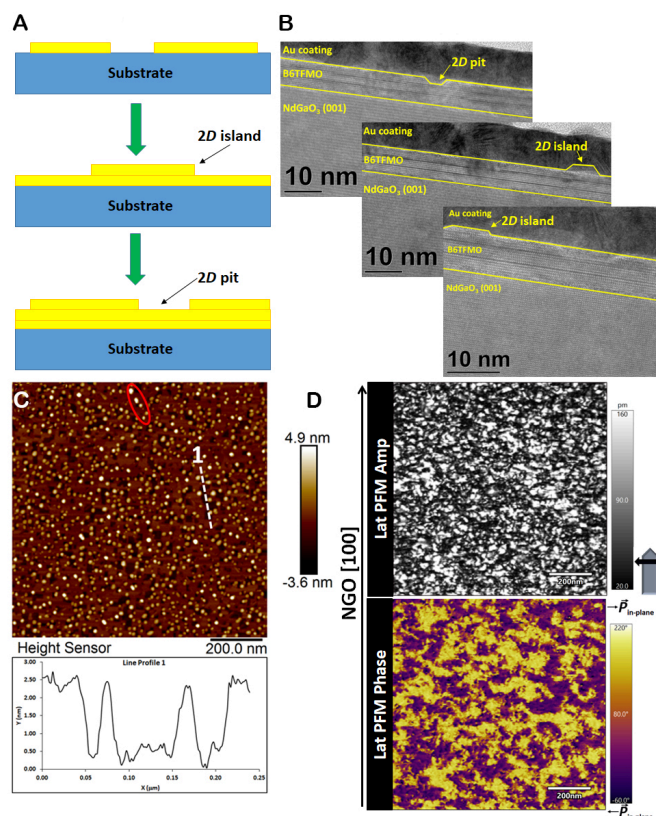


Figure 2. (A) A schematic of the 2D nucleation and layer-by-layer (Frank-Van der Merwe) growth mode. (B) Representative HR-TEM images demonstrating the presence of 2D islands and pits in the 7.9 nm thick B6TFMO film on NGO (001). (C) Representative AFM image of 5.6 nm thick B6TFMO film NGO (001) substrates. A line section profile 1 is shown in white through the 2D pits indicating a height of 2.5 nm, corresponding to half a u.c. ($c/2$) of the $m = 5$ Aurivillius structure (see Figure 1A). Small circular island-type inclusions (< 20 nm diameter) are encircled in red. (D) Lateral (Lat) PFM Amp and Phase images of the pristine surface of a 7.9 nm thick B6TFMO film.

Next, we performed PFM imaging of the 7.9 nm (1.5 u.c.) B6TFMO film as a function of nano-machined thickness. Lateral PFM results, scanned with the long-axis of the cantilever orientated parallel to the NGO [010] direction, are shown in Figure 3. While a randomly distributed piezoresponse without a favored domain orientation is observed for the pristine film surface [Figure 3A-C], on removal of 0.7 nm of the film surface [Figure 3D-F], it is revealed that spontaneous polarization orientates in distinct stripe domain configurations along the a - b plane, at 45° to the orthorhombic b -axis of NGO. Vertical PFM images [Supplementary Figure 2] demonstrate that a weaker component of the spontaneous polarization exists out of the a - b plane (along the c -axis). This observed vertical response is expected for an $m = 5$, an odd-layered Aurivillius phase^[47]. The measured domain widths are of the order of $0.14 \mu\text{m}$ for the nano-machined 7.9 nm (1.5 u.c.) B6TFMO sample. The 45° stripe domains were observed to persist at nano-machined depths of 2.0 nm [Figure 3G-I], 3.8 nm [Figure 3J-L], and 6.2 nm [Figure 3M-O]. It is only until the sample is nano-machined all the way through the film to the underlying NGO substrate that the PFM signal is lost. Note that great care was taken to ensure that the striped domain features angled at 45° were not artifacts created by the nano-machining process. Nano-machining investigations using intentionally aggressive load forces as a function of nano-machining angle (0° , 45° , 90°) were performed to distinguish the deliberately-created scan artifacts from the 45° stripe domains inherent to the B6TFMO films. Details establishing that 45° stripe ferroelectric domains are independent of topography and nano-machining scan artifacts are described in the Supplementary Material and Supplementary Figure 3.

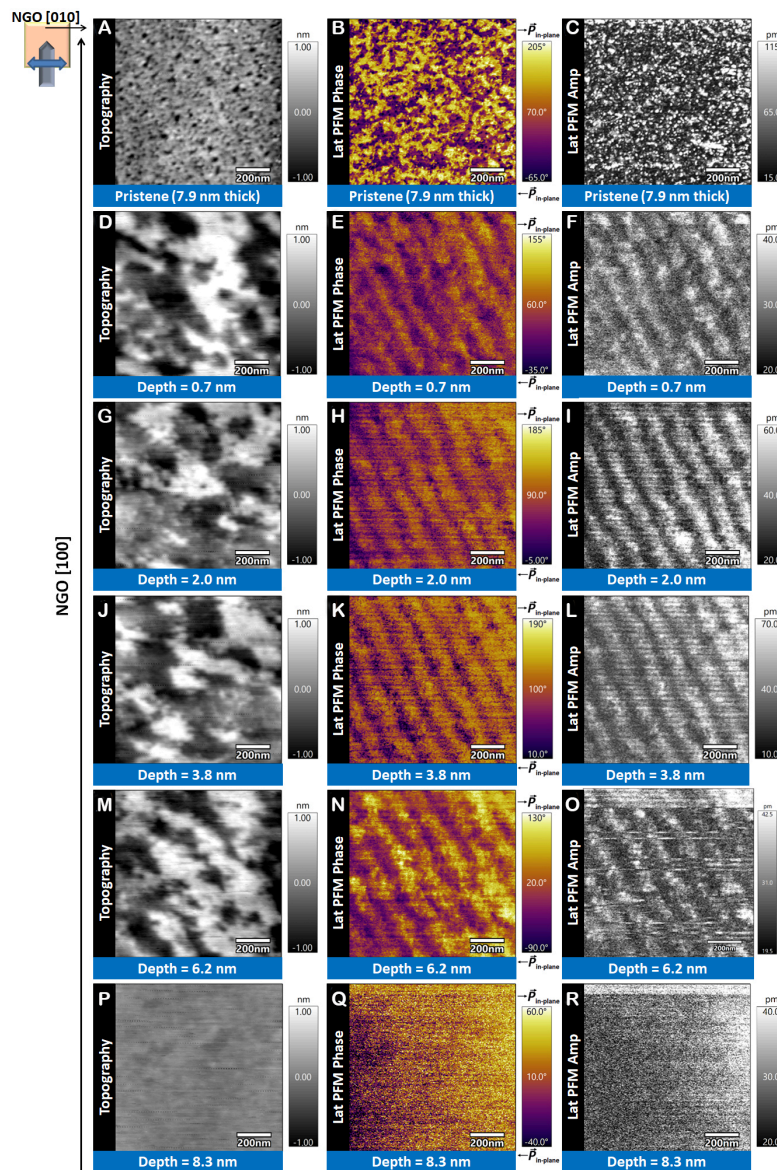


Figure 3. Representative topography and lateral (lat) DART-PFM phase and amplitude (amp) images of 7.9 nm (1.5 u.c.) B6TFMO on NGO (001) as a function of AFM-based nano-machined depth. The scanning direction of the cantilever was parallel with the $[010]_{\text{substrate}}$ axis.

Gradauskaite *et al.*^[29,30] and Keeney *et al.*^[27] previously observed stripe domains for one u.c. thick (5 nm) Aurivillius phase films that were terminated with complete Aurivillius layers and exhibited an atomically flat surface. It was deemed that domain patterns are stabilized by the underlying NGO substrate, where the lattice mismatch is progressively lost as film thickness increases. For films of two unit cells in thickness, an isotropic random distribution of 180° domains was observed^[29,30]. Therefore, the question arises as to whether the onset of 45° striped domain observation in this work happens solely due to the ability to image the B6TFMO film at decreased thickness, where the domain patterns are possibly stabilized by substrate strain effects. Alternatively, the onset of striped domain observation from the nano-machining process may be due to the removal of otherwise masking surface 2D islands, pits, and contaminants to reveal a smooth B6TFMO surface terminated with a complete Aurivillius layer.

To distinguish between the two possibilities, PFM imaging was performed on the thinner 5.6 nm (1 u.c.) B₆TFMO film, prepared by the same layer-by-layer growth process as the 7.9 nm (1.5 u.c.) thick B₆TFMO film. Lateral DART-PFM images, scanned with the long-axis of the cantilever orientated parallel to the NGO [100] direction, are shown in Figure 4. Based on the results of the 7.9 nm (1.5 u.c.) thick B₆TFMO films in Figure 3G-I, where the milled depth corresponds to a thickness of 5.9 nm and results from previous 5 nm-thick B₆TFMO films exhibiting an atomically flat surface^[27], we would expect to see 45° striped domain patterns for the 5.6 nm (1 u.c.) B₆TFMO film. However, a random mixture of piezoresponse with indiscriminate orientation is exhibited for measurements of the pristine surface of the 5.6 nm (1 u.c.) thick B₆TFMO film, as shown in Figure 4A-C. 180 degree phase contrast is displayed for oppositely polarized domains with average surface in-plane domain sizes of 209 nm² (SD = 274 nm²). Therefore, the observation of the randomly distributed piezoresponse in this work is due to the surface 2D islands, pits, and contaminants complicating the surface PFM signal. Stripe domain configurations along the *a-b* plane, at 45° to *b*-axis of the orthorhombic unit cell of NGO, are uncovered by PFM imaging on removal of surface contaminants by nanomachining at depths of 0.4 nm [Figure 4D-F], 3.7 nm [Figure 4G-I], 4.6 nm [Figure 4J-L], and 5.3 nm [Figure 4M-O]. We deduce that for the pristine film surfaces imaged in this work, the ferroelectric domains are not themselves inherently isotropic-type domains. Rather, the PFM probe is accessing fragmented Aurivillius phase structures (2D islands and pits); therefore, the piezoresponse and orientation cannot be visualized as continuous at the pristine surface. The differences in piezo-configuration between the pristine surface and exposed sub-surfaces can be attributed to the effectiveness of AFM-based nano-machining in removing growth surface artifacts, which, otherwise, obscure the domain configurations of the underlying planar B₆TFMO film.

The measured domain widths are of the order of 0.08 μm for the nano-machined 5.6 nm (1 u.c.) B₆TFMO sample; narrower than that observed for the thicker 7.9 nm (1.5 u.c.) B₆TFMO sample, consistent with the Landau-Lifshitz-Kittel scaling law^[48-50]. In the PFM images, striped domains are directed from the top left to the bottom right in the 7.9 nm (1.5 u.c.) B₆TFMO sample where the PFM cantilever was aligned parallel to the [010] substrate direction, whereas domains are directed from top right to bottom left in the 5.6 nm (1 u.c.) B₆TFMO sample, which was turned 90° so that the PFM cantilever was aligned parallel with the [100] NGO substrate direction. Topography images [Figure 4D] of the sample machined to a depth of 0.4 nm demonstrate that machining is somewhat “patchy” [with an RMS roughness value of 0.66 nm (±0.51 nm)] and did not completely remove the surface contaminants. PFM imaging [Figure 4E and F] shows a mixed image of domains with undefined orientation and 45° orientated stripe domains. Topography images [Figure 4M] of the sample machined to a depth of 5.3 nm show faint horizontal lines, which are scan artifacts of the nano-machining process as the film to substrate interface is approached. Remarkably, 45° striped domains and piezoresponse are also observed at this depth, which corresponds to less than half of an Aurivillius phase unit cell (< 2.5 nm). The nano-machining horizontal artifacts become more visible at machined depths of 7.2 nm [Figure 4P-R], correlating with the machining of the underlying NGO substrate and a loss in PFM signals. The 45° stripe domain configurations along the lateral *a-b* plane were observed to persist through the film, disappearing at depths consistent with the substrate. This is an interesting observation, as it suggests that the ferroelectric critical size limit may be absent for in-plane polarization directions in B₆TFMO, similar to observations in optimized HfO₂ and BiFeO₃ films and thickness-dependent tomographic PFM studies of *m* = 4 Aurivillius phase films^[7,51,52]. However, more detailed experiments correlating precise thickness measurements (e.g., using aberration-corrected scanning TEM) with PFM experiments are required in order to confirm whether or not a critical thickness exists for in-plane ferroelectricity in B₆TFMO.

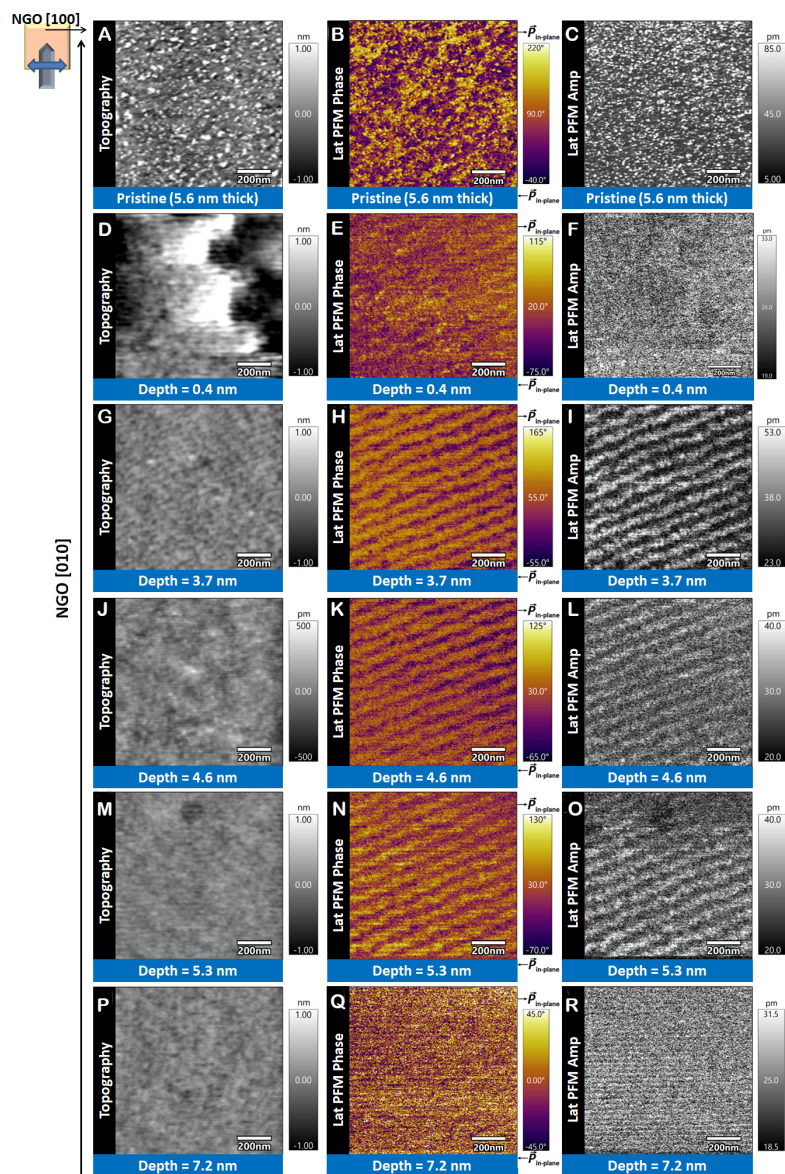


Figure 4. Representative topography and lateral (lat) DART-PFM phase and amplitude (amp) images of 5.6 nm (1 u.c.) B6TFMO on NGO (001) as a function of AFM-based nano-machined depth. The scanning direction of the cantilever scanning direction was parallel with the $[100]_{\text{substrate}}$ axis.

Crystal symmetry of the Aurivillius phases dictates that the major in-plane spontaneous polarization component lies entirely along the a axis (with a minor polarization along the out-of-plane c -axis in odd-layered structures)^[43]. Therefore, there must be another physical origination for the experimentally observed 45° striped domains. a - b crystal twinning is a common occurrence in layered materials such as the layered high temperature superconductors^[53] and Aurivillius phases^[54]. The lack of uniaxial polarization in this work indicates that crystal twinning is present in the B6TFMO thin films. The crystal twinning would originate from the orthorhombic crystal structure of the underlying (001) NGO substrate, which presents an anisotropic template for growth based on a pseudo-cubic unit cell^[53]. The a axis of the pseudo-cubic cell lies along the ab diagonals of the orthorhombic NGO crystal structure, and a pseudo-cubic lattice constant of 3.858 Å is presented for NGO. This provides a close lattice match to the a_p ' of B6TFMO (3.89 Å) to grow

under minimal strain^[27]; however, the angular anisotropy of the pseudo-cubic template would likely give rise to preferential twinning. The experimental observations of 45° orientated stripe domains, rather than expected in-plane uniaxial anisotropy, may be the result of crystal twinning in B6TFMO created by mimicking the pseudo-cubic symmetry of the underlying NGO substrate.

CONCLUSIONS

In summary, we demonstrate the use of AFM-based nano-machining using a commercially available diamond probe to remove surface contaminants from ultrathin B6TFMO films with nanometer-level precision. Complete Aurivillius layers are uncovered beneath the as-grown surface, with subsequent lateral PFM imaging revealing distinct stripe domain configurations along the *a-b* plane (at 45° to the NGO substrate *b*-axis), of stark contrast to the randomly distributed piezoresponse observed for the pristine film surface. We attribute the differences in piezo-configuration between the pristine surface and exposed sub-surfaces to the effectiveness of AFM-based nano-machining in removing growth surface artifacts (fractional Aurivillius phase 2D islands/pits and secondary phase contaminants) that, otherwise, mask the domain configurations of the underlying planar B6TFMO film. The experimental observations of 45° orientated stripe domains rather than in-plane uniaxial anisotropy are likely ensuing from the presence of crystal twinning in B6TFMO to conform to the pseudo-cubic symmetry of the underlying NGO substrate. The width of the 45° stripe domains is narrower for the 5.6 nm B6TFMO films (0.08 μm) compared to the 7.9 nm B6TFMO films (0.14 μm), consistent with the Landau-Lifshitz-Kittel scaling law^[48-50]. Moreover, while previous PFM investigations of multiferroic *m* = 5 B6TFMO films demonstrated the persistence of stable ferroelectricity close to the unit cell level (5 nm to 8 nm)^[27,28], the AFM-based nano-machining investigations in this work indicate that ferroelectricity persists at thicknesses lower than this. Stable sub-surface ferroelectric domain structures and piezoresponses persist along the in-plane directions throughout the film depth, down to less than half of an Aurivillius phase unit cell (< 2.5 nm). These findings, along with evidence for sub-unit cell ferroelectricity in exfoliated flakes^[26] and planar thin films^[29] of *m* = 4 Aurivillius phases, demonstrate the technological potential of Aurivillius phase B6TFMO for future miniaturized memory storage devices. For example, devices based on in-plane tunnel junctions are an appealing prospect, as they would not be expected to be obstructed by opposing depolarization fields upon thickness-scaling to ultrathin dimensions. This means that higher tunnelling current ratios could be achieved with non-destructive read processes. To date, no such in-plane devices have been commercialized; only theoretical device models based on monochalcogenides have been reported. However, it is difficult to synthesize high-quality ultra-thin monochalcogenides by scalable growth methods^[55-58]. As such, optimized multiferroic B6TFMO Aurivillius phases, which can be synthesized by scalable DLI-CVD growth methods, are perfect candidates for utilization in next-generation devices based on ultrathin multiferroic tunnel junctions.

DECLARATIONS

Acknowledgments

The authors gratefully acknowledge the support of the Royal Society-Science Foundation Ireland (SFI) University Research Fellowship URF\R\201008 and the SFI Frontiers for the Future Project 19/FFP/6475.

Authors' contributions

Conceiving and coordinating the project, developing the DLI-CVD processes, synthesizing the ultra-thin B6TFMO thin films, and performing AFM and PFM characterization and AFM-based nanomachining experiments; interpreting the results in discussion with the other authors; initially writing of the first draft of the manuscript, with the final version being crafted through contributions from all authors: Keeney L. Making substantial contributions to the conception and design of the AFM-based nanomachining studies: Colfer L.

Performing XRD characterization and interpreting the ultrathin B6TFMO films: Dutta D
Conducting FIB cross-sectioning of lamellae for TEM and performing HR-TEM analysis of the B6TFMO thin films: Schmidt M
Handling XRR analysis and interpreting the ultrathin B6TFMO films: Wei G
All authors have given their approval to the final version of the manuscript.

Availability of data and materials

The accepted publication is available on the open access University College Cork (UCC) CORA repository (<https://cora.ucc.ie/>).

Financial support and sponsorship

This work was supported by the Royal Society-Science Foundation Ireland (SFI) University Research Fellowship URF\R\201008 and the SFI Frontiers for the Future Project 19/FFP/6475.

Conflicts of interest

All authors declared that there are no conflicts of interest.

Ethical approval and consent to participate

Not applicable.

Consent for publication

Not applicable.

Copyright

© The Author(s) 2023.

REFERENCES

1. Scott JF. Future issues in ferroelectric miniaturization. *Ferroelectrics* 1998;206:365-79. DOI
2. Li S, Eastman JA, Vetrone JM, Foster CM, Newnham RE, Cross LE. Dimension and size effects in ferroelectrics. *Jpn J Appl Phys* 1997;36:5169. DOI
3. Qiao H, Wang C, Choi WS, Park MH, Kim Y. Ultra-thin ferroelectrics. *Mater Sci Eng R Rep* 2021;145:100622. DOI
4. Tybell T, Ahn CH, Triscone J. Ferroelectricity in thin perovskite films. *Appl Phys Lett* 1999;75:856-8. DOI
5. Fong DD, Stephenson GB, Streiffer SK, et al. Ferroelectricity in ultrathin perovskite films. *Science* 2004;304:1650-3. DOI
6. Choi KJ, Biegalski M, Li YL, et al. Enhancement of ferroelectricity in strained BaTiO₃ thin films. *Science* 2004;306:1005-9. DOI
7. Cheema SS, Kwon D, Shanker N, et al. Enhanced ferroelectricity in ultrathin films grown directly on silicon. *Nature* 2020;580:478-82. DOI
8. Vasudevan RK, Matsumoto Y, Cheng X, et al. Deterministic arbitrary switching of polarization in a ferroelectric thin film. *Nat Commun* 2014;5:4971. DOI
9. Guo YY, Gibbs AS, Perez-Mato JM, Lightfoot P. Unexpected phase transition sequence in the ferroelectric Bi₄Ti₃O₁₂. *IUCrJ* 2019;6:438-46. DOI PubMed PMC
10. Deepak N, Zhang PF, Keeney L, Pemble ME, Whatmore RW. Atomic vapor deposition of bismuth titanate thin films. *J Appl Phys* 2013;113:187207. DOI
11. Keeney L, Groh C, Kulkarni S, Roy S, Pemble ME, Whatmore RW. Room temperature electromechanical and magnetic investigations of ferroelectric Aurivillius phase Bi₅Ti₃(FexMn_{1-x})O₁₅ (x = 1 and 0.7) chemical solution deposited thin films. *J Appl Phys* 2012;112:024101. DOI
12. Keeney L, Kulkarni S, Deepak N, et al. Room temperature ferroelectric and magnetic investigations and detailed phase analysis of Aurivillius phase Bi₅Ti₃Fe_{0.7}Co_{0.3}O₁₅ thin films. *J Appl Phys* 2012;112:052010. DOI
13. Keeney L, Zhang PF, Groh C, Pemble ME, Whatmore RW. Piezoresponse force microscopy investigations of Aurivillius phase thin films. *J Appl Phys* 2010;108:042004. DOI
14. Zhang PF, Deepak N, Keeney L, Pemble ME, Whatmore RW. The structural and piezoresponse properties of c-axis-oriented Aurivillius phase Bi₅Ti₃FeO₁₅ thin films deposited by atomic vapor deposition. *Appl Phys Lett* 2012;101:112903. DOI
15. Wouters DJ, Maes D, Goux L, et al. Integration of SrBi₂Ta₂O₉ thin films for high density ferroelectric random access memory. *J Appl Phys* 2006;100:051603. DOI

16. Park BH, Kang BS, Bu SD, Noh TW, Lee J, Jo W. Lanthanum-substituted bismuth titanate for use in non-volatile memories. *Nature* 1999;401:682-4. DOI
17. Annual report pursuant to section 13 or 15(d) of the securities exchange act of 1934 for the fiscal year ended March 31, 2006 commission file number 1 - 6784. Available from: <https://www.sec.gov/Archives/edgar/data/63271/000119312506188347/d20f.htm> [Last accessed on 16 Oct 2023].
18. Fujii E, Uchiyama K. First 0.18 μm SBT-based embedded FeRAM technology with hydrogen damage free stacked cell structure. *Integr Ferroelectr* 2003;53:317-23. DOI
19. Pitcher MJ, Mandal P, Dyer MS, et al. Magnetic materials. Tilt engineering of spontaneous polarization and magnetization above 300 K in a bulk layered perovskite. *Science* 2015;347:420-4. DOI
20. Suwardi A, Prasad B, Lee S, et al. Turning antiferromagnetic $\text{Sm}_{0.34}\text{Sr}_{0.66}\text{MnO}_3$ into a 140 K ferromagnet using a nanocomposite strain tuning approach. *Nanoscale* 2016;8:8083-90. DOI
21. Choi EM, Maity T, Kursumovic A, et al. Nanoengineering room temperature ferroelectricity into orthorhombic SmMnO_3 films. *Nat Commun* 2020;11:2207. DOI PubMed PMC
22. Srihari NV, Vinayakumar KB, Nagaraja KK. Magnetoelectric coupling in bismuth ferrite - challenges and perspectives. *Coatings* 2020;10:1221. DOI
23. Keeney L, Maity T, Schmidt M, et al. Magnetic field-induced ferroelectric switching in multiferroic aurivillius phase thin films at room temperature. *J Am Ceram Soc* 2013;96:2339-57. DOI
24. Faraz A, Maity T, Schmidt M, et al. Direct visualization of magnetic-field-induced magnetoelectric switching in multiferroic aurivillius phase thin films. *J Am Ceram Soc* 2017;100:975-87. DOI
25. Moore K, O'Connell EN, Griffin SM, et al. Charged domain wall and polar vortex topologies in a room-temperature magnetoelectric multiferroic thin film. *ACS Appl Mater Interfaces* 2022;14:5525-36. DOI PubMed PMC
26. Keeney L, Smith RJ, Palizdar M, et al. Ferroelectric behavior in exfoliated 2D aurivillius oxide flakes of sub-unit cell thickness. *Adv Elect Materials* 2020;6:1901264. DOI
27. Keeney L, Saghi Z, O'sullivan M, Alaria J, Schmidt M, Colfer L. Persistence of ferroelectricity close to unit-cell thickness in structurally disordered aurivillius phases. *Chem Mater* 2020;32:10511-23. DOI
28. Keeney L, Colfer L, Schmidt M. Probing ferroelectric behavior in sub-10 nm bismuth-rich aurivillius films by piezoresponse force microscopy. *Microsc Microanal* 2022;28:1396-406. DOI
29. Gradauskaite E, Campanini M, Biswas B, et al. Robust in-plane ferroelectricity in ultrathin epitaxial aurivillius films. *Adv Materials Inter* 2020;7:2000202. DOI
30. Gradauskaite E, Gray N, Campanini M, Rossell MD, Trassin M. Nanoscale design of high-quality epitaxial aurivillius thin films. *Chem Mater* 2021;33:9439-46. DOI
31. Wang Y, Chen W, Wang B, Zheng Y. Ultrathin ferroelectric films: growth, characterization, physics and applications. *Materials* 2014;7:6377-485. DOI PubMed PMC
32. Lines ME, Glass AM. Principles and applications of ferroelectrics and related materials. Oxford: Oxford University Press; 1977. p.525. Available from: <https://academic.oup.com/book/25990> [Last accessed on 11 Oct 2023].
33. Venables JA, Spiller GDT, Hanbucken M. Nucleation and growth of thin films. *Rep Prog Phys* 1984;47:399. DOI
34. Binnig G, Quate CF, Gerber C. Atomic force microscope. *Phys Rev Lett* 1986;56:930-3. DOI PubMed
35. Steffes JJ, Ristau RA, Ramesh R, Huey BD. Thickness scaling of ferroelectricity in BiFeO_3 by tomographic atomic force microscopy. *Proc Natl Acad Sci USA* 2019;116:2413-8. DOI PubMed PMC
36. Wang J, Yan Y, Li Z, Geng Y, Luo X, Fan P. Processing outcomes of atomic force microscope tip-based nanomilling with different trajectories on single-crystal silicon. *Precis Eng* 2021;72:480-90. DOI
37. Iwata F, Saigo K, Asao T, et al. Removal method of nano-cut debris for photomask repair using an atomic force microscopy system. *Jpn J Appl Phys* 2009;48:08JB20. DOI
38. Robinson T, Dinsdale A, Bozak R, White R, Archuletta M. Nanomachining processes for 45, 32 nm mode mask repair and beyond. Proceedings of the Photomask and Next-Generation Lithography Mask Technology XV; 2008 May 19; Yokohama, Japan. DOI
39. Robinson T, Dinsdale A, Bozak R, Arruzza B. Advanced mask particle cleaning solutions. Proceedings of the SPIE Photomask Technology; 2007 Oct 30; Monterey, United States. DOI
40. Bartkowska JA, Bochenek D, Niemiec P. Multiferroic aurivillius-type $\text{Bi}_6\text{Fe}_{2-x}\text{Mn}_x\text{Ti}_3\text{O}_{18}$ ($0 \leq x \leq 1.5$) ceramics with negative dielectric constant. *Appl Phys A* 2018;124:823. DOI
41. Sader JE, Borgani R, Gibson CT, et al. A virtual instrument to standardise the calibration of atomic force microscope cantilevers. *Rev Sci Instrum* 2016;87:093711. DOI
42. Kalinin SV, Rodriguez BJ, Jesse S, et al. Vector piezoresponse force microscopy. *Microsc Microanal* 2006;12:206-20. DOI
43. Ismunandar, Kamiyama T, Hoshikawa A, et al. Structural studies of five layer Aurivillius oxides: $\text{A}_2\text{Bi}_4\text{Ti}_5\text{O}_{18}$ (A = Ca, Sr, Ba and Pb). *J Solid State Chem* 2004;177:4188-96. DOI
44. Holder CF, Schaak RE. Tutorial on powder X-ray diffraction for characterizing nanoscale materials. *ACS Nano* 2019;13:7359-65. DOI PubMed
45. Frank FC, van der Merwe JH. One-dimensional dislocations III. Influence of the second harmonic term in the potential representation, on the properties of the model. Proceedings of the Royal Society of London; 1949 Dec 22; London, UK. London: Royal; pp. 125-34.
46. Trolrier-mckinstry S. Crystal chemistry of piezoelectric materials. In: Safari A, Akdoğan EK, editors. Piezoelectric and acoustic materials for transducer applications. Boston: Springer US; 2008. pp. 39-56. DOI

47. Whatmore, R. Ferroelectric materials. In: Kasap S, Capper P, editors. Springer handbook of electronic and photonic materials. Springer International Publishing: Cham; 2017. p. 1. [DOI](#)
48. Landau L, Lifshitz E. 3 - on the theory of the dispersion of magnetic permeability in ferromagnetic bodies. In: Pitaevski LP editors. Perspectives in theoretical physics. The collected papers of E. M. Lifshitz. Amsterdam:Elsevier; 1992. pp. 51-65. [DOI](#)
49. Kittel C. Theory of the structure of ferromagnetic domains in films and small particles. *Phys Rev* 1946;70:965. [DOI](#)
50. Kittel C. Physical theory of ferromagnetic domains. *Rev Mod Phys* 1949;21:541. [DOI](#)
51. Wang H, Liu ZR, Yoong HY, et al. Direct observation of room-temperature out-of-plane ferroelectricity and tunneling electroresistance at the two-dimensional limit. *Nat Commun* 2018;9:3319. [DOI](#) [PubMed](#) [PMC](#)
52. Gradauskaite E, Meier QN, Gray N, et al. Defeating depolarizing fields with artificial flux closure in ultrathin ferroelectrics. *arXiv* 2022:2212.11073. [DOI](#)
53. Nam J, Hughes RA, Castellán JP, Gaulin BD, Britten JF, Preston JS. The origin of preferential twinning in $\text{YBa}_2\text{Cu}_3\text{O}_{7-\delta}$ thin films deposited on the (0 0 1) NdGaO_3 substrate. *J Appl Phys* 2005;97:123906. [DOI](#)
54. Zurbuchen MA, Cahill DG, Schubert J, Jia Y, Schlom DG. Determination of the thermal conductivity tensor of the $n = 7$ Aurivillius phase $\text{Sr}_4\text{Bi}_4\text{Ti}_7\text{O}_{24}$. *Appl Phys Lett* 2012;101:021904. [DOI](#)
55. Shen XW, Fang YW, Tian BB, Duan CG. Two-dimensional ferroelectric tunnel junction: the case of monolayer in:SnSe/SnSe/Sb:SnSe homostructure. *ACS Appl Electron Mater* 2019;1:1133-40. [DOI](#)
56. Chang K, Liu J, Lin H, et al. Discovery of robust in-plane ferroelectricity in atomic-thick SnTe. *Science* 2016;353:274-8. [DOI](#)
57. Liu J, Chang K, Ji SH, Chen X, Fu L. Apparatus and methods for memory using in-plane polarization. Available from: <https://www.osti.gov/servlets/purl/1438442> [Last accessed on 11 Oct 2023].
58. Shen H, Liu J, Chang K, Fu L. In-plane ferroelectric tunnel junction. *Phys Rev Appl* 2019;11:024048. [DOI](#)
59. Momma K, Izumi F. *VESTA 3* for three-dimensional visualization of crystal, volumetric and morphology data. *J Appl Crystallogr* 2011;44:1272-6. [DOI](#)

Research Article

Open Access



Influence of hydrogel and porous scaffold on the magnetic thermal property and anticancer effect of Fe₃O₄ nanoparticles

Man Wang^{1,2}, Rui Sun^{1,2}, Huajian Chen¹, Xiaohan Liu^{1,2}, Toru Yoshitomi¹, Masaki Takeguchi³, Naoki Kawazoe¹, Yingnan Yang⁴, Guoping Chen^{1,2}

¹Research Center for Macromolecules and Biomaterials, National Institute for Materials Science, Ibaraki 305-0044, Japan.

²Subprogram in Materials Science and Engineering, Doctoral Program in Engineering Sciences, Graduate School of Science and Technology, University of Tsukuba, Ibaraki 305-8577, Japan.

³Center for Basic Research on Materials, National Institute for Materials Science, Ibaraki 305-0044, Japan.

⁴Graduate School of Life and Environmental Science, University of Tsukuba, Ibaraki 305-8572, Japan.

Correspondence to: Prof./Dr. Guoping Chen, Research Center for Macromolecules and Biomaterials, National Institute for Materials Science, Ibaraki 305-0044, Japan. E-mail: Guoping.CHEN@nims.go.jp

How to cite this article: Wang M, Sun R, Chen H, Liu X, Yoshitomi T, Takeguchi M, Kawazoe N, Yang Y, Chen G. Influence of hydrogel and porous scaffold on the magnetic thermal property and anticancer effect of Fe₃O₄ nanoparticles. *Microstructures* 2023;3:2023042. <https://dx.doi.org/10.20517/microstructures.2023.46>

Received: 5 Sep 2023 **First Decision:** 20 Sep 2023 **Revised:** 27 Sep 2023 **Accepted:** 19 Oct 2023 **Published:** 10 Nov 2023

Academic Editors: Yin Xiao, Chun-Xia Zhao **Copy Editor:** Fangyuan Liu **Production Editor:** Fangyuan Liu

Abstract

Magnetic hyperthermia uses magnetic nanoparticles (MNPs) for conversion of magnetic energy into thermal energy under an alternating magnetic field (AMF) to increase local temperature for ablation of cancer cells. The magnetic thermal capacity of MNPs not only depends on the intrinsic properties of MNPs but is also affected by the microenvironmental matrices surrounding the MNPs. In this study, the influence of agarose hydrogels and gelatin porous scaffolds on the magnetic thermal property and anticancer effect of Fe₃O₄ nanoparticles (NPs) were investigated with a comparison to free Fe₃O₄ NPs. Flower-like Fe₃O₄ NPs were synthesized and embedded in agarose hydrogels and gelatin porous scaffolds. Under AMF irradiation, the free Fe₃O₄ NPs had the best magnetic thermal properties and the most efficiently increased the local temperature to ablate breast cancer cells. However, the Fe₃O₄ NPs embedded in agarose hydrogels and gelatin porous scaffolds showed reduced magnetic-thermal conversion capacity, and the local temperature change was decreased in comparison to free Fe₃O₄ NPs during AMF irradiation. The gelatin porous scaffolds showed a higher inhibitory influence than the agarose hydrogels. The inhibitory effect of agarose hydrogels and gelatin porous scaffolds on magnetic-thermal conversion capacity resulted in a decreased anticancer ablation capacity to breast cancer cells during AMF irradiation. The Fe₃O₄ NP-embedded gelatin scaffolds showed the lowest anticancer effect. The results suggested that the matrices used to



© The Author(s) 2023. **Open Access** This article is licensed under a Creative Commons Attribution 4.0 International License (<https://creativecommons.org/licenses/by/4.0/>), which permits unrestricted use, sharing, adaptation, distribution and reproduction in any medium or format, for any purpose, even commercially, as long as you give appropriate credit to the original author(s) and the source, provide a link to the Creative Commons license, and indicate if changes were made.



deliver MNPs could affect their performance, and appropriate matrices should be designed to maximize their therapeutic effect for biomedical applications.

Keywords: Fe₃O₄ NPs, hydrogel, scaffold, agarose, gelatin, magnetic hyperthermia, anticancer

INTRODUCTION

Magnetic nanoparticles (MNPs) can convert magnetic energy to thermal energy when subjected to alternating magnetic field (AMF)^[1,2]. The heat generated by MNPs under AMF irradiation increases the local temperature to ablate cancer cells, known as magnetic hyperthermia (MH)^[3-5]. MH has been developed as an effective approach for cancer treatment due to its good biocompatibility and deep strong tissue penetration. This approach has also been combined with radiotherapy, chemotherapy, and immunotherapy to further improve the anticancer effect^[6-12]. It is pivotal to increase magnetic-thermal conversion efficiency to achieve a maximized therapeutic effect with the minimized dosage of MNPs.

To achieve high magnetic-thermal conversion efficiency, many studies have reported the optimization of synthesis methods of MNPs^[13,14] by controlling their structure and magnetic characteristics, including shape, size, size distribution, dispersion and aggregation state, crystallinity, composition, and magnetic parameters^[15-26]. Except for the intrinsic properties of MNPs, their surrounding microenvironmental matrices can affect the magnetic-thermal conversion^[27,28]. Incorporation of MNPs in hydrogels has been reported to change their magnetic-thermal conversion property^[28-31]. Engelmann *et al.* immobilized them in acrylamide hydrogels and found that the heating efficiency of MNPs decreased when the hydrogel stiffness increased^[28]. Suto *et al.* compared the influence of polyvinyl alcohol hydrogel and water^[31]. The heating efficiency of MNPs dispersed in water was better than that dispersed in polyvinyl alcohol hydrogel, and their specific absorption rate value in hydrogel showed 67% less than that in water^[31]. These studies suggest the inhibitory effects of hydrogels on the magnetic-thermal conversion property of MNPs.

In recent years, localized delivery of photothermal nanoparticles (NPs) has been demonstrated as an efficient strategy to accumulate and constrain them in tumors to maximize the photothermal ablation effect while decreasing their side effect^[32-37]. Both hydrogels and porous scaffolds are good carriers for the local delivery of photothermal NPs. However, the influence of porous scaffolds on the magnetic-thermal conversion of MNPs remains elusive. It is desirable to compare the influence of aqueous solution, hydrogels^[38-45], and porous scaffolds^[46-48] on the magnetic-thermal conversion of MNPs to maximize their MH effect.

Based on the above considerations, in this study, different microenvironments of phosphate buffer saline (PBS), hydrogels, and porous scaffolds were used to investigate the magnetic-thermal conversion property and anticancer effect of MNPs under AMF irradiation [Figure 1]. The same concentration of Fe₃O₄ NPs was used in PBS, agarose hydrogels, and gelatin porous scaffolds to disclose the influence of the different matrices on magnetic thermal effects. Moreover, Fe₃O₄ NPs at different concentrations were incorporated in the same matrix to study the MNP concentration dependence. The free Fe₃O₄ NPs in PBS exhibited the best magnetic thermal property, while embedding in agarose hydrogels or gelatin porous scaffolds decreased the temperature change during AMF irradiation. The anticancer effect was investigated *in vitro* by incubating breast cancer cells (MDA-MB-231-Luc cells) with free Fe₃O₄ NPs, agarose/Fe₃O₄ hydrogels, and gelatin/Fe₃O₄ porous scaffolds under AMF irradiation. The free Fe₃O₄ NPs showed the highest anticancer effect under AMF irradiation, followed by Fe₃O₄ NPs in agarose hydrogels and then Fe₃O₄ NPs in gelatin porous scaffolds. The matrices for MNP delivery could affect the magnetic-thermal conversion property and anticancer effect of Fe₃O₄ NPs.

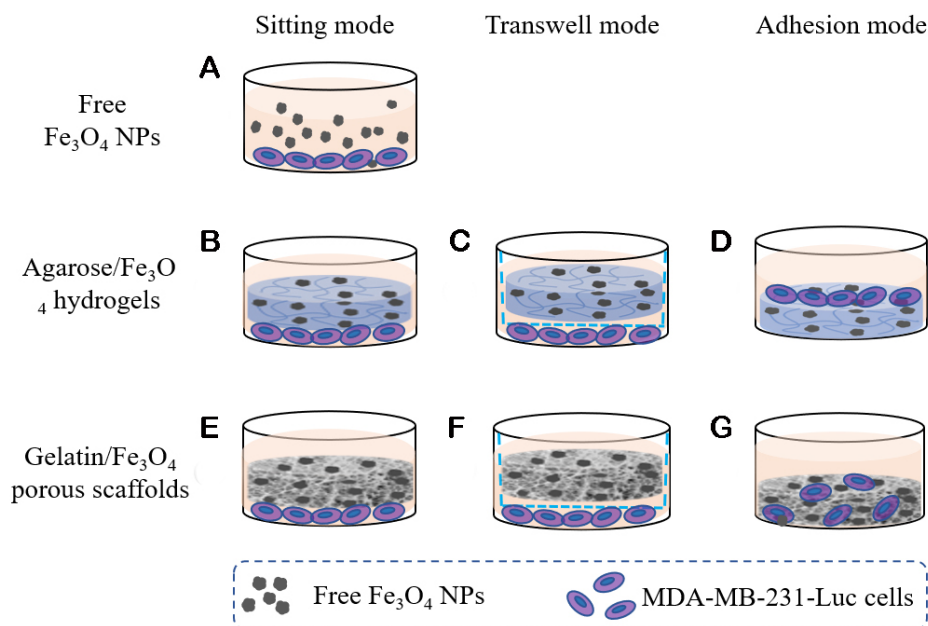


Figure 1. Anticancer experimental scheme of free Fe₃O₄ NPs (A), agarose/Fe₃O₄ hydrogels (B-D), and gelatin/Fe₃O₄ porous scaffolds (E-G). Three modes (sitting, transwell, and adhesion modes) were used to simulate the cells near or far away from or directly adhered to the matrices.

MATERIALS AND METHODS

Materials

Iron (II) chloride tetrahydrate (FeCl₂·4H₂O, ≥ 99%), iron (III) chloride hexahydrate (FeCl₃·6H₂O, ≥ 97%), and sodium citrate tribasic dihydrate (≥ 99%) were purchased from Sigma-Aldrich (St. Louis, MO, USA). Diethylene glycol (DEG, 99%), sodium hydroxide (NaOH, 99.99%), acetic acid, ethanol, ethyl acetate, 1-ethyl-3-(3-dimethylaminopropyl) carbodiimide (EDC), and N-hydroxysuccinimide (NHS) were obtained from Wako Pure Industries, Ltd. (Tokyo, Japan). N-methyldiethanolamine (NMDEA, 99%) was purchased from Tokyo Kasei. Kogyo Co., Ltd, and gelatin (porcine) was obtained from Nitta Gelatin (Osaka, Japan).

Synthesis and Characterization of Fe₃O₄ NPs

Fe₃O₄ NPs were synthesized using Fe (II) and Fe (III) in a mixture solution of DEG and NMDEA (1:1, v/v)^[49,50]. First, 4 mmol FeCl₂·4H₂O and 2 mmol FeCl₃·z'·6H₂O were added and dissolved in an 80 mL polyols mixture under a nitrogen atmosphere at room temperature. Next, 40 mL of 400 mM NaOH in a polyol mixture was dropped into the iron salts solution and stirred for 3 h. Then, the mixed solution was heated to 220 °C and reacted for 12 h under the protection of nitrogen. After the reaction, the black precipitates were collected and washed with ethanol/ethyl acetate solvent (1:1, v/v) three times to obtain bare Fe₃O₄ NPs. The obtained bare Fe₃O₄ NPs were redispersed in sodium citrate aqueous solution and reacted at 60 °C for 24 h to modify the Fe₃O₄ NPs with citrate anions. After centrifugation, washing, and lyophilization, the citrate-modified Fe₃O₄ NPs were obtained. The prepared Fe₃O₄ NPs were redispersed in PBS to obtain the Fe₃O₄ NPs colloidal solution at a concentration of 5 mg mL⁻¹, 10 mg mL⁻¹, and 20 mg mL⁻¹, which were named free Fe₃O₄-5 (5 mg mL⁻¹), free Fe₃O₄-10 (10 mg mL⁻¹), and free Fe₃O₄-20 (20 mg mL⁻¹), respectively. The structure and mean diameter of the citrate-modified Fe₃O₄ NPs were analyzed by a transmission electron microscope (TEM, JEOL 2100F, Japan). The hydrodynamic size of the citrate-modified Fe₃O₄ NPs was analyzed by dynamic light scattering (DLS, Beckman Coulter, USA).

Preparation and characterization of agarose/Fe₃O₄ hydrogels and gelatin/Fe₃O₄ scaffolds

The agarose/Fe₃O₄ hydrogels were prepared by dispersing the citrate-modified Fe₃O₄ NPs in agarose hydrogels. At first, 0.1 g agarose was dissolved in 5 mL PBS at 110 °C. After the temperature of the agarose solution was cooled to around 40 °C, the citrate-modified Fe₃O₄ NPs suspension solution was added to prepare 1% agarose solution with Fe₃O₄ NPs at 5 mg mL⁻¹, 10 mg mL⁻¹, and 20 mg mL⁻¹. Agarose hydrogels without Fe₃O₄ NPs were prepared as a control. After vortexing, the mixture was added into cylinder molds (Φ10 mm × H4 mm) and immediately transformed into a 4 °C refrigerator for 30 min to form agarose/Fe₃O₄ hydrogels. The obtained hydrogels with different NP concentrations were referred to as agarose/Fe₃O₄-5 (5 mg mL⁻¹), agarose/Fe₃O₄-10 (10 mg mL⁻¹), and agarose/Fe₃O₄-20 (20 mg mL⁻¹).

The porous scaffolds of gelatin and Fe₃O₄ NPs were prepared by using ice particulate porogen methods^[51-61]. Firstly, ice particulates with a diameter of 250-355 μm were obtained by spraying Milli-Q water into liquid nitrogen and sieved in a low-temperature chamber. Gelatin solution (8%, wt/v) in 70% acetic acid was mixed with the citrate-modified Fe₃O₄ NP suspension solution (1:1, v/v) to obtain gelatin/Fe₃O₄ NP mixture solution. Then, the temperature-balanced ice particulates (-4 °C) were added to the gelatin/Fe₃O₄ NP mixture solution (7:3, wt/v) in a -4 °C chamber, and the final concentrations of Fe₃O₄ NPs in the mixture solution were 5, 10, and 20 mg cm⁻³, respectively. The mixture was transformed into a silicone frame and frozen at -20 °C for 12 h and -80 °C for 4 h. Then, the lyophilized constructs were cross-linked by EDC (50.0 mM) and NHS (20.0 mM) in a series of ethanol/water mixture solvents [95/5, 90/10, and 85/5 (v/v)] each for 8 h. Finally, the cross-linked scaffolds were immersed in 0.1 M glycine solution to block the activated residual carboxyl groups. The lyophilized gelatin/Fe₃O₄ NPs composite scaffolds prepared with different concentrations of citrate-modified Fe₃O₄ NPs were referred to as gelatin/Fe₃O₄-5 (5 mg cm⁻³), gelatin/Fe₃O₄-10 (10 mg cm⁻³), and gelatin/Fe₃O₄-20 (20 mg cm⁻³). A control scaffold without Fe₃O₄ NPs was also prepared and referred to as a gelatin porous scaffold. An optical microscope (Olympus, Japan) and a scanning electron microscope (SEM, Hitachi S-4800, Tokyo, Japan) were used to observe the gross appearances and the inner pore structures of the lyophilized agarose/Fe₃O₄ hydrogels and gelatin/Fe₃O₄ scaffolds.

Magnetic thermal property of Fe₃O₄ NPs in different matrices

The magnetic thermal properties of free Fe₃O₄ NPs, agarose/Fe₃O₄ hydrogels, and gelatin/Fe₃O₄ porous scaffolds were investigated under AMF irradiation. First, 300 μL of free Fe₃O₄-5, Fe₃O₄-10, and Fe₃O₄-20 solutions were added in 0.5 mL Eppendorf tubes, respectively. The samples were placed in the center of Double H CoilSets AMF (Frequency: 373.6 kHz; Field intensity: 130 Gauss) for 10 min using a D5 series machine (nB nanoScale BioMagnetics, Zaragoza, Spain). Subsequently, the IR1 thermal imaging system (nB nanoScale Biomagnetics, Zaragoza, Spain) was used to record the temperature change of different samples. Triplicate samples were used for each measurement.

Similarly, 300 μL of aqueous agarose solution without or with 5 mg mL⁻¹, 10 mg mL⁻¹, and 20 mg mL⁻¹ of Fe₃O₄ NPs were added in 0.5 mL Eppendorf tubes, respectively. All samples were immediately transformed into a 4 °C refrigerator for 30 min to form agarose hydrogel, agarose/Fe₃O₄-5, agarose/Fe₃O₄-10, and agarose/Fe₃O₄-20 hydrogel samples. Before exposure to AMF, the agarose/Fe₃O₄ hydrogel samples were balanced at room temperature for 2 h. The temperature change of the agarose/Fe₃O₄ hydrogel samples was measured and recorded during 10 min AMF irradiation at 373.6 kHz of frequency and a field intensity of 130 Gauss. Triplicate samples were used for each measurement.

The gelatin/Fe₃O₄ porous scaffolds were molded into cylinder discs (Φ10 mm × H4 mm) and hydrated with pure water (300 μL/disc) in silicone frames. The gelatin/Fe₃O₄ porous scaffold discs were exposed to AMF for 10 min (Frequency: 373.6 kHz; Field intensity: 130 Gauss), and the temperature change was measured.

Triplicate samples were used for each measurement.

Anticancer effect of Fe₃O₄ NPs in different matrices

The anticancer effect of free Fe₃O₄ NPs, agarose/Fe₃O₄ hydrogels, and gelatin/Fe₃O₄ porous scaffolds was investigated by incubating breast cancer cells in the different matrices under AMF irradiation^[55-61]. Three culture modes were used to simulate the cells directly adhered to, near, or far away from the matrices [Figure 1]. The cells were seeded in wells of cell culture plates, and then free Fe₃O₄ NPs, agarose/Fe₃O₄ hydrogels, or gelatin/Fe₃O₄ porous scaffolds were added to the adhered cells. The hydrogels and porous scaffolds were sitting on the adhered cells (sitting mode), which simulated the cells near the matrices. The second mode was a transwell mode by seeding cells in the bottom wells of the transwell plates and placing the hydrogels and porous scaffolds in the inserts, which simulated the cells far away from the matrices. The third mode was an adhesion mode by seeding cells on the hydrogels or in the porous scaffolds to allow the cells to adhere to the hydrogels or in the pores of the porous scaffolds, which simulated the cells directly adhering to the matrices.

Anticancer effect of free Fe₃O₄ NPs

The free Fe₃O₄ NPs could only be added in the culture medium. Therefore, only the sitting mode was used for investigating the anticancer effect of free Fe₃O₄ NPs. The sub-cultured MDA-MB-231-Luc cells were harvested and resuspended in a culture medium at a concentration of 2.5×10^5 cells mL⁻¹. A 200 µL cell suspension solution was seeded in the wells of a 48-well plate (5×10^4 cells well⁻¹). After culture in a humidified incubator (5% CO₂, 37 °C) for 24 h, the culture medium was removed, and another 200 µL fresh culture medium was added. Then, 300 µL medium, without or with free Fe₃O₄-5, free Fe₃O₄-10 and free Fe₃O₄-20, was added to the wells, respectively. After co-incubation for 2 h, the wells were exposed to AMF (frequency: 373.6 kHz of; field intensity: 130 Gauss) for 10 min. Cell viability before and after AMF irradiation was visualized by live/dead staining and quantitatively analyzed by WST-1 assay. Triplicate samples were used for each measurement.

Anticancer effect of agarose/Fe₃O₄ hydrogels

The three culture modes were used for the investigation of the anticancer effect of the agarose/Fe₃O₄ hydrogel. For the sitting mode, the MDA-MB-231-Luc cells were seeded and cultured in the wells of a 48-well plate, as mentioned above. After the culture medium was changed with another 200 µL fresh medium, the agarose and agarose/Fe₃O₄ hydrogel discs (Φ10 mm × H4 mm) were placed on the cells. After co-incubation for 2 h, the wells were exposed to AMF (frequency: 373.6 kHz of; field intensity: 130 Gauss) for 10 min. Cell viability was investigated by live/dead staining and WST-1 assay before and after AMF irradiation. Triplicate samples were used for each measurement.

For the transwell mode, the MDA-MB-231-Luc cells were seeded in the centers of the wells of 24-well plate by using donut-shaped silicone rings (inner diameter 10 mm, outer diameter: 16 mm, height: 2 mm). The seeded cell number was the same (5×10^4 cells well⁻¹). The agarose/Fe₃O₄ hydrogel discs were placed on the transwell inserts and co-cultured with the cells on the bottom wells. The transwell plates containing cells and discs were irradiated by AMF (frequency: 373.6 kHz; magnetic field: 130 Gauss) for 10 min. Before and after AMF irradiation, cell viability was investigated, as mentioned above. Triplicate samples were used for each measurement.

For the adhesion mode, the agarose/Fe₃O₄ hydrogel discs (Φ10 mm × H4 mm) were put in the wells of a 48-well plate. Subsequently, 200 µL of cell suspension solution was seeded on the agarose/Fe₃O₄ hydrogel discs. After 2 h incubation, the plates were exposed to AMF (frequency: 373.6 kHz; magnetic field: 130 Gauss) for

10 min, and cell viability was investigated, as mentioned above. Triplicate samples were used for each measurement.

Anticancer effect of gelatin/Fe₃O₄ porous scaffolds

The three culture modes were also used for the investigation of the anticancer effect of the gelatin and gelatin/Fe₃O₄ porous scaffolds. All the experiment procedures were the same as those of agarose/Fe₃O₄ hydrogel discs by using the porous scaffold discs (Φ10 mm × H4 mm). Triplicate samples were used for each measurement.

RESULTS

Characterization of Fe₃O₄ NPs

The morphology and size of the citrate-modified Fe₃O₄ NPs were characterized by TEM. As shown in [Figure 2A-C](#), the NPs displayed a flower-like shape, which should have a good magnetic-thermal conversion capacity for MH. They had an average size of 30.8 ± 5.7 nm from the TEM images. The hydrodynamic size of the citrate-modified Fe₃O₄ NPs was measured in aqueous solution by DLS, and the hydrodynamic size was 108.5 ± 28.5 nm [[Figure 2D](#)].

Characterization of agarose/Fe₃O₄ hydrogels and gelatin/Fe₃O₄ porous scaffolds

The agarose/Fe₃O₄ hydrogel discs are shown in [Figure 3A](#). As the concentration of Fe₃O₄ NPs increased, the appearance of agarose/Fe₃O₄ hydrogel changed from transparent to black. SEM observation of the lyophilized agarose/Fe₃O₄ hydrogel discs showed that the agarose hydrogels with different amounts of Fe₃O₄ NPs had similar structures [[Figure 3B](#)]. They had spindle-shaped pores. The gelatin porous scaffold without Fe₃O₄ NPs was white, while the gelatin/Fe₃O₄ porous scaffolds became gray (gelatin/Fe₃O₄-5), dark gray (gelatin/Fe₃O₄-10), and black (gelatin/Fe₃O₄-20) [[Figure 3C](#)]. The gelatin and gelatin/Fe₃O₄ porous scaffolds had the same pore structures. They had large spherical pores that were surrounded by some small pores [[Figure 3D](#)]. The large spherical pores were controlled by the ice particulates that were used as a porogen material. The results indicated that the embedding of Fe₃O₄ NPs did not affect the pore structures of hydrogels and porous scaffolds.

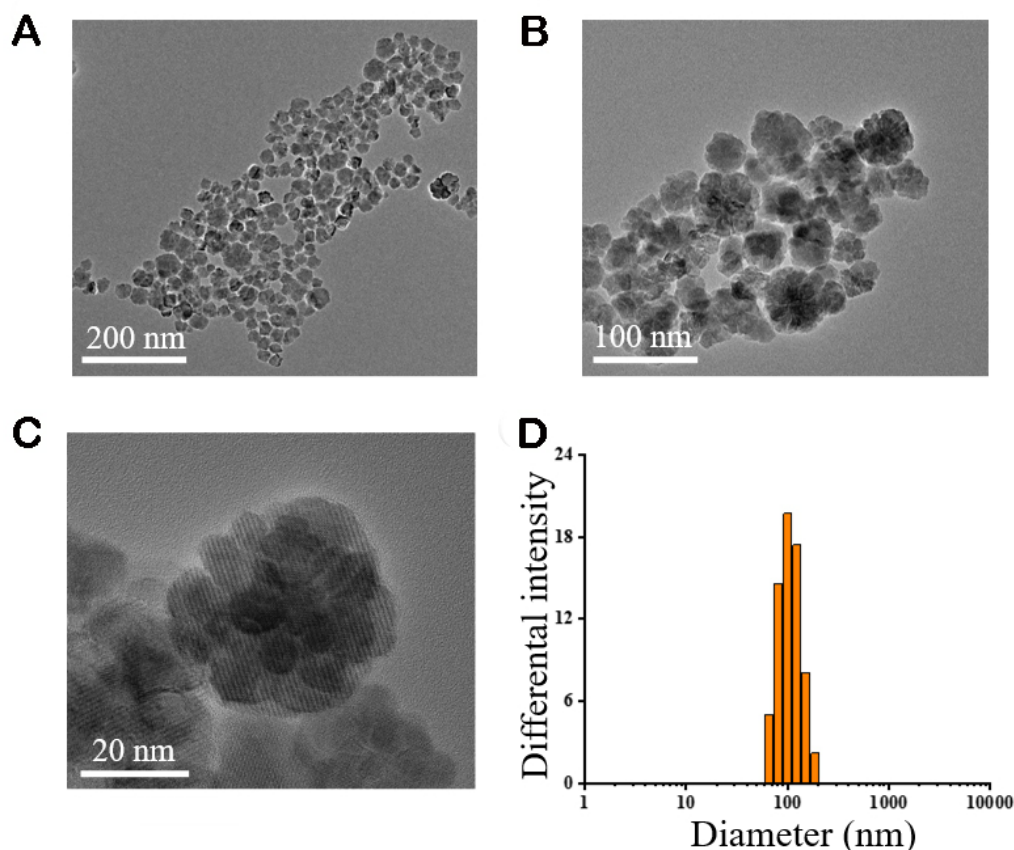
Magnetic thermal property of Fe₃O₄ NPs in different matrices

The magnetic thermal properties of Fe₃O₄ NPs in PBS, agarose hydrogels, and gelatin porous scaffolds were investigated by applying AMF (frequency: 373.6 kHz; field: 130 Gauss) for 10 min, and the results are shown in [Figure 4](#) and [Table 1](#). The temperature of PBS, agarose hydrogels, and gelatin porous scaffolds without Fe₃O₄ NPs had no obvious change after AMF irradiation [[Figure 4A](#) and [Table 1](#)]. The results suggested that PBS, agarose hydrogels, and gelatin porous scaffolds had no magnetic-thermal conversion capacity in the absence of Fe₃O₄ NPs. When Fe₃O₄ NPs were added to PBS, hydrogels, and porous scaffolds, the temperature change significantly increased under AMF irradiation.

The temperature change increased with the irradiation time and became plateau after 10 min AMF irradiation [[Figure 4B-D](#)]. The temperature change of free Fe₃O₄-5, agarose/Fe₃O₄-5, and gelatin/Fe₃O₄-5 was 24.1 ± 1.7 °C, 14.0 ± 0.3 °C, and 5.2 ± 0.3 °C, respectively, after 10 min AMF irradiation [[Figure 4B](#) and [Table 1](#)]. The temperature change of free Fe₃O₄-10, agarose/Fe₃O₄-10, and gelatin/Fe₃O₄-10 increased to 38.3 ± 1.1 °C, 22.8 ± 1.7 °C, and 9.1 ± 0.5 °C, respectively, after 10 min AMF irradiation [[Figure 4C](#) and [Table 1](#)]. The temperature change of free Fe₃O₄-20, agarose/Fe₃O₄-20, and gelatin/Fe₃O₄-20 increased to 65.7 ± 1.4 °C, 33.8 ± 1.0 °C, and 13.2 ± 0.4 °C, respectively, after 10 min AMF irradiation [[Figure 4D](#) and [Table 1](#)]. The results indicated that the temperature change of free Fe₃O₄ NPs, agarose/Fe₃O₄, and gelatin/Fe₃O₄ was positively correlated with the concentration of Fe₃O₄ NPs. Increasing the concentration of Fe₃O₄ NPs resulted in a bigger temperature change.

Table 1. Magnetic thermal property of Fe₃O₄ NPs in different matrices under AMF irradiation [Mean ± SD (n = 3)]

Sample	ΔT of PBS (°C)	ΔT of agarose hydrogel (°C)	Percentage compared to free NPs	ΔT of gelatin porous scaffold (°C)	Percentage compared to free NPs
No Fe ₃ O ₄ NPs	0.7 ± 0.2	1.0 ± 0.2	/	0.8 ± 0.2	/
Fe ₃ O ₄ -5 mg mL ⁻¹	24.1 ± 1.7	14.0 ± 0.3	58.1%	5.2 ± 0.3	21.6%
Fe ₃ O ₄ -10 mg mL ⁻¹	38.3 ± 1.1	22.8 ± 1.7	59.5%	9.1 ± 0.5	23.8%
Fe ₃ O ₄ -20 mg mL ⁻¹	65.7 ± 1.4	33.8 ± 1.0	51.5%	13.2 ± 0.4	20.1%

**Figure 2.** TEM images of citrate-modified Fe₃O₄ NPs at low (A), middle (B), and high magnifications (C). Hydrodynamic size distribution of citrate-modified Fe₃O₄ NPs (D).

The free Fe₃O₄ NPs in PBS showed the highest temperature change. The temperature change was reduced to 51.5%-59.5% when the Fe₃O₄ NPs were embedded in agarose hydrogels. The temperature change was further decreased to 20.1%-23.8% when the Fe₃O₄ NPs were embedded in gelatin porous scaffolds. The results indicated that the matrix where Fe₃O₄ NPs were embedded could significantly affect the magnetic-thermal conversion property of Fe₃O₄ NPs.

Anticancer effect of free Fe₃O₄ NPs

MH uses the Fe₃O₄ NPs to absorb and convert magnetic energy to heat and raise the local temperature, thereby killing the cancer cells. In this study, MDA-MB-231-Luc cells were cultured in a culture medium supplemented with free Fe₃O₄ NPs under different concentrations. Cell viability before and after AMF irradiation was investigated by live/dead staining and WST-1 assay [Figure 5]. Before AMF irradiation,

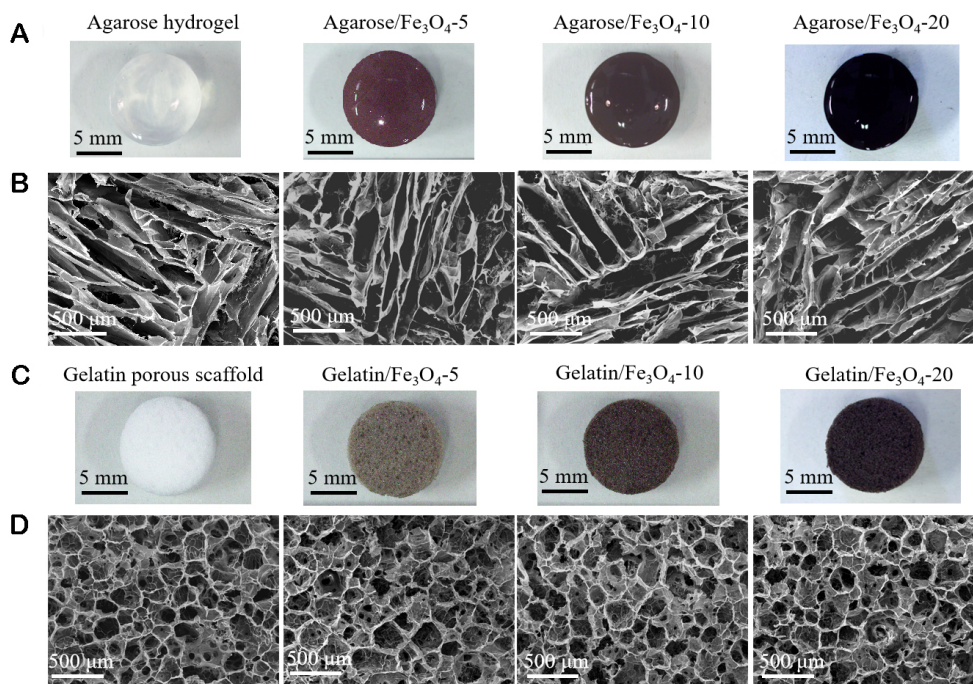


Figure 3. Gross appearances (A) and SEM images (B) of agarose and agarose/ Fe_3O_4 hydrogels with different concentrations of citrate-modified Fe_3O_4 NPs. Gross appearances (C) and SEM images (D) of gelatin and gelatin/ Fe_3O_4 porous scaffold with different concentrations of citrate-modified Fe_3O_4 NPs.

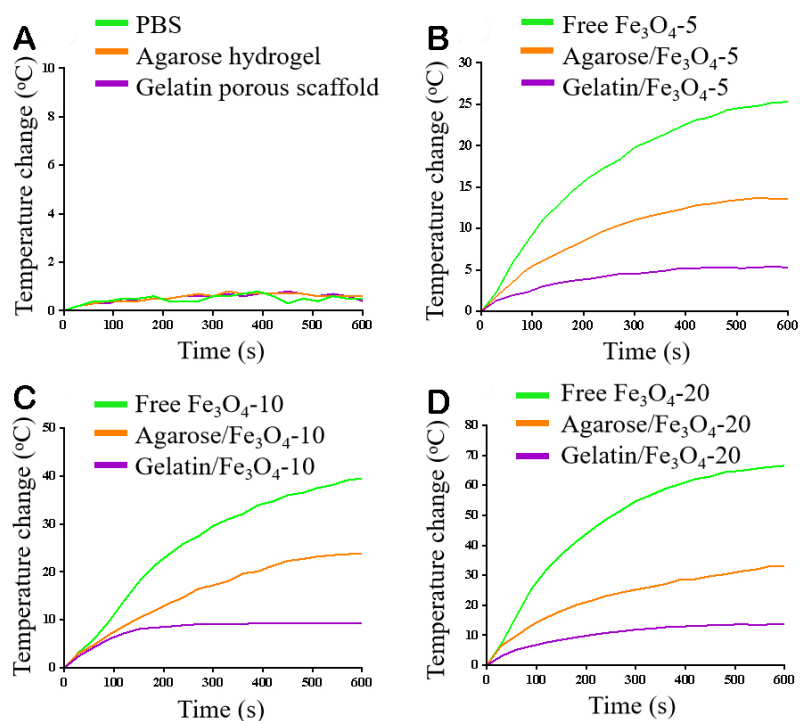


Figure 4. Heating curves of PBS, agarose hydrogels, and gelatin porous scaffolds without Fe_3O_4 NPs (A) and containing 5 mg mL^{-1} Fe_3O_4 NPs (B), 10 mg mL^{-1} Fe_3O_4 NPs (C), and 20 mg mL^{-1} Fe_3O_4 NPs (D) during AMF irradiation.

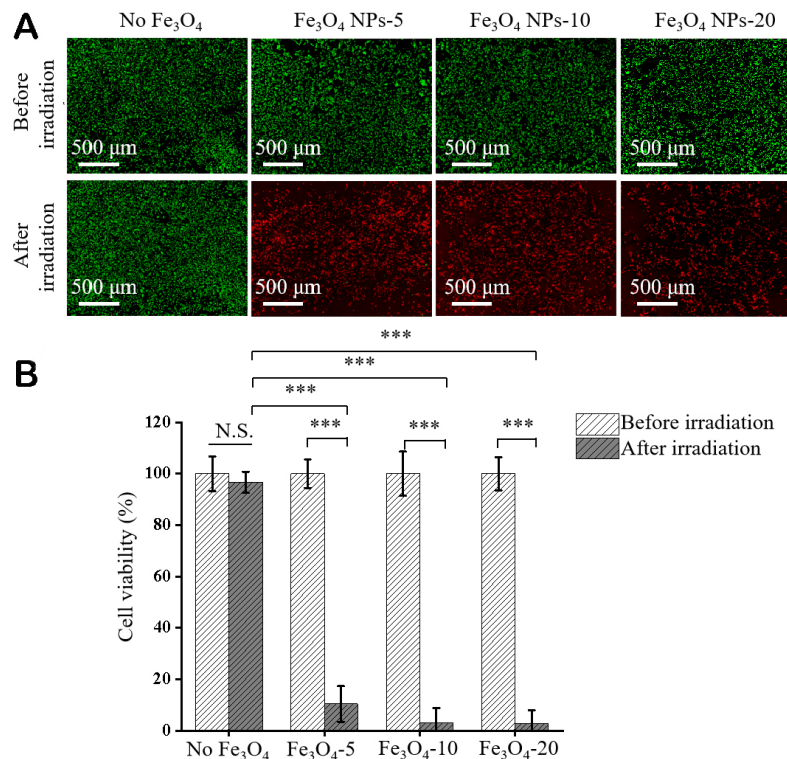


Figure 5. Anticancer effect of free Fe₃O₄ NPs. Live/dead staining of MDA-MB-231-Luc cells cultured without or with free Fe₃O₄ NPs before and after AMF irradiation (live cell: green fluorescence, dead cells: red fluorescence) (A). Quantified cell viability during culture without or with free Fe₃O₄ NPs before and after AMF irradiation (B). Cell viability was normalized to that cultured with PBS without free Fe₃O₄ NPs before AMF irradiation. Data are the mean ± SD (*n* = 3). Significant difference: ****P* < 0.001. N.S.: no significant difference.

almost all the cells were alive [Figure 5A]. After AMF irradiation, the cells cultured without Fe₃O₄ NPs were still alive, while almost all the cells cultured with Fe₃O₄-5, Fe₃O₄-10, and Fe₃O₄-20 were dead. The results indicated that the cells cultured with free Fe₃O₄ NPs at a concentration of 5, 10, and 20 mg mL⁻¹ were completely killed after AMF irradiation. Some of the dead cells cultured with 20 mg mL⁻¹ free Fe₃O₄ NPs detached from the culture wells.

The WST-1 assay showed that the cells cultured without or with free Fe₃O₄ NPs had the same high viability before AMF irradiation [Figure 5B]. After AMF irradiation, the viability of cells cultured without free Fe₃O₄ NPs did not change significantly, while the viability of cells cultured with free Fe₃O₄ NPs significantly decreased after AMF irradiation. Viability of cells cultured with 5, 10, and 20 mg mL⁻¹ free Fe₃O₄ NPs decreased to 10.3% ± 6.9%, 3.1% ± 5.8%, and 2.7% ± 5.2%, respectively. All the live/dead staining and WST-1 assay results indicated that the breast cancer cells could be killed by the free Fe₃O₄ NPs under AMF irradiation. A higher concentration of free Fe₃O₄ NPs resulted in a higher killing effect. The killing effect of free Fe₃O₄ NPs should be due to the high temperature generated by free Fe₃O₄ NPs during AMF irradiation [Figure 4]. A higher concentration of the Fe₃O₄ NPs could generate higher temperatures and enhance the killing efficiency.

Anticancer effect of agarose/Fe₃O₄ hydrogels

The interaction between cells and agarose/Fe₃O₄ hydrogels should be different from that between cells and free Fe₃O₄ NPs. The cells could be near the hydrogels without adhesion to the hydrogels. The cells could also

be far away from the hydrogels or directly adhere to the hydrogels. To simulate these interactions between the breast cancer cells and hydrogels, three culture modes were used to investigate the MH anticancer effect of the agarose/Fe₃O₄ hydrogels. When the MDA-MB-231-Luc cells were cultured near the agarose/Fe₃O₄ hydrogel discs (sitting mode), most of the cells near the agarose/Fe₃O₄-5 hydrogel discs were dead, and cell viability decreased significantly after AMF irradiation [Figure 6A and B]. Almost all the cells near the agarose/Fe₃O₄-10 and agarose/Fe₃O₄-20 were dead, and their viability further decreased to the lowest level. The cell viability near agarose/Fe₃O₄-5, agarose/Fe₃O₄-10, and agarose/Fe₃O₄-20 decreased to 11.3% ± 4.8%, 3.9% ± 2.2%, and 3.6% ± 5.1%, respectively, after AMF irradiation [Figure 6B]. However, the cells near the agarose hydrogel discs without Fe₃O₄ NPs were alive, and their viability did not change before and after AMF irradiation.

When the breast cancer cells were cultured far away from the agarose/Fe₃O₄ hydrogel discs (transwell mode), the agarose/Fe₃O₄ hydrogels with a high concentration of Fe₃O₄ NPs (agarose/Fe₃O₄-10 and agarose/Fe₃O₄-20) could kill almost all the cells and significantly decrease cell viability to very low level by AMF irradiation [Figure 6C and D]. However, only a small number of cells cultured with the agarose/Fe₃O₄-5 were killed by AMF irradiation. After AMF irradiation, cell viability in the transwell of agarose/Fe₃O₄-5, agarose/Fe₃O₄-10, and agarose/Fe₃O₄-20 decreased to 85.7% ± 5.7%, 6.0% ± 3.5% and 2.8% ± 5.9%, respectively [Figure 6D].

The breast cancer cells adhered on the agarose/Fe₃O₄ hydrogel discs (adhesion mode) were most efficiently killed by AMF irradiation. Almost all the cells cultured with all the agarose/Fe₃O₄ hydrogel discs were dead, and their viability was the lowest compared to the sitting and transwell modes [Figure 6E and F]. Viability of breast cancer cells adhered on the agarose/Fe₃O₄-5, agarose/Fe₃O₄-10, and agarose/Fe₃O₄-20 decreased to 7.1% ± 1.2%, 2.7% ± 4.6%, and 2.3% ± 6.5%, respectively, after AMF irradiation [Figure 6F]. This should be due to the direct heating effect of the cells by the agarose/Fe₃O₄ hydrogels when the cells adhered to the hydrogels.

Anticancer effect of gelatin/Fe₃O₄ porous scaffolds

The anticancer effect of gelatin/Fe₃O₄ porous scaffolds was investigated by using the same methods as those used for the agarose/Fe₃O₄ hydrogels [Figure 7]. The cells cultured with the gelatin porous scaffold before and after AMF irradiation and with the gelatin/Fe₃O₄ porous scaffolds before AMF irradiation were alive with high viability. However, after AMF irradiation, some dead cells were observed in the gelatin/Fe₃O₄-5 and gelatin/Fe₃O₄-10, and almost all the cells were dead in the gelatin/Fe₃O₄-20 when the cells were cultured near the scaffolds [Figure 7A] or adhered in the scaffolds [Figure 7E]. When the cells were cultured far away from the scaffolds, a small part of the cells cultured with the gelatin/Fe₃O₄-20 were killed [Figure 7C]. After AMF irradiation, the viability of breast cancer cells cultured with gelatin/Fe₃O₄-5, gelatin/Fe₃O₄-10, and gelatin/Fe₃O₄-20 was 94.2% ± 9.1%, 80.3% ± 7.8%, and 6.2% ± 5.2% in sitting modes [Figure 7B], 99.8% ± 5.0%, 96.0% ± 5.1%, and 87.0% ± 3.4% in transwell modes [Figure 7D] and 90.8% ± 2.5%, 67.8% ± 3.2%, and 4.7% ± 3.4% in adhesion modes [Figure 7F], respectively.

The above results indicated that the breast cancer cells could be killed by either free Fe₃O₄ NPs, agarose/Fe₃O₄ hydrogels, or gelatin/Fe₃O₄ porous scaffolds. However, the anticancer effect depended on the matrices and interactions. The free Fe₃O₄ NPs showed the highest killing effect, while the gelatin/Fe₃O₄ porous scaffolds showed the lowest. Matrices used to embed Fe₃O₄ NPs showed an inhibitory influence on the killing effect of Fe₃O₄ NPs. In particular, the porous scaffolds had a more inhibitory influence than the hydrogels. This should be due to the influence of matrices on the magnetic thermal property of the Fe₃O₄ NPs. The interaction between breast cancer cells and Fe₃O₄ NP-embedded hydrogels or porous scaffolds

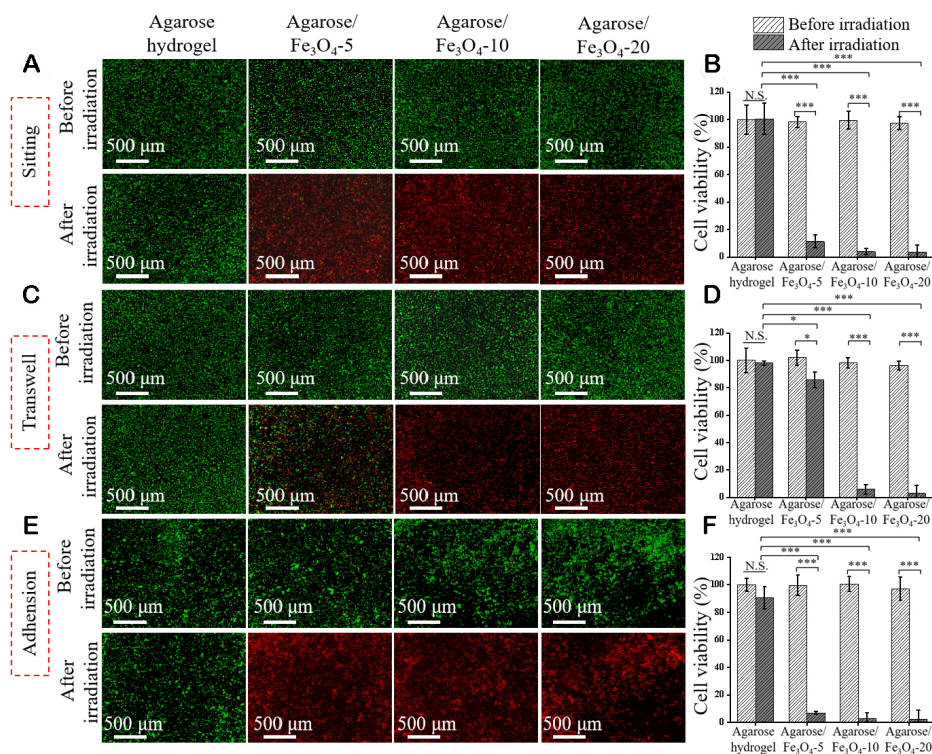


Figure 6. Anticancer effect of agarose/ Fe_3O_4 hydrogels. Live/dead staining of MDA-MB-231-Luc cells cultured with the agarose/ Fe_3O_4 hydrogel discs via sitting (A), transwell (C), and adhesion (E) modes before and after AMF irradiation (live cell: green fluorescence, dead cells: red fluorescence). Quantified cell viability during culture without or with agarose/ Fe_3O_4 hydrogel discs via sitting (B), transwell (D), and adhesion (F) modes before and after AMF irradiation. Cell viability was normalized to that cultured with agarose hydrogel without free Fe_3O_4 NPs before AMF irradiation. Data are the mean \pm SD ($n = 3$). Significant difference: * $P < 0.05$, *** $P < 0.001$. N.S.: no significant difference.

could also affect their killing effect. The cells directly adhered to the hydrogels or in the porous scaffolds could be more easily killed by AMF irradiation. The cells that were far away from the hydrogels or scaffolds were less affected by the heat generated by the Fe_3O_4 NP-loaded hydrogels or porous scaffolds.

DISCUSSION

Fe_3O_4 NPs have been widely used for MH because of their excellent magnetic-thermal conversion property. Investigation of the influence of matrices surrounding Fe_3O_4 NPs on the magnetic-thermal conversion property and anticancer effect of Fe_3O_4 NPs is important for the biomedical application of Fe_3O_4 NPs to maximize their therapeutic effect. In this study, the magnetic-thermal conversion property and anticancer effect of free Fe_3O_4 NPs and Fe_3O_4 NPs embedded in agarose hydrogels and gelatin porous scaffolds were compared because agarose hydrogels and gelatin porous scaffolds have been frequently used to embed therapeutic drugs and NPs. During AMF irradiation, the temperature change of free Fe_3O_4 NPs, agarose/ Fe_3O_4 , and gelatin/ Fe_3O_4 was positively correlated with the concentration of Fe_3O_4 NPs and irradiation time. Increasing the concentration of Fe_3O_4 NPs resulted in an increase of temperature alteration.

The matrices used to embed the Fe_3O_4 NPs could affect the magnetic thermal properties of Fe_3O_4 NPs. The free Fe_3O_4 NPs showed the best magnetic thermal properties. Embedding in hydrogels or porous scaffolds decreased the temperature change of Fe_3O_4 NPs during AMF irradiation. The temperature change of Fe_3O_4

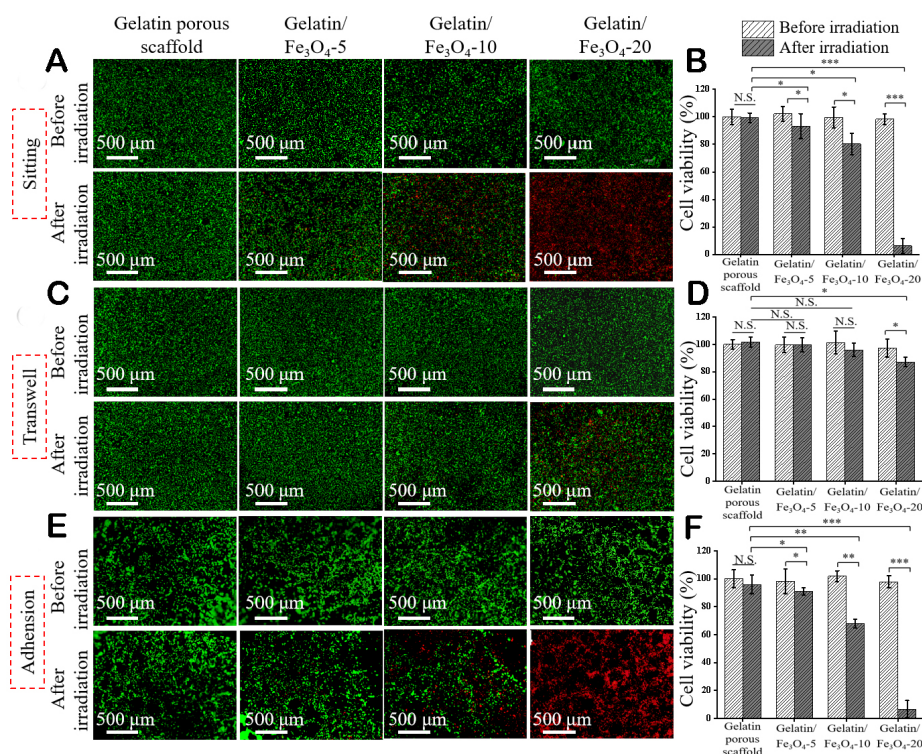


Figure 7. Anticancer effect of gelatin/Fe₃O₄ porous scaffolds. Live/dead staining of MDA-MB-231-Luc cells cultured with gelatin/Fe₃O₄ scaffold discs via sitting (A), transwell (C), and adhesion (E) modes before and after AMF irradiation (live cells: green fluorescence, dead cells: red fluorescence). Quantified cell viability after culture with gelatin/Fe₃O₄ scaffold discs via sitting (B), transwell (D), and adhesion (F) modes before and after AMF irradiation. Cell viability was normalized to that cultured with gelatin porous scaffold without free Fe₃O₄ NPs before AMF irradiation. Data are the mean ± SD (n = 3). Significant difference: *P < 0.05, **P < 0.01, ***P < 0.001. N.S.: no significant difference.

NPs in agarose hydrogels and porous scaffolds was decreased to 51.5%–59.5% and 20.1%–23.8% of that of free Fe₃O₄ NPs, respectively. The results of Fe₃O₄ NPs embedded in hydrogels were the same as the previously reported influence on their magnetic thermal property. Embedding in porous scaffolds further decreased the magnetic-thermal conversion capacity of Fe₃O₄ NPs.

The matrix influence should be due to the variation of Brownian relaxation of Fe₃O₄ NPs in the matrices. The heat generation mechanism of MNPs exposed to AMF includes Néel relaxation and Brownian relaxation^[62]. Néel relaxation refers to the heating due to the energy loss produced by the rotation of individual magnetic moments within the MNPs under AMF irradiation, and Brownian relaxation refers to the rotation of entire MNPs to produce heat^[63,64]. The Néel relaxation of Fe₃O₄ NPs in the hydrogels and porous scaffolds might not change. However, the matrices should affect the Brownian relaxation of Fe₃O₄ NPs. The Brownian relaxation of Fe₃O₄ NPs under AMF irradiation should be partially suppressed in the agarose hydrogel, leading to a decreased heating effect of Fe₃O₄ NPs. When the Fe₃O₄ NPs were embedded in gelatin porous scaffolds, the Fe₃O₄ NPs were tightly constrained in the gelatin fibers, and the Brownian relaxation of Fe₃O₄ NPs should be heavily inhibited. Therefore, the Fe₃O₄ NPs in the gelatin porous scaffolds generated heat predominantly through Néel relaxation.

Due to the influence of matrices on the magnetic thermal property of Fe₃O₄ NPs, the anticancer effect of Fe₃O₄ NPs was also dependent on the matrices. The breast cancer cells cultured with free Fe₃O₄ NPs were most efficiently killed by AMF irradiation. Embedding in agarose hydrogels and gelatin porous scaffolds

significantly decreased the killing effect of Fe₃O₄ NPs. Embedding in gelatin porous scaffolds showed the lowest killing effect. The decreased anticancer effects of Fe₃O₄ NPs embedded in agarose hydrogels and gelatin porous scaffolds could be explained by the decreased temperature change under AMF irradiation. The results of this study revealed that the magnetic thermal property and anticancer effect of Fe₃O₄ NPs were affected by their surrounding microenvironmental matrices. Although cancer cells and normal cells have different cytoplasmic properties^[65,66] and cancer cells are more sensitive to heat compared to normal cells^[67,68], the heat generated by Fe₃O₄ NPs under AMF irradiation should also affect viability of normal cells. The influence of Fe₃O₄ NP-embedded hydrogels and porous scaffolds on normal cell viability needs further investigation for controlling temperature to efficiently ablate cancer cells while minimizing negative effects on normal cells.

Furthermore, the interaction between the breast cancer cells and the Fe₃O₄ NPs could affect the killing effect. The free Fe₃O₄ NPs could be uptaken by breast cancer cells and generate heat inside the cells under AMF irradiation. When the Fe₃O₄ NP-embedded agarose hydrogels were applied, the breast cancer cells could be adhered to the hydrogel, near the hydrogels, or far away from the hydrogels. For the Fe₃O₄ NP-embedded gelatin porous scaffolds, breast cancers could enter the scaffolds and adhere in the scaffolds, near the scaffolds, or far away from the scaffolds. Three cultured models (sitting, transwell, and adhesion modes) were used to simulate the interaction between the cells and matrices. The Fe₃O₄ NPs embedded in the agarose hydrogels and gelatin porous scaffolds should be less or not uptaken by the cells if the hydrogels and scaffolds were not degraded. Therefore, the heat should be generated by the scaffolds and then transmitted to the breast cancer cells for ablation. The breast cancer cells adhered to the hydrogels or in the scaffolds were most efficiently ablated. The cells far away from the hydrogels and porous scaffolds were less affected. The results should be due to the heat transmission effect of the hydrogels and porous scaffolds.

CONCLUSION

In this study, the magnetic thermal property and ablation effect of free Fe₃O₄ NPs and Fe₃O₄ NPs embedded in agarose hydrogels and gelatin porous scaffolds were investigated to elucidate the influence of microenvironmental matrices on these properties. The flower-like Fe₃O₄ NPs were embedded in agarose hydrogels and gelatin porous scaffolds. Their magnetic thermal property and anticancer effects were compared with those of free Fe₃O₄ NPs. Under AMF irradiation, the free Fe₃O₄ NPs showed the highest temperature increase. Embedding in agarose hydrogels and gelatin porous scaffolds inhibited the heating capacity of Fe₃O₄ NPs and decreased the temperature change. The gelatin porous scaffolds had the highest inhibitory influence. The anticancer effect of Fe₃O₄ NPs was also dependent on the matrices. The free Fe₃O₄ NPs could most efficiently kill breast cancer cells under AMF irradiation. However, the ablation capacity of Fe₃O₄ NPs embedded in the agarose hydrogels and gelatin porous scaffolds significantly decreased under AMF irradiation compared to that of free Fe₃O₄ NPs. The reduced killing capacity of Fe₃O₄ NPs in agarose hydrogels and gelatin porous scaffolds was due to the inhibitory effect of the matrices on their magnetic thermal property. These results suggested that the matrices surrounding MNPs could affect the magnetic thermal property of MNPs and, therefore, affect their ablation capacity to cancer cells. The results should provide useful information for the design and application of MNPs for biomedical applications.

DECLARATIONS

Authors' contributions

Made substantial contributions to the conception and design of the study and performed data analysis and interpretation: Wang M, Sun R, Kawazoe N, Chen G

Performed data acquisition and provided administrative, technical, and material support: All authors

Availability of data and materials

Data will be made available upon request.

Financial support and sponsorship

This research was supported by the JSPS KAKENHI Grant Number 19H04475.

Conflicts of interest

All authors declared that there are no conflicts of interest.

Ethical approval and consent to participate

Not applicable.

Consent for publication

Not applicable.

Copyright

© The Author(s) 2023.

REFERENCES

1. Tong S, Quinto CA, Zhang L, Mohindra P, Bao G. Size-dependent heating of magnetic iron oxide nanoparticles. *ACS Nano* 2017;11:6808-16. [DOI](#) [PubMed](#)
2. Hervault A, Thanh NT. Magnetic nanoparticle-based therapeutic agents for thermo-chemotherapy treatment of cancer. *Nanoscale* 2014;6:11553-73. [DOI](#) [PubMed](#)
3. Cao Z, Wang D, Li Y, et al. Effect of nanoheat stimulation mediated by magnetic nanocomposite hydrogel on the osteogenic differentiation of mesenchymal stem cells. *Sci China Life Sci* 2018;61:448-56. [DOI](#)
4. Liu X, Zheng J, Sun W, et al. Ferrimagnetic vortex nanoring-mediated mild magnetic hyperthermia imparts potent immunological effect for treating cancer metastasis. *ACS Nano* 2019;13:8811-25. [DOI](#)
5. Liu X, Zhang Y, Wang Y, et al. Comprehensive understanding of magnetic hyperthermia for improving antitumor therapeutic efficacy. *Theranostics* 2020;10:3793-815. [DOI](#) [PubMed](#) [PMC](#)
6. Maier-Hauff K, Ulrich F, Nestler D, et al. Efficacy and safety of intratumoral thermotherapy using magnetic iron-oxide nanoparticles combined with external beam radiotherapy on patients with recurrent glioblastoma multiforme. *J Neurooncol* 2011;103:317-24. [DOI](#) [PubMed](#) [PMC](#)
7. Johannsen M, Gneveckow U, Thiesen B, et al. Thermotherapy of prostate cancer using magnetic nanoparticles: feasibility, imaging, and three-dimensional temperature distribution. *Eur Urol* 2007;52:1653-61. [DOI](#)
8. Ng EY, Kumar SD. Physical mechanism and modeling of heat generation and transfer in magnetic fluid hyperthermia through Néelian and Brownian relaxation: a review. *Biomed Eng Online* 2017;16:36. [DOI](#) [PubMed](#) [PMC](#)
9. Di Corato R, Espinosa A, Lartigue L, et al. Magnetic hyperthermia efficiency in the cellular environment for different nanoparticle designs. *Biomaterials* 2014;35:6400-11. [DOI](#)
10. Balakrishnan PB, Silvestri N, Fernandez-Cabada T, et al. Exploiting unique alignment of cobalt ferrite nanoparticles, mild hyperthermia, and controlled intrinsic cobalt toxicity for cancer therapy. *Adv Mater* 2020;32:e2003712. [DOI](#)
11. Lu N, Huang P, Fan W, et al. Tri-stimuli-responsive biodegradable theranostics for mild hyperthermia enhanced chemotherapy. *Biomaterials* 2017;126:39-48. [DOI](#)
12. Zhang J, Zhao B, Chen S, et al. Near-infrared light irradiation induced mild hyperthermia enhances glutathione depletion and DNA interstrand cross-link formation for efficient chemotherapy. *ACS Nano* 2020;14:14831-45. [DOI](#)
13. Chen S, Zhang Q, Nakamoto T, Kawazoe N, Chen G. Gelatin Scaffolds with controlled pore structure and mechanical property for cartilage tissue engineering. *Tissue Eng Part C Methods* 2016;22:189-98. [DOI](#)
14. Conde-leboran I, Baldomir D, Martinez-boubeta C, et al. A single picture explains diversity of hyperthermia response of magnetic nanoparticles. *J Phys Chem C* 2015;119:15698-706. [DOI](#)
15. de Sousa ME, Carrea A, Mendoza Zélis P, et al. Stress-induced gene expression sensing intracellular heating triggered by magnetic hyperthermia. *J Phys Chem C* 2016;120:7339-48. [DOI](#)
16. Munoz-Menendez C, Conde-Leboran I, Serantes D, Chantrell R, Chubykalo-Fesenko O, Baldomir D. Distinguishing between heating power and hyperthermic cell-treatment efficacy in magnetic fluid hyperthermia. *Soft Matter* 2016;12:8815-8. [DOI](#) [PubMed](#)
17. Domenech M, Marrero-Berrios I, Torres-Lugo M, Rinaldi C. Lysosomal membrane permeabilization by targeted magnetic nanoparticles in alternating magnetic fields. *ACS Nano* 2013;7:5091-101. [DOI](#) [PubMed](#)
18. Villanueva A, de la Presa P, Alonso JM, et al. Hyperthermia hela cell treatment with silica-coated manganese oxide nanoparticles. *J*

- Phys Chem C* 2010;114:1976-81. DOI
19. Baki A, Remmo A, Löwa N, Wiekhorst F, Bleul R. Albumin-coated single-core iron oxide nanoparticles for enhanced molecular magnetic imaging (MRI/MPI). *Int J Mol Sci* 2021;22:6235. DOI PubMed PMC
 20. Obaidat IM, Issa B, Haik Y. Magnetic properties of magnetic nanoparticles for efficient hyperthermia. *Nanomaterials* 2015;5:63-89. DOI PubMed PMC
 21. Bauer LM, Situ SF, Griswold MA, Samia AC. High-performance iron oxide nanoparticles for magnetic particle imaging - guided hyperthermia (hMPI). *Nanoscale* 2016;8:12162-9. DOI PubMed
 22. Coral DF, Zélis PM, Marciello M, et al. Effect of nanoclustering and dipolar interactions in heat generation for magnetic hyperthermia. *Langmuir* 2016;32:1201-13. DOI
 23. Gavilán H, Simeonidis K, Myrovali E, et al. How size, shape and assembly of magnetic nanoparticles give rise to different hyperthermia scenarios. *Nanoscale* 2021;13:15631-46. DOI
 24. Darwish MS. Effect of carriers on heating efficiency of oleic acid-stabilized magnetite nanoparticles. *J Mol Liq* 2017;231:80-5. DOI
 25. Bordet A, Landis RF, Lee Y, et al. Water-dispersible and biocompatible iron carbide nanoparticles with high specific absorption rate. *ACS Nano* 2019;13:2870-8. DOI PubMed PMC
 26. Gonçalves J, Nunes C, Ferreira L, et al. Coating of magnetite nanoparticles with fucoidan to enhance magnetic hyperthermia efficiency. *Nanomaterials* 2021;11:2939. DOI PubMed PMC
 27. Cabrera D, Lak A, Yoshida T, et al. Unraveling viscosity effects on the hysteresis losses of magnetic nanocubes. *Nanoscale* 2017;9:5094-101. DOI
 28. Engelmann UM, Seifert J, Mues B, et al. Heating efficiency of magnetic nanoparticles decreases with gradual immobilization in hydrogels. *J Magn Magn Mater* 2019;471:486-94. DOI
 29. Kaczmarek K, Mrówczyński R, Hornowski T, Bielas R, Józefczak A. The effect of tissue-mimicking phantom compressibility on magnetic hyperthermia. *Nanomaterials* 2019;9:803. DOI PubMed PMC
 30. Cabrera D, Coene A, Leliaert J, et al. Dynamical magnetic response of iron oxide nanoparticles inside live cells. *ACS Nano* 2018;12:2741-52. DOI
 31. Suto M, Hirota Y, Mamiya H, et al. Heat dissipation mechanism of magnetite nanoparticles in magnetic fluid hyperthermia. *J Magn Magn Mater* 2009;321:1493-6. DOI
 32. Dong S, Chen Y, Yu L, Lin K, Wang X. Magnetic Hyperthermia-synergistic H₂O₂ self-sufficient catalytic suppression of osteosarcoma with enhanced bone-regeneration bioactivity by 3D-printing composite scaffolds. *Adv Funct Mater* 2020;30:1907071. DOI
 33. Bigham A, Aghajanian AH, Saudi A, Rafienia M. Hierarchical porous Mg₂SiO₄-CoFe₂O₄ nanomagnetic scaffold for bone cancer therapy and regeneration: surface modification and in vitro studies. *Mater Sci Eng C Mater Biol Appl* 2020;109:110579. DOI PubMed
 34. Farzin A, Fathi M, Emadi R. Multifunctional magnetic nanostructured hardystonite scaffold for hyperthermia, drug delivery and tissue engineering applications. *Mater Sci Eng C Mater Biol Appl* 2017;70:21-31. DOI PubMed
 35. Serio F, Silvestri N, Kumar Avugadda S, et al. Co-loading of doxorubicin and iron oxide nanocubes in polycaprolactone fibers for combining magneto-thermal and chemotherapeutic effects on cancer cells. *J Colloid Interface Sci* 2022;607:34-44. DOI
 36. Eivazzadeh-Keihan R, Pajoum Z, Aghamirza Moghim Aliabadi H, et al. Magnetic chitosan-silk fibroin hydrogel/graphene oxide nanobiocomposite for biological and hyperthermia applications. *Carbohydr Polym* 2023;300:120246. DOI
 37. Sun R, Chen H, Zheng J, et al. Composite scaffolds of gelatin and Fe₃O₄ nanoparticles for magnetic hyperthermia-based breast cancer treatment and adipose tissue regeneration. *Adv Healthc Mater* 2023;12:e2202604. DOI
 38. Lu C, Zheng J, Yoshitomi T, Kawazoe N, Yang Y, Chen G. How hydrogel stiffness affects adipogenic differentiation of mesenchymal stem cells under controlled morphology. *ACS Appl Bio Mater* 2023;6:3441-50. DOI
 39. Wu H, Liu L, Song L, Ma M, Gu N, Zhang Y. Enhanced tumor synergistic therapy by injectable magnetic hydrogel mediated generation of hyperthermia and highly toxic reactive oxygen species. *ACS Nano* 2019;13:14013-23. DOI
 40. Gao F, Xie W, Miao Y, et al. Magnetic hydrogel with optimally adaptive functions for breast cancer recurrence prevention. *Adv Healthc Mater* 2019;8:e1900203. DOI
 41. Stocke NA, Sethi P, Jyoti A, et al. Toxicity evaluation of magnetic hyperthermia induced by remote actuation of magnetic nanoparticles in 3D micrometastatic tumor tissue analogs for triple negative breast cancer. *Biomaterials* 2017;120:115-25. DOI PubMed PMC
 42. Zhang X, Wei P, Wang Z, et al. Herceptin-conjugated DOX-Fe₃O₄/P(NIPAM-AA-MAPEG) nanogel system for HER2-targeted breast cancer treatment and magnetic resonance imaging. *ACS Appl Mater Interfaces* 2022;14:15956-69. DOI
 43. Lu J, Guo Z, Xie W, et al. Hypoxia-overcoming breast-conserving treatment by magnetothermodynamic implant for a localized free-radical burst combined with hyperthermia. *ACS Appl Mater Interfaces* 2021;13:35484-93. DOI
 44. Jalili NA, Jaiswal MK, Peak CW, Cross LM, Gaharwar AK. Injectable nanoengineered stimuli-responsive hydrogels for on-demand and localized therapeutic delivery. *Nanoscale* 2017;9:15379-89. DOI PubMed PMC
 45. Zheng J, Xie Y, Yoshitomi T, Kawazoe N, Yang Y, Chen G. Stepwise proliferation and chondrogenic differentiation of mesenchymal stem cells in collagen sponges under different microenvironments. *Int J Mol Sci* 2022;23:6406. DOI PubMed PMC
 46. Sun R, Chen H, Sutrisno L, Kawazoe N, Chen G. Nanomaterials and their composite scaffolds for photothermal therapy and tissue engineering applications. *Sci Technol Adv Mater* 2021;22:404-28. DOI PubMed PMC
 47. Zhang W, Chen Y, Li M, et al. A PDA-functionalized 3D lung scaffold bioplatfrom to construct complicated breast tumor

- microenvironment for anticancer drug screening and immunotherapy. *Adv Sci* 2023;10:e2302855. DOI PubMed PMC
48. Chen H, Sun R, Zeng T, et al. Stepwise photothermal therapy and chemotherapy by composite scaffolds of gold nanoparticles, BP nanosheets and gelatin immobilized with doxorubicin-loaded thermosensitive liposomes. *Biomater Sci* 2022;10:7042-54. DOI
 49. Lartigue L, Hugouenq P, Alloyeau D, et al. Cooperative organization in iron oxide multi-core nanoparticles potentiates their efficiency as heating mediators and MRI contrast agents. *ACS Nano* 2012;6:10935-49. DOI
 50. Hemery G, Keyes AC Jr, Garaio E, et al. Tuning sizes, morphologies, and magnetic properties of monocoresh versus multicore iron oxide nanoparticles through the controlled addition of water in the polyol synthesis. *Inorg Chem* 2017;56:8232-43. DOI
 51. Sutrisno L, Chen H, Chen Y, et al. Composite scaffolds of black phosphorus nanosheets and gelatin with controlled pore structures for photothermal cancer therapy and adipose tissue engineering. *Biomaterials* 2021;275:120923. DOI
 52. Li J, Zhang J, Chen Y, Kawazoe N, Chen G. TEMPO-conjugated gold nanoparticles for reactive oxygen species scavenging and regulation of stem cell differentiation. *ACS Appl Mater Interfaces* 2017;9:35683-92. DOI
 53. Zheng J, Sun R, Chen H, et al. Morphological dependence of breast cancer cell responses to doxorubicin on micropatterned surfaces. *Polymers* 2022;14:2761. DOI PubMed PMC
 54. Chen Y, Kawazoe N, Chen G. Preparation of dexamethasone-loaded biphasic calcium phosphate nanoparticles/collagen porous composite scaffolds for bone tissue engineering. *Acta Biomater* 2018;67:341-53. DOI PubMed
 55. Zheng J, Wang Y, Kawazoe N, Yang Y, Chen G. Influences of viscosity on the osteogenic and adipogenic differentiation of mesenchymal stem cells with controlled morphology. *J Mater Chem B* 2022;10:3989-4001. DOI
 56. Sutrisno L, Chen H, Yoshitomi T, Kawazoe N, Yang Y, Chen G. PLGA-collagen-BPNS bifunctional composite mesh for photothermal therapy of melanoma and skin tissue engineering. *J Mater Chem B* 2022;10:204-13. DOI
 57. Ma H, Zhuang H, Zhai D, et al. Xonotlite nanowire-containing bioactive scaffolds for the therapy of defective adipose tissue in breast cancer. *Nano Lett* 2023;23:7157-65. DOI
 58. Chen H, Sun R, Zheng J, Kawazoe N, Yang Y, Chen G. Doxorubicin-encapsulated thermosensitive liposome-functionalized photothermal composite scaffolds for synergistic photothermal therapy and chemotherapy. *J Mater Chem B* 2022;10:4771-82. DOI
 59. Chen H, Wang X, Sutrisno L, et al. Folic acid-functionalized composite scaffolds of gelatin and gold nanoparticles for photothermal ablation of breast cancer cells. *Front Bioeng Biotechnol* 2020;8:589905. DOI PubMed PMC
 60. Sutrisno L, Chen H, Yoshitomi T, Kawazoe N, Yang Y, Chen G. Preparation of composite scaffolds composed of gelatin and Au nanostar-deposited black phosphorus nanosheets for the photothermal ablation of cancer cells and adipogenic differentiation of stem cells. *Biomater Adv* 2022;138:212938. DOI
 61. Zhang J, Li J, Kawazoe N, Chen G. Composite scaffolds of gelatin and gold nanoparticles with tunable size and shape for photothermal cancer therapy. *J Mater Chem B* 2017;5:245-53. DOI
 62. Pinheiro IF, Brollo ME, Bassani GS, et al. Effect of viscosity and colloidal stability on the magnetic hyperthermia of petroleum-based nanofluids. *Fuel* 2023;331:125810. DOI
 63. Fortin JP, Gazeau F, Wilhelm C. Intracellular heating of living cells through Néel relaxation of magnetic nanoparticles. *Eur Biophys J* 2008;37:223-8. DOI PubMed
 64. Fortin JP, Wilhelm C, Servais J, Ménager C, Bacri JC, Gazeau F. Size-sorted anionic iron oxide nanomagnets as colloidal mediators for magnetic hyperthermia. *J Am Chem Soc* 2007;129:2628-35. DOI PubMed
 65. Wang X, Yang Y, Hu X, Kawazoe N, Yang Y, Chen G. Morphological and mechanical properties of osteosarcoma microenvironment cells explored by atomic force microscopy. *Anal Sci* 2016;32:1177-82. DOI
 66. Calzado-Martin A, Encinar M, Tamayo J, Calleja M, San Paulo A. Effect of actin organization on the stiffness of living breast cancer cells revealed by peak-force modulation atomic force microscopy. *ACS Nano* 2016;10:3365-74. DOI PubMed
 67. Qi G, Zhang Y, Xu S, et al. Nucleus and mitochondria targeting theranostic plasmonic surface-enhanced raman spectroscopy nanoprobe as a means for revealing molecular stress response differences in hyperthermia cell death between cancerous and normal cells. *Anal Chem* 2018;90:13356-64. DOI
 68. Danewalia SS, Singh K. Bioactive glasses and glass-ceramics for hyperthermia treatment of cancer: state-of-art, challenges, and future perspectives. *Mater Today Bio* 2021;10:100100. DOI PubMed PMC

Review

Open Access



Cryogenic atom probe tomography and its applications: a review

Ziyang Zhou^{1,2,4}, Zhengquan Wang^{2,3,4}, Ranming Niu^{2,5}, Pang-Yu Liu^{2,5}, Chao Huang^{2,5}, Yi-Hsuan Sun^{2,6},
Xiutong Wang⁴, Hung-Wei Yen⁶, Julie M. Cairney^{2,5}, Yi-Sheng Chen^{4,5,6}

¹State Key Laboratory for Strength and Vibration of Mechanical Structures, School of Aerospace Engineering, Xi'an Jiaotong University, Xi'an 710049, Shaanxi, China.

²Australian Centre for Microscopy and Microanalysis, The University of Sydney, Sydney 2006, Australia.

³Shaanxi Key Laboratory of Biomedical Metallic Materials, Northwest Institute for Non-Ferrous Metal Research, Xi'an 710016, Shaanxi, China.

⁴Key Laboratory of Marine Environmental Corrosion and Bio-Fouling, Institute of Oceanology, Chinese Academy of Science, Qingdao 266071, Shandong, China.

⁵School of Aerospace, Mechanical and Mechatronic Engineering, The University of Sydney, Sydney 2006, Australia.

⁶Department of Materials Science and Engineering, National Taiwan University, Taipei 106216, Taiwan.

Correspondence to: Prof. Yi-Sheng Chen, Australian Centre for Microscopy and Microanalysis, The University of Sydney, Sydney 2006, Australia. E-mail: yi-sheng.chen@sydney.edu.au

How to cite this article: Zhou Z, Wang Z, Niu R, Liu PY, Huang C, Sun YH, Wang X, Yen HW, Cairney JM, Chen YS. Cryogenic atom probe tomography and its applications: a review. *Microstructures* 2023;3:2023043. <https://dx.doi.org/10.20517/microstructures.2023.38>

Received: 1 Aug 2023 **First Decision:** 13 Sep 2023 **Revised:** 18 Sep 2023 **Accepted:** 27 Sep 2023 **Published:** 13 Nov 2023

Academic Editors: Lin Gu, Jiangyu Li **Copy Editor:** Fangling Lan **Production Editor:** Fangling Lan

Abstract

Cryogenic atom probe tomography (cryo-APT) is a new microstructure characterization technique with the potential to address challenges across various research fields. In this review, we provide an overview of the development of cryo-APT and the associated instrumentation that transforms conventional APT into cryo-APT. We start by introducing the APT principle and the instrumentation involved in the cryo-APT workflow, emphasizing the key techniques that enable cryo-APT specimen preparation. Furthermore, we shed light on the research made possible by cryo-APT, presenting several recent outcomes to demonstrate its capabilities effectively. Finally, we discuss the limitations of cryo-APT and summarize the potential research areas that can further benefit from this cutting-edge microstructural characterization technique.

Keywords: Atom probe tomography, cryogenic microscopy, microanalysis, materials characterization, hydrogen mapping



© The Author(s) 2023. **Open Access** This article is licensed under a Creative Commons Attribution 4.0 International License (<https://creativecommons.org/licenses/by/4.0/>), which permits unrestricted use, sharing, adaptation, distribution and reproduction in any medium or format, for any purpose, even commercially, as long as you give appropriate credit to the original author(s) and the source, provide a link to the Creative Commons license, and indicate if changes were made.



INTRODUCTION

Atom probe tomography (APT) is an advanced microanalysis technique that offers a remarkable way to visualize the distribution of atoms within materials at the nanoscale in three dimensions (3-D)^[1-4]. It boasts an impressive sub-nanometer spatial resolution and a high chemical resolution. The latter enables it to achieve precision levels of approximately 20 atomic parts per million (at. ppm) for all elements, regardless of their atomic masses^[2,5]. The combination of these unique abilities allows the research on the distributions of elements in materials, including those with low atomic mass, such as hydrogen, carbon, and lithium, which are difficult to analyze using conventional optical or electron microscopes^[6-8].

In 1955, Müller made a significant breakthrough by developing and utilizing a field ion microscope (FIM), which laid the groundwork for the APT technique^[9]. Using the FIM, they observed tungsten atoms on a tungsten tip surface and achieved the world's first atomic-scale image with an unprecedented magnification of over 10^6 times^[10]. Later, in 1968, Müller *et al.* further developed the atom-probe FIM^[1], integrating a mass spectrometer, which enabled the measurement of the time-of-flight (ToF) of evaporated ions and their mass-to-charge ratios (m/z). This addition provided a chemical resolution to complement the high spatial resolution of the FIM^[11]. In 1970, Brenner and McKinney^[12] also made a significant contribution to the development and application of FIM and APT for the advancements in surface science.

Over the following decades, the continuous improvement in computational power facilitated computer-assisted experimentation, leading to the development of modern APT instruments. The automation of ion evaporation experiments, data acquisition, and tomographic reconstruction became possible. The first commercial APT instrument was developed by the research group at the University of Oxford in the early 1990s^[13], which later led to the foundation of Oxford Nanoscience Ltd. with their products of Position-Sensitive Atom Probe and the subsequent Energy-Compensated Position-Sensitive Atom Probe. In 2001, Imago Scientific Instruments introduced the commercial APT module, making the APT technique more accessible to researchers^[14]. In 2006, Oxford Nanoscience was acquired by Imago Scientific Instruments. Subsequently, AMETEK acquired Imago Scientific Instruments in 2010 and merged it with CAMECA, which became the sole APT instrument manufacturer to date. Since Müller's pioneering work in the 1950s, APT has found extensive use in various fields of research and development. **Figure 1** depicts the increasing number of APT-related publications by year in the Web of Science database, reflecting the growing adoption of APT analyses. This technique has made significant contributions to advancements in materials science^[7,15], biology^[16], chemistry^[17], physics^[18,19], geoscience^[20], medicine^[21], and energy science^[15].

As depicted in **Figure 2**, to induce this field evaporation, a needle-shaped specimen with a tip diameter less than 100 nm is necessary. The required sharp tips can be created using either electropolishing or focused ion beam (FIB) annular milling techniques^[22]. In the APT process, a high voltage of 2-15 kilovolts (kV) is applied to the needle specimen, generating a powerful electric field at the apex of the tip. This electric field is strong enough to strip the outer-shell electron(s) from the atoms at the apex and ionize them. Once ionized, the charged particles are directed by the electric field toward a grounded, time-sensitive detector. The time taken for the ions to travel from the evaporation point to the detector gives the ToF information. To precisely determine the timing of the evaporation process, controlled pulsing with a marginal energy input is applied to the APT tip specimen. The tip is at a constant high voltage of several thousand volts, which is close to the threshold of the level required for field evaporation, and the ion evaporation only takes place when the additional pulsing energy is applied. This energy pulsing can be achieved by using either of the two methods -voltage pulsing and laser pulsing using a focused beam shed on the apex of the specimen, which leads to voltage mode and the laser mode of modern APT, respectively^[23].

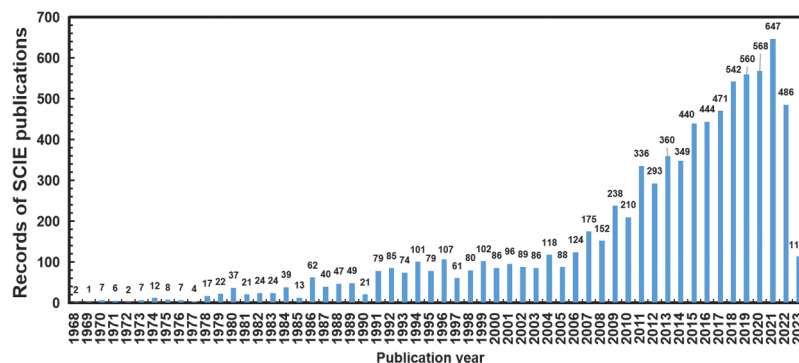


Figure 1. Numbers of Web of Science publications by year using a search term of “atom probe”.

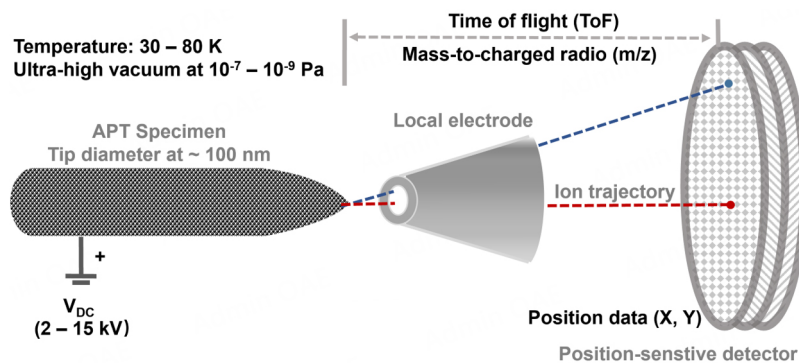


Figure 2. Schematic illustration of the principle and essential components of APT.

Both modes of APT experiments require conducting the analysis on a cryogenic stage [Figure 2] at a temperature range of 30 to 80 Kelvin (K). This low temperature is crucial to minimize thermal vibrations that could otherwise compromise the spatial resolution of the final ion images. In the case of laser-pulsing APT, special attention is needed because the laser beam can potentially heat up the apex, causing the actual tip temperature to deviate from the set temperature. To deduce the m/z of the detected ions in APT, the ToF and the flight path (L) of the APT instrument are taken into account. The m/z values are derived from the conservation of electric potential energy (E_e) and kinetic energy (E_k) of the ions, represented by the equation:

$$E_e = QeV = E_k = \frac{1}{2} mv^2$$

where Q represents the ionization state of the ion, e is the fundamental electric charge, V is the voltage at which ion evaporation takes place at the tip, m is the mass of the ion, and v is the speed of the ion from the tip to the detector over the flight length (L) during a ToF measurement. The m/z can be related to ToF (t) through:

$$\frac{m}{z} = 2eV \left(\frac{t}{L}\right)^2$$

Apart from providing excellent chemical resolution, the APT analysis also offers valuable spatial information. This is achieved by using a position-sensitive ion detector that enables the back projection of the spatial origins of ions based on the nominal ion trajectory path in the equipment [Figure 2]^[1,2]. As a result, a 3-D reconstructed atom map is produced, providing a detailed visualization of the atomic arrangement within the material under investigation.

To achieve the ultra-high vacuum required for ion evaporation and detection, the modern Local Electrode Atom Probe instrument (LEAP, developed by CAMECA) employs a three-chamber system^[13]. The first chamber, known as the “load lock”, is responsible for pumping down from ambient pressure to around 10^{-5} Pa. Once this step is completed, the APT specimen can be transferred to the second chamber, called the “buffer” chamber, which maintains a constant pressure of approximately 10^{-7} Pa. Finally, the APT specimen is moved to the “analysis chamber”, where the pressure is maintained below 10^{-9} Pa. This chamber is equipped with various components, including the specimen cooling system, the ion detector for ToF measurements, and the pulsing system.

In 2017, the groundbreaking development of cryogenic electron microscopy (cryo-EM) was honored with the Nobel Prize in Chemistry^[24]. This prestigious award recognized the seminal progress made in cryogenic specimen handling, enabling electron microscopy specimens to be rapidly cooled to extremely low temperatures and maintained in a “frozen” state throughout the transfer process. The key to this advancement lies in the ability to quickly quench the specimens, leading to the formation of amorphous ice from the water within them. This amorphous ice prevents ice crystallization, which could otherwise damage delicate structures during slow cooling processes^[25]. The innovation in cryo-specimen transfer has opened up exciting possibilities for preserving biological specimens in their natural states before observation in electron microscopes^[26]. This breakthrough also served as inspiration for the development of a cryo-specimen handling workflow dedicated to APT by Gerstl and Wepf^[27]. This adaptation of cryogenic techniques created opportunities to apply APT to soft matter and specimens containing diffusive solutes, which require low temperatures to immobilize them. Following their pioneering work at ETH Zurich, other APT laboratories have invested substantial efforts in enhancing and innovating cryo-workflows and applications, leading to the emergence of a new microanalysis technique called cryogenic APT (cryo-APT)^[28-32]. This cutting-edge approach represents a promising frontier in the field of microanalysis.

CRYO-APT

When it comes to cryo-APT analysis, the critical aspect lies in maintaining the low temperature of the specimen between its preparation and the actual APT analysis. This involves two key processes: the “cryo-transfer” (cryogenic transfer) to keep the specimen at a low temperature and the “cryo-specimen fabrication” to create the specific APT tip geometry. It is important to mention that the temperatures used for cryo-specimen fabrication and cryo-transfer can vary depending on the purpose, the type of coolant used, and the efficiency of thermal conduction from the coolant. Generally, temperatures ranging from 120 to 140 K are required for forming vitrified ice, which helps prevent damage during ice crystallization in biological specimens^[26]. On the other hand, temperatures around 150 K are necessary to inhibit the desorption of diffusive hydrogen solute from a metallic specimen^[33,34].

The cryo-transfer process involves plunge-freezing or direct cooling in liquid nitrogen, which allows the specimen to reach temperatures as low as 77 K. Using liquid helium enables reaching even lower temperatures of around 4 K. However, in an indirect cooling process, the lowest temperature that the specimen can achieve is somewhat compromised due to limitations in thermal conduction efficiency at various interfaces of the physical components. As a rule of thumb, utilizing copper bands for cooling with

liquid nitrogen can reach temperatures as low as 120 K. These experimental details are crucial to enable successful cryo-APT analysis and open up new possibilities for research in this field.

Cryo-transfer

The success of cryo-transfer for cryo-APT tips depends on three critical factors: environmental moisture that may come into contact with cryo-specimens, the cooling process, including potential heat absorption from the surroundings to the cryo-specimens, and the evacuation process required to reach the UHV levels necessary for the APT experiment^[29,35]. Out of these factors, the presence of moisture in the working space is particularly crucial in cryo-APT experiments. When a sharp tip is exposed to moisture, it can lead to frost formation on the surface of the tip, which compromises the required sharpness for APT field evaporation^[36]. Therefore, it is imperative to conduct cryo-transfer for APT specimens in an extremely dry environment. This can be achieved by using a glovebox purged with dry, non-reactive gases such as nitrogen and argon. [Figure 3A](#) provides an example image of a glovebox used for cryo-APT.

After preparing and treating the specimen inside a glovebox, the next step in cryo-APT involves transferring the cooled specimen from the glovebox to either a FIB system for further tip-shaping or directly to the APT measurement setup. To accomplish this, a specimen loading mechanism is utilized. As shown in the inset of [Figure 3A](#), this connection is achieved using a vacuum specimen carrier, often referred to as a "suitcase". The suitcase is equipped with a specimen stage containing a cold finger that connects to a dewar (indicated by the blue arrow). The cryo-and-vacuum suitcase requires a docking mechanism to connect it to the glovebox (shown as red circles in [Figure 3A](#)). Before the cryo-specimen is transferred into the suitcase through a loadlock (indicated by the green arrow in [Figure 3A](#)). The loadlock needs to be pre-evacuated to sufficiently low pressure, similar to that of the loadlock of the APT instrument, typically between 10^{-5} and 10^{-6} Pa. This ensures a seamless transition of the specimen into the APT vacuum chambers. Additionally, the loadlock of the glovebox must be connected to a dewar (blue arrow in [Figure 3A](#)) that can be filled with coolant to cool the specimen docking stage before it comes into contact with the cryo-specimen^[34]. Once the specimen reaches the desired low temperature and pressure, it is removed from the loadlock using a long magnetic-coupling transfer arm (the long rod on the left side of the inset in [Figure 3A](#)).

During the process of removing the specimen, the transfer arm operating at room temperature can inadvertently introduce heat, jeopardizing the cryogenic state of the specimen. To counteract this issue, it is necessary to use a thermos-insulating washer, which can be made of polyetheretherketone (PEEK), as shown by the red arrow in [Figure 3B](#), which also shows the APT specimen carrier "puck" (the orange component) for commercial LEAP instruments. In commercial LEAP systems, a carousel is employed to facilitate the movement of specimens across various chambers, including the loadlock, buffer, and analysis chambers. To handle cryo-specimens, the carousel also requires a thermo-insulating adaptation. [Figure 3C](#) illustrates the need for a special carousel with a cryo-specimen docking slot made of PEEK to ensure proper cryo-transfer (red arrow). In addition to the cryo-transfer workflow shown in [Figure 3](#) at the University of Sydney, Perea *et al.* developed a vacuum-cryo-transfer system at the Pacific Northwest National Laboratory in the US, which allows APT tips to expose a range of reactive gases such as hydrogen, oxygen, and carbon monoxide^[28]. This new instrumentation opens up the possibility of applying APT for catalytic research at the nanoscale, relatable to the dimension of APT tips.

Using the specialized cryo-transfer components mentioned earlier, a typical workflow for pre-sharpened tip specimens mounted on a puck unfolds as follows: Firstly, the specimen undergoes the desired treatment process inside the glovebox, such as electrolytic hydrogen charging as demonstrated in^[33,34]. Subsequently, the specimen is directly plunge-frozen in liquid nitrogen and then loaded into the pre-cooled loadlock of

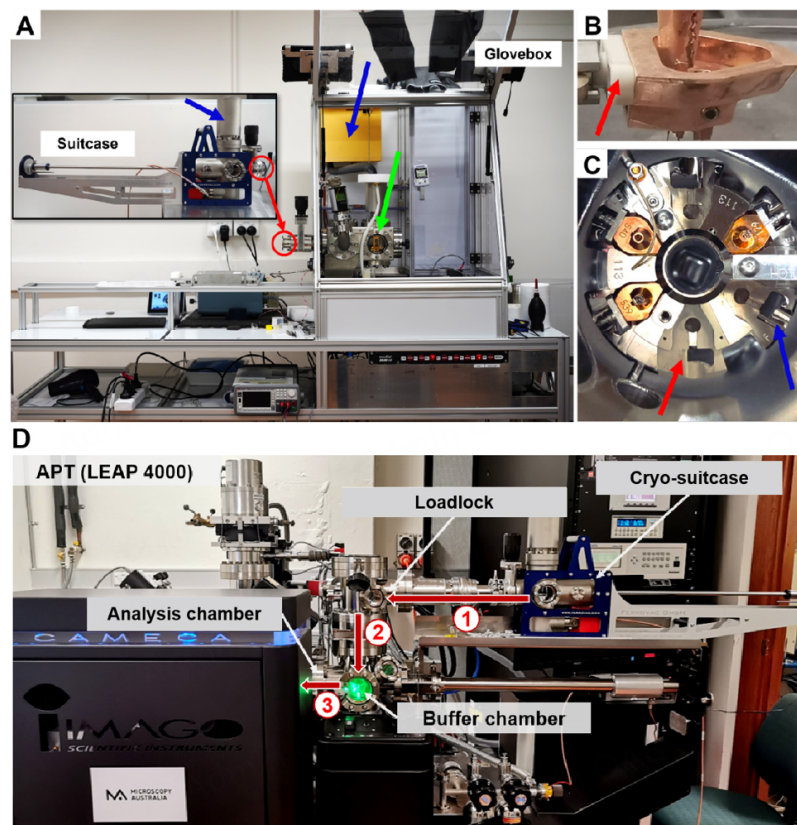


Figure 3. Auxiliaries for enabling cryogenic APT specimen transfer. (A) Glovebox with a dewar (blue arrow) and a loadlock (green arrow) with a cooling stage and turbo pump. The inset shows a specimen-transfer suitcase (by Ferrovac) equipped with a cooling finger connecting to a dewar (blue arrow). Red circles show the docking port connecting the loadlock and the suitcase. (B) Cryo-puck with a thermo-insulating washer (red arrow). (C) Cryo-carousel compatible with commercial APT system (LEAP by CAMECA) with a slot dedicated to cryo-specimen (red arrow), which is distinct from a normal metallic slot (blue arrow). (D) Commercial APT instrument (LEAP 4000 XS) with a suitcase attached.

the glovebox (indicated by the green arrow in [Figure 3A](#)). The loadlock is indirectly cooled with a cold finger, which needs to be pre-evacuated to sufficiently low pressure typically between 10^{-5} and 10^{-6} Pa, which is similar to the level of the loadlock of a commercial APT instrument. The puck, containing the cryo-specimens, is then evacuated within the loadlock before being transferred to the pre-cooled vacuum suitcase [[Figure 3A](#) inset] using the transfer arm. Next, the entire suitcase, along with the cryo-specimen, is transported to the APT instrument. A docking port is essential for accepting the specimen transferred from the suitcase (Arrow #1 in [Figure 3D](#)). Once the suitcase is connected to the APT loadlock, the cryo-specimen is moved into the pre-cooled PEEK slot within the cryo-carousel [[Figure 3C](#)]. The cryo-carousel is then shifted into the buffer chamber (Arrow #2 in [Figure 3D](#)) before loading the cryo-puck/specimen into the cryo-stage in the analysis chamber for APT measurement (Arrow #3 in [Figure 3D](#)). To measure the specimen temperature, a method utilizing the temperature response of the cryo-stage after cryo-specimen loading was demonstrated in^[34].

Cryo-specimen fabrication

The process of cryo-APT specimen fabrication is complex due to its stringent geometric requirements. The specimen must have a tip diameter of less than 100 nanometers while maintaining a low-temperature working condition. Electropolished metallic specimens with good mechanical strengths (see^[37,38] for electropolishing) can undergo direct plunge-freezing in coolants after treatments such as deuteration^[33,34]

and corrosion^[39]. After treatment, these specimens can proceed with cryo-transfer^[33,34,40]. However, this pre-sharpening method is most effective when the materials being studied have uniform distribution and high density of microstructural features of interest, such as nanosized precipitates or grain boundaries (GBs) in fine-grain materials^[33,34,40]. For specimens that require extracting a specific region of interest (ROI) from a bulk specimen, it is essential to use a FIB fabrication method that is compatible with low temperatures, often referred to as cryo-FIB^[41-46].

Cryo-FIB necessitates cooling not just the specimen stage but also the lift-out micromanipulator^[39]. Both can be achieved by connecting a flexible copper cold band finger to the coolant^[36]. The process of FIB lift-out involves trenching and extracting the ROI in a bar [Figure 4A1]. Subsequently, the bar is attached to the micromanipulator, which requires using a gas injection system (GIS) and targeted electron beam deposition to create the attachment or weld. Typically, this weld is made of platinum or carbon. After attachment to the micromanipulator, the bar is removed from the trench and placed onto the pre-sharpened microposts for further tip shaping.

However, working with both the specimen and the micromanipulator at cryogenic temperatures presents a challenge. The GIS deposition cannot function as usual since the injected gas will non-selectively condense onto the surfaces of both the specimen and the micromanipulator, hindering the site-specific attachment^[22]. To address this challenge, Schreiber *et al.* developed a method to lift out and attach a frozen specimen onto the micromanipulator and the cooled micropost^[39]. They utilized debris from the ion milling process of the cryo-specimen, which can re-deposit/condense onto the low-temperature surfaces. This creates site-specific nano-welds, enabling the cryo-specimen attachment to the micromanipulator and pre-sharpened micropost without requiring the GIS [Figure 4A2-A5]. This innovative method was successfully used to attach a lift-out bar containing frozen water and water-corroded glass onto a silicon (Si) micropost [Figure 4A6]. This breakthrough allowed for the fabrication and analysis of an APT tip incorporating both frozen water and corroded glass [Figure 4B1 and B2] after annular milling.

For cryo-specimens where the ROIs are not buried and are identifiable at the surface of the specimen (as shown in Figure 4), El-Zoka *et al.* developed a method using plasma FIB (PFIB)^[32,47]. PFIB offers higher ion milling efficiency compared to conventional gallium FIB, allowing for direct shaping of a tip from the surface of a bulk specimen. This approach avoids the need for a cryo-manipulator and cryo-attachments. The bulk specimen they worked with was nanoporous gold (NPG), which is inherently conductive and, hence, suitable for the APT field evaporation experiment. Additionally, the NPG incorporated frozen heavy water (D₂O ice) as the specimen for analysis within its nanopores^[32] (see^[15] for the need of using heavy water). The scanning electron microscope (SEM) images displayed in Figure 5 illustrate the specimen preparation process, showing the NPG before tip shaping [Figure 5A], during sharpening [Figure 5B], and after tip fabrication at low and high magnifications [Figure 5C and D, respectively]. The use of PFIB in cryo-preparation has expanded the possibilities for APT analysis of nanosized specimens that can be carried in water and subsequently frozen in ice^[32,47].

Besides the mentioned developments in cryo-FIB specimen preparation, significant progress has also been achieved in the cryo-electron microscopy community^[48-52]. On the APT side, there are noteworthy outcomes that deserve attention, such as those for biomineral materials^[53-58], poly(3-alkylthiophene)^[58,59], biomolecules adhered on aluminum substrate tips^[60], ferritin embedded in epoxy resin^[61], immunoglobulin (IgG) embedded in a silica glass matrix^[62], and mammalian cells fixed between gold layers^[63]. These breakthroughs have expanded the scope and capabilities of cryo-microscopy, facilitating the investigation and understanding of diverse biological and mineral specimens at fundamental scales.

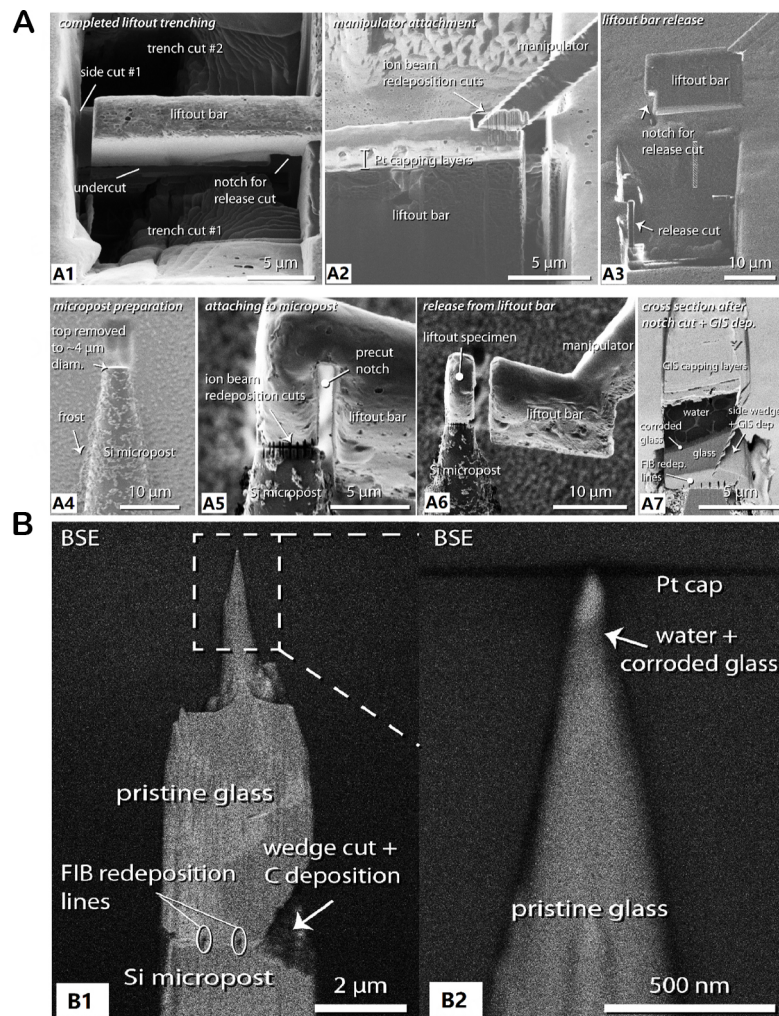


Figure 4. Micrographs from the cryogenic FIB lift-out process of a buried frozen water/solid interface: (A1) ROI trenching, (A2 and A3) lift-out, (A4) placing the lift-out bar on a silicon (Si) micropost, (A5) nano-welds by the re-deposition of the milled debris, (A6) detachment of the lift-out bar, and (A7) high-resolution image the cryo-specimen before annular milling. (B1) APT tip containing the interface of frozen water and corroded glass after annular milling, and (B2) the high-resolution image of (B1). Reproduced with the permission of Ref. [39] Copyright 2023, Elsevier.

RESEARCH ENABLED BY CRYO-APT

The advancements in cryo-transfer and cryo-specimen fabrication have resulted in groundbreaking scientific discoveries across various research fields. This section aims to showcase the successes achieved through the application of cryo-techniques, which have extended the utility of APT beyond its conventional areas of use.

Hydrogen in metals and alloys

Hydrogen can cause a reduction in the strength and ductility of metals and alloys, a phenomenon known as hydrogen embrittlement^[64,65]. Understanding the location of hydrogen atoms in materials is crucial as it allows for correlations with microstructural sites that may be susceptible to hydrogen-induced cracks or capable of trapping detrimental hydrogen solutes, preventing them from participating in the embrittling process. This knowledge has given rise to a material design concept for hydrogen-embrittlement-resistant alloys, where hydrogen "traps" are introduced to create safe sites that can accommodate hydrogen solutes in

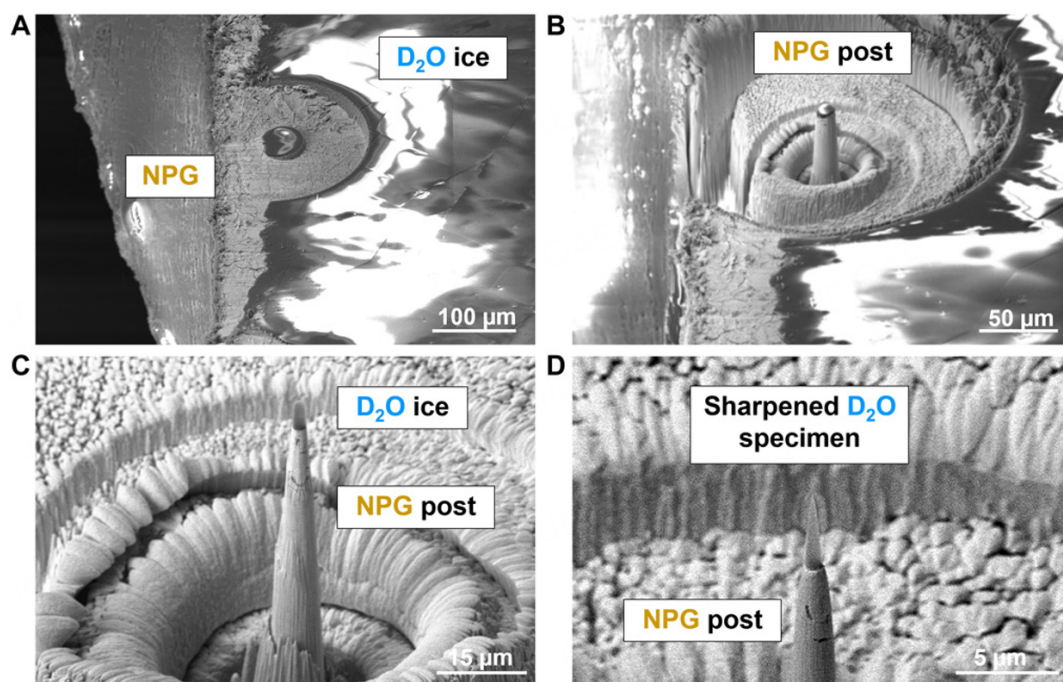


Figure 5. APT specimen preparation from a bulk nanoporous gold (NPG) with frozen heavy water (D_2O ice) in a plasma FIB. (A) NPG and D_2O ice before annular milling with the 200- and 75- μm milling patterns. (B) D_2O ice/NPG pillar during ion milling. (C) Ice/NPG tip after milling. (D) High-resolution view of the final APT tip. Reproduced with the permission of Ref. [32] Copyright 2023, Science Advances.

the metallic microstructure^[66]. Among these traps, dispersoids, such as second-phase precipitates, are of great interest as they enhance material toughness while reducing the diffusible hydrogen content in the matrix^[67].

APT exhibits exceptional sensitivity to light elements, including hydrogen, making it a promising technique for hydrogen mapping in materials. However, the high diffusivity of hydrogen in metals and alloys, regardless of the presence of traps, poses challenges, as hydrogen-charged metallic specimens are prone to desorption and signal loss. Recent advancements in cryo-transfer have enabled the study of frozen-in-place hydrogen atoms in metals and alloys using APT^[40,46,68-73]. To ensure high-quality APT hydrogen analyses, a key experimental requirement is introducing deuterium (2H or D) into APT tip specimens. Deuterium is a less-abundant isotope of hydrogen with a similar chemical reactivity but an additional neutron, resulting in higher atomic mass (and slightly lower diffusivity) than protium (1H), the most abundant hydrogen isotope. Charging deuterium into APT specimens allows the distinction of experimentally introduced signals from the hydrogen background noise arising from the residual gas in the APT chamber^[15]. While some studies have shown that using hydrogen charging can also provide qualitative measurements of hydrogen trapping^[74], deuterium charging has been demonstrated to reduce ambiguity in observations^[15]. Furthermore, deuterium charging must be combined with voltage-pulsed APT, as laser-pulsed APT can produce a significant amount of $^1H_2^+$ peak at 2 m/z, leading to confusion when assigning 2 m/z to deuterium ($^2H^+$)^[75]. A comprehensive discussion on using APT for high-quality hydrogen mapping can be found in a recent review^[15]. The following section will present several example findings made possible by cryo-APT.

Steels

In 2010, Takahashi *et al.* made a significant breakthrough by reporting the first high-resolution hydrogen mapping using APT in ferrite steel containing titanium carbides (TiC), as displayed in [Figure 6A](#)^[73]. They achieved this successful analysis by employing a custom gaseous deuteration cell with thermal control on the APT tip specimens. This allowed for controlled heating during tip deuteration and subsequent quenching, facilitating the uptake of deuterium and minimizing its desorption thereafter. The study revealed that the trapped deuterium atoms (represented by red spheres in [Figure 6A](#)) were localized in regions where titanium and carbon atoms clustered, indicating hydrogen trapping at TiC. Subsequently, Takahashi *et al.* demonstrated another successful analysis of trapped deuterium atoms in vanadium carbides (VC) within a VC precipitation-strengthened steel, as shown in [Figure 6B](#)^[76]. More recently, Takahashi *et al.* utilized cryo-APT to correlate VC-trapped deuterium with the crystal orientation of VC in a peak-aged VC steel, as depicted in [Figure 6C](#)^[77]. This study provided valuable insights into the specific (001) plane trapping of deuterium in the VC, further expanding the capabilities of cryo-APT in unraveling intricate hydrogen-microstructure relationships. These studies showcase the potential of cryo-APT in advancing our understanding of hydrogen behavior in steels.

Apart from the work by Chen *et al.* have also made contributions to observing hydrogen trapping in steels^[40]. Instead of using a custom gaseous charging deuteration cell, they opted for a route using heavy water electrolysis for tip deuteration^[40]. This approach generated a substantially higher deuterium pressure (or fugacity) compared to the gaseous method used by Takahashi *et al.*, leading to improved data statistics of deuterium atoms in APT reconstruction^[73]. This allowed for a more unambiguous observation of hydrogen trapping sites. As shown in [Figure 7A](#), Chen *et al.* utilized cryo-APT to demonstrate the presence of trapped deuterium within vanadium-molybdenum-mixed (V-Mo) carbides, which possess a rocksalt (NaCl) structure in a ferritic steel matrix^[40]. The left figure in [Figure 7A](#) represents a 10-nm-thick slice displaying deuterium and vanadium in red and blue, respectively. The right figure presents a statistical analysis, superimposing all identified V-Mo carbides from the APT dataset. This analysis reveals the distributions of deuterium in relation to other carbide-related elements (V, Mo, and C). The elemental distribution profile indicates that deuterium atoms mainly localize within the V-Mo carbides rather than at the interfaces of the carbides. As discussed, Chen *et al.* attributed this result to the presence of carbon vacancies in the V-Mo carbides^[15].

Subsequently, Chen *et al.* applied the same experimental method to examine hydrogen trapping in niobium carbide (NbC) precipitates, as shown in [Figure 7B](#)^[34]. Similar to the V-Mo carbides, the NbC also possesses a NaCl structure in a ferritic steel matrix but with fewer carbon vacancies. The top right figures in [Figure 8B](#) display 2-D slice views of the NbC precipitates and trapped deuterium (as schematized in the bottom left figure), revealing the hydrogen trapping at the NbC-ferrite interface. The bottom right figures in [Figure 7B](#) illustrate concentration profiles from two NbC precipitates (as schematized in the bottom left figure), confirming the interface hydrogen trapping of NbC. The combination of results from [Figure 7A](#) and [B](#) provides a comprehensive depiction of hydrogen trapping mechanisms in metal carbides with a NaCl structure. In addition, Chen *et al.* utilized cryo-APT to achieve the first-ever high-resolution observations of hydrogen segregation at dislocations and GBs, further demonstrating the power of cryo-APT in advancing research on hydrogen trapping and embrittlement in steels^[34]. These groundbreaking findings have opened up new avenues for understanding the behavior of hydrogen in complex materials and its implications for material performance and design.

Aluminum alloys

Pristine aluminum (Al) and its alloys have a natural ability to form a protective aluminum oxide layer when exposed to oxygen, which shields them from further oxidation or corrosion. However, when these metals

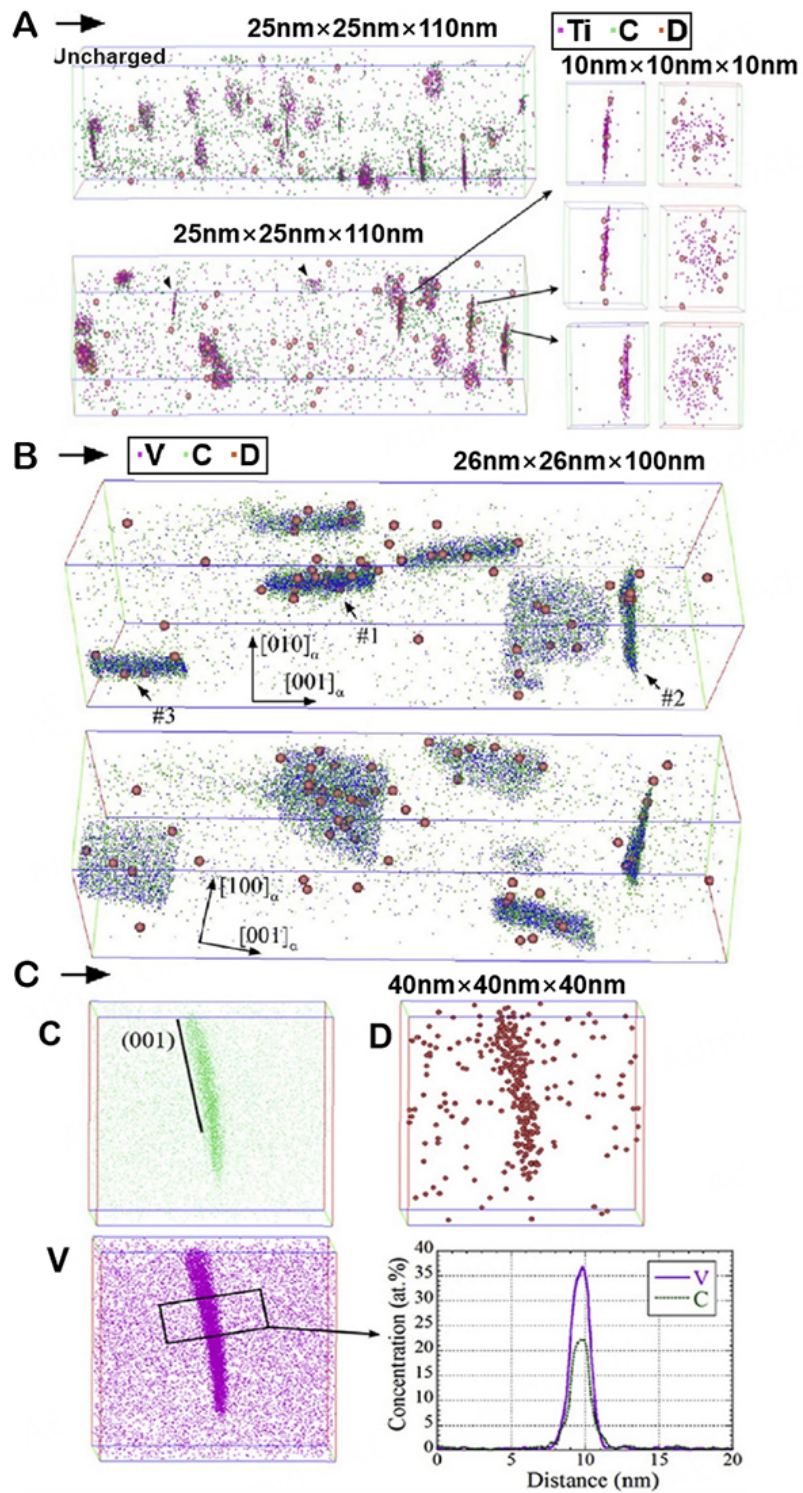


Figure 6. Observations of hydrogen (actually deuterium) atoms in steels by using cryo-APT. (A) 3-D atom maps of uncharged and deuterium-charged specimens of a TiC precipitation-strengthening steel. Reproduced with the permission of Ref.^[73] Copyright 2010, Elsevier. (B) 3-D atom maps of deuterium-charged specimens of the VC precipitation steel. Reproduced with the permission of Ref.^[76] Copyright 2012, Elsevier. (C) 3-D atom maps of a VC with trapped deuterium atoms. Reproduced with the permission of Ref.^[77] Copyright 2018, Elsevier.

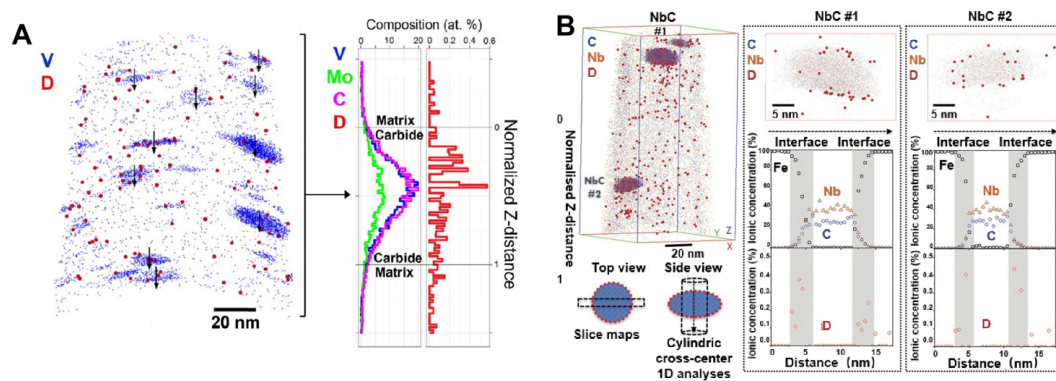


Figure 7. Cryo-APT observations of hydrogen trapping in metal carbides in ferrite steels. (A) APT analyses of a deuterium-charged ferritic steel containing V-Mo carbides. Reproduced with the permission of Ref.^[40] Copyright 2017, The American Association for the Advancement of Science. (B) APT analyses of a deuterium-charged ferritic steel containing NbC. Reproduced with the permission of Ref.^[34] Copyright 2020, The American Association for the Advancement of Science.

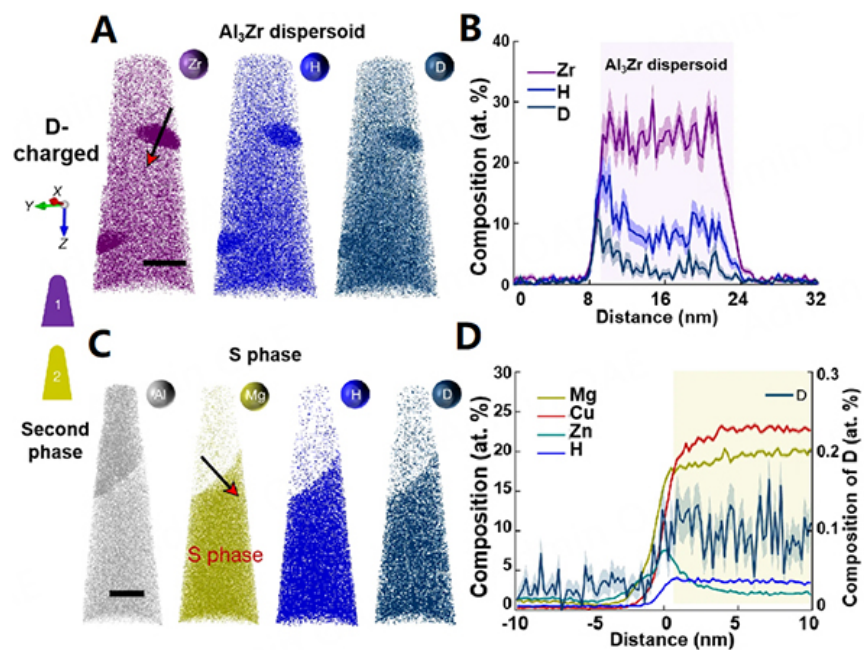


Figure 8. APT analyses deuterium-charged Al-Zn-Mg-Cu alloys. (A) 2-D slice views that include Al_3Zr dispersoids and (B) 1-D concentration profile from the arrow in (A). (C) 2-D slice views that include Al_2CuMg S phase and (D) 1-D concentration profile from the arrow in (C). Scale bars in (A, C) represent 30 nm. Reproduced with the permission of Ref.^[79] Copyright 2022, Springer Nature.

come into contact with water (H_2O) or oxidize in a moist environment, hydrogen can be produced as a by-product during the oxidation process. This hydrogen can then permeate the metal matrix and lead to hydrogen embrittlement, compromising the mechanical properties of materials^[78]. To enhance the microstructures of aluminum alloys and improve their resistance to hydrogen attack, it is crucial to investigate how hydrogen can be trapped within the material. Using APT plays a vital role in this endeavor.

Recently, Zhao *et al.* achieved success in using cryo-FIB to fabricate cryo-APT specimens and measure trapped deuterium in aluminum alloys^[79]. The team provided the first direct observations of hydrogen trapping in Al_3Zr dispersoids (shown in Figure 8A and B) and the Al_2CuMg second phase (commonly

referred to as the S phase, shown in [Figure 8C](#) and [D](#)). [Figure 8A](#) reveals co-located clusters of Zr, a component of the Al₃Zr dispersoids, along with hydrogen (H) and deuterium (D), indicating that hydrogen and deuterium are trapped within these dispersoids. [Figure 8B](#) displays a 1-D concentration profile across the dispersoid, confirming the presence of trapped hydrogen and deuterium. [Figure 8C](#) presents atom maps showing the distribution of Al (matrix), Mg (S phase), and the trapped hydrogen and deuterium. [Figure 8D](#) shows the corresponding 1-D concentration profile from the region marked in the Mg map of [Figure 8C](#). These findings offer valuable insights into the specific microstructures in aluminum alloys that have the capability to trap hydrogen, thus contributing to the development of materials that are more resistant to hydrogen embrittlement.

Titanium alloys

Titanium (Ti) alloys are highly sought after for aerospace applications due to their exceptional strength-to-weight ratio and corrosion resistance. However, Ti alloys are susceptible to hydrogen embrittlement, a phenomenon where hydrogen combines with the metal to form brittle hydride, leading to crack initiation and propagation^[65]. Characterizing the hydride and its impact in Ti alloys using conventional FIB and APT has been challenging, primarily because of the rapid formation of hydrides during specimen preparation, such as in FIB, where hydrogen is often present as a residual gas in the environment. This tendency to absorb environmental hydrogen and form artifact hydrides has caused significant confusion in material characterization when trying to identify the true origin of hydrides.

As such, Chang *et al.* developed specimen preparation methods using cryo-PFIB and cryo-APT to analyze commercially pure Ti (CP Ti) and a Ti-6Al-2Sn-4Zr-6Mo alloy (referred to as Ti6246) in their pristine states^[46]. The researchers employed hydrogen-sensitive APT to examine tip specimens prepared by electropolishing, conventional Ga FIB, Xe PFIB operating at room temperature, and cryo-PFIB. Their findings revealed that only cryo-PFIB provided hydride-free APT tips, as depicted in [Figure 9](#). [Figure 9A](#) and [B](#) displays the CP-Ti and Ti6246 samples prepared using conventional FIB, showing the presence of artifact hydrides or significant hydrogen uptake from the FIB environment. On the other hand, [Figure 9C](#) and [D](#) demonstrates that using cryo-PFIB produced hydride-free APT results for CP-Ti and Ti6246, allowing for the analysis of the beta phase, which is prone to hydrogen uptake, with low hydrogen content [[Figure 9D](#)]. These results suggest a promising path to enhance the quality of high-resolution hydrogen analysis in Ti-based alloys by utilizing cryo-APT and cryo-FIB.

Liquid and organic specimens

The research in analyzing mobile hydrogen atoms in metals has showcased the capabilities of cryo-APT and cryo-FIB workflows to achieve low temperatures. This breakthrough has paved the way for their application in the analyses and preparation of biological specimens, which predominantly consist of water and have poor conductivity. However, the existing knowledge of APT and its instrumentation is primarily geared towards conductive materials, especially metals. How organic and ice specimens can behave in APT evaporation experiments is still largely unknown, which could impede the data interpretation in the 3-D atom reconstruction.

As such, Schwarz *et al.* conducted APT analysis on ice using cryo-specimen fabrication and laser-pulsed APT, resulting in the collection of several tens of millions of atoms, as shown in the mass spectrum in [Figure 10A](#)^[80]. The analysis identified several primary peaks related to ice evaporation, with the top five peaks in relative intensity being H₃O⁺ at 19 m/z, (H₂O)H₃O⁺ at 37 m/z, (H₂O)₂H₃O⁺ at 55 m/z, (H₂O)₃H₃O²⁺ at 36.5 m/z, and (H₂O)₃H₃O⁺ at 73 m/z (note the logarithmic scale). Building upon this achievement, Schwarz *et al.* performed another analysis on an aqueous solution saturated with glucose (chemical formula: C₆H₁₂O₆) to demonstrate the ability of APT to distinguish glucose peaks from ice peaks^[81]. [Figure 10B](#) serves

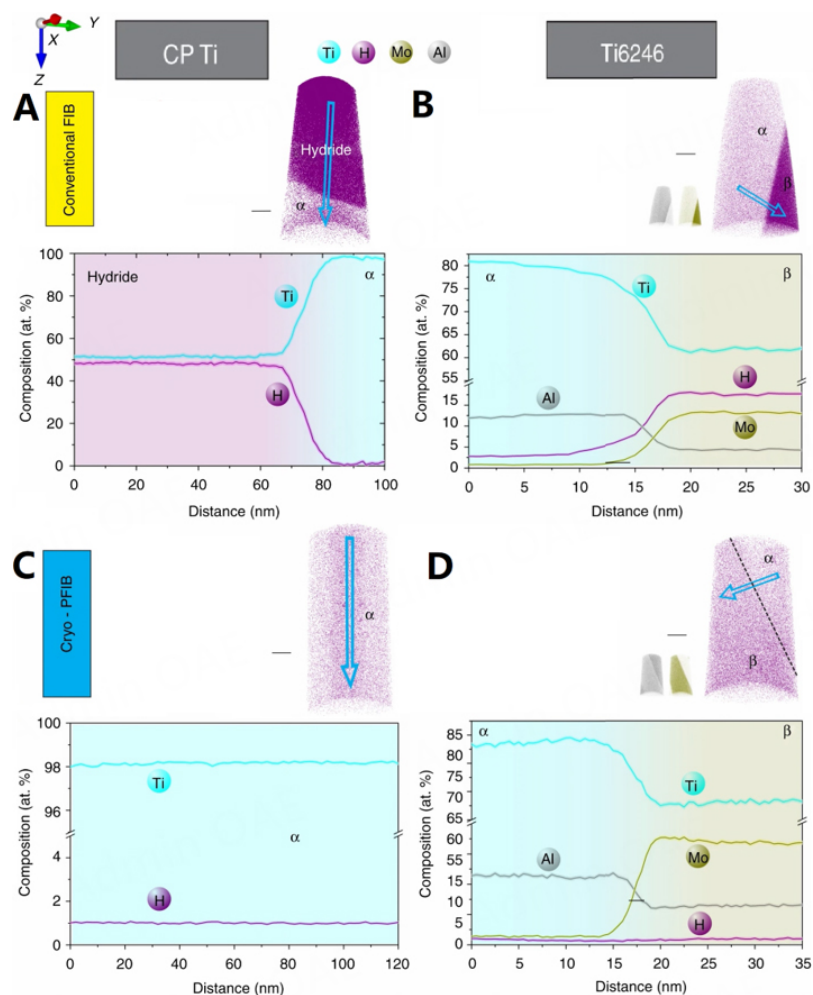


Figure 9. APT analyses of commercially pure Ti (CP Ti) and Ti6246 alloy. (A and B) are the atom maps and the corresponding concentration profiles of CP Ti and Ti6246, respectively, using conventional FIB specimen preparation at room temperature. (C and D) are the counterparts using cryo-PFIB, which show the low extent of hydrogen uptake from the specimen preparation processes. Scale bars are 20 nm. Reproduced with the permission of Ref.^[46] Copyright 2019, Springer Nature.

as a reference for the peaks related to ice, displayed on a logarithmic scale. Figure 10C presents the peaks associated with glucose, with higher m/z (> 100 m/z), depicted on a linear scale, and these peaks are clearly distinguishable from the ice peaks. These results exemplify the potential of APT in studying organic species encapsulated in an ice APT tip. Following the successes, Meng *et al.* further utilized cryo-APT and cryo-FIB to analyze organic specimens, focusing on the fragmentation behavior of linear alkane chains, such as n -tetradecanes^[42]. In their preliminary study, they discovered an extremely intricate fragmentation behavior, with numerous peaks associated with the C_xH_y ion species, where x can vary from 1 to 15. These findings open up new possibilities for studying organic compounds using cryo-APT and cryo-FIB techniques.

Schreiber *et al.* successfully employed the cryo-lift-out method (as shown in Figure 4) for cryo-APT specimens containing ice and non-homogeneous microstructures^[39]. Their success resulted in the first APT dataset that captured an interface between alkaline solution corroded glass and ice from the solution. In Figure 11A, the 3-D reconstruction of the APT dataset is depicted with purple isoconcentration surfaces (isosurfaces), highlighting areas rich in lithium (Li) and sodium (Na) that reveal the chemical heterogeneity in the alkaline ice. Additionally, green calcium ions are displayed in Figure 11A, representing the location of

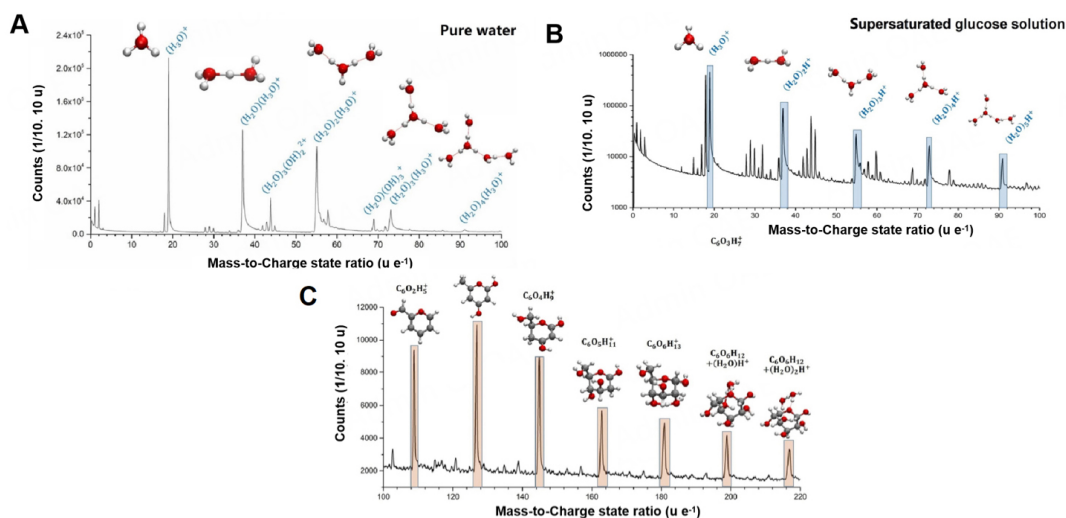


Figure 10. (A) APT mass spectrum of pure water. Reproduced with the permission of Ref.^[80] Copyright 2020, Springer Nature. (B and C) are APT mass spectra of a supersaturated glucose aqueous solution in a logarithmic scale from 0 to 100 m/z and in a linear scale from 100 to 220 m/z, respectively. Reproduced with the permission of Ref.^[81] Copyright 2021, Springer Nature.

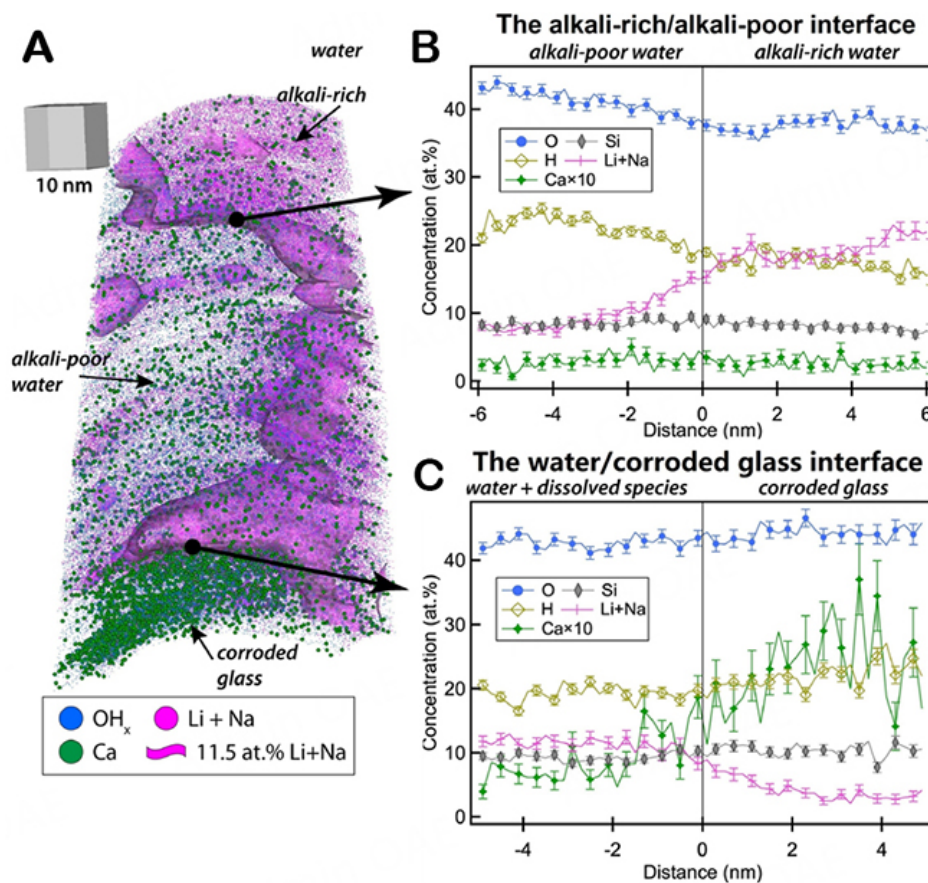


Figure 11. 3-D APT atom map and proximity histograms across the alkali-rich/alkali-poor interface in water and across the water/corroded glass interface. (A) 3-D APT atom map and proximity histograms across (B) the alkali-rich/alkali-poor interface in water and (C) across the water/corroded glass interface. Error bars indicate 1-sigma from standard counting error. Reproduced with the permission of Ref.^[39] Copyright 2018, Elsevier.

the corroded glass substrate at the bottom and their presence in the top ice region from the alkaline solution. **Figure 11B** presents the proximity histogram (proxigram) of local composition, confirming the variance of Li + Na concentration (magenta) and distinguishing it from the concentration profiles of other non-background elements such as Si and oxygen (O). In **Figure 11C**, the proxigram of the local composition near the solution-glass interface confirms the high concentration of calcium (Ca), indicating the location of the glass substrate. These results demonstrate the power of combining cryo-APT and cryo-FIB to site-specifically capture microstructural features of interest in ice, thereby opening up new applications for these techniques in biological specimens, such as cells that primarily consist of water.

Energy storage materials

The push to develop long-lasting and high-capacity energy storage materials in order to reduce reliance on carbon-based fossil fuels has gained significant momentum. APT, with its ability to offer high-resolution mapping of light elements such as Li, holds great promise in this research field for developing improved battery materials^[82].

However, when it comes to using APT for nanoscale Li mapping in battery materials, including anodes, cathodes, and electrolytes, a major challenge arises from in-situ delithiation and Li redistribution during APT experiments. The strong electrostatic field used in APT, along with the thermal migration caused by the laser beam, often leads to Li loss and inaccurate distribution in measurements, as observed in previous studies^[83,84]. Since many battery materials are reactive to air or ambient moisture, using glovebox, vacuum transfer, and cryo-transfer for accurate measurement of Li distribution has been considered. However, Kim *et al.* found that neither vacuum nor cryo-transfer provided satisfactory APT measurements^[85]. In one example dataset using a $\text{LiNi}_{0.8}\text{Co}_{0.1}\text{Mn}_{0.1}\text{O}_2$ (NMC811) cathode material and laser-pulsed APT with a specimen temperature of 60 K and low laser energy of 5 pJ, a nominally homogeneous distribution of Li was expected. However, a non-homogeneous distribution was measured, with higher Li concentration at the top and lower concentration underneath due to in-situ delithiation in APT [**Figure 12A**].

Interestingly, in **Figure 12B**, the authors observed contrasting results when the specimen was transferred in air and at room temperature, leading to the measurement of a nominally homogeneous Li distribution. They attributed this to the shielding effect of the surface layer, formed as a reaction with the ambient environment. Moreover, they found that cryo-FIB was necessary to prepare specimens with pristine compositions. In conclusion, Kim *et al.* emphasized the significance of electric-field shields and cryo-FIB, rather than cryo-APT, for obtaining high-quality APT results in Li mapping experiments^[85]. These findings highlight the importance of carefully considering the specimen preparation methods and environmental factors in APT studies of battery materials.

Using the experimental cryo-FIB method developed by Singh *et al.* further used cryo-FIB for preparing APT tips from NMC811 particles, which is a Li-containing cathode material^[86]. NMC811 particles are susceptible to corrosion in air, limiting their application in high-performance batteries. Additionally, similar to other lithium materials, NMC811 is also prone to electron beam damage during electron microscope observation, posing significant challenges in specimen preparation for APT.

To overcome these challenges, Singh *et al.* utilized the cryo-FIB method to prepare APT tips that incorporated the surface of an NMC811 particle [**Figure 13A and B**]^[86]. The particle was encapsulated in a chromium (Cr) layer deposited through physical vapor deposition (PVD) (shown in orange in **Figure 13B**). As a result, a layer consisting of Li, C, and O, representing corrosion products, was successfully captured in the APT data, as shown in **Figure 13C**. To provide detailed information about the composition of the layer,

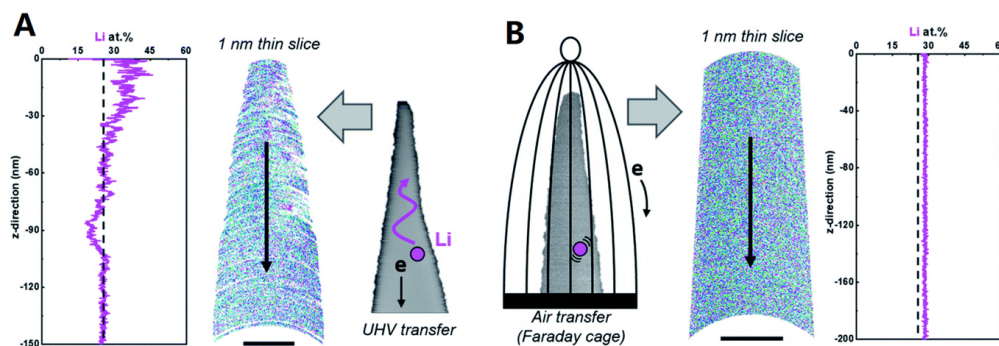


Figure 12. Li distribution of NMC811 specimens in APT. (A) APT data from a UHV transferred specimen with in-situ delithiation during the APT experiment. (B) APT data from an air-transferred specimen with the nominal Li composition and without delithiation, possibly due to the shielding effect of the surface corrosion product. The measurements were performed at a specimen temperature of 60 K and a pulsed laser energy of 5 pJ. Scale bars in (A and B) are 20 and 50 nm, respectively. Reproduced with the permission of Ref.^[85] Copyright 2022, Royal Society of Chemistry.

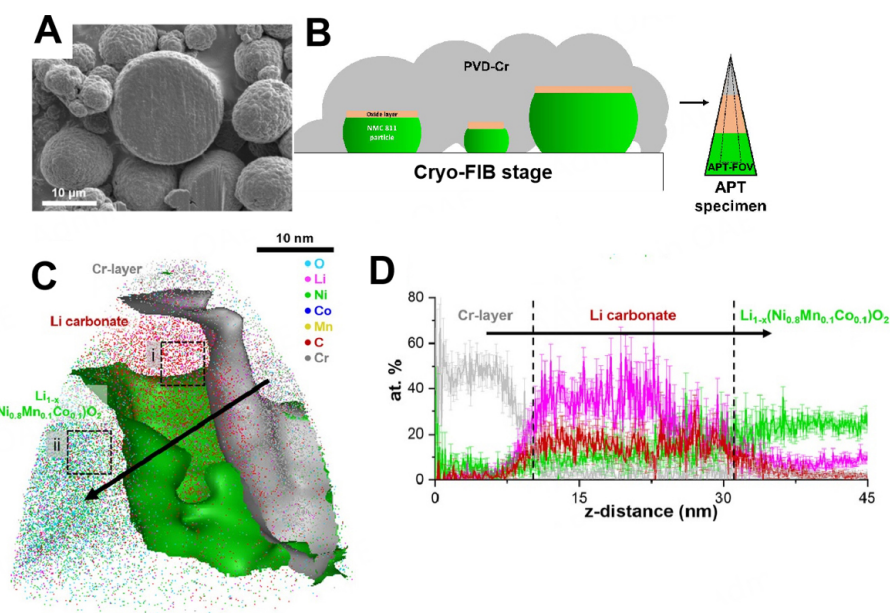


Figure 13. APT analysis of corroded $\text{LiNi}_{0.8}\text{Mn}_{0.1}\text{Co}_{0.1}\text{O}_2$ (NMC811) particle. (A) Scanning electron microscope image of the NMC811 particles. (B) Schematic illustrations of the APT specimen preparation method. The oxide layer of interest, as a corrosion product, is shown in orange. (C) 3-D reconstruction of the APT dataset of the tip incorporating the oxide later. (D) 1-D elemental concentration profile of the NMC oxide product from a cylindrical region of interest with 5 nm in diameter and 50 nm in length. Reproduced with the permission of Ref.^[86] Copyright 2022, Wiley-VCH GmbH.

a 1-D concentration profile was generated from the region indicated in [Figure 13C](#), as shown in [Figure 13D](#). This direct evidence shed light on the chemical origin of the NMC811 corrosion, revealing that it is related to both oxygen and carbon, rather than solely oxygen. Such valuable insights were challenging to obtain using conventional electron microscopy techniques due to their limited ability to detect light elements. By employing cryo-FIB and APT in this study, Singh *et al.* demonstrated the power of these advanced techniques in providing crucial information on the corrosion behavior of NMC811 particles, which could contribute significantly to the development of more stable and efficient battery materials^[86].

In battery research, there is a continuous effort to develop new anode materials that can outperform graphite, the current benchmark, while remaining cost-effective^[87]. In 1976, Lai *et al.* suggested that Si could be a promising candidate for anodes, as it has the potential to store more lithium than graphite^[88]. However, Si anode batteries suffer from poor charge-discharge cyclability due to significant volumetric changes during cycling, leading to cracking and degradation. There has been a lack of analytical techniques with sufficient spatial resolution to study the role of lithium in this degradation process, which hampers rational material design to address the issue.

Recently, Kim *et al.* made significant progress by utilizing cryo-FIB, cryo-transfer, and cryo-APT^[89], based on the experimental method developed by El-Zoka *et al.* [Figure 5]^[32]. They applied the technique to analyze the elemental distribution in a battery system comprising a liquid electrolyte and a single-crystal Si anode after various charge-discharge cycles. In Figure 14A, the researchers successfully analyzed the frozen pristine liquid electrolyte, which contains 1 M LiPF₆ with a mixture of ethylene carbonate, (CH₂O)₂CO, and diethyl carbonate, OC(OCH₂CH₃)₂, in a 1:1 volume ratio, using cryo-APT. They also provided a reference APT dataset of the single-crystal Si [Figure 14A]. After one cycle, a fragment consisting of Si and Si oxide species (SiO_x) was found in the frozen liquid electrode, indicating Si anode degradation [Figure 14B]. After 25 cycles, Figure 14C revealed a GB of Si nanocrystalline decorated with SiO_x, confirmed by transmission electron microscope (TEM) analysis. These high-resolution elemental analyses of battery materials were made possible through the use of cryo-APT, which is sensitive to light elements, in combination with cryo-FIB, allowing the analysis of liquid samples. This breakthrough paves the way for more applications in advancing other lithium-based energy storage devices using liquid electrolytes.

LIMITATIONS AND OUTLOOK

This article emphasizes the potential of cryo-APT and its combination with cryo-FIB specimen preparation for providing nanoscale elemental mapping of materials. Several examples were presented to showcase its applications in researching hydrogen in metals, liquid and organic specimens, and Li battery materials. However, it is important to acknowledge the limitations of APT. Firstly, the cryo-APT and cryo-FIB instrumentation is still under development and not yet optimal. Integrating temperature-tracking into commercial LEAP and FIB systems for a complete thermal history of specimens remains challenging. This affects the quantitative measurement of specimen temperature and precise control of ice sublimation for high-quality biological specimen preparation^[90].

Secondly, the data yield of APT experiments is limited by a high tip fracture rate. The success rate for analyzing hydrogen-charged steel tips is currently lower than 10%, and it can be even lower for less structurally robust specimens with heterogeneous interfaces or organic matter. Additionally, APT is a destructive technique, making it impossible to reproduce measurements on the same specimen. This leads to a comprehensive APT analysis being highly challenging and time-consuming. Thirdly, similar to other high-resolution microscopy techniques such as TEM, APT has a limited field of view 50 × 50 × 300 nm³. Meaningful APT observations require more sampling compared to other imaging methods, further complicated by the low data yield due to the high fracture rate.

Despite these challenges, the future of cryo-APT looks promising, with various potential applications that can provide new insights in crucial scientific areas. For instance, a correlative imaging workflow can be developed to combine APT with TEM, enabling a direct correlation of hydrogen location and its effects^[91,92]. It will also be interesting to correlatively apply imaging techniques that have wider fields of view than that of APT, such as X-ray-related techniques. This is vital for understanding hydrogen embrittlement and hydrogen storage. In analytical biology, cryo-FIB and cryo-APT can be utilized to study ionic transportation

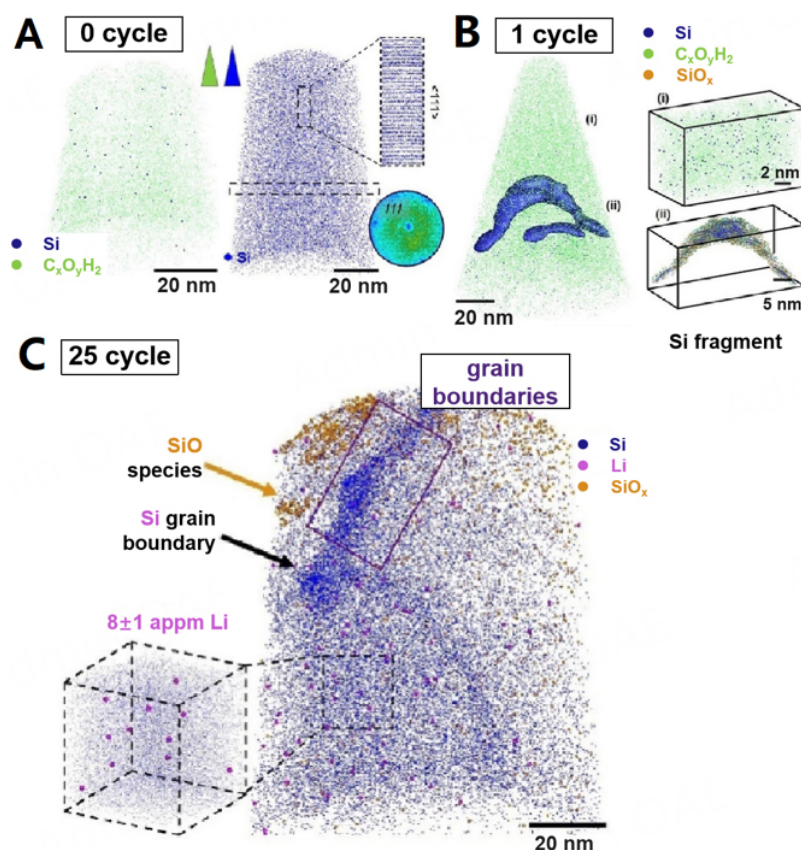


Figure 14. Cryo-APT (the protocol from Stephenson *et al.*^[36], mentioned above), along with cryo-FIB (the protocol from^[32], mentioned above), to understand the degradation of a model Si anode in a Li-ion battery at the atomic scale. (A) The result after 0 cycles; (B) The result after one cycle; (C) The result after 25 cycles. Reproduced with the permission of Ref.^[89] Copyright 2022, ACS publications.

at the sub-cellular level, providing valuable information previously only accessible through nanoscale secondary ion mass spectrometry (NanoSIMS) with sub-micrometer resolution^[93]. Moreover, the methods developed by Schreiber *et al.* and El-Zoka *et al.* offer a wide range of applications for studying corrosion in a liquid environment^[32,39]. Additionally, as more laboratories adopt cryo-workflows for APT, the accessibility of cryo-APT is rapidly increasing, leading to its widespread recognition and impact across the scientific community in the near future.

DECLARATIONS

Authors' contributions

Drafted the manuscript: Zhou Z, Wang Z

Cairney participated the writing and literature discussion: Niu R, Liu PY, Huang C, Sun YH, Wang X, Yen HW, Cairney JM

Coordinated the writing and finalized the manuscript: Chen YS

Availability of data and materials

Not applicable.

Financial support and sponsorship

The authors gratefully acknowledge funding from the Australian Research Council (Grants IE230100160, LP210300999, LE190100048, LP180100431, and FT180100232), the CITIC-CBMM Nb Steel Award Fund

Program (2018FWNB30064), Taiwan's Ministry of Education (Taiwan-University of Sydney Scholarship), the National Science and Technology Council (111-2119-M-002-020-MBK), Microscopy Australia, and the University of Sydney's Core Research Facility program.

Conflicts of interest

All authors declared that there are no conflicts of interest.

Ethical approval and consent to participate

Not applicable.

Consent for publication

Not applicable.

Copyright

© The Author(s) 2023.

REFERENCES

1. Müller EW, Panitz JA, McLane SB. The atom-probe field ion microscope. *Rev Sci Instrum* 1968;39:83-6. DOI
2. Gault B, Moody MP, Cairney JM, Ringer SP. Atom probe microscopy. Springer Science & Business Media; 2012. Available from: <https://link.springer.com/book/10.1007/978-1-4614-3436-8> [Last accessed on 31 Oct 2023].
3. Miller MK, Forbes RG. The local electrode atom probe. Springer; 2014. Available from: https://link.springer.com/chapter/10.1007/978-1-4899-7430-3_5 [Last accessed on 31 Oct 2023].
4. Lefebvre W, Vurpillot F, Sauvage X. Atom probe tomography: put theory into practice. Academic Press; 2016. Available from: <https://shop.elsevier.com/books/atom-probe-tomography/lefebvre/978-0-12-804647-0> [Last accessed on 31 Oct 2023].
5. De Geuser F, Gault B. Metrology of small particles and solute clusters by atom probe tomography. *Acta Mater* 2020;188:406-15. DOI
6. Gault B, Chiramonti A, Cojocaru-Miréidin O, et al. Atom probe tomography. *Nat Rev Methods Primers* 2021;1:51. DOI PubMed PMC
7. Kelly TF, Miller MK. Invited review article: atom probe tomography. *Rev Sci Instrum* 2007;78:031101. DOI PubMed
8. Geiser BP, Kelly TF, Larson DJ, Schneir J, Roberts JP. Spatial distribution maps for atom probe tomography. *Microsc Microanal* 2007;13:437-47. DOI PubMed
9. Müller EW. Resolution of the atomic structure of a metal surface by the field ion microscope. *J Appl Phys* 1956;27:474-6. DOI
10. Jacoby M. Atomic imaging turns 50. *Chem Eng News* 2005;83:13-6. Available from: <https://cen.acs.org/articles/83/i48/Atomic-Imaging-Turns-50.html#:~:text=By%20the%20early%201950s%2C%20far,with%20a%20field%20ion%20microscope.> [Last accessed on 31 Oct 2023]
11. Wagner A, Hall TM, Seidman DN. Simplified method for the calibration of an atom-probe field-ion microscope. *Rev Sci Instrum* 1975;46:1032-4. DOI
12. Brenner S, McKinney J. Construction and performance of an FIM-atom probe. *Surf Sci* 1970;23:88-111. DOI
13. Kelly TF, Panitz JA. The first fifty years of atom probe. *Microsc Today* 2017;25:12-7. DOI
14. Larson DJ, Prosa T, Ulfig RM, Geiser BP, Kelly TF. Local electrode atom probe tomography. New York: Springer Science; 2013. Available from: <https://link.springer.com/content/pdf/10.1007/978-1-4614-8721-0.pdf> [Last accessed on 31 Oct 2023].
15. Chen YS, Liu PY, Niu R, et al. Atom probe tomography for the observation of hydrogen in materials: a review. *Microsc Microanal* 2023;29:1-15. DOI
16. Grandfield K, Micheletti C, Deering J, Arcuri G, Tang T, Langelier B. Atom probe tomography for biomaterials and biomineralization. *Acta Biomater* 2022;148:44-60. DOI PubMed
17. Rajan K. Atom probe tomography - a high throughput screening tool for atomic scale chemistry. *Comb Chem High Throughput Screen* 2011;14:198-205. DOI PubMed
18. Miller M, Forbes R. Atom probe tomography. *Mater Charact* 2009;60:461-9. DOI
19. Silaeva EP, Karahka M, Kreuzer H. Atom probe tomography and field evaporation of insulators and semiconductors: theoretical issues. *Curr Opin Solid State Mater Sci* 2013;17:211-6. DOI
20. Reddy SM, Saxey DW, Rickard WDA, et al. Atom probe tomography: development and application to the geosciences. *Geostandard Geoanalytic Res* 2020;44:5-50. DOI
21. Liu J. Advances and applications of atomic-resolution scanning transmission electron microscopy. *Microsc Microanal* 2021;27:943-95. DOI
22. Thompson K, Lawrence D, Larson DJ, Olson JD, Kelly TF, Gorman B. In situ site-specific specimen preparation for atom probe tomography. *Ultramicroscopy* 2007;107:131-9. DOI PubMed
23. Tegg L, Breen AJ, Huang S, Sato T, Ringer SP, Cairney JM. Characterising the performance of an ultrawide field-of-view 3D atom

- probe. *Ultramicroscopy* 2023;253:113826. DOI PubMed
24. Shen PS. The 2017 nobel prize in chemistry: cryo-EM comes of age. *Anal Bioanal Chem* 2018;410:2053-7. DOI
 25. Moore EB, Molinero V. Structural transformation in supercooled water controls the crystallization rate of ice. *Nature* 2011;479:506-8. DOI PubMed
 26. Dubochet J, Adrian M, Chang JJ, et al. Cryo-electron microscopy of vitrified specimens. *Q Rev Biophys* 1988;21:129-228. DOI
 27. Gerstl S, Wepf R. Methods in creating, transferring, & measuring cryogenic samples for APT. *Microsc Microanal* 2015;21:517-8. DOI
 28. Perea DE, Gerstl SSA, Chin J, Hirschi B, Evans JE. An environmental transfer hub for multimodal atom probe tomography. *Adv Struct Chem Imaging* 2017;3:12. DOI PubMed PMC
 29. McCarroll IE, Bagot PAJ, Devaraj A, Perea DE, Cairney JM. New frontiers in atom probe tomography: a review of research enabled by cryo and/or vacuum transfer systems. *Mater Today Adv* 2020;7:100090. DOI PubMed PMC
 30. El-Zoka AA, Stephenson LT, Kim SH, Gault B, Raabe D. The fate of water in hydrogen-based iron oxide reduction. *Adv Sci* 2023;10:e2300626. DOI PubMed PMC
 31. Stender P, Gault B, Schwarz TM, et al. Status and direction of atom probe analysis of frozen liquids. *Microsc Microanal* 2022;28:1150-67. DOI
 32. El-Zoka AA, Kim SH, Deville S, Newman RC, Stephenson LT, Gault B. Enabling near-atomic-scale analysis of frozen water. *Sci Adv* 2020;6:eabd6324. DOI PubMed PMC
 33. Chen Y, Bagot PA, Moody MP, Haley D. Observing hydrogen in steel using cryogenic atom probe tomography: a simplified approach. *Int J Hydrog Energy* 2019;44:32280-91. DOI
 34. Chen YS, Lu H, Liang J, et al. Observation of hydrogen trapping at dislocations, grain boundaries, and precipitates. *Science* 2020;367:171-5. DOI
 35. Moody MP, Vella A, Gerstl SS, Bagot PA. Advances in atom probe tomography instrumentation: implications for materials research. *MRS Bull* 2016;41:40-5. DOI
 36. Stephenson LT, Szczeplaniak A, Mouton I, et al. The laplace project: an integrated suite for preparing and transferring atom probe samples under cryogenic and UHV conditions. *PLoS One* 2018;13:e0209211. DOI PubMed PMC
 37. Miller MK. Atom probe microanalysis, principles and applications to materials problems. *Mater Res Soc* 1989. Available from: https://inis.iaea.org/collection/NCLCollectionStore/_Public/19/064/19064040.pdf?r=1 [Last accessed on 31 Oct 2023].
 38. Melmed AJ. The art and science and other aspects of making sharp tips. *J Vac Sci Technol B* 1991;9:601-8. DOI
 39. Schreiber DK, Perea DE, Ryan JV, Evans JE, Vienna JD. A method for site-specific and cryogenic specimen fabrication of liquid/solid interfaces for atom probe tomography. *Ultramicroscopy* 2018;194:89-99. DOI PubMed
 40. Chen YS, Haley D, Gerstl SS, et al. Direct observation of individual hydrogen atoms at trapping sites in a ferritic steel. *Science* 2017;355:1196-9. DOI
 41. Zachman MJ, de Jonge N, Fischer R, Jungjohann KL, Perea DE. Cryogenic specimens for nanoscale characterization of solid-liquid interfaces. *MRS Bull* 2019;44:949-55. DOI
 42. Meng K, Schwarz TM, Weikum EM, Stender P, Schmitz G. Frozen *n*-tetradecane investigated by cryo-atom probe tomography. *Microsc Microanal* 2022;28:1289-99. DOI
 43. Ackerman AK, Vorontsov VA, Bantounas I, et al. Interface characteristics in an $\alpha + \beta$ titanium alloy. *Phys Rev Mater* 2020;4:013602. DOI
 44. Zhang S, Gervinskas G, Qiu S, et al. Methods of preparing nanoscale vitreous ice needles for high-resolution cryogenic characterization. *Nano Lett* 2022;22:6501-8. DOI
 45. Liliensten L, Gault B. New approach for FIB-preparation of atom probe specimens for aluminum alloys. *PLoS One* 2020;15:e0231179. DOI PubMed PMC
 46. Chang Y, Lu W, Guénolé J, et al. Ti and its alloys as examples of cryogenic focused ion beam milling of environmentally-sensitive materials. *Nat Commun* 2019;10:942. DOI PubMed PMC
 47. Halpin JE, Webster RWH, Gardner H, Moody MP, Bagot PAJ, MacLaren DA. An in-situ approach for preparing atom probe tomography specimens by xenon plasma-focussed ion beam. *Ultramicroscopy* 2019;202:121-7. DOI PubMed
 48. Marko M, Hsieh C, Schalek R, Frank J, Mannella C. Focused-ion-beam thinning of frozen-hydrated biological specimens for cryo-electron microscopy. *Nat Methods* 2007;4:215-7. DOI PubMed
 49. Rigort A, Bäuerlein FJ, Villa E, et al. Focused ion beam micromachining of eukaryotic cells for cryoelectron tomography. *Proc Natl Acad Sci USA* 2012;109:4449-54. DOI PubMed PMC
 50. Mahamid J, Schampers R, Persoon H, Hyman AA, Baumeister W, Plitzko JM. A focused ion beam milling and lift-out approach for site-specific preparation of frozen-hydrated lamellas from multicellular organisms. *J Struct Biol* 2015;192:262-9. DOI PubMed
 51. Parmenter CD, Fay MW, Hartfield C, Eltaher HM. Making the practically impossible “merely difficult”-cryogenic FIB lift-out for “damage free” soft matter imaging. *Microsc Res Tech* 2016;79:298-303. DOI PubMed
 52. Saxey DW, Cairney JM, McGrouther D, Honma T, Ringer SP. Atom probe specimen fabrication methods using a dual FIB/SEM. *Ultramicroscopy* 2007;107:756-60. DOI PubMed
 53. Gordon LM, Joester D. Nanoscale chemical tomography of buried organic-inorganic interfaces in the chiton tooth. *Nature* 2011;469:194-7. DOI PubMed
 54. Gordon LM, Tran L, Joester D. Atom probe tomography of apatites and bone-type mineralized tissues. *ACS Nano* 2012;6:10667-75. DOI PubMed

55. Gordon LM, Cohen MJ, MacRenaris KW, Pasteris JD, Seda T, Joester D. Dental materials. Amorphous intergranular phases control the properties of rodent tooth enamel. *Science* 2015;347:746-50. DOI PubMed
56. Fontaine A, Zavgorodniy A, Liu H, Zheng R, Swain M, Cairney J. Atomic-scale compositional mapping reveals Mg-rich amorphous calcium phosphate in human dental enamel. *Sci Adv* 2016;2:e1601145. DOI PubMed PMC
57. Langelier B, Wang X, Grandfield K. Atomic scale chemical tomography of human bone. *Sci Rep* 2017;7:39958. DOI PubMed PMC
58. Sundell G, Dahlin C, Andersson M, Thuvander M. The bone-implant interface of dental implants in humans on the atomic scale. *Acta Biomater* 2017;48:445-50. DOI PubMed
59. Prosa TJ, Keeney SK, Kelly TF. Atom probe tomography analysis of poly(3-alkylthiophene)s. *J Microsc* 2010;237:155-67. DOI PubMed
60. Rusitzka KAK, Stephenson LT, Szczepaniak A, et al. A near atomic-scale view at the composition of amyloid-beta fibrils by atom probe tomography. *Sci Rep* 2018;8:17615. DOI PubMed PMC
61. Perea DE, Liu J, Bartrand J, et al. Atom probe tomographic mapping directly reveals the atomic distribution of phosphorus in resin embedded ferritin. *Sci Rep* 2016;6:22321. DOI PubMed PMC
62. Sundell G, Hulander M, Pihl A, Andersson M. Atom probe tomography for 3D structural and chemical analysis of individual proteins. *Small* 2019;15:e1900316. DOI PubMed
63. Narayan K, Prosa TJ, Fu J, Kelly TF, Subramaniam S. Chemical mapping of mammalian cells by atom probe tomography. *J Struct Biol* 2012;178:98-107. DOI PubMed PMC
64. Martin ML, Connolly MJ, DelRio FW, Slifka AJ. Hydrogen embrittlement in ferritic steels. *Appl Phys Rev* 2020;7:041301. DOI PubMed PMC
65. Robertson IM, Sofronis P, Nagao A, et al. Hydrogen embrittlement understood. *Metall Mater Trans B* 2015;46:1085-103. DOI
66. Pressouyre G. Trap theory of hydrogen embrittlement. *Acta Metall* 1980;28:895-911. DOI
67. Bhadeshia HKDH. Prevention of hydrogen embrittlement in steels. *ISIJ Int* 2016;56:24-36. DOI
68. Chang Y, Breen AJ, Tarzimoghdam Z, et al. Characterizing solute hydrogen and hydrides in pure and alloyed titanium at the atomic scale. *Acta Mater* 2018;150:273-80. DOI
69. Chang Y, Zhang S, Liebscher CH, et al. Could face-centered cubic titanium in cold-rolled commercially-pure titanium only be a Ti-hydride? *Scr Mater* 2020;178:39-43. DOI
70. Haley D, Merzlikin S, Choi P, Raabe D. Atom probe tomography observation of hydrogen in high-Mn steel and silver charged via an electrolytic route. *Int J Hydrog Energy* 2014;39:12221-9. DOI
71. Breen AJ, Stephenson LT, Sun B, et al. Solute hydrogen and deuterium observed at the near atomic scale in high-strength steel. *Acta Mater* 2020;188:108-20. DOI
72. Sundell G, Thuvander M, Andrén HO. Hydrogen analysis in APT: methods to control adsorption and dissociation of H₂. *Ultramicroscopy* 2013;132:285-9. DOI PubMed
73. Takahashi J, Kawakami K, Kobayashi Y, Tarui T. The first direct observation of hydrogen trapping sites in TiC precipitation-hardening steel through atom probe tomography. *Scr Mater* 2010;63:261-4. DOI
74. Zhu X, Li W, Zhao H, Wang L, Jin X. Hydrogen trapping sites and hydrogen-induced cracking in high strength quenching & partitioning (Q&P) treated steel. *Int J Hydrog Energy* 2014;39:13031-40. DOI
75. Meier MS, Jones ME, Felfer PJ, Moody MP, Haley D. Extending estimating hydrogen content in atom probe tomography experiments where H₂ molecule formation occurs. *Microsc Microanal* 2022;28:1231-44. DOI
76. Takahashi J, Kawakami K, Tarui T. Direct observation of hydrogen-trapping sites in vanadium carbide precipitation steel by atom probe tomography. *Scr Mater* 2012;67:213-6. DOI
77. Takahashi J, Kawakami K, Kobayashi Y. Origin of hydrogen trapping site in vanadium carbide precipitation strengthening steel. *Acta Mater* 2018;153:193-204. DOI
78. Gangloff RP, Someday BP. Gaseous hydrogen embrittlement of materials in energy technologies: the problem, its characterisation and effects on particular alloy classes. Elsevier; 2012. Available from: <https://shop.elsevier.com/books/gaseous-hydrogen-embrittlement-of-materials-in-energy-technologies/gangloff/978-1-84569-677-1> [Last accessed on 31 Oct 2023].
79. Zhao H, Chakraborty P, Ponge D, et al. Hydrogen trapping and embrittlement in high-strength Al alloys. *Nature* 2022;602:437-41. DOI PubMed PMC
80. Schwarz TM, Weikum EM, Meng K, et al. Field evaporation and atom probe tomography of pure water tips. *Sci Rep* 2020;10:20271. DOI PubMed PMC
81. Schwarz TM, Dietrich CA, Ott J, et al. 3D sub-nanometer analysis of glucose in an aqueous solution by cryo-atom probe tomography. *Sci Rep* 2021;11:11607. DOI PubMed PMC
82. Devaraj A, Gu M, Colby R, et al. Visualizing nanoscale 3D compositional fluctuation of lithium in advanced lithium-ion battery cathodes. *Nat Commun* 2015;6:8014. DOI PubMed PMC
83. Pfeiffer B, Maier J, Arlt J, Nowak C. In Situ atom probe deintercalation of lithium-manganese-oxide. *Microsc Microanal* 2017;23:314-20. DOI PubMed
84. Greiwe GH, Balogh Z, Schmitz G. Atom probe tomography of lithium-doped network glasses. *Ultramicroscopy* 2014;141:51-5. DOI PubMed
85. Kim SH, Antonov S, Zhou X, et al. Atom probe analysis of electrode materials for Li-ion batteries: challenges and ways forward. *J Mater Chem A Mater* 2022;10:4926-35. DOI PubMed PMC

86. Singh MP, Kim SH, Zhou X, et al. Near-atomic-scale evolution of the surface chemistry in Li[Ni,Mn,Co]O₂ cathode for Li-ion batteries stored in air. *Adv Energy Sustain Res* 2023;4:2200121. [DOI](#)
87. McDowell MT, Lee SW, Nix WD, Cui Y. 25th anniversary article: understanding the lithiation of silicon and other alloying anodes for lithium-ion batteries. *Adv Mater* 2013;25:4966-85. [DOI](#) [PubMed](#)
88. Lai SC. Solid lithium-silicon electrode. *J Electrochem Soc* 1976;123:1196. [DOI](#)
89. Kim SH, Dong K, Zhao H, et al. Understanding the degradation of a model Si anode in a Li-ion battery at the atomic scale. *J Phys Chem Lett* 2022;13:8416-21. [DOI](#) [PubMed](#) [PMC](#)
90. Usukura J, Narita A, Matsumoto T, et al. A cryo-TSEM with temperature cycling capability allows deep sublimation of ice to uncover fine structures in thick cells. *Sci Rep* 2021;11:21406. [DOI](#) [PubMed](#) [PMC](#)
91. Kuzmina M, Herbig M, Ponge D, Sandlöbes S, Raabe D. Linear complexions: confined chemical and structural states at dislocations. *Science* 2015;349:1080-3. [DOI](#) [PubMed](#)
92. Huang L, Chen D, Xie D, et al. Quantitative tests revealing hydrogen-enhanced dislocation motion in α -iron. *Nat Mater* 2023;22:710-6. [DOI](#)
93. Greenwood DJ, Dos Santos MS, Huang S, et al. Subcellular antibiotic visualization reveals a dynamic drug reservoir in infected macrophages. *Science* 2019;364:1279-82. [DOI](#) [PubMed](#) [PMC](#)

Review

Open Access



Magnetic structures and correlated physical properties in antiperovskites

Sihao Deng^{1,2}, Hongde Wang^{1,5}, Lunhua He^{1,3,4}, Cong Wang⁵

¹Spallation Neutron Source Science Center, Dongguan 523803, Guangdong, China.

²Institute of High Energy Physics, Chinese Academy of Sciences, Beijing 100049, China.

³Institute of Physics, Chinese Academy of Sciences, Beijing 100190, China.

⁴Songshan Lake Materials Laboratory, Dongguan 523808, Guangdong, China.

⁵School of Integrated Circuit Science and Engineering, Beihang University, Beijing 100191, China.

Correspondence to: Prof. Lunhua He, Institute of Physics, Chinese Academy of Sciences, Beijing 100190, China, E-mail: lhhe@ihp.ac.cn; Prof. Cong Wang, School of Integrated Circuit Science and Engineering, Beihang University, Beijing 100191, China. E-mail: congwang@buaa.edu.cn

How to cite this article: Deng S, Wang H, He L, Wang C. Magnetic structures and correlated physical properties in antiperovskites. *Microstructures* 2023;3:2023044. <https://dx.doi.org/10.20517/microstructures.2023.42>

Received: 21 Aug 2023 **First Decision:** 5 Sep 2023 **Revised:** 11 Sep 2023 **Accepted:** 21 Sep 2023 **Published:** 10 Nov 2023

Academic Editor: Danmin Liu **Copy Editor:** Fangyuan Liu **Production Editor:** Fangyuan Liu

Abstract

Compounds with perovskite structures have become one of the focuses in both materials science and condensed matter physics because of their fascinating physical properties and potential functionalities correlated to magnetic structures. However, the understanding of the intriguing physical properties is still at an exploratory stage. Herein, owing to the magnetic frustration prompted by Mn_6N or Mn_6C octahedra, the abounding magnetic structures of antiperovskites, including collinear antiferromagnetic, collinear ferromagnetic, collinear ferrimagnetic, non-collinear magnetic, and non-coplanar magnetic spin configurations, are systematically introduced through the updated coverage. In addition, owing to the “spin-lattice-charge” coupling of antiperovskites, a large number of physical properties, such as anomalous thermal expansion, giant magnetoresistance, anomalous Hall effect, piezomagnetic/baromagnetic effects, magnetocaloric effect, barocaloric effect, etc., are summarized by combining the discussions of the determined magnetic structures. This review aims to clarify the current research progress in this field, focusing on the relationship between the magnetic structures and the correlated physical properties, and provides the conclusion and outlook on further performance optimization and mechanism exploration in antiperovskites.

Keywords: Antiperovskite, magnetic structures, physical properties, strong correlation material



© The Author(s) 2023. **Open Access** This article is licensed under a Creative Commons Attribution 4.0 International License (<https://creativecommons.org/licenses/by/4.0/>), which permits unrestricted use, sharing, adaptation, distribution and reproduction in any medium or format, for any purpose, even commercially, as long as you give appropriate credit to the original author(s) and the source, provide a link to the Creative Commons license, and indicate if changes were made.



INTRODUCTION

Since the 1980s, compounds with perovskite structures have become one of the focuses in both materials science and condensed matter physics because of their fascinating physical properties and potential functionalities. These properties include superconductivity, multiferroics, colossal magnetoresistance, negative thermal expansion (NTE), *etc.*^[1-4]. In the antiperovskite compounds (antiperovskites) similar to the perovskite structure, numerous interesting physical properties have also been observed, such as NTE^[5-25], giant magnetoresistance^[26-27], anomalous Hall effect^[28-30], piezomagnetic/baromagnetic effects^[23,31-35], magnetocaloric effect^[36-39], barocaloric effect^[40,41], nearly zero temperature coefficient of resistivity^[42-46], superconductivity^[47,48], *etc.* Therefore, antiperovskites have gained significant attention. Nevertheless, the understanding of these abnormal physical properties is still in the exploratory stage, and the accumulation of experimental data and further deepening of theoretical research are required.

The so-called antiperovskite structure refers to a structure that is similar to perovskite. As shown in [Figure 1](#), the face-centered position occupied by non-metallic elements, such as oxygen, in the original perovskite structure is occupied by transition group element atoms M, especially the magnetic element $M = \text{Mn, Fe, Ni, etc.}$ The body center position originally occupied by metal elements is occupied by non-metallic elements N or C, and the original vertex position is occupied by metal element X, thus forming a lattice belonging to a cubic unit cell with chemical formula $\text{M}_3\text{XN}(\text{C})$ ($M = \text{Mn, Fe, Ni; X = Zn, Ga, Cu, Al, In, Sn}$). Among them, face-centered magnetic atoms (such as Mn) and body-centered N (C) atoms can form NMn_6 or CMn_6 octahedra, and six magnetic atoms Mn are located at the six corners of the octahedron, which is prone to magnetic frustration. Thereby it generates the abounding magnetic structures, including collinear antiferromagnetic (AFM), collinear ferromagnetic (FM), collinear ferrimagnetic (FIM), non-collinear magnetic, and non-coplanar magnetic spin configurations^[49-51]. On the other hand, the abundant magnetic structures in antiperovskite $\text{Mn}_3\text{XN}(\text{C})$ compounds are very sensitive to changes in temperature, magnetic field, pressure, composition, and grain size. Its abnormal lattice change, magnetic phase transition, and electronic transport properties are interrelated and affect each other, showing its rich physical properties.

In this paper, we will summarize the magnetic structures and correlated physical properties in antiperovskites. We present the potential application of antiperovskites as novel materials in various emerging fields. In order to further optimize performance and explore mechanisms, the issues such as exploration of new magnetic structures, synthesis of single crystal samples, and practical application research for the in-depth research are deserved in the part of outlook.

MAGNETIC STRUCTURES IN MN-BASED ANTIPEROVSKITES

The research on the magnetic structures of antiperovskites mainly focuses on Mn-based compounds. Herein, the collinear, non-collinear, and non-coplanar magnetic structures in Mn-based antiperovskites will be introduced in this review.

Collinear magnetic structure

Both collinear AFM and collinear FM structures were determined by neutron diffraction in Mn_3GaC as early as the 1970s. Upon warming, Mn_3GaC displays several magnetic phase transitions: an AFM-intermediate (AFM-IM) phase transition at 160.1 K, an intermediate-FM (IM-FM) phase transition at 163.9 K, and a FM-paramagnetic (FM-PM) transition at 248 K^[52]. As shown in [Figure 2A](#), the determined magnetic moments m of AFM Mn_3GaC alternates along the [111] direction with a propagation vector $\mathbf{k} = (1/2, 1/2, 1/2)$, corresponding to $m = 1.8 \pm 0.1 \mu_B/\text{Mn}$ at 4.2 K reported by Fruchart *et al.* and $m = 1.54 \mu_B/\text{Mn}$ at 150 K revealed by Çakır *et al.*^[53-55]. As seen from [Figure 2B](#), the propagation vector for FM

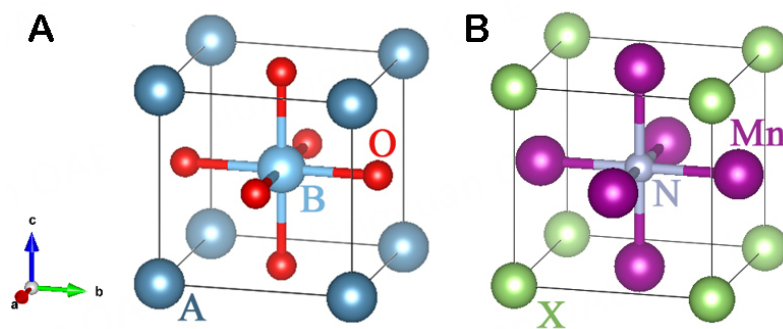


Figure 1. (A) Perovskite structure ABO_3 ; (B) antiperovskite structure Mn_3XN .

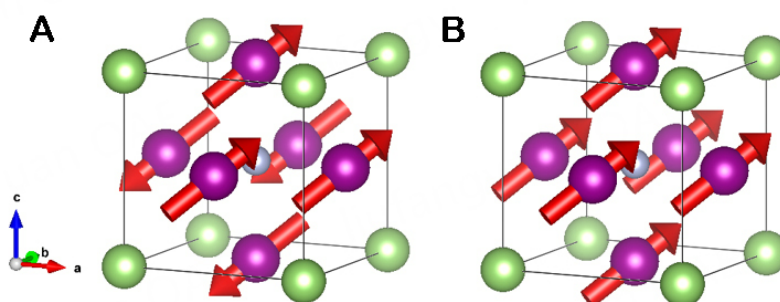


Figure 2. The collinear (A) AFM structure and (B) FM structure of Mn_3GaC .

Mn_3GaC is $k = (0, 0, 0)$, displaying $m = 1.3 \pm 0.1 \mu_B/Mn$ at 193 K^[53,54]. The direction [111] of easy magnetization is also confirmed by the Mössbauer effect^[56].

Mn_3ZnN is characterized by two first-order magnetic transitions: PM-AFM at 183 K and AFM-AFM at 140 K. As shown in [Figure 3A](#), the low temperature AFM phase is collinear within a $\sqrt{2}a, \sqrt{2}a, 2a$ sub-lattice of manganese, exhibiting two inequivalent magnetic atoms with different ordered magnetic moments^[57]. The values of moments $0.61 \mu_B$ on Mn1 (000) and $1.03 \mu_B$ on Mn2 (1/4, 1/4, 1/4) were clarified by Fruchart *et al.*^[58]. In 2012, we determined the ordered moments of $1.40 \mu_B$ on Mn1 and $2.44 \mu_B$ on Mn2 at 80 K for $Mn_3Zn_{0.99}N$ by neutron diffraction^[20]. Moreover, for $Mn_{3.19}Zn_{0.77}N_{0.94}$, we observed a collinear FIM structure with a propagation vector $k = (0, 0, 0)$ below 200 K [[Figure 3B](#)]. The magnetic moments alternate along the [111] direction with different values, corresponding to $0.5(1)$ (face-centered atom) and $1.3(7)$ (corner atom) μ_B/Mn for Mn atoms at 120 K^[21].

Non-collinear magnetic structures

It is worth noting that two non-collinear AFM phases belonging to Γ^{4g} and Γ^{5g} types, respectively, have been studied extensively in antiperovskites. In this case, the compounds remain cubic with the propagation vector $k = (0, 0, 0)$. For Γ^{5g} type shown in [Figure 4A](#), the magnetic moments of Mn atoms are located in the (111) plane with a triangular arrangement. As seen from [Figure 4B](#), the magnetic moments of Γ^{4g} are triangularly located in the (111) plane achieved by rotating 90° coherently from Γ^{5g} type. In Γ^{4g} and Γ^{5g} magnetic structures, two Mn atoms form an angle of 120° with each other in the (111) plane, and the magnetic moments of the three atoms cancel each other out to generate a zero net magnetic moment.

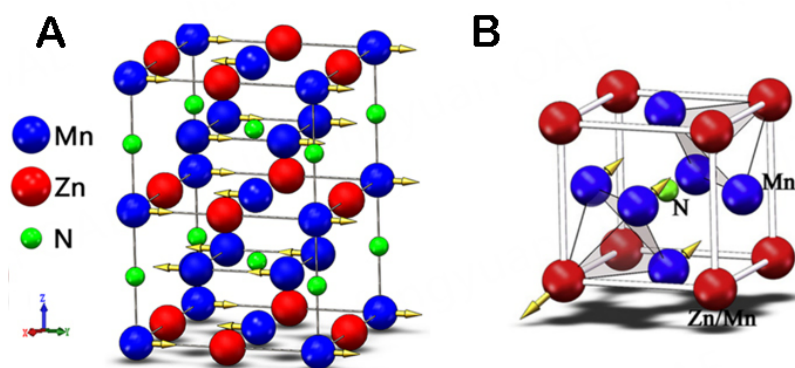


Figure 3. The collinear (A) AFM structure of Mn_3ZnN ^[57] and (B) the FIM structure of $\text{Mn}_{3.19}\text{Zn}_{0.77}\text{N}_{0.94}$ ^[21].

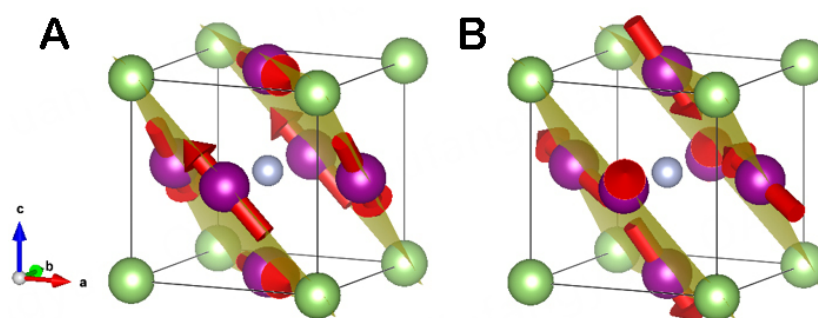


Figure 4. The non-collinear (A) Γ^{5g} and (B) Γ^{4g} AFM structures of antiperovskites.

So far, five typical undoped antiperovskites displaying the non-collinear magnetic structures of Γ^{4g} and Γ^{5g} types have been reported experimentally, including Mn_3NiN , Mn_3ZnN , Mn_3GaN , Mn_3AgN , and Mn_3SnN . The magnetic structure of Mn_3NiN below 163 K, Mn_3ZnN between 140 K and 183 K, Mn_3GaN below 298 K, and Mn_3AgN between 55 and 290 K belongs single-phase Γ^{5g} type, corresponding to the magnetic moments $0.98 \mu_B/\text{Mn}$ ($T = 77 \text{ K}$), $1.21 \mu_B/\text{Mn}$ ($T = 159 \text{ K}$), $1.17 \mu_B/\text{Mn}$ ($T = 4.2 \text{ K}$), and $3.1 \mu_B/\text{Mn}$ ($T = 4.2 \text{ K}$), respectively^[54]. This type of magnetic structure has had an important impact on the mechanism exploration of the NTE behavior, piezomagnetic effect, and barocaloric effect of antiperovskites. In addition, the magnetic structures of Mn_3NiN between 163 K and 266 K, Mn_3AgN below 55 K and Mn_3SnN between 237 K and 357 K are composed of Γ^{4g} and Γ^{5g} types, showing the magnetic moments $0.8 \mu_B/\text{Mn}$ at 250 K, $3.1 \mu_B/\text{Mn}$ and $2.5 \mu_B/\text{Mn}$ at 250 K at 4.2 K, respectively^[54]. It was suggested that the magnetic behavior of antiperovskites is very sensitive to the differences of sample composition. In $\text{Mn}_3\text{Ni}_{0.9}\text{N}_{0.96}$, the magnetic structure is a combination of Γ^{4g} and Γ^{5g} symmetries below $T_N = 264 \text{ K}$, and the moments undergo a rotation in the (111) plane upon warming^[59]. Moreover, for $\text{Mn}_3\text{Zn}_{0.6}\text{N}$, the sample fully transforms to the Γ^{5g} phase upon cooling below 185 K, and the low-temperature collinear magnetic structure existing in Mn_3ZnN disappears^[20].

The non-collinear Γ^{5g} AFM structure is also examined by both neutron diffraction and the correlated thermal expansion behavior in doped antiperovskites, such as $\text{Mn}_3\text{Cu}_{1-x}(\text{Ge}, \text{Sn})_x\text{N}$, $\text{Mn}_3\text{Zn}_{1-x}(\text{Ge}, \text{Sn})_x\text{N}$, and $\text{Mn}_3\text{Ga}_{1-x}\text{Sn}_x\text{N}$, etc.^[5-22]. Particularly, the undoped Mn_3CuN does not display the Γ^{5g} magnetic configuration. As shown in [Figure 5](#), a cubic structure with the Γ^{5g} magnetic configuration was determined by neutron study in $\text{Mn}_3\text{Cu}_{1-x}\text{Ge}_x\text{N}$ ($x \geq 0.15$), which is suggested to be a key ingredient of a large magnetovolume effect in antiperovskites^[18]. Meanwhile, the NTE behavior determined by Γ^{5g} magnetic order was also observed in

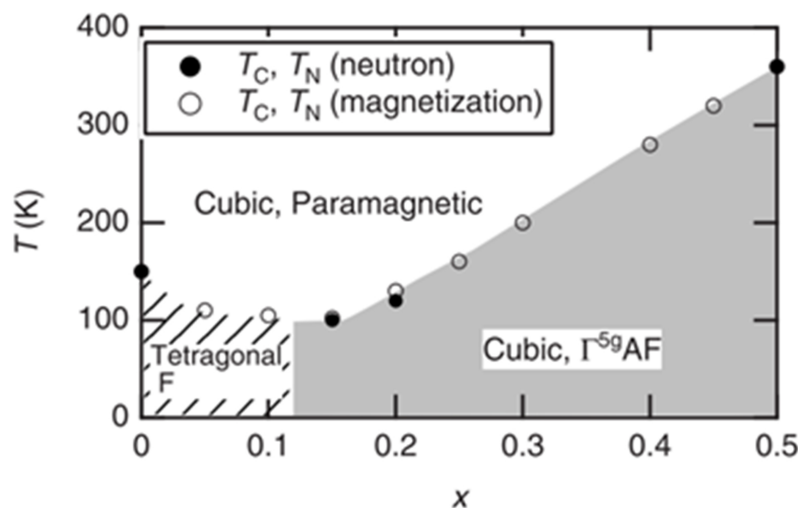


Figure 5. Phase diagram of $\text{Mn}_3\text{Cu}_{1-x}\text{Ge}_x\text{N}$. T_C and T_N denote the Curie and Néel temperatures, respectively^[18].

$\text{Mn}_3\text{Zn}_{1-x}\text{Ge}_x\text{N}$ ^[11,20]. In $\text{Mn}_3\text{Cu}_{1-x}\text{Sn}_x\text{N}$, the AFM transition closely coupled with the volume change is broadened upon Sn doping, producing the NTE behavior^[19]. The characterization of magnetic structures in doped systems still requires careful study by neutron scattering.

Non-coplanar magnetic structures

A non-coplanar FIM structure with the propagation vector $k = (1/2, 1/2, 0)$ has been reported in Mn_3CuN ^[54,60]. The magnetic ordering temperature of the Mn_3CuN compound is 143 K^[54]. With cooling, the compound shows a transition from a high-temperature cubic phase to a low-temperature tetragonal phase. Herein, the magnetic moment direction of Mn atoms in the $z = 0$ plane is along the $[001]$ direction, while the atoms in the $z = 0.5$ plane have two magnetic components, namely the FM arrangement in the $[001]$ direction and the “square” AFM arrangement in the $z = 0.5$ plane^[54]. It is worth noting that the antiperovskite Mn_3SnC with a magnetic ordering temperature of 294 K has the same type of magnetic structure as Mn_3CuN . Moreover, as shown in Figure 6A, an orthorhombic magnetic structure model with P_1 symmetry was determined in $\text{Mn}_3\text{Cu}_{0.89}\text{N}_{0.96}$. The sub-lattice of a magnetic structure is $2c \times 2a \times b$, where a , b , and c are nuclear lattice parameters. At 6 K, neutron diffraction revealed that the Mn moments show an AFM component of $3.65 \mu_B/\text{Mn}$ on the $z = 0.5$ plane and a FM component of $0.91 \mu_B/\text{Mn}$ parallel to the y -axis on the $x = 0.25$ and 0.75 planes^[39].

Figure 6B gives a non-collinear magnetic structure M-1 of $\text{Mn}_3\text{Ga}_{0.95}\text{N}_{0.94}$. The M-1 phase remains 79% in coexistence with Γ^{58} magnetic configuration between 6 K and 50 K^[35]. It can be seen that the sub-lattice of the M-1 phase is $\sqrt{2}a, \sqrt{2}a, a$, where a is the lattice parameter of the nuclear structure. For the M-1 phase, the results of neutron diffraction indicate that Mn atoms comprise three different locations, including Mn1 1a (0, 0, 0), Mn2 2b (0.5, 0.5, 0), and Mn3 4d (0.25, 0.25, 0.5). Mn1 and Mn2 display the AFM components along the z axis. Mn3 consists of two magnetic components; one is the “square” AFM component on the plane $z = 0.5$, and the other one is the FM component along a z axis direction. At 6 K, the AFM moment is $0.89 \mu_B/\text{Mn}$ for Mn1 and Mn2, while Mn3 includes a FM moment of $2.18 \mu_B/\text{Mn}$ and an AFM moment of $0.7 \mu_B/\text{Mn}$.

Recently, the non-collinear FIM structures were determined in the $(1-x)\text{Mn}_3\text{GaN} - x\text{Mn}_3\text{SbN}$ ($0.2 \leq x \leq 0.8$) heterogeneous system^[61] [Figure 6C]. Upon cooling, Mn_3SbN undergoes a PM-FIM phase transition at

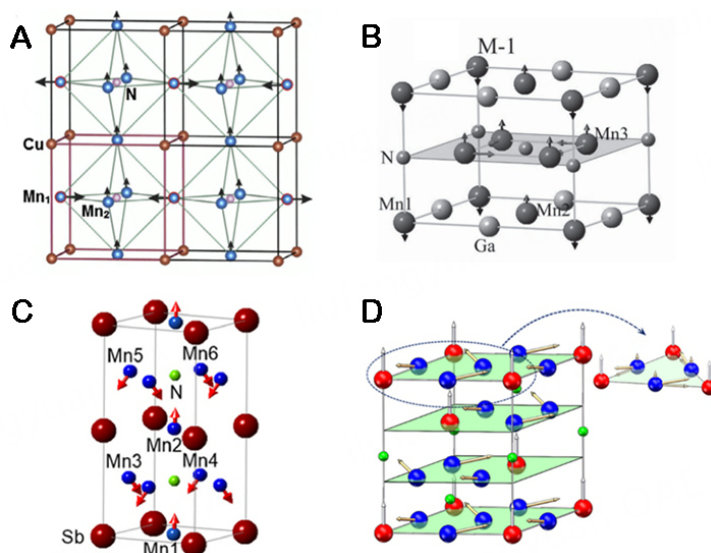


Figure 6. The non-coplanar FIM structures of (A) $\text{Mn}_3\text{Cu}_{0.89}\text{N}_{0.96}$ ^[39], (B) $\text{Mn}_3\text{Ga}_{0.95}\text{N}_{0.94}$ ^[35], (C) Mn_3SbN ^[61], and (D) $\text{Mn}_{3.39}\text{Co}_{0.61}\text{N}$ ^[62].

~353 K and FIM-M2 phase transition at ~250 K. Neutron diffraction pattern at 300 K reveals the non-collinear FIM phase with a sub-lattice $a, a, 2c$ where a and c are the lattice parameters of the tetragonal nuclear structure. The Mn atoms are located at six different types of sites with a P4 space group. Mn1 (0.5, 0.5, 0) and Mn2 (0.5, 0.5, 0.5) display the FM component $2.5 \mu_B/\text{Mn}$ along the z axis. Moreover, the tiled magnetic moments were uncovered for Mn3 (0.5, 0, 0.25), Mn4 (0, 0.5, 0.25), Mn5 (0.5, 0, 0.75), and Mn6 (0, 0.5, 0.75), corresponding to $(-2.47, 2.47, -2.16) \mu_B/\text{Mn}$, $(2.47, -2.47, -2.16) \mu_B/\text{Mn}$, $(2.47, -2.47, -2.16) \mu_B/\text{Mn}$, and $(-2.47, 2.47, -2.16) \mu_B/\text{Mn}$, respectively. At 5 K, another non-coplanar magnetic structure M2 with $\sqrt{2}a, \sqrt{2}a, a$ was revealed in Mn_3SbN . Herein, Mn atoms on the plane $z = 0.5$ show a “square” AFM arrangement with the moment $2.3 \mu_B/\text{Mn}$, while the other Mn atoms display the AFM component along the z axis with the moment $2.5 \mu_B/\text{Mn}$. The minor differences between the presented magnetic structure and the previously reported one may arise from the tiny elemental components^[54]. Even more interesting in antiperovskites is that the propagation vector $\mathbf{k} = (0, 0, k_z)$ of Mn_3SnN varies with temperature from $k_z = 0.25$ at 50 K to $k_z = 0.125$ at 237 K^[54].

The effect of magnetic element doping on the magnetic structure was also investigated in antiperovskites. For Mn-doped $\text{Mn}_{3+x}\text{Ni}_{1-x}\text{N}$ and $\text{Mn}_{3.39}\text{Co}_{0.61}\text{N}$ compounds [Figure 6D], a FM component along the [111] direction coexisting with canted Γ^{5g} AFM component was resolved by neutron diffraction technique^[15,62]. Table 1 summarizes the magnetic structures and corresponding temperature ranges of typical antiperovskites.

PHYSICAL PROPERTIES OF ANTIPEROVSKITES

The research on antiperovskite structure compounds can be traced back to the 1930s when there were not many studies on physical properties. Since the 1980s, this type of compound has been paid attention by scientists, and the basic physical properties of antiperovskites have been studied by means of neutron diffraction, X-ray diffraction (XRD), Mössbauer spectroscopy, and nuclear magnetic resonance. Extensive research of these basic physical properties mainly includes crystal structures, magnetic properties (magnetic structures), phase diagrams, *etc.* At the beginning of the 21st century, superconductivity, giant magnetoresistance, magnetocaloric effect, abnormal thermal expansion, and near-zero temperature coefficient of resistance behaviors were successively reported in antiperovskites. The discovery of these physical properties prompted more and more researchers to pay attention to antiperovskites and their

Table 1. Magnetic structures and corresponding temperature ranges in antiperovskites

Antiperovskites	Magnetic ordering	Spin configurations	Temperature range
Mn ₃ GaN ^[52]	Ferromagnetic intermediate antiferromagnetic	Collinear	163.9 K < T < 248 K 160.1 K < T < 163.9 K T < 160.1 K
Mn ₃ ZnN ^[58]	Antiferromagnetic	Γ^{5g} Collinear	140 K < T < 183 K T < 140 K
Mn ₃ NiN ^[54]	Antiferromagnetic	$\Gamma^{5g} + \Gamma^{4g}$ Γ^{5g}	163 K < T < 266 K T < 163 K
Mn ₃ GaN ^[54]	Antiferromagnetic	Γ^{5g}	T < 298 K
Mn ₃ AgN ^[54]	Antiferromagnetic	Γ^{5g} $\Gamma^{5g} + \Gamma^{4g}$	55 K < T < 290 K T < 55 K
Mn ₃ SnN ^[54]	Antiferromagnetic	Collinear $\Gamma^{5g} + \Gamma^{4g}$	357 K < T < 475 K 237 K < T < 357 K
Mn ₃ CuN ^[54]	Ferrimagnetic	Non-coplanar	T < 143 K

applications. In the past decade or so, a large number of physical properties correlated to magnetic structures have been reported.

Anomalous thermal expansion in manganese-based antiperovskites

Materials with zero thermal expansion (ZTE) and NTE behaviors have attracted widespread attention because of their broad applications in modern technology, such as high-precision optical instruments, microelectronics, aerospace devices, *etc.*^[63-69]. A great deal of work has focused on the discovery of new materials and the improvement of thermal expansion properties. Nevertheless, the investigations for the mechanism of anomalous thermal expansion (ATE) (mainly including ZTE and NTE) are still needed. For ZrW₂O₈^[67] and ScF₃^[68], the mechanism associated with the soft phonon mode of the frame structure is adopted; moreover, the ATE behavior of the material has a strong coupling effect with other physical properties, such as the valence state change in LaCu₃Fe₄O₁₂^[69], BiNiO₃^[70], and YbGaGe^[63] and the ferroelectric characteristics in PbTiO₃-BiFeO₃^[71]; in addition, the ATE behavior emerges with magnetic transitions in various materials, such as the NTE in La(Fe,Si,Co)₁₃^[72] and Ca₂Ru_{1-x}Cr_xO₄^[73] and near ZTE in FeNi Invar^[74] and SrRuO₃^[75]. It is worth noting that although a large number of studies have shown that the Invar effect is related to the magnetic properties of materials, an adequate understanding of this property is still required. Therefore, the exploration of new materials with ATE will contribute to the clarification of mechanisms^[75-80].

Some manganese nitrogen compounds (such as Mn₃ZnN at 185 K, Mn₃GaN at 298 K, *etc.*) are accompanied by a sudden change in volume during the magnetic transition, that is, the so-called magnetovolume effect. In 2005, Takenaka *et al.* reported the NTE behavior in the Ge-doped antiperovskite structure compound Mn₃Cu_{1-x}Ge_xN^[5]. For Mn₃CuN, the compound itself has no magnetovolume effect. Through the doping of Ge, the discontinuous volume change caused by the magnetic volume effect is broadened, thereby realizing the regulation of the thermal expansion coefficient and temperature range of the NTE behavior. With increasing the doping amount of Ge, the magnetovolume effect of Mn₃Cu_{1-x}Ge_xN was broadened and moved to the high temperature region, resulting in NTE behavior near room temperature. As shown in **Figure 7A** and **7B**, near room temperature, the linear expansion coefficient α of Mn₃Cu_{0.53}Ge_{0.47}N and Mn₃Cu_{0.5}Ge_{0.5}N are $-16 \times 10^{-6} \text{ K}^{-1}$ and $-12 \times 10^{-6} \text{ K}^{-1}$, respectively. In order to further reduce the material cost, Takenaka *et al.* used Sn as the dopant, which is cheaper than Ge. The doping of Sn can also broaden the NTE behavior of antiperovskites^[6].

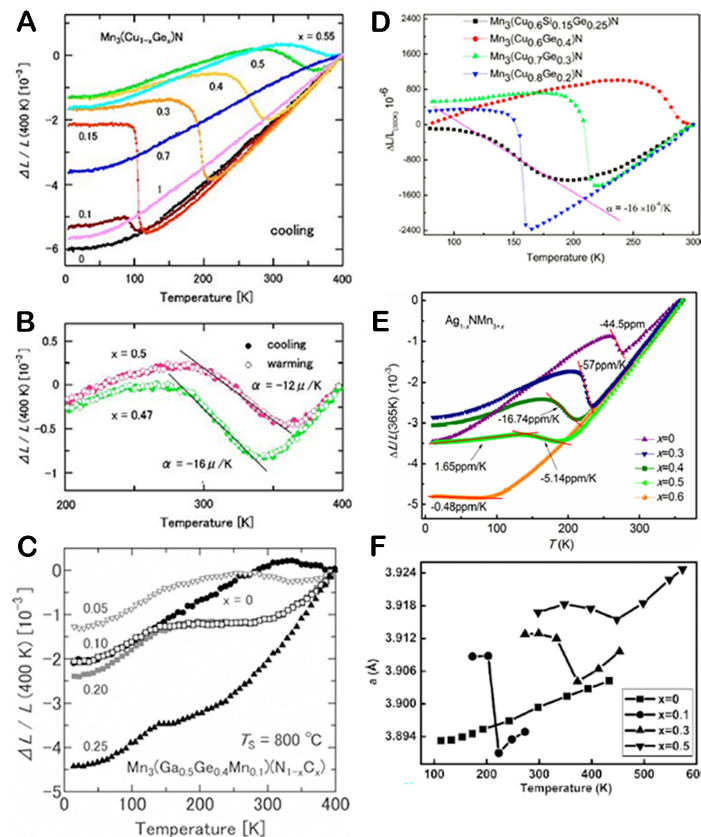


Figure 7. Linear thermal expansion of antiperovskites (A, B) $\text{Mn}_3\text{Cu}_{1-x}\text{Ge}_x\text{N}$ ^[5], (C) $\text{Mn}_3\text{Ga}_{0.5}\text{Ge}_{0.4}\text{Mn}_{0.1}\text{N}_{1-x}\text{C}_x$ ^[7], (D) $\text{Mn}_3\text{Cu}_{0.6}\text{Si}_x\text{Ge}_{0.4-x}\text{N}$ ^[8], (E) $\text{Mn}_{3+x}\text{Ag}_{1-x}\text{N}$ ^[9], and (F) $\text{Mn}_3\text{Zn}_{1-x}\text{Ge}_x\text{N}$ ^[11].

The thermal expansion behavior of $\text{Mn}_3\text{Ga}_{0.5}\text{Ge}_{0.4}\text{Mn}_{0.1}\text{N}_{1-x}\text{C}_x$ was also reported, and a single-phase ZTE material with a wider temperature range has been obtained^[7]. As shown in **Figure 7C**, the thermal expansion behavior of $\text{Mn}_3\text{Ga}_{0.5}\text{Ge}_{0.4}\text{Mn}_{0.1}\text{N}_{1-x}\text{C}_x$ changes with the doping of C. When $x = 0.1$, the compound exhibits low thermal expansion in the temperature range of 190–272 K with $|\alpha| < 0.5 \times 10^{-6} \text{ K}^{-1}$. In addition, a very close correlation between N content and NTE behavior was found in $\text{Mn}_3\text{Cu}_{0.5}\text{Sn}_{0.5}\text{N}_{1-\delta}$. The N content in the compound decreases with the increase of the sintering temperature. When the sintering temperature is 950 degrees, the linear expansion coefficient of the compound with the N content of about 0.8 in the temperature range of 307–355 K with $|\alpha| < 0.5 \times 10^{-6} \text{ K}^{-1}$.

Huang *et al.* carried out research on Ge and Si co-doped $\text{Mn}_3\text{Cu}_{0.6}\text{Si}_x\text{Ge}_{0.4-x}\text{N}$ and obtained a low-temperature NTE material^[8]. As shown in **Figure 7D**, with the co-doping of Si, the NTE temperature range of the compound moves to a lower temperature. When $x = 0.15$, $\text{Mn}_3\text{Cu}_{0.6}\text{Si}_{0.15}\text{Ge}_{0.25}\text{N}$ shows NTE behavior in a wide temperature range in the temperature range of 120–184 K, and its linear expansion coefficient is $\alpha = -16 \times 10^{-6} \text{ K}^{-1}$. Comparing $\text{Mn}_3\text{Cu}_{0.6}\text{Si}_x\text{Ge}_{0.4-x}\text{N}$ and $\text{Mn}_3\text{Cu}_{1-x}\text{Ge}_x\text{N}$, it can be seen that the single doping of Ge has a narrow volume mutation temperature range in the low temperature region (such as $\text{Mn}_3\text{Cu}_{0.8}\text{Ge}_{0.2}\text{N}$ around 155 K), while the co-doping of Si can make that the temperature range of the volume change of the compound is broadened and the behavior of NTE appears. The co-doping method provides a way to regulate the thermal expansion behavior of single-phase materials.

Lin *et al.* reported the thermal expansion and magnetic properties of antiperovskite manganese nitrides $\text{Mn}_{3+x}\text{Ag}_{1-x}\text{N}$ ^[9]. The substitution of Mn for Ag effectively broadens the temperature range of NTE and moves

it to low temperatures [Figure 7E]. When $x = 0.6$, the $\text{Mn}_3\text{Ag}_{0.4}\text{N}$ compound shows ZTE with $\alpha = -0.48 \times 10^{-6} \text{ K}^{-1}$ (temperature range 5 - 87 K). Moreover, Lin *et al.* revealed a giant NTE covering room temperature in nanocrystalline $\text{Mn}_3\text{Ga}_x\text{N}_x$ ^[10]. By reducing the average grain size to ~ 10 nm, the temperature window ΔT for NTE exceeds 100 K, and α remains as large as -30 ppm/K (-21 ppm/K) for $x = 1.0$ ($x = 0.9$).

The influence of Ge and Sn doping on the thermal expansion behavior of $\text{Mn}_3\text{Zn}_{1-x}\text{Ge}(\text{Sn})_x\text{N}$ has been investigated by us^[11,12]. Figure 7F shows the variation of lattice constant with temperature in $\text{Mn}_3\text{Zn}_{1-x}\text{Ge}_x\text{N}$. The doping of Ge broadens the magnetovolume effect of $\text{Mn}_3\text{Zn}_{1-x}\text{Ge}_x\text{N}$ and moves the temperature zone to the higher one, thereby realizing the regulation of NTE behavior. A similar behavior was also observed in Sn-doped $\text{Mn}_3\text{Zn}_{1-x}\text{Sn}_x\text{N}$ compounds^[12]. On the other hand, the regulation of the thermal expansion behavior of Mn_3NiN -based compounds has also been reported^[13,14]. Antiperovskite $\text{Mn}_3\text{Ni}_{0.5}\text{Ag}_{0.5}\text{N}$ shows NTE behavior in a wide temperature range (260-320 K) near room temperature with $\alpha = -12 \times 10^{-6} \text{ K}^{-1}$. The $\text{Mn}_3\text{Ni}_{0.5}\text{Cu}_{0.5}\text{N}$ exhibits NTE in the temperature range of 160-240 K ($\Delta T = 80$ K) with $\alpha = -22.3 \times 10^{-6} \text{ K}^{-1}$. Interestingly, a new type of Invar-like material exhibiting ZTE has been revealed in $\text{Mn}_{3+x}\text{Ni}_{1-x}\text{N}$ ^[15].

Song *et al.* revealed the ZTE behavior of $\text{Mn}_3\text{Cu}_{0.5}\text{Ge}_{0.5}\text{N}$ due to the size effect^[16]. When $\text{Mn}_3\text{Cu}_{0.5}\text{Ge}_{0.5}\text{N}$ was prepared from polycrystalline samples (average size of 2.0 μm) to ultra-nanocrystals (average size of 12 nm), the occupancy rate of Mn in the sample changed from 100% to 78.7% [Figure 8A]. Meanwhile, the ultra-nanocrystalline sample exhibits ZTE behavior in a wide temperature range $\Delta T = 218$ K (12-230 K) with $\alpha = 1.18 \times 10^{-7} \text{ K}^{-1}$.

The mechanism for the NTE of antiperovskites was investigated by Iikub *et al.* The neutron diffraction results indicate that the non-collinear Γ^{5g} AFM structure plays a key role in the magnetovolume effect of $\text{Mn}_3\text{Cu}_{1-x}\text{Ge}_x\text{N}$, which leads to the appearance of NTE behavior. Moreover, Iikub *et al.* further revealed that the local lattice distortion plays a very important role in the NTE of $\text{Mn}_3\text{Cu}_{1-x}\text{Ge}_x\text{N}$ ^[17] [Figure 8B]. As suggested by the pair distribution function (PDF) analysis, $\text{Mn}_3\text{Cu}_{1-x}\text{Ge}_x\text{N}$ maintains a cubic structure within a certain doping range, while the Mn_6N octahedrons in $\text{Mn}_3\text{Cu}_{1-x}\text{Ge}_x\text{N}$ rotate along the z-axis with Ge doping to form a local lattice distortion. This structural instability displays a strong correlation with the broadness of the growth of the ordered magnetic moment, which is considered as a trigger for broadening the volume change^[18]. Moreover, Tong *et al.* studied the magnetic transition broadening and local lattice distortion in $\text{Mn}_3\text{Cu}_{1-x}\text{Sn}_x\text{N}$ with NTE^[19]. The PDF results indicate that the distribution of Cu/Sn-Mn bonds is linked to the fluctuations of the AFM integral. This may account for the broadening of the volume change in antiperovskites.

Through the study of $\text{Mn}_3(\text{Zn}, \text{M})_x\text{N}$ ($\text{M} = \text{Ag}, \text{Ge}$), we revealed the quantitative relationship between thermal expansion and atomic magnetic moments in antiperovskites and realized the regulation of thermal expansion^[20]. A collinear AFM structure M_{PTE} and a non-collinear AFM structure Γ^{5g} are observed in $\text{Mn}_3\text{Zn}_x\text{N}$. Herein, the M_{PTE} phase displays PTE behavior, while the Γ^{5g} configuration shows NTE behavior. The NTE of Γ^{5g} phase can balance the contributions from PTE generated by the anharmonic vibration in the sample, producing the ZTE of antiperovskites. By introducing vacancies into $\text{Mn}_3\text{Zn}_x\text{N}$, the existence of a temperature range for Γ^{5g} configuration can be effectively regulated, thereby obtaining a ZTE material with a wider temperature range. In addition, we also discussed the quantitative relationship between the anomalous change of the lattice and the atomic magnetic moments for the Γ^{5g} phase. As shown in Figure 8C, both the lattice change $a_{\text{NTE}} - a_{\text{T}}$ and the atomic magnetic moment m in $\text{Mn}_3\text{Zn}_x\text{N}$ gradually decrease with the increase of temperature, and the change trends for both factors are consistent. By defining $r(T) = (a_{\text{NTE}} - a_{\text{T}})/m$, it is obtained that $r(T)$ hardly changes with temperature where a_{NTE} , a_{T} and m are the lattice constants and magnitude of the ordered magnetic moment, which confirms that there is a strong

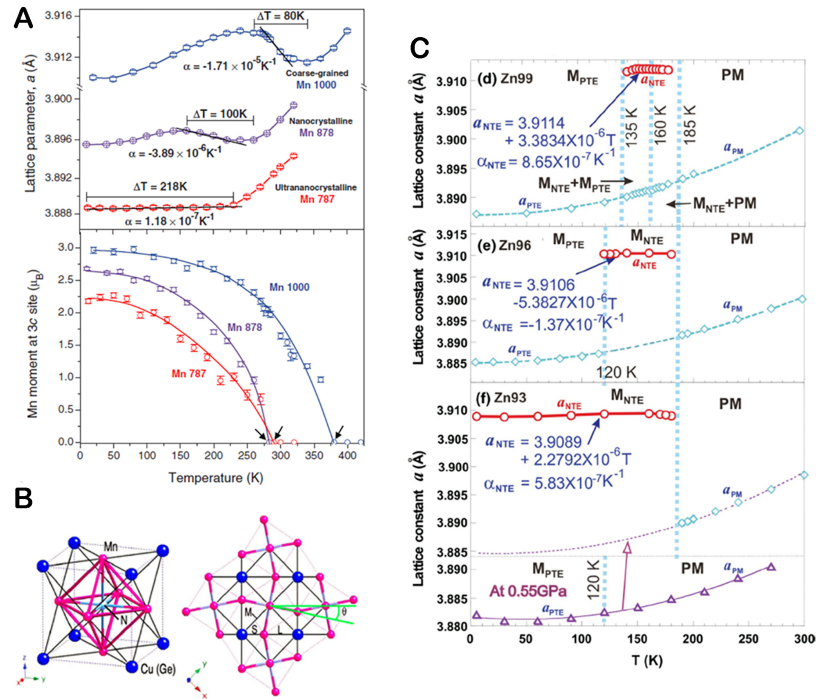


Figure 8. (A) ZTE behavior of $\text{Mn}_3\text{Cu}_{0.5}\text{Ge}_{0.5}\text{N}$ ^[16]; (B) local lattice distortion of $\text{Mn}_3\text{Cu}_{1-x}\text{Ge}_x\text{N}$ ^[17]; (C) the relationship between the anomalous change of the lattice and the atomic magnetic moments for Γ^{5g} phase of $\text{Mn}_3\text{Zn}_x\text{N}$ ^[20].

spin-lattice coupling between the lattice constant and the atomic magnetic moment in $\text{Mn}_3\text{Zn}_x\text{N}$. In addition, the strong spin-lattice coupling that can be tuned to achieve ZTE behavior was further confirmed in antiperovskite $\text{Mn}_{3+x}\text{Ni}_{1-x}\text{N}$ and $\text{Mn}_{3.15}\text{Zn}_{0.77}\text{N}_{0.94}$ within Γ^{5g} phase^[15,21]. Meanwhile, in $\text{Mn}_3\text{Ga}_{1-x}\text{Sn}_x\text{N}$ with Γ^{5g} phase, the increase of the phonon contribution to the thermal expansion induced by Sn doping and the corresponding decrease of dm/dT are revealed to be the key parameters for tuning the magnetovolume effect^[22].

The first-principle calculations have been adopted for understanding the NTE behavior of antiperovskites. The primary theoretical works focus on the comparison of differences in equilibrium volumes of antiperovskites with different magnetic structures. Lukashev *et al.* found that the equilibrium volume of the Γ^{5g} AFM state in Mn_3GaN is larger than that of the PM state, which confirms that the magnetic transition in the material can lead to volume change (magnetovolume effect)^[23]. Qu *et al.* calculated the energy-lattice curves of various magnetic configurations, and the results show that the Γ^{5g} AFM state has the largest volume. This work also confirms that the Γ^{5g} AFM state has the largest volume compared to other magnetic configurations^[24]. In addition, Mochizuki *et al.* constructed a classical spin model with frustrated exchange interactions and magnetic anisotropy to study the nontrivial magnetic orders in the antiperovskite Mn_3AN . With a replica-exchange Monte Carlo technique, the Γ^{5g} and Γ^{4g} spin configurations, known to trigger the NTE, have been reproduced^[25].

Electronic transport properties in antiperovskites

There is a strong correlation between the lattice, spin, and charge of Mn_3GaC . Therefore, a giant magnetoresistance effect was found near its collinear AFM - collinear FM magnetic transition^[26]. The size of magnetoresistance can be expressed by $[\rho(H) - \rho(0)]/\rho(0)$, and $\rho(H)$ and $\rho(0)$ represent the resistivity when the external magnetic field is finite and 0, respectively. As shown in Figure 9A, Mn_3GaC generates a

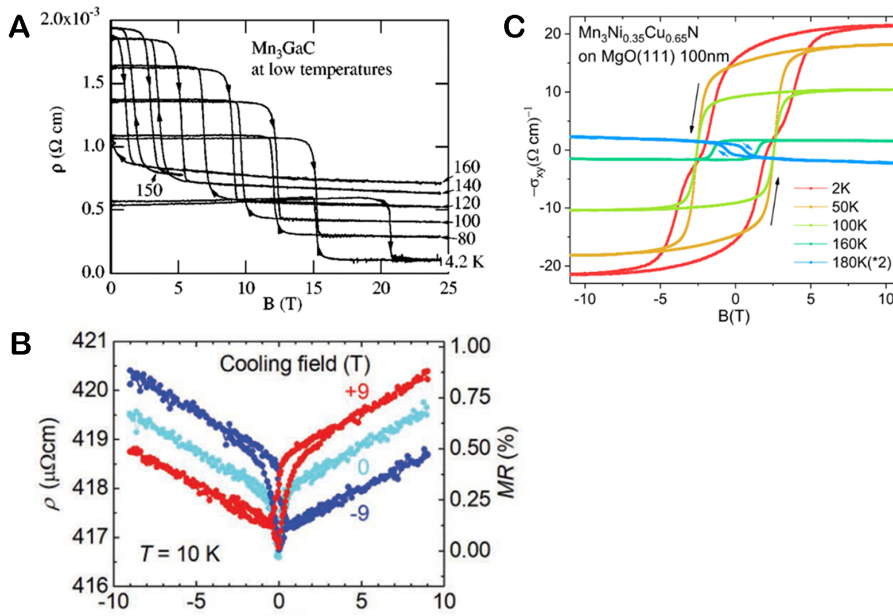


Figure 9. (A) Giant magnetoresistance effect of Mn_3GaC at selected temperatures^[26]; (B) magnetoresistance of $\text{Mn}_{3.338}\text{Ni}_{0.651}\text{N}$ after cooling in zero field and in $\pm 9 \text{ T}$ ^[27]; (C) anomalous Hall conductivity versus field measured in single crystalline $\text{Mn}_3\text{Ni}_{0.35}\text{Cu}_{0.65}\text{N}$ film on $\text{MgO}(111)$ substrate^[30].

magnetoresistance of about 50% under an external magnetic field of 3 kOe. With the further increase of the external magnetic field, the magnetoresistance value is almost unchanged, but its peak width is broadened and reaches 20 K at 50 kOe. Kamishima *et al.* suggested that the magnetoresistance effect in Mn_3GaC is aroused by the difference of resistivity between AFM and FM states, and the external magnetic field can induce the temperature shift of AFM-FM phase transition^[26]. In addition, an electroresistance-like behavior of the antiperovskite Mn_3GaC , revealed by a resistivity change of 50% due to the local Joule heating, is reported around the collinear AFM- intermediate phase transition. The currents significantly reduce the proportion of the higher resistivity AFM phase relative to the lower resistivity interphase with warming, showing a change in resistivity. On the other hand, for a non-coplanar magnet $\text{Mn}_{3.338}\text{Ni}_{0.651}\text{N}$ with triangular lattice, a high-resistivity state can be frozen along the direction of the cooling field while a low-resistivity state is determined in the reversed field direction, indicating an asymmetry with respect to H [Figure 9B]. This characteristic further demonstrates a switchable scalar spin chirality of $\text{Mn}_{3.338}\text{Ni}_{0.651}\text{N}$.

Recently, the anomalous Hall effect, originating from the nonvanishing momentum space Berry curvature, has been reported in the non-collinear AFM antiperovskites. Among the magnetic orders, a typical non-collinear AFM configuration is Γ^{4g} , whose atomic magnetic moments point to the triangle "inside" or "outside" in the triangular lattice of the antiperovskite (111) surface, forming a phase similar to that of Mn_3A ($X = \text{Sn}, \text{Ge}, \text{Pt}$) non-collinear magnets. Another typical AFM phase Γ^{5g} can be obtained by rotating the atomic magnetic moments in Γ^{4g} by 90 degrees in the (111) plane. Both of these two magnetic phases have zero scalar chirality, and theoretical studies show that the former and the latter magnetic order display a finite and zero anomalous Hall resistivity, respectively. In 2019, Gurung *et al.* used symmetry analysis and density functional theory to study the anomalous Hall conductance in non-collinear magnetic antiperovskites, revealing that the Γ^{4g} magnetic phase in Mn_3GaC shows a finite value of anomalous Hall conductivity, while the Γ^{5g} magnetic phase displays zero anomalous Hall conductivity^[28]. In 2020, Samathrakris *et al.* theoretically calculated the tailoring of the anomalous Hall effect in the non-collinear antiperovskite Mn_3GaC , revealing the large intrinsic anomalous Hall effect caused by the strain in the Γ^{5g}

and Γ^{4g} magnetic phases^[29]. In 2019, Zhao *et al.* experimentally observed the anomalous Hall effect in the non-collinear AFM $\text{Mn}_3\text{Ni}_{1-x}\text{Cu}_x\text{N}$, which is attributed to the nonzero Berry curvature of the Γ^{4g} magnetic phase in momentum space [Figure 9C]^[30]. The research on the anomalous Hall effect of antiperovskites is attracting widespread attention for novel spintronic applications.

Piezomagnetic/baromagnetic effects in antiperovskites

The piezomagnetic effect has been reported in non-collinear AFM antiperovskites^[23,33]. In 2008, Lukashev *et al.* predicted that the non-collinear magnetic structure of Mn_3GaN can be controlled by a small applied biaxial strain [Figure 10A]^[23]. Figure 10B shows the net magnetic moment of Mn_3GaN and the rotational angle of the magnetic moment of Mn atoms as a function of axial strain. It can be seen that the atomic magnetic moment rotates when the strain is applied. This piezomagnetic effect is linear and displays magnetization reversal with the applied strain. As the compressive strain is 1%, the magnetization is about $0.04 \mu_B/\text{f.u.}$ Therefore, this property can be utilized for the application of the magnetoelectric effect, such as a combination of piezomagnetic and piezoelectric phases or a combination of magnetostrictive and piezoelectric phases^[31,32]. In addition, Zemen *et al.* theoretically performed a systematic study of the piezomagnetic effect in nine cubic antiperovskites Mn_3XN ($\text{X} = \text{Rh}, \text{Pd}, \text{Ag}, \text{Co}, \text{Ni}, \text{Zn}, \text{Ga}, \text{In}, \text{Sn}$), revealing an extraordinarily large piezomagnetic effect in Mn_3SnN at room temperature^[33]. Boldrin *et al.* demonstrate experimentally that a giant piezomagnetic effect is indeed manifest in the AFM antiperovskite Mn_3NiN ^[34].

In 2016, the baromagnetic effect of $\text{Mn}_3\text{Ga}_{0.95}\text{N}_{0.94}$ was determined by both neutron diffraction analysis and magnetic measurements^[35]. Interestingly, $\text{Mn}_3\text{Ga}_{0.95}\text{N}_{0.94}$ displays a new tetragonal non-coplanar magnetic structure M-1 below 50 K, which is in coexistence with Γ^{5g} spin configuration under atmospheric pressure. As shown in Figure 10C and D, the sample exhibits the piezomagnetic effect. When the applied pressure is 750 MPa at 130 K, the magnetic phase transition from M-1 to Γ^{5g} AFM appears, generating the piezomagnetic characteristic of $0.63 \mu_B/\text{f.u.}$ Combined with the refined results of neutron diffraction, the change of Mn-Mn distance and spin rearrangement caused by pressure is considered to be the trigger of the observed baromagnetic effect.

Magnetocaloric effect

The magnetocaloric effect of antiperovskites was primarily reported in Mn_3GaC ^[36]. The collinear AFM-intermediate magnetic transition of Mn_3GaC showing a first-order characteristic can be controlled by an external magnetic field, generating the magnetocaloric effect. Figure 11A shows the temperature dependence of the maximum value of magnetic entropy change ΔS_{mag} . The peak of ΔS_{mag} reaches $17 \text{ J}/(\text{kg}\cdot\text{K})$ when the external magnetic field is 10 kOe, and the peak value broadens to a "platform" shape with further increase of the magnetic field. In addition, by introducing C vacancies, the magnetic properties of Mn_3GaC were changed, thereby affecting the magnetocaloric effect^[37]. The magnetic entropy of $\text{Mn}_3\text{GaC}_{0.78}$ decreased to $3.7 \text{ J}/\text{kg}\cdot\text{K}$ under a 5 T magnetic field. In $\text{Mn}_{3-x}\text{Co}_x\text{GaC}$, Co doping can reduce the first-order phase transition temperature from 164 K to 100 K without a significant decrease of magnetic entropy and realize the magnetocaloric effect covering a wider temperature range (50-160 K)^[38].

A large magnetic entropy change was observed in $\text{Mn}_3\text{Cu}_{0.89}\text{N}_{0.96}$ ^[39] [Figure 11B]. By introducing vacancies, the onset of the FIM-PM transition is slightly reduced from 150 K of Mn_3CuN to 147.7 K of $\text{Mn}_3\text{Cu}_{0.89}\text{N}_{0.96}$, and a new non-coplanar FIM structure with an orthorhombic symmetry was determined. The total entropy change of $\text{Mn}_3\text{Cu}_{0.89}\text{N}_{0.96}$ obtained by DSC is about $60 \text{ J}/\text{kg}\cdot\text{K}$, while the maximum magnetic entropy change ΔS_{mag} is $13.52 \text{ J}/\text{kg}\cdot\text{K}$ under a magnetic field of 50 kOe near the temperature of FIM-PM transition. Neutron diffraction results indicate that the magnetic entropy change of $\text{Mn}_3\text{Cu}_{0.89}\text{N}_{0.96}$ is caused by the magnetic transition from the AFM to the FM component in the tetragonal phase and the phase transition from cubic to tetragonal under a magnetic field.

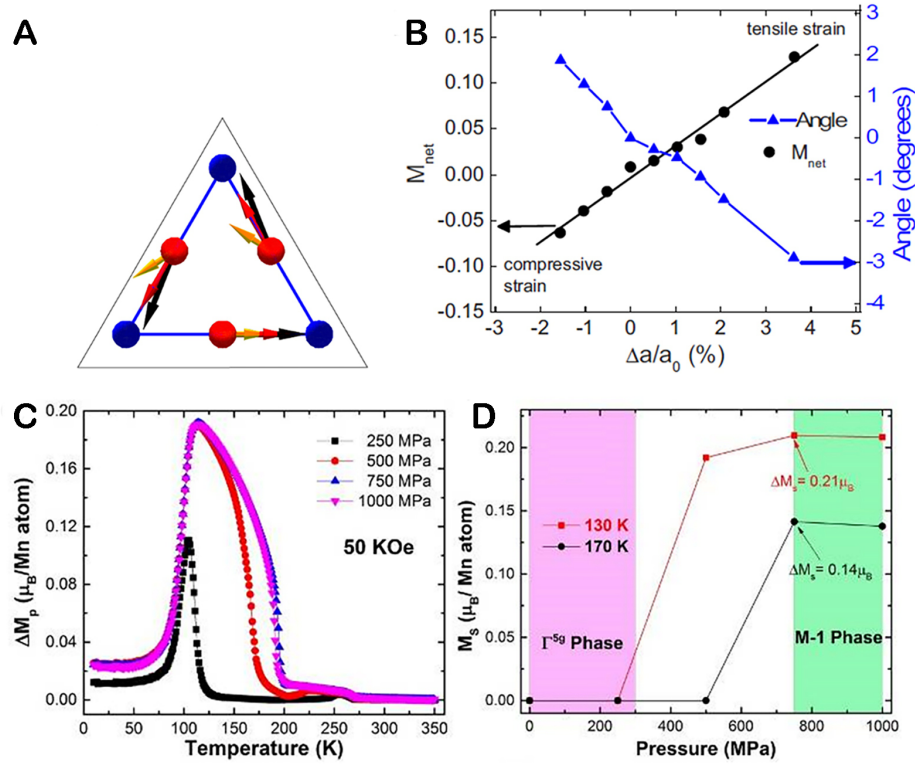


Figure 10. (A) Variation of magnetic moment of Mn Atoms in the (111) Plane of I^{5g} AFM Mn_3GaN with axial strain^[23]; (B) variation of net magnetic moment and rotation angle of Mn atomic magnetic moment with axial strain for Mn_3GaN ^[23]; (C) piezomagnetic effect determined by magnetization curve in $Mn_3Ga_{0.95}N_{0.94}$ ^[35]; (D) piezomagnetic effect of in $Mn_3Ga_{0.95}N_{0.94}$ at 130 K and 170 K^[35].

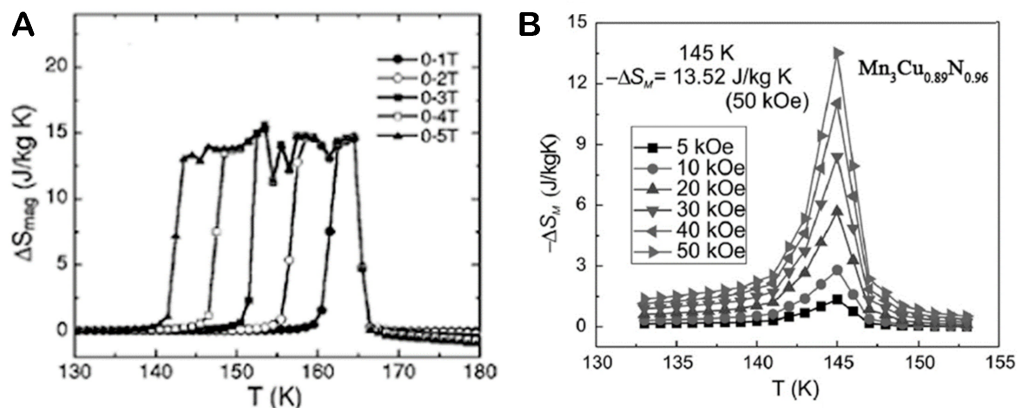


Figure 11. Magnetocaloric effect of (A) Mn_3GaC ^[36] and (B) $Mn_3Cu_{0.89}N_{0.96}$ ^[39].

Barocaloric effect

A significant barocaloric effect is expected when strong cross-correlations between the volume and magnetic order appear in materials. In 2015, Matsunami *et al.* reported the giant barocaloric effect enhanced by the frustration of the AFM phase in Mn_3GaN ^[40]. As shown in [Figure 12A](#), when a hydrostatic pressure change of 139 MPa is applied, Mn_3GaN exhibits an entropy change of $22.3 \text{ J kg}^{-1} \text{ K}^{-1}$. By applying a depressurization of 93 MPa, the change of adiabatic temperature is determined to be about 5 K.

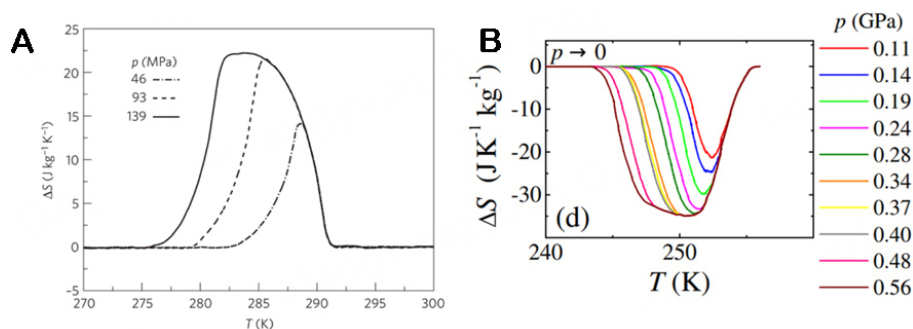


Figure 12. (A) The entropy change of Mn_3GaN under different hydrostatic pressures as a function of temperature^[40]; (B) isothermal entropy and adiabatic temperature changes^[41].

Matsunami *et al.* further suggests that the magnitude of the barocaloric effect of Mn_3GaN is determined by the volume change at the transition and stability of the AFM phase against the pressure^[40]. In 2018, Boldrin *et al.* further investigated the barocaloric effect in the geometrically frustrated antiferromagnet Mn_3NiN [Figure 12B]^[41]. It is worth noting that a large barocaloric entropy change, which is a factor of 1.6 than that of Mn_3GaN , is observed. Boldrin *et al.* proposed that the barocaloric effect of Mn_3NiN originates from multisite exchange interactions amongst the local Mn magnetic moments and their coupling with itinerant electron spins^[41].

CONCLUSION AND OUTLOOK

As reviewed in this article, owing to the magnetic frustration prompted by Mn_6N or Mn_6C octahedra, antiperovskites display the abounding magnetic structures, including collinear AFM, collinear FM, collinear FIM, non-collinear magnetic and non-coplanar magnetic spin configurations. In antiperovskites, the magnetic phase transition (magnetic structures), abnormal lattice change, and electronic transport properties are interrelated and affect each other, showing a large number of physical properties such as ATE, electronic transport properties, piezomagnetic/baromagnetic effects, magnetocaloric effect, barocaloric effect, *etc.* Therefore, antiperovskites will be an excellent candidate for exploring new smart materials. In order to further optimize performance and explore mechanisms, the following issues for in-depth research deserve attention and solutions:

Exploration of new magnetic structures. The examination of new physical properties is one of the important directions of the development of modern smart materials. Due to the strong correlation of "lattice-spin-charge", antiperovskites show a series of rich and unique physical properties within some specific magnetic structures. Although the determination of the magnetic structures is a central issue in antiperovskites, there is still a lack of systematic and in-depth research, especially on how the magnetic structures and correlated physical properties evolve in the case of elemental doping, varied temperatures, varied magnetic fields, and pressurization.

Synthesis of single crystal samples. The current research work on antiperovskites is mainly focused on polycrystalline. From the perspective of mechanism research and application, single crystal research has greater advantages. However, it is difficult to precisely control the nitrogen/carbon contents of antiperovskites in preparation, and the change of contents has a great influence on its physical properties. Therefore, the synthesis of three-dimensional single crystal materials with excellent physical properties is challenging.

Practical application research. Selecting some typical antiperovskites with fascinating physical properties, the practical applications can be explored in the fields of optics, microelectronics, refrigeration, aerospace, etc.

DECLARATIONS

Authors' contributions

Conceived and designed the manuscript: Deng S, He L, Wang C

Drafted and revised the manuscript: Deng S, Wang H, He L, Wang C

Availability of data and materials

Not applicable.

Financial support and sponsorship

This work was financially supported by the Guangdong Basic and Applied Basic Research Foundation (2022A1515140117), Large Scientific Facility Open Subject of Songshan Lake (Dongguan, Guangdong), the National Key R&D Program of China (Grant No. 2021YFA1600602 and No. 2021YFA1600603) and National Natural Science Foundation of China (Grant No. 52371190, No. U2032167, No. 12041202, No. U2032220, No. U1832219, and No. 52272264), the Sino-German Mobility Programme (No. M-0273), and the Key Program of the Chinese Academy of Sciences (CAS).

Conflicts of interest

All authors declared that there are no conflicts of interest.

Ethical approval and consent to participate

Not applicable.

Consent for publication

Not applicable.

Copyright

© The Author(s) 2023.

REFERENCES

1. Bednorz JG, Müller KA. Possible highT c superconductivity the Ba-La-Cu-O system. *Z Physik B Condens Matter* 1986;64:189-93. DOI
2. Ahn CH, Tybell T, Antognazza L, et al. Local, nonvolatile electronic writing of epitaxial Pb(Zr_{0.52}Ti_{0.48})O₃/SrRuO₃ heterostructures. *Science* 1997;276:1100-3. DOI
3. von Helmolt R, Wecker J, Holzapfel B, Schultz L, Samwer K. Giant negative magnetoresistance in perovskitelike La_{2/3}Ba_{1/3}MnO_x ferromagnetic films. *Phys Rev Lett* 1993;71:2331-3. DOI PubMed
4. Chen J, Nittala K, Forrester JS, et al. The role of spontaneous polarization in the negative thermal expansion of tetragonal PbTiO₃-based compounds. *J Am Chem Soc* 2011;133:11114-7. DOI
5. Takenaka K, Takagi H. Giant negative thermal expansion in Ge-doped anti-perovskite manganese nitrides. *Appl Phys Lett* 2005;87:261902. DOI
6. Takenaka K, Asano K, Misawa M, Takagi H. Negative thermal expansion in Ge-free antiperovskite manganese nitrides: Tin-doping effect. *Appl Phys Lett* 2008;92:011927. DOI
7. Takenaka K, Takagi H. Zero thermal expansion in a pure-form antiperovskite manganese nitride. *Appl Phys Lett* 2009;94:131904. DOI
8. Huang R, Li L, Cai F, Xu X, Qian L. Low-temperature negative thermal expansion of the antiperovskite manganese nitride Mn₃CuN codoped with Ge and Si. *Appl Phys Lett* 2008;93:081902. DOI
9. Lin JC, Tong P, Tong W, et al. Tunable negative thermal expansion related with the gradual evolution of antiferromagnetic ordering in antiperovskite manganese nitrides Mn_{3+x}Ag_{1-x}N (0 ≤ x ≤ 0.6). *Appl Phys Lett* 2015;106:082405. DOI

10. Lin JC, Tong P, Zhou XJ, et al. Giant negative thermal expansion covering room temperature in nanocrystalline GaN_xMn_3 . *Appl Phys Lett* 2015;107:131902. DOI
11. Sun Y, Wang C, Wen Y, Zhu K, Zhao J. Lattice contraction and magnetic and electronic transport properties of $\text{Mn}_3\text{Zn}_{1-x}\text{GexN}$. *Appl Phys Lett* 2007;91:231913. DOI
12. Sun Y, Wang C, Wen Y, et al. Negative thermal expansion and magnetic transition in anti-perovskite structured $\text{Mn}_3\text{Zn}_{1-x}\text{Sn}_x\text{N}$ compounds: rapid communications of the American ceramic society. *J Am Ceram Soc* 2010;93:2178-81. DOI
13. Ding L, Wang C, Sun Y, Colin CV, Chu L. Spin-glass-like behavior and negative thermal expansion in antiperovskite $\text{Mn}_3\text{Ni}_{1-x}\text{Cu}_x\text{N}$ compounds. *J Appl Phys* 2015;117:213915. DOI
14. Chu L, Wang C, Yan J, et al. Magnetic transition, lattice variation and electronic transport properties of Ag-doped $\text{Mn}_3\text{Ni}_{1-x}\text{Ag}_x\text{N}$ antiperovskite compounds. *Scr Mater* 2012;67:173-6. DOI
15. Deng S, Sun Y, Wu H, et al. Invar-like behavior of antiperovskite $\text{Mn}_{3-x}\text{Ni}_x\text{N}$ compounds. *Chem Mater* 2015;27:2495-501. DOI
16. Song X, Sun Z, Huang Q, et al. Adjustable zero thermal expansion in antiperovskite manganese nitride. *Adv Mater* 2011;23:4690-4. DOI
17. Iikubo S, Kodama K, Takenaka K, Takagi H, Takigawa M, Shamoto S. Local lattice distortion in the giant negative thermal expansion material $\text{Mn}_3\text{Cu}_{1-x}\text{Ge}_x\text{N}$. *Phys Rev Lett* 2008;101:205901. DOI PubMed
18. Iikubo S, Kodama K, Takenaka K, Takagi H, Shamoto S. Magnetovolume effect in $\text{Mn}_3\text{Cu}_{1-x}\text{Ge}_x\text{N}$ related to the magnetic structure: neutron powder diffraction measurements. *Phys Rev B* 2008;77:020409. DOI
19. Tong P, Louca D, King G, Llobet A, Lin JC, Sun YP. Magnetic transition broadening and local lattice distortion in the negative thermal expansion antiperovskite $\text{Cu}_{1-x}\text{Sn}_x\text{NMn}_3$. *Appl Phys Lett* 2013;102:041908. DOI
20. Wang C, Chu L, Yao Q, et al. Tuning the range, magnitude, and sign of the thermal expansion in intermetallic $\text{Mn}_3(\text{Zn}, \text{M})_x\text{N}$ ($M = \text{Ag}, \text{Ge}$). *Phys Rev B* 2012;85:220103. DOI
21. Deng S, Sun Y, Wu H, et al. Phase separation and zero thermal expansion in antiperovskite $\text{Mn}_3\text{Zn}_{0.77}\text{Mn}_{0.19}\text{N}_{0.94}$: an in situ neutron diffraction investigation. *Scr Mater* 2018;146:18-21. DOI
22. Shi K, Sun Y, Colin CV, et al. Investigation of the spin-lattice coupling in $\text{Mn}_3\text{Ga}_{1-x}\text{Sn}_x\text{N}$ antiperovskites. *Phys Rev B* 2018;97:054110. DOI
23. Lukashev P, Sabirianov RF, Belashchenko K. Theory of the piezomagnetic effect in Mn-based antiperovskites. *Phys Rev B* 2008;78:184414. DOI
24. Qu BY, Pan BC. Nature of the negative thermal expansion in antiperovskite compound Mn_3ZnN . *J Appl Phys* 2010;108:113920. DOI
25. Mochizuki M, Kobayashi M, Okabe R, Yamamoto D. Spin model for nontrivial types of magnetic order in inverse-perovskite antiferromagnets. *Phys Rev B* 2018;97:060401. DOI
26. Kamishima K, Goto T, Nakagawa H, et al. Giant magnetoresistance in the intermetallic compound Mn_3GaC . *Phys Rev B* 2000;63:024426. DOI
27. Deng S, Fischer G, Uhlarz M, et al. Controlling chiral spin states of a triangular-lattice magnet by cooling in a magnetic field. *Adv Funct Mater* 2019;29:1900947. DOI
28. Gurung G, Shao DF, Paudel TR, Tsybmal EY. Anomalous HALL conductivity of noncollinear magnetic antiperovskites. *Phys Rev Mater* 2019;3:044409. DOI
29. Samathrakris I, Zhang H. Tailoring the anomalous Hall effect in the noncollinear antiperovskite Mn_3GaN . *Phys Rev B* 2020;101:214423. DOI
30. Zhao K, Hajiri T, Chen H, Miki R, Asano H, Gegenwart P. Anomalous Hall effect in the noncollinear antiferromagnetic antiperovskite $\text{Mn}_3\text{Ni}_{1-x}\text{Cu}_x\text{N}$. *Phys Rev B* 2019;100:045109. DOI
31. Rani GM, Wu CM, Motora KG, Umapathi R. Waste-to-energy: utilization of recycled waste materials to fabricate triboelectric nanogenerator for mechanical energy harvesting. *J Clean Prod* 2022;363:132532. DOI
32. Gokana MR, Wu CM, Motora KG, Qi JY, Yen WT. Effects of patterned electrode on near infrared light-triggered cesium tungsten bronze/ poly(vinylidene)fluoride nanocomposite-based pyroelectric nanogenerator for energy harvesting. *J Power Sources* 2022;536:231524. DOI
33. Zemen J, Gercsi Z, Sandeman KG. Piezomagnetism as a counterpart of the magnetovolume effect in magnetically frustrated Mn-based antiperovskite nitrides. *Phys Rev B* 2017;96:024451. DOI
34. Boldrin D, Mihai AP, Zou B, et al. Giant Piezomagnetism in Mn_3NiN . *ACS Appl Mater Interfaces* 2018;10:18863-8. DOI
35. Shi K, Sun Y, Yan J, et al. Baromagnetic effect in antiperovskite $\text{Mn}_3\text{Ga}_{0.95}\text{N}_{0.94}$ by neutron powder diffraction analysis. *Adv Mater* 2016;28:3761-7. DOI
36. Tohei T, Wada H, Kanomata T. Negative magnetocaloric effect at the antiferromagnetic to ferromagnetic transition of Mn_3GaC . *J Appl Phys* 2003;94:1800-2. DOI
37. Yu M, Lewis LH, Moodenbaugh AR. Assessment of the magnetic entropy change in the metallic antiperovskite $\text{Mn}_3\text{GaC}_{1-\delta}$ ($\delta = 0, 0.22$). *J Magn Magn Mater* 2006;299:317-26. DOI
38. Tohei T, Wada H, Kanomata T. Large magnetocaloric effect of $\text{Mn}_{3-x}\text{Co}_x\text{GaC}$. *J Magn Magn Mater* 2004;272-76:E585-6. DOI
39. Yan J, Sun Y, Wu H, et al. Phase transitions and magnetocaloric effect in $\text{Mn}_3\text{Cu}_{0.89}\text{N}_{0.96}$. *Acta Mater* 2014;74:58-65. DOI
40. Matsunami D, Fujita A, Takenaka K, Kano M. Giant barocaloric effect enhanced by the frustration of the antiferromagnetic phase in Mn_3GaN . *Nat Mater* 2015;14:73-8. DOI PubMed
41. Boldrin D, Mendive-tapia E, Zemen J, et al. Multisite exchange-enhanced barocaloric response in Mn_3NiN . *Phys Rev X* 2018;8:041035. DOI
42. Chi EO, Kim WS, Hur NH. Nearly zero temperature coefficient of resistivity in antiperovskite compound CuNMn_3 . *Solid State Commun* 2001;120:307-10. DOI

43. Sun Y, Wang C, Chu L, Wen Y, Nie M, Liu F. Low temperature coefficient of resistivity induced by magnetic transition and lattice contraction in Mn_3NiN compound. *Scr Mater* 2010;62:686-9. DOI
44. Takenaka K, Ozawa A, Shibayama T, Kaneko N, Oe T, Urano C. Extremely low temperature coefficient of resistance in antiperovskite $\text{Mn}_3\text{Ag}_{1-x}\text{Cu}_x\text{N}$. *Appl Phys Lett* 2011;98:022103. DOI
45. Lin JC, Wang BS, Tong P, et al. Tunable temperature coefficient of resistivity in C- and Co-doped CuNMn_3 . *Scr Mater* 2011;65:452-5. DOI
46. Deng S, Sun Y, Wang L, et al. Near-zero temperature coefficient of resistivity associated with magnetic ordering in antiperovskite $\text{Mn}_{3+x}\text{Ni}_{1-x}\text{N}$. *Appl Phys Lett* 2016;108:041908. DOI
47. He T, Huang Q, Ramirez AP, et al. Superconductivity in the non-oxide perovskite MgCNi_3 . *Nature* 2001;411:54-6. DOI
48. Rosner H, Weht R, Johannes MD, Pickett WE, Tosatti E. Superconductivity near ferromagnetism in MgCNi_3 . *Phys Rev Lett* 2002;88:027001. DOI PubMed
49. Wu M, Isshiki H, Chen T, Higo T, Nakatsuji S, Otani Y. Magneto-optical Kerr effect in a non-collinear antiferromagnet Mn_3Ge . *Appl Phys Lett* 2020;116:132408. DOI
50. Balk AL, Sung NH, Thomas SM, et al. Comparing the anomalous Hall effect and the magneto-optical Kerr effect through antiferromagnetic phase transitions in Mn_3Sn . *Appl Phys Lett* 2019;114:032401. DOI
51. Feng W, Guo GY, Zhou J, Yao Y, Niu Q. Large magneto-optical Kerr effect in noncollinear antiferromagnets Mn_3X ($\text{X} = \text{Rh}, \text{Ir}, \text{Pt}$). *Phys Rev B* 2015;92:144426. DOI
52. Kamishima K, Bartashevich M, Goto T, Kikuchi M, Kanomata T. Magnetic behavior of Mn_3GaC under high magnetic field and high pressure. *J Phys Soc Jpn* 1998;67:1748-54. DOI
53. Fruchart D, Bertaut EF, Sayetat F, Nasr Eddine M, Fruchart R, Sénateur JP. Structure magnétique de Mn_3GaC . *Solid State Commun* 1970;8:91-9. DOI
54. Fruchart D, Bertaut EF. Magnetic studies of the metallic perovskite-type compounds of manganese. *J Phys Soc Jpn* 1978;44:781-91. DOI
55. Çakur Ö, Acet M. Reversibility in the inverse magnetocaloric effect in Mn_3GaC studied by direct adiabatic temperature-change measurements. *Appl Phys Lett* 2012;100:202404. DOI
56. Sénateur JP, Boursier D, L'héritier P, Lorthioir G, Fruchart ME, Le Caer G. Etude par spectrométrie mössbauer de ZnMn_3 et de la transition antiferro-ferromagnétique de GaMn_3C dopés au fer 57. *Mater Res Bull* 1974;9:603-14. DOI
57. Deng S, Sun Y, Wang L, et al. Frustrated triangular magnetic structures of Mn_3ZnN : applications in thermal expansion. *J Phys Chem C* 2015;119:24983-90. DOI
58. Fruchart D, Bertaut EF, Madar R, Fruchart R. Diffraction neutronique de Mn_3ZnN . *J Phys Colloques* 1971;32:C1-876. DOI
59. Wu M, Wang C, Sun Y, et al. Magnetic structure and lattice contraction in Mn_3NiN . *J Appl Phys* 2013;114:123902. DOI
60. Hua L, Wang L, Chen LF. First-principles investigation of Ge doping effects on the structural, electronic and magnetic properties in antiperovskite Mn_3CuN . *J Phys Condens Matter* 2010;22:206003. DOI
61. Han H, Sun Y, Deng S, et al. Effect of thermal stress on non-collinear antiferromagnetic phase transitions in antiperovskite Mn_3GaN compounds with Mn_3SbN inclusions. *Ceramics Int* 2022;48:15200-6. DOI
62. Sun Y, Hu P, Shi K, et al. Giant zero-field cooling exchange-bias-like behavior in antiperovskite $\text{Mn}_3\text{Co}_{0.61}\text{Mn}_{0.39}\text{N}$ compound. *Phys Rev Mater* 2019;3:024409. DOI
63. Salvador JR, Guo F, Hogan T, Kanatzidis MG. Zero thermal expansion in YbGaGe due to an electronic valence transition. *Nature* 2003;425:702-5. DOI
64. Mary TA, Evans JSO, Vogt T, Sleight AW. Negative Thermal Expansion from 0.3 to 1050 Kelvin in ZrW_2O_8 . *Science* 1996;272:90-2. DOI
65. Song Y, Shi N, Deng S, Xing X, Chen J. Negative thermal expansion in magnetic materials. *Prog Mater Sci* 2021;121:100835. DOI
66. Chen J, Hu L, Deng J, Xing X. Negative thermal expansion in functional materials: controllable thermal expansion by chemical modifications. *Chem Soc Rev* 2015;44:3522-67. DOI PubMed
67. Gava V, Martinotto AL, Perottoni CA. First-principles mode Grüneisen parameters and negative thermal expansion in $\alpha\text{-ZrW}_2\text{O}_8$. *Phys Rev Lett* 2012;109:195503. DOI PubMed
68. Li CW, Tang X, Muñoz JA, et al. Structural relationship between negative thermal expansion and quartic anharmonicity of cubic ScF_3 . *Phys Rev Lett* 2011;107:195504. DOI
69. Long YW, Hayashi N, Saito T, Azuma M, Muranaka S, Shimakawa Y. Temperature-induced A-B intersite charge transfer in an A-site-ordered $\text{LaCu}_3\text{Fe}_4\text{O}_{12}$ perovskite. *Nature* 2009;458:60-3. DOI
70. Gerhardt I, Liu Q, Lamas-Linares A, Skaar J, Kurtsiefer C, Makarov V. Full-field implementation of a perfect eavesdropper on a quantum cryptography system. *Nat Commun* 2011;2:349. DOI PubMed
71. Chen J, Fan L, Ren Y, et al. Unusual transformation from strong negative to positive thermal expansion in $\text{PbTiO}_3\text{-BiFeO}_3$ perovskite. *Phys Rev Lett* 2013;110:115901. DOI
72. Huang R, Liu Y, Fan W, et al. Giant negative thermal expansion in NaZn_{13} -type $\text{La}(\text{Fe}, \text{Si}, \text{Co})_{13}$ compounds. *J Am Chem Soc* 2013;135:11469-72. DOI
73. Qi TF, Korneta OB, Parkin S, De Long LE, Schlottmann P, Cao G. Negative volume thermal expansion via orbital and magnetic orders in $\text{Ca}_2\text{Ru}_{1-x}\text{Cr}_x\text{O}_4$ ($0 < x < 0.13$). *Phys Rev Lett* 2010;105:177203. DOI

74. Richter DD, Markewitz D, Trumbore SE, Wells CG. Rapid accumulation and turnover of soil carbon in a re-establishing forest. *Nature* 1999;400:56-8. [DOI](#)
75. Kiyama T, Yoshimura K, Kosuge K, Ikeda Y, Bando Y. Invar effect of SrRuO₃: itinerant electron magnetism of Ru 4d electrons. *Phys Rev B Condens Matter* 1996;54:R756-9. [DOI](#) [PubMed](#)
76. Taniguchi T, Mizusaki S, Okada N, et al. Anomalous volume expansion in CaRu_{0.85}Fe_{0.15}O₃: neutron powder diffraction and magnetic compton scattering. *Phys Rev B* 2007;75:024414. [DOI](#)
77. Klimczuk T, Walker HC, Springell R, et al. Negative thermal expansion and antiferromagnetism in the actinide oxypnictide NpFeAsO. *Phys Rev B* 2012;85. [DOI](#)
78. Uchishiba H. Antiferromagnetism of γ -phase manganese alloys containing Ni, Zn, Ga and Ge. *J Phys Soc Jpn* 1971;31:436-40. [DOI](#)
79. Yokoyama T, Eguchi K. Anisotropic thermal expansion and cooperative Invar and anti-Invar effects in mn alloys. *Phys Rev Lett* 2013;110:075901. [DOI](#) [PubMed](#)
80. Yu C, Lin K, Jiang S, et al. Plastic and low-cost axial zero thermal expansion alloy by a natural dual-phase composite. *Nat Commun* 2021;12:4701. [DOI](#) [PubMed](#) [PMC](#)

Research Article

Open Access



Temperature dependence of dielectric nonlinearity of BaTiO₃ ceramics

Ichiro Fujii^{1,2}, Susan Trolier-McKinstry²

¹Graduate Faculty of Interdisciplinary Research, University of Yamanashi, Kofu, Yamanashi 400-8510, Japan.

²Department of Materials Science and Engineering and Materials Research Institute, The Pennsylvania State University, University Park, PA 16802, USA.

Correspondence to: Prof. Ichiro Fujii, Graduate Faculty of Interdisciplinary Research, University of Yamanashi, Kofu, Yamanashi 400-8510, Japan. E-mail: ifujii@yamanashi.ac.jp

How to cite this article: Fujii I, Trolier-McKinstry S. Temperature dependence of dielectric nonlinearity of BaTiO₃ ceramics. *Microstructures* 2023;3:2023045. <https://dx.doi.org/10.20517/microstructures.2023.43>

Received: 21 Aug 2023 **First Decision:** 21 Sep 2023 **Revised:** 7 Oct 2023 **Accepted:** 19 Oct 2023 **Published:** 14 Nov 2023

Academic Editors: Dawei Wang, Fei Li **Copy Editor:** Fangyuan Liu **Production Editor:** Fangyuan Liu

Abstract

In many commercially utilized ferroelectric materials, the motion of domain walls is an important contributor to the functional dielectric and piezoelectric responses. This paper compares the temperature dependence of domain wall motion for BaTiO₃ ceramics with different grain sizes, point defect concentrations, and formulations. The grain boundaries act as significant pinning points for domain wall motion such that fine-grained materials show smaller extrinsic contributions to the properties below the Curie temperature and lower residual ferroelectric contributions immediately above the Curie temperature. Oxygen vacancy point defects make a modest change in the extrinsic contributions of undoped BaTiO₃ ceramics. In formulated BaTiO₃, extrinsic contributions to the dielectric response were suppressed over a wide temperature range. It is believed this is due to a combination of reduced grain size, the existence of a core-shell microstructure, and a reduction in domain wall continuity over the grain boundaries.

Keywords: Ferroelectrics, dielectric nonlinearity, grain size, ceramics

INTRODUCTION

It is well documented that the dielectric and piezoelectric responses of many ferroelectric materials include contributions from the motion of domain walls, even when the electric field used to excite the material is well below the coercive field^[1-6]. This motion of domain walls is important to understand, as it will govern much of the field, time, and frequency dependence of the properties of a ferroelectric material. As an



© The Author(s) 2023. **Open Access** This article is licensed under a Creative Commons Attribution 4.0 International License (<https://creativecommons.org/licenses/by/4.0/>), which permits unrestricted use, sharing, adaptation, distribution and reproduction in any medium or format, for any purpose, even commercially, as long as you give appropriate credit to the original author(s) and the source, provide a link to the Creative Commons license, and indicate if changes were made.



example, domain wall motion contributes substantially to the room temperature permittivity of BaTiO₃-based multilayer ceramic capacitors. Similarly, up to 75% of the piezoelectric response of soft PbZr_{1-x}Ti_xO₃ ceramics arises from domain wall motion, albeit at the expense of increased hysteresis. The relative extent of domain wall motion for a given material depends explicitly on the history of the sample, the sample microstructure^[7,8] and orientation, and the excitation conditions. For example, the following factors are critical to the observed extent of extrinsic contributions to the properties:

Electric field

Higher amplitudes of the AC electric field ($E_{AC\ 0-pk}$) act to drive domain walls more strongly and can substantially increase the extrinsic contributions to the properties. This increases the relative permittivity and loss tangent with the AC field, which is called dielectric nonlinearity. Often, the increase in relative permittivity is linear with AC electric field, producing the so-called Rayleigh regime (from a modified version of the Rayleigh law originally developed for magnetic materials)^[9], i.e.,

$$\varepsilon' = \varepsilon'_{init} + \alpha' E_{AC\ 0-pk}$$

where ε' is the relative permittivity, ε'_{init} is the reversible Rayleigh coefficient that includes both the intrinsic response and reversible motion of domain walls or phase boundaries, and α' is the irreversible Rayleigh coefficient^[10]. The Rayleigh law is typically observed up to modest electric fields under conditions where the domain structure is unchanged during the measurement and the distribution of the restoring forces for the domain walls is Gaussian^[11]. In cases where the domain wall density is changed by the applied field, the Rayleigh law will not be observed, and a more complex formalism, such as first-order reversal curves, needs to be employed^[12-16]. In many but not all ferroelectric materials, significant levels of domain nucleation are observed at $E_{AC\ 0-pk}$ exceeding ~a third to a half of the coercive field.

In contrast, because DC biases stabilize the domain state, they also act to suppress extrinsic contributions to the properties. This produces a far stronger DC bias dependence of the relative permittivity^[4] than would be predicted based on phenomenological descriptions of the field dependence of the intrinsic permittivity (e.g., intrinsic dielectric stiffening)^[17,18]. This progressive loss of the extrinsic contributions to the permittivity is problematic in multilayer ceramic capacitors where the voltage saturation significantly depresses the usable capacitance^[19]. In contrast, the suppression is very helpful in some piezoelectric sensing applications, as it increases the figure of merit = piezoelectric coefficient/relative permittivity^[20].

Temperature

There is a strong coupling between temperature and extrinsic contributions to the properties. First, domain wall motion is thermally activated such that domain walls become more mobile as temperature increases. Therefore, extrinsic contributions typically rise as the Curie temperature is approached. Other ferroelectric-ferroelectric phase transitions also tend to favor the motion of the mobile interfaces and will induce increases in the extrinsic contributions. Secondly, because domain wall and phase boundary motions are inherently dissipative, substantial levels of extrinsic contributions can increase the sample temperature^[21]. Thirdly, changes in temperature can perturb the domain structure and so de-age the material, increasing the extrinsic contributions temporarily.

Time

Domain structures, especially in ceramic materials, are rarely fully stable as a function of time. Thus, over the course of time, the domain structure progressively seeks lower energy configurations. As this occurs, the remaining domain walls tend to be less mobile. This is one of the contributions to the aging of the dielectric

or piezoelectric response^[22]. Time dependence is also observed in cases where poorly poled piezoelectrics are excited with unipolar waveforms, as is sometimes done in piezoelectric microelectromechanical systems. In this case, the sample poles progressively during use, increasing the remanent piezoelectric coefficient but decreasing the achievable strain during actuation due to progressive loss of the poling strain that is caused by polarization alignment. It is also critical to note that these factors of microstructure, time, temperature, and field are all inextricably linked such that the aging rates will depend on the amplitude of the field used for their characterization^[23].

This paper illustrates the temperature dependence of the domain wall contributions to the dielectric properties of BaTiO₃ ceramics, with an emphasis on the role of phase transitions, grain size, core-shell microstructures, and point defect concentrations in the response. The resulting temperature dependence of the dielectric response is a complex interplay between these factors.

EXPERIMENTAL PROCEDURE

Samples

Undoped BaTiO₃ ceramics were prepared using a BaTiO₃ powder (BT02, with a Ba/Ti ratio of 0.996, Sakai Chemical Industry Co., Ltd., Sakai, Japan). To study the effect of grain size, BaTiO₃ ceramics with grain sizes of 1.2 μm and 76 μm were prepared. The former was prepared by sintering a BaTiO₃ compact at 1,300 °C for 2 h and post-annealing the sintered body at 1,000 °C for 9.5 h^[24], while the latter was prepared by sintering the compact at 1,350 °C for 2 h^[25]. The grain sizes were measured from the microstructures of polished and chemically etched ceramic surfaces observed by scanning electron microscopy (SEM). **Figure 1A** and **B** shows the SEM images of the undoped BaTiO₃ ceramics. Two grain lengths were measured for each grain, and the average of these two lengths was calculated for more than 90 grains. The grain size given is the average of the two-length average, and the error bar for the grain size is the standard deviation. The grain sizes were calculated to be 1.2 ± 0.5 μm and 76 ± 37 μm for the BaTiO₃ ceramics sintered at 1,300 °C and 1,350 °C, respectively. To study the effect of oxygen partial pressure (pO₂) during sintering, BaTiO₃ ceramics were sintered at 10⁻⁹ atm pO₂ at 1,300 °C for 2 h^[24]. A microstructure similar to that of the undoped BaTiO₃ ceramics sintered at 1,300 °C in air (10⁻² atm pO₂) was observed by SEM, and the grain size was 1.2 ± 0.4 μm. The dielectric properties were compared with those of the air-sintered BaTiO₃ ceramics with a grain size of 1.2 μm. Formulated BaTiO₃ ceramics, which fulfill X7R specifications, were prepared using a BaTiO₃-based powder (EV540N, Ferro, Cleveland, OH, USA). The compact of the BaTiO₃-based powder was sintered at 1,300 °C for 2 h in the air (10⁻² atm pO₂) or at 10⁻⁹ atm pO₂^[24]. No reoxidation post-annealing was performed. **Figure 1C** and **D** shows the SEM images of the formulated BaTiO₃ ceramics. Two formulated BaTiO₃ ceramics had the same grain size of 0.5 ± 0.2 μm. The thickness of both undoped and formulated BaTiO₃ ceramics was about 0.5 mm. For dielectric measurements, 100 nm thick Au electrodes were formed by sputtering. The details of the sample preparation and additional electric data are described elsewhere^[24,25].

The grain size effect was also studied for model multilayer ceramics capacitors (MLCCs). The size of model MLCCs was 3.2 mm × 1.6 mm × 0.4 mm, and they consisted of ten 7.7-μm-thick BaTiO₃-based dielectric layers with X7R specifications and Ni internal electrodes. The grain sizes of the dielectrics were changed from 0.28 ± 0.1 μm, 0.36 ± 0.1 μm, and 0.39 ± 0.1 μm by changing the sintering temperature, while the composition of the dielectrics was held constant. The details for the model MLCCs can be found in Refs.^[26,27].

Measurement methods

For the undoped and formulated BaTiO₃ ceramics, the ac field dependence of the dielectric properties was measured using a lock-in amplifier (SR830, Stanford Research Systems Inc., Sunnyvale, CA, USA), a voltage

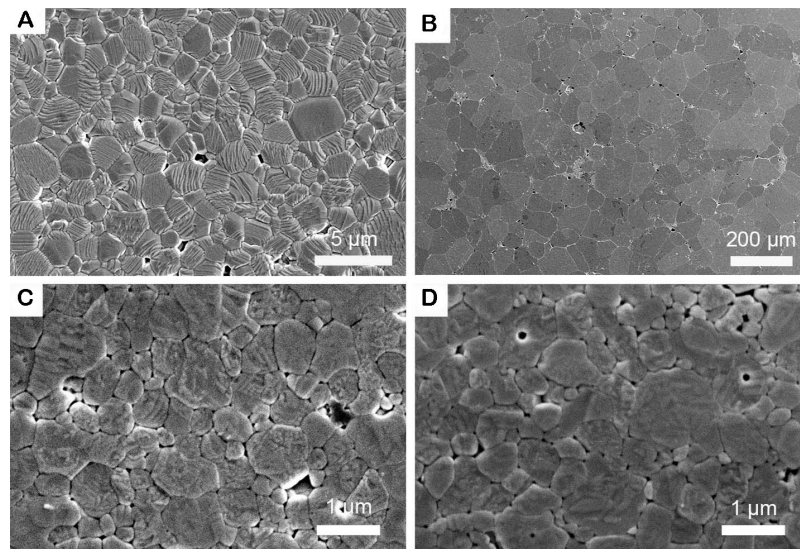


Figure 1. SEM images for undoped BaTiO₃ ceramics with grain sizes of (A) 1.2 μm and (B) 76 μm and formulated BaTiO₃ ceramics sintered at (C) 10⁻² atm pO₂ and (D) 10⁻⁹ atm pO₂.

amplifier, and a charge converter^[24]. An ac field frequency of 100 Hz was utilized. The ac field amplitude was increased up to 4 kV/cm; the coercive fields are 4 kV/cm for air-sintered undoped BaTiO₃ ceramics with 1.2 μm and 76 μm grain sizes, 3 kV/cm for undoped BaTiO₃ ceramics sintered at 10⁻⁹ atm pO₂ with a 1.2 μm grain size, and 5 kV/cm for formulated BaTiO₃ ceramics. The coercive fields were determined from polarization - electric field (P-E) loops measured by a custom-made measurement system at room temperature, as shown in [Figure 2](#).

For the model MLCCs, the ac field dependence of the dielectric properties was measured using an LCR meter (4284A, Agilent Technologies Inc., Santa Clara, CA) with a frequency of 1 kHz. The ac field amplitude was increased up to 12-15 kV/cm. The coercive fields of the samples were about 10-15 kV/cm.

The temperature dependence of the dielectric properties was measured upon cooling from 150 °C to -150 °C or -180 °C, and the temperature of the samples was controlled by a furnace (DELTA 9023, Delta Design, Poway, CA); the chamber was cooled with liquid nitrogen. The dielectric data were measured on cooling to reduce artifacts associated with condensed moisture.

RESULTS AND DISCUSSION

[Figure 3](#) illustrates the temperature dependence of the relative permittivity (ϵ') (prime) of a BaTiO₃ ceramic sample as a function of ac field amplitude. Several points are immediately apparent. First, at temperatures well above the Curie temperature $T_c \sim 125$ °C (i.e., measurements at 150 °C), where there should be no ferroelectric domains, there are no domain wall contributions to the properties. As a result, the dielectric permittivity shows very limited dependence on the amplitude of the ac electric field. As the temperature drops to the Curie temperature (data at 125 °C), it is apparent that there is a finite field dependence of ϵ' , which may be due to persistent micropolar regions^[28]. Below T_c in the tetragonal ferroelectric regime (data at 80 °C), there is a large population of mobile ferroelectric domain walls in the ceramics, and the nonlinearity in ϵ' increases. Near any of the phase transitions (apparent as peaks in the permittivity data), both the intrinsic polarizability and the domain wall contributions to the properties rise. The latter is clearly apparent as enhanced dielectric nonlinearity (for example, the data set at 20 °C). Substantial dielectric

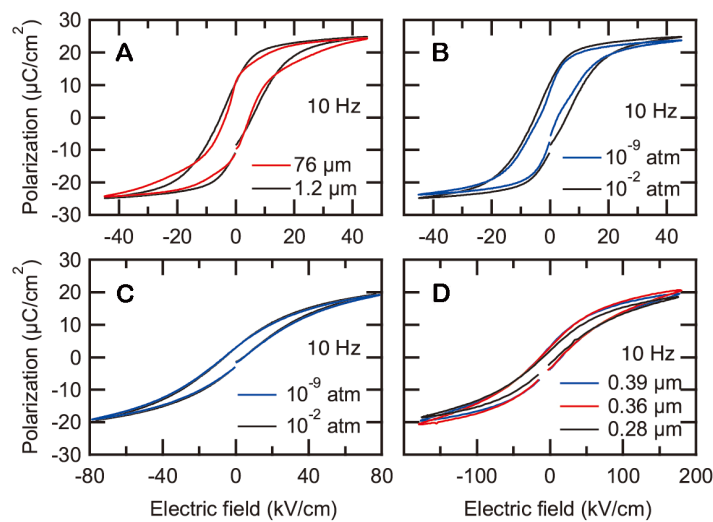


Figure 2. P-E loops measured at room temperature for (A) undoped BaTiO₃ ceramics with a grain size of 1.2 μm and 76 μm, (B) undoped BaTiO₃ ceramics sintered at 10⁻² atm pO₂ and 10⁻⁹ atm pO₂, (C) formulated BaTiO₃ ceramics sintered 10⁻² atm pO₂ and 10⁻⁹ atm pO₂, and (D) model MLCCs with various grain sizes. The ac frequency was 10 Hz.

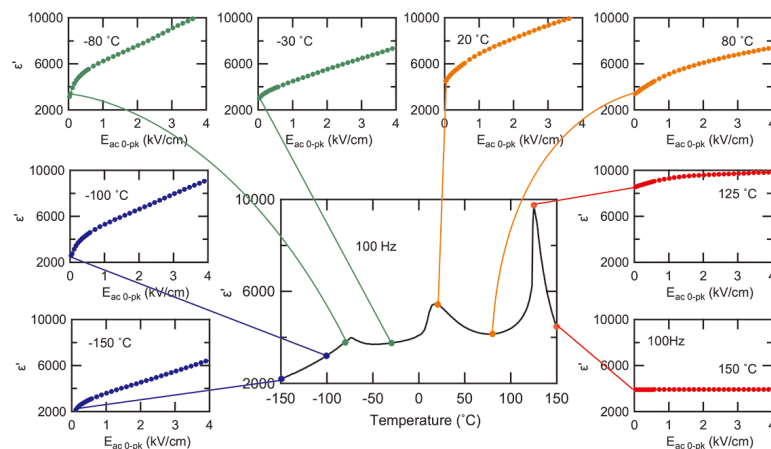


Figure 3. Temperature and the ac field dependence of the dielectric constant of a BaTiO₃ ceramics with a grain size of 1.2 mm. The ac field frequency was 100 Hz. The peaks in the permittivity correspond to the phase transition in BaTiO₃; on increasing temperature, the material transforms from a rhombohedral ferroelectric to an orthorhombic ferroelectric to a tetragonal ferroelectric to a paraelectric cubic structure.

nonlinearity is observed in the rhombohedral, orthorhombic, and tetragonal ferroelectric phases of BaTiO₃. Although not shown here, the domain wall motion contributions to the small signal properties are gradually lost as the temperature approaches 0 K^[29].

The magnitude of the temperature dependence of the extrinsic contributions to the properties is a function of the grain size of the ceramics, as can be seen in comparing the data in Figures 3-5 (Figure 3 uses the same data as Figure 5, and Figure 5 has more data). Figure 4 shows selected data for the dielectric nonlinearity for a large-grained (76 mm average grain size) BaTiO₃ ceramics. One consequence of the increased domain wall mobility in large-grained materials is that the electric fields at which the materials transition from Rayleigh-

like to non-Rayleigh-like behavior decreases. As a result, [Figure 4](#) shows marked departures from Rayleigh-like behavior at ac field magnitudes under 1 kV/cm in the tetragonal phase field for the BaTiO₃. Above these fields, the permittivity first rises very quickly as new domains are nucleated and then goes through a maximum before decreasing as the field amplitude is further increased. This is in contrast to the data in [Figures 3](#) and [5](#) for finer-grained ceramics, where no marked maximum in the relative permittivity is observed up to 4 kV/cm over the same temperature range.

[Figure 5](#) shows the ac field dependence of the dielectric properties of the undoped BaTiO₃ ceramics with a grain size of 1.2 μm measured at various temperatures. It was observed that the ac field dependence was suppressed compared to the large-grained sample over the whole temperature range, as has been reported elsewhere^[23]. Grain boundaries are regions where the crystallography of the material is disrupted, and in many cases, these grain boundaries act as pinning centers for the domain walls^[25,30-33].

The dielectric data for samples with different grain sizes were quantified by a pseudo-Rayleigh analysis that replaced ϵ_{init}' with ϵ_j' - the dielectric constant measured at a small field amplitude j . α' was replaced with α_i' - the slope for the dielectric constants measured at the field amplitudes j and i ($i > j$). In this case, pseudo refers to the fact that the permittivity does not increase truly linearly as a function of ac field. [Figure 6](#) shows the temperature dependence of the pseudo-Rayleigh parameters of the BaTiO₃ ceramics with a grain size of 1.2 μm and 76 μm. The field i was chosen to ~ 0.5 kV/cm or ~ 2 kV/cm to quantify domain wall contributions at subcoercive fields. The temperature dependence of the $\epsilon'_{0.03\text{kV/cm}}$ was similar to that of the small signal dielectric constant, except that no dielectric peak was observed at 125 °C for the large-grained ceramics due to its higher T_c of 128 °C^[25]. The observation that the $\epsilon'_{0.03\text{kV/cm}}$ of the 1.2 μm grain size sample is larger than that of the 76 μm grain size sample below T_c is due to the so-called grain size effect of BaTiO₃^[7]. For the 76 μm grain size sample, the α_i' values were larger than those of the 1.2 μm grain sample due to reduced domain wall pinning at grain boundaries. The α_i' values were increased at the rhombohedral to orthorhombic phase transition and orthorhombic to tetragonal phase transition temperatures. In addition, they were increased at 80 °C for the 76 μm grain size sample. This is probably due to a combination of increased domain wall mobility and decreased polarization with increasing temperature. For the 1.2 μm grain size sample, the increases at 80 °C were not observed due to suppressed domain wall mobility. For the 76 μm grain size sample, $\alpha'_{2\text{kV/cm}}$ is larger than $\alpha'_{0.5\text{kV/cm}}$ above -70 °C, indicating a superlinear ac field dependence. This, in turn, suggests a sublinear response below this temperature, which would be consistent with a restriction in long-range domain wall motion and/or a reduction in the nucleation of new domains.

Given that domain wall motion is a function of the concentration of pinning sites in the sample, it is also interesting to consider the effect of point defects as potential pinning points. Here, the oxygen vacancy concentration was varied by sintering undoped BaTiO₃ ceramics at different oxygen partial pressures, as described elsewhere^[24]. [Figure 7](#) shows the ac field dependence of the dielectric properties of BaTiO₃ ceramics sintered at 10⁻⁹ atm pO₂ with a 1.2 μm grain size measured at various temperatures. It was found that the response was similar to that of the sample sintered at 10⁻² atm pO₂, except that the larger increase in the dielectric properties at moderate ac fields than that of the sample sintered at 10⁻² atm pO₂ below T_c and larger loss above T_c .

The effect of the pO₂ on the dielectric nonlinearity was quantified at various temperatures, as shown in [Figure 8](#). Neither sample showed a true Rayleigh regime, presumably due to a combination of defect dipoles associated with oxygen vacancies, residual stresses^[34], and pinning from the grain boundaries. It was found that the temperature dependence of the pseudo-Rayleigh parameters was similar, except that the α_i' of 10⁻⁹ atm pO₂ sample were larger than those of the 10⁻² atm pO₂ sample, which is attributable to the de-

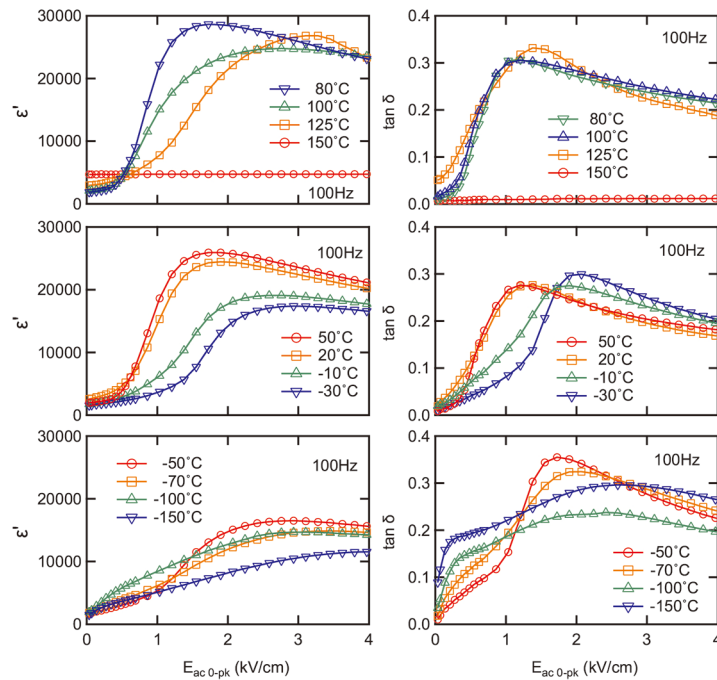


Figure 4. The ac field dependence of the dielectric properties of undoped BaTiO₃ ceramics with a grain size of 76 μm measured at various temperatures.

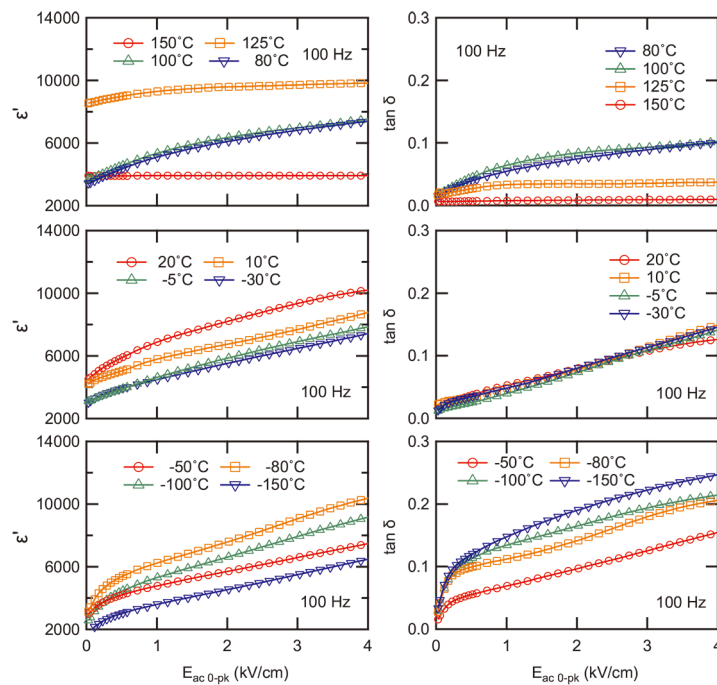


Figure 5. The ac field dependence of the dielectric properties of undoped BaTiO₃ ceramics with a grain size of 1.2 μm, measured at various temperatures.

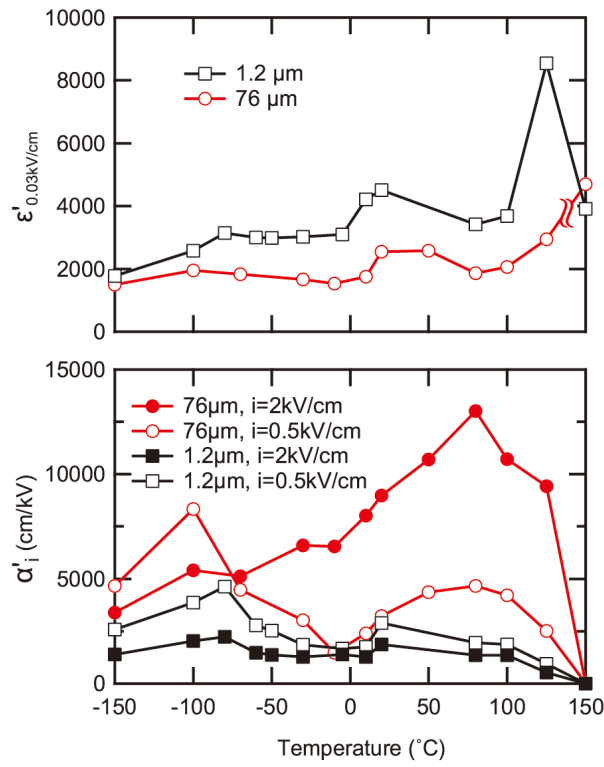


Figure 6. Temperature dependence of the pseudo-Rayleigh parameters of the BaTiO₃ ceramics with grain sizes of 1.2 μm and 76 μm.

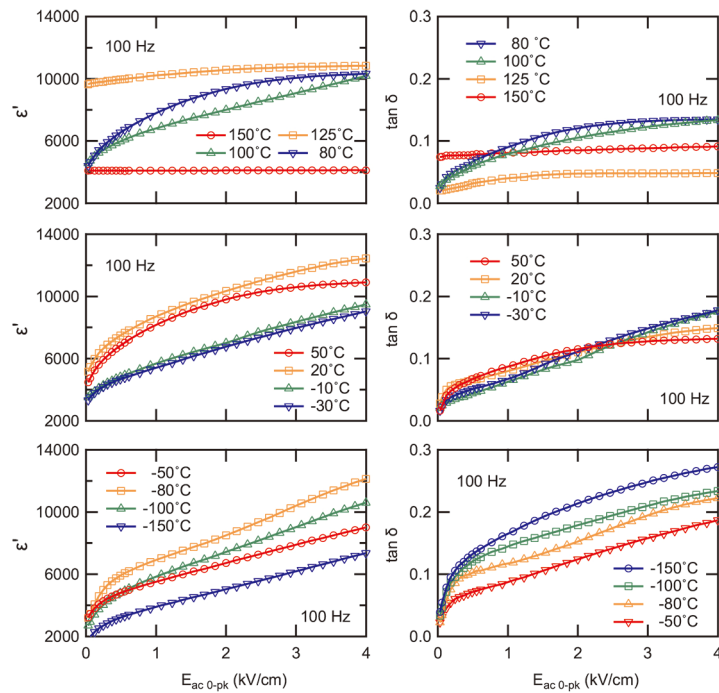


Figure 7. The ac field dependence of the dielectric properties of the undoped BaTiO₃ ceramics sintered at 10⁻⁹ atm pO₂ measured at various temperatures.

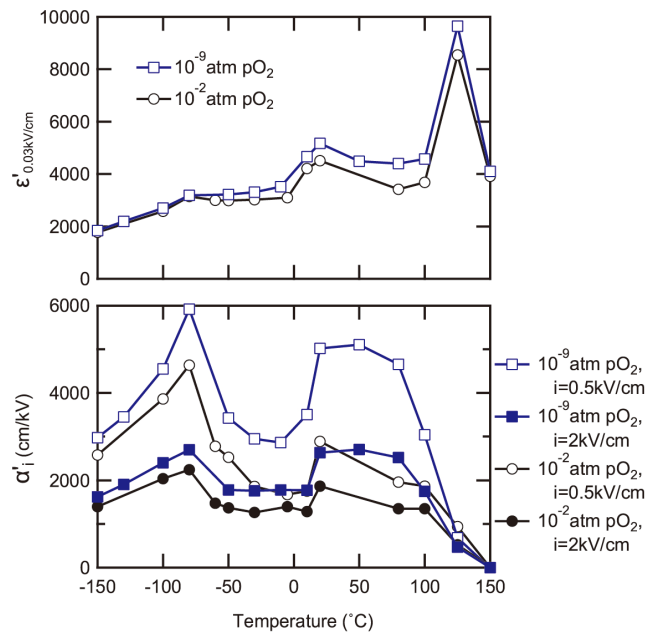


Figure 8. Temperature dependence of the pseudo-Rayleigh parameters of the BaTiO₃ ceramics sintered at 10⁻⁹ atm pO₂ and the BaTiO₃ ceramics sintered at 10⁻² atm pO₂ and post-annealed.

pinning of domain walls from weak pinning centers associated with the defect dipoles^[24].

In most multilayer ceramic capacitors, the BaTiO₃ is formulated to reduce the temperature dependence of the permittivity and increase the reliability when base metal electrodes are utilized^[35]. It is thus interesting to compare the temperature dependence of the extrinsic contributions of a formulated dielectric to that of undoped ceramics. Figure 9 shows the ac field dependence of the dielectric properties of formulated BaTiO₃ ceramics sintered at 10⁻² and 10⁻⁹ atm pO₂; these samples showed core-shell microstructures^[24]. Above T_c, the dielectric constant of both samples was independent of pO₂; the permittivities of the two samples were nearly identical in this regime due to the similar grain sizes (both samples had grain sizes of ~0.5 μm) and the absence of a large concentration of mobile interfaces. As expected, provided that the samples are far enough above T_c, there are few residual micropolar regions, and the nonlinear dielectric response of formulated and undoped ceramics is similar. In contrast, below T_c, the irreversible contributions to the permittivity were substantially suppressed in the formulated ceramics relative to the undoped materials. At 20 °C, the ac field dependence of the 10⁻² atm pO₂ sample was almost linear, while that of the 10⁻⁹ atm pO₂ sample was sublinear.

The dielectric responses were quantified using the pseudo-Rayleigh analysis, as shown in Figure 10. Below T_c, the ε'_{0.03kV/cm} of the 10⁻² atm pO₂ sample monotonically decreased with temperature, while that of the 10⁻⁹ atm pO₂ sample showed a core/shell response. This is consistent with the temperature dependence of the small signal dielectric permittivity of the samples^[24]. With decreasing temperature, α'_i increased up to the orthorhombic to rhombohedral phase transition and then decreased, which is consistent with the α'_i for the small-grained undoped BaTiO₃ ceramics (although the increase at the tetragonal to orthorhombic phase transition was smeared). It was found that the difference of the α'_i between the formulated samples was small above the T_c of the shell region. This suggests that the domain wall contributions are strongly influenced by the shell region. Note that near room temperature, α'_{2kV/cm} and α'_{0.5kV/cm} of the 10⁻² atm pO₂ sample were similar, which corresponds to the Rayleigh behavior.

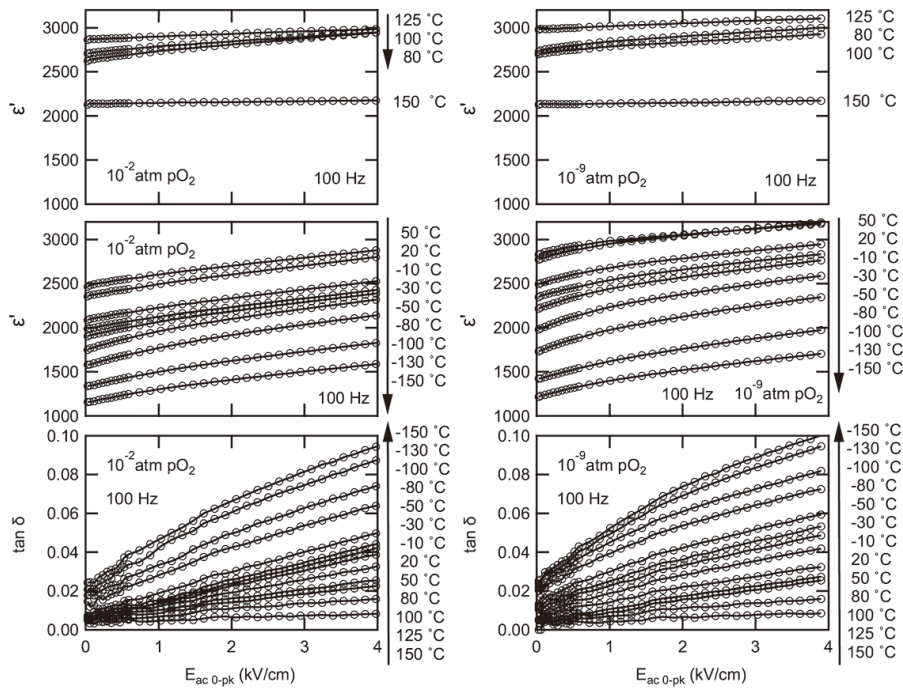


Figure 9. The ac field dependence of the dielectric properties of the formulated BaTiO₃ ceramics sintered at 10⁻² atm pO₂ and 10⁻⁹ atm pO₂ measured at various temperatures.

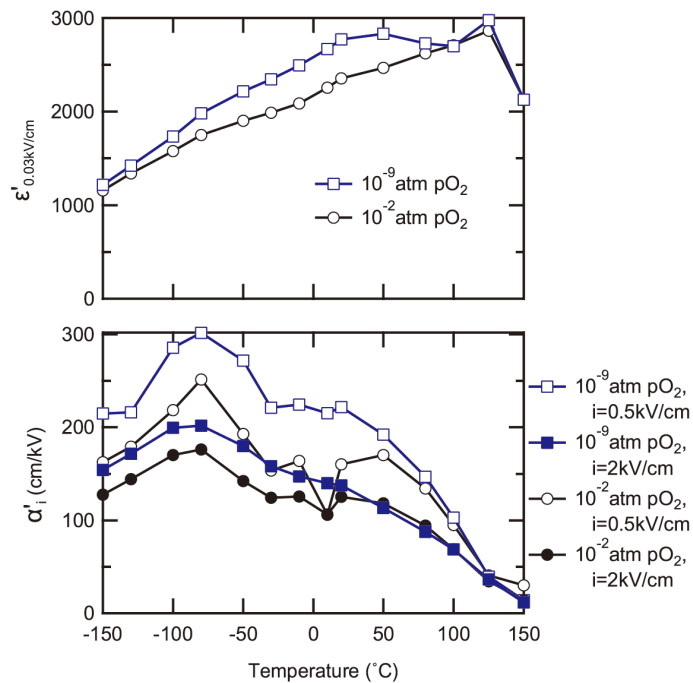


Figure 10. Temperature dependence of the pseudo-Rayleigh parameters of formulated BaTiO₃ ceramics sintered at 10⁻² atm pO₂ and 10⁻⁹ atm pO₂.

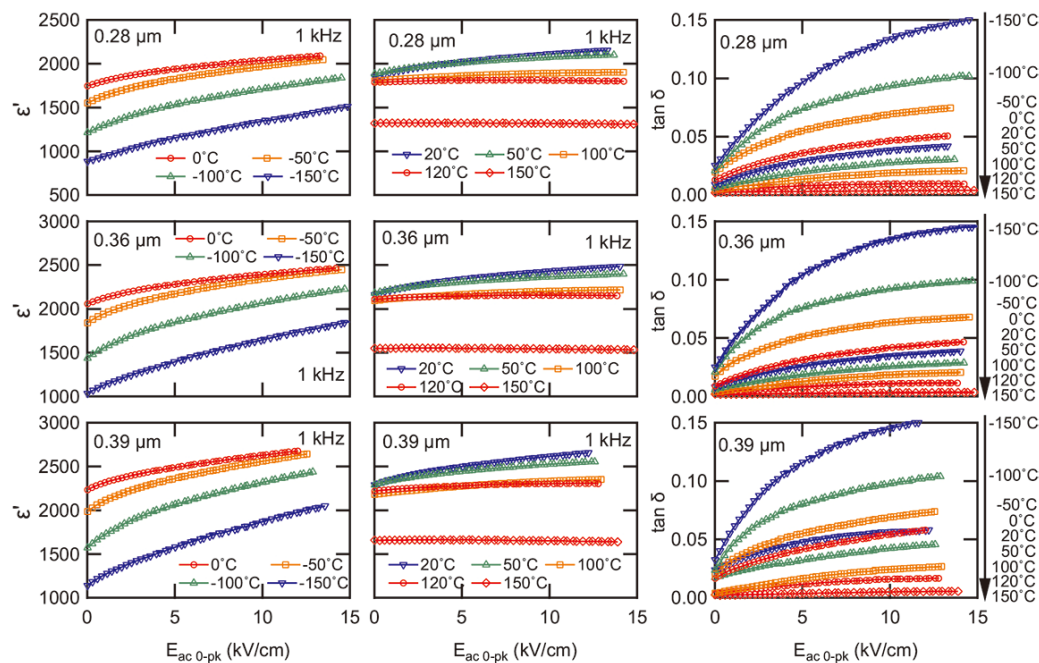


Figure 11. The ac field dependence of the dielectric properties of model MLCCs with different grain sizes measured at various temperatures.

It is also notable that the values for α'_i for these formulated BaTiO_3 ceramics are approximately an order of magnitude smaller than those of the undoped BaTiO_3 in the ferroelectric phases. There may be several reasons for this. First, the formulated ceramics had a small grain size of $\sim 0.5 \mu\text{m}$, which induced additional grain boundary dilution of the response. Secondly, the formulated BaTiO_3 has a lower volume fraction of the ferroelectric phase associated with the introduction of shell regions. These non-ferroelectric regions will also act as capacitors in series that suppress the extrinsic contributions to the response. Thirdly, it is also possible that the core-shell microstructures act to suppress the long coupling of the domain wall motion. It has been shown that domain walls often have some level of continuity across grain boundaries^[36] and that the resulting ensembles of domain walls often move as clusters rather than as isolated walls^[37,38]. It is not straightforward to separate the relative importance of each of these factors since the second and third, in particular, will also be functions of temperature themselves.

Figure 11 shows the ac field dependence of the dielectric constant for formulated BaTiO_3 MLCCs with various grain sizes measured at various temperatures. Above T_c , the dielectric constant was independent of the ac field amplitude. However, the permittivity data do not superimpose for the different grain sizes, presumably because of a difference in the grain boundary dilution of the response^[39]. Below T_c , the dielectric constant depends on the ac field, and the ac field dependence increases with decreasing temperature. The ac field dependence was quantified using pseudo-Rayleigh analysis, as shown in Figure 12. The ϵ'_i followed a core/shell response of the dielectric constant. With decreasing grain size, the ϵ'_i decreased. The temperature dependence of the α'_i was similar to the formulated BaTiO_3 ceramics. The peak at the orthorhombic to rhombohedral phase transition decreased with grain size. This is consistent with the grain size dependence of the undoped BaTiO_3 ceramics. It was observed that the grain size dependence of α'_i was relatively weak above the T_c of the shell. This result is consistent with the pO_2 dependence of α'_i for the formulated BaTiO_3 ceramics, suggesting the influence of the shell region on irreversible domain wall contributions.

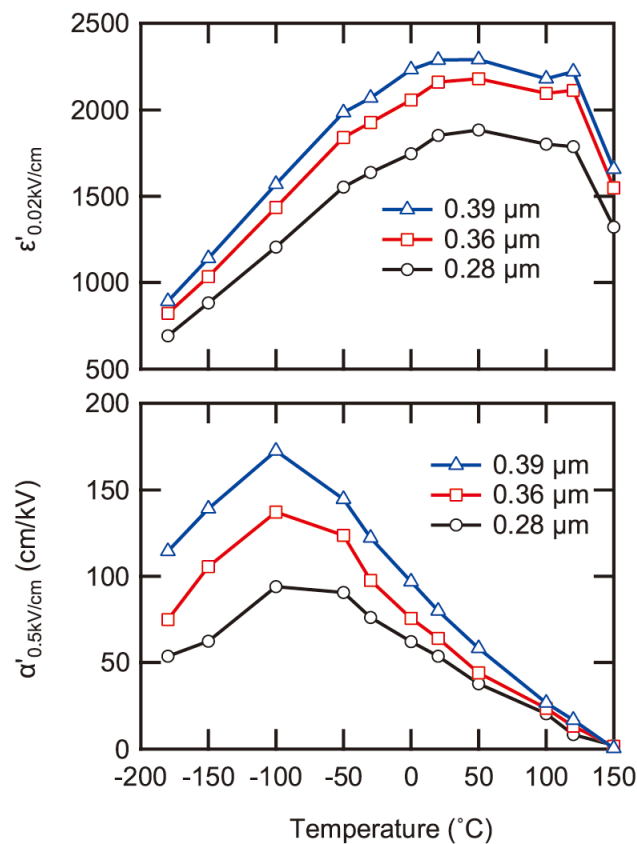


Figure 12. Temperature dependence of the pseudo-Rayleigh parameters of the MLCCs with various grain sizes.

CONCLUSIONS

In conclusion, this paper has demonstrated the temperature dependence of the extrinsic responses in both undoped and formulated BaTiO₃. Knowledge of this behavior is important to understand how the materials will perform in working conditions. Given that domain wall motion is thermally activated, it also depends on temperature. The relative magnitude of the extrinsic contributions to the properties is a strong function of the microstructure of the ceramics, especially the grain size and the existence of core-shell microstructures; it is a much weaker function of the concentration of oxygen vacancies.

DECLARATIONS

Acknowledgments

Model MLCC samples were provided from AVX Corporation, Myrtle Beach, SC, USA, for the Center for Dielectrics Studies at Penn State.

Authors' contributions

The conception and design of the work: Trolier-McKinstry S

The acquisition and analysis of data: Fujii I

The interpretation of data: Fujii I, Trolier-McKinstry S

The writing and revising: Fujii I, Trolier-McKinstry S

Availability of data and materials

The data that support the findings of this study are available from the corresponding author upon reasonable request.

Financial support and sponsorship

The experimental work was funded by the Center for Dielectrics Studies at Penn State. The interpretation of the results was supported by funding from the National Science Foundation and the Center for Dielectrics and Piezoelectrics under Grant No. IIP-1841466 and No. IIP-1841453 and the National Science Foundation grant DMR-2025439.

Conflicts of interest

Both authors declared that there are no conflicts of interest.

Ethical approval and consent to participate

Not applicable.

Consent to participate

Not applicable.

Copyright

© The Author(s) 2023.

REFERENCES

1. Hall DA. Review nonlinearity in piezoelectric ceramics. *J Mater Sci* 2001;36:4575-601. [DOI](#)
2. Herbiet R, Robels U, Dederichs H, Arlt G. Domain wall and volume contributions to material properties of PZT ceramics. *Ferroelectrics* 1989;98:107-21. [DOI](#)
3. Setter N, Damjanovic D, Eng L, et al. Ferroelectric thin films: review of materials, properties, and applications. *J Appl Phys* 2006;100:051606. [DOI](#)
4. Bassiri-Gharb N, Fujii I, Hong E, Trolier-Mckinstry S, Taylor DV, Damjanovic D. Domain wall contributions to the properties of piezoelectric thin films. *J Electroceram* 2007;19:49-67. [DOI](#)
5. Li S, Cao W, Cross LE. The extrinsic nature of nonlinear behavior observed in lead zirconate titanate ferroelectric ceramic. *J Appl Phys* 1991;69:7219-24. [DOI](#)
6. Otonicar M, Dragomir M, Rojac T. Dynamics of domain walls in ferroelectrics and relaxors. *J Am Ceram Soc* 2022;105:6479-507. [DOI](#)
7. Arlt G. The influence of microstructure on the properties of ferroelectric ceramics. *Ferroelectrics* 1990;104:217-27. [DOI](#)
8. Cao W, Randall CA. Grain size and domain size relations in bulk ceramic ferroelectric materials. *J Phys Chem Solids* 1996;57:1499-505. [DOI](#)
9. Rayleigh L. XXV. Notes on electricity and magnetism. - III. On the behaviour of iron and steel under the operation of feeble magnetic forces. Available from: <https://www.tandfonline.com/doi/abs/10.1080/14786448708628000> [Last accessed on 1 Nov 2023].
10. Taylor DV, Damjanovic D. Evidence of domain wall contribution to the dielectric permittivity in PZT thin films at sub-switching fields. *J Appl Phys* 1997;82:1973-5. [DOI](#)
11. Boser O. Statistical theory of hysteresis in ferroelectric materials. *J Appl Phys* 1987;62:1344-8. [DOI](#)
12. Preisach F. Über die magnetische Nachwirkung. *Z Physik* 1935;94:277-302. [DOI](#)
13. Robert G, Damjanovic D, Setter N. Preisach distribution function approach to piezoelectric nonlinearity and hysteresis. *J Appl Phys* 2001;90:2459-64. [DOI](#)
14. Mayergoyz ID. Mathematical models of hysteresis and their applications. Amsterdam: Elsevier Academic Press; 2003.
15. Fujii I, Hong E, Trolier-McKinstry S. Thickness dependence of dielectric nonlinearity of lead zirconate titanate films. *IEEE Trans Ultrason Ferroelectr Freq Control* 2010;57:1717-23. [DOI](#) [PubMed](#)
16. Stancu A, Ricinschi D, Mitoseriu L, Postolache P, Okuyama M. First-order reversal curves diagrams for the characterization of ferroelectric switching. *Appl Phys Lett* 2003;83:3767-9. [DOI](#)
17. Johnson KM. Variation of dielectric constant with voltage in ferroelectrics and its application to parametric devices. *J Appl Phys* 1962;33:2826-31. [DOI](#)
18. Narayanan M, Tong S, Ma B, Liu S, Balachandran U. Modified Johnson model for ferroelectric lead lanthanum zirconate titanate at very high fields and below Curie temperature. *Appl Phys Lett* 2012;100:022907. [DOI](#)

19. Tsurumi T, Yamamoto Y, Kakemoto H, Wada S, Chazono H, Kishi H. Dielectric properties of BaTiO₃-BaZrO₃ ceramics under a high electric field. *J Mater Res* 2002;17:755-9. [DOI](#)
20. Cheng C, Peters T, Dangi A, et al. Improving PMUT receive sensitivity via dc bias and piezoelectric composition. *Sensors* 2022;22:5614. [DOI](#) [PubMed](#) [PMC](#)
21. Hirose S, Aoyagi M, Tomikawa Y, Takahashi S, Uchino K. High power characteristics at antiresonance frequency of piezoelectric transducers. *Ultrasonics* 1996;34:213-7. [DOI](#)
22. Mokřý P, Wang Y, Tagantsev AK, Damjanovic D, Stolichnov I, Setter N. Evidence for dielectric aging due to progressive 180° domain wall pinning in polydomain Pb(Zr_{0.45}Ti_{0.55})O₃ thin films. *Phys Rev B* 2009;79:054104. [DOI](#)
23. Wu K, Schulze WA. Effect of the ac Field level on the aging of the dielectric response in polycrystalline BaTiO₃. *J Am Ceram Soc* 1992;75:3385-9. [DOI](#)
24. Fujii I, Ugorek M, Han Y, Trolrier-McKinstry S. Effect of oxygen partial pressure during firing on the high AC field response of BaTiO₃ dielectrics. *J Am Ceram Soc* 2010;93:1081-8. [DOI](#)
25. Fujii I, Ugorek M, Trolrier-McKinstry S. Grain size effect on the dielectric nonlinearity of BaTiO₃ ceramics. *J Appl Phys* 2010;107:104116. [DOI](#)
26. Nies C, Berolini M. Factors in improved DC bias performance in X7R capacitors. In: The 12th US-Japan seminar on dielectric piezoelectric ceramics, 2005 Nov 6-9; Annapolis, USA.
27. Fujii I, Trolrier-McKinstry S, Nies C. Effect of grain size on dielectric nonlinearity in model BaTiO₃-based multilayer ceramic capacitors. *J Am Ceram Soc* 2011;94:194-9. [DOI](#)
28. Garten LM, Lam P, Harris D, Maria JP, Trolrier-McKinstry S. Residual ferroelectricity in barium strontium titanate thin film tunable dielectrics. *J Appl Phys* 2014;116:044104. [DOI](#)
29. Zhang QM, Wang H, Kim N, Cross LE. Direct evaluation of domain-wall and intrinsic contributions to the dielectric and piezoelectric response and their temperature dependence on lead zirconate-titanate ceramics. *J Appl Phys* 1994;75:454-9. [DOI](#)
30. Randall CA, Kim N, Kucera JP, Cao W, Shrout TR. Intrinsic and extrinsic size effects in fine-grained morphotropic-phase-boundary lead zirconate titanate ceramics. *J Am Ceram Soc* 1998;81:677-88. [DOI](#)
31. Ghosh D, Sakata A, Carter J, et al. Domain wall displacement is the origin of superior permittivity and piezoelectricity in BaTiO₃ at intermediate grain sizes. *Adv Funct Mater* 2014;24:885-96. [DOI](#)
32. Marincel DM, Zhang H, Jesse S, et al. Domain wall motion across various grain boundaries in ferroelectric thin films. *J Am Ceram Soc* 2015;98:1848-57. [DOI](#)
33. Hennessey G, Peters T, Tipsawat P, Checa M, Collins L, Trolrier-McKinstry S. Domain wall motion across microstructural features in polycrystalline ferroelectric films. *Acta Mater* 2023;250:118871. [DOI](#)
34. Demartin M, Damjanovic D. Dependence of the direct piezoelectric effect in coarse and fine grain barium titanate ceramics on dynamic and static pressure. *Appl Phys Lett* 1996;68:3046-8. [DOI](#)
35. Kishi H, Mizuno Y, Chazono H. Base-metal electrode-multilayer ceramic capacitors: past, present and future perspectives. *Jpn J Appl Phys* 2003;42:1-15. [DOI](#)
36. Mantri S, Daniels JE. Ferroelectric domain continuity over grain boundaries for tetragonal, orthorhombic, and rhombohedral crystal symmetries. *IEEE Trans Ultrason Ferroelectr Freq Control* 2018;65:1517-24. [DOI](#) [PubMed](#)
37. Bintachitt P, Jesse S, Damjanovic D, et al. Collective dynamics underpins Rayleigh behavior in disordered polycrystalline ferroelectrics. *Proc Natl Acad Sci USA* 2010;107:7219-24. [DOI](#) [PubMed](#) [PMC](#)
38. Peters T, Zhu W, Checa M, Collins L, Trolrier-McKinstry S. Influence of doping and thickness on domain avalanches in lead zirconate titanate thin films. *Appl Phys Lett* 2023;122:132906. [DOI](#)
39. Frey MH, Xu Z, Han P, Payne DA. The role of interfaces on an apparent grain size effect on the dielectric properties for ferroelectric barium titanate ceramics. *Ferroelectrics* 1998;206:337-53. [DOI](#)

Research Article

Open Access



Varied domain structures in $0.7\text{Pb}(\text{Mg}_{1/3}\text{Nb}_{2/3})\text{O}_3$ - 0.3PbTiO_3 single crystals

Dawei Zhang^{1,2,#} , Lei Wang^{1,#} , Linglong Li³, Pankaj Sharma^{4,5} , Jan Seidel^{1,2} 

¹School of Materials Science and Engineering, UNSW Sydney, Sydney, NSW 2052, Australia.

²ARC Centre of Excellence in Future Low-Energy Electronics Technologies, UNSW Sydney, Sydney, NSW 2052, Australia.

³Key Laboratory of Quantum Materials and Devices of Ministry of Education, School of Physics, Southeast University, Nanjing 211189, Jiangsu, China.

⁴College of Science and Engineering, Flinders University, Bedford Park, Adelaide, SA 5042, Australia.

⁵Flinders Institute for Nanoscale Science and Technology, Flinders University, Adelaide, SA 5042, Australia.

#Authors contributed equally.

Correspondence to: Prof. Jan Seidel, School of Materials Science and Engineering, UNSW Sydney, Sydney, NSW 2052, Australia.
E-mail: jan.seidel@unsw.edu.au

How to cite this article: Zhang D, Wang L, Li L, Sharma P, Seidel J. Varied domain structures in $0.7\text{Pb}(\text{Mg}_{1/3}\text{Nb}_{2/3})\text{O}_3$ - 0.3PbTiO_3 single crystals. *Microstructures* 2023;3:2023046. <https://dx.doi.org/10.20517/microstructures.2023.57>

Received: 13 Oct 2023 **First Decision:** 13 Nov 2023 **Revised:** 20 Nov 2023 **Accepted:** 28 Nov 2023 **Published:** 1 Dec 2023

Academic Editor: Shujun Zhang **Copy Editor:** Fangyuan Liu **Production Editor:** Fangyuan Liu

Abstract

Single crystals of $0.7\text{Pb}(\text{Mg}_{1/3}\text{Nb}_{2/3})\text{O}_3$ - 0.3PbTiO_3 (PMN-30PT) with a composition close to the morphotropic phase boundary have demonstrated remarkable electromechanical properties, stimulating intensive research interest in the field of piezoelectrics. Domain structures have long been associated with their overall piezoelectric properties, thereby garnering particular research interest for the enhancement of piezoelectric properties. Here, we report on three distinct domain structures in this material. Through a combination of X-ray diffraction reciprocal space mapping and piezoresponse force microscopy measurements, an M_A crystal structure has been confirmed. The three-dimensional polar vectors of the three domain structures have been reconstructed with two $4M_A$ and one $2M_A$ domain structures. Correlations between different domain structures and their local electrical switching properties have been revealed. Our study of the PMN-30PT single crystal examines diverse domain structures at the mesoscale in detail, which provides valuable insight into the relationship between structures and properties of the material.

Keywords: Ferroelectrics, PMN-PT single crystal, domain structures, piezoresponse force microscopy



© The Author(s) 2023. **Open Access** This article is licensed under a Creative Commons Attribution 4.0 International License (<https://creativecommons.org/licenses/by/4.0/>), which permits unrestricted use, sharing, adaptation, distribution and reproduction in any medium or format, for any purpose, even commercially, as long as you give appropriate credit to the original author(s) and the source, provide a link to the Creative Commons license, and indicate if changes were made.



INTRODUCTION

Relaxor ferroelectric solid solutions of $(1-x)\text{Pb}(\text{Mg}_{1/3}\text{Nb}_{2/3})\text{O}_3-x\text{PbTiO}_3$ (PMN- x PT) have long been the research focus over the last few decades by virtue of their superb piezoelectric and electromechanical performance that is closely related to their complex microstructure^[1-6]. In pursuit of high piezoelectric properties, normally two approaches are adopted: the intrinsic one through composition tuning of the solid solution or doping^[5,7,8] and the extrinsic one through domain/domain wall engineering^[9-11]. To achieve high electromechanical properties in the PMN- x PT system, regarding the intrinsic approach, the composition x is usually tuned to a composition of $x\sim 0.3$ near the morphotropic phase boundary (MPB), which separates the rhombohedral and tetragonal phases. The improved piezoelectric performance has been attributed to the intermediate monoclinic phase bridging the adjacent rhombohedral and tetragonal phases, thus allowing easy polarization rotation^[2,8,12]. The resulting domain structures at the MPB region in various systems have also demonstrated beyond-binary multilevel switching and memristive behavior, which is promising for the new paradigms of non-volatile memory applications^[13,14]. When it comes to the extrinsic approach, both direct current (DC) poling and an emerging alternating current (AC) poling approach, along with various other approaches, have been utilized to enhance the piezoelectricity through domain wall engineering^[1,3,15-28].

Therefore, PMN-30PT is of particular research interest for revealing its structure-property relationship. This interest stems not only from its status as an MPB composition but also from its rich domain structures. From the composition perspective, the hierarchy of domain structures has been known to evolve with different Ti concentrations. $\text{Pb}(\text{Mg}_{1/3}\text{Nb}_{2/3})\text{O}_3$ (PMN) and PbTiO_3 (PT) are typical relaxors and classic ferroelectric systems featuring short-range-ordered polar nanoregions and long-range-ordered domains, respectively. The increased concentration of PT leads to an increased off-center polar displacement within the unit cell accompanied by mechanical stress^[29,30]. To accommodate the elastic strain, smaller domains are self-assembled into larger ones with orientations along the polarization variants. Bian *et al.* have investigated the domain structures of PMN- x PT systems at diverse compositions and their associated local piezoresponse^[31]. From the domain engineering perspective, significant effort has been made to examine the relationship between the domain structure and the electromechanical performance in PMN- x PT systems. The piezoelectric response of PMN-PT has been enhanced more than three times by increasing the domain wall density through DC poling^[1,16]. Recently, it has been found that three varied domain structures can be induced by the DC poling on the patterned electrodes^[32]. Under AC poling, it is suggested that the field-induced M_A phase contributes to the enhanced piezoelectricity in PMN-PT^[22]. It has also been discovered that with increasing AC poling cycles, the domain structure can evolve from 4R to 2R with a concomitant increasing length of 109° domain walls^[23]. To note, 4R/2R denotes that there are four/two possible spontaneous polarization directions along the polar axis in the rhombohedral phase^[23]. Additionally, the elimination of light-scattering 71° domain walls has been used to fabricate transparent PMN-PT single crystals under AC poling^[3,33].

In this work, three distinctive domain structures have been revealed in different regions of PMN-30PT single crystals using piezoresponse force microscopy (PFM). X-ray diffraction (XRD) reciprocal space mappings (RSM), a series of rotational in-plane (IP) PFM, and trailing field experiments have been used to confirm the M_A structure of the crystal, and three-dimensional (3D) polar domain variants have been reconstructed. The correlation between the domain structures and the local electrical switching properties has been revealed using switching spectroscopy PFM (SSPFM).

EXPERIMENTAL METHODS

PMN-30PT single crystals with (100) orientation were obtained from MTI Corporation, China. The crystals were synthesized by an improved Bridgman method. The size of the crystals is 5 mm × 5 mm × 0.2 mm, two-sided polished with a surface roughness (Ra) less than 10 Å.

High-resolution θ -2 θ XRD studies and RSMs were carried out using a PANalytical X'Pert Pro diffractometer with $\text{CuK}\alpha_1$ radiation. The optical images were taken using a Nikon ECLIPSE LV100POL optical microscope.

All measurements were performed by two commercial AFM systems, an AIST-NT Smart scanning probe microscopy (SPM) 1000 and an Asylum Research MFP-3D Infinity at room temperature under ambient conditions. The IP PFM signal depends on the sample orientation with respect to the cantilever. It means that only the projected component of the IP polarization vector perpendicular to the cantilever contributes to the IP PFM signal, as IP PFM modes rely on the torsional vibration of the cantilever. Therefore, in order to resolve the IP polarization vectors, angle-resolved PFM measurements were carried out by changing the azimuthal angle between the cantilever and the sample. Consequently, the directions of the IP polarization variants have been resolved by high-resolution PFM images acquired at the quasi-identical region by changing the cantilever-sample orientation from 0° to 360° with an interval of 45°. To note, during the angle-resolved PFM measurements, the orientation of the cantilever is fixed, and only the angle of the sample is rotated with respect to the cantilever. The angle-resolved PFM measurements were performed with an AC excitation bias between 1.0 to 2.0 V (peak to peak) with platinum-coated tips (HQ:NSC35/Pt, Mikromasch) at an off-resonance frequency of 100 kHz to avoid any crosstalk from the topography or resonance frequencies. For SSPFM measurements, commercial silicon tips with conductive Ti/Ir coating (ASYLEEC.01-R2, Asylum Research) were used.

RESULTS AND DISCUSSION

The composition of PMN-30PT single crystals is at the MPB that separates the rhombohedral and tetragonal phases, and the existence of intermediate monoclinic phases at this regime is argued to facilitate the rotation path between these two phases. To analyze the polarization variants in the sample, RSMs were performed to determine the crystal structure. A twofold and a threefold peak splitting were observed around 310 and 311 reflections, respectively, confirming a monoclinic A (M_A) structure [Supplementary Figure 1]^[34,35].

Type 1 domain structures with a typical zigzag feature on the topography are shown in Figure 1. The long vertical zigzag stripes [Figure 1A], with an average stripe/domain width of 2.5 μm , can be observed in the majority of the sample regions, as evidenced by the optical image shown in Figure 1G. Coinciding with the topography, the out-of-plane (OOP) phase shows the same zigzag domain structure, with a clear 180° phase reversal between the adjacent two stripe domains [Figure 1B]. Such topography-domain correlation originates from a mechanochemical polishing effect that leads to a polarization-dependent mechanical property upon polishing. Of note, the downward polarization demonstrates a higher surface height in comparison to the upward polarization, as confirmed in the OOP poling experiment in Supplementary Figure 2. Two sets of IP PFM images [Figure 1C-F] were obtained by changing the tip-sample rotation angle from 0 to 90 to resolve the IP polarization variants as the polarization component perpendicular to the cantilever leads to a torsional movement of the cantilever that can be sensitively detected. The 0° and 90° rotation IP PFM phase signals in Figure 1C and E show checkerboard domain structures with four-color contrast, indicating four polarization variants. Figure 1C and E is then binarized to Figure 1D and F with only black and white contrast. The trailing field, which is equivalent to an IP

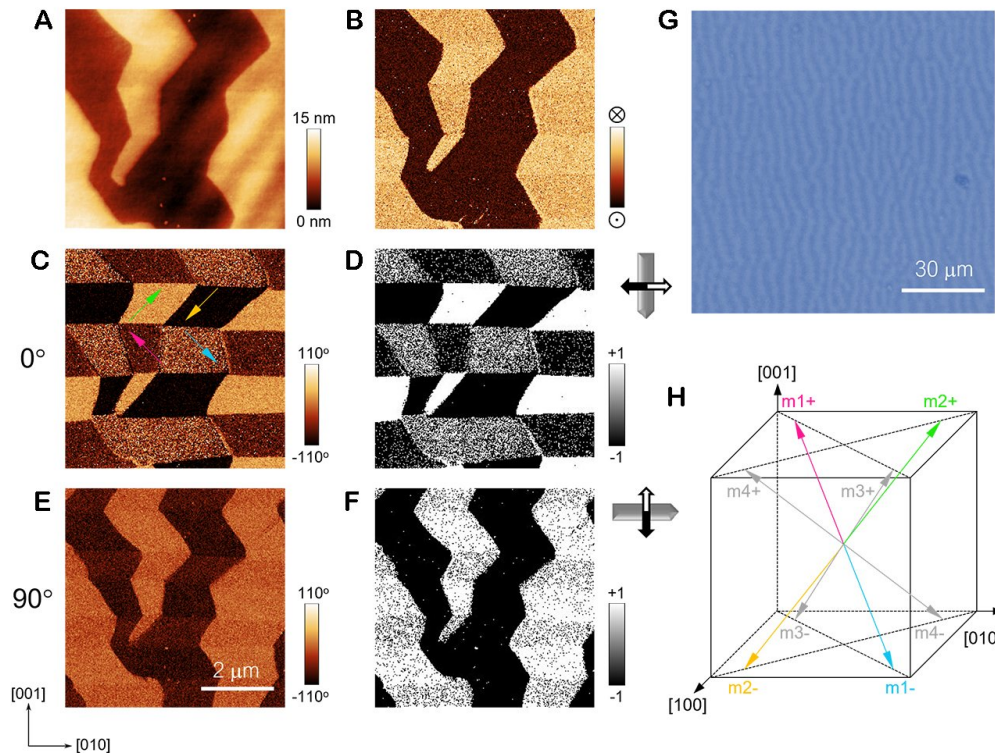


Figure 1. Type 1 domain structure. (A) Topography of type 1 domain structure. (B) The corresponding OOP phase signal. (C) IP phase signal measured at a tip-sample orientation of 0. The IP polarization variants are denoted on each domain. (D) The binarized version of (C). (E) IP phase signal measured at a tip-sample orientation of 90. (F) The binarized version of (E). (G) The optical image of type 1 domain. (H) The reconstructed three-dimensional polarization vectors for type 1 domain.

electric field with a direction co-determined by the tip motion direction and the polarity of the tip bias, has been used to resolve the directions of the binary black and white contrast [Supplementary Figure 3]^[36]. All the PFM signals in this paper were measured at off-resonance frequency to avoid the crosstalk from the topography and possible phase flipping near the resonance frequency. By combining the two IP directions, as denoted in Figure 1D and F, the polarization vectors for each domain can be established in this (100) oriented M_A PMN-PT sample. The IP projections of the four variants are shown in Figure 1C. Additionally, in Supplementary Figure 4, full angle-resolved PFM measurements were performed at the quasi-identical region by altering the cantilever-sample orientation from 0° to 360° at an interval of 45°. IP phase values of the four domains are plotted as a function of tip rotation angle, and then trigonometric fitting is used to resolve the relative phase differences between each of the four domains. The same reconstruction result of the polarization vectors is obtained and shown in Supplementary Figure 5, which is also confirmed by the trailing field experiments shown in Supplementary Figures 6 and 7. The domain structure shows a $4M_A$ domain configuration with non-charged head-to-tail 71° domain walls (m1+ and m2+, m1- and m2-) and 180° domain walls (m2+ and m2-, m1+ and m1-), which can be seen from the reconstructed four polarization vectors shown in Figure 1H. There are no 109° domain walls in this type 1 domain structure. To note, the PMN-30PT is an MPB composition with an M_A structure, which closely resembles the rhombohedral structure due to the slight structural deviations; therefore, the names of domain wall types still conform to the conventional usage, denoted as 71, 109, and 180, as defined within a pseudocubic structure^[37,38].

Type 2 domain structures with a checkerboard feature in the topography are shown in [Figure 2](#). The alternating yellow and brown quadrilateral patterns [[Figure 2A](#)], with an average base/height of 1.5/3 mm, can only be observed in a minority of the sample regions embedded in the matrix of type 1 domain configurations. The OOP phase image shows the same alternating checkerboard domains in comparison with the topography, exhibiting distinct 180° phase differences [[Figure 2B](#)]. The optical image shows a consistent checkerboard pattern [[Figure 2G](#)]. Two sets of IP PFM images with different tip-sample orientations, i.e., 0° and 90° , were measured to determine the polarization vectors [[Figure 2C](#) and [E](#)]. Based on the binarized IP phase values [[Figure 2D](#) and [F](#)], the reconstructed four polarization vectors with both upward and downward directions are shown in the schematic in [Figure 2H](#). The IP polarization projections are denoted in corresponding domains in [Figure 2C](#). Compared to the type I domain structure, 71° domains are non-existent, but 109° domain walls emerge (m_{1+} and m_{3+} , m_{1-} and m_{3-}) in addition to the 180° domain walls that are present in both type 1 and type 2 domain structures. The existence of 180° domain walls in both type 1 and 2 domain structures is due to the allowed polarization states in both upward and downward directions.

Type 3 domain structures have a prominent horizontal long stripe domain arrangement along $[010]$, as shown in [Figure 3A](#). The stripes have a typical width of around 1-2 mm. Not all stripe domains are continuous, as some of them terminate or merge to form larger stripes. The OOP phase also demonstrates a clear 180° phase difference between adjacent stripe domains, as shown in [Figure 3B](#). The optical image also shows a consistent structure, as shown in [Figure 3C](#). It should be noted that the type 3 domain only emerges at certain regions that are adjacent to the sample edge, as denoted by the red dashed boxes in [Supplementary Figure 8](#). The same rotational experiments were done and are shown in [Figure 3D-G](#). The 0° rotational IP phase signals [[Figure 3D](#) and [E](#)] show the same phase contrast as the OOP phase signal [[Figure 3B](#)]. The 90° rotational IP phase signals [[Figure 3F](#) and [G](#)], by contrast, present a uniform bright phase contrast. This indicates that the polarization components perpendicular to the cantilever from all variants now have the same direction with respect to the cantilever. The reconstructed polarization vectors with only two allowed directions, sharing the same m_{1+} and m_{3+} variants as compared to the type 2 domain, are shown in the schematic in [Figure 3H](#). In this domain configuration, only non-charged 109° domain walls exist due to the existence of only two polarization variants.

A PMN-xPT system is a well-known relaxor ferroelectric system, and the hierarchy of domain structures is known to vary on length scales from nanometer to millimeter with different Ti concentrations. PMN is a pure relaxor with short-range-ordered polar nano regions (PNRs), while PT is a classical ferroelectric with long-range-ordered large domain structures. The introduction of Ti^{4+} increases the off-center displacement, and the distortion inside the PNRs results in a mechanical mismatch between regions with different polarization orientations. To accommodate the generated mechanical strain or minimize the elastic energy, the small PNRs tend to amalgamate into larger domains of micrometer sizes, such as the observed stripe domains or checkerboard patterns, following their macroscopic symmetries^[31]. The observed domain configurations in all three types of domains show macroscopic domain structures, which is consistent with previous studies^[3,21,31,32]. On a close inspection, type 1 and 2 domain structures, while both showing a clear four-variant domain configuration, are slightly different from the commonly reported ones^[3,21,32]. A very typical four-rhombohedral domain configuration after DC or AC poling will have four allowed polarization orientations only in the OOP directions^[3,21], either upward or downward. A checkerboard domain structure along $[110]$ directions and alternating long stripe domains along $[010]$ directions are presented for the OOP and IP domain structures, respectively. The coexistence of 71° and 109° domains and the absence of 180° domains are seen. By comparison, a type 1 domain shows zigzag and checkerboard domain structures in the OOP and IP images, respectively, with a coexistence of 71° and 180° domains. Type 2 does show a

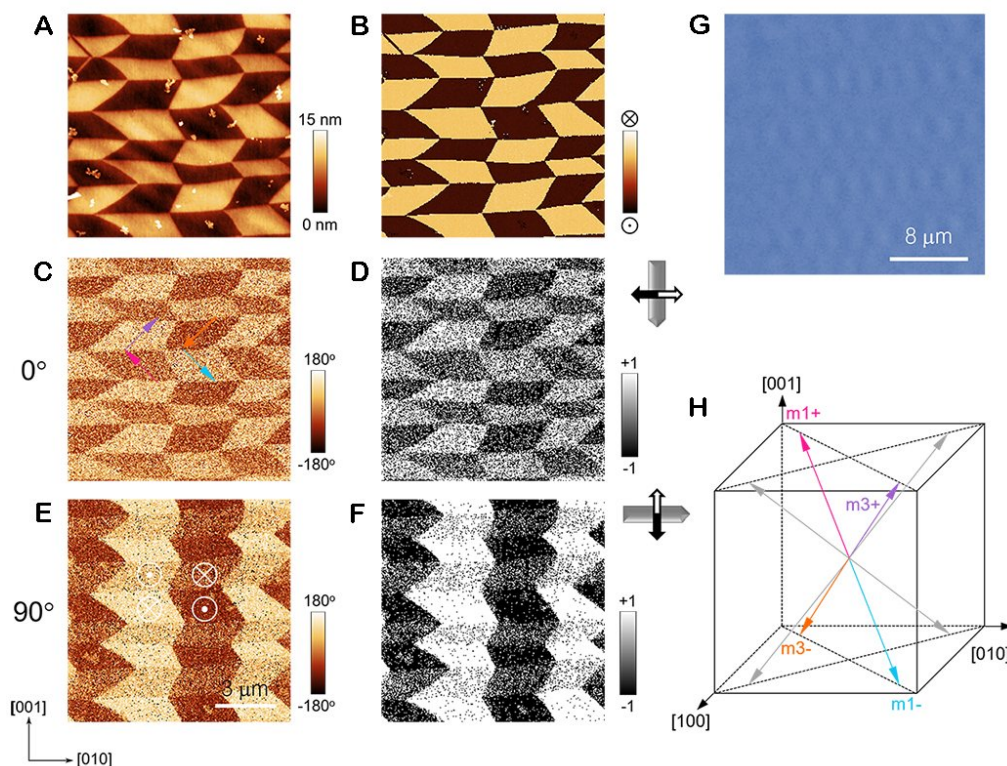


Figure 2. Type 2 domain structure. (A) Topography of type 2 domain structure. (B) The corresponding OOP phase signal. (C) IP phase signal measured at a tip-sample orientation of 0. The IP polarization variants are denoted on each domain. (D) The binarized version of (C). (E) IP phase signal measured at a tip-sample orientation of 90. (F) The binarized version of (E). (G) The optical image of type 2 domain. (H) The reconstructed three-dimensional polarization vectors for type 2 domain.

checkerboard domain structure in the OOP plane but no alternating stripe domains, with a coexistence of 109° and 180° domains. A Type 3 domain structure is consistent with the reported 2M configuration, showing long stripe domains in both OOP and IP directions. One unique feature of the type 3 domain is the existence of pure 109° domain walls that do not induce light scattering in comparison to 71° domain walls, making transparent crystals possible^[3]. However, due to the small fraction of the type 3 domain, the transparency of the region is not very apparent under the optical microscope [Supplementary Figure 8]. The formation of a type 3 domain structure may be due to the unusual strain state at the edge of the dented region [Supplementary Figure 8]. It is known that strain can effectively modify the domain structures or even alter the phase in the PMN-PT system^[39,40], which is especially prominent in the PMN-30PT system, which is close to the MPB and, therefore, has a small anisotropy.

The local ferroelectric properties are further probed by SSPFM mappings of the three different types of domains [Figure 4]. The imprint field mappings calculated from the SSPFM mapping ($V_i = (|V_p| - |V_n|)/2$), where V_p and V_n are positive and negative switching voltages, are also shown. The typical topography image for type I domain structures with OOP polarization directions is shown in Figure 4A. The corresponding V_i mapping exhibits a nice correlation with the topographical feature, which also resembles the domain structure in the OOP direction, as shown in Figure 4A. Figure 4C shows the SSPFM curve averaged over 200 groups of data (100 groups of data each for downward and upward domains). Figure 4D-I contain the same information on the topography, the V_i imprint mapping, and the averaged SSPFM curve for type II and type III domain structures, respectively. The extracted critical fields for each domain type have been summarized in Table 1. $V_{i-SSPFM}$ and V_{i-map} are the imprint fields extracted from the averaged SSPFM curve

Table 1. Local switching properties of the three types of domain structures

Type	$V_{i-SSPFM}$ (V)	V_{i-map} (V)	$V_{c-SSPFM}$ (V)	V_{c-map} (V)
Type 1	-0.6	-1.28	7.1	7
Type 2	-3.55	-3.5	13.77	14
Type 3	-0.95	1.5	11.9	11.5

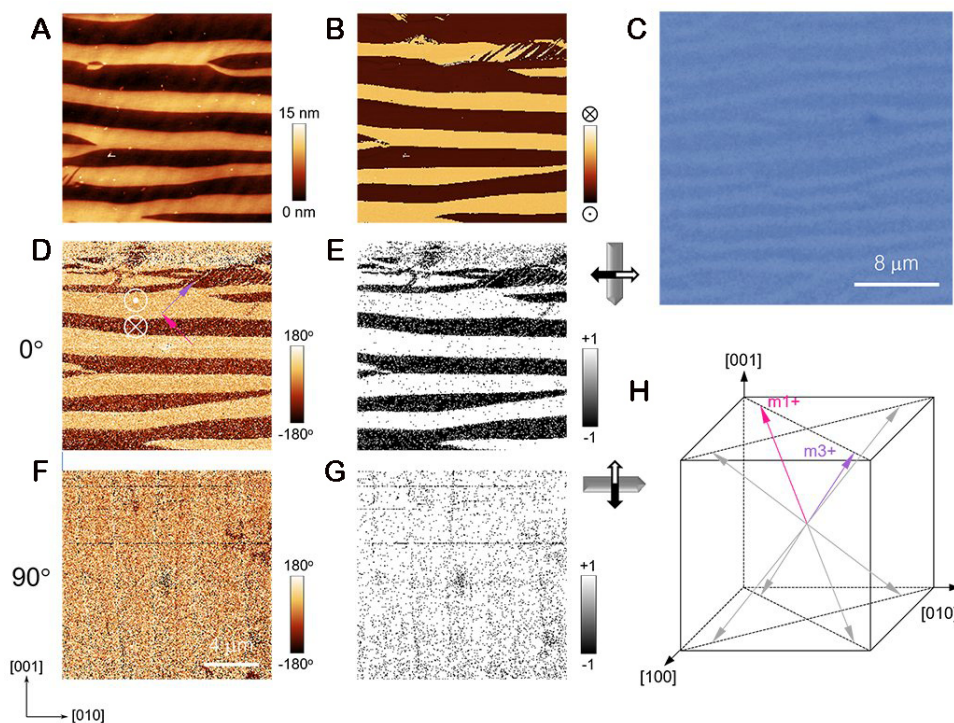


Figure 3. Type 3 domain structure. (A) Topography of type 3 domain structure. (B) The corresponding OOP phase signal. (C) The optical image of type 3 domain. (D) IP phase signal measured at a tip-sample orientation of 0. The IP polarization variants are denoted on each domain. (E) The binarized version of (D). (F) IP phase signal measured at a tip-sample orientation of 90. (G) The binarized version of (F). (H) The reconstructed three-dimensional polarization vectors for type 3 domain.

and the SSPFM mappings, respectively. $V_{c-SSPFM}$ and V_{c-map} are coercive fields extracted from the averaged SSPFM curve and the SSPFM mappings, respectively, where $V_c = (|V_p| + |V_n|)/2$. From the imprint mappings [Figure 4B, E, H], it can be seen that in all three types of domain structures, the downward domains consistently have a negative imprint while the upward domains have a positive imprint, which may be due to the alignment of the high concentration of defect dipoles, e.g., oxygen vacancies, during the DC switching processes. V_{i-map} for type 1, 2, and 3 domain structures are -1.28, -3.5, and 1.5 V, respectively. As a comparison, $V_{i-SSPFM}$ shows a similar trend (-0.6, -3.55, and -0.95 V), and the deviation might originate from different sample sizes as the $V_{i-SSPFM}$ is based on only 200 groups of datasets. The coercive fields, $V_{c-SSPFM}$ and V_{c-map} , show that a type I domain structure has the smallest coercive field, around 7 V, compared to about 14 and 11 V for type 2 and 3 domain structures. The divergence is probably due to the different polarization variants in type 1, m1 and m2, in contrast to m1 and m3 in type 2 and 3 domain structures. The resultant vectors m1+ and m2+ or m1- and m2- are closer to the OOP direction of the electric field along the [100] directions than m1 and m3 pairs, which allows the electrical switching at a lower voltage. The coercive field of the type 3 domain is slightly smaller than that of the type 2 domain. It is possible that a larger domain size

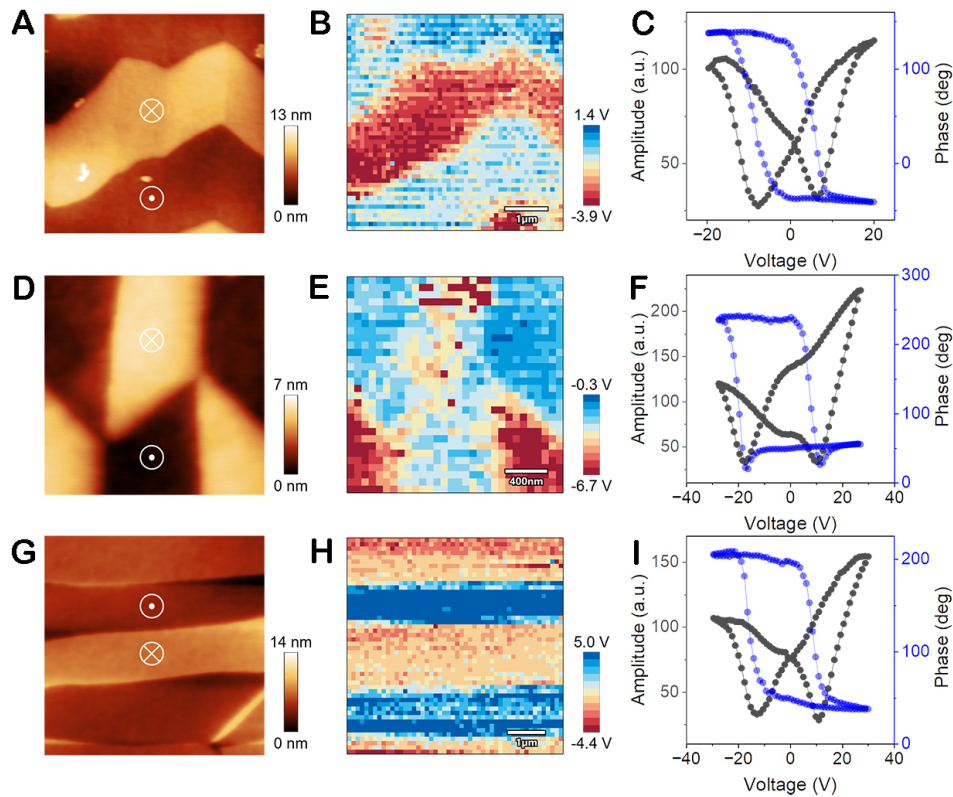


Figure 4. Local electrical switching properties for three types of domains. (A-C) The topography, SSPFM mapping, and averaged SSPFM curves for type 1 domain. (D-F) The topography, SSPFM mapping, and averaged SSPFM curves for type 2 domain. (G-I) The topography, SSPFM mapping, and averaged SSPFM curves for type 3 domain.

in the type 3 domain leads to a larger depolarization field and elastic energy, which makes the domain unstable and easier to switch. The detailed V_{c-map} mappings and averaged SSPFM loops for upward and downward domains are shown in [Supplementary Figure 9](#). The cross-boundary regions between type 1 and type 3, alongside those type 1 and type 2, are shown by the optical microscope images in [Supplementary Figure 10](#).

CONCLUSION

In summary, three different types of domain structures have been systematically studied using SPM in PMN-30 PT single crystals with an M_A crystal structure. High-resolution PFM and trailing field experiments were performed to reconstruct the polarization variants in 3D space for three different domain structures. Type 1 and 2 domain structures have been shown to possess two varying $4M_A$ domain structures featuring a $180^\circ/71^\circ$ domain wall type and a $180^\circ/109^\circ$ domain wall type. A Type 3 domain structure has a pure 109° domain wall type. Detailed electrical switching properties have been studied through the SSPFM mappings, and the divergence of coercive fields in different types of domains is likely to be associated with different domain sizes and types. Furthermore, the perfect correlation between the morphology and ferroelectric domains allows for pinpointing diverse domain structures using optical microscopy. The detailed study of PMN-30PT single crystal at mesoscale can provide a better understanding of various domain structures and insight into the structure-property relationship of the material.

DECLARATIONS

Authors' contributions

Experimental design: Zhang D, Seidel J

Experiments and data collection: Zhang D, Wang L

Data analysis: Zhang D, Wang L, Li L, Sharma P

Manuscript writing and revision: Zhang D, Wang L, Li L, Sharma P, Seidel J

Supervision: Seidel J

Availability of data and materials

The data that support the findings of this study are available from the corresponding author upon reasonable request.

Financial support and sponsorship

This work was supported by the Australian Research Council through Discovery Grants and the ARC Centre of Excellence in Future Low Energy Electronics Technologies (FLEET), the National Natural Science Foundation of China (No. 12204096), the Natural Science Foundation of Jiangsu Province (BK20220797), the Open Research Fund Program of the State Key Laboratory of Low-Dimensional Quantum Physics (No. KF202203), the open research fund of Key Laboratory of Quantum Materials and Devices (Southeast University), Ministry of Education, the Fundamental Research Funds for the Central Universities, an Australian Government Research Training Program (RTP) Scholarship, the Flinders University start-up grant. Some of the data presented in this work was acquired using instruments at the Mark Wainwright Analytical Centre (MWAC) of UNSW Sydney with the assistance of personnel, which is in part funded by the Research Infrastructure Programme of UNSW.

Conflicts of interest

All authors declared that there are no conflicts of interest.

Ethical approval and consent to participate

Not applicable.

Consent for publication

Not applicable.

Copyright

© The Author(s) 2023.

REFERENCES

1. Park SE, Shrout TR. Ultrahigh strain and piezoelectric behavior in relaxor based ferroelectric single crystals. *J Appl Phys* 1997;82:1804-11. [DOI](#)
2. Fu H, Cohen RE. Polarization rotation mechanism for ultrahigh electromechanical response in single-crystal piezoelectrics. *Nature* 2000;403:281-3. [DOI](#) [PubMed](#)
3. Qiu C, Wang B, Zhang N, et al. Transparent ferroelectric crystals with ultrahigh piezoelectricity. *Nature* 2020;577:350-4. [DOI](#)
4. Li F, Cabral MJ, Xu B, et al. Giant piezoelectricity of Sm-doped $\text{Pb}(\text{Mg}_{1/3}\text{Nb}_{2/3})\text{O}_3$ - PbTiO_3 single crystals. *Science* 2019;364:264-8. [DOI](#)
5. Li F, Lin D, Chen Z, et al. Ultrahigh piezoelectricity in ferroelectric ceramics by design. *Nat Mater* 2018;17:349-54. [DOI](#)
6. Li L, Yang Y, Zhang D, et al. Machine learning-enabled identification of material phase transitions based on experimental data: exploring collective dynamics in ferroelectric relaxors. *Sci Adv* 2018;4:eaap8672. [DOI](#) [PubMed](#) [PMC](#)
7. Zhang S, Shrout TR. Relaxor-PT single crystals: observations and developments. *IEEE Trans Ultrason Ferroelectr Freq Control* 2010;57:2138-46. [DOI](#) [PubMed](#) [PMC](#)
8. Singh AK, Pandey D. Evidence for M_B and M_C phases in the morphotropic phase boundary region of $(1-x)[\text{Pb}(\text{Mg}_{1/3}\text{Nb}_{2/3})\text{O}_3]$ - $x\text{PbTiO}_3$: a rietveld study. *Phys Rev B* 2003;67:064102. [DOI](#)

9. Sun E, Cao W. Relaxor-based ferroelectric single crystals: growth, domain engineering, characterization and applications. *Prog Mater Sci* 2014;65:124-210. DOI PubMed PMC
10. Wada S, Yako K, Kakemoto H, Tsurumi T, Kiguchi T. Enhanced piezoelectric properties of barium titanate single crystals with different engineered-domain sizes. *J Appl Phys* 2005;98:014109. DOI
11. Wada S, Suzuki S, Noma T, et al. Enhanced piezoelectric property of barium titanate single crystals with engineered domain configurations. *Jpn J Appl Phys* 1999;38:5505. DOI
12. Vanderbilt D, Cohen MH. Monoclinic and triclinic phases in higher-order Devonshire theory. *Phys Rev B* 2001;63:094108. DOI
13. Park MH, Lee YH, Kim HJ, et al. Morphotropic phase boundary of $\text{Hf}_{1-x}\text{Zr}_x\text{O}_2$ thin films for dynamic random access memories. *ACS Appl Mater Interfaces* 2018;10:42666-73. DOI
14. Sarott MF, Rossell MD, Fiebig M, Trassin M. Multilevel polarization switching in ferroelectric thin films. *Nat Commun* 2022;13:3159. DOI PubMed PMC
15. Chang WY, Chung CC, Yuan ZY, et al. Patterned nano-domains in PMN-PT single crystals. *Acta Mater* 2018;143:166-73. DOI
16. Yamamoto Y, Itsumi K, Hosono Y. Effects of manganese oxides/gold composite electrode on piezoelectric properties of lead magnesium niobate titanate single crystal. *Jpn J Appl Phys* 2011;50:09NC05. DOI
17. Luo C, Wan H, Chang WY, et al. Effect of low-frequency alternating current poling on 5-mm-thick $0.7\text{Pb}(\text{Mg}_{1/3}\text{Nb}_{2/3})\text{O}_3$ - 0.3PbTiO_3 single crystals. *Appl Phys Lett* 2019;115:192904. DOI
18. Wan H, Luo C, Chang WY, Yamashita Y, Jiang X. Effect of poling temperature on piezoelectric and dielectric properties of $0.7\text{Pb}(\text{Mg}_{1/3}\text{Nb}_{2/3})\text{O}_3$ - 0.3PbTiO_3 single crystals under alternating current poling. *Appl Phys Lett* 2019;114:172901. DOI
19. Yamashita Y, Yamamoto N, Hosono Y, Itsumi K. Piezoelectric transducer, ultrasonic probe, and piezoelectric transducer manufacturing method. 2015. Available from: <https://patents.google.com/patent/US20150372219> [Last accessed on 1 Dec 2023].
20. Yamamoto N, Yamashita Y, Hosono Y, Itsumi K, Higuchi K. Ultrasonic probe, piezoelectric transducer, method of manufacturing ultrasonic probe, and method of manufacturing piezoelectric transducer. 2014. Available from: <https://patents.google.com/patent/US20140062261A1/en> [Last accessed on 1 Dec 2023]
21. Deng C, Ye L, He C, et al. Reporting excellent transverse piezoelectric and electro-optic effects in transparent rhombohedral PMN-PT single crystal by engineered domains. *Adv Mater* 2021;33:e2103013. DOI
22. Chang WY, Chung CC, Luo C, et al. Dielectric and piezoelectric properties of $0.7\text{Pb}(\text{Mg}_{1/3}\text{Nb}_{2/3})\text{O}_3$ - 0.3PbTiO_3 single crystal poled using alternating current. *Mater Res Lett* 2018;6:537-44. DOI
23. Wan H, Luo C, Liu C, Chang WY, Yamashita Y, Jiang X. Alternating current poling on sliver-mode rhombohedral $\text{Pb}(\text{Mg}_{1/3}\text{Nb}_{2/3})\text{O}_3$ - PbTiO_3 single crystals. *Acta Mater* 2021;208:116759. DOI
24. Xu J, Deng H, Zeng Z, et al. Piezoelectric performance enhancement of $\text{Pb}(\text{Mg}_{1/3}\text{Nb}_{2/3})\text{O}_3$ - 0.25PbTiO_3 crystals by alternating current polarization for ultrasonic transducer. *Appl Phys Lett* 2018;112:182901. DOI
25. Zhuo F, Zhou X, Gao S, et al. Anisotropic dislocation-domain wall interactions in ferroelectrics. *Nat Commun* 2022;13:6676. DOI PubMed PMC
26. Zhuo F, Zhou X, Gao S, et al. Intrinsic-strain engineering by dislocation imprint in bulk ferroelectrics. *Phys Rev Lett* 2023;131:016801. DOI
27. Zhang D, Sando D, Pan Y, Sharma P, Seidel J. Robust ferroelectric polarization retention in harsh environments through engineered domain wall pinning. *J Appl Phys* 2021;129:014102. DOI
28. Zhang D, Sando D, Sharma P, et al. Superior polarization retention through engineered domain wall pinning. *Nat Commun* 2020;11:349. DOI PubMed PMC
29. Bai F, Li J, Viehland D. Domain hierarchy in annealed (001)-oriented $\text{Pb}(\text{Mg}_{1/3}\text{Nb}_{2/3})\text{O}_3$ - $x\%\text{PbTiO}_3$ single crystals. *Appl Phys Lett* 2004;85:2313-5. DOI
30. Rodriguez BJ, Jesse S, Morozovska AN, et al. Real space mapping of polarization dynamics and hysteresis loop formation in relaxor-ferroelectric $\text{PbMg}_{1/3}\text{Nb}_{2/3}\text{O}_3$ - PbTiO_3 solid solutions. *J Appl Phys* 2010;108:042006. DOI
31. Bian JH, Xue P, Zhu R, et al. Fingerprints of relaxor ferroelectrics: characteristic hierarchical domain configurations and quantitative performances. *Appl Mater Today* 2020;21:100789. DOI
32. Luo CT, Chang WY, Gao M, et al. Multi-layered domain morphology in relaxor single crystals with nano-patterned composite electrode. *Acta Mater* 2020;182:10-7. DOI
33. Finkel P, Cain MG, Mion T, et al. Simultaneous large optical and piezoelectric effects induced by domain reconfiguration related to ferroelectric phase transitions. *Adv Mater* 2022;34:e2106827. DOI
34. Liu HJ, Chen HJ, Liang WI, et al. Structural study in highly compressed BiFeO_3 epitaxial thin films on YAlO_3 . *J Appl Phys* 2012;112:052002. DOI
35. Christen HM, Nam JH, Kim HS, Hatt AJ, Spaldin NA. Stress-induced *R-MA-MC-T* symmetry changes in BiFeO_3 films. *Phys Rev B* 2011;83:144107. DOI
36. Chen C, Chen D, Li P, et al. Deterministic manipulation of multi-state polarization switching in multiferroic thin films. *Adv Funct Mater* 2023;33:2208244. DOI
37. Sharma P, Zhang Q, Sando D, et al. Nonvolatile ferroelectric domain wall memory. *Sci Adv* 2017;3:e1700512. DOI PubMed PMC
38. Li L, Xie L, Pan X. Real-time studies of ferroelectric domain switching: a review. *Rep Prog Phys* 2019;82:126502. DOI
39. Khakpash N, Khassaf H, Rossetti GA, Alpay SP. Misfit strain phase diagrams of epitaxial PMN-PT films. *Appl Phys Lett* 2015;106:082905. DOI

40. Belhadi J, Gabor U, Ursic H, et al. Growth mode and strain effect on relaxor ferroelectric domains in epitaxial $0.67\text{Pb}(\text{Mg}_{1/3}\text{Nb}_{2/3})\text{O}_3$ - $0.33\text{PbTiO}_3/\text{SrRuO}_3$ heterostructures. *RSC Adv* 2021;11:1222-32. DOI PubMed PMC

AUTHOR INSTRUCTIONS

1. Submission Overview

Before you decide to publish with *Microstructures*, please read the following items carefully and make sure that you are well aware of Editorial Policies and the following requirements.

1.1 Topic Suitability

The topic of the manuscript must fit the scope of the journal. Please refer to Aims and Scope for more information.

1.2 Open Access and Copyright

The journal adopts Gold Open Access publishing model and distributes content under the Creative Commons Attribution 4.0 International License. Copyright is retained by authors. Please make sure that you are well aware of these policies.

1.3 Publication Fees

Microstructures is an open access journal. When a paper is accepted for publication, authors are required to pay Article Processing Charges (APCs) to cover its editorial and production costs. The APC for each submission is \$600. There are no additional charges based on color, length, figures, or other elements. For more details, please refer to OAE Publication Fees.

1.4 Language Editing

All submissions are required to be presented clearly and cohesively in good English. Authors whose first language is not English are advised to have their manuscripts checked or edited by a native English speaker before submission to ensure the high quality of expression. A well-organized manuscript in good English would make the peer review even the whole editorial handling more smoothly and efficiently.

If needed, authors are recommended to consider the language editing services provided by Charlesworth to ensure that the manuscript is written in correct scientific English before submission. Authors who publish with OAE journals enjoy a special discount for the services of Charlesworth via the following two ways.

Submit your manuscripts directly at <http://www.charlesworthauthorservices.com/~OAE>;

Open the link <http://www.charlesworthauthorservices.com/>, and enter Promotion Code “OAE” when you submit.

1.5 Work Funded by the National Institutes of Health

If an accepted manuscript was funded by National Institutes of Health (NIH), the author may inform editors of the NIH funding number. The editors are able to deposit the paper to the NIH Manuscript Submission System on behalf of the author.

2. Submission Preparation

2.1 Cover Letter

A cover letter is required to be submitted accompanying each manuscript. It should be concise and explain why the study is significant, why it fits the scope of the journal, and why it would be attractive to readers, etc.

Here is a guideline of a cover letter for authors' consideration:

In the first paragraph: include the title and type (e.g., Research Article, Review Article, etc.) of the manuscript, a brief on the background of the study, the question the author sought out to answer and why;

In the second paragraph: concisely explain what was done, the main findings and why they are significant;

In the third paragraph: indicate why the manuscript fits the Aims and Scope of the journal, and why it would be attractive to readers;

In the fourth paragraph: confirm that the manuscript has not been published elsewhere and not under consideration of any other journal. All authors have approved the manuscript and agreed on its submission to the journal. Journal's specific requirements have been met if any.

If the manuscript is contributed to a special issue, please also mention it in the cover letter.

If the manuscript was presented partly or entirely in a conference, the author should clearly state the background information of the event, including the conference name, time and place in the cover letter.

2.2 Types of Manuscripts

There is no restriction on the length of manuscripts, number of figures, tables and references, provided that the manuscript is concise and comprehensive. The journal publishes Research Article, Review Article, Editorial, Perspective etc. For more details about paper type, please refer to the following table.

Manuscript Type	Definition	Abstract	Keywords	Main Text Structure
Research Article	A Research Article describes detailed results from novel research. All findings are extensively discussed.	Structured abstract including Aim, Methods, Results and Conclusion. No more than 250 words.	3-8 keywords	The main content should include four sections: Introduction, Materials and Methods, Results and Discussion.
Review Article	A Review Article summarizes the literature on previous studies. It usually does not present any new information on a subject.	Unstructured abstract. No more than 250 words.	3-8 keywords	The main text may consist of several sections with unfixed section titles. We suggest that the author include an "Introduction" section at the beginning, several sections with unfixed titles in the middle part, and a "Conclusion" section in the end.
Meta-Analysis	A Meta-Analysis is a statistical analysis combining the results of multiple scientific studies. It is often an overview of clinical trials.	Structured abstract including Aim, Methods, Results and Conclusion. No more than 250 words.	3-8 keywords	The main content should include four sections: Introduction, Methods, Results and Discussion.
Technical Note	A Technical Note is a short article giving a brief description of a specific development, technique or procedure, or it may describe a modification of an existing technique, procedure or device applied in research.	Unstructured abstract. No more than 250 words.	3-8 keywords	/
Commentary	A Commentary is to provide comments on a newly published article or an alternative viewpoint on a certain topic.	Unstructured abstract. No more than 250 words.	3-8 keywords	/
Editorial	An Editorial is a short article describing news about the journal or opinions of senior editors or the publisher.	None required.	None required.	/
Letter to Editor	A Letter to Editor is usually an open post-publication review of a paper from its readers, often critical of some aspect of a published paper. Controversial papers often attract numerous Letters to Editor.	Unstructured abstract (optional). No more than 250 words.	3-8 keywords (optional)	/
Opinion	An Opinion usually presents personal thoughts, beliefs, or feelings on a topic.	Unstructured abstract (optional). No more than 250 words.	3-8 keywords	/
Perspective	A Perspective provides personal points of view on the state-of-the-art of a specific area of knowledge and its future prospects. Links to areas of intense current research focus can also be made. The emphasis should be on a personal assessment rather than a comprehensive, critical review. However, comments should be put into the context of existing literature. Perspectives are usually invited by the Editors.	Unstructured abstract. No more than 150 words.	3-8 keywords	/

2.3 Manuscript Structure

2.3.1 Front Matter

2.3.1.1 Title

The title of the manuscript should be concise, specific and relevant, with no more than 16 words if possible. When gene or protein names are included, the abbreviated name rather than full name should be used.

2.3.1.2 Authors and Affiliations

Authors' full names should be listed. The initials of middle names can be provided. Institutional addresses and email addresses for all authors should be listed. At least one author should be designated as corresponding author. In addition, corresponding authors are suggested to provide their Open Researcher and Contributor ID upon submission. Please note that any change to authorship is not allowed after manuscript acceptance.

2.3.1.3 Highlights

Highlights are mandatory because they can help increase the discoverability of your article through search engines. They consist of a short collection of bullet points that capture the novel results of your research as well as new methods that were used during the study (if any). They should be submitted in a separate editable file in the online submission system. Please use 'Highlights' in the file name and include 3 to 5 bullet points (maximum 85 characters per bullet point, including spaces).

2.3.1.4 Abstract

The abstract should be a single paragraph with word limitation and specific structure requirements (for more details please refer to Types of Manuscripts). It usually describes the main objective(s) of the study, explains how the study was done, including any model organisms used, without methodological detail, and summarizes the most important results and their significance. The abstract must be an objective representation of the study: it is not allowed to contain results which are not presented and substantiated in the manuscript, or exaggerate the main conclusions. Citations should not be included in the abstract.

2.3.1.5 Graphical Abstract

The graphical abstract is essential as this can catch first view of your publication by readers. We recommend you to submit an eye-catching figure. It should summarize the content of the article in a concise graphical form. It is recommended to use it because this can make online articles get more attention. The graphic abstract should be submitted as a separate document in the online submission system. Please provide an image with a minimum of $730 \times 1,228$ pixels (h \times w) or proportionally more. The image should be readable at a size of 7×12 cm using a regular screen resolution of 96 dpi. Preferred file types: TIFF, PSD, AI, JPG, JPEG, EPS, PNG, ZIP and PDF files.

2.3.1.6 Keywords

Three to eight keywords should be provided, which are specific to the article, yet reasonably common within the subject discipline.

2.3.2 Main Text

Manuscripts of different types are structured with different sections of content. Please refer to Types of Manuscripts to make sure which sections should be included in the manuscripts.

2.3.2.1 Introduction

The introduction should contain background that puts the manuscript into context, allow readers to understand why the study is important, include a brief review of key literature, and conclude with a brief statement of the overall aim of the work and a comment about whether that aim was achieved. Relevant controversies or disagreements in the field should be introduced as well.

2.3.2.2 Materials and Methods

Materials and Methods should contain sufficient details to allow others to fully replicate the study. New methods and protocols should be described in detail while well-established methods can be briefly described or appropriately cited. Experimental participants selected, the drugs and chemicals used, the statistical methods taken, and the computer software used should be identified precisely. Statistical terms, abbreviations, and all symbols used should be defined clearly. Protocol documents for clinical trials, observational studies, and other non-laboratory investigations may be uploaded as supplementary materials.

2.3.2.3 Results and Discussion

This section should contain the findings of the study and discuss the implications of the findings in context of existing research and highlight limitations of the study. Future research directions may also be mentioned. Results of statistical analysis should also be included either as text or as tables or figures if appropriate. Authors should emphasize and summarize

only the most important observations. Data on all primary and secondary outcomes identified in the section Methods should also be provided. Extra or supplementary materials and technical details can be placed in supplementary documents.

2.3.2.4 Conclusions

It should state clearly the main conclusions and include the explanation of their relevance or importance to the field.

2.3.3 Back Matter

2.3.3.1 Acknowledgments

Anyone who contributed towards the article but does not meet the criteria for authorship, including those who provided professional writing services or materials, should be acknowledged. Authors should obtain permission to acknowledge from all those mentioned in the Acknowledgments section. This section is not added if the author does not have anyone to acknowledge.

2.3.3.2 Authors' Contributions

Each author is expected to have made substantial contributions to the conception or design of the work, or the acquisition, analysis, or interpretation of data, or the creation of new software used in the work, or have drafted the work or substantively revised it.

Please use Surname and Initial of Forename to refer to an author's contribution. For example: made substantial contributions to conception and design of the study and performed data analysis and interpretation: Salas H, Castaneda WV; performed data acquisition, as well as provided administrative, technical, and material support: Castillo N, Young V.

If an article is single-authored, please include "The author contributed solely to the article." in this section.

2.3.3.3 Availability of Data and Materials

In order to maintain the integrity, transparency and reproducibility of research records, authors should include this section in their manuscripts, detailing where the data supporting their findings can be found. Data can be deposited into data repositories or published as supplementary information in the journal. Authors who cannot share their data should state that the data will not be shared and explain it. If a manuscript does not involve such issue, please state "Not applicable." in this section.

2.3.3.4 Financial Support and Sponsorship

All sources of funding for the study reported should be declared. The role of the funding body in the experiment design, collection, analysis and interpretation of data, and writing of the manuscript should be declared. Any relevant grant numbers and the link of funder's website should be provided if any. If the study is not involved with this issue, state "None." in this section.

2.3.3.5 Conflicts of Interest

Authors must declare any potential conflicts of interest that may be perceived as inappropriately influencing the representation or interpretation of reported research results. If there are no conflicts of interest, please state "All authors declared that there are no conflicts of interest." in this section. Some authors may be bound by confidentiality agreements. In such cases, in place of itemized disclosures, we will require authors to state "All authors declare that they are bound by confidentiality agreements that prevent them from disclosing their conflicts of interest in this work." If authors are unsure whether conflicts of interest exist, please refer to the "Conflicts of Interest" of *Microstructures* Editorial Policies for a full explanation.

2.3.3.6 Copyright

Authors retain copyright of their works through a Creative Commons Attribution 4.0 International License that clearly states how readers can copy, distribute, and use their attributed research, free of charge. A declaration "© The Author(s) 2023." will be added to each article. Authors are required to sign License to Publish before formal publication.

2.3.3.7 References

References should be numbered in order of appearance at the end of manuscripts. In the text, reference numbers should be placed in square brackets and the corresponding references are cited thereafter. If the number of authors is less than or equal to six, we require to list all authors' names. If the number of authors is more than six, only the first three authors' names are required to be listed in the references, other authors' names should be omitted and replaced with "et al.". Abbreviations of the journals should be provided on the basis of Index Medicus. Information from manuscripts accepted but not published should be cited in the text as "Unpublished material" with written permission from the source.

References should be described as follows, depending on the types of works:

Types	Examples
Journal articles by individual authors	Weaver DL, Ashikaga T, Krag DN, et al. Effect of occult metastases on survival in node-negative breast cancer. <i>N Engl J Med</i> 2011;364:412-21. [DOI: 10.1056/NEJMoa1008108]

Organization as author	Diabetes Prevention Program Research Group. Hypertension, insulin, and proinsulin in participants with impaired glucose tolerance. <i>Hypertension</i> 2002;40:679-86. [DOI: 10.1161/01.hyp.0000035706.28494.09]
Both personal authors and organization as author	Vallancien G, Emberton M, Harving N, van Moorselaar RJ; Alf-One Study Group. Sexual dysfunction in 1,274 European men suffering from lower urinary tract symptoms. <i>J Urol</i> 2003;169:2257-61. [DOI: 10.1097/01.ju.0000067940.76090.73]
Journal articles not in English	Zhang X, Xiong H, Ji TY, Zhang YH, Wang Y. Case report of anti-N-methyl-D-aspartate receptor encephalitis in child. <i>J Appl Clin Pediatr</i> 2012;27:1903-7. (in Chinese)
Journal articles ahead of print	Odibo AO. Falling stillbirth and neonatal mortality rates in twin gestation: not a reason for complacency. <i>BJOG</i> 2018; Epub ahead of print [DOI: 10.1111/1471-0528.15541]
Books	Sherlock S, Dooley J. Diseases of the liver and biliary system. 9th ed. Oxford: Blackwell Sci Pub; 1993. pp. 258-96.
Book chapters	Meltzer PS, Kallioniemi A, Trent JM. Chromosome alterations in human solid tumors. In: Vogelstein B, Kinzler KW, editors. The genetic basis of human cancer. New York: McGraw-Hill; 2002. pp. 93-113.
Online resource	FDA News Release. FDA approval brings first gene therapy to the United States. Available from: https://www.fda.gov/NewsEvents/Newsroom/PressAnnouncements/ucm574058.htm . [Last accessed on 30 Oct 2017]
Conference proceedings	Harnden P, Joffe JK, Jones WG, editors. Germ cell tumours V. Proceedings of the 5th Germ Cell Tumour Conference; 2001 Sep 13-15; Leeds, UK. New York: Springer; 2002..
Conference paper	Christensen S, Oppacher F. An analysis of Koza's computational effort statistic for genetic programming. In: Foster JA, Lutton E, Miller J, Ryan C, Tettamanzi AG, Editors. Genetic programming. EuroGP 2002: Proceedings of the 5th European Conference on Genetic Programming; 2002 Apr 3-5; Kinsdale, Ireland. Berlin: Springer; 2002. pp. 182-91.
Unpublished material	Tian D, Araki H, Stahl E, Bergelson J, Kreitman M. Signature of balancing selection in Arabidopsis. <i>Proc Natl Acad Sci U S A</i> . Forthcoming 2002.

For other types of references, please refer to U.S. National Library of Medicine.

The journal also recommends that authors prepare references with a bibliography software package, such as EndNote to avoid typing mistakes and duplicated references.

2.3.3.8 Supplementary Materials

Additional data and information can be uploaded as Supplementary Materials to accompany the manuscripts. The supplementary materials will also be available to the referees as part of the peer-review process. Any file format is acceptable, such as data sheet (word, excel, csv, cdx, fasta, pdf or zip files), presentation (powerpoint, pdf or zip files), image (cdx, eps, jpeg, pdf, png or tiff), table (word, excel, csv or pdf), audio (mp3, wav or wma) or video (avi, divx, flv, mov, mp4, mpeg, mpg or wmv). All information should be clearly presented. Supplementary materials should be cited in the main text in numeric order (e.g., Supplementary Figure 1, Supplementary Figure 2, Supplementary Table 1, Supplementary Table 2, etc.). The style of supplementary figures or tables complies with the same requirements on figures or tables in main text. Videos and audios should be prepared in English, and limited to a size of 500 MB.

2.4 Manuscript Format

2.4.1 File Format

Manuscript files can be in DOC and DOCX formats and should not be locked or protected.

2.4.2 Length

There are no restrictions on paper length, number of figures, or number of supporting documents. Authors are encouraged to present and discuss their findings concisely.

2.4.3 Language

Manuscripts must be written in English.

2.4.4 Multimedia Files

The journal supports manuscripts with multimedia files. The requirements are listed as follows:

Video or audio files are only acceptable in English. The presentation and introduction should be easy to understand. The frames should be clear, and the speech speed should be moderate.

A brief overview of the video or audio files should be given in the manuscript text.

The video or audio files should be limited to a size of up to 500 MB.

Please use professional software to produce high-quality video files, to facilitate acceptance and publication along with the submitted article. Upload the videos in mp4, wmv, or rm format (preferably mp4) and audio files in mp3 or wav format.

2.4.5 Figures

Figures should be cited in numeric order (e.g., Figure 1, Figure 2) and placed after the paragraph where it is first cited; Figures can be submitted in format of TIFF, PSD, AI, EPS or JPEG, with resolution of 300-600 dpi;

Figure caption is placed under the Figure;

Diagrams with describing words (including, flow chart, coordinate diagram, bar chart, line chart, and scatter diagram, etc.) should be editable in word, excel or powerpoint format. Non-English information should be avoided;

Labels, numbers, letters, arrows, and symbols in figure should be clear, of uniform size, and contrast with the background; Symbols, arrows, numbers, or letters used to identify parts of the illustrations must be identified and explained in the legend;

Internal scale (magnification) should be explained and the staining method in photomicrographs should be identified;

All non-standard abbreviations should be explained in the legend;

Permission for use of copyrighted materials from other sources, including re-published, adapted, modified, or partial figures and images from the internet, must be obtained. It is authors' responsibility to acquire the licenses, to follow any citation instruction requested by third-party rights holders, and cover any supplementary charges.

2.4.6 Tables

Tables should be cited in numeric order and placed after the paragraph where it is first cited;

The table caption should be placed above the table and labeled sequentially (e.g., Table 1, Table 2);

Tables should be provided in editable form like DOC or DOCX format (picture is not allowed);

Abbreviations and symbols used in table should be explained in footnote;

Explanatory matter should also be placed in footnotes;

Permission for use of copyrighted materials from other sources, including re-published, adapted, modified, or partial tables from the internet, must be obtained. It is authors' responsibility to acquire the licenses, to follow any citation instruction requested by third-party rights holders, and cover any supplementary charges.

2.4.7 Abbreviations

Abbreviations should be defined upon first appearance in the abstract, main text, and in figure or table captions and used consistently thereafter. Non-standard abbreviations are not allowed unless they appear at least three times in the text. Commonly-used abbreviations, such as DNA, RNA, ATP, etc., can be used directly without definition. Abbreviations in titles and keywords should be avoided, except for the ones which are widely used.

2.4.8 Italics

General italic words like vs., et al., etc., in vivo, in vitro; t test, F test, U test; related coefficient as r, sample number as n, and probability as P; names of genes; names of bacteria and biology species in Latin.

2.4.9 Units

SI Units should be used. Imperial, US customary and other units should be converted to SI units whenever possible. There is a space between the number and the unit (i.e., 23 mL). Hour, minute, second should be written as h, min, s.

2.4.10 Numbers

Numbers appearing at the beginning of sentences should be expressed in English. When there are two or more numbers in a paragraph, they should be expressed as Arabic numerals; when there is only one number in a paragraph, number < 10 should be expressed in English and number > 10 should be expressed as Arabic numerals. 12345678 should be written as 12,345,678.

2.4.11 Equations

Equations should be editable and not appear in a picture format. Authors are advised to use either the Microsoft Equation Editor or the MathType for display and inline equations.

2.5 Submission Link

Submit an article via <https://oaemesas.com/login?JournalId=microstructures>.



Microstructures

Los Angeles Office

245 E Main Street ste122, Alhambra,
CA 91801, USA

Tel: +1 323 9987086

E-mail: editorialoffice@microstructj.com

Website: <https://www.oaepublish.com/microstructures>

